A real-time 5G Testbed at Millimetre-wave

Rodolfo Vitorino Gomes

Faculty of Computing, Engineering & Science
University of South Wales

This thesis is submitted for the degree of
Doctor of Philosophy

October 2019

A real-time 5G Testbed at Millimetre-wave

Rodolfo Vitorino Gomes, Faculty of Computing, Engineering & Science
University of South Wales

Director of Studies:	Akram Hammoudeh[1]
Supervision team:	Rafael Caldeirinha[1,2]
	Carlos Ribeiro[2]
Advisors:	Telmo Fernandes[1,2]
	Leshan Ugalla[1]

[1]Faculty of Computing, Engineering & Science, University of South Wales (USW), Pontypridd, Wales, United Kingdom.

[2]Instituto de Telecomunicações (IT), Delegação de Leiria and Polytechnic Institute of Leiria (IPL), Leiria, Portugal.

Abstract

This thesis highlights the research carried out on the design and implementation of a real-time 5G testbed at mmWave. This work is part of a research program registered at the University of South Wales submitted in fulfilment of the requirements for the degree of Doctor of Philosophy, in collaboration with Instituto de Telecomunicações in Leiria, Portugal.

This page is intentionally left blank.

Certificate of Research

This is to certify that, except where specific reference is made, the work described in this thesis is solely the result of the candidate. Neither this thesis, nor any part of it, has been presented, or is currently submitted, in candidature for any degree at any other university.

(Rodolfo Vitorino Gomes)

October 2019

This page is intentionally left blank.

This thesis is dedicated to my parents, brother and girlfriend.

This page is intentionally left blank.

Acknowledgements

I would like to start by express my gratitude to all members of my supervision team, Doctors Akram Hammoudeh, Rafael Caldeirinha, Carlos Ribeiro and Telmo Fernandes for their continuous advice, support, motivation and knowledge, resulting in so many enthusiastic and stimulating discussions. Their guidance was indispensable in the research and in the writing up of this thesis. In particular, I would like to express my sincere gratitude to Dr. Rafael Caldeirinha, who was the responsible for the beginning of my Ph.D. journey. He believed in my skills, recommended me for a Ph.D. student position at University of South Wales and kept track of my progress all over these years with all the necessary support. A special word goes to Dr. Akram Hammoudeh, in the position of DOS, for believing in my capacities to deliver for the project. Thanks for all the support, stimulation and enormous effort in obtaining the necessary funds to cover this research. I would like to thank Dr. Telmo Fernandes for his constant comfort, confidence and incentive during the times of my staying at Wales. It is always tough to be far from our beloved ones and he had always a friendly word to say. Finally, I would like to express my deepest gratitude to Dr. Carlos Ribeiro to be my mentor. Thanks for kindly sharing his expertise that went beyond hardware design and implementation. We spent long working hours together solving issues that would have been very difficult to overcome without his support.

A very special thanks to my cousin João Reis, whom I had the privilege to share this journey, to provide me encouragement in all struggling times. He was always there for me.

I would like to acknowledge the University of South Wales for providing me the facilities and a full-time Ph.D. grant which allowed me to do my researcher without any other concerns. I would also like to acknowledge Instituto de Telecomunicações in Leiria for hosting me since 2016 to date, which enabled me the extension of my Ph.D. program for 2 more years. From then on all the developments were funded by the *5G TESTBED (UID/EEA/50008/2013)* project.

A special mention to David Ferreira, my friend and colleague from Instituto de Telecomunicações - Leiria, for helping and sharing his research experience with me. I am truly grateful for that. I also would like to thank the following university staff: Mr. John Williams and Marco Santos (Instituto Politécnico de Leiria) who always helped me with hardware related issues. To the people who worked in the Wireless and Optoelectronic Research and Innovation Centre during my stay, Mr. A. Alfadreek, Mr. M. Abdurahman, Mr. A. Buba, I would like to thank the friendly environment and their sympathy. Finally, I wish to express my gratitude to Dr. Manuel García and Isabel Pérez for their collaborative work in this research project. Such allowed the realisation of very specific 60 GHz measurements, using cutting-edge RF equipment available in

the Radio Systems laboratory at University of Vigo, which otherwise, would have been very difficult to obtain.

A very special gratitude goes to my parents and brother who have encouraged me in the first place to accept this life challenge and for providing me emotional and financial support throughout this journey. I owe it all to you. Finally, to my love Inês Lemos for accepting me in her life even knowing that I would be $>$ 2000 km away from her for at least 3 years. You were always present in the good and bad moments. Your unconditional support and patience were of the most importance to complete this challenge.

Summary

This thesis presents the work developed by the author on the design, development and implementation of a Millimetre-wave (mmWave) Wireless Radio System targeting 5G applications. The feasibility of the developed real-time 5G testbed is assessed over the air, particularly at carrier frequencies of 60 GHz. A maximum data rate of 1 Gigabits per second (Gbps), enabling Quadrature Amplitude Modulation (QAM) modulation up to 256-QAM has been achieved, where Orthogonal Frequency Division Multiplexing (OFDM) is the adopted transmission scheme due its well known relatively higher spectral efficiency and simpler equalisation algorithms in comparison with other schemes. The work presented herein can be summarised into five distinct parts, as follows.

Firstly, the effect that both RF and channel impairments, from 60 GHz transmissions, have on the performance of OFDM, Single Carrier with Frequency-Domain Equalisation (SC-FDE), and Frequency Spreading Filter Bank Multi-Carrier (FS-FBMC), is assessed based on simulations, where the former is a promising candidate to be the transmission scheme adopted by the 5^{th} Generation (of mobile network) (5G). To this end, proper modelling for non-linearities from Power Amplifier (PA), In-phase and Quadrature-phase (IQ) imbalances, Phase-Noise (PN) have been considered.

The second part introduces the developed mmWave testbed system, which is composed of a baseband processing unit, Software-Defined Radio (SDR), and a RF front-end at both TX/RX ends. In particular, SDR is a re-programmable hardware platform controlled by software which has the potential to implement the ideal radio architecture. That is, typical hardware components of a radio communication system, e.g. mixers, filters, amplifiers, detector, are implemented by software, in the digital domain and fully reconfigurable. This allows such agile radio system front-end to be completely independent from any standard and operate at any frequency band. Details of the OFDM baseband implementation/ integration in the VC707 FPGA board, one of the most powerful (with more logic resources) Xilinx FPGA's available on the market, at the time of this thesis, are also given.

The third part evaluates whether RF Front-Ends really cope with 5G requirements at mmWave. To this end, a thorough comparative analysis between 60 GHz cutting-edge commercial off-the-shelf and reference RF front-ends, taking into account their intrinsic

RF impairments and their impact on the overall system performance degradation, is presented.

The fourth part assesses the feasibility of the developed mmWave OFDM communication is assessed in a typical classroom indoor scenario, towards five User Equipment (UE) devices. EVM, SNR, and path loss measurements are considered for Quality of Service (QoS) evaluation.

Finally, it is introduced a novel and highly scalable multi-Gigabit/s Real-Time (RT) Wideband MIMO processing chain which explores logical resources to boost MIMO OFDM systems Hardware (HW) utilization. A significant hardware footprint saving is achieved, when compared with conventional design MIMO-OFDM methods.

List of acronyms and abbreviations

2G	2^{nd} Generation (of mobile network)
3G	3^{rd} Generation (of mobile network)
3GPP	3^{rd} Generation Partnership Project
4G	4^{th} Generation (of mobile network)
5G	5^{th} Generation (of mobile network)
ACF	Autocorrelation Function
AD	Analogue Devices
ADC	Analogue-to-Digital Converter
ACI	Adjacent Channel Interference
AGC	Automatic Gain Controller
AM-AM	Amplitude Modulation–Amplitude Modulation
AM-PM	Amplitude Modulation–Phase Modulation
AOA	Angle of Arrival
AOD	Angle of Departure
AP	Access Point
AR	Augmented Reality
ASIC	Application-Specific Integrated Circuit
ASK	Amplitude Shift Keying
AV	Audio Visual
AWGN	Additive White Gaussian Noise
AXI	Advanced Extensible Interface
B2B	Back-to-Back
$\mathbf{B_c}$	Coherence bandwidth
BER	Bit Error Rate
BF	Beamforming
BPSK	Binary Phase Shift Keying

BS	Base Station
BSP	Board Support Package
B	Bandwidth
CAZAC	Constant Amplitude Zero Autocorrelation
CDF	Cumulative Distribution Function
CEF	Channel Estimation Field
CES	Channel Estimation Sequence
CFO	Carrier Frequency Offset
CFR	Channel Frequency Response
CI	Clock Input
CIR	Channel Impulse Response
CMOS	Complementary Metal-Oxide-Semiconductor
CMS	Common Mode Signalling
CO	Clock Output
CORDIC	Coordinate Rotational Digital Computer
COTS	Commercial Off-The-Shelf
CP	Cyclic Prefix
CPR	Common Phase Rotation
CQI	Channel Quality Indicator
CRAN	Centralised (Cloud) Radio Access Networks
CRC	Cyclic Redundancy Check
CW	Continuous Wave
D2V	Device-to-Vehicle
DAC	Digital-to-Analogue Converter
DC	Direct Current
DDC	Digital Down-Conversion
DDR	Double Data Rate
DDS	Direct Digital Synthesiser
DFT	Discrete Fourier Transform
DL	Downlink
DMG	Directional Multi-Gigabit
DSP	Digital Signal Processing
DUC	Digital Up-Conversion

DUT	Device Under Test
EGC	Efficient *Golay* Correlator
EIRP	Effective Isotropic Radiated Power
eMBB	enhanced Mobile Broadband
ENOB	Effective Number Of Bits
EVM	Error Vector Magnitude
ETSI	European Telecommunications Standards Institute
FBMC	Filter Bank Multi-Carrier
FCF	Frequency Correlation Function
FCS	Frame Check Sequence
FDD	Frequency Division Duplex
FDE	Frequency-Domain Equalisation
FEC	Forward Error Correction
FFs	Flip-Flops
FFT	Fast *Fourier* Transform
FIFO	First-In First-Out
FIR	Finite Impulse Response
FMC	FPGA Mezzanine Card
FoV	Field-of-View
FPGA	Field Programmable Gate Array
FR	Frequency Response
FS-FBMC	Frequency Spreading Filter Bank Multi-Carrier
FSK	Frequency Shift Keying
FSM	Finite State Machine
GaAs	Gallium Arsenide
Gbps	Gigabits per second
GFLOPS	Giga Floating Point Operations per Second
GMACS	Giga Multiply-Accumulate operations per Second
GPRS	General Packet Radio Service
GPUs	Graphics Processing Units
GSM	Global System for Mobile
GSPS	Giga Samples Per Second

GUI	Graphical User Interface
HDMI	High-Definition Multimedia Interface
HetNets	Heterogeneous Networks
HMDs	Head Mounted Devices
HPC	High Pin Count
HSI	High Speed Interface
HW	Hardware
I2C	Inter-Integrated Circuit
IC	Integrated Circuit
ICI	Inter-Carrier Interference
IEEE	Institute of Electrical and Electronics Engineers
IF	Intermediate Frequency
IFFT	Inverse Fast *Fourier* Transform
IIR	Infinite Impulse response
ILA	Integrator Logic Analyser
IMD	Intermodulation Distortion
IMT	International Mobile Telecommunications
IoT	Internet of Things
IP	Intellectual Property
IPL	Polytechnic Institute of Leiria
IQ	In-phase and Quadrature-phase
ISI	Inter-Symbol Interference
IT	Instituto de Telecomunicações
ITU	International Telecommunication Union
JTAG	Joint Test Access Group
KPI	Key Performance Indicator
LDPC	Low Density Parity Check
LFM	Linear Feet per Minute
LNA	Low-Noise Amplifier
LO	Local Oscillator
LOS	Line-Of-Sight
LPC	Low Pin Count
LTE	Long Term Evolution
LTE-Advanced	Long Term Evolution Advanced

LTI	Linear Time-Invariant
LTV	Linear Time-Variant
LUTs	Look-Up Tables
LVDS	Low Voltage Differential Signal
LVPECL	Low-Voltage Positive-referenced Emitter Coupled Logic
M2M	Machine-to-Machine
MAC	Medium Access Control
MAWP	Modular Architecture for Wireless Prototyping
Mbps	Megabits per second
MCS	Modulation and Coding Scheme
MIMO	Multiple-Input Multiple-Output
MMCM	Mixed-Mode Clock Manager
MMSE	Minimum Mean Square Error
mMTC	massive Machine Type Communication
mmWave	Millimetre-wave
MU	Multi-user
NLOS	Non-Line-Of-Sight
NR	New Radio
OBO	Output-Back-off
OFDM	Orthogonal Frequency Division Multiplexing
OFDMA	Orthogonal Frequency-Division Multiple Access
OHMD	Optical Head Mounted Displays
OOBEs	Out-Of-Band Emissions
OQAM	Offset QAM
OTA	Over-The-Air
P2MP	Point-to-Multi-Point communication
P2P	Peer-to-Peer
PA	Power Amplifier
PAE	Power Added Efficiency
PAM	Pulse Amplitude Modulation
PAPR	Peak-to-Average Power Ratio
PD	Pre-Distortion

pdf	probability density function
PDP	Power Delay Profile
PHY	Physical Layer
PL	Path Loss
PLL	Phase-Locked Loop
PN	Phase-Noise
PNC	Piconet Coordinator
PPN	Polyphase Network
PRBs	Physical Resource Blocks
PSD	Power Spectral Density
PSK	Phase Shift Keying
PSNR	Peak Signal-to-Noise Ratio
PW	Pilot Word
PCB	Printed Circuit Board
QAM	Quadrature Amplitude Modulation
QoS	Quality of Service
QPSK	Quadrature Phase-shift Keying
RCC	Root Raised Cosine
RE	Recurring Expenses
RF	Radio Frequency
RMS	Root-Mean-Square
RT	Real-Time
RX	Receiver
S/P	Serial-to-Parallel
SA	Spectrum Analyser
SC	Single-Carrier
SC-FDE	Single Carrier with Frequency-Domain Equalisation
SD	Spatial Diversity
SDR	Software-Defined Radio
SFDR	Spurious-Free Dynamic Range
SiGe	Silicon Germanium
SINAD	Signal-to-Noise and Distortion ratio
SISO	Single-Input Single-Output
SNIR	Signal-to-Noise-plus-Interference Ratio

SNR	Signal-to-Noise Ratio
SPI	Serial Peripheral Interface
STF	Short Training Field
SV	Saleh-Valenzuela
SysGen	System Generator
TBCC	Tail-Biting Convolutional Codes
TDD	Time Division Duplex
TG	Task Group
THD	Total Harmonic Distortion
TOA	Time of Arrival
TRN	Training field
TRX	Transceiver
TRxP	Transmission Reception Point
TSM	Transmit Spectrum Mask
TX	Transmitter
TXOP	Transmission Opportunities
UART	Universal Asynchronous Receiver-Transmitter
UE	User Equipment
UHD	Ultra-High-Definition
UL	Uplink
UMs	Usage Models
UMTS	Universal Mobile Telecommunications System
URLLC	Ultra-Reliable and Low-Latency Communications
US	Uncorrelated Scatterers
USW	University of South Wales
UWB	Ultra-Wide Band
V2I	Vehicle-to-Infrastructure
V2V	Vehicle-to-Vehicle
VCO	Voltage-Controlled Oscillator
VGA	Variable Gain Amplifier
VHDL	VHSIC Hardware Description Language
VNA	Vector Network Analyser
Vpp	Voltage peak-to-peak

VR	Virtual Reality
VSG	Vector Signal Generator
V2X	Vehicle to everything
WB	WideBand
WG	Working Group
WiGig	Wireless Gigabit Alliance
WiMAX	Worldwide Interoperability for Microwave Access
WLAN	Wireless Local Area Network
WMAN	Wireless Metropolitan Area Network
WPAN	Wireless Personal Area Network
WSS	Wide-Sense Stationary
WSSUS	Wide-Sense Stationary Uncorrelated Scattering
WWAN	Wireless Wide Area Network
X-MWblocks	Modular Drop-In Building Blocks
ZF	Zero Forcing

Contents

This page is intentionally left blank.

List of figures

This page is intentionally left blank.

List of tables

CHAPTER 1

Introduction

1.1 Background of study and motivation

Mobile communications has become one of the utmost important enterprises in modern history [1]. In fact, after twenty years after the deployment of the 2^{nd} Generation (of mobile network) (2G) standard, where *texting* was one of the mainstream applications and Global System for Mobile (GSM) and General Packet Radio Service (GPRS) radio access technologies became available with data rates of few kbps, radio communications have constantly been evolving. In fact, this former achievement has led to a revolution in the wireless digital data transmission, where 3^{rd} Generation (of mobile network) (3G) has been put in place to support mobile Internet connections with speeds of hundreds of kbps at the beginning of its deployment, and several Mbps with 3.5G. As consequence, mobile broadband has been enabled and mobile services became very popular [2]. Currently, Long Term Evolution Advanced (LTE-Advanced) standard is the 4^{th} Generation (of mobile network) (4G). In such technology, data rates of 3 Gbps can be provided in downlink scenarios [3]. All these mobile technology evolutions has led to breakthroughs in semiconductors processes, and also to worldwide agreements between national frequency spectrum regulators [4]. Furthermore, it is expected that by 2021, the number of mobile devices will reach 3.5 per capita [5].

Nevertheless, the wireless innovation might be just beginning. There is a huge demand for technologies that can provide solutions for the expected explosive growth of mobile data users, and consequently massive data traffic to be accommodated by the mobile network. For example, official standardisation bodies such as 3GPP are developing 5G standards which are expected to appear in Q2 2019. However, one can already predict some of the key concepts of 5G [6, 7]. A massive inter-connection of users and devices is expected in the upcoming network generation, merging the key applications in a globalised service including: Internet of Things (IoT) and Machine-to-Machine (M2M) communication, Gigabit wireless connectivity, Tactile Internet, Centralised (Cloud)

Radio Access Networks (CRAN) and Heterogeneous Networks (HetNets) [6–9]. The anticipated architecture and applications will require 5G to be "flexible, scalable, robust, reliable, and efficient in terms of energy and spectrum" [10], and capable of providing a comprehensive list of specifications, targeting low latencies ($< 1\ ms$) and peak data rates ($\geq 10\ Gbps$) with a minimum of 100 Mbps at cell edge [11], high bandwidths (1 GHz [12]), high energy efficiency and service reliability [7, 8, 10]. In this context, multi-Gigabit/s data transmission, hardware and energy efficiencies are seen as the most promising Key Performance Indicator (KPI) metrics for future mobile terminals and networks [13].

Moreover, to compensate for the expected growth of users and devices and the consequent overloading of the frequency spectrum that will come aside with 5G, the use of the unlicensed mmWave spectrum (especially the 60 GHz band) has also been exploited for 5G applications, providing high bandwidths and high data rates [6–8]. In particular, the continuous 7 GHz of spectrum, between 57 and 64 GHz, for wireless communications, allows users to exploit such band without buy a license from the regulator. Therefore, this unlicensed spectrum allows the reduction of costs in high-data rates operation links. Furthermore, radio signal propagation in this band has unique characteristics that allow many other benefits, such as excellent immunity to inter-system interference, high security and frequency re-use [14]. Hence, the mmWave portion of the Radio Frequency (RF) spectrum which in the past was not exploited for commercial purposes is currently being given great attention and a large number of manufacturers are now producing mmWave products [15]. Thus, the design, development and implementation of a mmWave wireless radio system prototype for Gigabit/s multimedia applications is cutting edge topic and may contribute to important knowledge among the scientific and industry communities.

1.2 Aims and objectives

To this extent, working on the development of technology capable of providing such applications, is both timely and topical in the scientific wireless community. The availability of new rapid design, validation flows and related real-time prototyping experiments are of significant interest for performance validation and proof-of-concept of the various proposed communication techniques. The focus of this research programme aims at the design, implementation, and development of a prototype wireless radio communication system at millimetre wave frequencies. Such would not rely on a single wireless communication standard. In fact, it should adapt its own communication parameters to meet the user's needs. For example, with the completely design of the

transmitted waveform in the digital domain, not only the flexibility of the radio is enhanced, but also its reconfigurability and efficiency.

As aforementioned, radio communication systems are envisaged at 60 GHz due to the wide available bandwidths to accommodate multi-Gigabit transmission rates and to the possibility of highly integrated transceivers at these frequencies. However, at these high frequencies, performing up-conversion/down-conversion by digital signal processing algorithms becomes impracticable, since a minimum sampling rate of 120 Giga Samples Per Second (GSPS) would be required to comply with the *Nyquist* criteria. Therefore, for such high frequencies, RF conversions are preferably implemented in hardware. In this context, the identification of non-idealities coming from Radio RF front-ends, as well as, their study impact on the performance of the system should be evaluated. Furthermore, in addition to all algorithms needed for an over-the-air transmission, namely, timing and frequency synchronisation, channel estimation and equalisation, Carrier Frequency Offset (CFO) compensation should also be considered. It is impossible to have two distinct oscillator references operating exactly at the same frequency. Finally, Multiple-Input Multiple-Output (MIMO) can be employed to enhance the system robustness against doubly selective channels.

At the outset, the aims of this work are as follows:

1. Development of a complete multi-Gigabit/s wireless communication system in a simulation environment, considering the more appropriate impairment models, present in the literature. Such tool should be capable to estimate and evaluate the performance of several waveforms under severe RF and channel impairments;

2. Development of a novel FPGA based SDR (testbed) for prototyping future wireless communications, while enabling transmissions at distinct RF carrier frequencies;

3. Development of a complete real-time multi-Gigabit/s wireless mmWave SISO radio link;

4. Definition of measurements for short-range Gigabit/s link at 60 GHz (at the outset of this work, such frequency spectrum was thought to be the key solution for the next-generation, i.e., 5G in terms of data rate [16, 17])), for an appropriate framework performance assessment and optimisation;

5. Evolvement of the SISO RF system architecture in order to enable MIMO communications;

6. Timely dissemination of the work being performed, in several conferences and journal publications with relevant scientific reputation and peer-reviewed, to validate the outcomes and importantly obtain expertise feedback on the field.

Finally, the main key objectives of this work are present below:

1. Identification of the preferred choices of waveforms for high data rate transmissions presented in the literature, understanding its advantages and drawbacks;

2. Identification of the adopted RF architectures presented in both commercial and academic solutions for mmWave RF front-ends. Understanding their main limitations and the impact they might have in the performance of a communication system. In particular, the source of main critical non-idealities presented, in both Transmitter (TX)/ Receiver (RX), should be investigated;

3. Study of the theoretical modelling for PN, PA non-linearities, and IQ imbalances, in particular for 60 GHz RF front-end technologies. Moreover, a proper literature review should also be conducted in the modelling of multi-path fading channels for wideband mmWave transmissions;

4. Study on the practical implementation of a multi-Gigabit/s SDR. Special focus should be given to the features of the embedded system (processor engine) and of both Digital-to-Analogue Converter (DAC)/ Analogue-to-Digital Converter (ADC). The processor unit should not only has a considerable quantity of logical resources, but should also operate at significant high clock frequency signals. To this extent, the selection criteria of both converters should be based on sampling rate, binary resolution and compatibility with embedded systems;

5. Getting familiarised with the main components of a SDR. Since the SDR would be developed from the scratch (not a commercial solution), special focus should be given on the connectivity between the FPGA and both ADC/DAC.

6. Familiarisation with various tools and programs for hardware design and configuration. In particular, getting familiar with the ultra efficient fully pipelined modular architecture proposed in [18], for the implementation of advanced signal processing algorithms. Integration of the OFDM engine reported in [18], into the SDR system developed in 6);

7. Fully characterisation of the considered DAC/ ADC. Consideration should be given to the design and implementation of an analogue Automatic Gain Controller (AGC) to be placed before the ADC converter, thus avoiding the operation of the ADC at a very low performance;

8. Study on commercial cutting-edge RF front-ends at 60 GHz, in order to choose the best one to perform both up-conversion/ down-conversion stages on the prototype system. Such system should deal with a wide range of carrier frequencies centred at 60 GHz, high order modulations and relatively low noise figure;

9. Fully characterisation and modelling of the RF impairments induced by the adopted mmWave RF front-end. Radio calibration inside an anechoic chamber. Evaluation of the OFDM system performance in RT at 60 GHz in order to obtain the first preliminary results of Quality of Service (QoS) indicators and link-budget;

10. Study, design, and hardware implementation of a (massive) MIMO architecture capable to re-utilized the main functional DSP blocks of a Single-Input Single-Output (SISO) OFDM processing chain.

1.3 Thesis outline

This thesis is structured as follows:

Chapter 2 starts by presenting a literature review covering not only some relevant concepts regarding the propagation phenomena of mmWave frequencies, but also presenting both current and future wireless standard specifications. Particularly, the role of mmWave technology in the 5G New Radio (NR) is well detailed. NR adopts OFDM modulation with different numerologies to address a wide range of frequencies bands, depending on the deployment scenario and application. For example, mmWave is intend to be deployed in enhanced Mobile Broadband (eMBB) scenarios. Moreover, a state-at-art on mmWave testbeds is also presented, highlighting the importance of high spectral efficient transmissions to attain multi-Gigabit/s of data rate.

Chapter 3 is devoted to the work carried out on the implementation of a framework tool to predict the performance of mmWave communication systems, based on the IEEE 802.15.3c standard. It starts by introducing OFDM, SC-FDE, and FS-FBMC transmission schemes, and the RF impairment modelling at 60 GHz. A thorough study on the performance evaluation of aforementioned transmission schemes, under both RF and channel impairments is presented. This study particularly aims to characterise the performance boundaries of mmWave wireless communications, with the presence and absence of Forward Error Correction (FEC) codes, the use of different order modulations, and different conditions of Signal-to-Noise Ratio (SNR). These features allow to assess which is the most robust waveform under PA, PN, IQ imbalances over a particular 60 GHz multipath fading channel. Communication theory necessary to only in the development of the aforementioned simulation framework, but also for the subsequent chapters, covering radio, signal processing and digital communication fundamentals, has been compiled in the Appendix A. In particular, a critical review on the most common techniques for up-converting and down-converting RF signals is presented, and a mathematical formulation of the effect of RF impairments induced in an In-Phase and Quadrature-phase demodulation is performed.

Chapter 4 introduces the software-defined radio concept followed in this thesis. All the hardware components and firmware modifications to build a digital waveform engine to comply with the 5G specifications, introduced in previous chapters, is described. For example, analogue bandwidth of the SDR is set to 625 MHz, but might go up to 2.5 GHz. In particular, connectivity issues between the VC707 FPGA with the both adopted DAC and DAC are outlined, as well as their workaround. Furthermore, a complete characterisation of the proposed SDR in both frequency and time domains is given. Finally, a multi-rate low-IF up/ down-conversions Field Programmable Gate Array (FPGA) algorithm is presented.

Chapter 5 outlines the multi-Gigabit/s 5G testbed developed in this work, herein designated *USW/IT*, designed to tackle the 5G requirements for mmWave transmissions. An extensive over-the-air characterisation performance of this system is considered over a Line-Of-Sight (LOS) scenario, for different conditions of Signal-to-Noise-plus-Interference Ratio (SNIR), and considering a link distance of 74.5 cm, placed inside an anechoic chamber.

Chapter 6 provides an extensive characterisation of a 60-GHz cutting-edge commercial off-the-shelf RF front-end solution. Firstly, its transmitter is assessed in terms of output power and gain, intermodulation distortion products, carrier and side-band leakages. Subsequently, a loop-back overall IF-IF frequency response magnitude, and IQ/ DC offset values, induced by this device, are evaluated. In addition, a comparative analysis between such and a reference RF front-end is carried out, as the degradation performance of real-time over-the-air multi-Gigabit/s wideband wireless OFDM system. Based on the results obtained from appropriate RF measurements, a practical EVM link budget formulation, which takes into account both PA and PN impairment effects, is proposed.

Chapter 7 is dedicated to assess the feasibility of the proposed mmWave testbed to deliver both Augmented Reality (AR) and Virtual Reality (VR) applications, which are in fact services envisaged to be enabled by the 5G network (round-trip latencies should be below 20 ms). In this context, QoS of the designed OFDM downlink communication towards five UE devices, placed at different locations inside an indoor classroom environment scenario, have been assessed. KPI(s) as Error Vector Magnitude (EVM), SNR, and path loss are considered as figures of merit.

Chapter 8 introduces the design of a highly scalable MIMO multi-Gigabit/s RT WideBand (WB) processing chain for 5G applications. MIMO is seen as a promising solution to boost either spectral efficiency (data rate) or increase the system spatial diversity. The proposed architecture can be easily integrated on the SISO system developed in previous chapters, by re-using the main OFDM transceiver chain resources among all antenna paths. This is of paramount importance since in typical MIMO architectures the usage of logical resources increases proportionally to the antenna configuration, which might lead to enormous amount of digital processing resources and

energy consumption. For example, it is demonstrated that the proposed MIMO-OFDM method saves more than 80% of DSP48E1 slices, when compared with conventional design methods.

Chapter 9 presents a summary and main conclusive remarks of this complete research work. An overview of all reported developments is provided and compared with initial aims and objectives, as well as the identification of all major contributions to the scientific community. Consideration is also given regarding topics that require further investigation, or are envisaged as possible relevant developments in the near future, and as an extension of the work presented in this thesis. It is worth to mention that, a 26 GHz RF front-end has been designed, but due to time constraints, such was not integrated with the proposed OFDM engine. The same happen to the FPGA 2×2 *Alamouti* design, presented in this chapter.

This page is intentionally left blank.

CHAPTER 2

Literature review

2.1 Introduction

The first wireless radio transatlantic experiment transmission was performed in 1901 by Marconi, from Cornwall, England, to Newfoundland, Canada [19]. Since this huge historical mark, wireless communication systems have been evolving at a colossal pace, mostly enabled by the advancements on semiconductor and radio connectivity technologies. For example, this leads to a life cycle of every generation of cellular networks to be typically 10 years [12]. Nowadays, wireless communications become indispensable in peoples' daily routine life interactions, where wireless services and applications are widely available in large and small geographical areas.

In general, wireless networks can be divided into four main classes, Wireless Wide Area Network (WWAN), Wireless Metropolitan Area Network (WMAN), Wireless Local Area Network (WLAN) and Wireless Personal Area Network (WPAN), depending on their operating range [20]. In this context, WWAN is the one that covers larger geographic area, providing wireless services for city-wide access. This is in fact, enabled by the use of mobile cellular technologies such as Long Term Evolution (LTE), Universal Mobile Telecommunications System (UMTS), GSM and GPRS. For the purpose of large scale broadband wireless access, Institute of Electrical and Electronics Engineers (IEEE) has created the IEEE 802.16 standard, in 2001 [21], which is considered a WMAN due its small-to-medium cell coverage size (below 50 km) [22]. To this extent, Worldwide Interoperability for Microwave Access (WiMAX) forum developed both WiMAX fixed and mobile specifications to ensure interoperability among devices from different vendors [21]. This enabled low-cost mobile Internet applications [23]. Finally, both WLAN and WPAN technologies aim short-range over the air communications, which constrains their coverage to building-wide cell size. However, unlike WLAN, WPAN applications do not require any particular infrastructure. In other words, connections in this local area do not involve any exchange of data to users from

other radio links, which results in small, power-efficient, inexpensive solutions to be implemented for a wide range of devices [24]. On the other hand, WLAN aims to maximize both transmission range and data rate, resulting in expensive infrastructure with higher power consumption [24].

Furthermore, the WPAN Working Group (WG) 802.15 [25] began to develop the Bluetooth (IEEE 802.15.1 [26]), around 1998, as an IEEE standard for connecting computer peripherals, this task was in fact accomplished by the Task Group (TG) [27]. A few years later, the same WG developed two WPAN technologies to target both high data rate, HR-WPAN (IEEE 802.15.3), and low data rate applications, LR-WPAN (ZigBee over IEEE 802.15.4 [28]) [27]. While the first aims to provide support for portable digital imaging and multimedia applications, the former is intended for wireless sensor networks [27].

Particularly for HD uncompressed video transmission, relatively high bandwidth and low latency are required to enable high data throughput as high as several Gbps [29]. In order to meet such requirements, one solution could have been the wireless USB based on Ultra-Wide Band (UWB) radio technology [30]. However, such standard only supports a maximum data date of 480 Megabits per second (Mbps) [31]. Later on, in 2009, TG3c [32] was created to develop the IEEE 802.15.3c, which supports multi-Gigabit/s of data rate based on the mmWave technology [33]. A comparison of the most relevant wireless protocols available in the literature in terms of nominal range, channel B, frequency band and maximum supported data rate, is presented in Table 2.1.

Additionally, in Fig. 2.1 it is depicted the relation between typical operational range and data rate for the wireless standards outlined in Table 2.1. From this figure, it becomes clear that data rates over 4 Gbps is only supported by three standards, namely, the IEEE 802.15.3c, Wireless Gigabit Alliance (WiGig), and Wireless HD. This is due to the use of the 60 GHz band, which is characterised by more than 7 GHz of continuous spectrum. For example, at lower frequency bands, only 500 MHz of bandwidth is available at 5 GHz, whereas only 85 MHz of free spectrum in the 2.4 GHz band (in most regions) [34]. To this end, it is presented in this chapter not only an overview regarding the propagation phenomena of electromagnetic waves at mmWave frequencies and its spectrum regulation, but also the role that such band has in current multi-Gigabit/s communications and might has in future wireless standards, namely: IEEE 802.11.ay (next generation of Wi-Fi) and 5G NR. This leads to the introduction of mmWave testbeds, where a list of the most relevant prototype systems available in the literature are outlined.

Table 2.1
Comparison of the most relevant wireless protocols in terms of nominal range, channel B, frequency band and maximum supported data rate.

Ref.	Standard	Network	IEEE Specification	First Release	Latest Release	Nominal Range	Channel BW	Frequency Band	Max data rate*
[35]	Wi-Fi	WLAN	802.11a/b/g/n/ac	1999	2013	100 m	20/40/80/160 MHz	2.4†/5 GHz	1.3 Gbps
[36]	UMTS	WWAN	N/A	1999	2010	> 50 km	5/20** MHz	1885-2025/2110-2200 MHz	84.4 Mbps‡
[21, 23]	Mobile WiMAX	WMAN	802.16	2001	2011	< 50 km	3.5/5/7/10 MHz	1999	100 Mbps
[24, 33]	Bluetooth	WPAN	802.15.1	2002	2005	10 m	1 MHz	2.4 GHz	1 Mbps
[24, 33]	ZigBee	WPAN	802.15.4	2003	2009	10-100 m	0.3/0.6; 2 MHz	868/915 MHz; 2.4 GHz	250 kbps
[31, 30]	Wireless USB	WPAN	N7A	2005	N/A	10 m	500 MHz	3.1-10.6 GHz	480 Mbps
[37]	LTE	WWAN	N/A	2008	2017	> 50 km	1.4 - 20/100†† MHz	700-3800 MHz	3 Gbps‡
[38]	Wireless HD	WPAN	N/A	2008	N/A	10 m	1.76 GHz	57-64 GHz	4 Gbps
[34, 39]	WiGig	WLAN	802.11.ad	2009	2012	10 m	2.16 GHz	57-66 GHz	7 Gbps
[40]	IEEE 802.15.3c	WPAN	802.11.3c	2009	2016	10 m	2.14 GHz	57-66 GHz	5.3 GHz

* Considering the latest standard release specifications;
† Not supported in the 802.11.ac;
** With carrier aggregation of five channels;
‡ DL only;
†† with carrier aggregation of five 20 MHz channels;

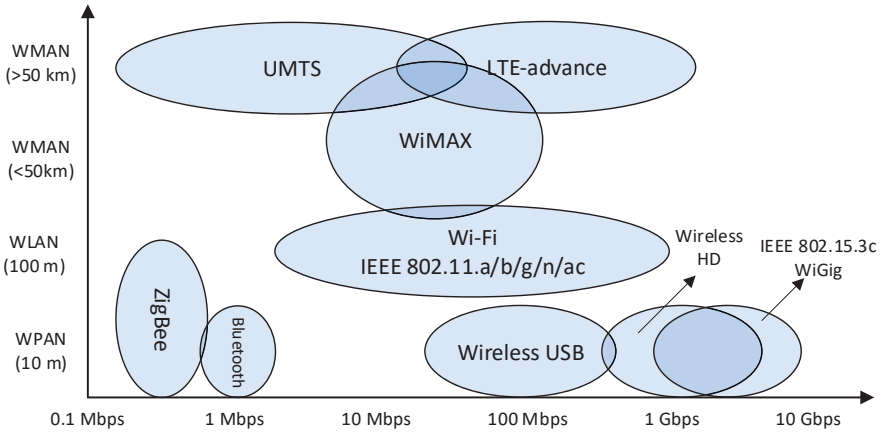

FIGURE 2.1: Typical operational range for area network standards.

2.2 The mmWave spectrum: overview

MmWave technology has been recognised for many decades, but it was mainly considered for military applications [19]. The main reason to this was that, at the time, mmWave technology was not evolved well enough to provide affordable low-cost integration solutions. Recently, with advances in process technologies, this issue is no longer a constraint [14]. Therefore, mmWave solutions start to attract a great deal of interest, due their capability to provide continuous large channel bandwidths. As consequence, this technology can provide multi-Gigabit/s of transmission rate, discussed in the previous subsection. Mmwave frequencies are the part of the electromagnetic spectrum from 30 to 300 GHz. Nevertheless, this work will be particularly focused on the 26 and 60 GHz bands.

The main benefit of considering the 60 GHz over other bands, is not only its huge unlicensed bandwidth. From Fig. 2.2, it can be seen that more than 5 GHz of continuous spectrum is available in almost all countries (except in Australia), despite of the constraints in terms of transmitted power [19]. Although UWB technology (3.1-10.6 GHz) can provide a frequency band comparable to the one allocated for the 60 GHz, its transmitted power is subject to very strict regulations [19], leading to, typical, lower values of Effective Isotropic Radiated Power (EIRP). This is also noted when compared to WLAN systems, as it can be verified in Table 2.2. Furthermore, maximum EIRP values established for the 60 GHz band can vary from one country to another, as it is outlined in Table 2.3, for USA, Japan, Australia and Europe. For example in Europe, the maximum EIRP in outdoor scenarios is 32 dB less than the one allowed in Japan.

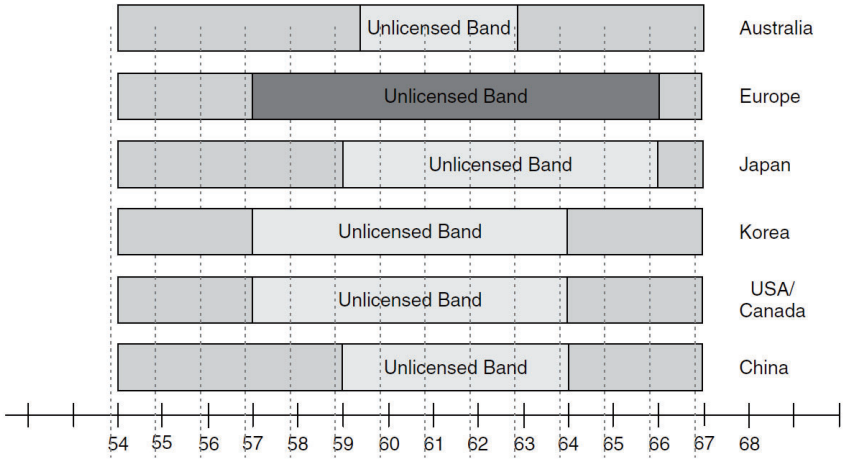

FIGURE 2.2: Worldwide frequency allocation for the 60 GHz band (image extracted from [19]).

TABLE 2.2
TYPICAL OUTPUT POWER, ANTENNA GAIN AND EIRP VALUES FOR 60 GHZ, UWB AND WI-FI TECHNOLOGIES, ACCORDING TO [19].

Technology	**PA output [dBm]**	**Antenna Gain [dBi]**	**EIRP [dBm]**
60 GHz	10	25	35
UWB	-11.5	1.5	-10
IEEE 802.11n	22.0	3.0	25

TABLE 2.3
MAXIMUM EIRP VALUES FOR THE 60 GHZ BAND FOR USA, JAPAN AUSTRALIA, AND EUROPE REGIONS, ACCORDING TO [40, 41].

Region	**Max. EIRP value [dBm]**	
	Indoor	**Outdoor**
USA	27	40
Japan	N/A	57
Australia	N/A	51.8
Europe	40	25

2.2.1 Propagation characteristics of mmWave signals

The available unlicensed bandwidth at 60 GHz may accommodate the entire radio communications operating from nearly DC up to 9 GHz. However, while signals from conventional sub-6 GHz band systems can propagate for many kms, mmWave signals can only travel few kms. This is mainly due to its relatively high free-space signal path loss and from the high absorption of electromagnetic waves by the oxygen and other gasses molecules, presented in the atmosphere [42]. Atmospheric absorption of electromagnetic waves, at sea level, versus frequencies from few MHz up to 400 GHz, is depicted in Fig. 2.3. On one hand, it is clearly noted that at certain mmWave frequencies, atmospheric abortion only arises from the $1-2$ dB excess loss per km, in relation to that usually obtained directly from *Friis'* space loss formula. On the other hand, as it is highlighted in Fig. 2.3, around 60, 120, 180 GHz signals suffer significant attenuation over distance due to the molecules resonances, making this frequencies only well suited for short-range communications.

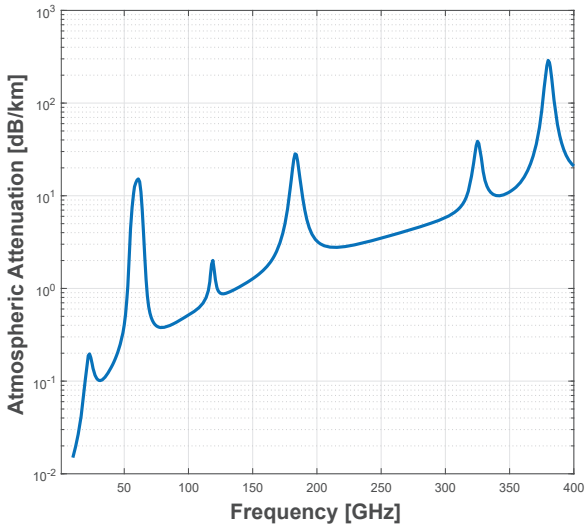

FIGURE 2.3: Atmospheric absorption of electromagnetic waves at sea level versus frequency (image adopted from [42]).

In addition, depending on the rainfall rate, rain can also induce attenuation in electromagnetic wave transmissions. According to [43], rain rate of 0.25, 25, and 50 mm/h are considered on the modelling of light, heavy, and extreme rainfalls, respectively. From Fig. 2.4, light rainfall does not create relevant additional path loss, whereas at heavy rainfall (25 mm/h) 4 and 9.7 dB/km of attenuation is expected at 26 GHz, and 60 GHz, respectively.

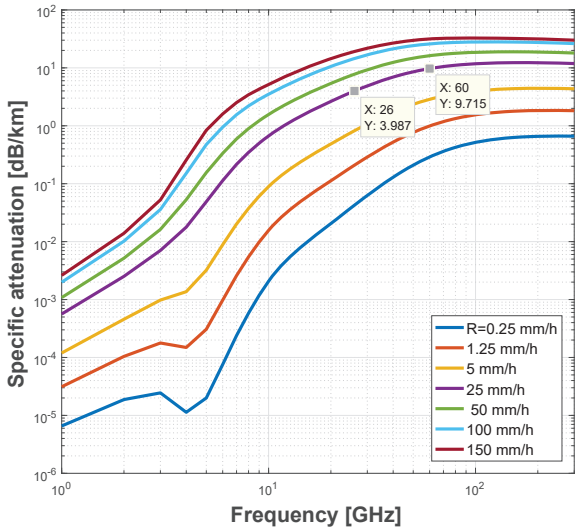

FIGURE 2.4: Rain attenuation in dB/km versus carrier frequency for several rainfall rates (using the ITU model reported in [44], considering 1 km as path distance).

Furthermore, work reported in [42], demonstrates that penetration loss into buildings is another constrain when considering the mmWave band for wireless communications. It is claimed that at 38 GHz, both tinted glass window and glass door, lead to signal attenuations around 25 and 37 dB, respectively. Even in indoor propagation environments, there is a relatively high free-space signal path loss and high attenuation by walls, furniture and other objects [45].

In order to overcome the drawbacks of the utilisation of the mmWave spectrum, relatively high transmitted power is required, which goes in line the EIRP specification values presented in Table 2.3. In other words, the challenge of such technology is overcoming the propagation path loss presented in the radio link, which, can be estimated considering the following *Friis'* formula [34], and taking into account the aforementioned additional path loss values as fading margins.

Nevertheless, severe high path loss can be leveraged in mmWave systems. For example, in an outdoor environment scenario the limitation in terms of the maximum range of coverage within a network cell can be overcome through the implementation of small RF coverage cells. This would also reduce signal congestion, since fewer users will be assigned per cell, and simplify the frequency reuse factor over small distances [45]. Also in [42], it is claimed that both spectral and energy efficiencies increase with the number of small cells. Another advantage is that, due to the fact wavelengths at mmWave frequencies are from 10 to 1 mm, size of devices can be highly reduced. For instance, high antenna gain values, which scales inversely with the square of the

wavelength, as represented in (2.1) [34], with relatively small apertures are feasible.

$$G = \frac{4\pi A_e}{\lambda^2}, \tag{2.1}$$

where A_e is the effective aperture area, which for example, is approximately the geometrical area of the surface, for parabolic antenna [46].

Consequently, antenna arrays can be composed with more elements in comparison with at lower frequencies, while keeping the same physical dimensions. In indoor scenarios the utilisation of mmWave signals can result in some advantages as well. For example, confining the system operation within a room would result in the reduction of effective interference levels when compared to those systems operating at sub-6 GHz bands [19].

Moreover, E and H beam-width plane values become narrower when both effective aperture area and wavelength are decreased, as it is formulated in (2.2) for a rectangular aperture or linear array [47, 48]. Therefore, relatively good mobile radio coverage, using mmWave, might be difficult to support. This is, movement of people can easily block and attenuate such narrow-beam signal [14]. However, such constraint can be overcame with the adoption of either multi-beam or beam-steerable antennas, as it will be addressed in the following subsections.

$$\begin{cases} \theta_H = \frac{51\lambda}{a}[^\circ] \\ \theta_E = \frac{51\lambda}{b}[^\circ] \end{cases}, \tag{2.2}$$

where both θ_H and θ_E are the theoretical beam-width values for each H and E planes. Both a and b are the length width of the aperture, respectively.

In particular, the 60 GHz band can offer the following key benefits to a wireless communication system:

- According to the European Telecommunications Standards Institute (ETSI) documentation reported in [49], the 60 GHz band is characterised by mostly unlicensed or light licence around the world. For example, in UK, wireless communications from 57.1 to 63.4 are licence exempt [50];
- Relatively high path loss, narrow antenna beam-width, and difficult to penetrate wall buildings lead to highly secure short transmissions [14];
- It enables a high level of frequency re-use in cellular communications, resulting in an increased network capacity, where data rate transmissions are close to ones from typical fibre optic links [14];
- It is a mature technology;

2.3 Gigabit/s wireless communication standards

As aforementioned, 60 GHz communication systems, due to a significant continuous allocated bandwidth are the key enabler for multi-Gigabit/s applications. As consequence, the requirement of a very high spectral efficiency transmission is not as strict as in the sub-6 GHz bands. This might lead to simpler system designs, implementations and low-cost solutions. Typically, to increase the spectral efficiency, in a limited bandwidth, techniques such as MIMO/ Massive MIMO are considered [51]. However, such techniques require a relatively high signal processing complexity and hardware. For example, in the massive MIMO testbed reported in [52, 53] and shown in Fig. 2.5, 145.6 (bits/s)/Hz on a 20 MHz radio channel at 3.51 GHz, has been provided, while requiring a 128-antenna array (employed at the base station), and a massive number of SDRs. Furthermore, in Table 2.4 it is summarised the spectral efficiency required by a system using the 60 GHz, UWB and 2.4 GHz bands to achieve 1 and 4 Gbps of transmission data rate [19]. It is verified, that the two most popular 60 GHz standards, IEEE 802.15.3c and WiGig (over IEEE 802.11.ad), only require approximately 0.5 and 2 bps/Hz to achieve 1 Gbps and 4 Gbps, respectively, against 25 and 100 bps/Hz using a typical 2.4 GHz Wi-Fi system.

FIGURE 2.5: Picture of the Lund's university massive MIMO BS (image extracted from [54]).

Table 2.4
Target data rate vs required spectral efficiency, for 2.4 GHz, UWB (3.1-10.6 GHz) and 60 GHz band systems.

Technology	Channel Bandwidth	Spectral efficiency [bit/s/Hz] @ 1Gbps	@ 4Gbps
2.4 GHz - IEEE802.15.n	40	25	100
60 GHz - IEE802.15.3c/ WiGig	2160	0.463	1.85
UWB - Wireless USB	500	2	8

2.3.1 WiGig - IEEE 802.11.ad

The Wireless Gigabit Alliance is the latest generation of WLAN, and it has been the outcome between the cooperation of both WiGig (industry consortium) and Wi-Fi Alliances bodies, to develop a standard for multi-Gigabit/s wireless networking. In this context, IEEE 802.11ad standard [39] specifies both Physical Layer (PHY) and Medium Access Control (MAC) layers, to bring consumer wireless communications to the mmWave band. This enables applications such as: high speed video streaming, Gigabyte file data transfer, and wireless bus, as illustrated in Fig. 2.6 [34]. Remarkably, a file transfer of 2 GB takes only 30s, at a minimum system throughput of 0.53 Gbps.

In fact, both PHY and MAC layers are modifications of the IEEE 802.11 standard. Thus, WiGig specification enables a Wi-Fi device to operate in the 2.4 GHz, 5 GHz and 60 GHz bands, which maintains interoperability among other device technologies [55]. On top of that, IEEE 802.11ad defines a directional communication scheme that employs a Beamforming (BF) algorithm to cope with the relatively high signal attenuation experienced by 60 GHz signals. With this, both transceiver devices, placed at both base and mobile stations, are able to choose the best propagation path (the one that ensures a better QoS) in a full-duplex communication, as illustrated in Fig. 2.7a. This is enabled by a highly directional reconfigurable switch-beam antenna, which divides 360° azimuth coverage plane in virtual sectors, as it is also illustrated in Fig. 2.7b. Consequently, not only the high path losses experienced at mmWave are mitigated, but also interference among other users is significantly reduced [56]. Nevertheless, since the same WiGig device incorporate modes for point-to-point communications between two wireless devices and the wireless network access, whenever longer ranges are required, the WiGig network can switch from a 60 GHz carrier to either a 5 GHz or 2.4 GHz.

To meet the requirements of the applications outlined in Fig. 2.6, IEEE 802.11.ad established several settings for different device classes. Table 2.5 summarises the number of sectors, expected range, maximum data rate and number of antenna arrays defined for each application device. Moreover, it is specified three different PHY layers: the

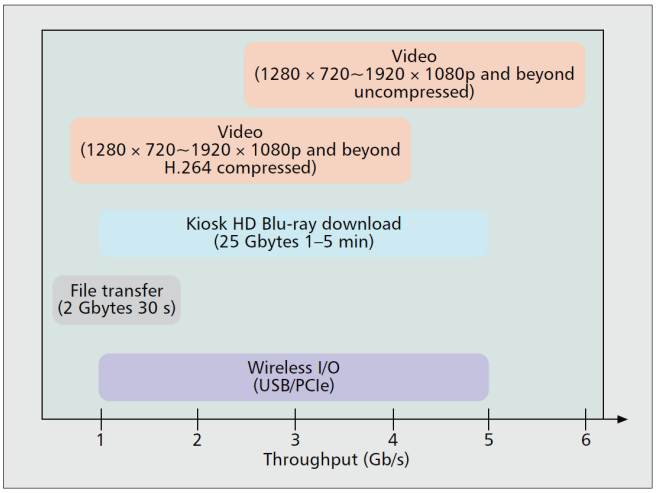

FIGURE 2.6: Main WiGig applications (image extracted from [34]).

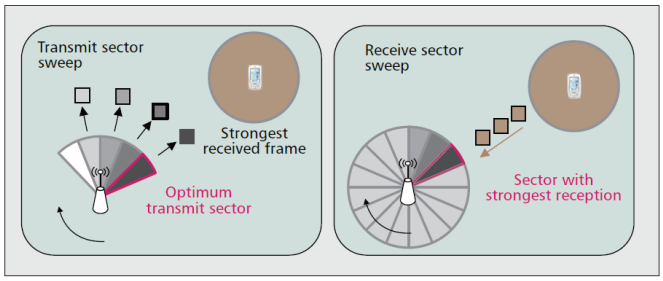

(a)

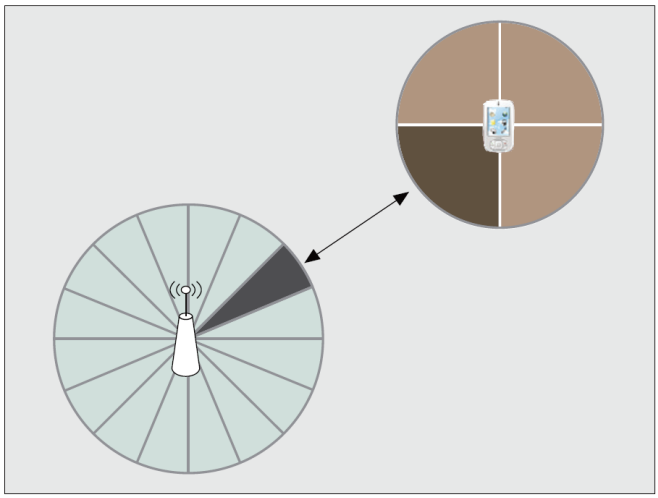

(b)

FIGURE 2.7: (a) BF algorithm protocol and (b) virtual antenna sectors from both TX/RX devices (images extracted from [56]).

Table 2.5
Typical WiGig device configurations, according to [56].

Device	Antenna Sector	Expected range [m]	Expected max. data rate [Gbps]	Nº antenna arrays
AP, docking station	32 to 64	20	7	≤ 3
Wireless peripherals	≤ 4	0.5 to 2	4.6	1
Wireless display-TV	32 to 64	5 to 10	7	≤ 2
Notebook	16 to 32	5 to 10	4.6 to 7	≤ 2
Tablets	2 to 16	2 to 5	4.6	1
Smartphone, camera	≤ 4	0.5 to 2	1.2 to 4.6	1

control, Single-Carrier (SC) and OFDM modes [39]. The first mode is designed for low SNR conditions, prior to BF, and for the control of frame transmissions. Second mode enables low-power and low complexity transceivers, while OFDM mode ensures a better system performance over frequency selective channels, and consequently higher data rate transmissions [56]. For example, SC mode enables maximum data rates of 4.6 Gbps, while OFDM can boost such value to 7 Gbps. Nevertheless, both modes share same packet structure and preamble to promote interoperability among PHY layers [34].

Finally, Low Density Parity Check (LDPC) codes with rates of 1/2, 5/8, 3/4, and 13/16, are also considered for channel coding [34]. These wide range of code rates allows the communication system to choose the best trade off between reliability and target data rate, in a particular fading channel condition.

2.3.2 IEEE 802.15.3c

The TG3c was formed in 2005, to develop a mmWave based alternative for the existing IEEE 802.15.3-2003 WPAN standard. The outcome was the IEEE 802.15.3c standard [40], which was the first communication system specification addressing multi-Gigabit/s transmissions [15]. Unlike the IEEE 802.11.ad, the IEEE 802.15.3c targets a WPAN. In other words, it only allows a number of independent devices to communicate with each other, just like in a piconet network. Therefore, a complex infrastructure is not required. It is only necessary a single device to coordinate the network. Such is known as Piconet Coordinator (PNC), which is responsible for the maintenance, synchronisation and to add new members in the network [58]. Utilising the 60 GHz

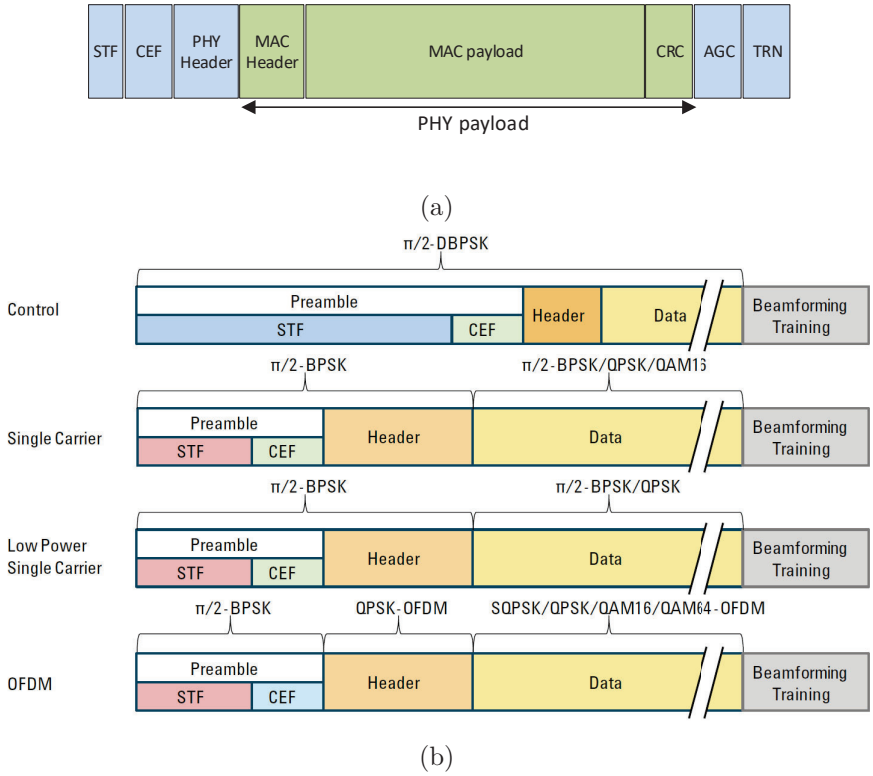

FIGURE 2.8: Both generic a) and detailed b) WiGig frame structures for each PHY mode (images extracted from [57]).

band, support from 2 up to 5 Gbps of data exchange rate among devices, depending on the propagation scenario, is attained.

In terms of channelisation, the unlicensed 60 GHz band is divided into four channels of 2160 MHz of bandwidth, as it is depicted in Fig. 2.9. Such is also common to the IEEE 802.11.ad standard. From the aforementioned figure, it can be seen that each channel is centred at 58.32, 60.48, 62.64 and 64.8 GHz, and in other to prevent adjacent-channel interference in other bands, a lower band of 240 MHz and upper band of 120 MHz have been also established.

Furthermore, the main key applications, Usage Models (UMs), for IEEE 802.15.3c standard are illustrated in Fig. 2.10 and in Fig. 2.11, while their full description is find next [59]:

- **UM1) Uncompressed video streaming:** transmission of HDTV contents, eliminating the need for video cables from the video players to the display devices. The range should be around 10 m;
- **UM2) Uncompressed multivideo streaming:** similar to **UM1)**, however multiple video signals could be supplied by a single transmitter;

- **UM3) Office desktop:** This UM aims the communication of a personal computer with external computer peripherals, e.g. printers and hard disks;
- **UM4) Conference ad hoc:** In this UM, the target scenario is where many computers are communicating each other;
- **UM5) Kiosk file downloading:** Aims the connection of portable devices with electronic kiosks, enabling data uploads and downloads with their fixed antennas. This model requires at least 1 m of range.

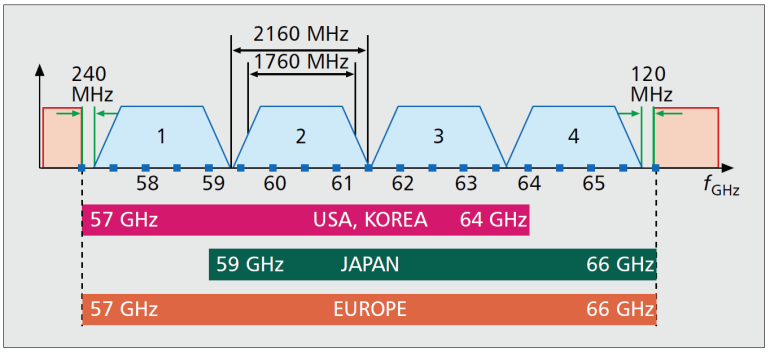

FIGURE 2.9: Channelisation of IEEE 802.15.3c in the 60 GHz unlicensed band (image extracted from [15]).

Similarly to the WiGig standard, IEEE 802.15.3c standard also specifies three PHY modes. These are: SC, High Speed Interface (HSI) and Audio Visual (AV) PHY modes, which were designed to meet the different UMs requirements. While SC mode is the one more suitable for UM3 and UM5, AV PHY is designed to enable high data rate transmissions for video streaming. Finally, HSI PHY mode is established for UM4, to provide wireless communications in Non-Line-Of-Sight (NLOS) scenarios with relatively low latencies [15]. The comparison of the different PHY configurations for each mode can be found in Table 2.6. It is noted that the main difference between modes is the transmission scheme, channel coding and data rate transmissions. For example, both HSI and AV modes consider OFDM modulation, whereas in SC mode it is employed SC-FDE instead. Once again similar to WiGig, this mode leads to a relatively low cost and complexity of the transceiver's architecture.

Furthermore, in order to promote coexistence among these PHY modes, a low data (25 Mbps) Common Mode Signalling (CMS) mode is also defined. This signal is modulated by $\pi/2$ Binary Phase Shift Keying (BPSK) and transmitted using SC-FDE scheme, which is also used to periodically transmit beacon frames. So the PNC device can deal with the interference from other cells [15]. Identically to the WiGig standard,

(a)

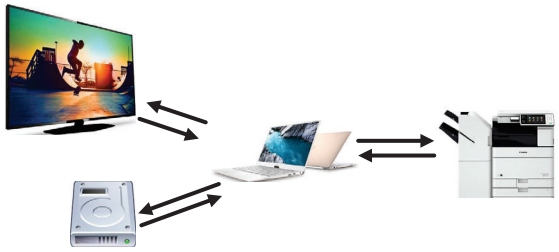

(b)

FIGURE 2.10: Main IEEE 802.15.3c applications for: (a) uncompressed video transmission (UM1) and (b) office desktop (UM3) (images adopted from [59]).

(a)

(b)

FIGURE 2.11: Main IEEE 802.15.3c applications for: (a) conference ad-hoc (UM4) and (b) kiosk file downloading (images adopted from [59]).

BF capabilities are also supported in all modes, to find the optimum transmit and received beams that ensure a good QoS. The packet/ frame structure is common to all modes, and it is illustrated in Fig. 2.12. The preamble is used for frame detection, channel estimation, frequency recover, and timing acquisition, which are mainly composed by

TABLE 2.6
MAIN FEATURES OF THE IEEE802.15.3C PHY MODES, ACCORDING TO [15, 40].

	SC PHY	**HSI PHY**	**AV PHY**
UM number	3, 5	3, 4	1, 2
Occupied Bandwidth	1760 MHz	1760 MHz	1815 MHz
Type of constellation	BPSK, (G)MSK, QPSK, 8PSK, 16-QAM	QPSK, 16-QAM 64-QAM	QPSK 16-QAM
Data rate	0.3 Mbps - 5.28 Gbps*	1.54 - 5.28 Gbps*	0.95 - 3.8 Gbps*
Transmission scheme	SC-FDE	OFDM	OFDM
Channel coding	RS, LDPC	LDPC	RS, convolutional

* Depending on the Modulation and Coding Scheme (MCS).

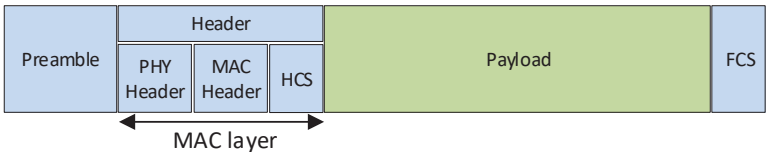

FIGURE 2.12: SC, AV and HSI frame structure, adapted from [58, 60].

Golay sequences [26]. Frame Check Sequence (FCS) is necessary to indicate whenever the frame ends, which can also operates as a Cyclic Redundancy Check (CRC).

Finally, a network performance comparison between WiGig and IEEE 802.15.3c will be addressed in the following section.

2.3.3 IEEE 802.15.3c versus IEEE 802.11.ad: a comparative analysis

As it has been discussed above, IEEE 802.15.3c and IEEE 802.11.ad standards specify both PHY and MAC layers to support multi-Gigabit/s transmissions over the 60 GHz band. In this section, not only a comparison of both standards is performed in terms of PHY/ MAC layers specification values, but they are also evaluated in terms of system's delay and throughput, for a similar usage case scenario, based on the study report in [55].

A comparison of the main specifications of IEEE 802.15.3c and IEEE 802.11.ad standards are given in Tables 2.7 and 2.8. From these information, it can be verified that both standard are, in fact, very similar. They both have similar RF channelisation, transmissions schemes (depending on the target application), data rates, and both support NLOS and LOS scenarios.

Moreover, it is fundamental that radio communications coexist without interfering with each other. Therefore, in the WiGig protocol, an Access Point (AP) can only establish an infrastructure/network once there is no other radio signals (from other

Table 2.7
Comparison of both OFDM and SC modes present in both standards, based on [57, 58, 60].

OFDM mode					
IEEE 802.11.ad			**IEEE 802.15.3c**		
Coding	Modulation	Data rate	Coding	Modulation	Data rate
1/2 LDPC	SQPSK	from	1/2 LDPC	QPSK	from
5/8 LDPC	QPSK	693 Mbps	5/8 LDPC	16-QAM	1540 Mbps
3/4 LDPC	16-QAM	to	3/4 LDPC	64-QAM	to
13/16 LDPC	64-QAM	6756 Mbps	7/8 LDPC		5775 Mbps
SC mode					
IEEE 802.11.ad			**IEEE 802.15.3c**		
1/2 LDPC 2x	$\pi/2$ BPSK	from	RS (255,239)	$\pi/2$ BPSK	from
1/2 LDPC	$\pi/2$ QPSK	385 Mbps	1/2 LDPC	$\pi/2$ QPSK	405 Mbps
5/8 LDPC	$\pi/2$ 16-QAM	to	3/4 LDPC	$\pi/2$ 8PSK	to
3/4 LDPC		4620 Mbps	7/8 LDPC	$\pi/2$ 16-QAM	5180 Mbps
13/16 LDPC			14/15 LDPC		

* Geographical region dependent.

Table 2.8
A comparative analysis of the main specifications of both standards, based on [55, 57, 58, 60].

Feature	**IEEE 802.15.3c**	**IEEE 802.11.ad**
Frequency Band	57-66 GHz	57-66 GHz
Number of channels	4*	4*
PHY mode and max. data rate	CMS (32.1 Mbps) SC (5.18 Gbps) HSI (5.775 Gbps) AV (3.807 Gbps)	control (27.5 Mbps) SC (4.6 Gbps) OFDM (6756 Gbps)
MAC channel access	centralised†	centralised†
LOS/NLOS support	yes	yes
Coexistence feature	No	yes
Backward compatibility**	No	yes

* Geographical region dependent - different countries have their own authority to allocate and authorize channels;
† Contention channel access and scheduled access;
** Multi frequency band support.

services) interfering in its communication channel. In other words, if a transmission is detected from a different mmWave technology device, both AP and network devices' can use one of the following features: change of the operating channel, beam forming, moving

beacon interval time or change the schedule of service period to mitigate interference with that device [55]. Unfortunately, IEEE 802.15.3c does not offer this type of interference management to its piconet.

Finally, in [55] both communication networks (including both PHY and MAC layers) were evaluated, in a video transmission usage case (similar to UM1), in terms of transmission delay and system throughput. Moreover, it was also considered that a HDTV video display is operating as the PNC. Simulation results of this study are depicted in Fig. 2.13, where both IEEE 802.15.3c and IEEE 802.11.ad achieved the same performance (plot lines and planes overlap in the four graphs).

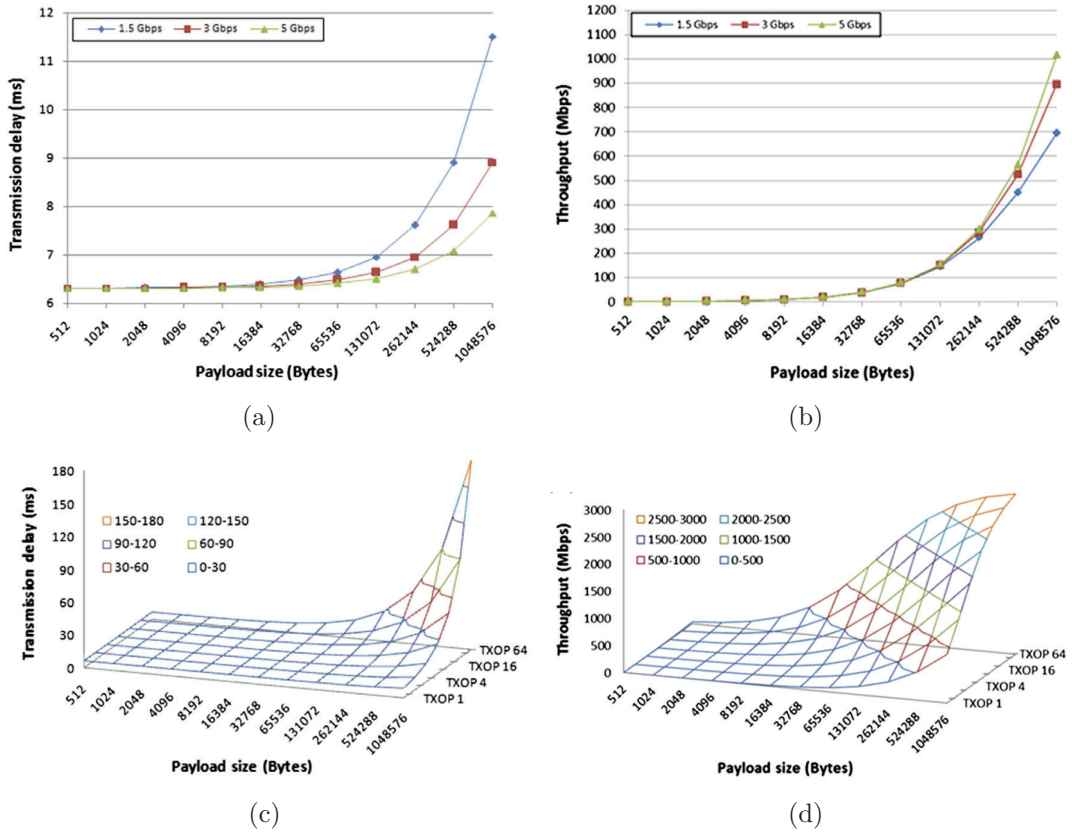

FIGURE 2.13: Performance of IEEE 802.15.3c and IEEE 802.11.ad: (a) transmission delay versus payload size, (b) throughput versus payload, (c) TXOP versus transmission delay and payload size, and (d) TXOP (multiple data frames are sent in a single transmission cycle) versus throughput and payload size (images extracted from [55]).

2.4 Future wireless communication systems

The amount of Internet protocol data traffic handled by wireless networks in 2010 was around 3 exabytes, and estimated 190 in 2018 [6]. In future, such traffic is expected to be increased to 500 exabytes (in 2020)[6], driven by new type of mobile services, such as 4k Ultra-High-Definition (UHD) video streaming, holograms and both VR AR [61]. In order to accommodate this volume of data, official standardization bodies such as 3^{rd} Generation Partnership Project (3GPP) are developing 5G standards, which first release appeared in 2018.

In Fig. 2.14 it is illustrated the IMT-2020 vision on 5G, reported in the ITU M.2083 recommendation [62]. Based on this document, 5G network is envisaged to be composed by three main verticals: enhancement of the mobile network capacity, the need for massive devices connectivity and innovative solutions for ultra-high reliability and low latency communications. Therefore, 5G technology is expected to provide broadband services up to 20 Gbps per cell (at least 0.1 Gbps per user) [61], provide ultra-low latency (below 1 ms) and high reliability solutions for M2M, Vehicle to everything (V2X), and healthcare. These features would enable for example, real-time remote-control of machines and remote medical surgeries [62]. Additionally, one million of connected devices per square kilometre is thought to be accommodated with the development of IoT [61].

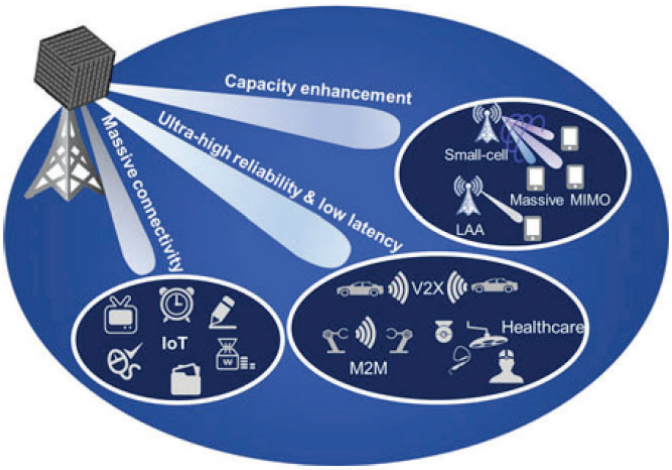

FIGURE 2.14: 5G vision of IMT 2020 (image extracted from [61]).

As result, autonomous vehicles might become a reality in the near future, where data from many in-vehicle sensors gathered in each car will become available in the

cloud, so it can be shared and computed in each vehicle [63]. Finally, different carrier frequency and signal bandwidths would be used to support the aforementioned usage cases. In particular, it is suggested that in services where GHz of continuous spectrum is required, carrier frequencies above 6 GHz should be considered [62].

In terms of system requirements, each 5G vertical is envisaged to meet:

- **eMBB:** high user density, very high traffic data capacity and low mobility, particularly for hotspot environment. Whether the target scenario is a wide range of coverage, the system should address high mobility with less data rate constraints [62];
- **Ultra-Reliable and Low-Latency Communications (URLLC):** strict requirements latency and reliability. According to [64], data be must transported fast and error-free to the recipient, with high levels of integrity, authenticity and confidentiality. Target latency and outage probability should be below 1 ms and $10^{-}5$, respectively;
- **massive Machine Type Communication (mMTC)** scalable and efficient connectivity for a massive number (around tens of billions) of wireless devices. The network should be characterised by a wide and deep indoor penetration coverage, delivering tens of kbps [65]. Small low-cost devices associated with the IoT will be used to perform less delay sensitive communications, with short periodical data bursts (transmission of short packets is required) in order to maximise battery lifetime.

Finally, Fig. 2.15a summarises the most relevant usage scenarios, while 2.15b shows the relation between them and the required 5G system requirements [62]. As it can be seen from both figures, different applications will result in a wide diversity and variety of requirements. The overall target performance indicators for 5G are illustrated in Fig. 2.15c. In sum, key design principles are flexibility and diversity, which lead to device and base station densifications, and a very high number of antennas at both TX and RX [6].

2.4.1 Enabling high data rate in 5G systems

Regarding the 5G requirements outlined in Section 2.4, the one that is in the scope of this research work, is the demand for solutions to enable high data rate transmissions. In fact, one of the innovative solutions to meet such requirement is utilisation of the mmWave technology, which, as it was discussed in Section 2.2, enable Gbps transmission of data rates, at a relatively low spectral efficiency. However, 5G technology will not be limited to indoor coverage solutions. In fact, according to [42], this technology

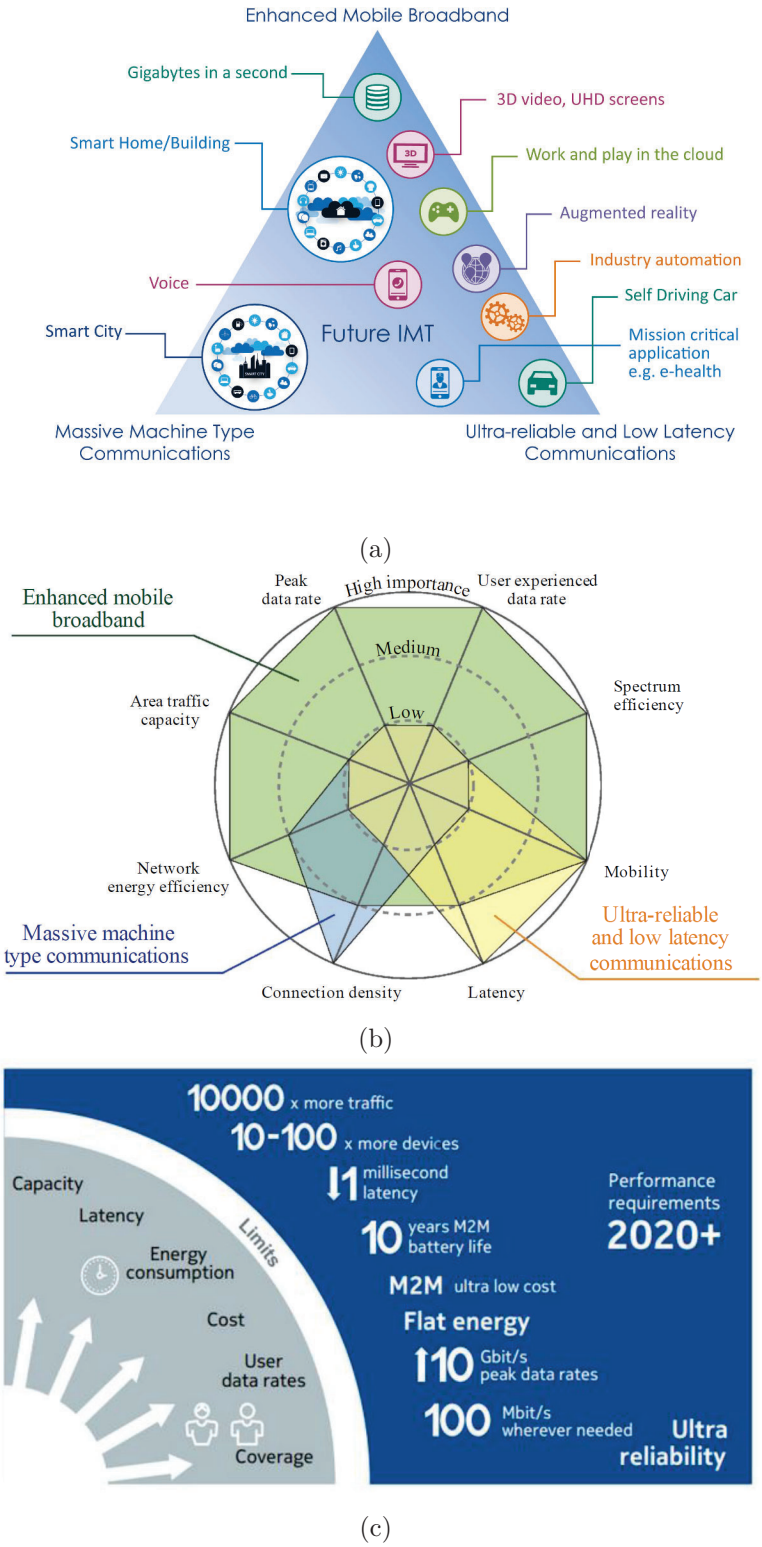

FIGURE 2.15: Illustration of the 5G most relevant: (a) usage case scenarios, (b) key system requirements, and (c) performance indicators (images extracted from [11, 62, 66]).

will use mmWave frequencies to offer unprecedented spectrum and multi-Gbps data rates to a mobile equipment, and thus increase the network capacity. Therefore, this section will be particularly focused in eMBB usage case architecture solutions, where this requirement is a demand.

5G unlike 4G, where only incremental improvements and small amounts of new spectrum was achieved, in comparison with previous mobile communication standards [6], will not rely in a single technology [42]. It will integrate several existing technologies, as it is illustrated Fig. 2.16, to enable new applications with much lower system latencies, such as Vehicle-to-Vehicle (V2V) [67], Vehicle-to-Infrastructure (V2I) [68], and M2M communications [69]. This can be attained, according to [42], by connecting Wi-Fi offloading, small cells, and wideband data distribution (femtocells) to servers, at the edge on the network. Therefore, the next generation of mobile networks will have to be highly integrative and flexible, tying any new 5G air interface and spectrum together with current LTE-Advanced, Wi-Fi, and mmWave technologies. This will provide the high-data rate necessary to accommodate the heavy data traffic expected in future wireless communications [6]. In particular the role of mmWave transmissions in future wireless communications will be addressed in the section below.

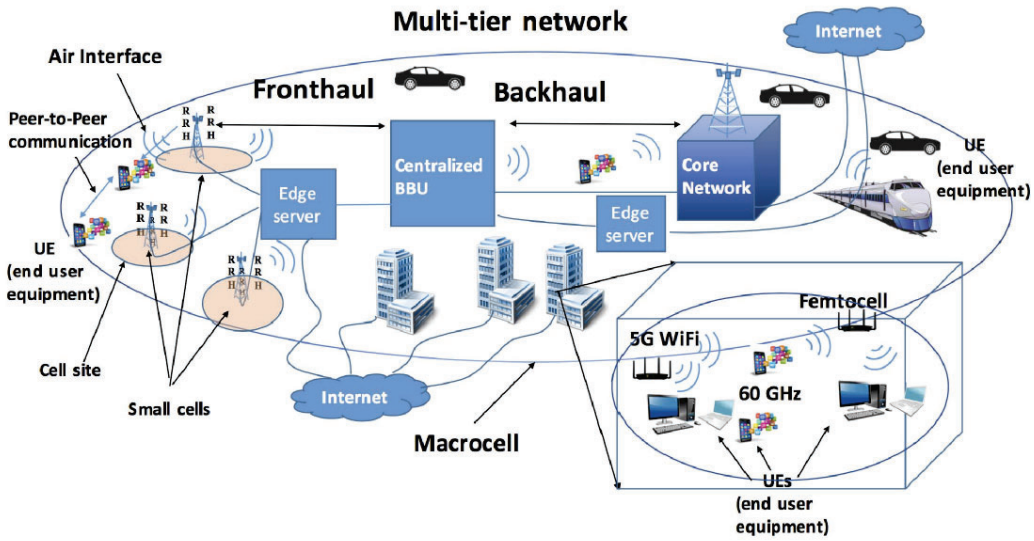

FIGURE 2.16: Evolution of the 4G mobile network towards 5G (image extracted from [42]).

In sum, according to [42], the main innovative features of the aforementioned network can be summarised as follows:

- **Backhault and Fronthaul:** modern cellular network will support a more flexible deployment of radio resources, by distributing them using a cloud radio access network. Mwave wireless backhaul will offer fiber-like data rates. In fact, the source of traffic congestion, in LTE systems, is the backhault link, where Ethernet links provide approximately 1 Gbps;
- **Small cells:** it is well known that one possible approach to increase the area spectral efficiency is to shrink the cell coverage size, and by increasing the number of BS per unit area. With this, spectrum is re-utilised and delivered for few number of cell subscribers;
- **Multi-tier architecture:** allow different tier users to have various channel access priorities and types of connections, such as: macrocells, small cells and peer-to-peer communications. These will result in the support of higher data rate, lower latency, higher energy efficiency and interference management, from the network;
- **Air interface:** a new PHY design is required in consequence of strict latencies, rapid BF and synchronisation, with better spectral efficiency and smaller time slots. OFDM considered in 4G will therefore be evolved;
- **Unlicensed Wi-Fi:** IEEE 802.11 ac/ad show the suitability to support Gbps communications. Hence, it should be integrated in the 5G network.

The role of mmWave technology

In Section 2.2, it has been discussed that propagation of electromagnetic waves at mmWave are characterised by strong pathloss, as a result of relatively high atmospheric and rain absorptions, and penetration and free space losses. Due to this fact, mmWave communications were only considered for indoor applications by employing WiGig and IEEE 802.15.3c standards, and fixed wireless communication technologies (backhaul links), used to connect base stations in outdoor scenarios. In other words, mmWave spectrum was not seen as an reliable solution for mobile communications [6]. However, mmWave have recently attracted the interest of the scientific community to support the 5G network.

For example, the study reported in [70], suggests that mmWave spectrum could be used as an alternative to the overloading of frequency spectrum at lower frequencies, particularly below 6 GHz. In addition, it is also claimed that the combination of cost-effective mmWave semi-conductors technology with high gain and steerable antennas at both BS and UE, will enhance the feasibility of mmWave mobile communications [70].

Moreover, in [12], it has been demonstrated, from an extensive propagation measurement campaign in the urban environment of New York city, that maximum radio link coverage ranges of 200 m (typical LTE cell size in urban environments), can be achieved at both 28 and 38 GHz bands. In such study, the target coverage area was divided into sectors corresponding to the location of the transmitters devices, as it is illustrated in Fig. 2.17a. Consequently, signal has been acquired in all RX positions, denoted as circles in this figure. Results of maximum coverage distance, at 28 GHz, versus combination of TX/ RX antenna gains, for a target SNR of 10 dB, are depicted in Fig. 2.17b. From them, it can be demonstrated that relatively high coverage distances can be achieved using mmWave frequencies which, as expected, it increases with the increasing of combined antennas gain, and decreases with the path loss exponential (n). More details about this path loss modelling parameter are presented in Appendix A.

Results shown in Fig. 2.17b are one of the examples, available in the literature review, which demonstrate that 5G mmWave mobile communications are feasible. To this end, authors of the work reported in [6], propose the innovative heterogeneous network solution illustrated in Fig. 2.18, where a wide cell coverage is achieved by the deployment of several phantom cells (nodes) at different locations from the macrocell. The presence, discovery and usage of the phantom cells are controlled dynamically by the macrocell site, in a master-slave configuration [71]. Moreover, the mmWave BSs will be mainly responsible for the payload transmission (U-plane), while the microwave BS would be in charge of the network signalling and control (C-plane), since it is required a more reliable coverage. These would significantly increase the area spectral efficiency due to frequency re-use, and consequently the overall network capacity. Nevertheless, the microwave BS will also support both planes, to ensure data is always retrieved whenever interruptions occur on the mmWave links [71].

Although phantom cells are a very promising solution to enable mobile communications at mmWave, the support of good mobility and connectivity between the mmWave BS and the UE, employing large antenna arrays with very directional beams, are not trivial. Both directional TX/ RX antenna beams should be always properly aligned, regardless the user's mobility speed. According to [6, 12, 42, 71], such can be achieved through the exploitation of new signal processing techniques, namely MIMO and adaptive BF. The performance of active BF systems are significantly improved when combined with MIMO techniques [72]. For example, in a MIMO communication system, the support of Multi-user (MU) can be enabled with the design of advanced BF precoding algorithms, where multiple beams are provided by the array antenna to deliver simultaneous multiple data streams to different users [72].

In general, MIMO BF systems can be implemented using either a fully digital or analogue approaches, or considering a hybrid architecture [73]. On one hand, a relatively higher degree of freedom, which consequently offers a better performance [72], can be

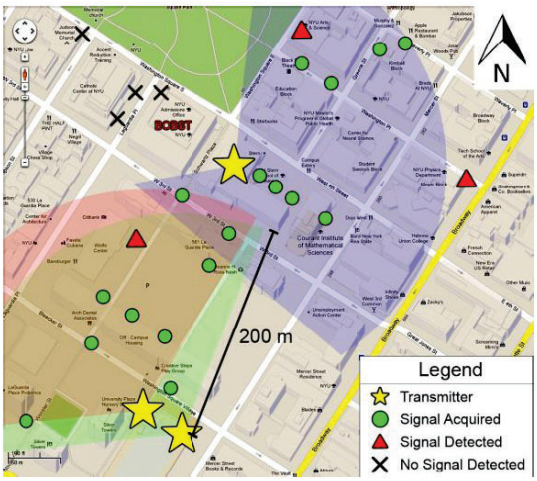

(a)

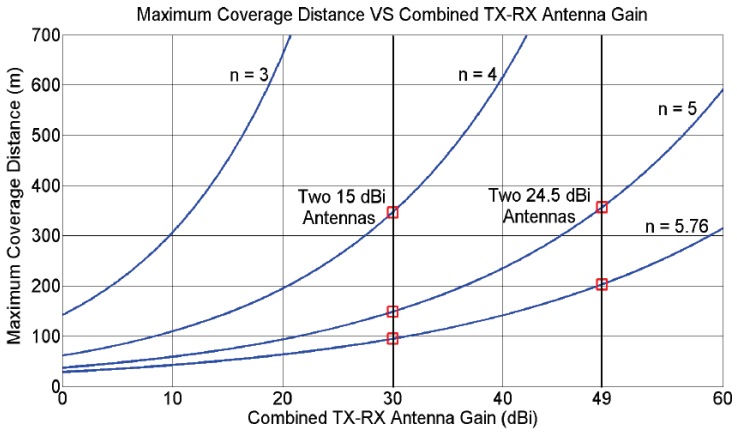

(b)

FIGURE 2.17: New York city measurement campaign: (a) mapping coverage area, and (b) maximum coverage distance results, *vs.* combined TX/ RX antenna gains, considering SNR = 10 dB, at 28 GHz (images extracted from [12]).

attained using only digital algorithms. However, having customary fully DACs, ADCs, and dedicated processing blocks per each antenna chain, might lead to an impractical solution, due to system's implementation complexity and cost. On the other hand, a BF architecture requiring only analogue components, would be simpler, cheaper, but less flexible. Therefore, there is a trade-off between flexibility/ performance and simplicity in the design of MIMO transceivers with BF capabilities. In this context, a hybrid architecture might be the preferable choice, when compared to both exclusive digital and analogue BF techniques.

One of the most relevant mmWave hybrid BF architectures presented in the literature, is the one proposed in [74]. In this work, the steering of TX/ RX highly directional beams is performed with the aid of analogue phase shifters, as illustrated in Fig. 2.19a.

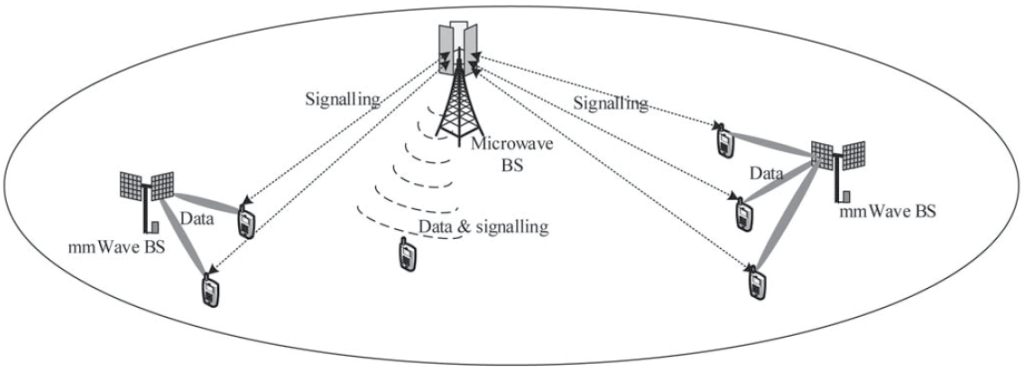

FIGURE 2.18: Mmwave mobile cell concept employing phantom cells (image extracted from [6]).

Moreover, the picture of this MIMO BF prototype system is depicted Fig. 2.19b, where antenna arrays at both TX/RX ends are composed by 32 radiating elements, arranged as a planar array with 8 horizontal and 4 vertical elements, with dimensions of $60mm \times 30mm$. This relatively small footprint was enabled by the consideration of an operational centre frequency of 27.925 GHz. Finally, considering the outdoor measurement scenario shown in Fig. 2.20, this prototype system not only enabled coverage areas of few hundred meters of radius in both outdoor/ indoor environment and in both LOS and NLOS scenarios, but also provided data rates higher than 500 Mbps. However, such performance is only guaranteed for an UE's speed below 8 km/h.

An example of a fully digital architecture can be found in [72], where a 64 MIMO BF transceiver, at 27.95 GHz, was implemented according to the system's block diagram depicted in Fig. 2.21. The performance of such prototype communication system was evaluated by considering two distinct experimental trials, over the surroundings of the Shanghai Bell laboratories, as shown in Fig. 2.22. Firstly, the tracking capabilities of the prototype were evaluated, in a single user mode, where an UE was moving and its QoS being constantly monitored in terms of data rate and received signal constellation. Block diagram of such measurement is depicted in Fig. 2.21a. Secondly, the system's support for multi-Gbps of data rates was assessed following the block diagram depicted in Fig. 2.23b. Each UE was assigned to multiple sharp beams. In terms of results, in a mobility scenario, 5.3 Gbps of steady throughput was delivered to the UE, while in a static environment, a overall peak data rate of 50.73 Gbps was obtained by the employing of 20 data streams, and a signal bandwidth of 500 MHz modulated using 64-QAM OFDM. This lead to a spectral efficiency of 101.5 bps/Hz. Finally, a maximum cell coverage radius of 300 m was achieved.

Although it is possible to pack a large number of antennas into a small space (e.g. in [75], a 256-element antenna chip only occupies $41.4mm \times 42mm$), when it comes to the cellular handsets, placing multiple mmWave radio chains inside an operating cellular

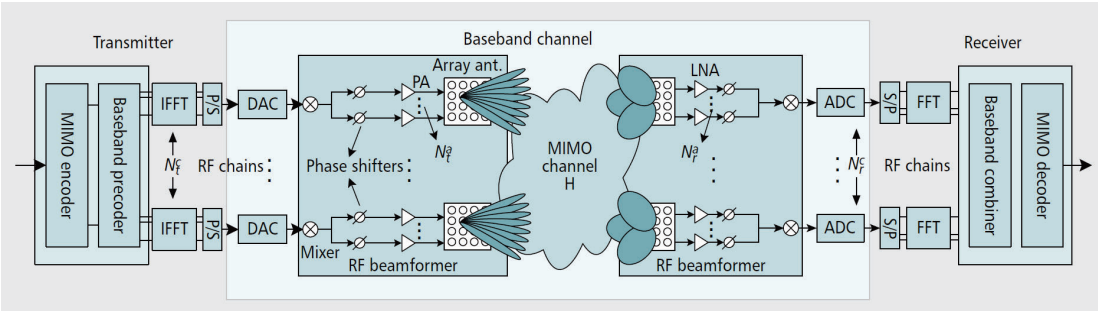

(a)

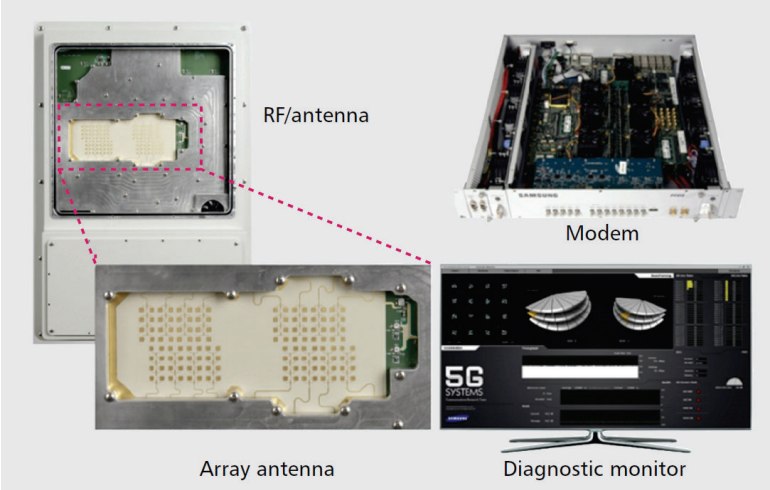

(b)

FIGURE 2.19: Block diagram a) and picture of the end-to-end fully hybrid adaptive beamforming prototype system reported in [74] (images extracted from [74]).

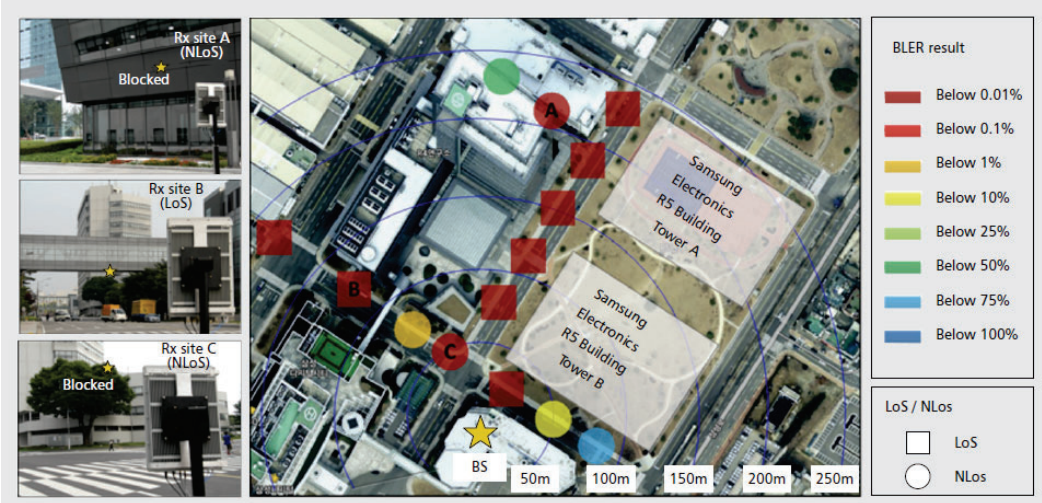

FIGURE 2.20: Outdoor measurement scenario for coverage assessment, employing the mmWave beamforming prototype system presented in [74] (image extracted from [74]).

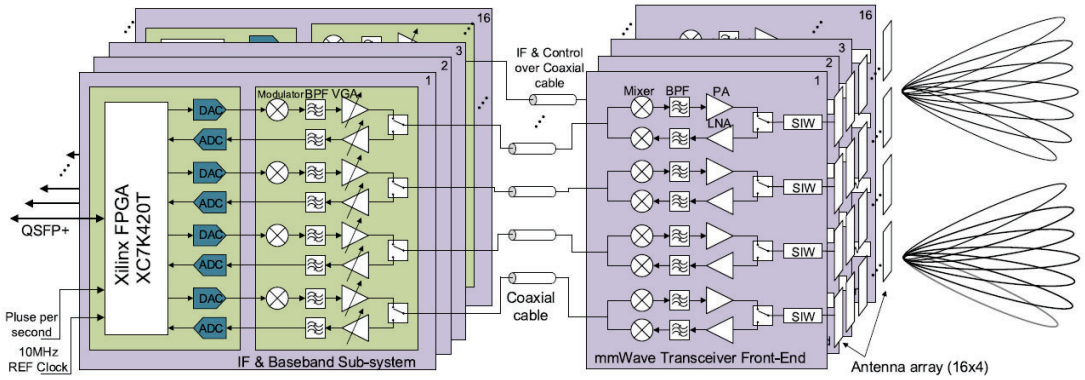

(a)

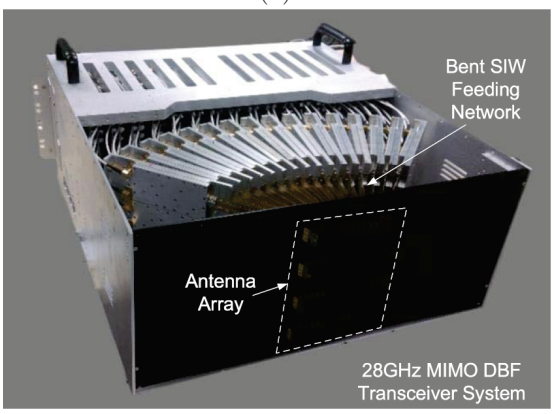

(b)

FIGURE 2.21: Block diagram a) and b) picture of the fully digital adaptive beamforming transceiver prototype presented in [72] (images extracted from [72]).

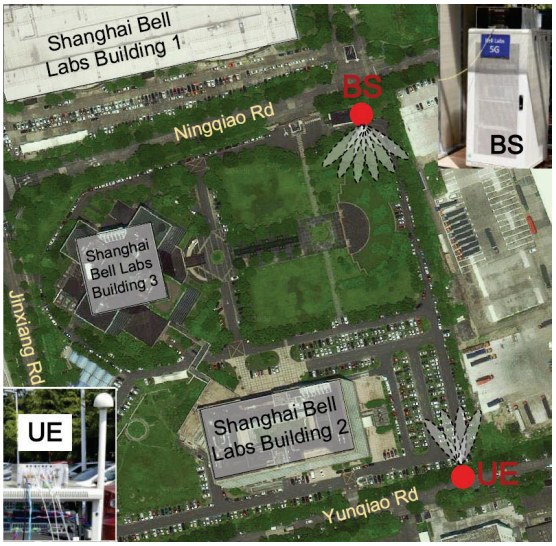

FIGURE 2.22: Outdoor measurement scenario for coverage assessment, employing the mmWave beamforming prototype system presented in [74] (image extracted from [74]).

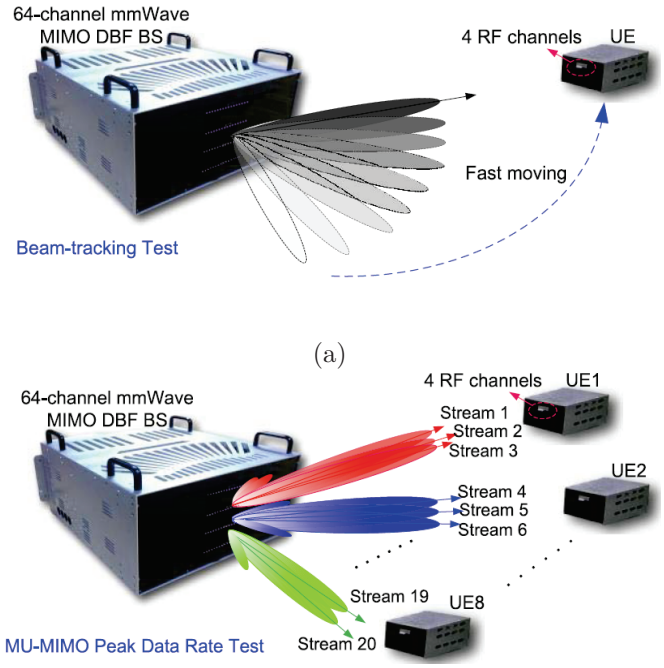

FIGURE 2.23: Beam-tracking a) and b) MU-MIMO measurements scenarios, respectively [72] (images extracted from [72]).

cellphone, size is still a major constraint. For example, the MIMO BF prototypes presented in both Fig. 2.19b and Fig. 2.21b, could only be adopted as base stations, in a real 5G deployment scenario. In [76], an overview of mmWave 5G antennas for cellular handset is provided for the first time. In addition, authors propose two end-fire 60 GHz phased-arrays to be placed in opposing corners of the cellular device, as exemplified in Fig. 2.24, to enable either spatial diversity, or multichannel MIMO or carrier aggregation. Particularly, in Fig. 2.24b, it is seen that both phased arrays are connected to the baseband processor of the cell phone by wired connections. Moreover, each antenna array design is composed by 8 vertically and 8 horizontal oriented endfire antenna elements, as shown in Fig.2.25a. The prototype system, see Fig. 2.25b, has been evaluated under different conditions as shown in Fig. 2.25a: scenario 1, 2, and 3. While in scenario 1 it is assessed the effect of holding the cellular phone on the phased array performance, scenarios 2 and 3 evaluate the loss of data rate by obstructing the LOS of both phased array antennas. Results of these measurements are summarised in Fig.2.26b, where it is shown that 3 Gbps peak rates are obtained in absence of signal obstruction (reference plot line). However, attenuation caused by the human presence could significant reduce the payload rate, at the handset.

With the aforementioned results, it is clearly demonstrated that the usage of mmWave frequencies in future cellular communications are not only feasible, but will also bring disruptive advantages to the network subscribers. However, particularly at the handset

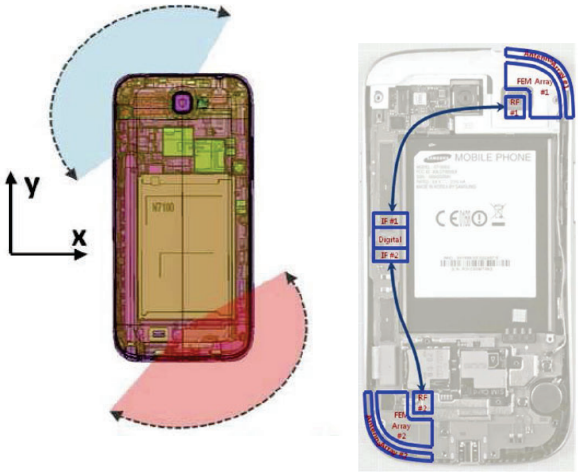

(a) (b)

FIGURE 2.24: A vision of what could be the: a) schematic and b) radio layout of a 5G cellular handset, according to [76] (images extracted from [76]).

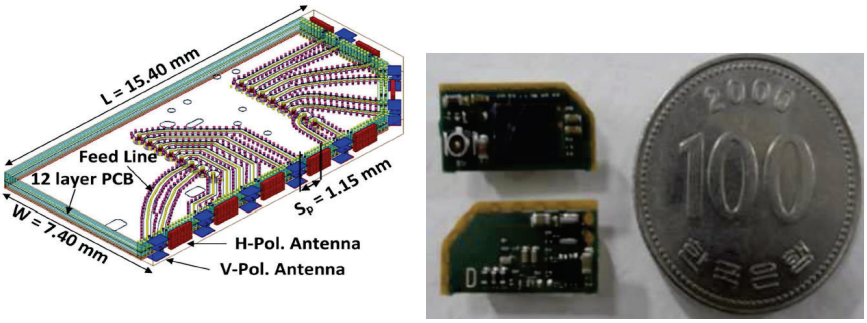

(a) (b)

FIGURE 2.25: Both phased array a) schematic and b) prototype developed in [76] (images extracted from [76]).

(a)

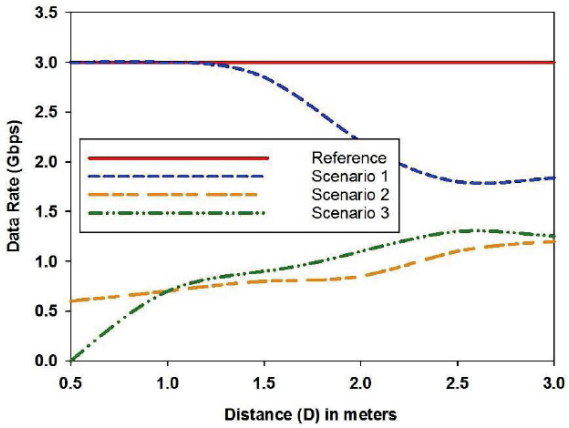

(b)

FIGURE 2.26: Performance assessment: a) scenarios and b) results in term of data rate vs distance, of the handset presented in [76] (images extracted from [76]).

device side, mmWave solutions should be further evolved to overcome the negative effect that signal obstruction caused by human presence has in the communication performance.

5G New Radio specifications: overview

In order to meet the aforementioned performance requirements of IMT-2020, 3GPP is currently working on the establishment of technical specifications for the 5G NR [77]. To support multiple and distinct usage cases, such as eMBB, mMTC, and URLLC, as it was cited above, 5G needs to be more than an evolution of the previous mobile broadband standard [78]. In this context, the 5G NR PHY layer, in order to address diverse scenarios and deployments, needs to be flexible to target a wide range of carrier frequencies and channel bandwidths, and the support of different combinations of latency, capacity, reliability, coverage areas and a massive number of connected devices [78, 79]. Moreover, since it might be very difficult for one band of spectrum to meet all these requirements, 5G will joint both sub-6GHz band (from 0.45 to 6 GHz) and mmWave (24 to 52.6 GHz) bands [78, 79]. For example, whenever relatively large coverage is required per base station (macro sites), a lower carrier frequency will be used, otherwise small and phantom base stations will be operating at higher carrier frequencies [78].

The roadmap of the development of the 5G NR standard is outlined in Fig. 2.27, while Rel. 16 will address new types of services/ devices, new deployment/ business models, such as vehicle communications for autonomous driving use cases, and new spectrum bands/types [80], a commercial deployment of 5G is only expected to start somewhere in 2020, with the Rel. 17 [81]. In particular, at the time of this thesis, 3GPP NR specifications releases 14, 15 (Phase 1) have been already published. While Rel. 14 is a study item stage, i.e., describes all the necessary research to define the appropriate channel models, scenarios and systems requirements for 5G, and Rel. 15 presents the first non-standalone NR operation specification [79, 81]. According to [77, 79, 80], first NR deployments will first rely on LTE for initial access and mobility, mainly focusing in the eMBB usage case and URLLC, while adding the 5G carrier.

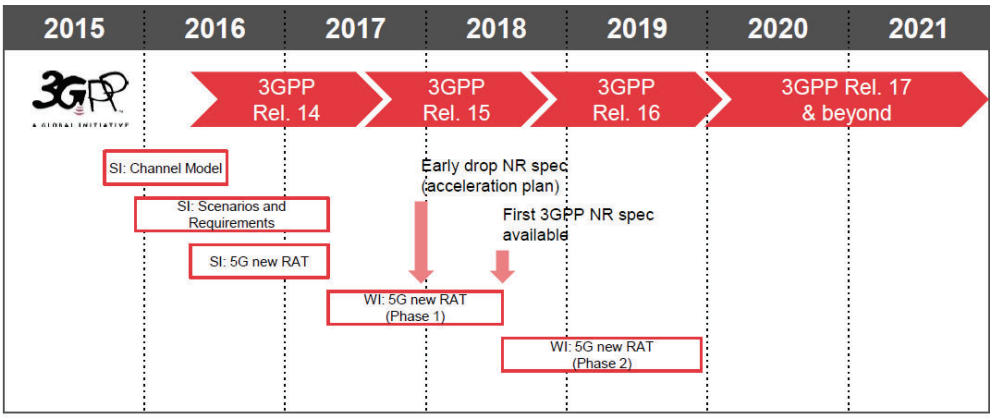

FIGURE 2.27: 3GPP 5G NR Roadmap (image extracted from [77]).

In [82], a scalable PHY layer adopting OFDM was proposed and evaluated in several link types, namely: Uplink (UL), Downlink (DL), Device-to-Vehicle (D2V) and backhaul, against other multi-carrier waveforms. It was concluded that due to the a better time localization and spectral efficiency, low-complexity transceiver design, and easy integration with MIMO technologies, that OFDM is the most suitable waveform for the first 5G specifications. Additionally, it is well known that OFDM suffers from a relatively high Peak-to-Average Power Ratio (PAPR), but such might be reduced with the consideration DFT-OFDM [82]. In fact, this is an optional feature in NR, which uses such precoding technique to reduce the OFDM PAPR and thus, boosting the power amplifier efficiency [79]. These are some of the main reasons for the adoption of OFDM as the waveform, for both UL and DL directions (similarly to 4G), in the 5G NR's Rel. 15 [77–79, 83].

As aforementioned, NR is envisioned to operate in a wide range of frequencies bands, depending on the deployment scenario and application. In this context, it is not feasible for a single waveform numerology to fulfil all service requirements, and thus, a flexible OFDM numerology is adopted in the NR [78]. More in detail, this new radio interface supports scalable OFDM sub-carrier spacing and bandwidth (always wider when compared to LTE), which are, for instance, straight related to latency, data rate of the supported services. The relation between sub-carrier spacing, cyclic prefix, channel bandwidth and frequency band in NR, is represented in Table. 2.9, where n is a integer value parameter and Δf denotes the sub-carrier spacing. This former feature is calculated according to (2.3) [79]. Moreover, it can be verified that, 15, 30, 60 kHz are the sub-carrier spacing for the sub-6 GHz systems, which are characterised with a maximum channel bandwidth of 200 MHz, whereas, 60, and 120 kHz are established for mmWave communications, with channel bandwidths up to 400 MHz.

$$\Delta f = 15 \times 2^n [kHz] \tag{2.3}$$

Table 2.9
Relation between sub-carrier spacing, channel bandwidth and frequency band in the NR standard, based on [77, 79].

n	Δf **[kHz]**	**Freq. Band [GHz]**	**Max. Bandwidth [MHz]**
0	15	0.45-6	50/100/200
1	30		
2	60	0.45-6/24-52.6	
3	120	24-52.6	200/400
4	240		
5	480	N/A*	N/A *

* Specified but not supported in Rel. 15.

It is worth noting that, when considering $n = 0$ in (2.3), the OFDM numerology is exactly the same as in 4G systems. Moreover, the summary of 5G NR OFDM sub-carrier numerology versus frequency band, cell size and system latency is illustrated in Fig. 2.28. As it can be seen, multiple services with different requirements might be supported by considering distinct OFDM numerologies. Low system latencies can also be accomplished in larger cells when higher sub-carrier spacings are considered.

Nevertheless, lower sub-carrier values, of at least 3.75 kHz ($n = -2$), are also supported by 5G NR, which is necessary to meet meet the IoT modes specifications (e.g., higher power efficiency) [78, 84]. Consequently, smaller the sub-carrier spacing, higher tolerance of NR to deal with time dispersion caused by a multipath environment [83].

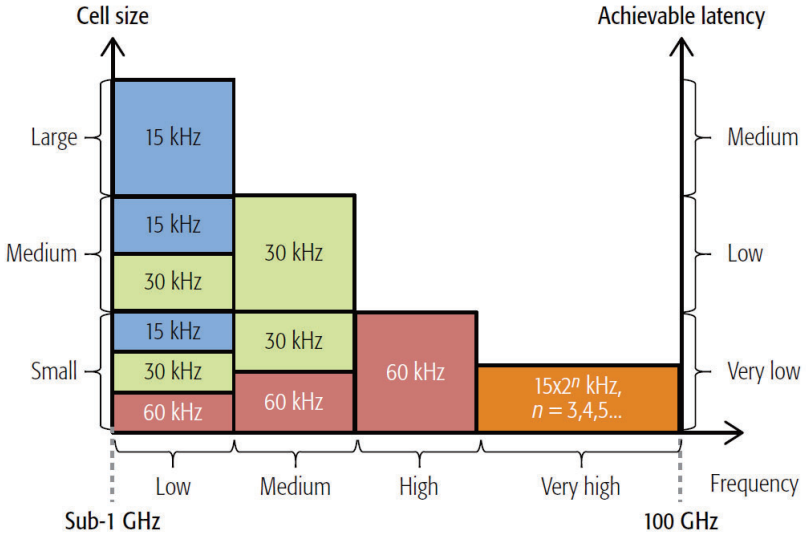

FIGURE 2.28: 5G NR OFDM sub-carrier numerology versus frequency band, cell size and system latency (image extracted from [78]).

Additionally, the 5G NR frame has a duration of 10 ms divided into ten 1 ms sub-frames, which are further divided into time slots consisting of 14 OFDM symbols [77]. As it can been seen in Fig. 2.29a, the duration of each slot also depends on the sub-carrier numerology, since a slot is composed by a fixed number of OFDM symbols. Therefore, higher the sub-carrier spacing, shorter are the time slots, which consequently leads to higher number of slots per subframe. Moreover, it is also verified, from Fig. 2.29a, that an integer number of slots of one numerology fits into a slot of another. For example, two time slots when $\Delta f = 30$ kHz has the same duration of one time slot in the 15 kHz numerology. According to [78], this time alignment is particular important in Time Division Duplex (TDD) uplink-downlink network duplex schemes. Nevertheless, NR will support both Frequency Division Duplex (FDD) and TDD. Particularly, when $\Delta f = 15$ kHz has a duration of 1 ms, resulting into the same duration of an LTE subframe, which promote the NR-LTE coexistence [79].

From Fig. 2.29a, it can also be verified that each slot is composed by signalling symbols. Hence, DL and UL transmission directions can be flexible and dynamically changed on a per-slot basis [84]. From its 14 OFDM symbols, either the first or/ and the

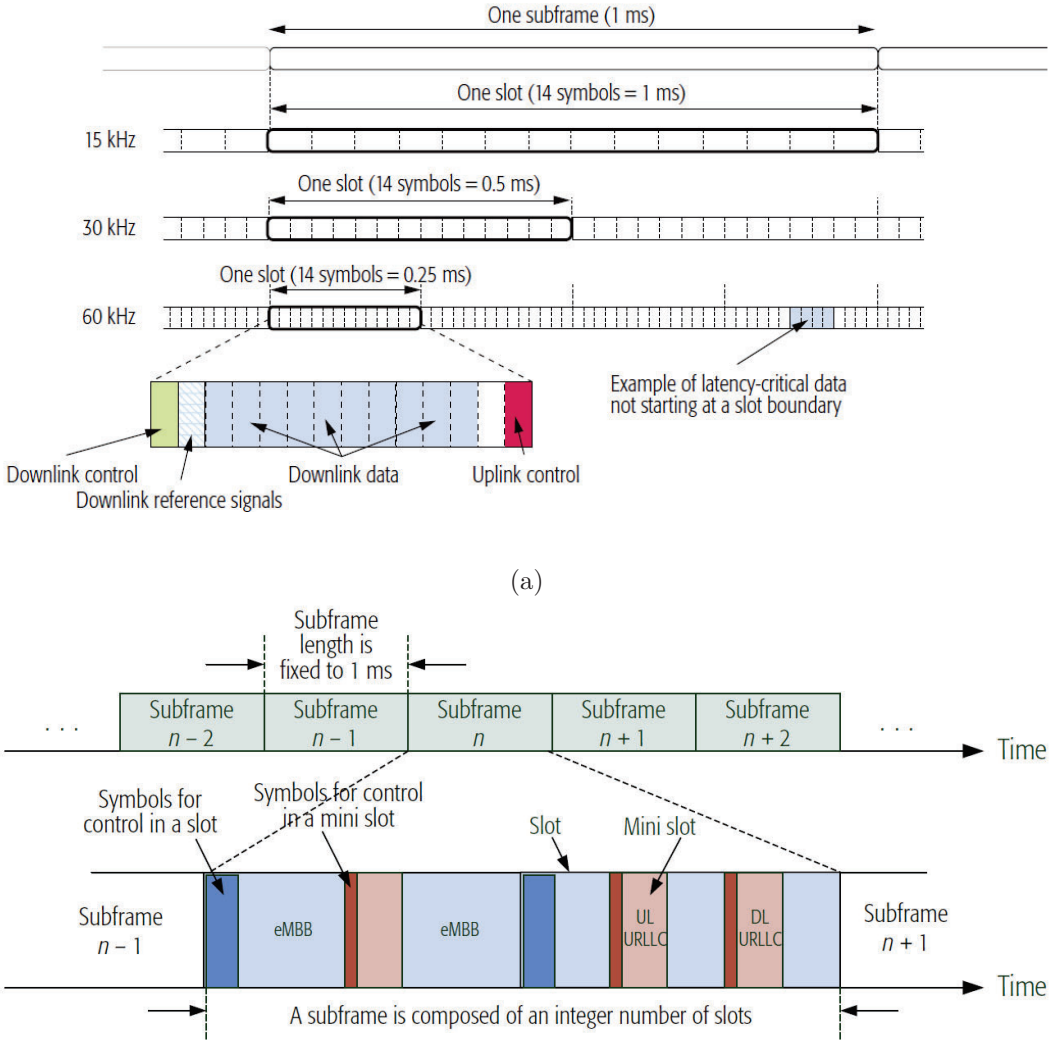

FIGURE 2.29: 5G NR: a) frame structure (assuming TDD), and b) "mini-slot" illustration within a subframe, according to [79, 84] (images extracted from [79, 84]).

last one are considered for control purposes [84], and unlike in 4G, cell-specific (reference) signals are only transmitted if there is data ready to transmit. As consequence, the energy efficiency of the overall network is improved and interference reduced. In addition, 3GPP has introduced the concept of "mini-slot" in the NR PHY layer [85], as it is illustrated in Fig. 2.29b, to enable a ultra low latency communication system. To this extent, small size packet transmissions aiming URLLC applications, which are shorter than regular slot durations, can be enabled at any OFDM symbol. In order words, such feature allows the base station to immediately allocate resources for very low latency services [78, 79, 84]. According to [77], a "mini-slot" can be composed of either 7, or 4 or 2 OFDM symbols, which also be used to convey control data before transmitting the payload, as it is depicted in Fig. 2.29b.

In sum, this disruptive feature can bring the following capabilities into the 5G network [78, 79]:

- In URLLC applications, transmissions can start immediately without waiting for the beginning of a slot boundary;
- In unlicensed spectrum communications, after listen-before-talk, necessary to ensure that the intended radio channel is not occupied for other services, the communication can be prompt established, once again there is no need to wait for the beginning of a slot boundary;
- Particularly at mmWave band communications, a few OFDM symbols might be enough to carry the majority of the payload packets.

As aforementioned, time slot duration, in the NR frame, decreases with the increase of the sub-carrier spacing. Relation between this numerology with OFDM and CP symbol durations, along with number of slots per frame and their duration is summarised in Table 2.10. Since the ratio between Cyclic Prefix (CP) and OFDM symbol samples is kept for all numerologies, CP is longer when $\Delta f = 15$ kHz ($4.69\mu s$) than when $\Delta f = 60$ kHz ($1.17\mu s$). This is particularly relevant when sub-6 GHz carriers are considered, since at mmWave, electromagnetic wave propagation from very directive antennas is dominated by the LOS path and first order reflections from strong reflecting materials, and thus, multipath delay spread lower when compared to lower frequencies [56, 83]. Therefore, longer CP duration is less crucial at mmWave carriers. In fact, this is one of the reasons sub-carriers of higher than 60 kHz were selected for the NR high frequency band, as verified in Fig. 2.28. In terms of Fast *Fourier* Transform (FFT) size and number of active sub-carriers, the maximum values, established in [86], are 4000 and 3300, respectively. Notwithstanding, in case the number of active sub-carriers is reduced, smaller FFT size might be considered [78].

In terms of air radio interface, Orthogonal Frequency-Division Multiple Access (OFDMA) is also considered (at least in Rel. 15), where a time/ frequency resource block is assigned to one user only [84]. In this context, resource elements are arranged into Physical Resource Blocks (PRBs), where each PRB consists of 12 sub-carriers. Since multiple sub-carrier numerologies are supported in 5G NR, different range of PRBs bandwidth are also supported. Relation between sub-carrier spacing and PRB bandwidth is given in Table 2.11. Remarkably, when $n = 5$, the bandwidth of a single PRB is higher than the 5 MHz LTE's channel.

Finally, a comparison of the main operating parameters of LTE versus 5G NR, according to [77], is given in Table. 2.12. Particularly, the adoption of LDPC for the payload and polar codes for control signals in the NR's PHY layer, rather than turbo codes and Tail-Biting Convolutional Codes (TBCC) as in LTE, respectively, will improve

Table 2.10
Relation between sub-carrier spacing with OFDM and CP symbol durations, along with number of slots per frame and their duration in the 5G NR standard, according to [78, 83].

Δf	**15 kHz**	**30 kHz**	**60 kHz**	$n = 3, 4, ...$
OFDM symbol duration [s]	66.67μ	33.33μ	16.67μ	$66.67/2^n\mu$
Cyclic prefix duration [s]	4.69μ	2.34μ	1.17μ	$4.69/2^n\mu$
OFDM with CP [s]	71.35μ	35.68μ	17.84μ	$71.35/2^n\mu$
Nº OFDM symbol/slot	14	14	14	14
Slot duration [s]	1000μ	500μ	250μ	$1000/2^n\mu$
Nº slot/subframe	1	2	4	2^n
Nº slot/frame	10	20	40	$2^n \times 10$

Table 2.11
Relation between sub-carrier spacing and PRB bandwidth.

n	Δf **[kHz]**	**PRB Bandwidth [kHz]**
0	15	180
1	30	360
2	60	720
3	120	1440
4	240	2880
5	480	5760

the system data rate and both reliability and latency [83]. Moreover, 5G NR will support BF particularly when the mmWave band is used. To this extent, it is expected that massive MIMO antenna configurations, which employs hundreds of radiating elements, are deployed in 5G NR systems [79].

2.4.2 Next generation of 60 GHz communications: IEEE 802.11.ay

While WiGig specifications enabled multi-Gigabit/s wireless communications, as introduced in Section 2.3.1, recent applications, such as VR/ AR and wireless backhauling, are requiring even greater demand for higher system throughput, reliability and lower

Table 2.12
Comparison of the main operating parameters of LTE versus 5G NR, according to [77].

	LTE	**5G NR**
Max. channel BW [MHz]	20	50, 100, 200, 400
Sub-carrier spacing [kHz]	15	15×2^n
Waveform	OFDM (DL) SC-FDMA (UL)	OFDM (DL); OFDM /DFT-OFDM (UL)
Max. nº of active sub-carriers	1200	3300
Subframe length [ms]	1	1
Latency [ms]	10	1
Slot length [nº OFDM symbols]	7	14 2, 4, 7 ("mini-slot")
Channel coding	Turbo code (data) / TBCC (control)	LDPC (data) / Polar codes (control)
Initial access	No BF	BF
Max. MIMO config.	8×8	8×8
Duplex scheme	FDD, static TDD	FDD, Dynamic TDD

latencies [87]. In this context, IEEE 802.11 TG is currently developing the IEEE 802.11ay standard, stating that:

> "Task Group ay is expected to develop an amendment that defines standardized modifications to both the 802.11 physical layers (PHY) and the 802.11 medium access control layer (MAC) that enables at least one mode of operation capable of supporting a maximum throughput of at least 20 Gigabits per second, while maintaining or improving the power efficiency per station (STA). [88]"

The proposed use cases for the IEEE 802.11ay standard are summarised in Table. 2.13, along with the required propagation condition, system throughput and topology for each one, based on the information reported in [89]. Comparing Table 2.5, typical WiGig device configurations, with Table 2.13, it is clearly seen that data will be delivered faster and in a longer range. Also, unlike IEEE 802.11ad, this new standard will be not only addressing communication systems over indoor environments, but also enabling tens of Gigabit/s communications over outdoor scenarios, where both Peer-to-Peer (P2P) and Point-to-Multi-Point communication (P2MP) transmissions, are considered to meet the requirements of people's daily information exchange and entertainments [90].

In sum, IEEE 802.11.ay will be an evolution of both PHY and MAC layers of the current IEEE 802.11ad (WiGig) standard, using the same unlicensed 60 GHz band spectrum. For this reason, backward compatibility and coexistence of IEEE 802.11ay

Table 2.13
Summary of the proposed use cases for the IEEE 802.11.ay, according to [89].

Applications and Characteristics	Propagation Conditions	Throughput [Gbps]	Topology
Ultra short range comm.	Indoor: LOS only with range < 10 cm	≈ 10	P2P
8k UHD streaming	Indoor: LOS/ NLOS with range < 5 m	> 28	P2P
AR and VR	Indoor: LOS/ NLOS with range < 10 m	≈ 20	P2P
Data centre Inter-rack connectivity	Indoor: LOS only with range < 10 m	≈ 20	P2P P2MP
Video/Mass Data distribution	Indoor/outdoor: LOS/NLOS with range < 100 m	> 20	P2P P2MP
Mobile Wi-Fi offloading	Indoor/outdoor: LOS/NLOS with range < 100 m	> 20	P2P P2MP
Mobile Fronthauling	Outdoor: LOS with range < 200 m	≈ 20	P2P P2MP
Office Docking	Indoor: LOS/NLOS with range < 3 m	≈ 13.2	P2P P2MP
Backauling in single hop multi-hop	Outdoor: LOS with range < 1 km with range < 150 m	$\approx 2 - 20$	P2MP P2P

with existing deployed 60 GHz devices will also be ensured [87]. According to [87], IEEE 802.11ay will include unique and disruptive design parameters, in comparison to the WiGig one, namely: channel bonding, and improved channel access, and enhanced MIMO BF capabilities. With this technologies, IEEE 802.11ay is expected to enable a Wi-Fi device to achieve 100 Gbps of data rate transmission, while reaching distance over 300 m. These main proposed enhancements to the current WiGiG standard are discussed below. Finally, specifications for this next generation of 60 GHz Wi-Fi standard are expected to be released in November 2019 [91].

Channel bonding and aggregation

As seen in Section 2.3, channelisation of IEEE 802.11ad specifies four single channels with 2.16 GHz of bandwidth, over the frequency from 57 up to 66 GHz. Nonetheless, such channel bandwidth is not enough to provide the data rate for the usage cases envisaged

for IEEE 802.11.ay, as it is outlined in Table 2.13. To achieve such requirements, IEEE 802.11 TG has decided to include mechanisms for channel bonding and aggregation [87]. This is, the creation of a wider channel from multiple relatively narrow channels. For instance, a two-channel bonding would result into a 4.32 GHz channel, which can enable a maximum data rate of 25.92 Gbps, when considering 64-QAM. Consequently, if a four-channel bonding is considered instead, this rate would be increased to 51.84 Gbps. In this context, channelisation expected for the IEEE 802.11ay standard is illustrated in Fig. 2.30, where a continuous spectrum of approximately 13 GHz is divided into channels of 2.16, 4.32, 6.48 and 8.64 GHz. Moreover, the centre frequency of the narrow channels are: 58.32, 60.48, 62.64, 64.80, 66.96, and 69.12 GHz [87]. Similarly, carrier aggregation utilises the combination of multiple channels, but there is a spectrum gap between them [87]. Nevertheless, control and management of the network can only be performed in single channels, also known as primary channel, which is common to all devices that are members of a particular base station [90].

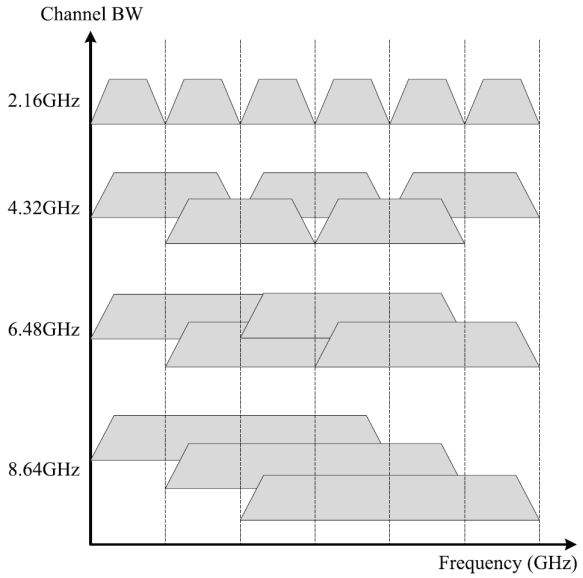

FIGURE 2.30: Channelisation envisaged for the IEEE 802.11ay standard (image extracted from [90]).

PHY and MAC layers: overview

Another difference between both IEEE 802.11ay and IEEE 802.11ad standard, is that the former one does not support SU/ MU MIMO technologies [90], it only addresses BF mechanisms. However, IEEE 802.11ay will include both BF and multiplexing gains. This

will increase even more the network capacity. For example, the boost in terms of data rate, due to a four-channel bonding technology, would ideally be boosted to 414.72 Gbps. This considering eight simultaneous streams modulated with 64 QAM, towards a UE (SU MIMO). Therefore, improvements and consideration of new algorithms in the design of both PHY and MAC layers from IEEE 802.11ad are necessary.

The main innovative features of this new standard are highlighted as follows [87, 90]:

- Inclusion of pre-coding schemes at the baseband for efficient digital/hybrid beamforming architectures;
- Support of channel bonding, channel aggregation and SU/ MU MIMO, considering both OFDM and SC transmission schemes;
- Addition of channel access for MIMO and multiple channel operations (channel allocation) in the MAC layer, addressing both spatial sharing and interference mitigation technologies;
- Consideration of polarisation diversity;
- Design of efficient and intelligent beam tracking methods. If the BF training algorithm requires significant amount of time to stablish the more appropriate directional communication link, the quality of service is severely compromised.

The generic packet structure that is expected to be adopted by the IEEE 802.11.ay is depicted in Fig. 2.31. As it can be seen from this figure, such frame is similar to the one illustrated in Fig. 2.8a for WiGig systems. This is, the inclusion of a Non-EDMG portion (refers to devices that are not compatible with IEEE 802.11.ay), is considered to guarantee the interoperability among WiGig devices [87]. Once again, Short Training Field (STF) and Channel Estimation Field (CEF) refer to the necessary sequences needed for synchronisation and channel estimation purposes, respectively. In other words, EDMG packet portion will include all the necessary fields to support the additional new features (cited above) of IEEE 802.11.ay. In particular and according to [87], *Header-A* sequence will carry information regarding the signal bandwidth, modulation, coding scheme and number of spatial streams, while *Header-B* will enable the MU MIMO system capability. In addition, Training field (TRN) field will be a new redefined training sequence to enable more flexible and efficient BF algorithms for TX/ RX beam tracking. Finally, similar to IEEE 802.11ad, this new version of 60 GHz Wi-Fi technology will also adopt both OFDM and SC transmissions schemes for the payload, with QAM orders up to 64.

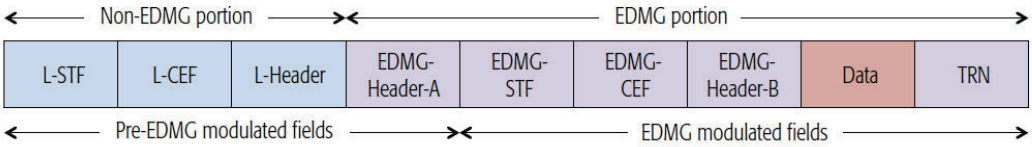

FIGURE 2.31: Block diagram of the IEEE 802.11ay's standard packet structure (image extracted from [87]).

2.5 Related works: state of the art on mmWave testbed system specifications

The 5G network minimum technical performance specifications have already been established in [81], and are summarised in Table 2.14, in particular for eMBB and URLLC usage cases. For example, the peak data rate and spectral efficiency in DL is 20 Gbps and 30 bps/Hz, respectively. For UL connection, values are half the DL ones. User data rate and average spectral efficiency should be 100 Mbps (DL) and 50 Mbps (UL), and 7.8 bit/s/Hz (DL) and 5.4 bit/s/Hz, respectively, in a dense urban environment. System bandwidth should be at least 100 MHz, and the spectrum ranging from 24 to 100 GHz [81].

As discussed in Section 2.4.1, 5G is envisaged to deliver hundreds MHz of continuous spectrum and multi-Gbps transmission rates to mobile devices where, to fulfil such requirement, mmWave frequency spectrum will be one of the enabling key technologies [42]. In this context, it has been conducted a state of the art on mmWave testbeds available in the scientific literature, in particular at 28 and 60 GHz, having into consideration the KPI values given in Table 2.14. For example, in [93] a prototype testbed, see Fig. 2.32, was developed to mimic an unidirectional transmission from an access point to an UE device at 60 GHz. Particularly, the NI PXIe 1085 [94] Commercial Off-The-Shelf (COTS) baseband unit solution was considered, which includes all the necessary components for the design of a customised wireless communication system. It is composed of two-channel 8 bit 1.5 GSPS ADC, two-channel 14 bit 1.25 GSPS ADC and a FPGA module. With this, it was implemented an Over-The-Air (OTA) SC scheme, with bandwidths up to 750 MHz. For system performance assessment RX was placed in different distances from the TX, under LOS scenario and in an indoor meeting room environment, as it is shown in Fig. 2.33a. Under such conditions, the system's QoS was assessed in terms of the received scatter constellation plots for: BPSK, Quadrature Phase-shift Keying (QPSK) and 16-QAM, and SNR. Results for a link distance of 1 m are depicted in Fig. 2.33b.

Similarly, in [95], a SC 60 GHz short-range testbed system is presented. Particularly in this case, authors have build a complete customised system, from the baseband unit

Table 2.14
Summary of the minimum technical performance requirements of IMT 2020 for 5G, according to [81].

KPI	Usage case	Values
Peak data rate	eMBB	DL: 20 Gbps UL: 10 Gbps
Peak spectral efficiency	eMBB	DL: 30 bps/Hz UL: 15 bps/Hz
User experienced data rate	eMBB	DL: 100 Mbps UL: 50 Mbps
5 % User spectral efficiency	eMBB	DL: 0.3 bps/Hz, UL: 0.21 bps/Hz* DL: 0.225 bps/Hz, UL: 0.15 bps/Hz† DL: 0.12 bps/Hz, UL: 0.045 bps/Hz**
Average (TRxP) spectral efficiency††	eMBB	DL: 9 bps/Hz, UL: 6.75 bps/Hz* DL: 7.8 bps/Hz, UL: 5.4 bps/Hz† DL: 3.3 bps/Hz, UL: 1.6 bps/Hz**
Area traffic capacity	eMBB	DL: 10 Mbps/m^{2}*
User plane latency	eMBB URLLC	eMBB: 4 ms URLLC: 1 ms
Control plane latency	eMBB URLLC	eMBB: 20 ms URLLC: 20 ms
Connection density	URLLC	1 M devices per km^2
Reliability	URLLC	$1 - 10^{-}5$ success probability
Mobility	eMBB	up to 500 km/h
Mobility interruption time	eMBB URLLC	0 ms
Signal bandwidth	eMBB	$>$ 100 MHz# up to 1 GHz§

* In an indoor Hotstop environment;
† In a dense Urban environment;
** In a rural environment;
†† Average number of data bits that can be sent per unit time, unit frequency bandwidth, cell, and Transmission Reception Point (TRxP) [92];
# below 6 GHz carrier frequencies;
§ above 6 GHz carrier frequencies.

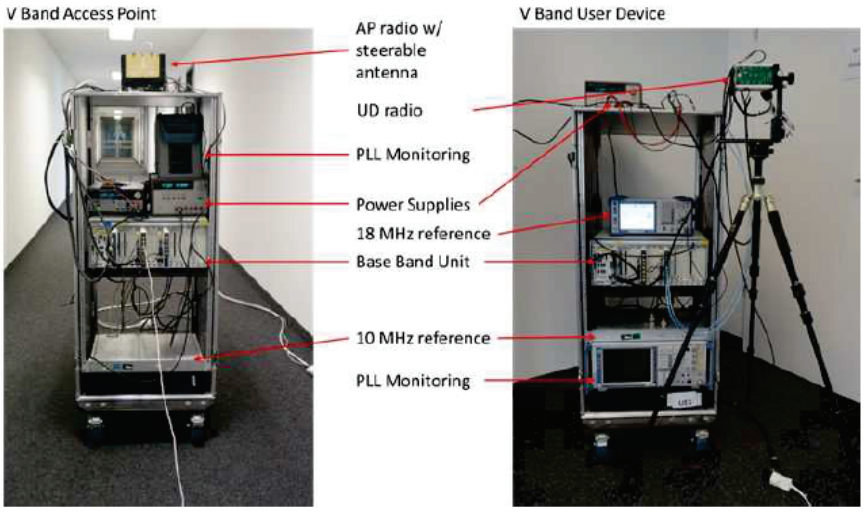

FIGURE 2.32: Picture of both TX/ RX prototypes developed in [93] (image extracted from [93]).

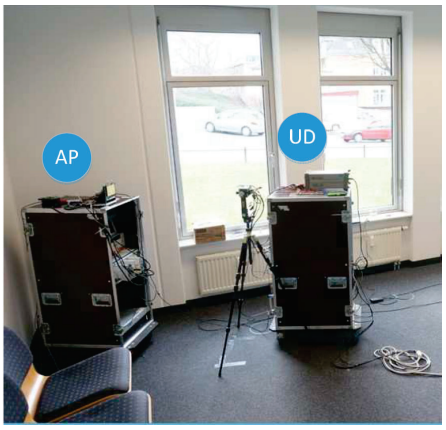

(a)

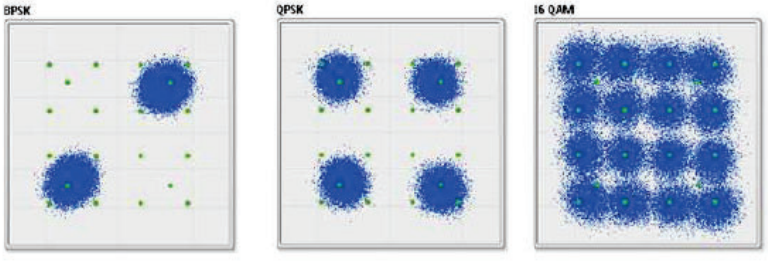

(b)

FIGURE 2.33: MiWaveS tesbed evaluation performance: a) picture of the measurement setup environment, and b) received scatter constellation plots for: BPSK, QPSK and 16-QAM, at a link distance of 1 m (images extracted from [93]).

to the RF front-end. For example, the transmitter chain is composed of a 12 GHz I/Q quadrature modulator, a 48 GHz up-conversion mixer, and a PA, designed in a single printed circuit board, as it is depicted in Fig.2.34a. Performance of the transceiver was evaluated in terms of received QPSK scatter constellation plots, and EVM measurements. Results at a link distance of 6 m are depicted in Fig. 2.34b.

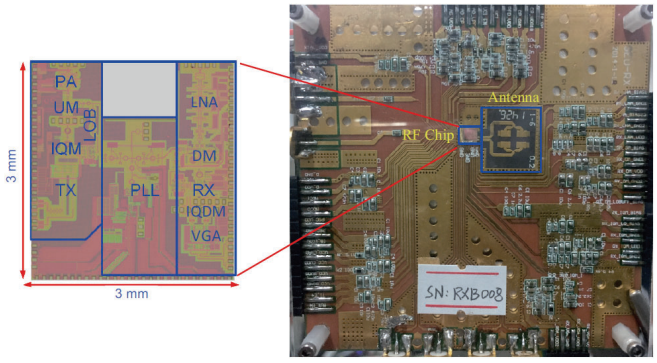

(a)

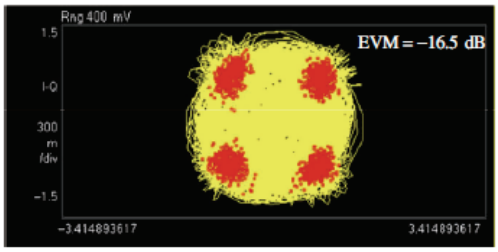

(b)

FIGURE 2.34: Developed testbed in [95]: picture of the transceiver, and b) received scatter constellation plots for: QPSK, at a link distance of 6 m (images extracted from [95]).

The aforementioned testbeds, are just two examples of mmWave prototype radio system were spectral efficiency is rather limited (maximum QAM constellation order is 16-QAM). Nevertheless, a list of the most relevant mmWave testbeds available in the literature is presented in Table 2.15, along with their system specifications. Each testbed/ prototype is summarised in terms of its affiliation, frequency band, base-band real-time signal processing, transmission scheme, system bandwidth, whether the transmission is over-the-air or not, and both system's maximum spectral efficiency per stream (not considering MU-MIMO) and SNR. Whenever the SNR was not presented, this has been extrapolated from the minimum achieved EVM in the system performance. Testbed systems listed in Table 2.15 demonstrate that it is possible to utilise the mmWave spectrum to successfully establish a radio link. However, only the testbeds reported in

[61, 96–98] consider a modulation bandwidth higher than 100 MHz, real-time baseband processing, and consider OFDM (the adopted waveform for the 5G New Radio (NR) [79]) as the transmission scheme. Moreover, it is evident that when using the 60 GHz band, there is a lack of testbeds which comply with the above specifications. Nonetheless, in all reported testbeds, spectral efficiency is rather low, i.e., the maximum QAM order is 64. Even in the listed 28 GHz testbed systems, such requirement should be further improved to meet the DL specification of 7.8 bit/s/Hz envisaged for 5G.

Finally, from this table 2.15, it is evident that the *USW/IT* 60 GHz OFDM testbed (outcome of the research work presented in this thesis) meets the minimum technical performance requirements of IMT-2020 in terms of average spectral efficiency. Remarkably, despite the existence of a large number testbeds published in the literature, to the best of author acknowledge, at the time of this thesis submission, our testbed is the only one that fulfils the gap in terms of spectral efficiency. In other words, no other prototype system can process a signal B of 150 MHz in real-time, with modulation orders up to 256 QAM, using OFDM as transmission scheme in over-the-air scenario. The development and implementation of this wireless radio system prototype, will be documented throughout the thesis, in particular in Chapter 4.

2.6 Interim conclusions

This chapter presents an extensive literature review addressing the most relevant topics for this research work. It reviews the current wireless communication standards, giving particular emphasis to the role of mmWave spectrum in enabling multi-Gigabit/s data rates, which are a demand in the enhanced mobile broadband 5G usage case. Moreover, the NR PHY layer is extensively described, and a comparison, with the 5G testbed proposed in this thesis with the most relevant mmWave radio prototype systems available, in the scientific literature, is carried out.

A fundamental overview of electromagnetic wave propagation in the millimetre wave is introduced. It was verified that both additional path losses due to atmospheric absorption and rain can induce significant additional excess loss per km, in relation to the *Frii's* space loss equation, particularly at frequencies of 60, 120, and 180 GHz. Therefore, wireless systems considering such bands for data transmission, are limited to short-range communications. Nevertheless, at other frequency bands, such as the 28 GHz, those additional losses are negligible. Besides this, it is also documented that in general, the use of the mmWave spectrum leads to the reduction of the physical dimensions of the antenna, which consequently reduce its aperture area, and leads to the generation of sharper beams. As consequence, the movement of people or other obstacles can easily block the specular propagation path, resulting in relatively poor

Table 2.15
Current mmWave testbeds.

Ref.	Affiliation	Freq. Band [GHz]	Main Features					
			Transmission scheme	BW [GHz]	real-time	over the air	MAx. Spectral eff. [bit/s/Hz]	Max. SNR [dB]
[99]	Tokyo Institute of Technology	**60**	OFDM	2.16	no*	no	6	25.8
[100]	OpenMili	**60**	OFDM	0.0005	yes	yes	1	30
[95]	UESTC	**60**	SC	2.16	yes	yes	2	16.5
[96]	Samsung/ NTT DOCOMO	28	OFDM	0.8	yes	yes	4	21† / <28††
[97]	NTT DOCOMO	28	OFDM	0.8	N/A	yes	6	N/A
[61]	ONRGET	28	OFDM	0.125	yes	yes	6	28
[98]	mmMAGIC	28	OFDM	0.12288	yes	yes	4	28
[98]	mmMAGIC	82	OFDM	0.12288	yes	yes	4	24
[93]	MiWaveS	**60**	SC	0.75	yes	yes	4	16.5
[101]	HUB/UFAF	**60**	OFDM	0.625	no*	yes	1	N/A
[102]	KTH / BLUEWAVE	**60**	OFDM	0.022	no*	yes	2	13.5
[103]	UG	**60**	SC	0.035	yes	yes	4	28.5
[104]	Nokia /NTT DOCOMO	73.5	SC	1	yes	yes	4	18
[J2]	**USW/IT*** tesbed**	**60**	**OFDM**	**0.156**	**yes**	**yes**	**8**	**37.81**

(*) OFDM TX/RX processing is performed off-line by an host PC; (†) Outdoor environment;
** With carrier aggregation of five channels; (††) Indoor environment; (***) Testbed developed in this work;

QoS. To this end, either multi-beam or beam-steerable antennas must employed, at both TX/ RX ends, to enable the support of mobile communications.

Subsequently, current multi-Gigabit/s wireless communication standards at 60 GHz, are detailed in Section 2.3, targeting in particular indoor short-range applications. Although both IEEE 802.15.3c and IEEE 802.11ad standards have slightly different MAC and PHY layers specifications, they provide the same network's throughput and delay. However, IEEE 802.11ad seems to be the preferable choice, from a industry point of view, since offers add-on features of coexistence with other systems operating in the 60 GHz band and backward compatibility. Due to this fact, it is highly likely that IEEE 802.11ad will become the most widely deployed 60 GHz technology for indoor environments, in a very close future. Nevertheless, if the purpose of the radio link is to stablish a private and secure multi-Gigabit/s WPAN, IEEE 802.15.3c seems to be a better solution. There is no need for a network infrastructure, i.e., communication is only established within the local devices added by the PNC.

After having introduced the current multi-Gigabit/s specifications, a literature review on network architectures envisaged for the next generation of mobile networks, in particular for 5G, is outlined. In this context, it is expected that 5G will integrate new radio air interfaces and spectrum together with current wireless technologies, such as LTE, and Wi-Fi. To this end, new applications, namely: V2V, V2I and M2M communications, where ultra low system latency is a demand, will be enabled. Additionally, the role of mmWave spectrum in increasing the overall capacity of mobile radio cells, at relatively high link distances, is addressed. In this matter, it is study the deployment of phantom cells to increase the area spectral efficiency of a radio cell, and the support of multi-Gigabit/s of transmissions towards mobile equipments. In this context, two end-to-end mmWave fully adaptive BF MIMO prototypes, which can be used as mmWave sites in a phantom network, are outlined. One addresses an hybrid architecture solution and other a digital one, and despite different architectures, both systems demonstrate to provide tens of Gigabit/s data rates and few hundred meters of cell coverage radius. However, the support of mobility is a limitation in these systems, where target UEs should travel at speeds below 8 km/h, in particular, when hybrid architecture system is considered. Finally, the reliability of mmWave handset technology solution is also evaluated. In this regard, a 60 GHz phase array chip-set solution is also presented. It is verified that when this antenna is connected to the processor engine of a cutting edge mobile phone, data rates higher than 1 Gbps are achieved. Notwithstanding, it is also proved that the major limitation of such system is the effect of the human interaction with the handset, which leads to significant attenuations of the transmitted signal level. In sum, mmWave technology can seen as a promising alternative to the sub-6 GHz bands, where both mmWave base stations and UE equipments (with further

improvements on the mobility support capability) will bring disruptive advantages to the mobile network.

A massive inter-connection of users and devices is expected in the upcoming network generation, merging the key applications in a globalised service including: IoT and M2M communication, Gigabit/s wireless connectivity, Tactile Internet, CRAN and HetNets. To meet such demands, 3GPP is currently developing the 5G NR, which is expected to be deployed in 2020. Nevertheless, Rel. 14 and Rel. 15 are already available, and detailed in Section 2.4. In sum, the main innovative features of 5G NR are the employment of scalable OFDM sub-carrier spacing and bandwidth, instead of a single waveform numerology, and the consideration of the mmWave spectrum. While the first, allows the NR to adjust the waveform settings depending on the 5G usage case (target latency, and data rate) and channel condition, i.e, multipath delay spread, the second allows signal transmission with higher bandwidth (in the sub-6 GHz band spectrum is a very scarce resource).

Finally, in Section 2.5, a detailed state-of-the-art literature review is presented on mmWave testbeds, including a comparison of their system specification with the minimum technical performance requirements defined by IMT-2020 for 5G. The references presented in this review are summarised in Table 2.14. Special attention was given to the capability of those systems to deliver spectral transmissions efficiency higher than 7.8 bit/s/Hz. It is evident (at the time of this thesis writing) that the *USW/IT*, to the best of author acknowledge, appears to be one of the most promising and feasible testbeds to meet the 5G requirements, as it will be detected in the subquent chapters.

This page is intentionally left blank.

CHAPTER 3

Proposed simulation framework for 60 GHz radio communications

The performance assessment of either existing or future wireless communication systems can be a very time-consuming task, since it, usually, requires the development of hardware prototypes and carry out extensive indoor/ outdoor field experiments. However, such can be significantly reduced by the consideration of an accurate simulation tool. In this context, in this work, it has been developed a simulation framework capable to predict the performance of the most relevant transmissions schemes, namely: OFDM, SC-FDE and FBMC, under both channel and RF impairments at 60 GHz. Particularly, obtained results, herein, were an important guidance for the development of the proposed mmWave real-time 5G testbed, addressed in Chapter 5, and were disseminated in six paper publications, corresponding to the work performed in the following sections of this chapter.

The implementation of a realistic simulation tool using *Matlab/ Simulink*, an user-friendly graphical environment which enables the rapid development of models from an Intellectual Property (IP) block based library [105], for mmWave wideband communication systems, is addressed. The implementation is based on the 60 GHz PHY layer specifications of the IEEE 802.15.3c standard [40], following the work reported in [106–108]. From Fig. 3.1, it can be seen the required *Simulink* blocks to develop the IEEE 802.15.3c's OFDM mode. Nevertheless, the inherent simulator's modular architecture enables the study of customised waveforms (not defined in this standard), and the consideration of several different channel and RF impairments conditions, which are essential for appropriate RF system design and modelling. In addition, the tool allows several parametric studies such as, the use of different order modulations, lengths of CP and FFT size. As outputs, the system delivers Bit Error Rate (BER), SNR, Peak Signal-to-Noise Ratio (PSNR) (when uncompressed video frames are transmitted) metrics, and operating range.

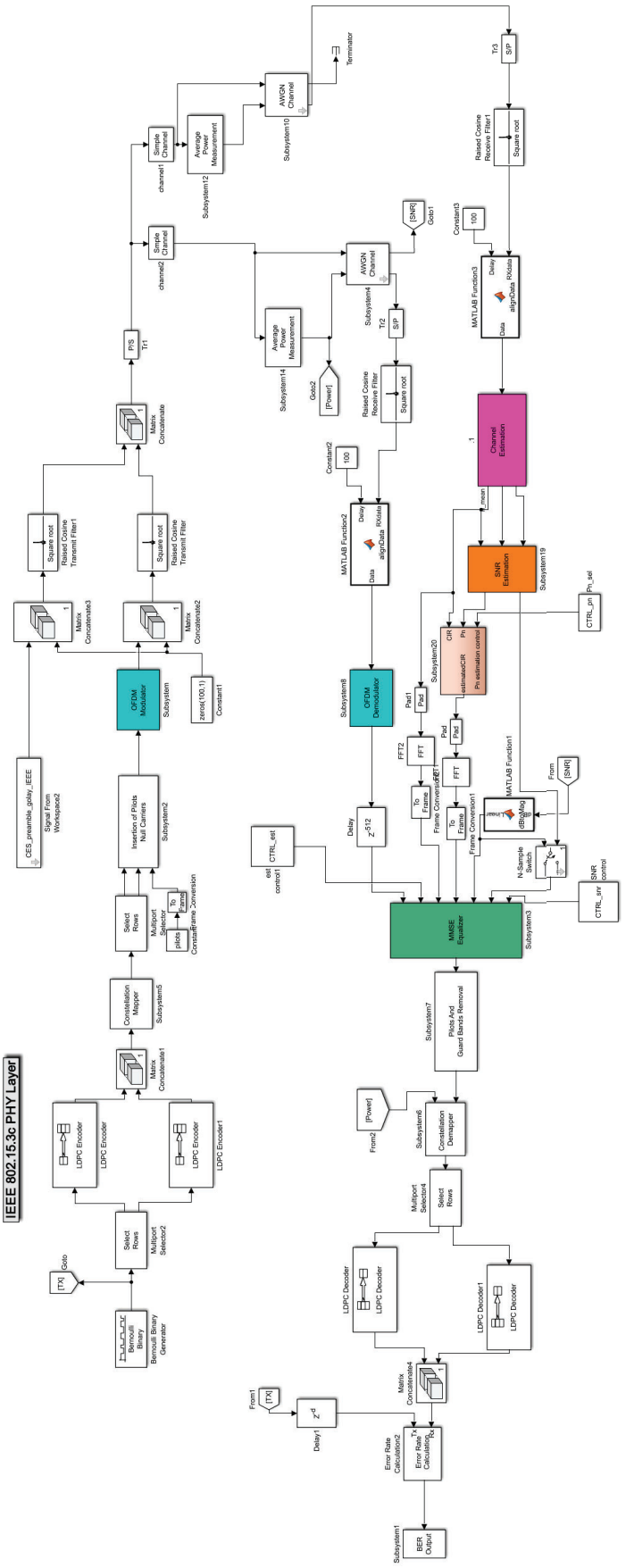

FIGURE 3.1: Simulation framework for OFDM communications, based on the IEEE 802.15.3c standard.

3.1 Introduction to OFDM, SC-FDE and FS-FBMC

Multi-carrier modulation such as OFDM and Filter Bank Multi-Carrier (FBMC) can be described as synthesis-analysis filter bank [109], where at the transmitter side, the synthesis filter bank comprises of parallel transmit filters and, at the receiver, the analysis filter bank is composed by matched receive filters.

The prototype filter, presented in Fig. 3.2, is usually defined in the time domain by $p_{Tx}(t)$ and by $p_{Rx}(t)$, at the transmitter and at the receiver, respectively, is applied for each individual M sub-carrier of a multi-carrier system [109]. In the time domain, this is accomplished by an Inverse Fast *Fourier* Transform (IFFT) operation, present in both OFDM and FBMC systems, as it is depicted in Fig. 3.3a. In the frequency domain this corresponds to the frequency offset of f_k between adjacent sub-carriers [10].

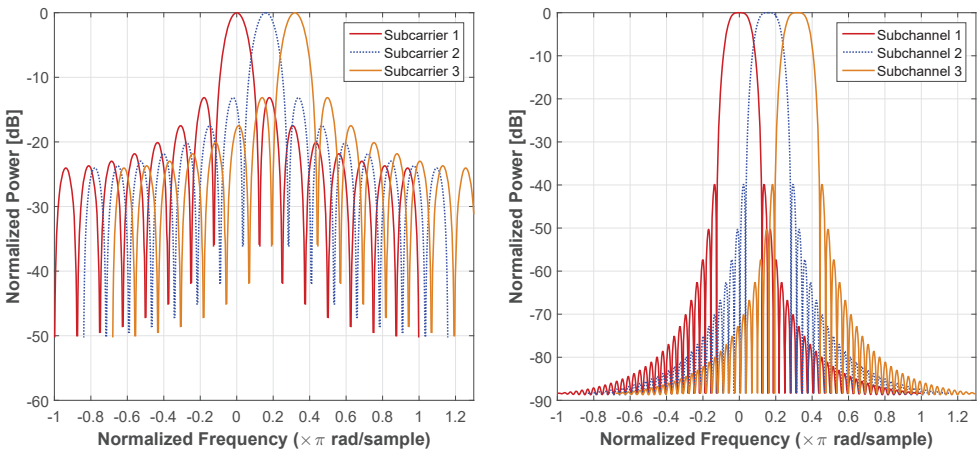

(a) (b)

FIGURE 3.2: Frequency response of a *Nyquist* filter used as prototype filter for: (a) OFDM and (b) FBMC, in frequency domain, for 3 consecutive sub-carriers.

Traditionally in an OFDM system, the prototype filters $p_{Tx}(t)$ and $p_{Rx}(t)$ have the form of a rectangular window in time domain and cardinal sine function (sinc) in the frequency domain according to the properties of the *Fourier* transform (discussed in section A.3.1). This, leads to undesirable frequency responses with large side lobes, characteristic of the mathematical sinc function [109]. In this context, OFDM output signal is considered as a linear sum of M independent streams transmitted over M orthogonal sub-carriers. In the input data stream, bits are mapped to constellation symbols through a QAM, and thus, modulated and demodulated applying the IFFT and the FFT, respectively.

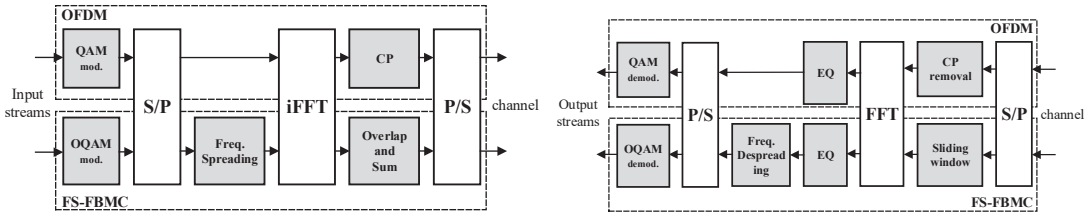

(a) (b)

FIGURE 3.3: Generic block diagrams of: (a) transmitter and (b) receiver, for both OFDM and FS-FBMC waveforms, illustrating the blocks common to both schemes (hatched white).

The transmitted OFDM signal, in time domain, can be expressed as (3.1) [19].

$$x(t) = \frac{1}{\sqrt{M}} \sum_{k=0}^{\infty} p(t - kT_s) \sum_{m=0}^{M-1} X_m(k) e^{j2\pi f_m (t-kT_s)}, \tag{3.1}$$

where $X_m(k)$ is the frequency domain complex symbol sequence, transmitted on the m^{th} sub-carrier of the k^{th} OFDM symbol, with the corresponding frequency $f_m = m/T_s$, M is the total number of sub-carriers, and T_s is the OFDM symbol period. In the time domain, $p(t)$ is a rectangular window defined by (3.2), which represents the prototype filter for OFDM.

$$p(t) = \begin{cases} 1 & if \quad 0 \leq t \leq T_s \\ 0 & other \end{cases}, \tag{3.2}$$

Equation (3.1) can be characterised in the discrete time domain [19] and represented by:

$$x(mT_s) = \sum_{n=0}^{M-1} X_n e^{j2\pi nm/M}, \tag{3.3}$$

where X_n defined from $n = 0, 1, ..., M-1$ is the complex sequence corresponding to a two-dimensional QAM constellation. From (3.3), one can note that a total of M QAM symbols are modulated by applying an IFFT of length M, corresponding to M active sub-carriers. This generates an OFDM symbol of M samples, in the time domain. In the receiver side, the FFT with the same length is used to demodulate the data symbols.

SC-FDE can be seen as a traditional digital transmission scheme in which data symbol is transmitted at a fixed symbol rate. However, equalisation is performed by a linear frequency domain equaliser on a block of data to minimise the ISI from the multipath [110], making this concept very similar to OFDM, as it can be verified in

Fig. 3.4. Evidently, the difference between both systems is mainly in the IFFT block placement, enabling both systems to operate on a dual-mode wireless system. This brings many advantages such as:

- Lower sensitivity to carrier frequency offset [111];
- When OFDM is employed in the downlink, most of the signal processing complexity is concentrated at the base station, when compared to SC-FDE;
- When SC-FDE is used in the UL, power efficiency on the user equipment is higher, reducing the cost of the power amplifier and enhancing battery life.

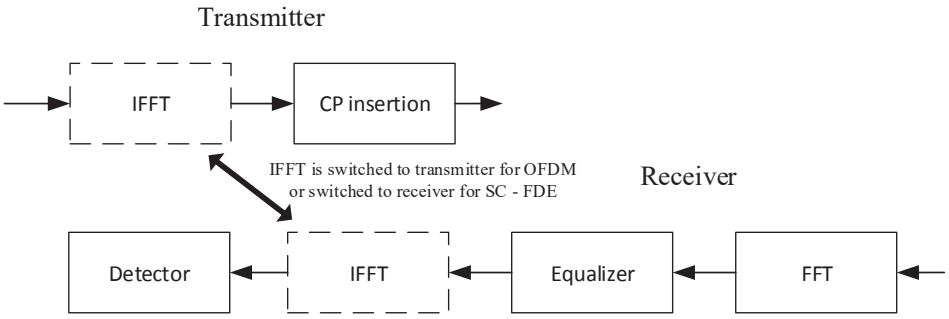

FIGURE 3.4: Conversion between OFDM and SC-FDE.

On the other hand, FBMC systems apply enhanced prototype filters [109, 112], with smoother edges or lower side lobes, in order to enhance the Out-Of-Band Emissions (OOBEs) and, consequently, reduce Inter-Carrier Interference (ICI). Furthermore, by employing such elaborated filtering techniques in addition to the Offset QAM (OQAM), the cyclic-prefix used in OFDM to mitigate multi-path phenomena i.e. reduce Inter-Symbol Interference (ISI), can be removed and sub-carriers can be better localised, improving consequently the spectral and power efficiency in FBMC waveform [10]. The use of an OQAM modulation in FBMC imposes that the real and imaginary part of the complex transmitted symbol are interleaved in time and frequency ensuring orthogonality at the transmitter as alternative to the CP used in OFDM [109].

FBMC can be implemented using two different architectures: Polyphase Network (PPN-FBMC) or Frequency Spreading (FS-FBMC). The first provides a time domain analysis of the filter banks, allowing a reduction of computational complexity by keeping the size of the FFT similar to the equivalent OFDM case [113]. Additional processing e.g. sub-channel multi-tap equalisation is carried out by the Polyphase Network (PPN) network introducing undesirable transmission delays [114]. On the other hand, filter

coefficients in FS-FBMC and therefore channel-equalisation are treated in the frequency domain. This increases the robustness and flexibility of the system at the cost of increasing the size of the FFT. Even with larger computational complexity (due to the larger IFFT/FFT operations) the FS-FBMC is easier to implement using FPGA hardware. For this reason, this work will only be focused on frequency FS-FBMC.

Besides the use of OQAM modulation to ensure symbol orthogonality, FS-FBMC also differs from OFDM by implementing an efficient pulse shaping through the use of a non-rectangular prototype filters with a length extending over multiple symbol periods in time domain, as previously mentioned.

The *Nyquist* filter implemented in this work [10, 113] satisfies the discrete time impulse response (3.4), and its H_k coefficients are detailed in (3.5). Moreover, K defines the overlapping factor of the filter and, σ^2 is the residential interference power due to the non-orthogonality of the carriers beyond the neighbouring sub-channels.

$$p(m) = 1 + 2\sum_{k=1}^{K-1} H_k cos(2\pi km/KM), \tag{3.4}$$

$$\begin{cases} K = 4 \\ H_0 = 1 \\ H_1 = 0.971960 \\ H_2 = 0.707 \\ H_3 = 0.235147 \\ \sigma^2 = -65\ dB \end{cases} \tag{3.5}$$

Consequently, the overlap in the time domain is caused on the transmitter side by spreading $P = 2K - 1$ coefficients over the IFFT OQAM input data. The frequency spreading technique alters the filter shape at the expense of increasing the size of the IFFT by $L = KM$, where M is the number of sub-channels, as illustrated in Fig. 3.5a. According to the latter, real and pure imaginary input parts of the symbols are mapped accordingly to each OQAM sub-channel, ensuring orthogonality between adjacent carriers since coefficients of the prototype filter are real [109]. In addition, to match the bit rates, the IFFT/FFT in FBMC runs at twice the rate as in equivalent OFDM case. Finally, at the output of the IFFT KM samples are buffered for each N_c FBMC symbol, delayed by $M/2$ and finally overlapped and summed for data transmission.

At the receiver side, Fig. 3.5b, to recover the transmitted data a sliding window operation is performed in the time domain, in which L points are selected every $M/2$

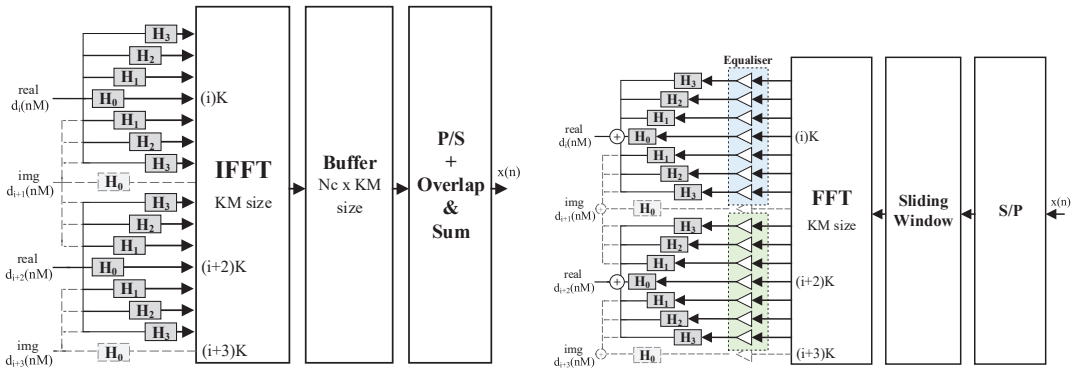

FIGURE 3.5: Block diagram of: a FS-FBMC (a) modulator and (b) demodulator.

samples to feed the FFT input. At the output of the FFT, data are recovered by despreading it according to (3.6), i.e. by summing the result of the multiplication of the FFT output by the filter coefficients.

For an ideal transmission, considering that the transmitter is connected back-to-back to the receiver, the delay of the FS-FBMC transceiver is estimated by the time that the memory of the FFT takes to be filled. However, if equalisation is considered to compensate for radio channel impairments, no additional delay is required since it is usually performed by applying an equaliser coefficient in addition to the despreading after the FFT operation [114].

$$\frac{1}{K}\sum_{k=-K+1}^{K-1}|H_k|^2 = 1, \tag{3.6}$$

To this extent, equation (3.6) is only valid when considering an ideal propagation channel. However, if in the presence of a multipath fading channel, an equaliser is needed before this mathematical operation. Thus, a post-FFT sub-channel equaliser is implemented in the frequency domain, as illustrated in Fig. 3.5b, where its coefficients (EQ) are just the inverse of the transmission channel response over KM sub-carriers, given by:

$$EQ(i+K+k) = \frac{1}{C(iK+k)} \tag{3.7}$$

3.2 RF models for 60 GHz communications

Behavioural modelling and simulation of non-linear systems play an important role in the evaluation of an overall communication system design and performance. In this section, modelling of both channel and RF impairments is presented.

3.2.1 Phase-noise and IQ imbalances

In typical radio communication systems operating at the sub-6 GHz band, the IQ mixing and up-conversion/ down-conversion stages are being replaced by software implementations, making the system less susceptible to hardware imperfections and non-linearities. However, at 60 GHz, performing up-conversion/ down-conversion by digital signal processing algorithms is impracticable, since a minimum sampling rate of 120 GSPS would be required to comply with the *Nyquist* criteria. Therefore, for such high frequencies, RF conversions are preferably implemented in hardware. For instance, oscillators for the RF conversions and IQ mixers for the QAMs are required, and thus their hardware imperfections should be taken into account in a mmWave system design. For example, it is very unlikely to have two oscillators operating at the exact same carrier frequency and thus distortion in the OFDM signal due to this effect is always present, causing ICI and Common Phase Rotation (CPR) [115], also known as phase-noise.

Since the characterisation and modelling of a mmWave Phase-Locked Loop (PLL) in terms of PN behaviour is beyond the scope of this research project. To the best of the author knowledge such is a research project itself, as it can be verified from the work documented in [116]. Therefore, in this work, it is adopted the 60 GHz PN models validated and suggested in [117]. By performing an interpolation of the data obtained from measurements at 60 GHz, it has been demonstrated that PN can be modelled as a high-pass filter, given by [117]:

$$PSD(f) = PSD(0)\frac{[1 + (f/f_z)^2]}{[1 + (f/f_p)^2]}, \tag{3.8}$$

where $PSD(0)$ is the low frequency phase noise, f_p is the pole filter frequency and f_z is the zero filter frequency. Thus, by considering different values of $PSD(0)$, the PN spectral density model can be adjusted for different competing Integrated Circuit (IC) technologies, such as 0.25 μm/0.13 μm Complementary Metal-Oxide-Semiconductor (CMOS) VCOs, 0.25 μm BipolarCMOS (BiCMOS) PLL with frequency tripler and a SiGe PLL, as is depicted in Fig. 3.6, according to [117].

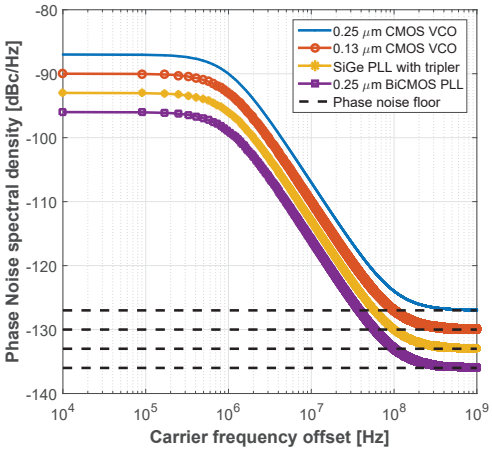

FIGURE 3.6: Power spectral density for different VCO and PLL CMOS/SiGe IC technologies.

As mentioned in Section A.2.4, IQ imbalances are described by the phase and amplitude offset between I and Q branches, in quadrature amplitude modulators/ demodulators. The complex baseband output signal, which suffers from this mismatch, can be defined by [19]:

$$y(t) = [\cos(\Delta\phi) + j\Delta g \sin(\Delta\phi)]x(t) + [\Delta g \cos(\Delta\phi) - j \sin(\Delta\phi)]x^*(t), \tag{3.9}$$

where $x(t)$ is the input signal, $x^*(t)$ is its complex conjugate and, Δg and $\Delta\phi$ are the gain and phase mismatches, respectively. From (3.9), it can be seen that $x(t)$ is interfered with its image signal, $x(t)^*$, causing attenuation and a rotation of the desired signal.

3.2.2 Power amplifier

As it is discussed in Section A.2.4, radio signals are subject to both amplitude and phase distortions when passing a power amplifier. Such distortions are visible not only in the signal bandwidth but also as out of band emissions. For a generic amplifier stage, the input signal $x(t)$, given by $x(t) = A(t)\cos[2\pi f_c t + \theta(t)]$, is amplified and characterised by $y(t) = G[A(t)]\cos(2\pi f_c t + \theta(t) + \psi[A(t)])$, where $G[A(t)]$ is the amplitude distortion, also known as Amplitude Modulation–Amplitude Modulation (AM-AM) and $\psi[A(t)]$ characterises the Amplitude Modulation–Phase Modulation (AM-PM).

Similarly to the PN phenomenon induced by mmWave PLL's, characterisation and modelling of a PA at these frequencies is also beyond the scope of this work. For example, in [118, 119], extensive analysis and modelling on the non-linear effects of RF power amplifiers is outlined. In this context, the adopted 60 GHz PA models are the ones validated and suggested in [117], where the *Rapp* model for AM-AM [120] has

been used and modified to extend it to include the AM-PM effects. Spectral regrowth and distortions on the constellation scheme of a 60 GHz PA can be therefore modelled by [117]:

$$F_{AM-AM}(|x[n]|) = \frac{G|x[n]|}{(1+(\frac{|x[n]|}{V_{sat}})^{2s})^{\frac{1}{2s}}}, \tag{3.10}$$

$$F_{AM-PM}(|x[n]|) = \frac{\alpha|x[n]|^{q_1}}{(1+(\frac{|x[n]|}{B})^{q_2})}, \tag{3.11}$$

where G is the voltage gain of the PA, V_{sat} is the saturation voltage level, $|x[n]|$ is the input voltage level, s ($s > 0$) is the smoothness factor that controls the transition from the linear zone to the saturation zone, α, B and q are constants and representing fitting parameters.

In order to mitigate the distortion introduced by the power amplifier, its quiescent operating point should be set to operate in the linear region, otherwise out-of-band emissions (intermodulation products) will appear in the output signal spectrum. And thus, leading to a high Adjacent Channel Interference (ACI) and ISI, contributing to the degradation of the transmitted signal. In addition, if the input signal envelope is not constant, the operation point of the PA will vary. In practice to avoid (or at least to reduce) the effects of non-linearities, the PA should be operated at a given OBO set to a specific level keeping the signal within the linear region, at the expense of less power efficiency.

The PA OBO is given by:

$$OBO = 10\log 10(\frac{P_{sat}}{P_{out}}), \tag{3.12}$$

where P_{out} is the average output power from the PA and P_{sat} corresponds to the maximum output power (saturating power). The OBO parameter is highly important, since OFDM systems are characterised by large signal amplitude fluctuations, which make it susceptible to system non-linearities. Such amplitude fluctuations are characterised by the PAPR of the signal. The PAPR measures instantaneous power compared to the average power of the OFDM symbols and for the discrete-time signal is expressed as:

$$PAPR(x[n]) = max_{0\leq n\leq N_c-1}\frac{|x[n]|^2}{E[|x[n]|^2]}, \tag{3.13}$$

where $|x[n]|^2$ is the maximum instantaneous power, $E[.]$ is the average power and N_c is the number of the sub-carrier per OFDM signal.

The Power Added Efficiency (PAE), denoted by η, is defined as the ratio of the amplified output signal power to the DC power supplied to the amplifier, which is expressed by:

$$\eta = \frac{P_{out} - P_{in}}{P_{DC}}, \tag{3.14}$$

where P_{in} is the input power, P_{out} is the desired output power in the band of interest and P_{DC} is the DC input power.

The values characterising the PA non-linearities, given in Table 3.1, for two competing IC technologies have been calculated by fitting data obtained from 60 GHz measurements on Gallium Arsenide (GaAs) pHEMT [121] and a 65 nm CMOS [122] to the models presented in (3.10) and (3.11). The power and voltage characteristics for both GaAs and CMOS PA models, together with the AM/AM transfer functions assuming a 50Ω input impedance, are given in Fig. 3.7a and Fig. 3.7b, respectively. In addition, the AM/PM characteristics of the amplifiers are depicted in Fig. 3.7c.

Table 3.1
Modelling parameters for the considered PA models.

Model	**Gain [dB]**	V_{sat}**[V]**	**s**	α	**B**	q_1	q_2
GaAs	25.6	1.98	0.81	-48000	0.123	3.8	3.7
CMOS	13.3	0.82	0.81	2560	0.114	2.4	2.3

According to Fig. 3.7b, the voltage AM/AM curves exhibit a linear characteristic for low input signal amplitudes, followed by a transition towards a constant saturated output. Additionally, it is evident that as the smoothness function becomes increasingly large ($s \to \infty$), the *Rapp* model converges towards a perfect Pre-Distortion (PD) technique. This is verified for both PA technologies and observed when $s = 100$.

The PA is the main power consuming device in a transceiver. Therefore it is important to operate it close to its saturation point. However, as it was cited above, distortions occur due to the signal high PAPR., and a trade-off between the PA OBO and efficiency must be taken into account. This trade-off is shown in Fig. 3.7d for both PA models, with and without employing PD. Results for the CMOS PA have been obtained with the DC power value of 14.59 dBm [122]. As no DC power value is reported in literature for GaAs PA, its value was interpolated from reference (blue

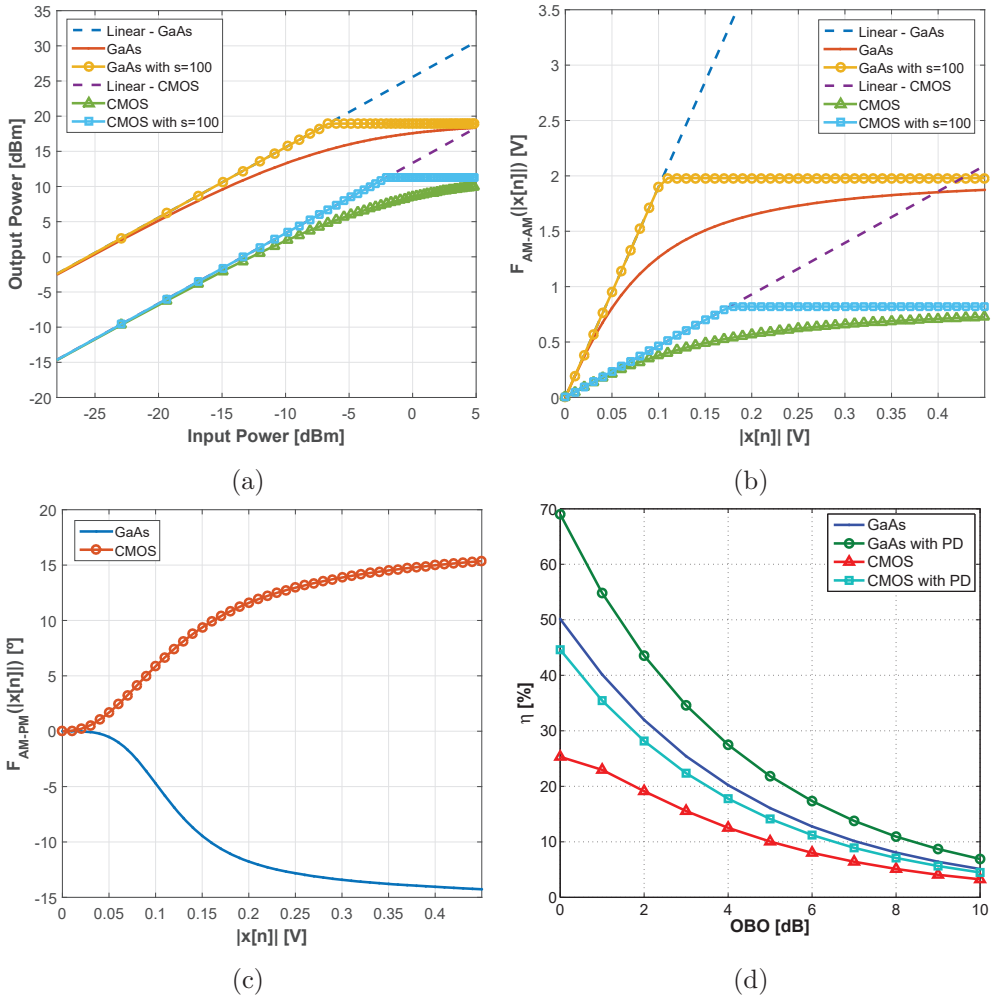

FIGURE 3.7: PA characteristic curves of: AM/AM for (a) power and (b) voltage, (c) AM/PM in function of input voltage and (d) relation between PAE and OBO for GaAs and CMOS model amplifiers.

curve), assuming OBO = 0 and $\eta = 50\%$. Fig. 3.7d shows that the GaAs PA has much higher PAE than the CMOS model and when employing a PD technique, the PAE increases significantly, i.e. CMOS PA has an increased PAE of about 20%.

3.2.3 Channel modelling

This section presents the channel modelling proposed by TG3c at 60 GHz for the following indoor environments: office, residential and kiosk [123]. These channel models are based on a frequency sweep technique performed using a Vector Network Analyser (VNA) to measure the frequency response of the radio channel. The centre frequency and the bandwidth considered in these measurements were 62.5 GHz and 3 GHz, respectively. For each environment, both LOS and NLOS scenarios were considered, except in the kiosk environment, where only LOS has been considered. In such indoor scenarios,

multipath components are mainly obtained from reflected or scattered signals from furniture, floor and ceiling.

Moreover, the IEEE 802.15.3c standard has adopted the generic Channel Impulse Response (CIR) based on the clustering of propagation phenomena in both time and spatial domains, as observed in measurement data [123]. The cluster model is based on the extension of the *Saleh-Valenzuela* model [124] to the angular domain by *Spencer* [125], discussed in Section A.2.2 and described by (A.12). Hence, the IEEE 802.15.3c channel modelling group [126] proposed a statistical channel model dependent on the temporal and spatial domains, where signals arrive at the receiver first in a LOS component, calculated with a two-ray model, and then in clusters (modified S-V model). This 60 GHz channel modelling is utilised in this work, allowing the performance evaluation of distinct waveforms over different multipath environments. Additionally, each indoor environment has been mapped onto a channel model and scenario, as presented in Table 3.2.

Table 3.2
Mapping of environment to channel model and scenario, according to [59].

Environment	**Channel Model**	**Scenario**
Residential	CM1	LOS
	CM2	NLOS
Office	CM3	LOS
	CM4	NLOS
Kiosk	CM9	LOS

Several channel realisations may be considered to yield different Power Delay Profile (PDP) for the same multipath environment. This occurs due to the fact that the considered channel modelling tool [126] takes into account the uniform distribution in terms of the scatters movements between transmitter and receiver and at different antennas height. Consequently, in this work, an averaged PDP is obtained from 100 quasi-static channel realisations, and analysed in terms of averaged RMS delay spread ($\bar{\tau}_{RMS}$), coherence bandwidth for signal correlation of 0.9 ($\bar{B}_{c_{0.9}}$) and *Rician* factor ($\bar{K}$). Such metrics have been calculated from the equations presented in section A.2.2. Moreover, the dynamic range of the average PDP is estimated considering all multipath components which are 10 dB above the thermal noise of the system as threshold, which is defined by (3.15), and considering a EIRP of 40 dB, which is the maximum valuer for Europe regions, see Table 2.3, and a receiver gain antenna (G_{RX}) of 10 dBi (typical

value of gain on-chip antennas at 60 GHz) [16]. This method is illustrated in Fig. 3.8, considering a single channel realisation for both CM1 and CM9 models.

$$N = K.T.B\ [W], \tag{3.15}$$

where N, K, T and B are the noise power, the *Boltzmann* constant, the temperature in *Kelvin* and the transmitted signal bandwidth, respectively. The system noise floor is -81 dBm, considering $T = 290$ K and $BW =$ 1.8 GHz. Summary of the average Channel Quality Indicator (CQI) values of each model are presented in Table 3.3, where HPBW is the Half Power Beamwidth of $TX/\ RX$ antennas.

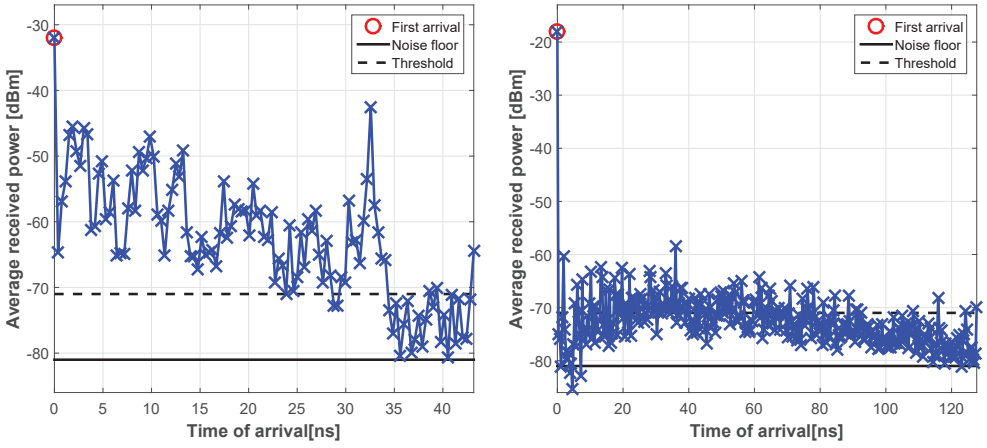

(a) (b)

FIGURE 3.8: PDP calculation method for the channel models: a) CM1 b) CM9.

TABLE 3.3
AVERAGED CHANNEL QUALITY INDICATOR PARAMETERS FOR EACH MULTIPATH ENVIRONMENT.

CM #	$\bar{\tau}_{rms}$ (ns)	$\bar{\tau}_{max}$ (ns)	$\bar{B}_{c_{0.9}}$ **(MHz)**	$\bar{\mathbf{K}}$ (dB)	**HPBW°** **(TX/RX)**
1	3.5	67.42	14.6	14.6	(360,15)
2	2.73	68.9	7.33	-	
3	22.75	464	0.88	14.61	(30,30)
4	57.7	651	0.35	-	(30,15)
9	2.7	183	7.41	30.9	(30,30)

Additionally, to estimate the maximum operation range of a particular wireless communication system, the PL between the transmitter and receiver must be known. As discussed in section A.2.2, PL describes the attenuation of mean power as function of distance, and according to the TG3c group [123], and it is modelled by (A.13) by replacing the term $\sum_{q=1}^{Q} X_q$ by X_σ. Such is a zero mean *Gaussian* distributed random variable with a standard deviation σ_s, which in this work, X_σ is chosen to be 80% of σ_s [127]. The representation of PL as function of travelled distance is depicted in Fig. 3.9 for each CM, taking into account the values of each variable presented in Table 3.4. From this figure, it is clearly noted that NLOS scenarios induce much higher losses than LOS ones.

TABLE 3.4
TYPICAL VALUES OF n, $PL_{d_0}|_{dB}$ AND $X_\sigma|_{dB}$ FOR DIFFERENT ENVIRONMENTS AND SCENARIOS [19].

CM #	**n**	PL_{d_0} **(dB)**	σ_s **(dB)**
1	1.53	75.1	1.5
2	2.44	86	6.2
3	1.16	84.6	5.4
4	3.74	56.1	8.6
9*	2	68	5

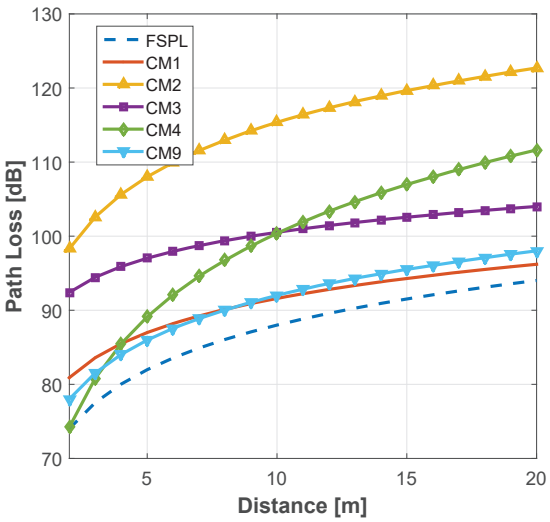

FIGURE 3.9: Path loss in function of distance for each channel model.

Consequently, the PL value in its maximum range can also be obtained from a link budget equation, represented in (3.16) [128]:

$$PL = EIRP + G_{RX} - P_N - E_b/N_o - IL - M \ [dB], \tag{3.16}$$

where P_N is the average noise power per bit, where $P_N = N + N_f$ and $N = -174 + 10\log_{10}(R_b[bps])$, N_f is the receiver noise figure, R_b is the system throughput, IL is the implementation loss of the transceiver and M is the link (shadowing) margin. In case human blockage is present, additional losses must be taken into account, thus according to [127], losses caused by a person moving and crossing the propagation path varies from 18-36 dB, at 60 GHz in indoor environments. Furthermore, N_f and IL are usually characterised by 8 dB and 2 dB, respectively [123]. Finally, relating both equations (A.13) and (3.16), the maximum operation range for a required E_b/N_o is calculated using the following equation [128]:

$$d = 10^{\frac{(PL - PL_{d_0})/10n}{}}[m], \tag{3.17}$$

where PL_{d_0} is the path loss at a reference distance (d_0), usually $d_0 = 1$ m.

For example, the maximum operating range vs E_b/N_o of 6.2 Gbps throughput system over the aforementioned multipath channels in either absence or presence of human shadowing, is given in Fig. 3.10.

3.3 Performance of OFDM under both channel and RF impairments

Detailed analysis on the impact of RF and channel impairments on the performance of UWB wireless OFDM systems based on the IEEE 802.15.3c standard, for high data rate applications using the 60 GHz millimetre frequency band is presented in this section. The impact of impairments is evaluated, in terms of some of the most important key performance indicators, including spectral efficiency, power efficiency, required coding overhead and system complexity, OOBEs, BER target and PSNR. Additionally, joint distortion effects of coexisting PN, mixer IQ imbalances and PA non-linearities, on the performance degradation of a mmWave radio transceiver, combined with various multipath fading channels, are investigated. Subsequently, the power efficiency of the system is evaluated by estimating values of the PA OBO needed to meet the requirements for the Transmit Spectrum Mask (TSM) and BER target. Finally, a comparison of the system overall performance between uncoded and coded OFDM systems combined with

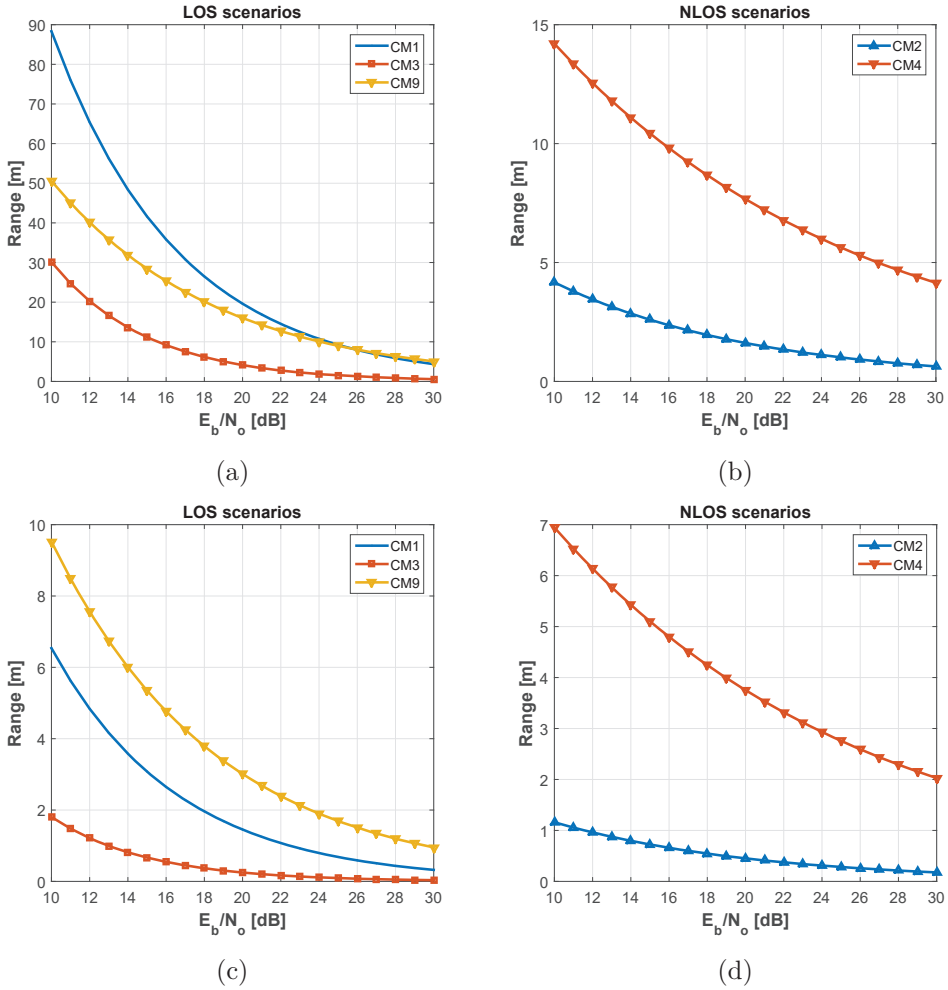

FIGURE 3.10: Estimated maximum operating range of a 6.2 Gbps throughput system versus E_b/N_o for each channel model: (a) and (b) without human blockage ; (c) and (d) with human blockage (36 dB).

QAMs (16 and 64 QAM) and its maximum operable range are evaluated by transmitting a Full HD uncompressed video frame under five different RF impairment conditions over the CM9 channel model.

3.3.1 mmWave system model based on IEEE 802.15.3c standard

The developed OFDM system model is illustrated in Fig. 3.11, with the physical operating parameters given in Table 3.5 [40], for both 16-QAM and 64-QAM. Their constellations are mapped to *Gray*-code and their output values are obtained by multiplying the constellation points with a normalisation factor. The FEC codes, bit and tone interleaver blocks are directly provided by the standard. In order to shape the OFDM signal Power Spectral Density (PSD) the sub-carriers are allocated into the IFFT according to [40]. The wireless channel employed is based on the IEEE model proposed in [123]. The

received signal, $y(t)$, after being processed using a K- point FFT, is converted into its frequency domain, $Y(k)$. The received OFDM signal, Y_l, is given by:

$$Y_l(k) = H_l(k).X_l(k) + Z_l(k) \tag{3.18}$$

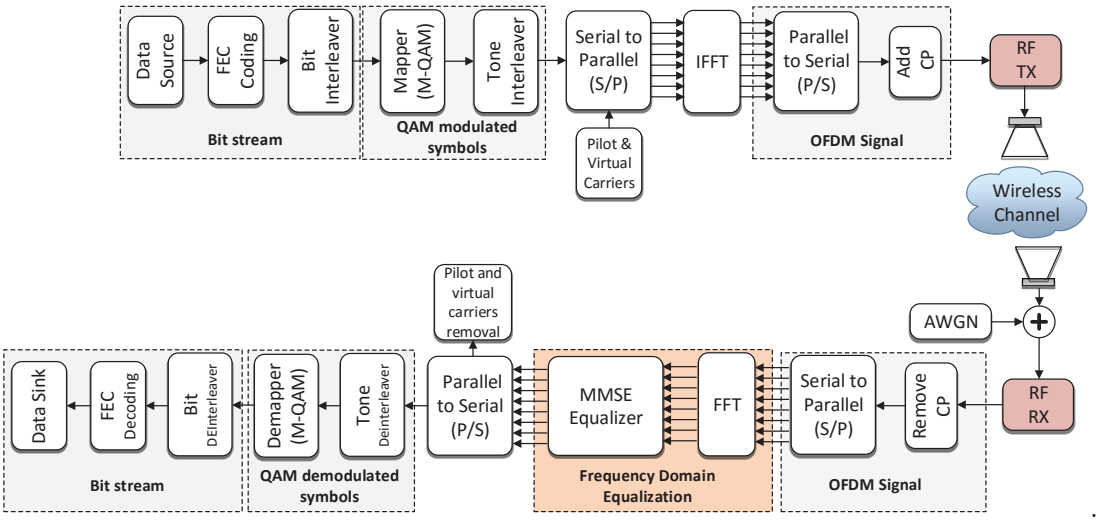

FIGURE 3.11: OFDM block diagram.

TABLE 3.5
MAIN PARAMETERS CONSIDERED IN THE DESIGN OF UNCODED OFDM SYSTEM BASED ON IEEE 802.15.3C STANDARD.

Parameter	**Value**
FFT size block (N_{fft})	512
Cyclic prefix (N_{cp})	64 samples
Sampling rate	2640 MHz
Nominal Used Bandwidth	1815 MHz
Sub-carrier bandwidth	5.15 MHz
Cyclic prefix time (T_{cp})	24.24 ns
Symbol time	218.18 ns

Considering that $T_{cp} \geq \tau_{max}$, where, T_{cp} is the cyclic prefix interval time, τ_{max} corresponds to the maximum excess delay from a generic multipath channel, k denotes the sub-carrier frequency component of the l^{th} transmitted OFDM signal, $H_l(k)$ is

the Channel Frequency Response (CFR) and $Z_l(k)$ is the Additive White Gaussian Noise (AWGN) in the frequency domain. The original transmitted information, $X_l(k)$ can be recovered employing a Frequency-Domain Equalisation (FDE) technique [129], which is performed as a K-branch linear feed-forward equaliser with $C(k)$ being the complex coefficient of the k^{th} sub-carrier. Minimum Mean Square Error (MMSE) equaliser is considered, where for this criterion, $C(k)$ is defined by (3.19).

$$C_{MMSE}(k) = \frac{\hat{H}(k)^*}{|\hat{H}(k)|^2 + \frac{1}{\eta}} \tag{3.19}$$

where $\hat{H}(k)$, η, * and $|.|$ denote the estimated CFR, SNR, conjugate transpose and modulus, respectively.

Table 3.6
Sub-carrier allocation in the frequency spectrum domain.

sub-carrier type	**Number of sub-carriers**	**Logical sub-carrier indexes**
Null	141	[-256:-186]∪[186:255]
DC	3	-1;0;1
Pilot	16	[-166:22:-12]∪[12:22:166]
Guard	16	[-185:-178]∪[178:185]
Data	336	All others

A mmWave multi-Gigabit transmission requires the employment of a FEC technique to ensure a high quality performance under PN, IQ imbalances, PA non-linearities and channel impairments. FEC schemes should be determined considering the trade-off between higher coding gain, hardware complexity and code rate. Two families of linear block codes are proposed in the standard: RS codes (mandatory) and LDPC codes (optional) with several coding rates. RS codes are known for their good capability of burst error correction at a relatively high SNR. LDPC codes, despite having high complexity, with its iterative decoding process, ensures a better error correction performance than *Reed Solomon* codes or turbo codes [130] and its performance is very close to the *Shannon* coding limit [131]. For each modulation scheme, FEC with three different coding rates are considered as detailed in Table 3.7. The RS coding scheme (outer code) is combined with a convolutional coding (inner code).

TABLE 3.7
SUMMARY OF THE OFDM FEC SCHEMES.

FEC	Overall code rate	Modulation	Throughput [Gbps]
RS (224,216)	9/14	16-QAM	3.96
LDPC (672,336)	1/2	16-QAM	3.08
		64-QAM	4.62
LDPC (672,504)	3/4	16-QAM	4.62
		64-QAM	6.93

Model Validation

A comparison between the simulated BER results and those obtained from the analytical expressions presented in (A.91) and (A.92), for uncoded OFDM employing M-ary QAM modulations over AWGN and *Rayleigh* fading channels is shown in Fig. 3.12a and in Figs. 3.12b and 3.12c, for 16 and 64-QAM respectively . Such results exhibit a relatively good agreement. Results for the *Rayleigh* channel are obtained using an average of 100 random channel realisations.

Additionally, the small difference between simulated and theoretical results over AWGN channel are caused by the insertion of CP. This discrepancy can be calculated using (3.20) [132], obtaining a difference of 0.51 dB.

$$L_{CP} = 10\log_{10}(\frac{T_{OFDM}}{T_{total}})\ [dB], \tag{3.20}$$

where T_{OFDM} is the OFDM symbol time without the insertion of the CP samples and T_{total} is the transmitted frame time. However, in this work, the OFDM symbol is power boosted to compensate for the wastage of energy (L_{cp} losses) associated with the insertion of CP.

The BER simulation results for the coded OFDM (C-OFDM) system are depicted in Fig. 3.13. It is evident that LDPC clearly outperforms RS even with higher code rate. Results for 64-QAM with RS coding are not considered due to their higher sensitivity to errors.

3.3.2 Impact of individual non-linearities at 60 GHz

Therefore, this section presents a study of performance degradation due to the inclusion of individual RF impairments on the uncoded OFDM, namely, PN, IQ imbalances and power amplifier non-linearities. The effect of the RF impairments, is implemented based on the models introduced in Section 3.2. This is achieved through BER analysis for 16

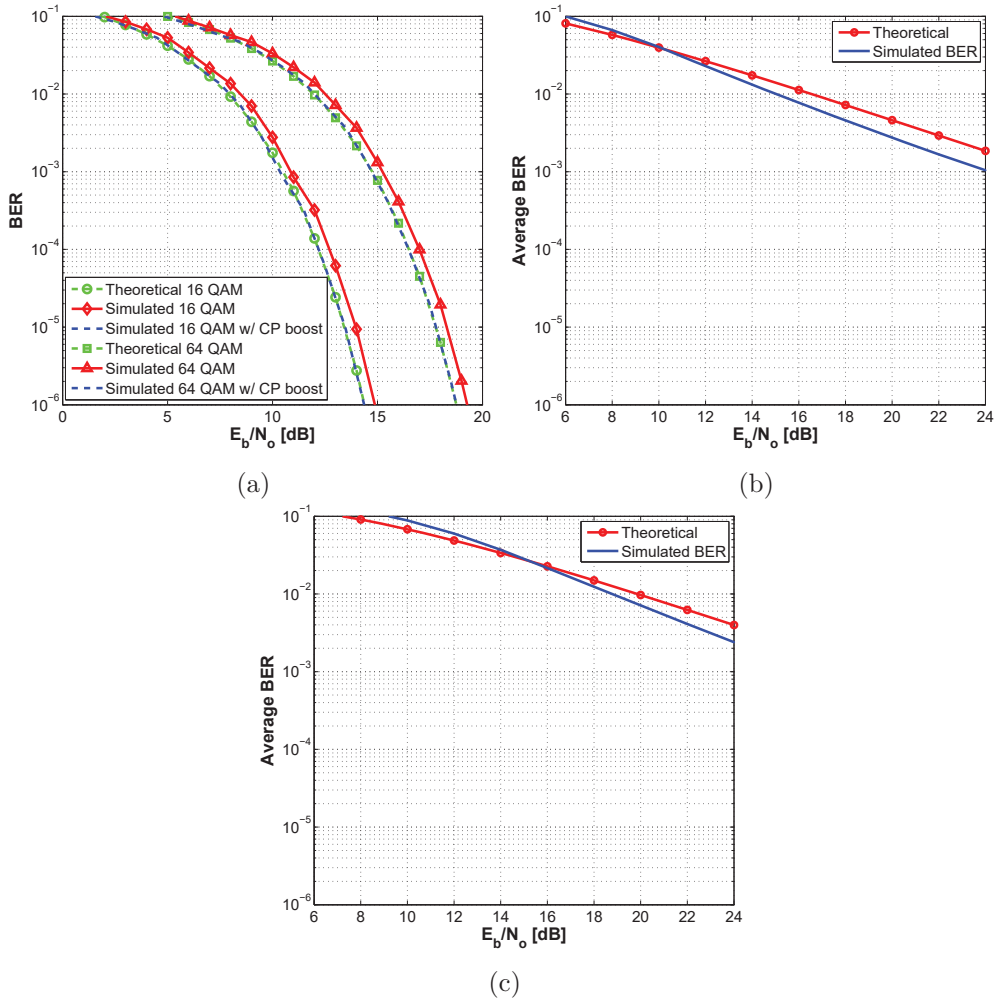

FIGURE 3.12: Comparison of the theoretical and simulated E_b/N_0 results for uncoded OFDM: a) over AWGN channel and over the *Rayleigh* channel for: b) 16-QAM c) 64-QAM modulations.

and 64-QAM, under an AWGN channel. The considered BER target, recommended for video streaming applications is 10^{-6} [123].

Phase-noise and IQ imbalances

The impact of phase noise on the performance of OFDM using 16-QAM (Fig. 3.10a) and 64-QAM (Fig. 3.10b), for four low frequency PN constants: -87, -90, -93 and -96 dBc/Hz [121], where -87 and -96 represent the worst and best case scenarios, respectively. It can be clearly seen that the presence of PN degrades the overall system performance, requiring larger E_b/N_0 values to achieve a desired BER. i.e for the worst case scenario (PSD (0) = -87 dBc/Hz), the degradation of the OFDM performance is about 1.5 dB for 16-QAM, while in the 64-QAM system, the BER target is not achievable.

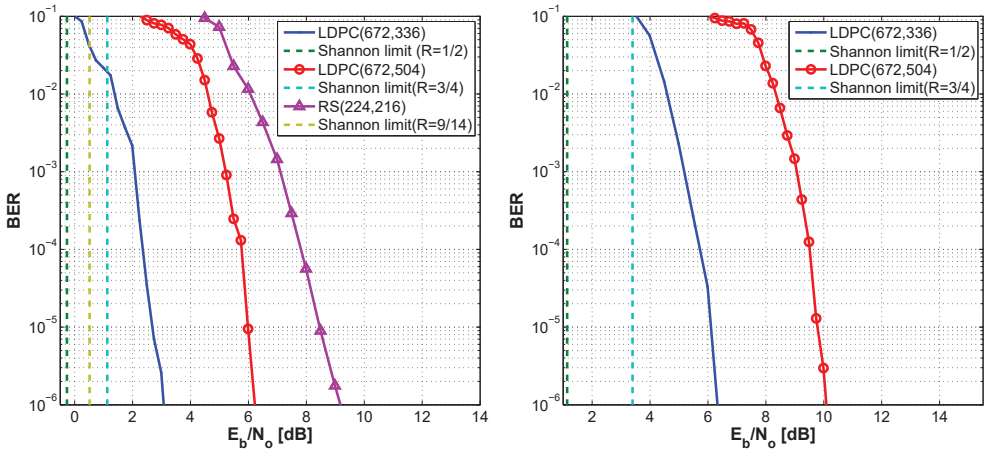

FIGURE 3.13: BER performance for C-OFDM for: a) 16-QAM and b) 64-QAM, over an AWGN channel.

The effect of IQ imbalances on BER analysis depends on the type of IQ mixers and the number of upconversion/downconversion stages present in the RF front-end architecture. The phase gain mismatch (Δg) and phase mismatch ($\Delta\theta$) values vary from 0 to 0.5 dB and from 0 to 6 degrees, respectively [121]. Figures 3.14c and 3.14d demonstrate the effect of IQ imbalances considering both modulation orders, where the OFDM system employing 16-QAM is slightly more robust against IQ imbalances than 64-QAM (to achieve the required BER of 10^{-6}). 16-QAM requires approximately 8.5 dB lower value of E_b/N_0 for the worst case scenario ($\Delta g = 0.5$ dB and $\Delta\theta = 6°$), in comparison with the 64-QAM.

Power amplifier

The effects of the in-band and out-of-band distortions, due to the non-linear PA response, modelled in Section 3.2.2, for uncoded OFDM, are presented in this section. The out-of-band emissions do not have a direct impact on the system performance, but may harm communication systems operating in the adjacent frequency channels. Nevertheless in-band emissions introduce ISI. In order to minimise the effect of out of band emissions, the spectrum of the transmitted signal must be below the TSM defined by the IEEE 802.15.3c standard [40]. The estimation of such spectrum was performed by calculating the transmitted signal Power Spectral Density (PSD).

The transmitted OFDM signal amplitude might exhibit high peak values, since many sub-carrier components are added in the IFFT operation. However, a discrete representation of the OFDM signal does not necessarily contain the maximum amplitude values of the continuous time domain signal. Therefore, an oversampled version of the

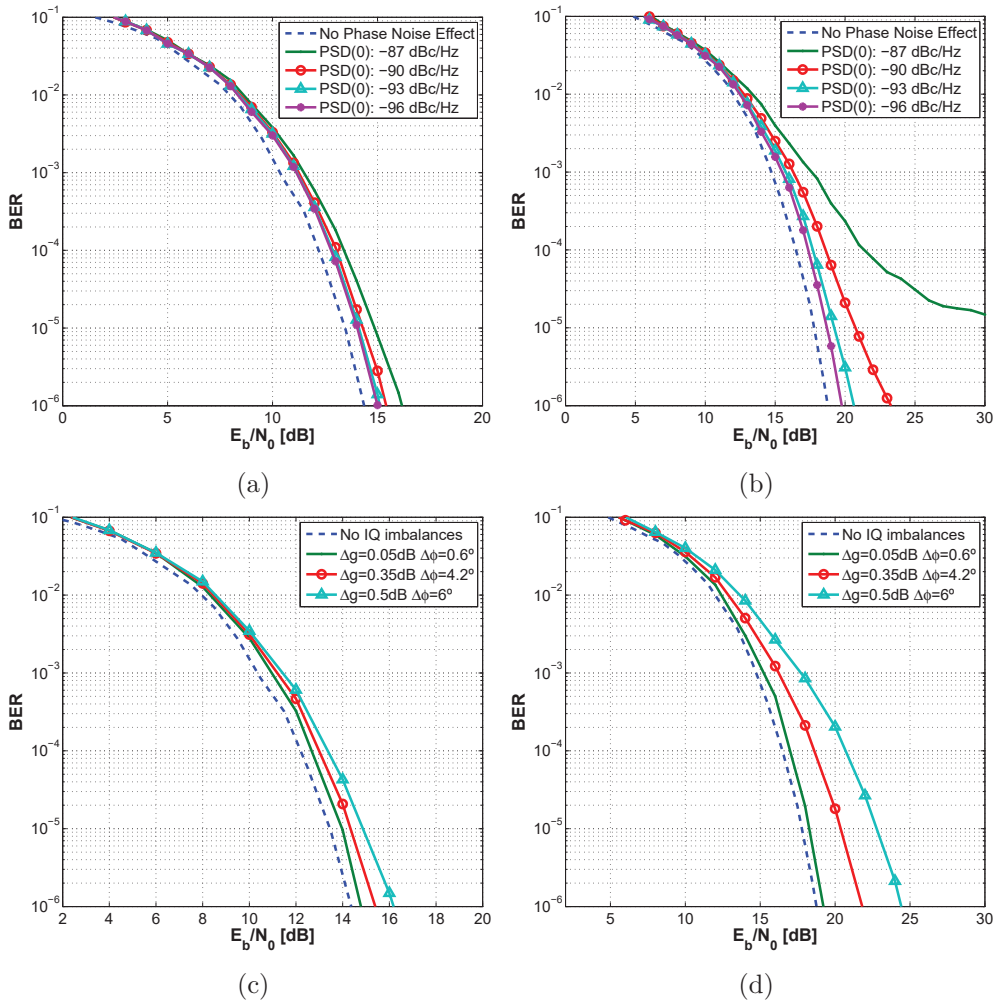

FIGURE 3.14: BER performance under PN and IQ imbalances effect, respectively, for (a) (c) 16-QAM, and (b) (d), 64- QAM.

discrete signal is considered, yielding a more accurate PAPR distribution of the OFDM signals. An oversampling factor of L = 4 is considered for both QAM modulations.

The PSD has been computed for both PA technologies. Estimated OBO values for both PA models and both modulations are summarised in Table 3.8, and illustrated, in particular for 16-QAM, in Fig. 3.15a and in Fig. 3.15b without and with PD, respectively. Results show that the minimum estimated Output-Back-off (OBO) values, which meet the TSM requirements are slightly higher for 64-QAM, as expected. The PAPR distribution employing 64 QAM has slightly higher values than 16 QAM. In addition, introducing a PD technique reduces the OBO values for both amplifier technologies and consequently increases their power efficiency, e.g. for the GaAs model the PAE increases from 8.25% to 19.95% (16-QAM). Furthermore, both PA models present similar OBO values to meet the TSM requirements. i.e., for the GaAs model using PD, the lowest values of PA OBO are 5.5 and 6 dB for both modulation schemes, whereas the CMOS model requires OBO values of 5.5 and 5.9 dB, respectively.

TABLE 3.8
OBO REQUIRED TO MEET TSM REQUIREMENTS FOR 60 GHZ OFDM SYSTEMS.

PA model	**Modulation**	**PD**	**OBO [dB]**	η [%]
GaAs	16-QAM	yes	5.5	19.95
		no	9.2	8.25
	64-QAM	yes	6	17.78
		no	9.5	7.7
CMOS	16-QAM	yes	5.5	12.56
		no	9.5	4.58
	64-QAM	yes	5.9	11.45
		no	9.6	4.48

A summary of PA non-linearity impact on BER results against PA OBO for both PA models, is presented in Table 3.9. In this table, the performance degradation is characterised by $\triangle E_b/N_o$, which is the difference between the required E_b/N_0 in the presence and absence of non-linearities. Simulated results have shown that the PA OBO has a significant impact on the BER performance. A trade-off is noticed between the PA operating point, $\triangle E_b/N_o$ and PAE, i.e, in order to mitigate the effects of the PA non-linearities on the system, the power efficiency of the PA is significantly decreased. Pre-distortion employment allows to reduce the signal degradation for lower PA OBO values, making the system more power efficient and more robust against this impairment, as demonstrated with the comparison between Fig. 3.15c and Fig. 3.15d.

Additionally, when comparing the BER simulation results for both PAs, it is noticed that the GaAs PA is a better choice for the RF front-end, as it is capable to achieve the desirable BER target with lower PA OBO values at a higher power efficiency. The system requires 6 and 8 dB of PA OBO (optimum values) using GaAs model and PD for 16 and 64-QAM, respectively. On the other hand, the CMOS model requires 7 and 12 dB for 16 and 64-QAM, respectively. This can be justified by the fact that CMOS PA model is being characterised by a high phase distortion on its AM-PM curve, as is evident in Fig. 3.7c.

Effects of channel impairments

In this section, the uncoded OFDM system performance over the IEEE CM9 model [123] (typical indoor LOS kiosk environment) is assessed in terms of averaged BER. Results are depicted in Fig. 3.16, where it is possible to conclude that BER curves varies from one channel realization to another, since each CIR is characterised with different statistical values of τ_{RMS}, K, and $B_{c_{0.9}}$. Due to the statistical nature of the model [126], introduced in Section 3.2.3, it is expected that BER curves converge with the

TABLE 3.9
SUMMARY OF PA NON-LINEARITY IMPACT ON BER RESULTS FOR 60 GHZ OFDM SYSTEMS.

PA model	M-ary	PD	E_b/N_0 [dB]	$\triangle E_b/N_o$ [dB]	OBO [dB]	η %
GaAs	16	yes	20.5	6.1	6	17.7
		no	26	11.6	9	8.6
	64	yes	26.2	7.45	8	11.2
		no	32	13.25	13	3.44
CMOS	16	yes	23.7	9.3	7	8.89
		no	21.6	7.2	11	3.26
	64	yes	28.65	9.9	12	2.81
		no	26	7.25	15	1.3

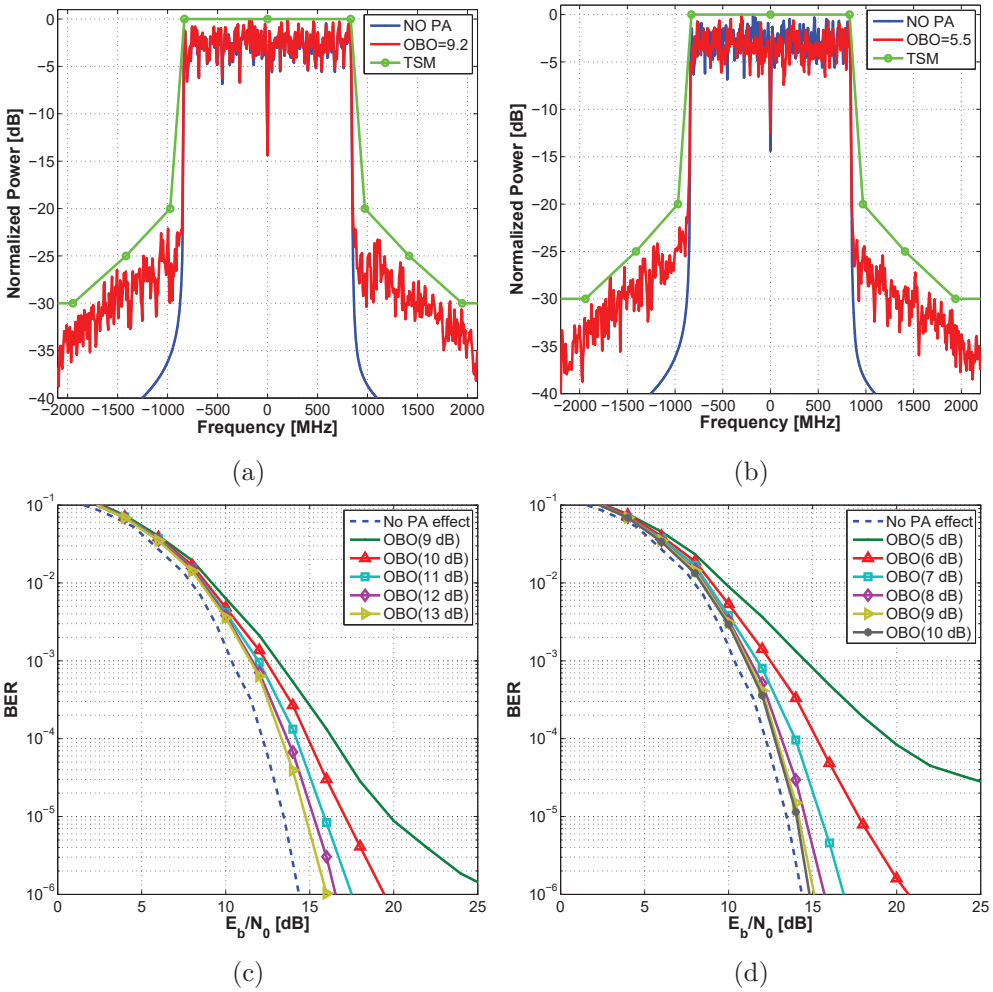

FIGURE 3.15: (a) (b) estimated OOBEs and (c) (d) OFDM BER performance employing GaAs PA without and with PD for 16-QAM.

increase of the number of iterations. Therefore, 100 realisations were considered in this work respecting a relatively good commitment between simulation time and accuracy.

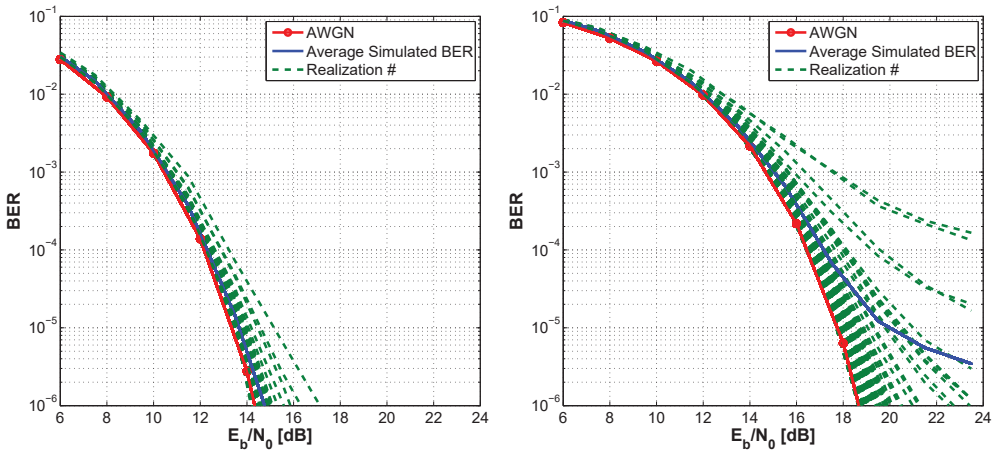

(a) (b)

FIGURE 3.16: Average BER for the considered fading channel for: a) 16-QAM b) 64-QAM.

In order to assess the effect of the kiosk multipath environment on the OFDM system, the average of BER performance is conducted. With this, it is verified that 16-QAM uncoded OFDM BER performance is similar to that obtained with AWGN. This is explained by the fact the former is characterised by a very high *Rician* factor and a relatively high coherence bandwidth, as it is also verified in Section 3.2.3. Whereas, the performance of the 64-QAM uncoded OFDM system is inferior rendering it to be inoperable for BER below 10^{-6}.

3.3.3 Impact of RF front-end non-linearities at 60 GHz

In this section, the effect of RF impairments on the quality of uncompressed wireless video streaming for UM1 application, defined by the IEEE 802.15.3c standard [59], is evaluated and demonstrated under different impairment conditions (case studies) over CM9 channel. Hence, it is possible to accurately estimate the impact of a realistic RF front-end on a wireless mmWave OFDM (uncoded and coded) communication system, under various scenarios for a combination of optimum and non-optimum non-linearity values based on results presented in Section 3.3.2.

Therefore, five distinct case studies (A to E) have been built based on a combination of different QAM modulation order, PA OBO values, IQ imbalances and PSD(0) modelling values. Those are thoroughly reported in Table 3.10.

The quality of the transmitted uncompressed video content, in Full HD, is assessed through BER and PSNR analysis. Moreover, it is possible to estimate the minimum value of E_b/N_0 to ensure a relatively good subjective quality considering a reference video frame. This is achieved by using the relation between the PSNR (objective quality

Table 3.10
Case study RF impairments values.

Case studies	**M-ary**	**PA OBO [dB]**	**IQ (Δg [dB], $\triangle\theta$ [°])**	**PSD(0) [dBc/Hz]**
A	16	6	(0.05,0.6)	-96
	64	8		
B	16	6	(0.5,6)	-96
	64	8		
C	16	6	(0.05,0.6)	-87
	64	8		
D	16	6	(0.5,6)	-87
	64	8		
E	16	5.5	(0.5,6)	-87
	64	6		

assessment metric) and the subjective quality assessment based on viewer's impression, presented in Table 3.11 [133].

Table 3.11
Relation between subjective and objective quality indicators.

PSNR [dB]	**ITU Quality scale**
> 37	5 - Excellent
$31 - 37$	4 - Good
$25 - 31$	3 - Satisfactory
$20 - 25$	2 - Poor
< 20	1 - Very poor

The uncoded OFDM BER results, computed for each case study, are displayed in both Fig. 3.18a and Fig. 3.18b, for 16-QAM and 64 QAM, respectively, where "Ideal RF front-end" means that only the effect of the multipath propagation is taking into account. It is evident from these results that the desired BER is only achievable using 16-QAM for case study A, which corresponds to a maximum system range of 10.2 m, according to (3.17). In order to minimise ISI, in particular, in cases where the BER target is not achieved and consequently increasing operation range, FEC code schemes RS(224,216), LDPC(672,336) and LDPC(672,504) with coding rates of 9/14, 1/2 and 3/4, respectively, are considered.

In Fig. 3.18c and Fig. 3.18d, it is clearly shown that the C-OFDM outperforms the uncoded OFDM under both RF and channel impairments, but at the expense of system

FIGURE 3.17: Reference frame from the Full HD Cactus.yuv video sequence for the PSNR calculation.

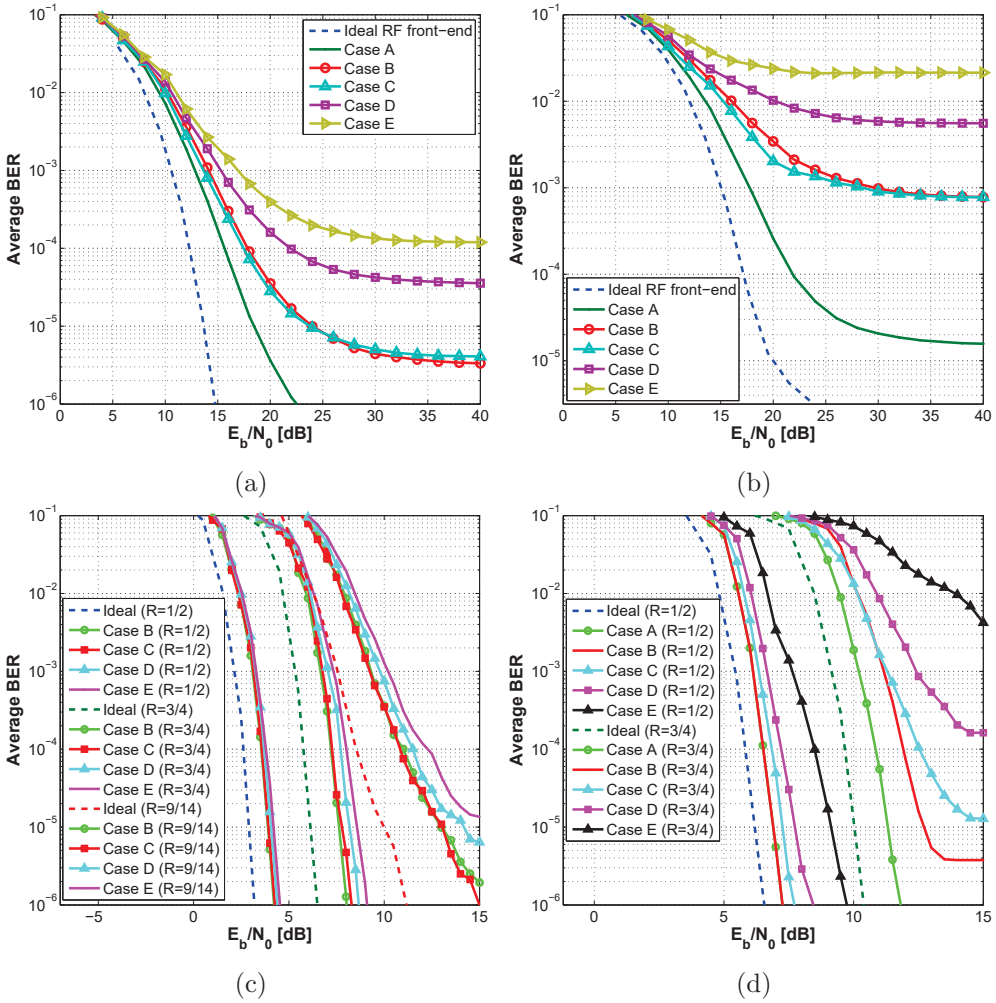

FIGURE 3.18: BER performance for various case studies: uncoded OFDM for a) 16-QAM b) 64-QAM and Coded OFDM for c) 16-QAM and d) 64-QAM modulations.

throughput. Moreover, as expected the LDPC coding with its iterative decoding and

exploitation of frequency diversity leads to impressive results. For example, using RS FEC coding, 16-QAM OFDM BER performance fails to meet the BER target for C, D and E case scenarios. However, for the 64-QAM system with LDPC (672,504), the BER target is only achieved for case study A, whereas, the 16-QAM OFDM system is able to achieve the BER target in all case scenarios, making the wide-band wireless transmission reliable regardless of the impact of non-linearities. A summary of RF front-end non-linearity impact over CM9 channel on the BER results and maximum range for 60 GHz coded OFDM systems, using 16 and 64-QAM, are shown in Table 3.12 and Table 3.13, respectively.

Table 3.12
Summary of RF front-end non-linearity impact on the BER results for 60 GHz coded OFDM systems for 16-QAM.

Case Studies	**Coding**	E_b/N_0 [dB]	$\triangle E_b/N_o$	d_{max} **[m])**
B	R=3/4	8	1.51	73.7
	R=9/14	15	4	35.6
C	R=3/4	8.1	1.6	72
	R=9/14	-	-	-
D	R=1/2	4.05	1.05	143.1
	R=3/4	8.6	2.1	68.8
	R=9/14	-	-	-
E	R=1/2	4.15	1.15	139.7
	R=3/4	9.1	2.6	64.1
	R=9/14	-	-	-

Table 3.13
Summary of RF front-end non-linearity impact on the BER results for 60 GHz coded OFDM systems for 64-QAM.

Case Studies	**Coding**	E_b/N_0 **[dB]**	$\triangle E_b/N_o$	d_{max} **[m])**
A	R=1/2	7.1	1.1	82.6
	R=3/4	12	2	38
C	R=1/2	7.5	1.45	79.1
D	R=1/2	8.2	2.2	72.1
E	R=1/2	9.6	3.6	61.3

In order to evaluate the effectiveness of uncoded OFDM in ensuring a good QoS, at appropriate PSNR values, the degradation of the quality of the video frame for the best case scenario (case A), has been studied. The video frame content (Fig. 3.19a) is divided into several transmitting OFDM symbols and then transmitted over the channel model. PSNR results are depicted in Fig. 3.19c, for both modulation schemes together with those obtained for an ideal RF front-end, where dash curves show the BER results over AWGN. It be can seen that both RF and channel impairments have significant impact on the degradation of the quality of reference video frame, where the presence of distorted pixels is clearly visible when compared to those of Fig. 3.19a and Fig. 3.19b, and a maximum achievable PSNR of about 24 dB (for an $E_b/N_o = 24$ dB) for both modulations. This characterises the video frame subjective quality as poor (Table 3.11), while the effective objective quality degradation ($\triangle PSNR$), which is the difference between the PSNR in absence and presence of non-linearities to achieve an excellent video quality, is about 17 dB for same E_b/N_0. Therefore, in order to ensure reliable QoS ($PSNR > 31$) and consequently reducing the necessary SNR to meet this quality requirement, FEC schemes are selected based on their BER performance, complexity and system throughput. Based on results presented in Fig. 3.18 for the worst case scenarios, i.e case study D and E, 16-QAM RS (224,216) lend itself to be the preferred option, since 64-QAM requires LDPC (672,336). Although both modulation schemes operate approximately at the same throughput rate, LDPC (672,336) increases significantly the overall system complexity in comparison with RS (224,214). The 16-QAM C-OFDM system ensures an excellent and satisfactory QoS under the worst case scenarios (D and E) with $E_b/N_o = 24$, as demonstrated in Fig. 3.19d, which restricts the maximum distance between T_X/R_X to 12.62 m. In other words, for a satisfactory QoS the streaming video device and a TV/projector or other receiver equipment should be at a distance smaller than 12.62 m.

3.3.4 Results discussion

In this section, a study of the impact of RF impairments on a 60 GHz OFDM (uncoded and coded) system, implemented according to the IEEE 802.15.3c standard, for high data rate applications, and considering 16-QAM and 64-QAM, was presented. Degradation in system performance due to phase-noise characteristics, IQ imbalances and power amplifier non-linearities, was evaluated. Such impairments were modelled and used to characterise a realistic generic RF front-end system. The performance assessment of the OFDM system was conducted through BER and PSNR analysis considering the transmission of an uncompressed Full HD video frame over an AWGN radio channel model.

It has been shown that PA non-linearities induce the largest performance degradation in the OFDM system, when compared with PN and IQ imbalances. This limitation has

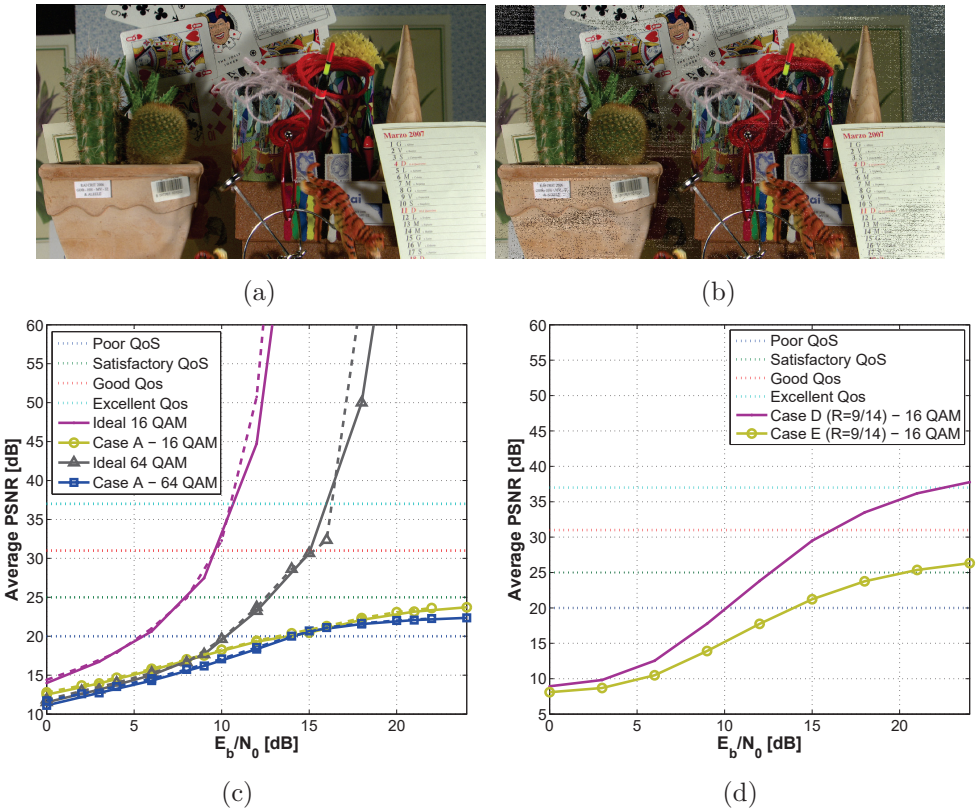

FIGURE 3.19: Subjective video quality performance assessment of the received video frame for an "Ideal RF front-end" a) and under impairments b) for an $E_b/N_o = 24$ dB using 16-QAM. In c) and d) the impact of impairments on the objective quality of the received frame vs E_b/N_0 is conducted for uncoded and coded OFDM, respectively.

been compensated for by the introduction of a PA PD technique, which allows to achieve a good communication quality, reducing the required PA OBO value which, however, remains above those of 6 dB and 8 dB estimated using a GaAs PA for 16 QAM and 64-QAM, respectively. It is concluded that, in order to decrease further these values, a PAPR reduction technique should be considered in the system design, together with PD. This is particularly important if a mobile equipment is used as either TX or RX, since the efficiency of PA should be as high as possible to overcome battery saving requirements.

It is also concluded that the modulation order is important in OFDM system design, in particular at high frequencies and in uncoded systems, since high order modulations present higher sensitivity to bit errors in presence of impairments. For example, it has been shown that for channels with small time dispersion characteristics such as the CM9, BER values of 10^{-6} cannot be achieved for 64 QAM OFDM without FEC schemes. Whereas a performance similar to that of AWGN is noted for uncoded 16-QAM system. This makes the system performance impractical in some cases. For example, 64-QAM with coded OFDM, which enhance the spectral efficiency of the system, just ensures a reliable wireless communication system for worst case scenarios considering LDPC

(672,336) coding. This makes the system to operate at approximately the same rate as the 16-QAM with RS (224,216), but with higher complexity.

Additionally, it is concluded that a coded 16-QAM OFDM system operating under RF and channel impairments is robust enough to provide a relatively good quality of service in streaming uncompressed video for wireless applications, for a range shorter than 13 m. Hence, PN, IQ imbalances and PA non-linearities have direct impact on the potential OFDM system throughput. Both uncoded 16-QAM and 64-QAM OFDM systems fail to achieve the required performance target (for all RF impairment combinations), and coded 64-QAM systems require large coding rates.

3.4 Performance comparison between f-OFDM and SC-FDE over mmWave channels

In this section it is introduced a dual-mode f-OFDM/SC-FDE 60 GHz mmWave PHY layer to provide transmission data rates above 10 Gbps. Such feature goes towards one of the vertical requirements for future wireless communications, such as 5G. The system is evaluated and assessed through metrics of required E_b/N_0 for a target BER of 10^{-5}, under both residential LOS and NLOS scenarios.

For a fair comparison between different transmission schemes, both f-OFDM and SC-FDE are compared considering the same symbol rate, sampling rate, modulation, guard time interval, and common receiver algorithm structure, i.e., channel and SNR estimations and equalisation. To enable this, channel equalisation is performed in the frequency domain, employing a MMSE equaliser, which ensures better performance than Zero Forcing (ZF) at lower SNR. Additionally, both channel and SNR estimations required in the MMSE technique are yield from the auto-correlation properties of a transmitted Channel Estimation Sequence (CES), preamble defined in the IEEE 802.15.3c. Finally, LDPC FEC codes are considered in order to increase robustness in both transmission schemes over frequency selective multipath channels.

3.4.1 Channel frequency response and SNR estimation based on *Golay* sequences

Golay complementary sequences are suggested by the IEEE 802.15.3c standard to be used in the PHY preamble for synchronisation and channel estimation purposes. According to [40], the recommended CES is given by (3.21), and should be transmitted prior to the data for channel estimation purposes at the receiver. In this work, each *Golay* sequence pair was obtained through the recursive complementary sequence generator algorithm

presented in [134], considering all the coefficients $W_n = 1$, where n is the number of delay line blocks.

$$CES = [\mathbf{a}_{256}\mathbf{b}_{256}\mathbf{a}_{256}\mathbf{b}_{256}\mathbf{b}_{128}], \tag{3.21}$$

where the first transmitted bit is the leftmost bit of $\mathbf{a}_{256}$. Hence, the CES sequence consists of the *Golay* pair $(\mathbf{a}_{256}, \mathbf{b}_{256})$ repeated twice and preceded by the cyclic prefix $\mathbf{b}_{128}$. Such pair of *Golay* sequences has an attractive property that the sum of their auto-correlations has maximum peak with zero side-lobes [135]. Let $\mathbf{a}_N$ and $\mathbf{b}_N$ be the pairs of *Golay* sequences of length equals to $N = 2^M$ (M natural number) and $[\mathbf{R}_a, \mathbf{R}_b]$ the auto-correlation of each pair respectively, where the sum both auto-correlations is defined:

$$\mathbf{R}_{ab}(i) = \mathbf{R}_a(i) + \mathbf{R}_b(i) = 2N\delta(i - N), \tag{3.22}$$

where $i \in [0, ..., N-1]$ and $\delta_{(i)}$ is the *Kronecker* delta function. At the receiver, the counterpart of the *Golay* sequence generator, which is known as Efficient *Golay* Correlator (EGC) algorithm [134] was considered. Such digital signal algorithm outputs a CIR from each sum of the auto-correlation of each transmitted pair. Thus two estimated CIRs, $\hat{h}_1(t)$ and $\hat{h}_2(t)$ are obtained. After an FFT operation on both CIRs, the average CFR is estimated according to (3.23):

$$\hat{H}(k) = \frac{1}{M}\sum_{m=1}^{M}\hat{H}(m,k), \tag{3.23}$$

where $\hat{H}(k)$ is the CFR estimated average magnitude for the k^{th} sub-carrier, M is the number of *Golay* pair repetitions in the transmitted CES sequence, which specifically for this case equals 2, and finally, m is the index of each pair.

Additionally, to estimate SNR (η) at the receiver, both the signal power, P_s, and the noise power, P_n, must be estimated. According to [129], such values are obtained from the estimated CFR and given by:

$$P_s = \frac{1}{MK}\sum_{m=1}^{M}|\hat{H}(k)|^2, \tag{3.24}$$

$$P_n = \frac{1}{MK}\sum_{m=1}^{M}\sum_{k=1}^{K}|\hat{W}(m,k)|^2, \tag{3.25}$$

where $\hat{W}(m,k) = \hat{H}(k) - \hat{H}(m,k)$, $m \in [2:M]$ and K is the FFT length.

Furthermore, an enhancement on the CIR estimation under presence of noise is also considered. By comparing the average power estimated on each individual CIR path, $|\hat{h}(k)|^2$, with a predefined threshold, λ, only the significant CIR paths are selected as inputs to the K - point FFT. The value of λ is determined by the average noise power at receiver (3.25). Therefore, the average power estimation values which are below the threshold, are assumed to contain only noise samples, and thus set to null. As a result, the accuracy of the average estimated CFR is significantly increased. The mathematical representation is presented in (3.26).

$$\hat{H}(k) = \begin{cases} \hat{H}(k), & |\hat{H}(k)|^2 > \lambda \\ 0, & otherwise \end{cases} \tag{3.26}$$

3.4.2 System models

The SC-FDE system mode suggested in this work is developed based on the OFDM PHY parameters described in the IEEE 802.15.3c standard [40], with the necessary adjustments to the transmitter and receiver block chains that ensures a fair performance comparison between both. Such modes share the same PHY operating parameters, as depicted in Table 3.14. Particularly for the SC-FDE mode, stuff symbols are inserted to match the data length of an OFDM symbol.

The considered dual-mode f-OFDM/SC-FDE system has been developed in *Matlab* and its block diagram can be found in Fig. 3.20. In this figure, white blocks indicate those that are common to both transmission schemes, the grey ones are specific to SC-FDE, while green ones are OFDM specific blocks. At the transmitter, data source are coded with a FEC block and subsequently mapped into QAM symbols. Following this, and only for OFDM, QAM symbols are mapped into K sub-carriers through 512-points IFFT. Next, a cyclic extension is inserted, namely CP in OFDM and Pilot Word (PW) in SC-FDE, between data. Finally, a *Golay* CES is prefixed to the payload sequence, and a Root Raised Cosine (RCC) is considered in order to limit the bandwidth and output band emissions of the transmitted signal. In particular for OFDM waveforms, such process results in smoothing the discontinuities between adjacent OFDM symbols in frequency domain.

At the receiver, a matched filter, similar to the one used at the transmitter, is considered. The CIR is estimated according to those algorithms (described in Section 3.4.1), and data is equalised. In the SC-FDE system unlike f-OFDM, after equalisation data, is transformed to time domain for data decision by applying the IFFT prior to QAM demodulation.

TABLE 3.14
SUMMARY OF THE MAIN PARAMETERS CONSIDERED IN THE DESIGN OF OFDM/SC-FDE DUAL MODE SYSTEM BASED ON IEEE 802.15.3C STANDARD.

Parameter	Value
FFT size block (N_{fft})	512
Data block size	336
Symbol rate	2640 MHz
Sub-carrier bandwidth	5.15 MHz
Modulation	16-/64-/256-QAM
Stuff symbols (SC-FDE only)	112
Guard time interval*	114/116 samples
FEC code	LDPC(504,672)
Maximum throughput	11.3 Gbps
FIR filter	RCC with interpolation factor 4X
Roll-off factor	0.25
Sampling rate	10560 MHz

(*) number of samples required to meet the maximum excess delay spread of CM2 and CM1, respectively.

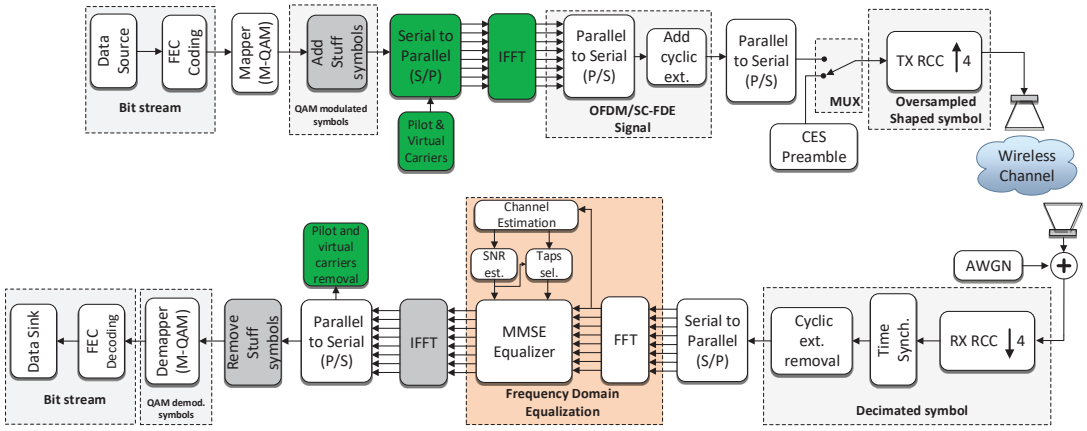

FIGURE 3.20: Dual mode system block diagram.

Received signal and frequency domain equalisation

According to [19], SC-FDE system is equivalent to an OFDM system with a linear FFT pre-coding, where original transmitted information can be recovered with a FDE for both systems. From [129], FDE is performed as a K-branch linear feed-forward equaliser with $C(k)$ as the complex coefficient at the k^{th} sub-carrier. In this work, the FDE approach is the MMSE equaliser, which criterion, $C(k)$ is defined by (3.19).

3.4.3 Effect of channel impairments

In this section, both uncoded and coded f-OFDM and SC-FDE transmission schemes are assessed over a particular CIR realisation from CM1 and CM2 models, which led to the PDPs and frequency responses depicted Fig. 3.21, for each model. Consequently, Table 3.15 presents the CQI for the considered PDPs, where it can be seen that CM2 is the most frequency selective channel, i.e., $B_{c_{0.9}}|CM2 << B_{c_{0.9}}|CM1$.

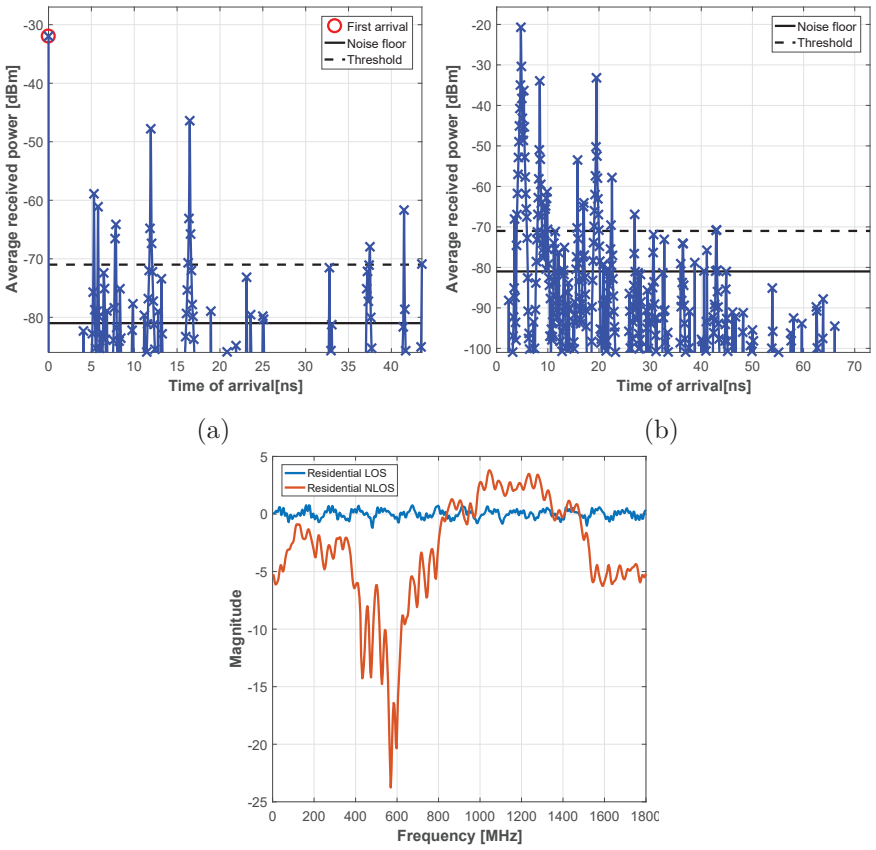

FIGURE 3.21: PDP calculation method for the channel models: a) CM1 b) CM2.

Prior to the aforementioned evaluation, *Golay* sequences accuracy, in estimating CIR and SNR, are evaluated in terms of overall demodulation performance, i.e., through BER analysis. For this, a comparison between BER results from an ideal versus channel and SNR estimations for uncoded SC employing 256-QAM modulation over CM1 is considered. From Fig. 3.22a, it can be seen that such results and are in good agreement, which validates *Golay* complementary pair sequences as a good choice for channel and SNR estimations.

TABLE 3.15
CQI PARAMETERS FOR THE CONSIDERED MULTIPATH FADING CHANNELS.

CM #	τ_{RMS} (ns)	$B_{c_{0.9}}$ **(MHz)**	τ_m (ns)
1	3.92	36	43.6
2	3.1	18	43

Furthermore, noise mitigation on estimated CIR samples, method suggested in (3.26), is assessed. For that, λ is obtained through the following parametric study. First, a reference threshold is considered as P_n, and then it is decreased in dB steps of 1, until an optimised value of BER is achieved. From Fig. 3.22b, it can be verified that such optimised BER is attained for λ equals to 10 dB below P_n.

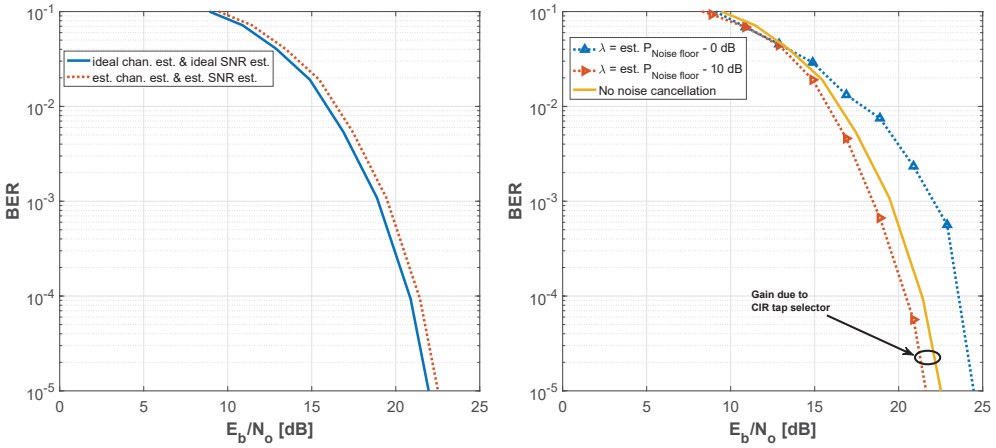

(a) (b)

FIGURE 3.22: *Golay* pair sequences performance on estimating both CIR and SNR using 256-QAM for SC-FDE (a), and its enhanced performance using a noise cancellation method (b).

Uncoded Systems

BER comparison performance of uncoded SC-FDE and f-OFDM modes over CM1 and CM2, employing 16, 64 and 256 QAM, is depicted in Fig. 3.23a and Fig. 3.23b, respectively. As it can be verified from these results, f-OFDM is significantly more effected by CM2 than SC-FDE, due to the lack of frequency diversity. Such feature is an intrinsic characteristic of SC systems, since one single symbol shares all channel

bandwidth, whereas, in f-OFDM systems every sub-carrier experience different attenuation levels caused by the CFR. Thus, when several sets of sub-carriers are experiencing a frequency null in the CFR, all the information contained in them are lost except if, at receiver, SNR values are higher than the corresponding attenuation values. For example, considering the CFR of CM2, (see Fig. 3.21c), SNR values above 10 dB at the receiver must be ensured, otherwise all the information around 425 and 620 MHz will be lost. This explains the fact that over CM2 channel model, SC-FDE clearly outperforms f-OFDM BER results. On the other hand, for a relatively flat CFR such as the CM1, both systems perform similarly.

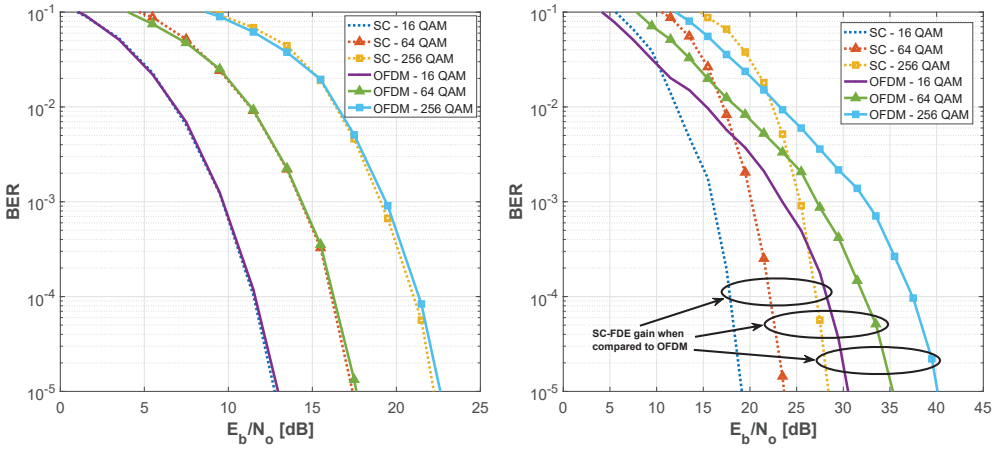

FIGURE 3.23: BER comparison performance uncoded f-OFDM and SC-FDE employing 16-/64-/256-QAM modulations over: a) CM1; b) CM2.

Coded Systems

In order to enhance the lack of frequency diversity of f-OFDM demonstrated in previous results, LDPC(504,672) FEC codes are employed. BER results of coded SC-FDE and f-OFDM are shown in Fig. 3.24. From these, it can be seen that the performance of f-OFDM is now closer to the SC-FDE when channel coding is employed. However, SC-FDE still outperforms f-OFDM over both CM1 and CM2 channel models, as summarised in Table 3.16. For example, considering 256-QAM modulation, it has 6 dB of E_b/N_0 gain in comparison with f-OFDM, under the same conditions.

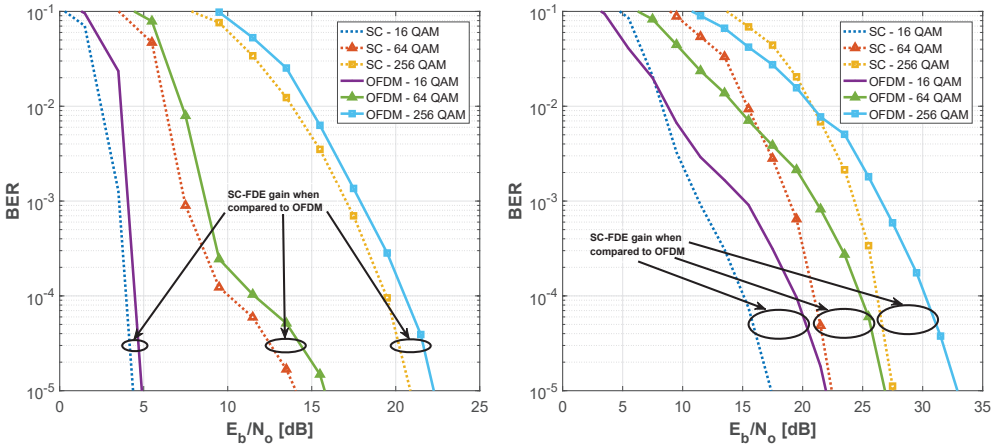

(a) (b)

FIGURE 3.24: BER comparison performance coded f-OFDM and SC-FDE employing 16-/64-/256-QAM modulations over: a) CM1 and b) CM2.

TABLE 3.16
SUMMARY OF THE REQUIRED E_b/N_0 DB FOR CM1 AND CM2 CHANNEL MODELS, EMPLOYING BOTH F-OFDM AND SC-FDE MODES.

Channel model [#]	**Modulation order**	**Required SC-FDE** E_b/N_0 **[dB]***	**SC-FDE Gain [dB]**†
1	16	5	0.5
	64	15.5	1.5
	256	21.5	1.5
2	16	17.5	4
	64	21.5	5.5
	256	27.5	6

(*) considering a BER target of 10^{-5};
(†) difference between the required SC-FDE E_b/N_0 with f-OFDM one, under the same conditions.

3.4.4 Results discussion

A detailed comparative study on the system performance of f-OFDM and SC-FDE systems at a 60 GHz, considering *Golay* sequences for channel and SNR estimations under mmWave environments, has been presented.

In this work it has been shown that *Golay* sequences, presented as PHY preamble, are a relatively good choice for channel and SNR estimations for mmWave signals, operating at multi-Gigabit/s data rates. Moreover, it has also been demonstrated,

through BER analysis, that by removing the effect of noise on estimated CIR samples, the FDE overall performance significantly increases.

Finally, SC-FDE and f-OFDM modes yield similar BER performances over non frequency selective channels, while SC-FDE mode proved to be more robust against frequency selective multipath fading channels. Even with improvements from frequency diversity introduced by channel coding, the f-OFDM cannot achieve the SC-FDE performance, under similar conditions. Therefore, SC-FDE should be seen as a serious alternative to f-OFDM, specially, in deployment scenarios where high PA efficiency is required, since it does not suffers from high PAPR values.

Furthermore, 11 Gbps data transmission throughput over mmWave channels using both f-OFDM and SC-FDE seems possible. This is achieved with limited design refinements, from the original IEEE 802.15.3c proposal, which indicates that wireless communications systems providing multi-Gigabit/s data rates, transmitted at millimetre wave frequencies, will eventually work on 5G networks.

3.5 Evaluation of FS-FBMC against OFDM for high data rate applications at 60 GHz

In the scope of 5G, this section introduces and examines a FS-FBMC waveform based on OFDM physical layer specifications present on the IEEE 802.15.3c standard for 60 GHz high data rate applications [40]. The transmission channel is modelled according to both CM1 and CM9 models, which are LOS indoor residential and kiosk, respectively. The performance of an end-to-end 5G system is presented for a realistic application, where a comparison of the effect of non-linearities of a typical RF power amplifier at 60 GHz is presented for both OFDM and FS-FBMC. In particular, the sensitivity to non-linear effects caused by the RF power amplifier is investigated and compared between both transmission schemes, using OOBEs and BER as metrics to assess the overall system performance. Despite the existence of articles addressing the effect of PA non-linearities in both OFDM and FBMC system, to the authors' knowledge, none of them present a comprehensive critical comparison analysis on the performance of both transmission schemes at 60 GHz. For example, in [136], the comparison is performed without considering the proposed standard specifications [40] and appropriate RF impairment models for 60 GHz communication systems, reported in [117] and [121]. Similarly, in [136] a *Rayleigh* fading channel model is considered whereas realistic mmWave multipath fading channels are considered in this work.

3.5.1 System model architecture

To full-fill these requirements, new waveforms based on filter bank techniques, e.g. FBMC, have been proposed [10]. As evident by all the activities in 5G on the air interface, there is a need to overcome the limitations that OFDM imposes in a traditional multi-carrier system, such as strict synchronisation requirements and use of CP to keep sub-carrier orthogonality, low spectral efficiency and high spectral leakage [109], which currently fails to meet the rejection level requirements of, e.g. 55 dB of adjacent channel leakage ratio [137]. These limitations form the basis of the issues addressed in this paper.

The FS-FBMC system model proposed in this work is developed based on the OFDM architecture described in the IEEE 802.15.3c standard [40], with the necessary adjustments to the transmitter and receiver as suggested in Section 3.1 and illustrated in Fig.3.5. The implemented OFDM/ FS-FBMC system has been developed in *Matlab* and its block diagram can be found in Fig. 3.25.

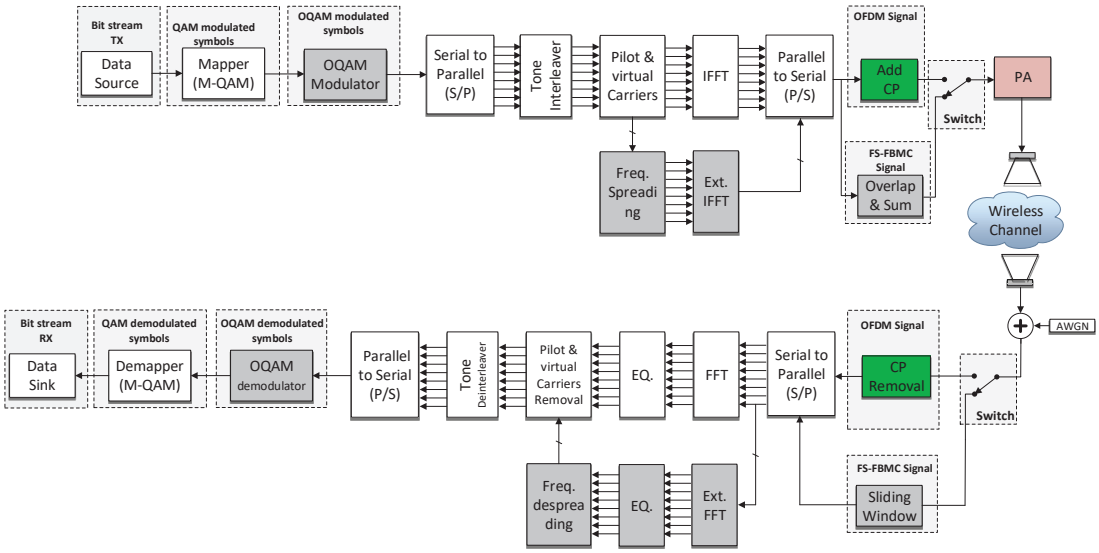

FIGURE 3.25: Block diagram of the implemented OFDM/FS-FBMC systems.

In the above figure, white blocks indicate those that are common to both transmission schemes, the grey ones are those specific to FS-FBMC, while green ones are OFDM specific blocks. Evidently, the difference between both systems mainly in the employment of an OQAM modulator/demodulator and extended IFFT/FFT operations, enabling both systems to operate on a dual-mode wireless system. This brings many advantages such as [109]:

- In either down-link or up-link, OFDM offers lower complexity, while FBMC provides higher bandwidth efficiency;
- In a duplex communication system, if the transmission scheme used for the down-link is FS-FBMC, it means that most of the signal processing complexity is concentrated at the base station;
- If the FS-FBMC is used as up-link scheme, due to its higher bandwidth efficiency and relatively lower out-of-band emissions, the noise level at the user receiver equipment is not overwhelmed by the presence of high level neighbouring signals and is able to identify accurately the spectrum holes;
- In up-link, synchronisation requirement among signals from different nodes is less stringent when using FS-FBMC, i.e., interference cancellation technique is not necessary. Moreover, because of the complexity of interference mitigation algorithms in general, OFDM system becomes more complex when compared to the FBMC.

The physical operating parameters for both system models are given in Table 3.17 [40]. Their constellations, tone interleaver blocks are directly provided by the standard [40]. In order to shape both OFDM and FS-FBMC signal PSD, sub-carriers/ sub-channels are allocated into the IFFT according to Table 3.6 [40]. The wireless channel model employed is an AWGN channel combined with the multipath fading channels presented in Section 3.2.3. Perfect frequency and time synchronisation is assumed at the receiver. The power amplifier considered in the model is described in detail in the next section.

Table 3.17
Main parameters considered for the OFDM and FS-FBMC systems design based on IEEE 802.15.3c standard.

Parameter	**OFDM**	**FS-FBMC**
Overlapping Factor (K)	n/a	4
FFT size block (N_{fft})	512	2048
Sub-channels	n/a	512
Cyclic prefix (N_{cp})	64 samples	n/a
Cyclic prefix time (T_{cp})	24.24 ns	n/a
Modulation	16-QAM	16 OQAM
Throughput	6.2 Gbps	**6.93 Gbps**
Nominal Used Bandwidth	1815 MHz	1815 MHz
Sub-carrier bandwidth	5.15 MHz	1.2875 MHz

At the receiver, the original transmitted information is recovered with a frequency domain equalisation for both systems. A ZF technique has been chosen due to its inherent simplicity. For such criterion, $C(k)$ is defined by:

$$C_{ZF}(k) = \frac{\hat{H}(k)^*}{|\hat{H}(k)|^2} \tag{3.27}$$

where $\hat{H}(k)$, where $k = 0, ..., M-1$ and $k = 0, ..., KM-1$ for OFDM and FS-FBMC, receptively * and $|.|$ denote the estimated CFR, SNR, conjugate transpose and module, respectively.

3.5.2 Model validation

The main feature of FS-FBMC is the extremely low out-of-band radiation, allowing for more efficient spectrum sharing between opportunistic users, due to relatively lower adjacent-channel leakage from one user to another in comparison with OFDM. To this extent and in order to validate the framework, the difference of the PSD between OFDM and FS-FBMC is depicted in Fig. 3.26a, illustrating the capability of the considered FS-FBMC system to reject the OFDM out-of-band emissions of up to 65 dB.

Moreover, a comparison between the simulated BER results and those obtained from the analytical expressions presented for uncoded OFDM and FBMC employing M-ary QAM modulations over AWGN channels are presented in Fig. 3.26b. For the OFDM case, the small difference between simulated and theoretical results over AWGN channel are caused by the insertion of CP.

In this work, the OFDM symbol is power boosted to compensate for the wastage of energy (L_{cp} losses) associated with the insertion of CP. Thus, both OFDM and FBMC systems, employing M-ary QAM/OQAM modulations, show similar BER results and are in agreement with those reported in [138] and theoretical expressions in [106].

The PAPR of each transmission scheme is represented in Fig. 3.26c as a Cumulative Distribution Function (CDF) of the amplitude variations. Clearly both OFDM and FS-FBMC practically have the same distribution, i.e. for 90% of cases OFDM PAPR is below 9.5 dB whereas in FS-FBMC is 9.3 dB.

3.5.3 PA non-linearities effect in OFDM/ FS-FBMC

The importance of operating a PA as close as possible to its saturation point is vital, since it is the point where its power efficiency is highest. As referred in Section 3.2.2, distortion occurs if the signal has a high PAPR due to the PA non-linear response. Therefore, in this section the performance of both OFDM and FS-FBMC is assessed

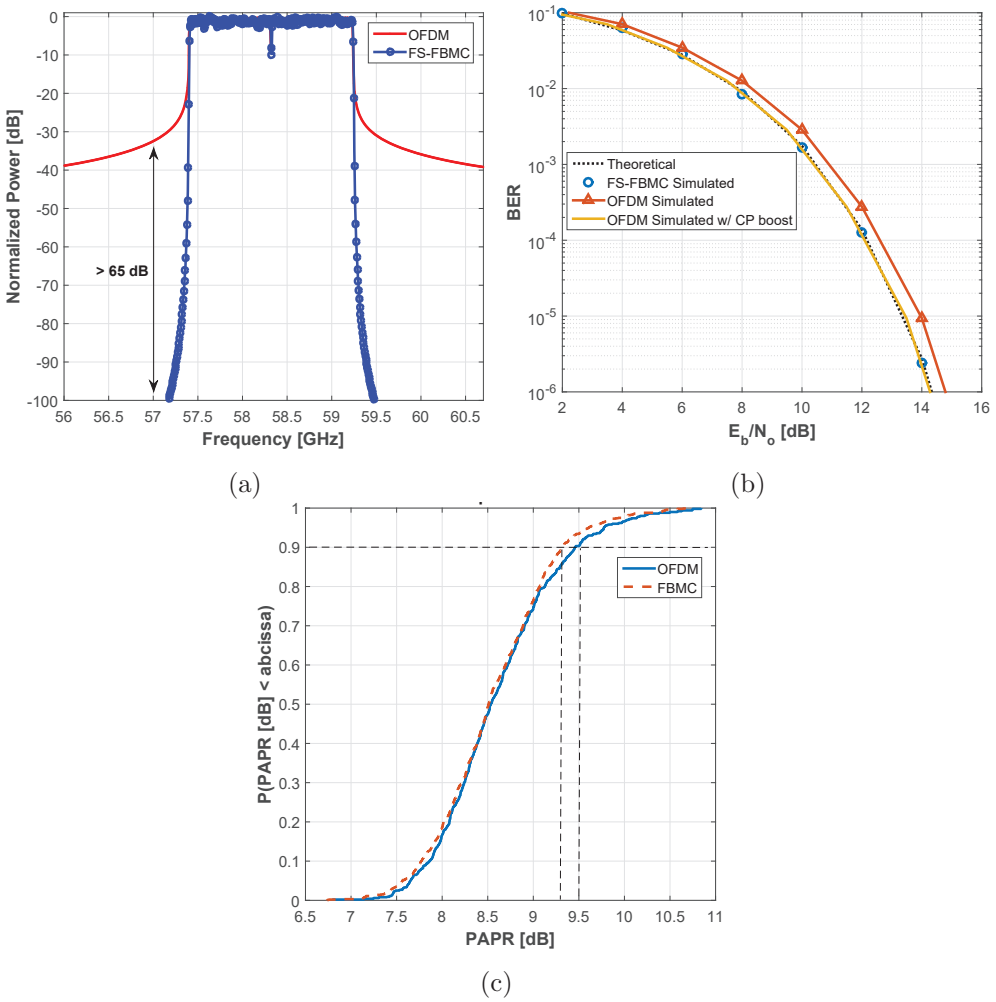

FIGURE 3.26: FS-FBMC validation curves in comparison with OFDM: (a) normalised power spectrum, (b) theoretical and simulated E_b/N_o over an AWGN channel (using 16-QAM/OQAM) and (c) PAPR distribution.

through BER, OOBE and power efficiency analysis over CM1 and CM2 channel models, presented in Section 3.2.3, considering both PA in-band and out-of-band distortions. Additionally, as it was performed in other system's analysis, all BER simulation results are averaged over 100 realisations.

Unlike in-band distortions, where ISI is introduced, out-of-band emissions do not have a direct impact on the system performance, but might however interfere with other networks operating in adjacent frequency channels. Therefore, for 60 GHz communication networks, a TSM is defined in [40] to ensure that this phenomena will not occur. In order to investigate when the spectral growth of both signals exceeds this mask in the PA OBO curves, PSD is calculated, averaging 400 multi-carrier symbols. Results illustrated in Fig. 3.27, considering the GaAs PA model introduced in Section 3.2.2, show that the minimum value of PA OBO for OFDM and FS-FBMC without PA pre-distortion is 9 dB and 13 dB, respectively. In addition, when PA

pre-distortion is employed, both values drop to 5 dB and 9.5 dB, where FS-FBMC appears to be more sensitive against those impairments than OFDM.

Similar analysis is carried out on the impact in-band PA distortions have on both transmissions schemes. Results of BER vs PA OBO are presented in Fig. 3.28, over AWGN, CM1 and CM9 channel models, where the influence of PD technique is evaluated.

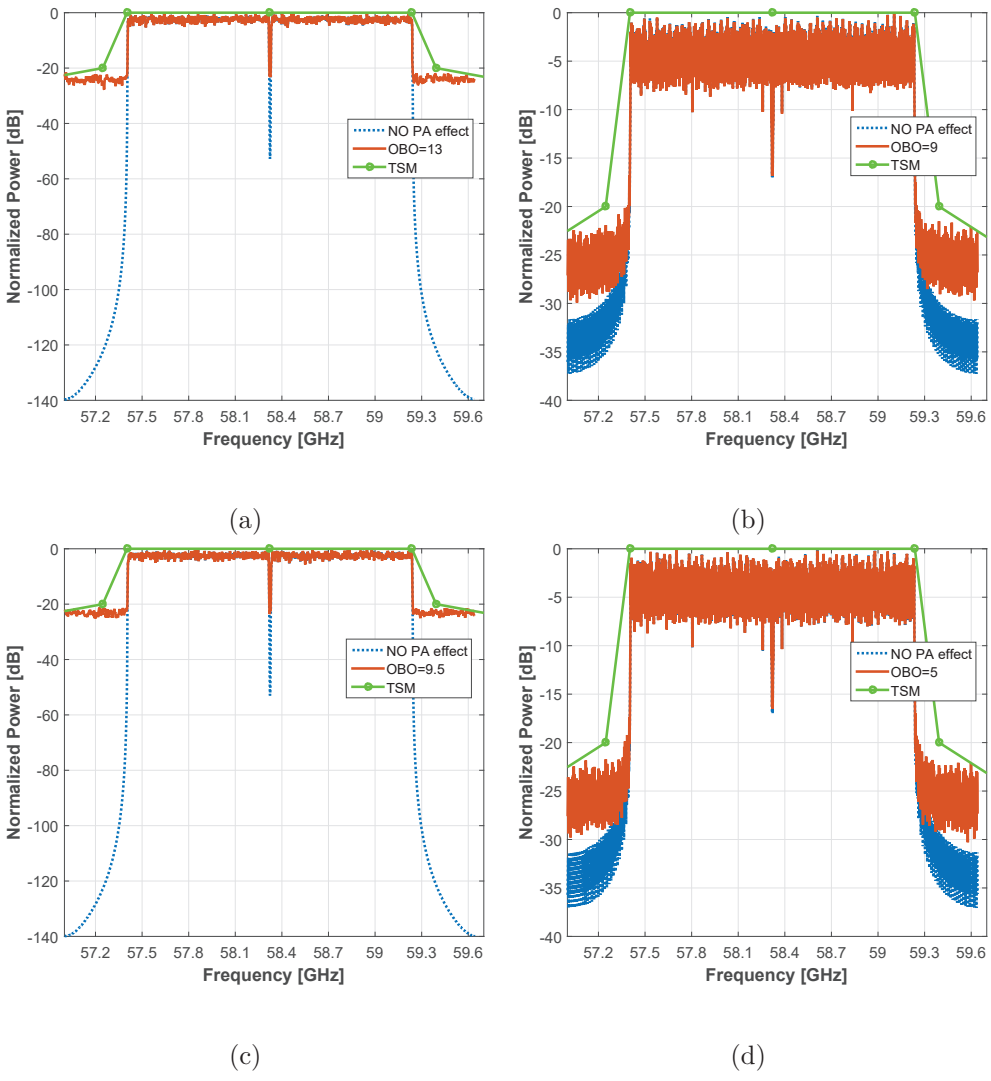

FIGURE 3.27: Estimated OOBEs using GaAs PA model: (a) and (b) without PD; (c) and (d) considering PD, for FS-FBMC and OFDM (employing 16-QAM/OQAM), respectively.

It can be clearly noticed that FS-FBMC is more sensitive to PA non-linearities than OFDM, i.e. ISI in FS-FBMC is higher than for OFDM for the same PA OBO value, leading to higher BER. A summary of PA non-linearity impact on OOBE and BER

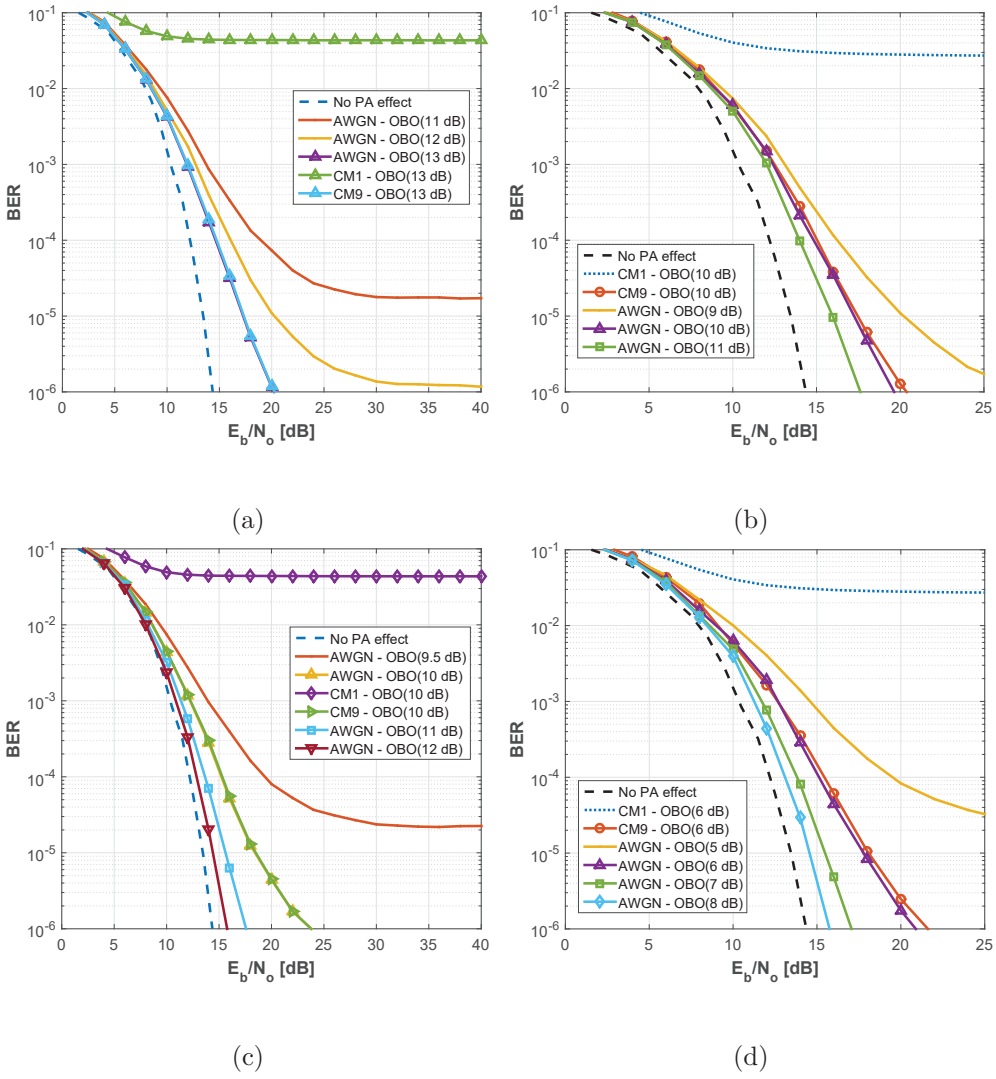

FIGURE 3.28: BER performance using GaAs PA model: (a) and (b) without PD; (c) and (d) considering PD, for FS-FBMC and OFDM (employing 16-QAM/OQAM), respectively.

results, against PA OBO for both systems, is presented in Table 3.18. In this table, E_b/N_o values are obtained for a minimum possible PA OBO, which meets a BER target of 10^{-6}. Performance degradation is characterised by $\triangle E_b/N_o$, which is the difference between the required E_b/N_o in the absence and presence of non-linearities.

It is evident from results that PA OBO has a significant impact both in OOBE and BER performance. Additionally, it is verified that FS-FBMC system, under presence of PA distortion, loses its enhanced spectral efficiency, i.e. the rejection of the out-of-band emissions presented in an OFDM system as shown in Fig. 3.26a is no longer verified. In fact, it can also be concluded that OFDM might be a better choice since according to Table 3.18, it offers lower values of PA OBO to meet the TSM, making GaAs PA to operate at higher values of η than FS-FBMC. Moreover, both OFDM and FS-FBMC

Table 3.18
Summary of PA non-linearity impact on BER and OOBE results for 60 GHz OFDM and FS-FBMC systems.

Transmission Scheme	**Channel**	**PD**	E_b/N_o **[dB]**	$\triangle E_b/N_o$ **[dB]**	**OBO [dB]**	η **%**
FS-FBMC	AWGN	no	20	5.6	13	3.4
		yes	24	9.6	10	7.07
	CM1/CM9	**no**	**N/A / 20**	**N/A / 5.6**	**13**	**3.4**
		yes	**N/A / 24**	**N/A / 9.6**	**10**	**7.07**
OFDM	AWGN	no	19.5	5.1	10	6.8
		yes	21	6.6	5	17.7
	CM1/CM9	**no**	**N/A / 20.4**	**N/A / 6**	**10**	**6.8**
		yes	**N/A / 22**	**N/A / 7.6**	**5**	**17.7**

are affected by the considered propagation channel. For example, OFDM performance over CM1 at PA $OBO = 10\ dB$, when no PD is employed, fails to meet the BER target. Despite CM1 being characterised by a relatively low RMS delay, since CP interval time is shorter than the maximum delay spread of the multipath channel, the equaliser is not able to deal with the resulting ISI. However, under the same conditions OFDM meets the performance target over CM9, due to the fact that such channel is characterised by a *Rician* factor 30 dB higher (Table 3.3) and consequently lowest frequency selectivity, when compared to CM1.

3.5.4 Spectrum analysis for mmWave signals: a case study

In this subsection, a FS-FBMC system based on IEEE 802.15.3c standard specifications [40], is suggested to be candidate for 5G networks operating at mmWave spectrum. Such transmission scheme provides higher spectral efficiency, due to the CP removal, system throughput, enhanced time, better sub-carriers frequency localization, and less strict orthogonality requirements, when compared to OFDM systems. Networks operating at these frequencies are usually associated with very high path losses and typically resulting in less coverage distances for a given transmission power and antenna gain than at lower frequencies. This in fact can be seen as an advantage in such networks, since that helps in increasing the frequency re-use density [45], and very wide signal bandwidth is available.

Simulation results presented in Section 3.5.3 show that FS-FBMC is relatively more sensitive to non-linearities than OFDM, i.e. FS-FBMC requires much higher PA OBO values to ensure significant attenuation of the sides lobes presented in the frequency power spectrum of OFDM, leading to reduced power efficiency of the PA. This is particularly important in a mobile equipment, where battery saving requirements are

mandatory. Therefore, for future radio communication (5G), OFDM could be utilised for up-link since it ensures higher power efficiency whereas FS-FBMC could be used for down-link in the PHY layer in order to avoid multiple access interference and higher data rates.

To demonstrate the advantages of this concept, the following study has been considered. At the base station information towards three different users, UE1, UE2 and UE3 are being transmitted over three 60 GHz channels, which are presented in Table 3.19 [40]. At the receiver each mobile equipment is acquiring the intended information at a normalised average power of 0, -50 and -30 dB, respectively.

Table 3.19
mmWave PHY channelisation.

Channel ID	**Start Frequency [GHz]**	**Centre Frequency [GHz]**	**Stop Frequency [GHz]**
1	57.24	58.32	59.4
2	59.4	60.48	61.56
3	61.56	62.64	63.72

As depicted in Fig. 3.29, higher adjacent channel interference is presented between UE1 and UE2, i.e., information received from UE2 is masked by the Channel Interference (CI) from UE1 and UE3. The content transmitted to UE2 will be lost unless advanced interference cancellation techniques are employed. On the other hand, the FS-FBMC receiver is not blinded by the presence of high level neighbouring signals and it is capable to identify accurately the spectrum holes through a simple energy detector. Additionally, in the employment FS-FBMC, the number of null sub-carriers could be decreased, resulting in an increased throughput, since according to Fig. 3.29, there is a "clean gap" $\triangle f$ between adjacent wireless channels.

3.5.5 Results discussion

The results presented in this work provide an important guidance for OFDM/FBMC 5G radio communication design principles at mmWave.

A detailed study of the degradation of system performance at a 60 GHz OFDM and FS-FBMC systems, implemented based on the IEEE 802.15.3c standard for high data rate applications, has been presented for the first time. In particular, power amplifier non-linearities are modelled to characterise a realistic PA to be embedded in the system. The performance assessment of both OFDM and FS-FBMC systems was conducted

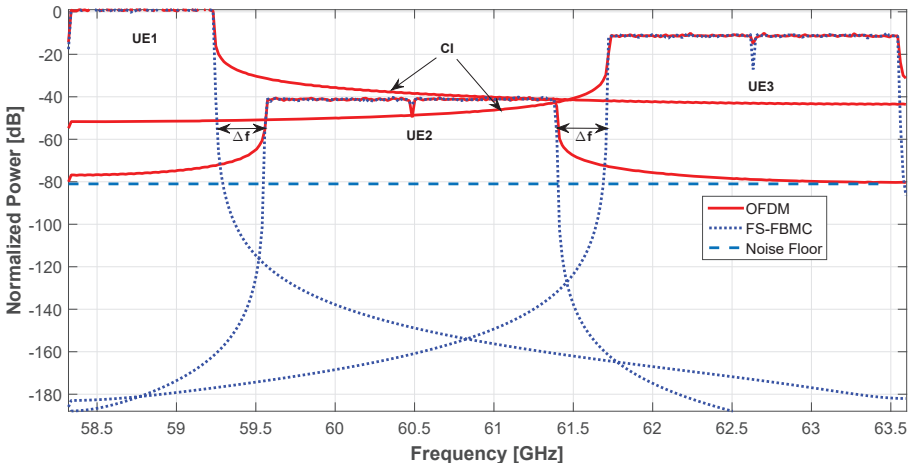

FIGURE 3.29: Normalised power spectrum comparison between OFDM and FS-FBMC, considering three different users over three 60 GHz channels, according to Table 3.19.

through OOBEs and BER analysis over an AWGN channel. Moreover, a radio access for future radio generations employing OFDM and FS-FBMC for up-link and down-link, respectively, has been proposed and analysed.

It has been shown that PA non-linearities induce very significant degradation on both systems but more accentuated in the FS-FBMC. This limitation has been compensated for, by the introduction of a PA pre-distortion technique which allows a reduction in the the required PA OBO values. However, for FS-FBMC, in order to ensure its enhanced spectral efficiency, along with PD, the overall system should include also a PAPR reduction and forward error correction techniques to make the system more robust in terms of BER.

Furthermore, the suitability of mmWave using FS-FBMC as a transmission scheme is good a candidate for the down-link transmissions, since it ensures higher spectral efficiency, despite being more sensitive to PA non-linearities. Such negative effects must be compensated either with high valuer of PA OBO or employing PD techniques. Consequently, FS-FBMC distance range could also be increased due to the reduction in the power sensitivity of the mobile equipment. Moreover, due to the inherent capability of reducing adjacent channel interference, the system throughput by using FS-FBMC can be potentially increased as a result of increasing the number of available data sub-carriers and CP removal.

3.6 Interim conclusions

The work presented in this chapter puts the efforts in assessing the feasibility of multi-Gigabit/s transmissions at 60 GHz (at the time of the framework development, this

frequency spectrum was thought to be the key solution for the next-generation in terms of data rate [16, 17]). This was achieved by simulations, since it is impractical to test the effect of individual RF impairments in the performance of an real end-to-end OTA communication system. Such would be subject to the contribution of imperfections from all hardware components present in the architecture of both TX/ RX RF front-ends. Moreover, since wireless communication technology is evolving relatively fast, by the means of simulations, it was possible to obtain promising results while reducing the time to market.

As discussed in Section A.2.3, 5G imposes distinct requirements than earlier generations. That is, it is expected a high level of integration, flexibility, costs and power consumption. To this context, the proposed framework provides a clear identification of the main limiting factors in the performance of a multi-Gigabit/s communication. In general, it has been demonstrated that PA, PN and IQ impairments are a very restrictive factor in 60 GHz transmissions, limiting both data rate and spectral efficiency. Therefore, in order to enable high-performance solutions for 5G, RF architectures should be evolved in a way that the aforementioned non-linearities are mitigated. For example, PA and PN impairments can be compensated by backing off the PA input power, and choosing a very stable LO, while IQ imbalances should be completely mitigated either by performing the IQ mixing process in the digital domain or by the consideration of other techniques for its estimation and compensation. Otherwise it would be very challenging to enable data rate communications over 10 Gbps.

The work performed in this chapter has been disseminated in three international journals and three conference publications, as follows:

J. R. Gomes, J. R. Reis, Zaid Al-Daher, A. Hammoudeh, R. F. S. Caldeirinha, **"5G: Performance and Evaluation of FS-FBMC against OFDM for High Data Rate Applications at 60 GHz**, *IET Signal Processing*, vol. 12, no. 5, pp. 620-628, Feb. 2018. doi: 10.1049/iet-spr.2016.0671 . **Impact Factor = 1.25, Q2;**

J. R. Gomes, Akram Hammoudeh , R. F. S. Caldeirinha, Zaid Al-Daher, T. Fernandes, J. R. Reis, **"Towards 5G: Performance evaluation 60 GHz UWB OFDM communications under both channel and RF impairments"**, *Physical Communication-Elsevier*, vol. 25, no. 2, pp. 527-538, Oct. 2017. doi: 10.1016/j.phycom.2017.10.011. **Impact Factor = 1.522, Q2;**

J. R. Gomes, R. F. S. Caldeirinha, Akram Hammoudeh, Pedro Pires, **"Performance Evaluation of 60 GHz OFDM Communications under Channel Impairments over Multipath Fading Channels at 60**

GHz", *Sensors & Transducers Journal and Magazine*, vol. 204, no. 9, pp. 29-38, Sept.2016;

C. R. Gomes, K. Sobaihi, R.F.S Caldeirinha and A. Hammoudeh, **"Performance Evaluation of a Dual-Mode OFDM and SC-FDE System at mmWave enabling Joint Radar and 5G Multi-Gigabit/s Wireless Communications"**, 2019 6th International Conference on Signal Processing and Integrated Networks (SPIN), India, 2019.

C. R. Gomes, R. F. S. Caldeirinha, Akram Hammoudeh, **"Uncompressed Full HD Video Transmission using Uncoded OFDM over Multipath Fading Channels at 60 GHz"**, *IARIA SIGNAL 2016*, vol. 0, no. 0, pp. 0-0, June 2016;

C. R. Gomes, Zaid Al-Daher, Akram Hammoudeh, Khaled Sobaihi, R. F. S. Caldeirinha, T. Fernandes, **"Performance and evaluation of OFDM and SC - FDE over an AWGN propagation channel under RF impairments using simulink at 60GHz"**, *Loughborough Antennas and Propagation Conference (LAPC)*, Loughborough, 2014, pp. 685-689. doi: 10.1109/LAPC.2014.6996487

This page is intentionally left blank.

CHAPTER 4

A software-defined radio for future wireless communication systems

4.1 Introduction

In this chapter, a novel FPGA based SDR (testbed) for prototyping future wireless communications is introduced, following the 5G system requirements outlined in Section 2.5. A software-defined radio is a common term given to a system which employ the majority of physical layer functionalities using digital signal processing algorithms implemented in an embedded system, with the aid of a specific software. In this context, typically analogue stages such as: mixing, amplification, filtering, modulators/ demodulators, essential to establish a wireless radio link, are digitally implemented rather than using discrete analogue hardware components. Therefore, an ideal SDR is composed of very reduced hardware at the RF front-end, i.e., only an antenna and a very high speed sampler that is capable of capturing and digitising a wideband radio signals [139]. However, relatively large coverage distances might be only attained by the employment of amplifiers prior to both DAC/ ADC stages, as it is depicted in Fig. 4.1. For example, at the receiver, a Low-Noise Amplifier (LNA) must be consider to reduce the converter quantisation noise and thus maximise the SNR at the digital domain (after sampling), only then the signal is converted to its binary form. Next, data is processed on a number of dedicated computational units, inside the embedded system, enabling the implementation of crucial methods for demodulation, synchronisation, decoding, which are required to recover the transmitted information from advanced modulation techniques.

Nevertheless, the main drawback of this architecture is that in the digital domain computational complexity and precision are limited. However, translating hardware discrete analogue components functionalities into an embedded platform, brings several advantages for a wireless communication system designer, such as [140]:

1. **Design Flexibility:** with the recent availability of very fast and accurate DACs/ ADCs, traditional hardware circuitry such as: filtering, analogue modulators/ demodulators can now be tuned;

2. **Reliability:** in general hardware components functionalities vary according to temperature, manufacturing variations and ageing, which might lead to performance losses for the communication system. On other hand, if such functionalities are implemented in a SDR platform, system's performance is expected to remain the same over the years;

3. **Upgradability:** Upgrading and improving a wireless system which is composed only by discrete components usually means replacing hardware, whereas using SDR a particular system might be upgraded without any additional cost, which lead to a more cost effective solution;

4. **Re-usability:** once a PHY is designed and tested in software, its deployment can be implemented in several hardware platforms;

5. **Reconfigurability:** current SDR implementations offers the capability of reconfigurable hardware to support several wireless standards and waveforms;

6. **Lower Cost:** less number of hardware components are necessary to be acquired in order to build a communication system from the scratch. Such devices are usually more expensive than the acquisition of SDR products.

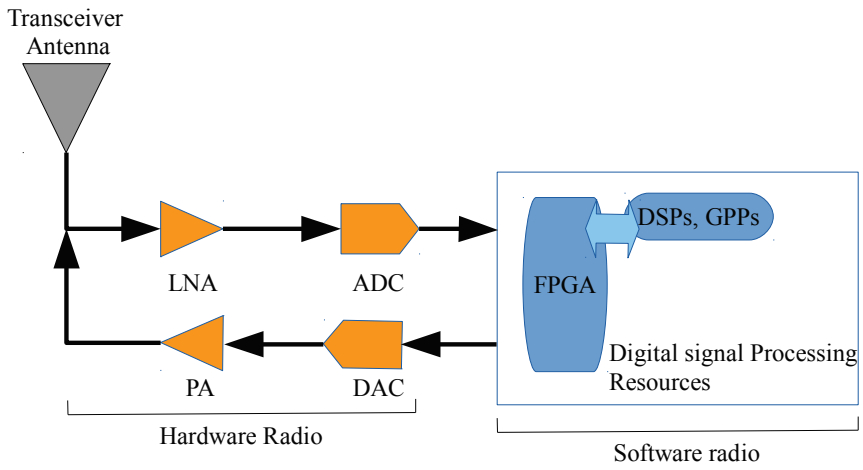

FIGURE 4.1: Block diagram of the ideal software-defined radio transceiver (image adapted from [141]).

A complete description of the developed SDR is outlined, where a special focus is given to the adopted connectivity firmware between the embedded system with both GSPS DAC/ ADC boards. Also, an extensive characterisation of the SDR in terms of SNR, Spurious-Free Dynamic Range (SFDR), Signal-to-Noise and Distortion ratio (SINAD) and Effective Number Of Bits (ENOB) is given, along with the proposed hardware design for OFDM systems based on the LTE-Advanced downlink PHY layer. Finally, OFDM performance in both Back-to-Back (B2B) and over-the-air (all digital radio) scenarios is assessed in terms of EVM and received scatter constellation plots for 4-/ 256-QAM.

4.2 The hardware choice

An ideal SDR is composed of an embedded platform engine, which can be either an Application-Specific Integrated Circuit (ASIC) or a FPGA [142], and at least by one pair DAC/ ADC, to translate signals from digital domain to analogue domain and vice-versa. While a FPGA is an integrated circuit, intended for a general purpose use, that contains programmable logic blocks which form higher-level functions (e.g., lookup tables, multiplexers, adders, multipliers, and RAM memories), and a hierarchy of reconfigurable interconnection between them [143]. The ASIC is specific HW solution designed for a particular use of application and require higher development costs [144]. Moreover, unlike the FPGA chip-set, they are not reprogrammable and therefore a chip modification requires Recurring Expenses (RE). In order to ease the decision of choosing between FPGA and ASIC, it has been drawn the Table 4.1, based on the *Xilinx* documentation presented in [144].

From Table 4.1, it can be verified that FPGA platforms bring three main benefits for the designer, such as: faster time-to-market (no layout for manufacturing needed), simpler design (the software handles much of the routing, placement, and timing), and field re-programmability (a new bitstream can be uploaded remotely). Traditionally, all the above features would become available at the expense of chip performance, i.e., clock speed. However, in recent *Xilinx's* FPGA technology digital clock values can now go over the 500 MHz performance barrier [143].

In particular, FPGA technology has been the preferable choice, due to the fact that time-to-market and costs, are crucial for this research project, which mainly consists on the prototyping of a novel multi-Gigabit/s wireless communication system. Nevertheless, once a final product is achieved, its functionality can be re-mapped into an ASIC relatively easy and improving its performance (bandwidth/ clock speed), optimising size, unit cost, and power consumption.

TABLE 4.1
FPGA VS ASIC: DESIGN ADVANTAGES.

Feature	FPGA	ASIC
Faster time-to-market	Fast	Slow
No upfront NRE	Low	High
Simpler design cycle	Simple	Complex
Field reprogramability	High	N/A
Full custom capability	N/A	High
Lower unit costs	High	Low
Smaller form factor	High	Low
Power consumption	High	Low
Performance	Medium	High

4.2.1 FPGA

One of the main challenges faced by embedded systems developers is the diversity of external I/O interfacing requirements, which might be either Ethernet, optical, analogue conversion, or Gigabit serial [145]. Thus, in order to enable data transfer between the embedded system and other hardware devices, the creation of external I/O interface is needed. In this context, unless that is implemented on a daughter board (mezzanine module), replacing the physical I/O components and connectors would require constantly changing the FPGA board design, and consequently increasing the system costs [146]. To overcome this, the VITA 57 FPGA Mezzanine Card (FMC) connectivity ANSI/ VITA standard was developed in 2008, to provide a modular standard mezzanine I/O interfacing solution to a FPGA located on a carrier board [146]. This brought several benefits including [145]:

- **Maximum data throughput:** individual signalling speeds up to 10 Gbps, reaching overall bandwidths up to 40 Gbps between the FMC and FPGA;
- **Minimal latency and reduced design complexity:** there is no need for protocol overhead;
- **System cost reduction:** design is simplified.

Furthermore, two type of populated FMC connectors are available, namely Low Pin Count (LPC) and High Pin Count (HPC). The difference is that the first has 160 pins, whereas the second one has 400 available pins. Moreover, LPC connector provides 68/ 34 user-defined signals for single-ended and differential signals, respectively. It also provides one serial transceiver pair, clocks, and both Joint Test Access Group (JTAG) interface and Inter-Integrated Circuit (I2C) interfaces. The HPC has similar features,

however provides twice the user-defined signals of the LPC connector, and 10 serial transceiver pairs.

The most recent and powerful *Xilinx* FPGA (with more logic resources) available on the market, at the time of this document, is the Virtex FPGA's family, namely Ultrascale [143]. For example, the XCVU9P-L2FLGA2104E chip provides more than 2000 k logic cells [147]. However, it is relatively expensive, and thus it has been decided to acquire the Virtex-7 VC707 evaluation kit instead [148]. This board, is characterised to be highly-flexible, high-speed serial based platform using the XC7VX485T-2FFG1761C chip-set, which is in fact a good compromise between cost and available logical resources (HW), as it can be verified in Table. 4.2.

Table 4.2
Product table comparison of the most relevant *Xilinx* Virtex FPGA chip-sets, based on [147, 149].

	FPGA technology	
Feature	**XC7VX485T**	**XCVU9P**
Logic Cells	485k	2586k
DSP Slices	2800	6840
Memory (Mb)	37.08	345.9
GTX TRX	56 †	120(*)
I/O Pins	700	832
Price [USD]	**3495**	6995

(†) 12.55 Gbps;
(*) 32.75 Gbps.

Particularly, the VC707 FPGA evaluation board has two HPC connectors, denoted by FMC1 and FMC2, as it can be seen in Fig. 4.2. FMC1 has the full HPC connectivity capabilities, whereas, in FMC2 it is only implemented a subset of the FMC1, i.e, it has less 22 HB I/O pairs than FMC1. Notwithstanding, the following features are provided to both FMC ports:

- 80 differential user-defined pairs;
- 34 LA pairs;
- 24 HA pairs;
- 8 GTX Transceiver (TRX);
- 2 GTX clocks;
- 2 differential clocks.

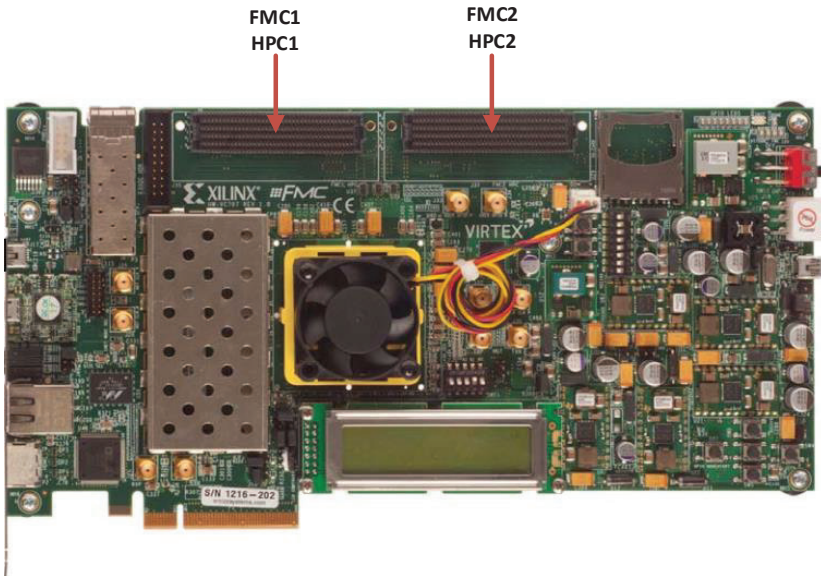

.

FIGURE 4.2: Picture of the VC707 evaluation board, highlighting the FMC port connectivity (image extracted from [148])

It is worth noting that FMC2 might bring some connectivity issues when connected to FMC daughter boards, such as DAC, ADC, RF board, etc..., which usually requires a fully populated HPC I/O pin connector type.

4.2.2 DAC/ ADC

The selection of both DAC and ADC was based on the criteria of speed, bit resolution and the most important one, the compatibility with VC707 FPGA board. According to the *Xilinx* documentation [150], the FMC 230 (DAC) [151] and FMC 126 (ADC) [152] from 4DSP, were the only available converters meeting such requirements in the market, at the outset. Table 4.3 summarises the main converters features, where it can be noticed that the maximum bandwidth of the proposed SDR is restricted to 2.5 GHz.

TABLE 4.3
SUMMARY OF THE MAIN FMC CONVERTS FEATURES [153, 154].

Features	**FMC 126**	**FMC 230**
Bit resolution	10	14
Max. sampling rate	5 GSPS	5.7 GSPS
Maximum signal bandwidth	**2.5 GHz**	2.85 GHz
Number of channels	4	2
Connector FMC type	HPC	HPC

FMC126 overview

The FMC126 is a four channel 1.25 GSPS 10-bit resolution ADC daughter board compliant to the HPC standard VITA 57.1. The design is based on four EV10AQ190 Quad 1.25 GSPS ADC chip-sets [155], which are characterised by Double Data Rate (DDR) Low Voltage Differential Signal (LVDS) outputs [153]. Moreover, each core can operate either individually or in pair or even all interleaved together, enabling sample rates of 1.25, 2.5 and 5 GSPS, respectively.

In order to achieve such rates the ADC requires a reference sample clock of 2.5 GHz, as it is indicated in Fig. 4.3. Furthermore, information going to each core is provided by the analogue input ports A, B, C, and D (see the operational block diagram of this board presented in Fig. 4.4). In this figure, it can also be noticed that the FMC126 board not only includes the Quad ADC IC core itself, but also other peripherals, such as a clock tree IC circuit, source of the necessary digital clocks, and all the electronic needed for ADC control purposes and temperature monitoring, performed via serial I2C communication [153].

In particular, the clock distribution is carried out by the AD9517 IC circuit from Analogue Devices (AD) [156], detailed in Fig. 4.5. By default it has an internal PLL (locked at a input reference - $REFIN$) and a 2500 MHz internal VCO to generate the sampling clock source. However, such clock can also be provided from an external VCO. Finally, AD9517 $OUT1$ output is connected to the Clock Output (CO) physical pin of the board, $OUT3$ drives the ADC (sample rate clock), $OUT4$ is used for synchronisation with the FPGA, and $OUT6$ is used to drive the monitoring temperature circuit.

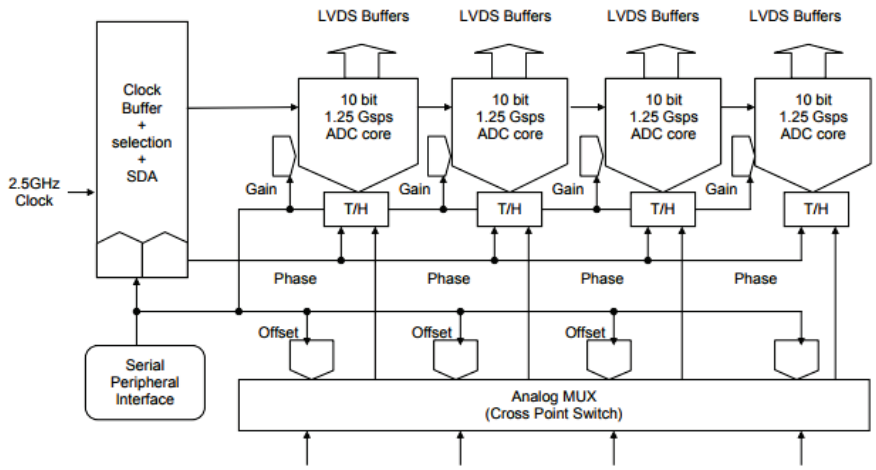

FIGURE 4.3: Operational block diagram of the EV10AQ190 chip-set [155].

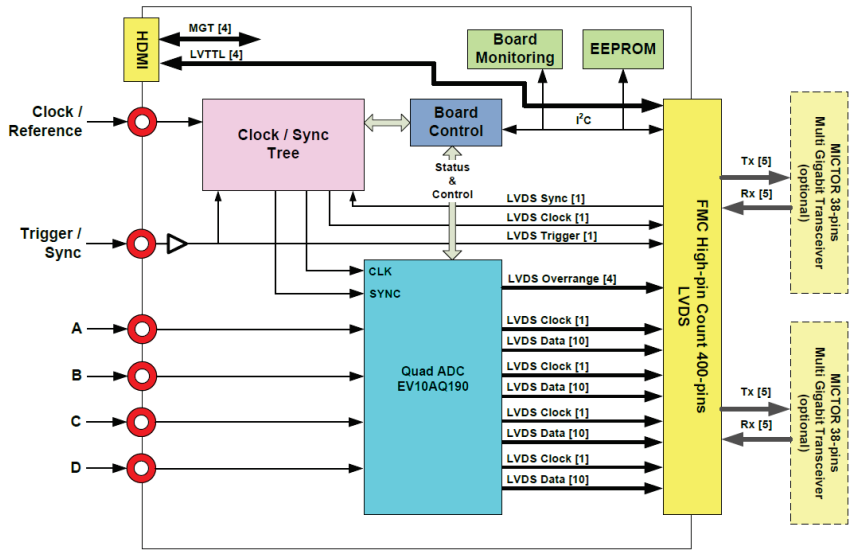

FIGURE 4.4: Operational block diagram of FMC126 (image extracted from [153]).

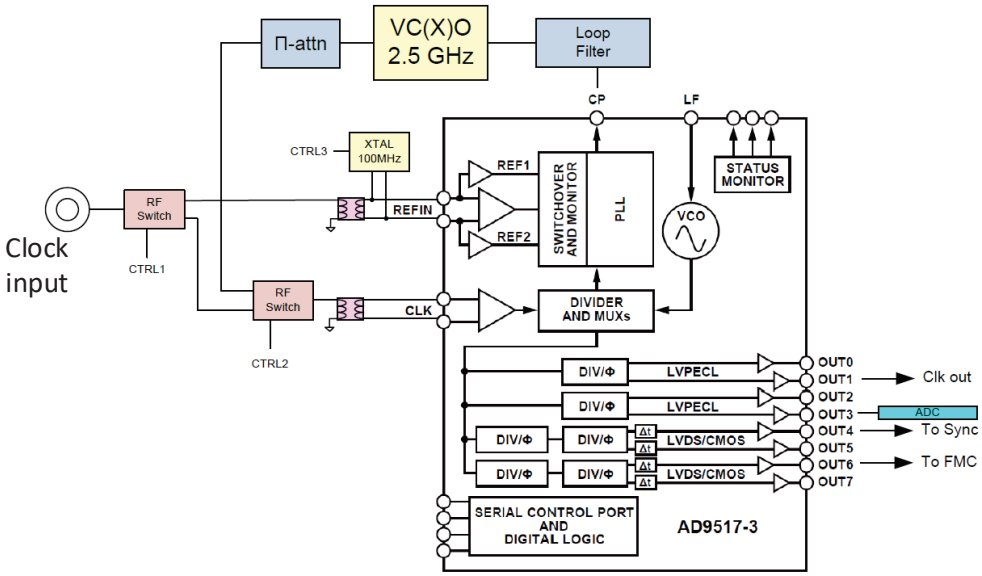

FIGURE 4.5: Operational block diagram of the clock distribution circuit (image extracted from [156]).

FMC230 overview

The FMC230 is a two channel 14-bit DAC daughter board, which is controlled through a single Serial Peripheral Interface (SPI) communication bus [154]. Similar to the FMC126, it can also be locked either by an external clock source or by an internal IC clock circuit. The board design is based on two AD9129 single-channel 14-bit 5.7 GSPS DAC with DDR LVDS inputs [157], and it is illustrated in Fig.4.6. Furthermore, FMC230 reference sample clock is also provided by a AD9517 IC circuit as in the FMC126, however, unlike the ADC board, its internal PLL reference is 30.72 MHz

(rather than 100 MHz), and its internal VCO is locked at 2457.60 MHz (rather than 2500 MHz). Therefore, for the 4DSP default configuration, sampling rate is limited to 2.457 GSPS, but it can be increased up to 5.7 GSPS, by considering an external reference sampling signal. Finally, DAC analogue outputs are provided by MMCX coax connectors on the front panel (AC-coupled).

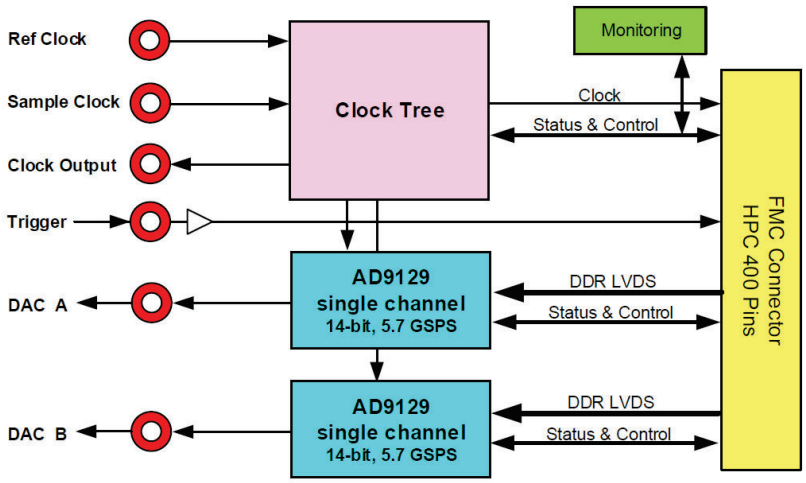

FIGURE 4.6: Operational block diagram of FMC230 (image extracted from [154]).

Board support packages overview

In this subsection, it is introduced the Board Support Package (BSP), provided by 4DSP, required to successfully test both FMC126 (ADC) and FMC230 (DAC) devices. For example, when considering the DAC's BSP, a sine-wave is transmitted at both of its output analogue channels, at a specific fundamental frequency. Similarly, for the ADC, the acquisition of signals, from its analogue input channels, are enabled, processed, and displayed in a Graphical User Interface (GUI).

To accomplish the above calibration tests, both Device Under Test (DUT) must be attached in HPC1 FMC connector of the VC707, and the bitstream (containing the firmware of the target application) of each device must be downloaded into the FPGA via JTAG interface (e.g. using the hardware manager task of *Vivado*). Finally, a C++ software routine programme must be run, in order to configure the devices and to generate/ display data. Subsequently, this information is exchanged with the target FPGA via Ethernet protocol, and processed in an host PC. Furthermore, FPGA firmware for the aforementioned reference applications, is provided for each converter [158, 159], which were designed based on the 4DSP Stellar IP software. This tool is

a block-based integration solution, similar to *Xilinx Vivado* IP integrator [160], used to simplify complexity of hardware designs. To this end, well-structured and reusable intellectual property blocks are available in a library, leading to a high level of abstraction to users, which significantly speeds-up the firmware design and its debugging.

In Stellar IP environment, the top level of a firmware design is denoted as *constellation*, and *star* is the name given to the logic blocks presented in the *constellation*, and connections between *stars* are called *wormholes*. Both FMC126 and FMC230 reference firmware designs are shown in Fig. 4.7a and 4.7b, respectively. From these figures, it is evident that several *stars* are common to both designs, only block such as: sip_fmc230, sip_fmc126 and the router *stars* are distinct to each converter. In this context, it is predicted that both FPGA designs might be merge in a single one in a relatively easy (scope of following subsection).

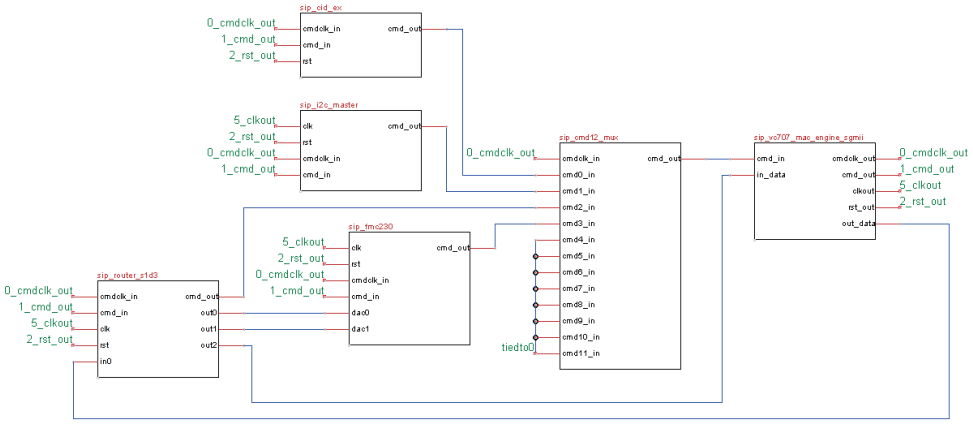

(a)

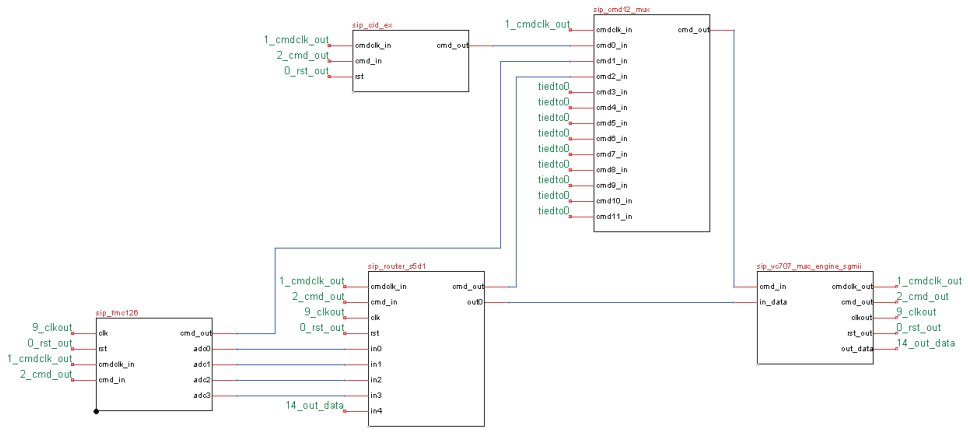

(b)

FIGURE 4.7: Both Stellar IP firmware designs for a) DAC and b) ADC (images extracted from [158, 159]).

The main description of the *stars* present in both reference FPGA designs is given below [158, 159]:

- **Constellation ID** (*sip_cid*) - is a memory holding information about the constellation ID, star ID's, star address range, etc.;
- **MAC engine** (*sip_vc*707*_mac_engine_sgmii*) - distributes register read and register write commands coming from the Ethernet MAC entity, in addition, it also transfers data to/ from the host PC. It also generates and distributes the clock and reset signals for the other *stars*;
- **1-to-3 Router** (*sip_router_s*1*d*3) - routes data from the input port to any of the three outputs;
- **FMC230** (*sip_fmc*230) - is responsible for the communication with the FMC230 daughter board. It sends data to the DAC and provides burst size control. It uses an internal waveform memory in the DAC path to accommodate the data, which is constantly being play back to the its core (data is transmitted cyclically);
- **I2C master** (*sip_i*2*c_master*) - is the I2C master bus, which is connected to the control, voltage and temperature monitoring circuit of the FMC230 board;
- **Command multiplexer** (*sip_cmd*12$_m$*ux*) - merges the command output *wormholes* of all stars and connects a single command output to the MAC engine entity;
- **5-to-1 Router** (*sip_router_s*5*d*1) - routes data from any of the five inputs ports to the output, it acts like a multiplexer;
- **FMC126** (*sip_fmc*126) - is responsible for the communication with the FMC126 daughter board.

Finally, Stellar IP is also compatible with *Vivado*, i.e., automated tasks are available in the software to translate the VHSIC Hardware Description Language (VHDL) (VHSIC stands for Very-High-Speed Integrated Circuit) sources from each *star* into a new top level entity in a new generated *Vivado* project [161]. This flow is illustrated in Fig. 4.8, where a decrypted folder containing constellation descriptions, *star* library, etc..., is converted into a new *Vivado* project.

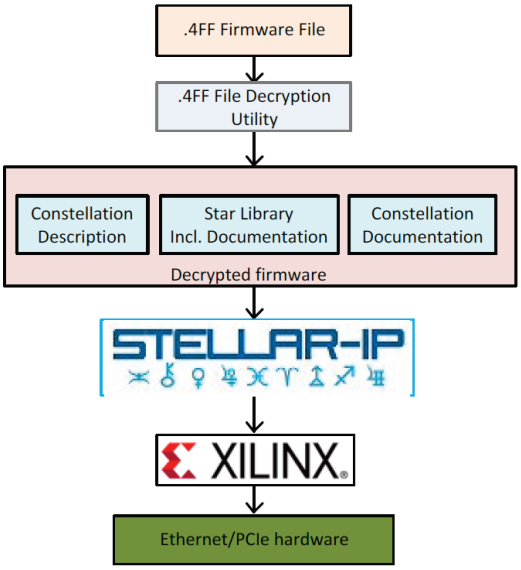

FIGURE 4.8: Firmware compilation chain (image extracted from [161]).

Cooling SDR system acrylic box

In order to avoid the damage of the aforementioned both daughter boards due to overheating, they must be operating in a conduction-cooled environment. According to [153], a minimum airflow of 300 Linear Feet per Minute (LFM) is recommend. Hence, it was necessary to design and manufacture a cooling box for the proposed SDR, where the required airflow must be provided across both FMC boards. To this end, the duct cross sectional area (A_T) of the developed cooling box, was calculated according to (4.1).

$$A_T[m^2] = \frac{Q\,[m^3/s]}{v\,[m/s]}, \tag{4.1}$$

where Q is the airflow, fixed to $0.0069 m^3/s$ (provided by the acquired fan), and v is the air-flow velocity. Converting 300 LFM to m/s, v becomes equal to 1.52 m/s, and consequently, (4.1) can be simplified as:

$$A_T = \frac{0.0069}{1.52} = 0.0046\,m^2, \tag{4.2}$$

Considering the result of (4.2), the overall A_T was divided into four individual rectangles, as it is illustrated in Fig. 4.9a (highlighted as number 2). Finally, a picture of the developed acrylic cooling prototyping box system is depicted in Fig. 4.9b.

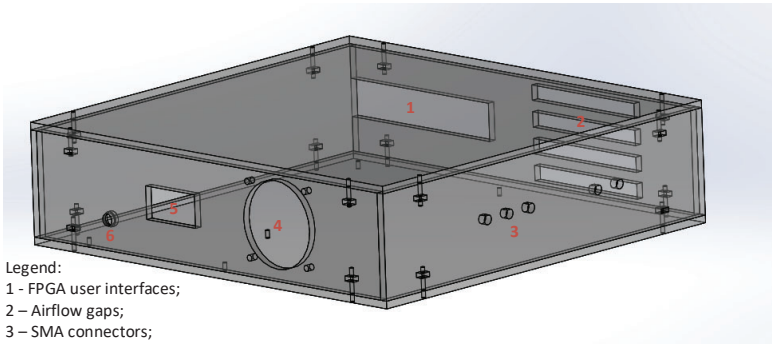

Legend:
1 - FPGA user interfaces;
2 – Airflow gaps;
3 – SMA connectors;
4 – Fan;
5 – FGPA power switch;
6 – DC power FAN.

(a)

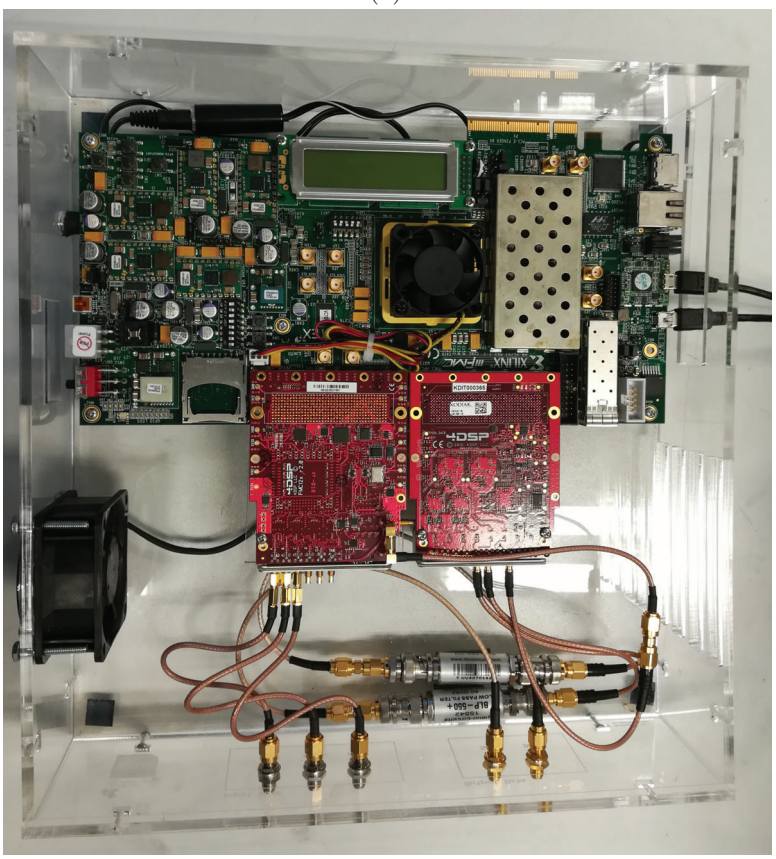

(b)

FIGURE 4.9: Proposed acrylic cooling system: a) design, and b) picture of the developed box.

4.3 Connectivity between Virtex 7 and FMC230/ FMC126

The reference designs provided by 4DSP, introduced in the previous Section, are rather limited, since they were only developed to successfully evaluate both DAC/ ADC boards. Firstly, both FMC cards are set to be utilised in the same VC707 HPC1 connector, and thus they cannot operate simultaneously (using the same FPGA). Secondly, Ethernet interface is used to either exchange initialization commands or data to both devices. Thus, a physical dependency must always exists between an host PC and the software-defined radio. Thirdly, both ADC/ DAC are set by default to operate at different sampling rates, which leads to loss of samples when connected together. Finally, the most relevant limitation is that data being sent to the DAC and received by the ADC, is not processed in real-time. For example, in the reference design of the DAC, a memory is implemented to store the data coming from a host PC and then cyclically played it back towards the AD9129 core entity. In order to overcome the aforementioned reference firmwares limitations, several modifications are required, which are addressed in the subsections below.

4.3.1 Physical dependency removal between an host PC and the SDR

As mentioned above, 4DSP reference firmwares target Ethernet communication as the protocol to perform the initialization of both devices and to transmit/ receive data. Consequently, such architecture demands a host PC to be always connected to the FPGA, which is impractical in a wireless communication transceiver.

Therefore, Ethernet connection must be replaced by a new VHDL entity capable to play back initialization commands that were previously sent by the MAC engine to the FMC board entities (*stars*). This approach is highlighted in the block diagram illustrated in Fig. 4.10, where all the connections in red are the ones that must be removed from the original FMC230 and FMC126 reference designs, illustrated in Fig. 4.7. The MAC engine *star* is now just considered to generate clock and reset signals to the others *stars*, and due to this fact, it has been decided not to be removed.

In this work, the aforementioned new entity is a processor engine, since the BSP's C++ routine can be run in this logic processor entity with minor modifications, which allows the configuration commands of both converters to be send (in real-time) from the FPGA to either ADC or the DAC (placed in HPC1 slot). Moreover, a Integrator Logic Analyser (ILA) was used as debugging tool, to make sure the commands being sent would match the original ones.

Nevertheless, the design and implementation of a processor hardware engine architecture is not a straightforward task. It is usually composed of a *microBlaze* processor,

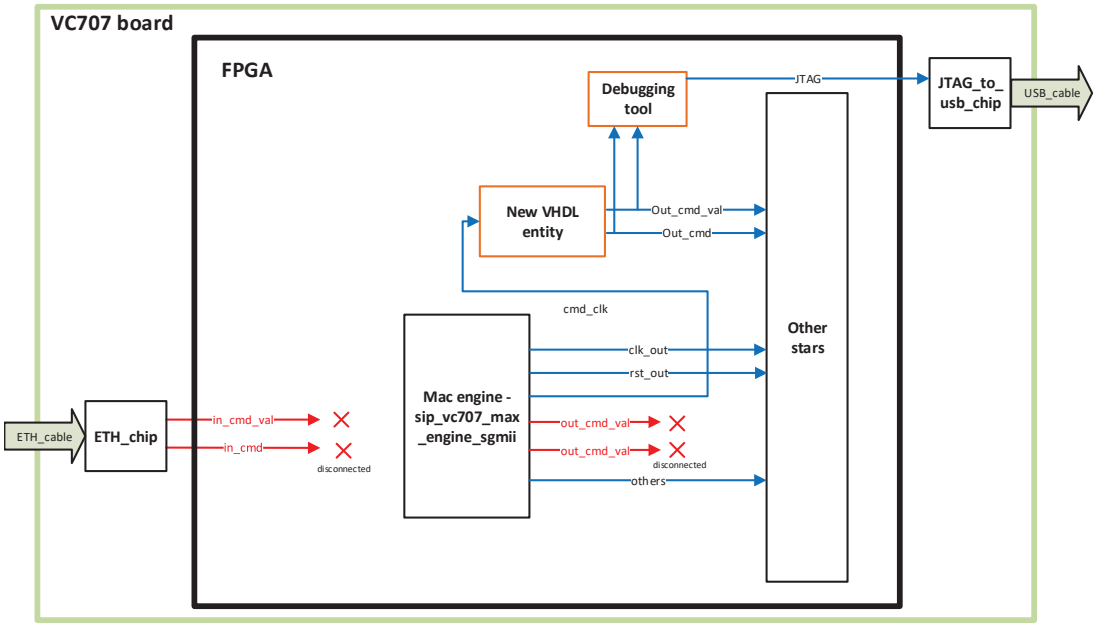

FIGURE 4.10: Block diagram of the adopted modifications common to both FMC126/ FMC230 reference firmwares.

peripherals, reset, clocking and debugging blocks, which are connected together using an Advanced Extensible Interface (AXI)4-Stream [162]. Such interface is characterised by a 32 bit data width format for easy, direct access to fabric and hardware acceleration (very small footprint) [163]. It is worth noting, that this interface/ protocol is not a bus, and thus a custom user block is also necessary to convert the AXI data, coming from the processor engine, to the bus format given in Fig. 4.10. This bus has a 64 bit width word, and *cmd_word* can have the following hexadecimal values (register status): $0x1, 0x2, 0x4$ for write, read and read with acknowledge, respectively. The processor architecture design has been designed using *Xilinx Vivado* IP integrator, and a print-screen of its design is depicted Fig. 4.12.

Description of the considered *Xilinx* IP blocks are given below [162]:

- **Cloking Wizard** (*clk_wiz_0*) - is a Mixed-Mode Clock Manager (MMCM) module used to generate multiple clocks with defined phase and frequency related to a given input clock (reference). In this work, such block is used to generate the 100 MHz *microBlaze* clock signal (*clk_out1*), from a *clk_200_uB* reference signal coming from a 200 MHz LVDS oscillator placed on the VC707 board;
- **Processor System Reset** (*rst_clk_wiz_0_100M*) - it distributes (from a reference input reset port) a synchronous reset signal to the processor engine and its associated peripheral blocks;

- **MicroBlaze Debug Module** (*mdm_1*) - is a debug interface for *microBlaze* applications, and it is controlled by the system debugger tool through the JTAG port of the FPGA, where debug signals are grouped in a debug bus;
- **MicroBlaze Local Memory** (*microblaze_0_local_memory*) - the processor engine uses two Local Memory Bus (LMB) to connect both instruction and data ports to high-speed peripherals, primarily on-chip block RAM;
- **MicroBlaze** (*microblaze_0*) - where the processing is carried out. In addition, it also defines the address map to communicate with the peripherals and the location of the application code in the memory space (either a block RAM or an external memory);
- **AXI interconnect** (*microblaze_0_axi_periph*) - This block behaves as a router, e.g., it can connect/ integrate a master entity (*microbaze* block) to several slaves (peripherals);
- **AXI Uartlite** (*axi_uartlite_0*) - Universal Asynchronous Receiver-Transmitter (UART) serial protocol port is also used for debug purposes. For example, data read from a register will be shown on the console terminal by *xil_printf* instruction on the embedded application code, it is useful to double check data sent from the processor to the write address channels;
- **Block Memory Generator** (*axi_bram_ctrl_0_bram*) - dedicated to run and store the user's software routine;
- **Custom user IP** (*myip_AXI2BUS_0*) - is a fully customised block used to enable the communication between the processor engine and the *stars*. In other words, information from two writing registers are concatenated to a single output command in order to match the required bit bus format from 4DSP (see Fig. 4.11). In addition, it has implemented a cross clock domain VHDL architecture. While the processor entity is operating at 100 MHz, all the 4DSP *stars* are clocked at 125 MHz.

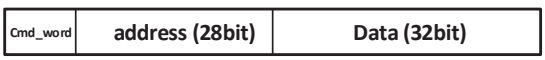

FIGURE 4.11: 4DSP command format.

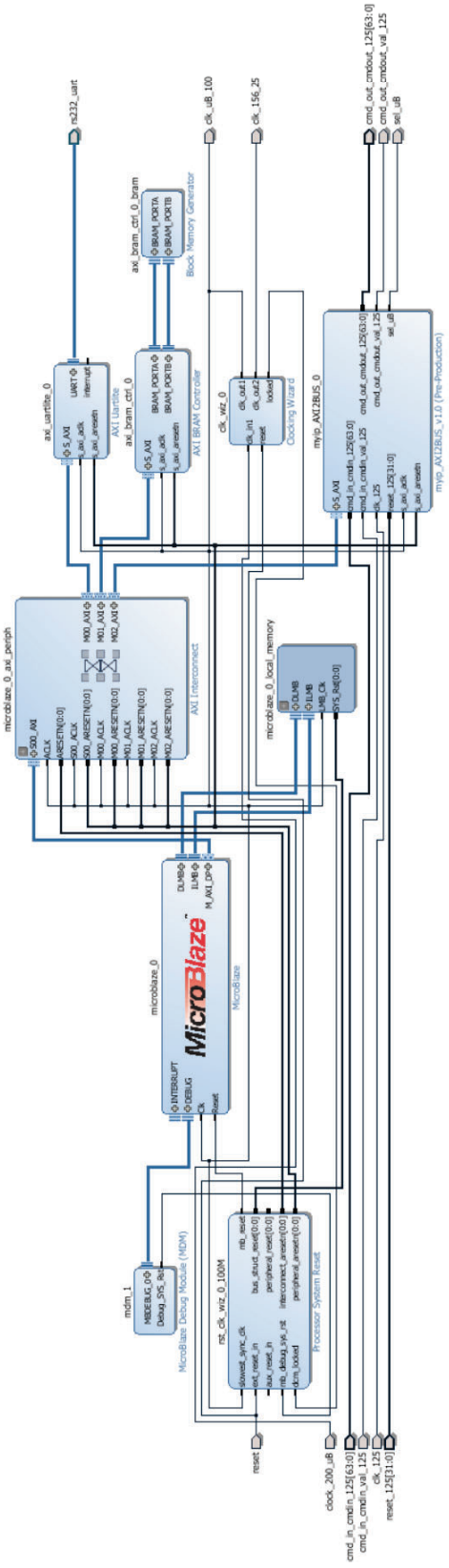

FIGURE 4.12: Proposed *microBlaze* architecture design.

4.3.2 Transceiver firmware design

As it is mentioned in Section 4.2.1, the VC707's HPC2 connector is not fully populated, i.e., it has a reduced pin-out in comparison with the standard HPC connector. As consequence, if the FMC230 is placed in this connector, only one out of two DAC channels is available. On the other hand, if the FMC126 is connected to it instead, only three out of four ADC channels are available.

Considering that the most relevant modern digital modulation techniques employ I/Q modulations, to achieve higher spectral efficiency (as discussed in Section A.4.2), two channels are required in both DAC/ ADC boards. Therefore, FMC230 and FMC126 have been connected to the FMC1 and FMC2 slots of the VC707 board, respectively. In order to merge the individual 4DSP FPGA firmwares in a transceiver design, the I/O pins connections from the FMC126 original firmware require to be assigned to the HPC2 pin-out instead (achieved by updating the original ADC's *.xdc* file). Moreover, all the logic associated with the fourth ADC channel must to be removed. The block diagram illustrating these firmware modifications is depicted in Fig. 4.13, showing, particularly, how the configuration commands are now exchanged among the *stars* from both DAC/ ADC boards.

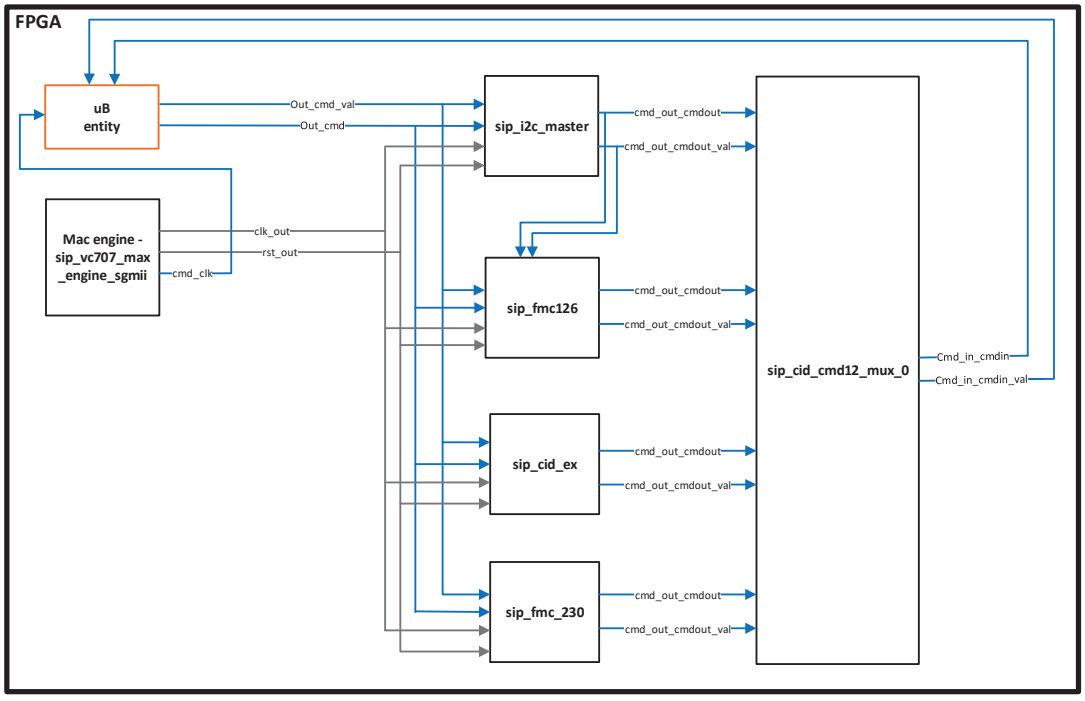

FIGURE 4.13: Block diagram of the developed transceiver firmware.

Furthermore, as previously discussed, FMC126 board is configured by I2C communication protocol, where clock (SCL) and data (SDA) are carried out in distinct wires. These signals, which are being sent to the VC707's HPC1 connector, in the original firmware, must be now driven to FMC2 (HPC2). This can be achieved by changing the configuration of the VC707's I2C switch, PCA9548A [164]. As depicted in Fig. 4.14, the *sip_i2c_master* entity connects I2C signals to this IC, which consequently routes them to either FMC1 or FMC2 connectors, depending if channel 0 or 1 are selected. For this application in particular, PCA9548A IC was configured, through the following 4DSP command: $0x1000740000000004$, to select channel 1.

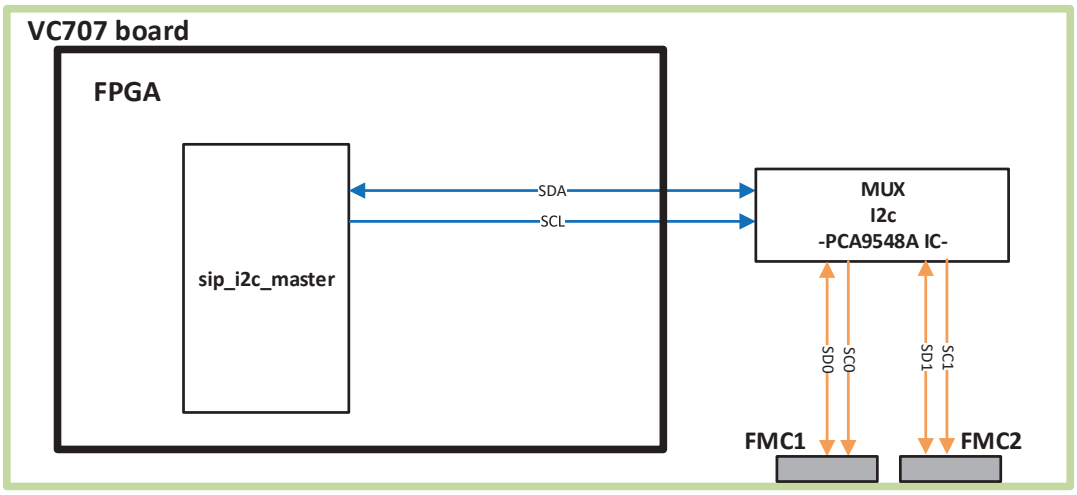

FIGURE 4.14: Illustration of the I2C communication towards VC707's FMC1 and FMC2.

4.3.3 Sample rate synchronisation

The sampling process at the receiver might be subject to severe timing imperfections such as acquisition of erroneous information or loss of transmitted samples, depending on the different between both DAC/ ADC sampling rates [139]. The acquisition of erroneous information can occur when the ADC rate is higher than the DAC whereas loss of transmitted samples might happen if the ADC rate is lower than the DAC. In this context, sampling rate of both considered converter boards in the proposed SDR, should match.

The easiest solution, found in this work, to meet the above requirement is to configure the clock tree of the FMC230 to drive a 1.25 GHz clock signal into both AD9129 cores. This would be a very straightforward task if the internal VCO of the AD9517-1 could

generate a 1.25 GHz operating frequency (maximum rate achievable by FMC126 without phase interleaving) or integer multiples of this frequency. From Fig. B.1, it is seen that the DAC sample clock, driven by the $fDAC\_CLK$ path, is provided by the $OUT2$ output of AD9517-1. This port provides clock frequencies from 2457.6 MHz down to 12.8 MHz, which are the result of configuring either both block divisors VCO_div and $div1$ or alternatively, bypassing VCO_div and using $div1$, or vice-versa. However, only integer values are acceptable in such block dividers, and thus, is not possible to obtain a divisor combination where $OUT2$ port is at 1.25 GHz. Therefore meeting the ADC sample clock in the FMC230 is only possible considering an external signal as sample clock reference.

As a workaround, the clock tree of the FMC126 has been configured to enable a CO signal, with Low-Voltage Positive-referenced Emitter Coupled Logic (LVPECL) waveform type, at 1.25 GHz, to be connected to the Clock Input (CI) port of FMC230. Although the AD9517-3 circuit can be easily configured to enable $OUT1$ as CO, this port is not connected to any external connector in the FMC126 board. To overcome this, an additional SSMC connector has been soldered to the CO port pad in the reverse side of the device PCB. The adopted clock synchronisation method between both FMC126 and FMC230 is shown in Fig. 4.15.

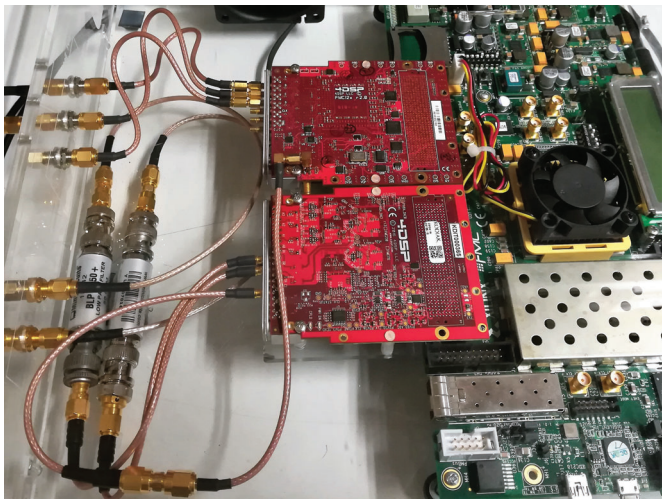

FIGURE 4.15: Sample rate clock synchronisation configuration between both FMC126 and FMC230.

4.4 Integration with *Xilinx System Generator* tool

According to the *Xilinx* information reported in [165], System Generator (SysGen) is the state-of-the-art tool for the design, test and implementation of high-performance DSP algorithms on FPGAs. It enables a rapid prototyping of very complex FPGA design by considering the *Mathworks* model-based design environment, namely *Simulink*, with total abstraction of the chip-set complexity [105, 166]. In addition, such provides pre-existing optimised IPs, in a dedicated *Xilinx* block-set library, for the target FPGA fabric [165]. These blocks can be tuned by the user, without requiring any knowledge in VHDL programming, and are both bit- and cycle-true. This means that the model simulation results in *Simulink* will be the ones experienced in hardware, and thus there is no need to download the bit-stream to the target FPGA whenever the user intends to debug its design [166]. This is a remarkable feature, since such is usually a very time-consuming task. Furthermore, after the system is completed and validated, the synthesis, place and route of the HW design, and even timing and resource analysis can also be performed using SysGen [165]. Nevertheless, in cases where this is not desired, the user can export its design as a customised IP block and integrate it into a larger HW design. SysGen automatically compiles the design into efficient low-level hardware description language (VHDL/Verilog).

In this context, the design of the proposed multi-Gigabit/s real-time OFDM TRX engine (testbed) is performed using SysGen, and then packed into a customised IP, in order to be integrated into the transceiver *Vivado's* firmware introduced in Section 4.3.2. To do so, it is required an extensive study in terms of data connectivity/ interface present in both FMC126/ FMC230 VHDL entities (*stars*), which will be described in the sections below.

4.4.1 FMC126/ FMC230 data interface

It is well known that operating FPGA logic at GHz of clock frequencies is impractical, since very low rising interval times would result into failing design timing requirements, where data integrity would not be ensured. As it has been referred before, *Xilinx's* FPGA clock performance barrier is around 500 MHz, considering their state-of-art device (chip-set). Hence, 4DSP adopted a parallel data path architecture in both original FMC230/FMC126 firmwares, which significantly reduces data clock frequencies to MHz, depending on the number of paths. For example, from the functional block diagram of the FMC230 (see Fig. B.1), two parallel data DDR interface paths coming from the FMC connector (FPGA), namely: $DAC0\_p0\_p/DAC0\_p0\_n$ and $DAC0\_p1\_p/DAC0\_p1\_n$ (operating at $fDACCLK/4$), are then multiplexed into a

single data stream by the assembler entity, which is clocked at $fDACCLK/2$, where $fDACCLK/$ represents the DAC sampling rate value (F_s).

A detailed block diagram of the FPGA data connectivity, required in the DAC's firmware, in terms of required VHDL entities, is depicted in Fig. B.2. From that figure, it is verified that data source is generated in the $Ad9129\_wfm\_inst0$ entity, driven by the wfm_out_data bus signal. This bus is in fact, a 16 words of 16 bit width in parallel, building a bus of 256 bits ($Odata\_reg$) clocked at $txclkdiv8$. Such clock value is equals to $DAC0\_dco$ value divided by 4 or DAC $\frac{F_s}{16}$. Since the bit resolution of the AD9129 is 14 bits, the two most significant bits which were previously set to 0, are then discard in the $Ad9129\_io\_buf\_v7\_inst0$ entity. In this entity, the 256 data bit bus ($Odata\_reg$) is serialised, using two sets of fourteen parallel to serial structures of Oserdeses2 (high-speed source-synchronous output fabric interfaces) operating in DDR mode. This results in two buses of 14 bits, ($DAC0\_p0\_p/DAC0\_p0$ and $DAC0\_p1\_p/DAC0\_p1$), clocked at $txclkdiv2$ clock, which are then connected to the FMC230 board throughout the FMC1 pin-out connection (see Fig B.1). In sum:

- Two 14 bit LVDS data ports are used to sample de-interleaved data from the host on the rising and falling edges of the host Dac_dci clock signal;
- Interface data buses inside the FPGA operate at 1/16 the sampling rate of the DAC ($fDAC\_CLK$), which is the same as $Dac\_dci/4$. Thus, if F_s is equal to 2.456 GSPS (default), $txclkdiv8 = 153.5$ MHz and $txclkdiv2 = 614$ MHz;
- The AD9129 also provides to the host (FPGA) with DAC_dco signal clock (which is equal to Dac_dci value), to establish a synchronisation operation.

The data interface of the FMC126 with the FPGA is rather similar to the FMC230 ones, however 8 parallel data paths are considered instead. This is, data going to the FMC230 is a 256 bit bus, whereas, data coming from the FMC126 is a 128 bit bus. This leads to a mismatch of the clock value in both DAC and ADC firmware channel paths. For example, considering a target sampling rate of 1.25 GHz, buses are clocked at 78.125 MHz and at 156.25 MHz for FMC230 and FMC126, respectively. To overcome this issue, the number of data paths in the FMC230 firmware were reduced to 8 (matching the ones from the FM126), and thus entities namely, $ad9129\_mmcm\_isnt$, $ad9129\_phy0\_dac0\_inst0$, and $ad9129\_io\_buf\_v7\_isnt0$ have been updated accordingly, where $txclkdiv8$ value is now given by $\frac{F_s}{8} = Dac\_dci/2$.

4.4.2 Proposed architecture for the prototype communication system: SysGen design and integration

The proposed communication transceiver prototype is based on the digital IF architecture referred in Section A.2.3. It offers more flexibility compared to the traditional RF architectures, and it is not sensitive to DC offset, LO leakage and flicker noise. Moreover, since I/Q up-conversion/ down-conversion is digitally performed in an IF stage, negative effects induced by IQ imbalances, critical in advanced modulation techniques, are therefore limited. Block diagram of the proposed digital IF transceiver architecture to be implemented in the SDR, introduced in previous sections, is illustrated in Fig. 4.16. Note that both Digital Up-Conversion (DUC) and Digital Down-Conversion (DDC) stages are performed to relatively low centre IF frequencies (limited by the sampling rate of both DAC/ ADC), however, up-conversions to mmWave can be accomplished by an external analogue mixer.

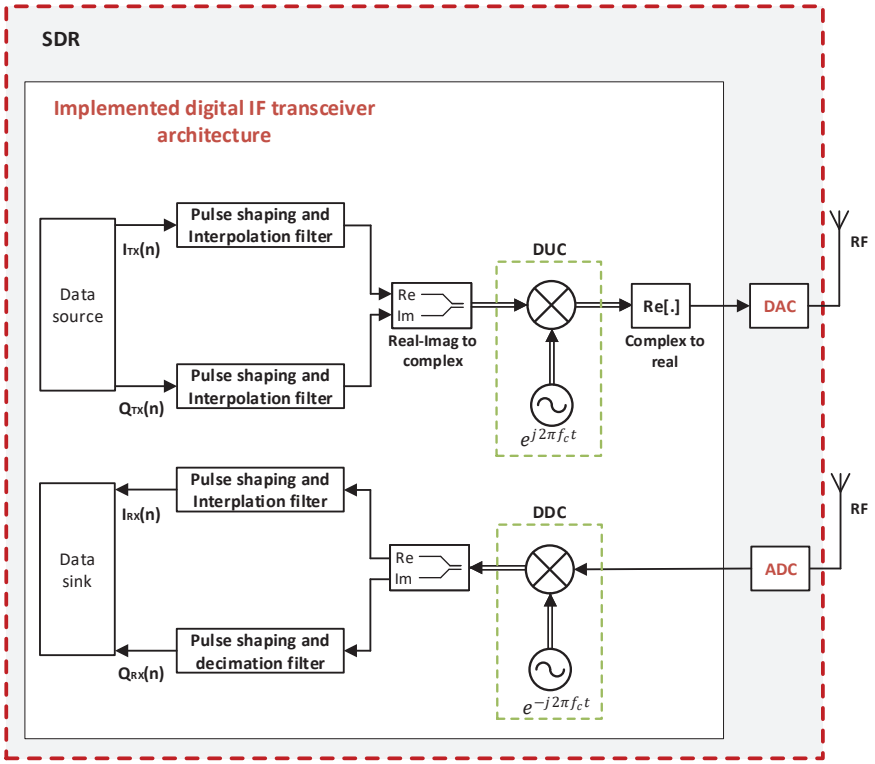

FIGURE 4.16: Block diagram of the proposed digital IF RF transceiver architecture.

In other to design and implement the aforementioned communication system prototype using SysGen, it is required to understand how a real-time data source engine would be integrated to the data interface of both ADC/ DAC reference designs, which

considers 8 parallel processing paths, each one being sampled at 156.25 MHz. This has been discussed in Section 4.4.1, for a sampling rate of 1.25 GSPS. In this context, at the transmitter, a DSP interpolation filter is necessary which would be capable to interpolate the sample rate of 156 MHz to 1.25 GHz (absolute value of the DAC core sampling rate). The solution, considered in this work, is the implementation of an architecture composed of Finite Impulse Response (FIR) filter banks (clocked at 156.25 MHz) by following the polyphase decomposition algorithm reported in [167]. This not only increases the sampling rate, but also attenuates the generated spectral images from the up-sampling process (present at integers values of the original sampling rate) using a low-pass filter, which also shapes the bandwidth of the transmitted signal [139]. At the RX, the counter part must be implemented. This is, ADC sampling rate is decreased using a down-sampling operation followed by a low-pass filter, which removes undesired components that would otherwise overlap (aliase) into the band of interest. These two operations together result into a decimation filter [139]. It is worth noting that, if I/Q up-/down- conversion is required, 16 (two banks) distributed FIR filters are necessary.

A filter bank is characterised by a parallel arrangement of low-, band-, or high-pass filters, required to decompose the spectral content of a certain signal into multiple sub-bands [168]. When the filter bank is implemented based on a low-pass prototype filter, which corresponds to the 0^{th} band, the other uniform sub-bands are obtained by frequency shifting the prototype filter frequency response [169]. In this case, such is known as DFT filter bank, and the graphical representation of its frequency response is illustrated in Fig. 4.17a. Moreover, as it can be seen from Fig. 4.17b, the process of splitting the bandwidth of the original signal $x(n)$ into M different sub frequency bands, performed by a set of $H_k(z)$ filters, is called analysis. Subsequently, its counterpart, i.e., the reconstruction of the original signal ($x'(n)$), is called synthesis, which also requires M parallel filter channels $F_k(z)$ [168].

Furthermore, the polyphase decomposition algorithm [167], can be employed to enable an efficient real-time implementation of uniform filter banks, while ensuring the perfect-reconstruction of the analysis/ synthesis process. Essentially, it represents the transfer function of a digital filter, $H(z)$, in the following M-component form [167]:

$$H(z) = \sum_{M-1}^{k=0} z^{-k} H_k(z^M), \tag{4.3}$$

where $H_k(z)$ represents the polyphase components. The coefficients of each of the M-filters are calculated according to [167]:

$$h_k(n) = h(nM + k), \quad 0 \leqslant k \leqslant M - 1, \tag{4.4}$$

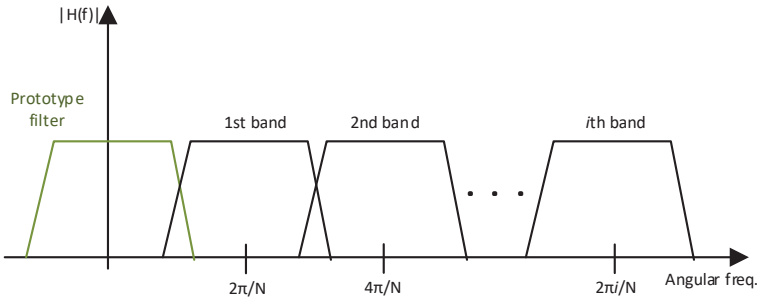

(a)

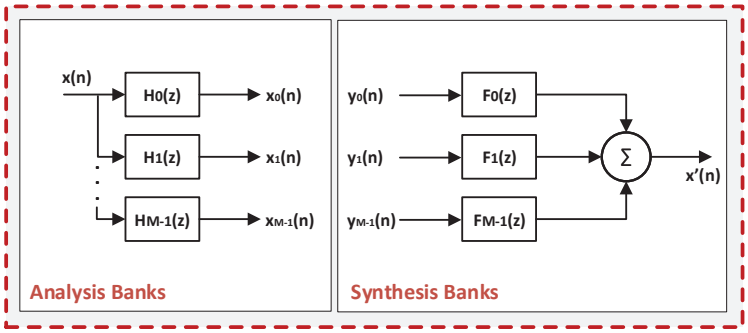

(b)

FIGURE 4.17: Uniform filter banks: a) graphical representation (image adapted from [169]) and b) block diagram of both analysis and synthesis filter banks (images adapted from [168]).

where for example, $h_0(n)$ (impulse response of the prototype filter) is, in fact, a $M-$ fold decimated version of $h(n)$.

In order to combine the y_k signals (highlighted in Fig. 4.17b) in a way that aliasing distortion is negligible, the relation between sub-band filters H_k and F_k, must meet the following condition [167].

$$F_k(z) = H_{M-1-k}(z) \tag{4.5}$$

The overall frequency response of the aforementioned interpolation/ decimation bank of filters, operating at a relatively low clock rate, is the result of the combination of the shifted versions of $H_0(z)$. Since 8 parallel signal processing paths are required per I/Q path, 8 analysis/ synthesis FIR filters were carefully designed and implemented, considering the following procedure:

1. **Filter response type** - it is well known that pulse shaping with raised cosine is characterised by a zero-ISI [139]. This is, despite its impulse response extending over several other symbol periods, at the decision points, there is neither constructive nor destructive interference. Therefore, in this work, a square root raised

cosine matched filter pair was considered, which have the same zero-ISI properties of the raised cosine [139];

2. **Filter order and frequency specifications of** $H(z)$ - the interpolation/ decimation filter was designed with the aid of the *Matlab* FDAtool algorithm, where its frequency specifications can be found in Fig. 4.18. As it can be seen from this figure, the normalised cut-off bandwidth of the low-pass filter was set to 0.125, which is the relation between the clock rates of a single processing path with the DAC core. Moreover, both *Kaiser* window Beta, and filter roll-off values were set to 2 and 0.25, respectively, since this configuration was found to be the best compromise between passband ripple, stop-band attenuation, and transition band. Finally, filter order was chosen to be 62, since it was also a compromise between system complexity (greater the order, greater the amount of computation in the filter implementation), stop-band attenuation and transition band;

3. **Implementation of the interpolation filter bank** - the filter bank was implemented by multiple parallel FIR digital filters, which IP block is available in the *Xilinx* SysGen IP block library. Coefficients for each filter were "distributed" according to (4.4), which resulted in the following array equation: $a_i = coef_{single}[i : 8 : f_{TAPS}]$, where i is the index of each of M parallel FIR filters ($1 \leqslant k \leqslant 8$), and $coef_{single}$ and f_{TAPS} are the array of coefficients and number of taps of $H(z)$, respectively. The SysGen implementation of the interpolation distributed filters can be found in Fig. C.1.

4. **Implementation of the decimation filter bank** - similar to the interpolation filter architecture, it requires the implementation of multiple FIR filters, however the filter coefficients were "distributed" according to (4.5), which led to: $a_i = coef_{single}[(9 - i) : 8 : f_{TAPS}]$.

Furthermore, both IQ up-/down- conversion stages can be performed by the multiplication of the desired signal by a complex exponential operating at a certain centre frequency (f_c), as it is illustrated in Fig. 4.16. At the transmitter, the baseband signal spectrum is frequency shifted to be centred at (f_c), resulting in a non-symmetric spectra [139]. Consequently, applying $e^{-j2\pi f_c}$ at the receiver, will move the spectra of the transmitted signal to be centred at DC, and thus converting the received signal back to baseband.

The complex exponential function can be digitally designed and implemented using a Coordinate Rotational Digital Computer (CORDIC) DSP algorithm (also available in the SysGen IP block library) [170]. This block is responsible for implementing an IQ-mixer, with angular frequency proportional to the desired f_c value. However, since both DAC/ ADC converters employ a 8 parallel processing path technique, similar

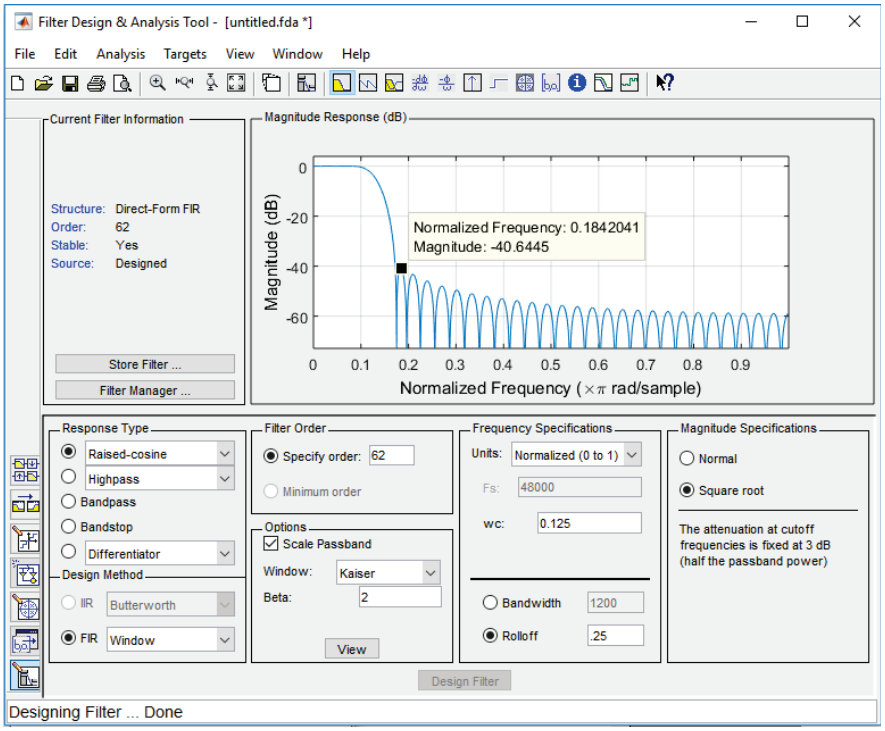

FIGURE 4.18: Square root raised cosine filter design.

to the FIR filter introduced above, it is also required a distributed CORDIC with 8 paths (which one operating at 156 MHz) to perform either an up-conversion or down-conversion. To this end, the distributed CORDIC must generate samples of the same complex exponential, but at shifted sample instants (phase) in each processing path. It is worth noting that, each CORDIC path in the TX FPGA firmware should be connected to the parallel structure of OSERDES (mentioned in the previous section), in order to perform the data serialisation required in the data interface of the FMC230. In the RX firmware, a similar distributed CORDIC is required but with negative phase increment (in order to shift the signal to baseband). Such should be connected to a parallel structure of ISERDES, a serial to parallel FPGA fabric primitive, which enables data parallelism and consequently reduction of the data clock.

The mathematical expression for the aforementioned distributed CORDIC is given below:

$$C(i, N_c) = \exp\left(j \underbrace{2\pi N_c \frac{n}{N}}_{\text{angular freq.}} + j \underbrace{2\pi \frac{i}{N}}_{\text{initial phase}}\right), \tag{4.6}$$

where n is the sample index of the carrier signal, N_c is the number of distributed (parallel) CORDICs, i is the index of each CORDIC, N is the number of samples per period of the carrier signal). Moreover, the angular frequency given by $2\pi \frac{N_c}{N} n$

and the initial phase shift present in each CORDIC is given by $2\pi\frac{i}{N}$. For example if $f_c = 156$ MHz, N becomes approximately 8 samples/ period. Finally, both designs of the TX/ RX distributed CORDICs are shown in Fig. C.3 and Fig. C.4, respectively.

Finally, in order to integrate the developed SysGen RF architecture with the transceiver firmware (introduced in Section 4.3.2), it was necessary to package and export it into two distinct TX/ RX IP customised blocks. A high-level block diagram with the integration approach is illustrated in Fig. 4.19. Particularly for the DAC, a more detailed block diagram of the transmitter implementation is shown in Fig. B.3, where the SysGen block is highlighted in red. In addition, it can be verified in this figure that all the logic related with the $Ad9129\_wfm\_inst0$ entity, which implements a ROM with stored sine-wave samples (as introduced in Section 4.3) is still considered. This allows to switch between the original 4DSP test mode and an user real-time IP customised solution (e.g. a simple Direct Digital Synthesiser (DDS) used to generate sine-waves or a more complex baseband signal generator) through the implementation of an additional multiplexer ($Data\_mux$). Similar changes have been done in the ADC entity, enabling either a reference test mode or data processing in real-time.

4.5 SDR characterisation

In this section, it is not only evaluated the performance boundaries of both FMC126 and FMC230 boards, based on the characterisation metrics introduced in Section A.3.5, but also the modifications performed on the original firmwares of both DAC/ ADC are validated. The block diagram of the measurement setup, considered for this purpose, is depicted in Fig. 4.20.

At TX, an oscilloscope and a Spectrum Analyser (SA) are used to measure the time and frequency responses of the DAC, at multiple tones. At the RX, a signal generator is used to generate sine-wave signals with tunable amplitude and frequency (from a few kHz up to 15 MHz), which are connected to the ADC input channels, allowing the assessment of both time and frequency domain responses of the ADC (after post-processing the received data).

Moreover, a DDS SysGen IP had to be implemented, as the real-time TX engine (see Fig. 4.19) to enable the generation and transmission of sinusoidal signals in both FMC230 channels 0 and 1. It is worth noting that, by considering an IF modulation stage, sine-wave fundamental frequencies can go up to 890 MHz (considering a sample rate of 2.456 GHz). At the receiver, received samples are acquired with the aid of a real-time debugging tool. A *Xilinx* ILA has been implemented to perform several sample acquisitions and transmit them to a host PC, for post-processing in *Matlab*.

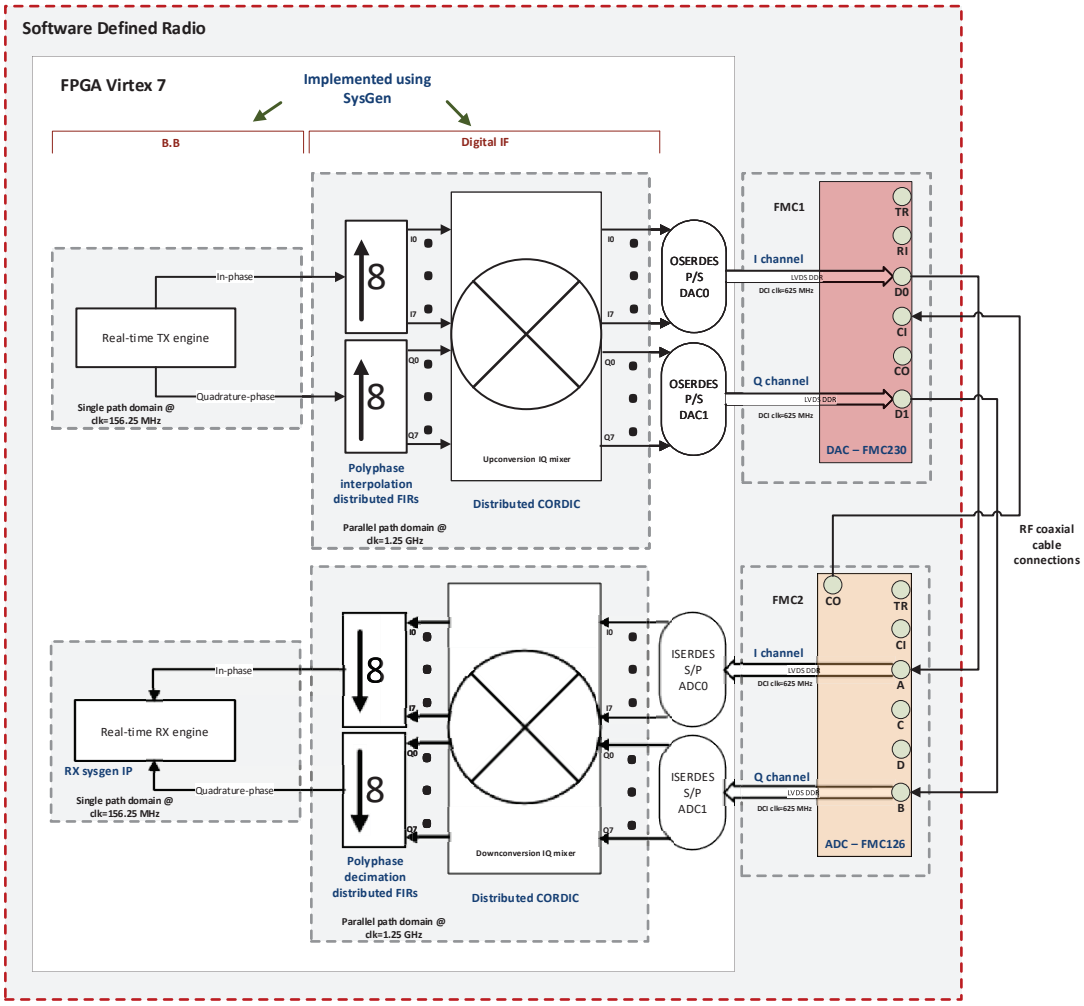

FIGURE 4.19: Block diagram of the implemented digital IF RF transceiver architecture, and its integration with both DAC/ ADC firmwares.

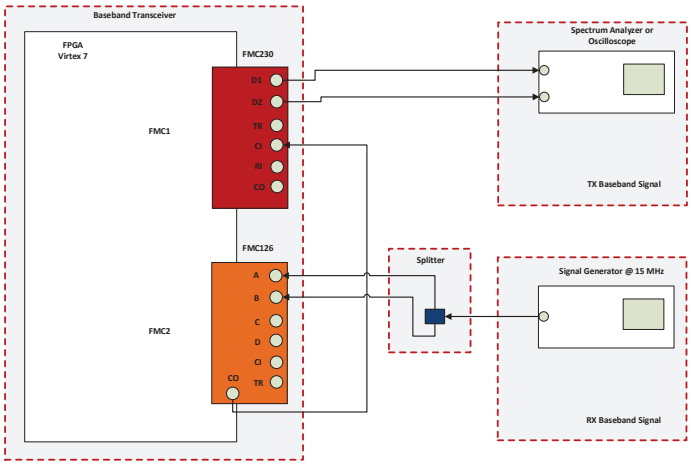

FIGURE 4.20: Block diagram of the utilised setup for the assessment performance of both FMC230 and FMC126 boards.

4.5.1 Measured SFDR, SINAD, SNR and ENOB

As discussed in Section A.3.5, the SDR's TX dynamic range can be evaluated by the SFDR of the DAC, which is measured as the difference between the RMS power level of the transmitted tone and the most significant spur signal, presented in the DAC's frequency response. A example of a SFDR measurement result, for the FMC230, can be seen in Fig. 4.21, considering the D1 channel and a frequency tone of 134.3 MHz.

Additionally, FMC230 was also characterised in terms of SINAD, SFDR, and ENOB, for various frequency tones. Results are summarised in Table 4.4 and plotted in both Figs 4.22a and 4.22b, considering a sampling rate of 2456 MHz, and the DAC's D1 output channel. Obtained average values for SFDR, SINAD and ENOB measurements, are 56.93 dB, 69.61 dB, and 11.34 bits (2.66 bits less than the specifications from 4DSP), respectively, which represent, therefore, the DAC performance boundaries. In addition, from the aforementioned figures, it is evident that both DAC's SFDR, measured SNR and ENOB values are tone dependent.

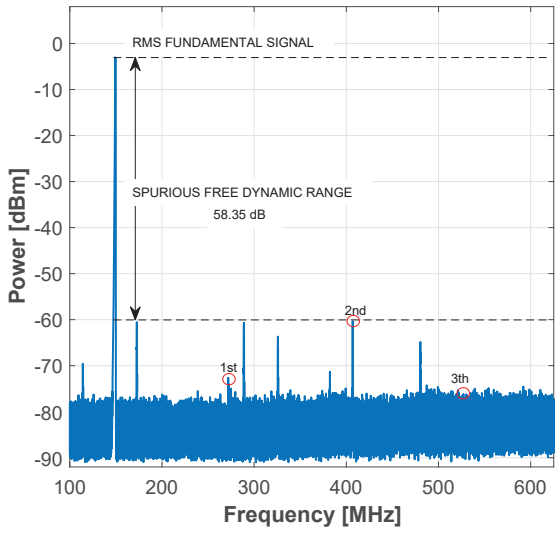

FIGURE 4.21: DAC SFDR for a tone signal of 134.3 MHz, considering the DAC's D1 channel.

For the FMC126, similar measurements were conducted. However, it was necessary to ensure that the ADC frequency response results were not being masked by undesired signals from the signal generator. To this end, a 11 MHz low-pass filter was placed at the signal generator's output, and thus all its harmonics and interfering signals were significantly attenuated, which otherwise could compromise the measurement results. As consequence, the reference signal connected into both ADC's channel A and B,

TABLE 4.4
FMC230 PERFORMANCE BOUNDARIES VERSUS FREQUENCY TONE, FOR THE D1 CHANNEL.

Freq. [MHz]	**Carrier Power(*) [dBm]**	**SFDR [dB]**	**SINAD [dB]**	**ENOB [bits]**
18	-3.5	54.2	75.48	12.25
134.3	-2.68	58.35	64.77	10.47
282.8	-4.37	57.36	68.75	11.13
589.3	-3.16	57.84	71.03	11.51
893.9	-4	53	68.05	11.01

(*) Average value, considering a SA resolution bandwidth of 3 kHz.

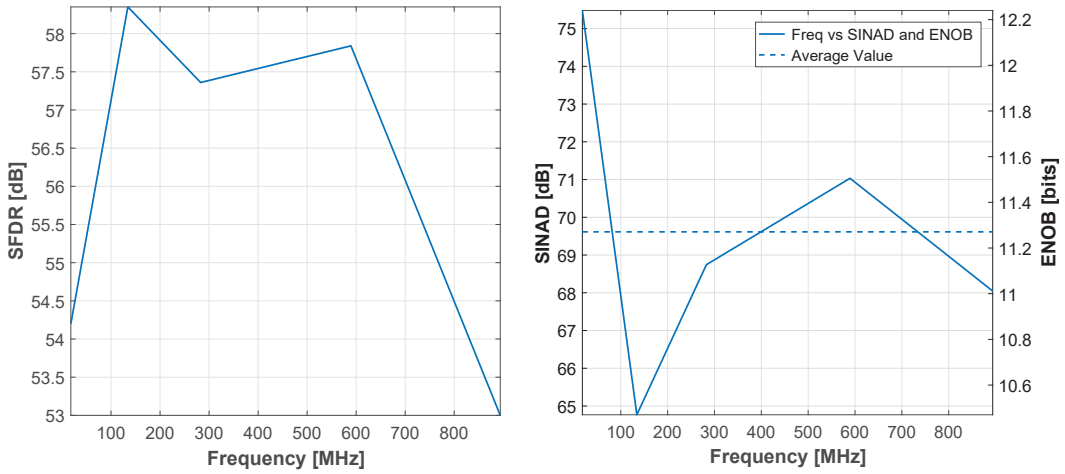

(a) (b)

FIGURE 4.22: FMC230 performance boundaries versus frequency tone: (a) SFDR and (b) SINAD versus ENOB.

was characterised by 72.5 dB of SFDR which in this case it is limited by the SNR of the considered signal generator equipment (Fig. 4.23a), for a signal power level of -2 dBm (ADC full-scale input value). Since, no other connectorised filters were available, FMC126's SFDR, SNR and ENOB measurements, were only conducted for this single frequency tone.

Moreover, comparing both Figs 4.23a and 4.23b, it is verified that the ADC sampling and quantisation processes induce a performance degradation of 12.7 dB in terms of SFDR, leading to a maximum dynamic range of 59.8 dB. Measured results for SNR and ENOB are depicted in Fig. 4.24, where it can be seen that the maximum value for SNR and ENOB is 48.8 dB and 7.8 bits, respectively, and as expected, it is also noticed that ENOB decreases linearly with the decreasing of the SNR value at the input of the ADC. For this experiment, a 0-50 dB variable attenuator between the low-pass filter and the ADC input, as considered.

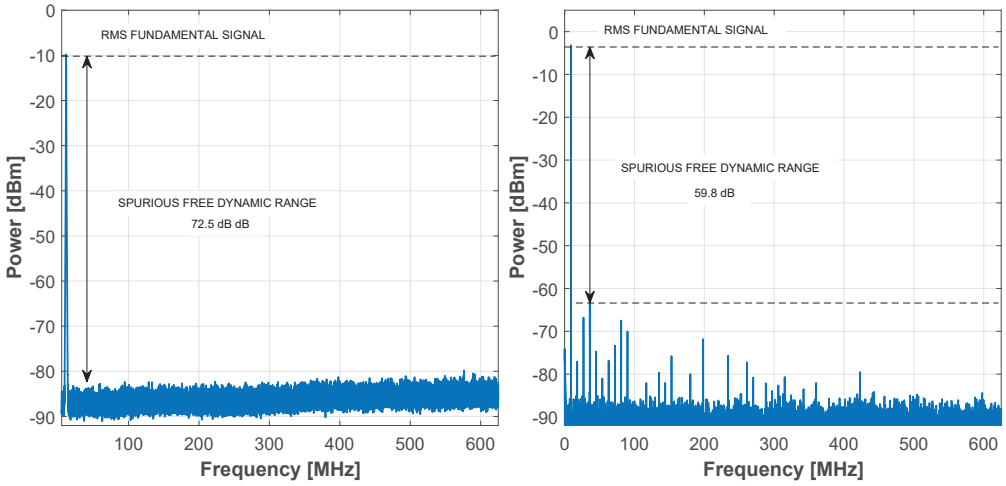

(a) (b)

FIGURE 4.23: SFDR measurement results at: a) the input, and b) output of the FMC126, considering channel A.

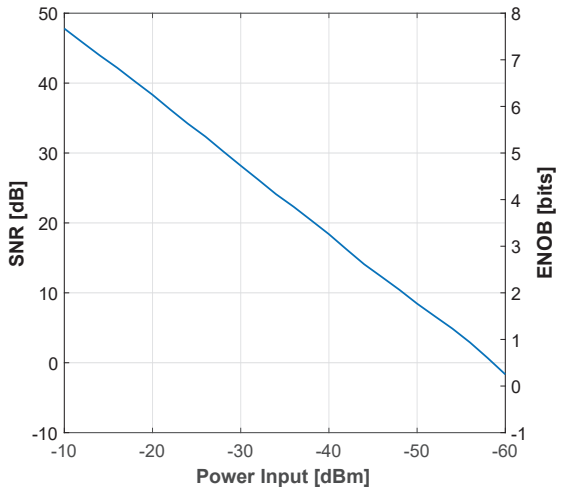

FIGURE 4.24: FMC126: measured SNR versus ENOB, considering channel A.

4.5.2 Magnitude frequency response

In a wireless communication system, both DAC and ADC might also induce non-linearities to the baseband signal, affecting the demodulation performance of advanced digital modulation techniques. For example, considering the OFDM TRX engine that will be introduced in following section, both DAC/ ADC frequency responses are particularly relevant. A time-domain Constant Amplitude Zero Autocorrelation (CAZAC) *Zadoff-Chu* sequence is used for synchronisation and CFO estimation. This sequence is composed by a set of sub-carriers around DC, and therefore if significant attenuation is experienced around this frequency, severe performance degradation in estimating both the beginning of OFDM frame samples and CFO value, will be introduced.

In this context, magnitude frequency response of FMC230 channel 1, is shown in Fig. 4.25a, where it is clearly seen that Voltage peak-to-peak (Vpp) is not constant for different frequency tones. From Fig. 4.25b, it is also verified a poor DAC performance around DC, exhibiting a maximum of 46 dB of signal attenuation at 50 kHz, and 10 dB from 224 MHz up to 312 MHz. The same analysis has been conducted for the FMC126 daughter board, and it is presented in Fig. 4.26. From these results, it is evident that ADC also attenuates signals around DC.

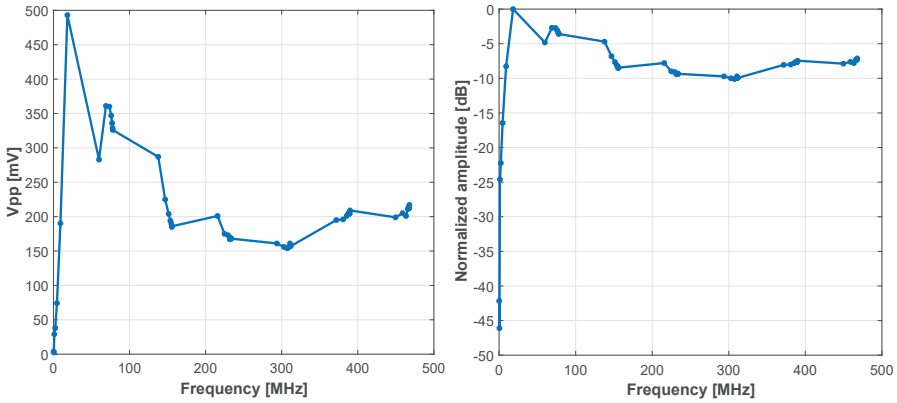

(a) (b)

FIGURE 4.25: DAC magnitude frequency response representation for the DAC0 channel in: a) Vpp, and b) normalised amplitude.

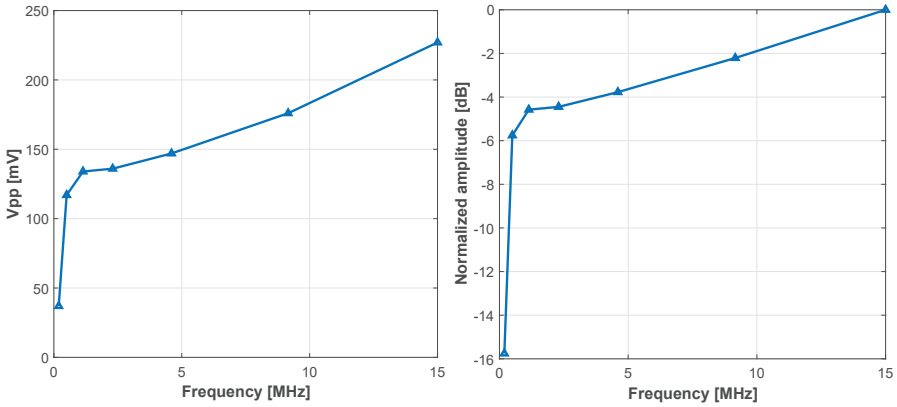

(a) (b)

FIGURE 4.26: ADC magnitude frequency response representation for the ADC channel A in: a) Vpp, and b) normalised amplitude.

4.6 SDR: a complete low-IF real-time multi-Gigabit/s OFDM system

Following the specification presented in [81] for 5G pre-trials, i.e., B higher than 100 MHz, a multi-Gigabit/s real-time OFDM TRX engine, implemented in the VC707 evaluation board, was developed. In particular, the design of the OFDM baseband engine, was based on the work reported in [18], with the necessary modifications to increase the OFDM bandwidth from 61.44 to 156.25 MHz, in addition to its implementation in the *Xilinx* Virtex7 XC7VX485T FPGA instead. This led to a 1 Gbps of real-time transmission rate (considering 256-QAM). Moreover, all algorithms needed for an OTA transmission, namely, timing and frame synchronisation, channel estimation and equalisation, and CFO compensation were implemented, by also following the work presented in [18].

The main SDR system specifications are outlined in Table 4.5, accomplished by integrating both OFDM modulator/ demodulator (TX/ RX real-time engines), with the digital IF architecture illustrated in Fig. 4.19, using a disruptive modular fully pipelined hardware architecture (see Fig. C.5), which will be described in Chapter 8.

Table 4.5
Main SDR system specifications.

Feature	Value
Processing BW	1.25 GHz
Transmission BW	150 MHz
ADC/DAC sampling rate	1.25 GSPS
Modulation	OFDM 4-/16-/64-/256-QAM
Max spectral eff.	8 bits/s/Hz/user
IF freq.	DC-612 MHz
User configuration	Single
Antenna configuration	SISO
Number of DAC/ADC channels	2/3
Resolution of DAC/ADC	14/10 bits

Moreover, the considered OFDM main design operating parameters, particularly the FFT and data size block values, are based on the LTE-Advanced standard (targeting the downlink PHY layer [3]), and are given in Table 4.6. Nevertheless, due to the inherent agile capabilities of the developed SDR, such waveform parameters can be

easily re-designed to match other RF communication systems standards such as: IEEE 802.15.3c and WiGig (for 60 GHz wireless links).

TABLE 4.6
MAIN PARAMETERS CONSIDERED IN THE DESIGN OF OFDM SYSTEM.

Parameter	Value
FFT size block	1024
Data block size	800
Sub-carrier bandwidth	152 kHz
Modulation	16-/64-/256-QAM
Guard time interval	256 samples
Maximum data rate	1 Gbps
Nominal signal bandwidth	122 MHz
OFDM symbol duration	8.2μs
CP duration	1.64μs

Finally, performance of the OFDM TRX engine can be evaluated considering two configurations, namely: B2B, and all digital radio (OTA), as it is as illustrated in Fig. 4.27.

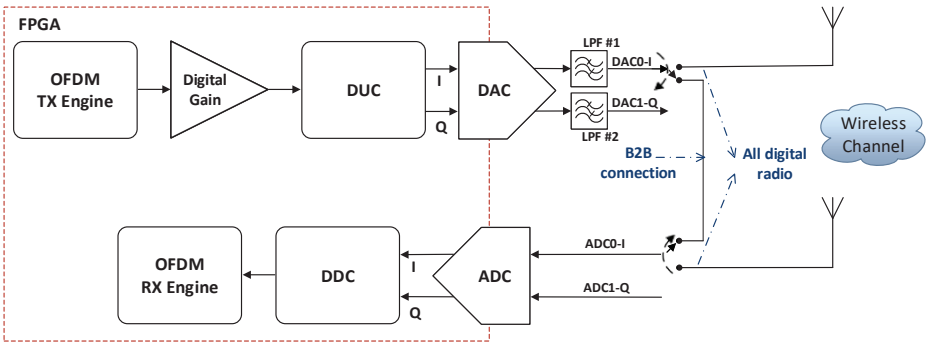

FIGURE 4.27: SDR configurations for the evaluation of the OFDM TRX engince.

4.6.1 Back-to-back system performance

The TRX performance of the OFDM testbed, in a B2B configuration (see Fig. 4.27), is evaluated using EVM as QoS assessment metric. Moreover, OFDM IF possibilities,

such as: zero IF (DC), IF2 (156.25 MHz), IF4 (312.5 MHz), and IF6 (468.75 MHz) were considered, where a digitally controlled amplification stage was also implemented to have control over the transmitted OFDM signal power level. Figure 4.28 shows the output power transfer curve as a function of selected gain and IF modulations, where it is verified that OFDM modulation centred in IF2 provides higher DAC output power than the remaining IF frequencies, since less signal attenuation occurs at this frequency, in comparison with the other IF values (see Fig. 4.25b). Particularly, transmitted OFDM signal spectrum centred at IF4 and considering a gain select of 7, can be seen in Fig. 4.29.

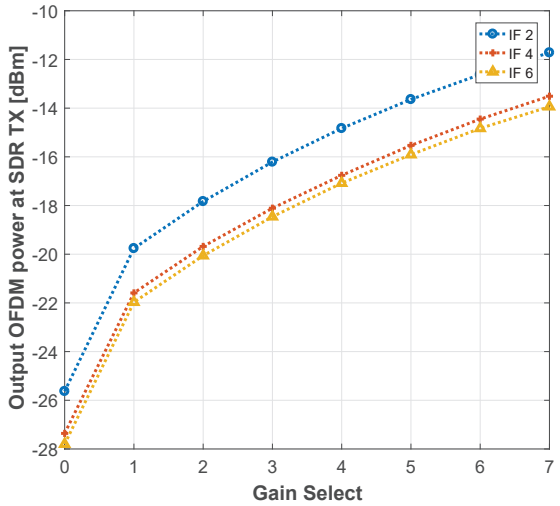

FIGURE 4.28: OFDM transmitted signal power versus digital gain and IF frequency.

In Table 4.7, EVM results are summarised for a digital gain of 7 (maximum gain), and for the four different IF configurations. Additionally, when either I or Q channels are used to transmit and receive data, EVM results are denoted $EVM\ I$ or $EVM\ Q$, respectively. That is, connecting DAC0 to ADC0 is considered as the *I branch*, and connecting DAC1 to ADC1 channels is the *Q branch*, as illustrated in Fig. 4.27. Additionally, for a quadrature transmission, both I/Q channel branches are used simultaneously. These results show that a minimum EVM of approximately -42 dB is obtained for all low IF modulations, except for zero-IF, in which synchronisation algorithms fails to estimate the beginning of frame, due to the nulls obtained on both DAC/ ADC frequency responses. As expected, for other IFs, no OFDM performance degradation is verified, even when an IQ transmission configuration is considered, indicating that very low distortion is present on received signal constellations.

Finally, from Fig.4.30, it can be seen that, 4- and 256-QAM constellations do not present significant scattering distortion on the received symbols, for IF2 frequency and

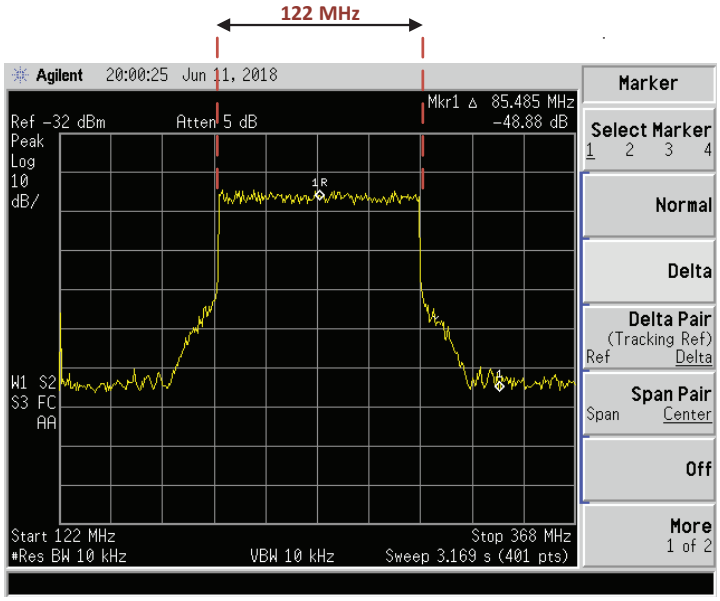

FIGURE 4.29: Frequency spectrum of the transmitted OFDM signal, for an IF4 and gain select of 7.

TABLE 4.7
SUMMARY OF THE OFDM SYSTEM PERFORMANCE, IN B2B CONFIGURATION, FOR VARIOUS IF VALUES, DAC/ADC CHANNEL CONFIGURATIONS, AND MAX. DIGITAL GAIN.

IF config.	**EVM I** [%]	[dB]	**EVM Q** [%]	[dB]	**EVM IQ** [%]	[dB]
0	-	-	-	-	320.76	11.17
2	0.85	-41.29	**0.77**	**-42.21**	4.36*	-27.16*
4	**0.84**	**-41.51**	0.78	-42.10	0.87	-41.23
6	0.97	-41.22	0.90	-40.86	**0.72**	**-42.75**

(*) Received level power exceeds the ADC saturation point.

a maximum digital gain. This subjective quality evaluation indicates that the OFDM SDR system is thus very accurate.

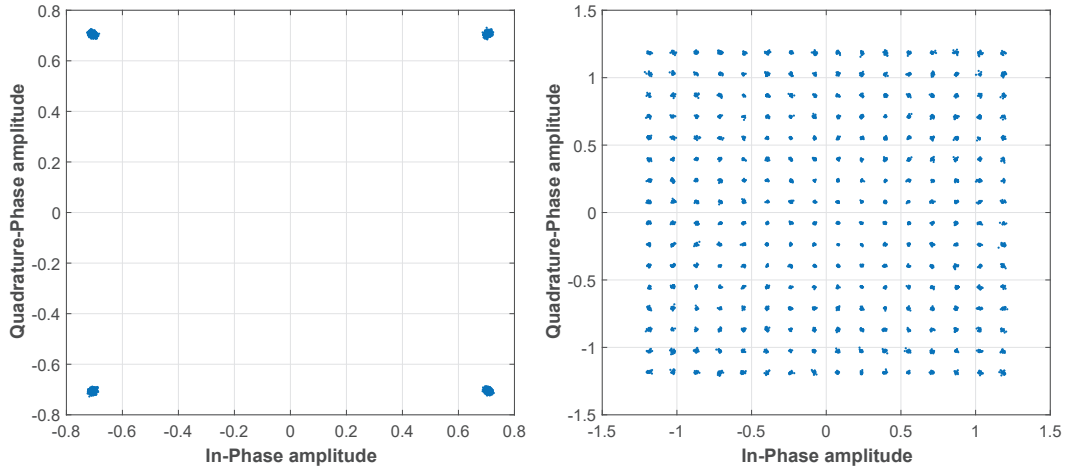

(a) (b)

FIGURE 4.30: B2B scatter constellation plots for: a) 4-QAM and b) 256-QAM, considering $IF2$ and maximum digital gain.

TABLE 4.8
SUMMARY OF THE ALL DIGITAL RADIO PERFORMANCE IN TERMS OF EVM AND SNR RESULTS, IN A B2B CONFIGURATION, FOR DIFFERENT GAIN SELECTION VALUES.

Centre Frequency	**RX power [dBm]**	**gain sel.**	$\overline{EVM}$ **[dB]**	$\overline{SNR}$ **[dB]**
	-17	2	-32.7	40
	-16	3	-32.8	40
368.64 MHz	-15	4	-33	40
	-14	5	-33.4	42
	-13	6	-34.3	42
	-12.5	7	**-35.4**	43

4.7 All digital radio

The proposed all-digital system is composed by two of the described above SDRs. Each of TX and RX radios is composed by a VC707 FPGA board, and a pair of FMC 230 and FMC 126 boards, as it can be seen in Fig. 4.31. Prior to evaluating the system OTA, the DL OFDM communication was assessed in a B2B configuration (a coaxial cable was connecting both TX and RX SDRs) with physical independent TX and RX, as function of the digital gain selection at TX. Results in terms of average EVM, SNR and RX baseband power level, considering a carrier frequency of 368.4 MHz, are detailed in Table 4.8. From these results it can be verified that the maximum EVM performance of the radio system is -35.4 dB. This indicates the feasibility of the system.

Moreover, in an OTA OFDM transmission, path losses must be mitigated with the aid of automatic gain controllers at the receiver (in the analogue domain), otherwise

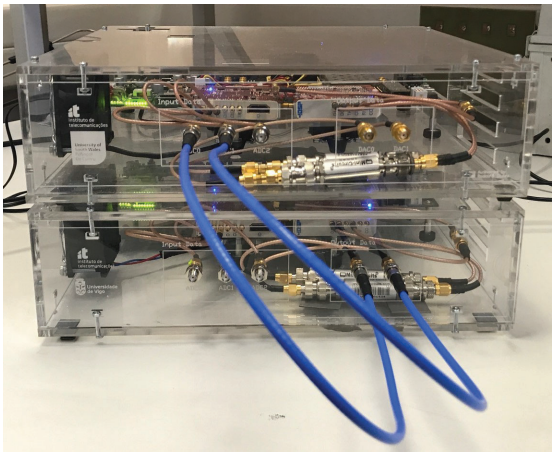

FIGURE 4.31: Photograph of the developed SDR systems for the all digital radio configurations.

EVM results will be severely affected by the quantisation noise of the ADC. As it is demonstrated in Section A.4.3, there is a relationship between received power level (SNR) and EVM. From Fig. 4.24, it is clearly seen that the ADC input signal power must be higher than -44 dBm, if an EVM around -15 dB is required. For instance, for a better QoS, i.e, $EVM < -30dB$, power level must be higher than -28 dBm. Thus, it is necessary to control the average received signal power level to accurately demodulate the transmitted signals. In this context, a dual channel AGC with an output signal power set to -10 dBm, 8 dB below the full-scale input power of the ADC to avoid its saturation due to the relatively high OFDM PAPR (as discussed in Section 3.3), as been developed and introduced in the following section.

4.7.1 Analogue AGC prototype system

An AGC is a device that amplifies the average power level of an arbitrary input signal to a specific output power value (defined by the user), which is typically considered at the receiver communication chain to prevent either quantisation noise or saturation of the ADC. Nevertheless, the first condition is only verified in the AGC's dynamic range.

The most common AGC architecture is known as a closed-loop feedback [171], and is the one considered in this work. It is usually composed of three main components: a Variable Gain Amplifier (VGA), an envelope detector and an integrator [171]. After the input signal is amplified by the VGA, it is passed through an envelope detector that retrieves signal power level, and converts the VGA's signal output power level to a voltage, enabling the comparison of such DC signal with a reference (adjusted by the user). Such produces an error control signal (proportional to the desired output power) that is driven back to the VGA. A picture of the developed prototype AGC system is shown in Fig. 4.32. It is composed of two MAX2090 analogue VGAs [172], a dual-port

power detector (HMC1030 [173]), and potentiometer to adjust the reference control voltage, while requiring only a single 12V power supply.

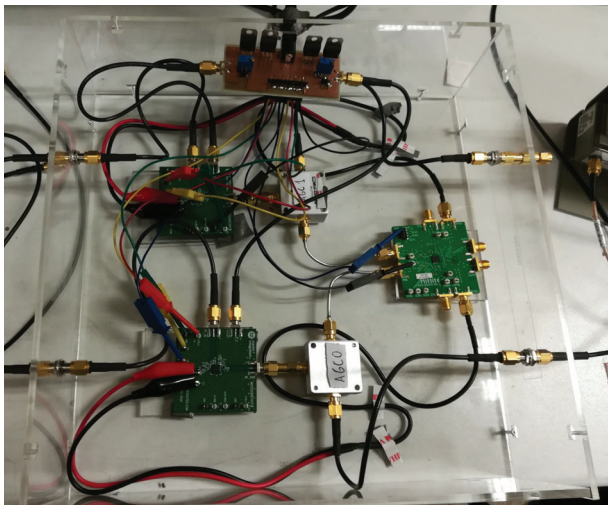

FIGURE 4.32: Developed AGC device.

According to [174], an AGC scheme at the receiver may result into significant OFDM performance degradation due to a relatively long gain convergence time. However, comparing the CP duration of the implemented OFDM system, 1.64 μs, with response time of the MAX2090, 0.22 μs [172], it is verified that the proposed AGC converge time is within the CP period, and thus significant additional EVM degradation due to this amplification stage is not expected.

Before the integration of the developed AGC in the SDR system, dynamic range of such controlled amplification stage was assessed. To this end, at the input of both VGAs, a signal with power levels ranging from -40 dBm up to -12 dBm, was connected. Results are presented in Fig. 4.33a, where it is clearly verified that the proposed analogue AGC has a relatively good performance for input power levels above -32 dBm (lower boundary of its input dynamic range).

Next, similar analysis was carried out, but now integrating this analogue amplification stage with the OFDM SDR's receiver. Obtained EVM results are depicted in Fig. 4.33b, where it is verified that when AGC is not considered, EVM increases linearly, in dB, as the OFDM received power level decreases, whereas, when AGC is placed prior to the ADC, EVM values remain approximately the same, regardless its power level. This is a good indication that the proposed AGC will enhance the OFDM system performance over multipath fading channels.

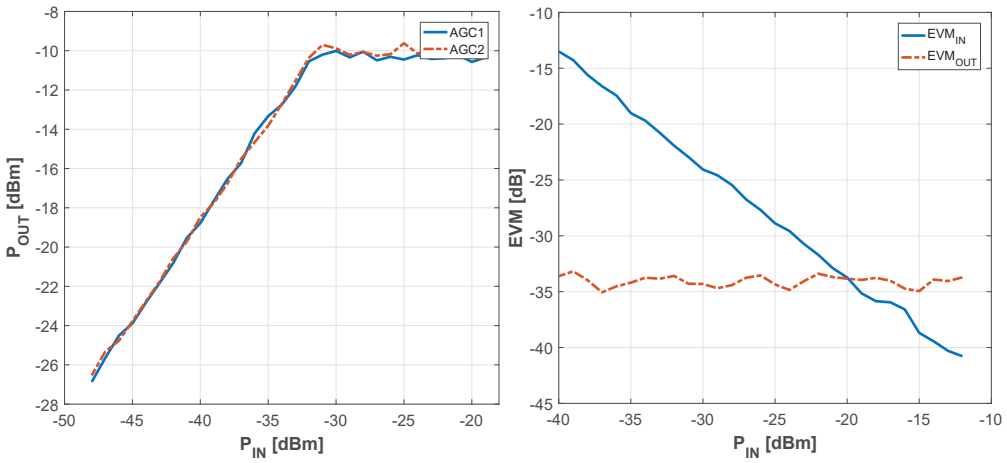

(a) (b)

FIGURE 4.33: AGC performance results: input power versus (a) output power and (b) EVM.

4.7.2 Over-the-air results

The performance of the aforementioned all-digital radio testbed has been evaluated for a link distance of 1 m, inside an anechoic chamber. A detailed high-level block diagram of the setup is presented in Fig. 4.34, and the picture of the measurement setup at its room-plan are depicted in Fig. 4.35. Moreover, the TX radio was configured with a digital gain of 7 (Table 4.8), and under such conditions, a 491.5 Mbps (16-QAM) OFDM transmission obtained an EVM of -26 dB (5%). The comparison of received scatter constellation plot of 16-QAM for both B2B and over-the-air configurations are depicted in Fig. 4.36. The degradation of the RX constellation of the over-the-air, when compared to the B2B constellation is explained by the narrow signal bandwidth of the considered UHF antennas, see Fig. D.1. This lead to an increased transmitted signal attenuation and consequently the reduction of the SNR, even after signal amplification.

4.7.3 Discussion results

This section details an experimental trial on an OFDM all-digital radio communication. It has been shown through EVM and SNR measurements, that the proposed all digital radio system is a promising solution for the 5G NR. Subsequent work to the research present herein aims to exploit the second and third *Nyquist* zones of both DAC and ADC, which enable carrier frequencies up to 1.29 GHz and 2.9 GHz in the digital domain, respectively. This would meet, for example, the frequency band established for 5G outdoor macro applications.

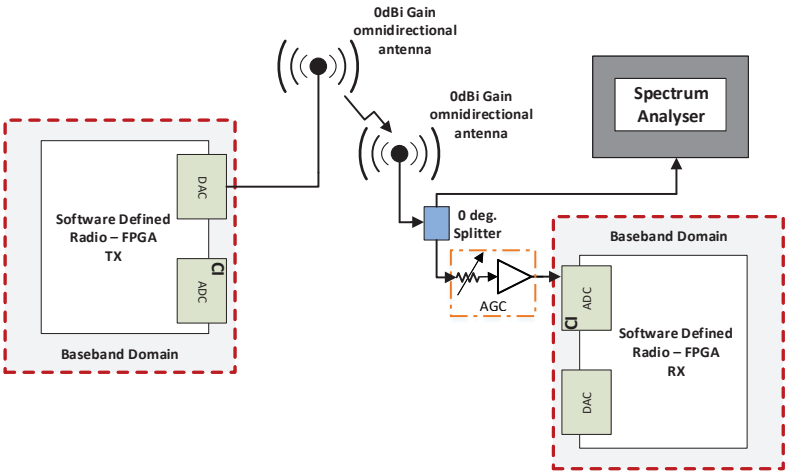

FIGURE 4.34: Detailed block diagram of the proposed all-digital radio architecture.

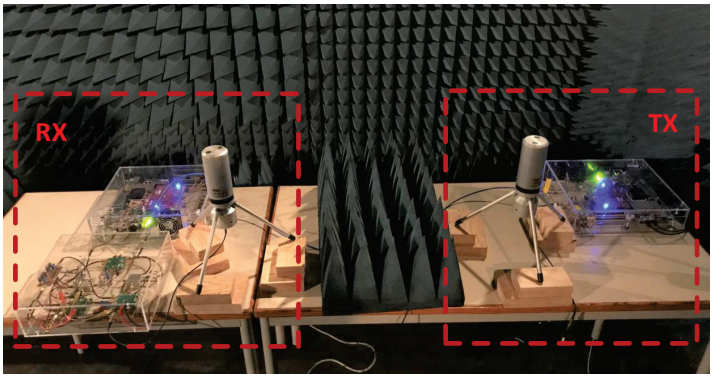

(a)

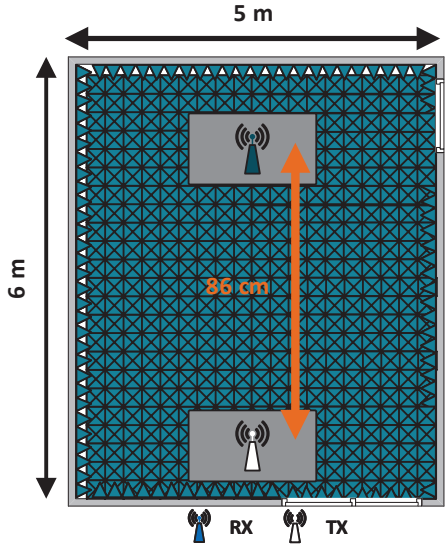

(b)

FIGURE 4.35: Radio performance measurement setup: a) picture, and b) anechoic chamber room-plan.

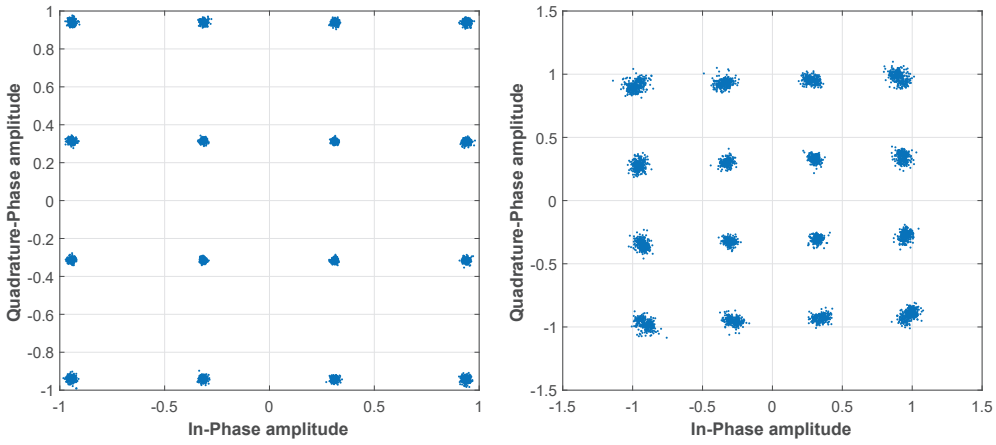

(a) (b)

FIGURE 4.36: Received scatter constellation plot of 16-QAM for: a) B2B configuration, and b) over-the-air.

4.8 Interim conclusions

In this chapter, a novel software-defined radio solution for future wireless communication systems is presented and validated by the implementation of a complete multi-Gigabit/s radio in-the-loop OFDM transmission scheme.

The SDR hardware choice was based on the overall criteria of low time-to-market and reduced development costs. On one hand, VC707 FPGA was the choice for the embedded DSP engine, since, at the time of such decision, it was the best compromise between available logic resources, highly-flexible, high-speed serial bus I/O interface, and cost. In addition, both FMC230/ FMC126 were selected based on their inherent high sampling rates, bit resolution, and their compatibility with the VC707 FMC I/O interface connectivity.

Moreover, firmware connectivity issues between the embedded system and both FMC230/ FMC126 have been outlined, as well as, the considered workarounds to enable a GSPS real-time communication system. Currently, the SDR is limited to 1.25 GSPS, but can be tuned to 5 GSPS with some additional firmware modifications. Moreover, both converters were deeply characterised in terms of SNR, ENOB, SINAD and SFDR, and the advantages of a digital IF RF architecture has been extensively discussed.

Additionally, a complete multi-Gigabit/s radio in-the-loop OFDM communication system, implemented according to the LTE advanced, for high data rate applications, and considering 4-, 16-, 64-, 256-QAM, was validated, considering both B2B and OTA configurations. EVM results in both scenarios were below 2 %, which is quite remarkable, since the EVM values required by sub-6 GHz Wi-Fi (IEEE 802.11.ac) to employ 256-QAM OFDM transmissions is 2.5% [175].

This page is intentionally left blank.

CHAPTER 5

A real-time multi-Gigabit/s OFDM testbed at 60 GHz

5.1 Introduction

This chapter introduces a novel 5G mmWave testbed, designated *USW/IT* herein, aimed to tackle the 5G communication requirements. The proposed system is composed of a baseband/ low-IF processing unit, and a RF front-end at both TX/ RX ends, as it is illustrated in Fig. 5.1. In fact, such was of the result of the integration of the SDR OFDM system introduced in Chapter 4, with a RF front-end designed for mmWave. From Fig. 5.1, it is evident that the low-IF waveform generation/ demodulation is completely independent from the RF up-conversion/ down-conversion. This modular approach was adopted to enhance the flexibility of the prototype radio system to enable signal transmissions at distinct frequency bands. That is, the mmWave carrier frequency can be tuned (to match other RF communication systems standards) by only changing the RF front-end.

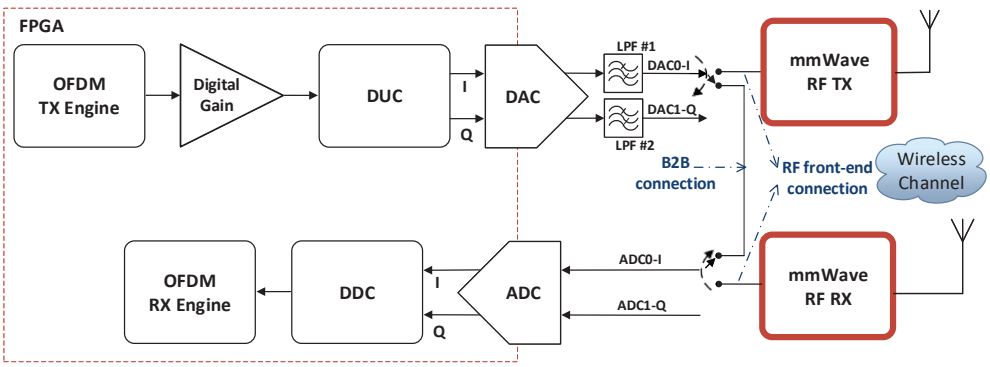

FIGURE 5.1: Block diagram of the *USW/IT* testbed.

Moreover, as it has been demonstrated in Section 3.3 (through simulations), analogue up-conversion/ down-conversion stages presented in on-chip RF architectures, induce a severe performance degradation on OFDM communications. This led to the design and development a more academic RF front-end approach, herein designated Instituto de Telecomunicações (IT) RF front-end. Such device is composed of several connectorised HXI analogue components rather than a COTS chip-set approach. This alternative is intended to provide a multi-Gibabit/s radio in-the-loop at 60 GHz. Such frequency band, at the outset of this project, was thought to be the key solution for the next-generation [16, 17]. Due to the large available bandwidth (from 55 to 66 GHz), mmWave band is very attractive for future 5G wireless communication systems, which might provide transmission data rates over 10 Gbps and network latency below 1 ms. Effectively, even if a 2 GHz channel in the 60 GHz band is used to transmit data employing both 4-QAM, and 16-QAM modulations, data rate would still be limited to 4, and 8 Gbps, respectively. Therefore, there is demand for improving both system reliability and data rates (over 10 Gbps is the target for 5G). In this context, an architecture overview, and system performance of the IT RF front-end will be presented in the following section.

5.2 IT RF front-end: architecture overview

At the TX, it has been considered a typical direct-conversion (in order to avoid IQ imbalance effects on transmitted signals), also known as, homodyne architecture. It is composed by a PLL operating at 15 GHz, a $4X$ multiplier, which brings the LO signal to 60 GHz, and a up-conversion mixer. Also, an external 10 MHz reference clock is required for the PLL. The block diagram of the transmitter, as well as, the specification of each analogue component is illustrated in fig. 5.2. Moreover, in order to reduce the presence of PA non-linearities, an amplification stage at 60 GHz is not considered.

Regarding the receiver, a two stage heterodyne architecture is employed. An LNA is used to amplify received signals, followed by a down-conversion to a 6 GHz IF stage, performed by a first mixing stage process with a 54 GHz LO signal. In a second down-conversion stage, received signals are shifted to baseband/low IF frequencies. Therefore, unlike the transmission architecture, two PLLs operating at 13.5 and 6 GHz are needed in this one, as it can be seen in Fig. 5.3.

Furthermore, the external clock references for both TX/ RX PLLs are generated by a PRS10M rubidium oscillator. Such reference clock signals are characterised by very low phase noise, as verified in Table 5.1, and very high frequency stability (≈0.05ppb), being, therefore, very reliable clock sources. Moreover, in an independent clock configuration between TX/ RX (presence of CFO), two rubidium oscillators were also considered. Fig. 5.4 depicts the experimental characterisation of the IT's RF front-end in terms

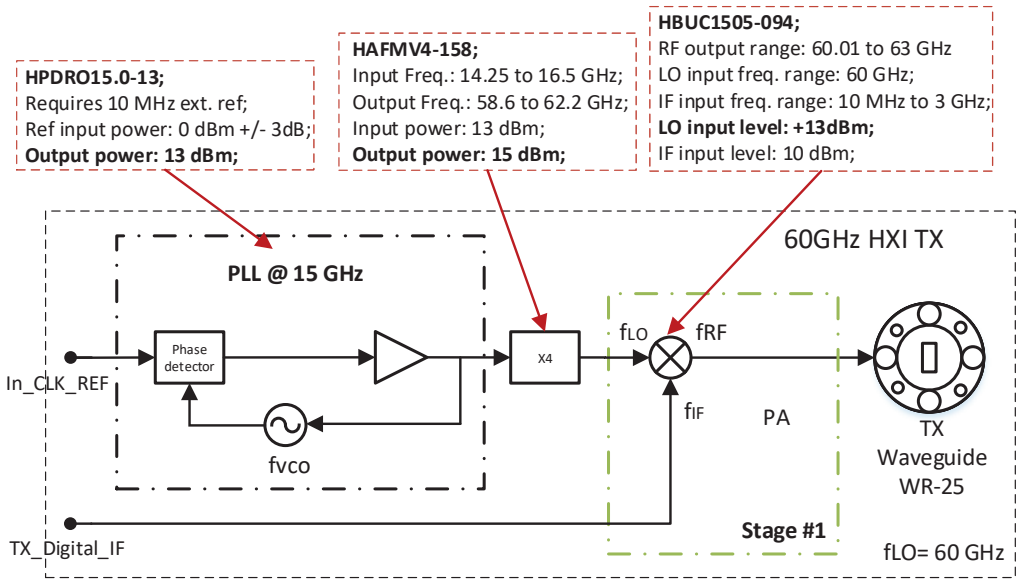

FIGURE 5.2: IT homodyne architecture transmitter.

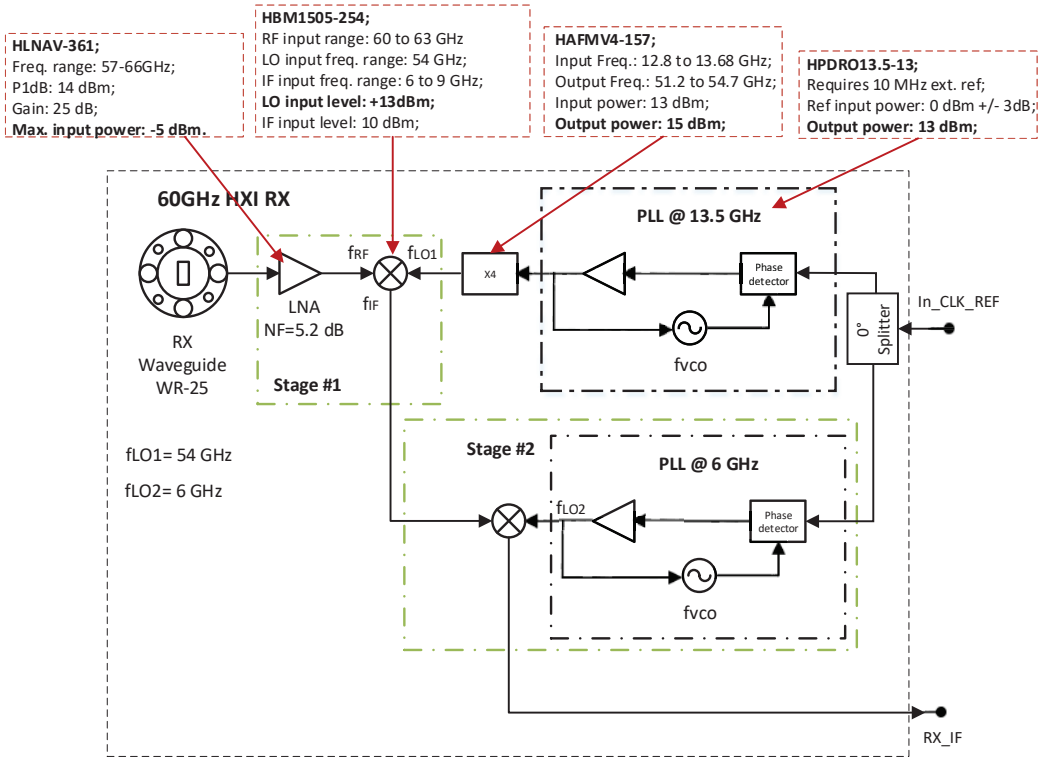

FIGURE 5.3: IT two-step superheterodyne architecture receiver.

of PN, considering both shared and independent clock configurations. Such not only indicate the stability of the analogue demodulator when a CW signal is transmitted, but also the presence of very low power spurious regardless the clock configurations. In

addition, CFO is negligible when IT RF front-end is operating with independent clock sources.

TABLE 5.1
MEASURED PN OF THE RUBIDIUM OSCILLATOR SIGNAL.

Freq. Offset [Hz]	**Phase Noise [dBc/Hz]**
10	-78
100	-80
1000	-81
10000	-100
100000	-122
1000000	-128

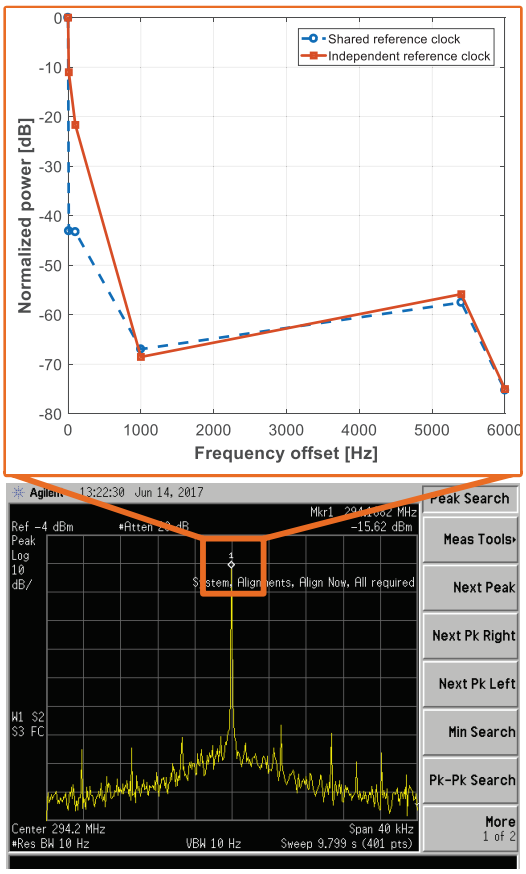

FIGURE 5.4: Results of IT signal frequency stability assessment considering both shared and independent clock configurations.

5.2.1 *USW/IT* tesbed: OTA OFDM system performance

The effect of RF impairments on the quality of TRX OFDM system, outlined in Section 4.6, over-the-air at 60 GHz, is evaluated and demonstrated for different conditions of RX SNIR, for 4-, 16-, 64- and 256-QAM modulations. To reduce possible OFDM performance degradation due to multipath effect, transmission is established inside an anechoic chamber under LOS conditions. Hence, it is possible to accurately assess the impact of the RF front-end on a wireless mmWave OFDM communication system. The QoS is assessed through EVM, and spectral efficiency per stream analysis. BER is estimated using the relation between this metric and EVM, given in Table 5.2 [18]. The experimental setup is shown in Fig. 5.5, where due to the lack of a PA at the TX, 25 dBi antennas have been employed at both TX/ RX terminals, leading to a system usable distance range to 74.5 cm.

Table 5.2
Relation between EVM, BER and digital modulation, according to [18].

BER [%]	Digital Modulation	EVM [dB]
10^{-3}	4-QAM	-10
	16-QAM	-17
	64-QAM	-24
	256-QAM	-32
10^{-4}	4-QAM	-12
	16-QAM	-19
	64-QAM	-26
	256-QAM	-34

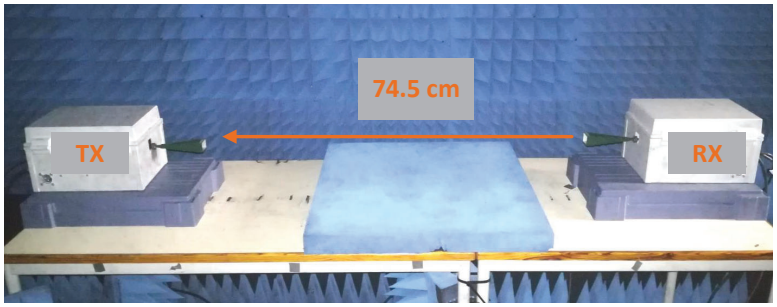

Figure 5.5: MmWave link used for OFDM performance assessment, using IT RF front-end.

EVM results have been computed for each OFDM IF modulated signal under different SNIR and in either the presence or absence of CFO. For example, Table 5.3 shows the measured average EVM values (EVM), for an IF OFDM modulated signal at 312.5 MHz (IF4). These results were obtained with the aid of an ILA, i.e., a *Xilinx* IP block that enables multiple sample acquisitions and data transmission to a host PC for post-processing. In this particular case, three consecutive ILA acquisitions with a memory depth of 12k samples, were considered. The minimum average EVM value, -32.99 dB, is verified for an input power of -14.83 dBm when both TX/ RX devices are clocked using different sources. This indicates that IT RF front-end can handle QAM modulations up to 256-QAM, meaning that 1 Gbps of data transmissions are possible with the proposed mmWave OFDM testbed.

For a subjective quality assessment metric of this EVM value, 4-, 16-, 64-, 256-QAM received constellations, are depicted in Fig. 5.6a, Fig. 5.6b, Fig. 5.6c, and Fig. 5.6d, respectively. When comparing these results with the ones obtained in a B2B configuration, see Fig. 4.30, constellations present a slightly additional scattering distortion on the received symbols. However, even for 256-QAM, all constellations exhibit a well defined point scattering area, indicating therefore, that the probability of decoding erroneous bits will be relatively low.

Furthermore, in Figs. 5.7a and 5.7b it is shown the minimum average EVM and its degradation for the remaining IF OFDM modulations. For IF values of 312.5 and 468.75 MHz, EVM is below 3%, representing a performance degradation below 2% when compared to a back-to-back configuration. This is quite remarkable, since the EVM values at 60 GHz are lower than the 2.5 % required by sub-6 GHz Wi-Fi (IEEE 802.11.ac) to employ 256-QAM OFDM transmissions [175]. To the best of the author knowledge, this spectral efficiency per stream and SNR results go significantly beyond the state-of-the-art, when compared to the current mmWave testbeds presented in table 2.15. Finally, for the proposed link budget the received power versus digital modulation, for a BER of 10^{-3}, is presented in Table 5.4.

Finally, in Fig. 5.8, it is shown the input power operating range of the IT RF front-end considering IF4, where it is clearly seen that such system operates with a relatively wide input dynamic power range, considering an EVM threshold of -10 dB, which is enough for a error-free QPSK demodulation.

5.2.2 Results discussion

From the above results, it is demonstrated that it is possible to successfully use the mmWave spectrum to achieve multi-Gigabit/s, while considering relatively high spectral efficient modulations, and signal bandwidths greater than 100 MHz. For example, from the testbeds listed in Table 2.15, only 28 GHz testbeds reported in [61, 96–98], consider

Table 5.3
SNIR vs EVM results using IF4 OFDM modulation for both shared and independent clock configurations, for IT RF front-end.

Gain Sel.	**Analogue*** **Att. [dB]**	**TX Input Power [dBm]**	**Analogue RX SNIR [dB]**	$\overline{EVM}^{\dagger}$ [%]	$\overline{EVM}^{\dagger}$ [dB]	$\overline{EVM}^{\ddagger}$ [%]	$\overline{EVM}^{\ddagger}$ [dB]
0	0	-25.63	28.70	6.83	-23.30	5.40	-25.34
	5	-30.63	22.90	11.56	-18.74	9.43	-20.51
	10	-35.63	18.80	20.57	-13.73	16.50	-15.65
1	0	-19.76	33.79	3.67	-28.72	3.01	-30.42
	5	-24.76	29.78	5.75	-24.81	4.79	-26.39
	10	-29.76	24.06	10.49	-19.58	8.28	-21.64
2	0	-17.83	36.00	3.11	-30.13	2.62	-31.60
	5	-22.83	31.00	4.87	-26.26	3.96	-28.05
	10	-27.83	25.19	8.48	-21.45	6.67	-23.52
3	0	-16.21	36.67	2.74	-31.21	2.30	-32.52
	5	-21.21	32.42	4.40	-27.12	3.37	-29.43
	10	-26.21	26.74	7.14	-22.93	5.64	-24.98
4	0	-14.83	**37.81**	2.35	-32.58	**2.23**	**-32.99**
	5	-19.83	34.00	3.44	-29.27	3.00	-30.44
	10	-24.83	29.30	6.04	-24.38	4.81	-26.36
5	0	-13.64	38.48	2.50	-32.36	2.31	-32.70
	5	-18.64	34.22	3.08	-30.22	2.84	-30.93
	10	-23.64	29.96	5.05	-25.94	4.45	-26.98
6	0	-12.62	38.08	2.69	-31.36	2.26	-32.87
	5	-17.62	34.00	3.07	-30.15	2.57	-31.78
	10	-22.62	31.42	4.57	-26.80	3.95	-28.06
7	0	-11.72	39.00	2.55	-31.87	2.37	-32.46
	5	-16.72	36.02	2.58	-31.75	2.37	-32.48
	10	-21.72	32.63	4.06	-27.82	3.64	-28.77

(*) Variable attenuator placed between the SDR and transmitter;
(†) Shared clock source configuration;
(‡) Independent clock source configuration.

Table 5.4
Minimum received power at RX vs digital modulation, using IT RF Front-End.

Digital Modulation	**Minimum received Power [dBm]**
4-QAM	-84.09
16-QAM	-66.65
64-QAM	-59.09
256-QAM	-48.35

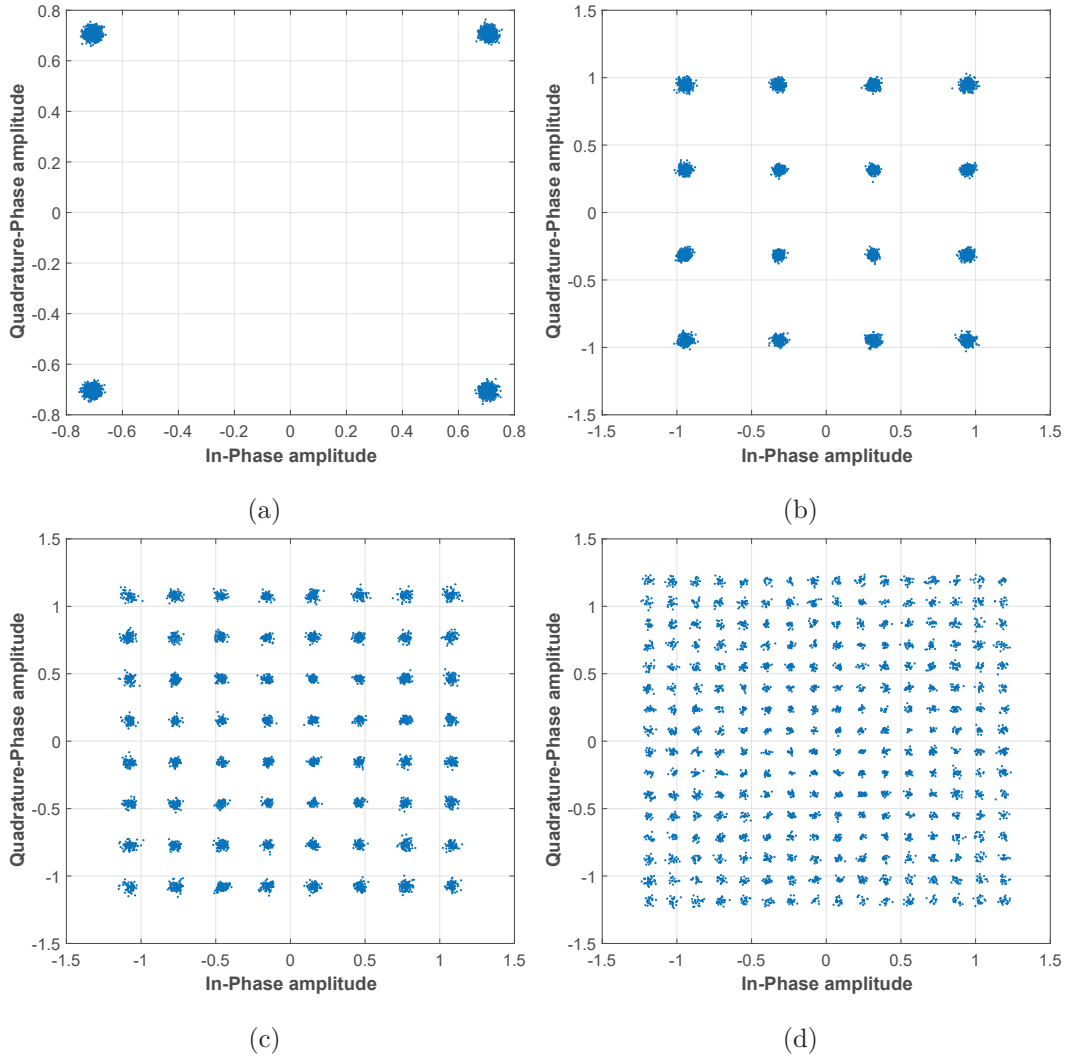

FIGURE 5.6: Received scatter constellation plots for: a) 4-QAM, b) 16-QAM, c) 64-QAM, d) 256-QAM, considering an IF4 OFDM power transmission of −14.83 dBm on the IT RF front-end.

a modulation bandwidth higher than 100 MHz, real-time baseband processing, and consider the 5G NR waveform as the transmission scheme (OFDM). On the other hand, at 60 GHz, it is evident a lack of testbeds which comply to the minimum technical performance requirements of IMT 2020 for 5G, see Table 2.14. Considering the proposed OFDM testbed, the 5G peak spectral efficiency value of 7.8 bit/s/Hz [81] was achieved, and thus, the gap verified in testbeds operating at 60 GHz has been fulfilled. In other words, no other prototype system can process a signal BW of 150 MHz in real-time, with modulation orders up to 256 QAM, using OFDM as transmission scheme in an over-the-air scenario. It is worth noting that, even in the listed 28 GHz testbed systems, do not meet the DL specification of 7.8 bit/s/Hz.

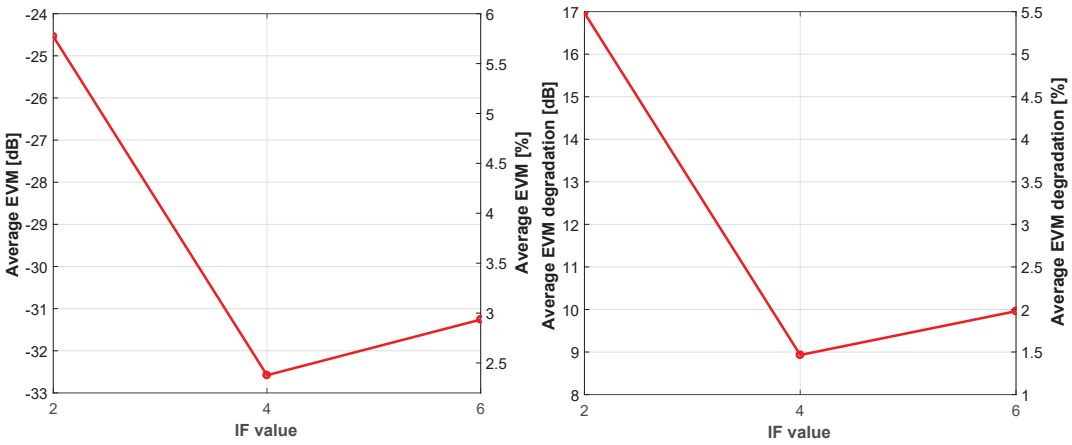

(a) (b)

FIGURE 5.7: Results of EVM: a) performance, and b) degradation, with absence of CFO and the considering IT RF front-end.

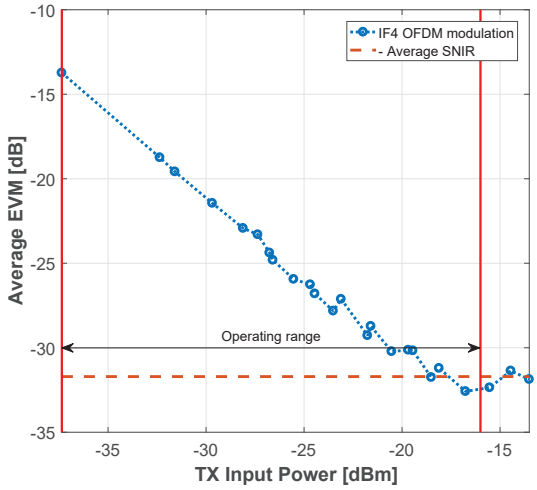

FIGURE 5.8: IT RF front-end input power versus EVM, for IF4 OFDM with absence of CFO.

5.3 Interim conclusions

In this chapter, a novel 5G mmWave testbed solution was presented, and its feasibility assessed over-the-air, particularly considering the 60 GHz band. Through the performance assessment of OFDM, under different conditions of SNIR, it was demonstrated that the proposed prototype communication system is robust (enables QAM modulations up to 256-QAM), and it is capable to provide data rates up to 1 Gbps. Moreover, at the time of this thesis writing, to the best of the author acknowledge, *USW/IT* testbed appears to be one of the most promising and feasible testbeds to meet the 5G requirements.

The work performed in this chapter was successfully demonstrated in real-time, see Fig. 5.9, where a KPI monitoring tool has been also developed (see Fig. E.1), in four showcases:

D. Demonstrator: **"Design, Development and Implementation of a Milimetre Wave Wireless Radio System Prototype for Gigabit/s Multimedia Applications at 60 GHz"** – *2016 Engineering Showcase* – 20 April 2016 – University of South Wales, United Kingdom;

D. Demonstrator: **"A complete Multi-Gigabit/s End-to-End 5G TESTBED at mmWave - the first Portuguese trials"** – *Techdays Aveiro 2017 Centro Exposições* – 12-14 October 2017 – Aveiro, Portugal, in a collaboration with TWEVO;

D. Demonstrator: **"An End-to-End Multi-Gigabit/s 5G TESTBED at mmWave – the First Portuguese Trials"** – *encontro Ciência 2018 Centro de Congressos de Lisboa* – 2-4 July 2018 – Aveiro, Portugal, in a collaboration with TWEVO;

D. Demonstrator: **"Showcase of a full-duplex 5G Radio TESTBED at mmWave: GbE-based OTA Live Streaming of 8 HD Videos"** – *Techdays ISWCS 2018 conference* – 28-31 December 2018 – Lisboa, Portugal, in a collaboration with TWEVO;

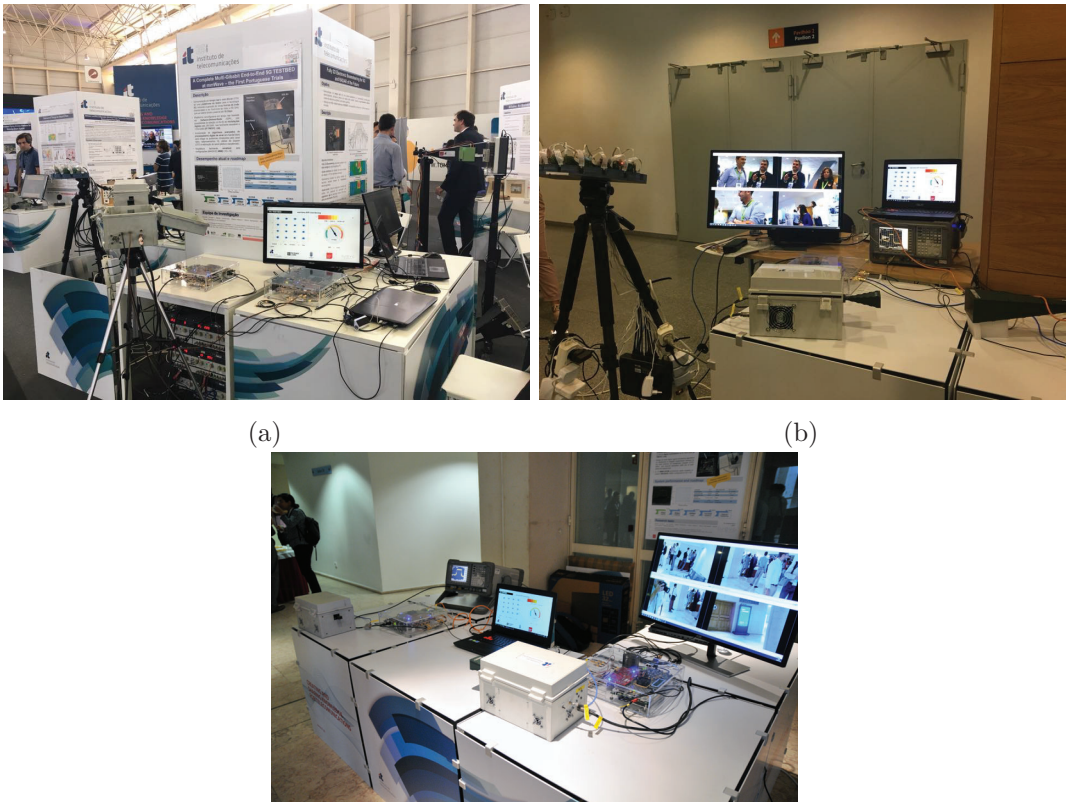

(a) (b)

(c)

FIGURE 5.9: Photograph of the *USW/IT* testbed demonstrator: (a) on the IT stand at Techdays 2017, Aveiro, Portugal, (b) on the IT stand at Ciência 2018, Lisboa, Portugal, and (c) at ISWCS 2018 conference, Lisboa, Portugal.

This page is intentionally left blank.

CHAPTER 6

Radio front-end evaluation and assessment at 60 GHz

6.1 Introduction

In this chapter, a commercial off-the-shelf mmWave RF front-end, is experimentally evaluated, using the *USW/IT* testbed, outlined in the Chapter 5. With this, a thorough comparative analysis between 60 GHz cutting-edge COTS and the IT RF front-ends, the later also introduced in the previous chapter, taking into account their intrinsic RF impairments and their impact on the overall system performance degradation, is presented. With this, it is also possible to verify whether readily available system on chip technology for RF circuits is ready for 5G systems.

As discussed before, non-linearities of RF front-ends, at these frequencies, severely affect the performance of transmission schemes. Therefore, PN, mixer IQ imbalances and PA non-linearities, from the PEM009 VUBIQ RF system, are extensively measured. In addition, OFDM performance degradation induced by this COTS RF front-end is evaluated considering important key performance indicators for QoS in digital communications. Finally, based on the results obtained from appropriate RF measurements, a practical EVM link budget formulation for mmWave systems, which takes into account both PA and PN impairment effects, is proposed.

6.2 The COTS RF front-end choice

The 60 GHz band for a few decades has been considered as an alternative to lower frequency signals [176] [177] due to its large and worldwide unlicensed bandwidth availability [4, 178, 179]. However, its utilisation in previous generations of mobile communications was impractical due to large costs associated with RF chip-set manufacture [4]. Recent evolutions in integrated circuits technology and design techniques [180],

led to more cost effective implementations of such chips. Additionally, the inherent small form factor, enables a massive number of antennas to be placed on a chip at both ends of the radio link, and therefore massive MIMO solutions for 5G. Furthermore, as it was discussed in Chapter 2, the development of mmWave frequency standards such as IEEE 802.11ad (also known as WiGig) [39], IEEE 802.15.3c [40] and IEEE 802.11ay [88], demonstrate that 60 GHz band technology is mature enough to reach the open market. For example, RF devices complying with WiGig are increasing in number. The availability of WiGig routers, such as the TP-Link Talon AD7200 [181] and the Netgear Nighthawk R9000-100EUS [182], and WiGig laptops such as the Dell Latitude [183], bring to practice multi-Gbps implementation of radio links for indoor scenarios.

However, the offer of RF COTS products for research purposes at mmWave band is yet to be satisfactory. To author knowledge, there are only two (cutting-edge) RF front-ends at 60 GHz available, namely EK1HMC6350 [184] and VUBIQ PEM009 [185], supplied by AD, and Pasternack, respectively. In both development systems, analogue up-conversion/ down-conversion stages are implemented in a single TX/ RX chip-set, with the claimed specifications presented in Table 6.1. From this table, it can be seen that both mmWave RF front-ends have similar features. However, differences arise in terms of noise figure value, where EK1HMC6350 has 2 dB more than PEM009, and surprisingly, supporting higher modulation orders.

Table 6.1
RF Front-ends features at 60 GHz.

Feature	**Value**	
Model	EK1HMC6350	PEM009
Technology	BiCMOS	CMOS
Frequency Range [GHz]	57 to 64	57 to 64.8
I/Q Interface	✓	✓
Suggested Modulation	Up to 64-QAM	4/16-QAM
Modulation Bandwidth [GHz]	1.8	1.8
RX Noise Figure	8 dB	6 dB

Despite the fact that in the datasheet of EK1HMC6350 system, 64-QAM capability is claimed, the work reported in [102], shows that signal modulation using such front-end is limited to 4-QAM (EVM at RX higher than 24%). Moreover, a literature survey reveals a lack of documentation addressing the usage of EK1HMC6350 system is presented in

the literature. In fact, to the author's knowledge, only [102] was found. On the other hand, several scientific articles might be found on the VUBIQ system. For example, in [186–188] such system is employed for high precision tracking of people and objects while in [189, 190] it is used for beamforming and beamsteering. Finally, in [191] it is used to assess received signal power in beamforming and interference measurement setups. Based on such wide availability of information, the PEM009 is considered in this work.

6.3 PEM009 architecture overview

The VUBIQ PEM009 RF Front-End, is a TX/ RX 60 GHz development system, which can be configured by a host PC via USB interface [185]. A GUI allows to change multiple parameters such as: signal attenuation, baseband filter bandwidth, channel spacing and centre frequency. Both boards (TX and RX) have built-in reference clocks at 308.571 MHz. However, in order to ensure that the clock signal can be used in a shared TX/RX configuration (avoiding CFO between TX/ RX boards), a Clock (CLK) generator board using an external clock crystal was developed with the same frequency of the built-in clock. This reference clock enables centre frequency (f_C) steps from 57.24 to 64.8 GHz. In the following subsections, details regarding TX/ RX boards and the developed clock board are given.

6.3.1 TX board

At the VUBIQ TX board, both IQ differential baseband signals are up-converted into a 60 GHz RF signal through a two mixer stage, as it can be seen in Fig. 6.1. First an IF IQ mixer, operating at a Local Oscillator (LO) frequency (f_{LO1}), translates and combines both IQ baseband signals, at Baseband Frequency (f_{BB}), into a single signal centred at an intermediate frequency (f_{IF}). Next, an amplification stage is presented followed by a bandpass filter to suppress unwanted image signals. The gain in this IF branch might also be reduced through an IF attenuator (IF_{Att}). Finally, this intermediate signal is modulated to a central carrier frequency, f_C, through a second mixing stage (operating at f_{LO2}). Both f_{LO1}, f_{LO2} and Voltage-Controlled Oscillator (VCO) frequencies (f_{VCO}) are generated in the built-in synthesiser, which requires a external differential reference clock signal ($In\_CLK\_REF^+$/$In\_CLK\_REF^-$), to lock its PLL. The relation between

all these signal frequencies is given by the following equations:

$$\begin{cases} f_{LO1} = f_{VCO} \times \frac{1}{2} \\ f_{LO2} = 3 \times f_{VCO} \\ f_{VCO} = f_C \times \frac{2}{7} \\ f_{RF} = f_C + f_{BB} \\ f_{IF} = f_{LO1} + f_{BB} \end{cases} \tag{6.1}$$

where f_{RF} is the transmitted signal frequency.

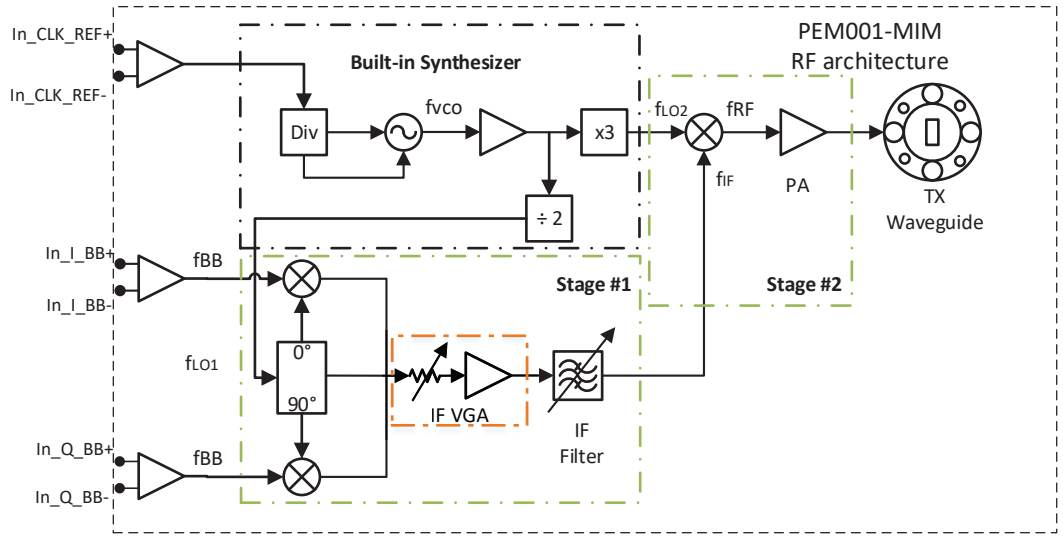

FIGURE 6.1: PEM009 transmitter two-step superheterodyne architecture (adapted from [185]).

6.3.2 RX board

At RX, the counterpart of the TX up-conversion process is performed, in two stages. Firstly, the received mmWave signal is amplified by a LNA. Secondly, a frequency down-conversion is made with the first LO moving the RF signal down to the IF band. This is followed by amplification and filtering stages, which suppress image signals and adjust signal levels for optimum I/Q demodulation. Next, down-conversion to baseband with an I/Q mixer is carried out. Finally, additional gain-control and anti-aliasing filtering might be performed in the demodulated baseband signal, as illustrated in Fig. 6.2.

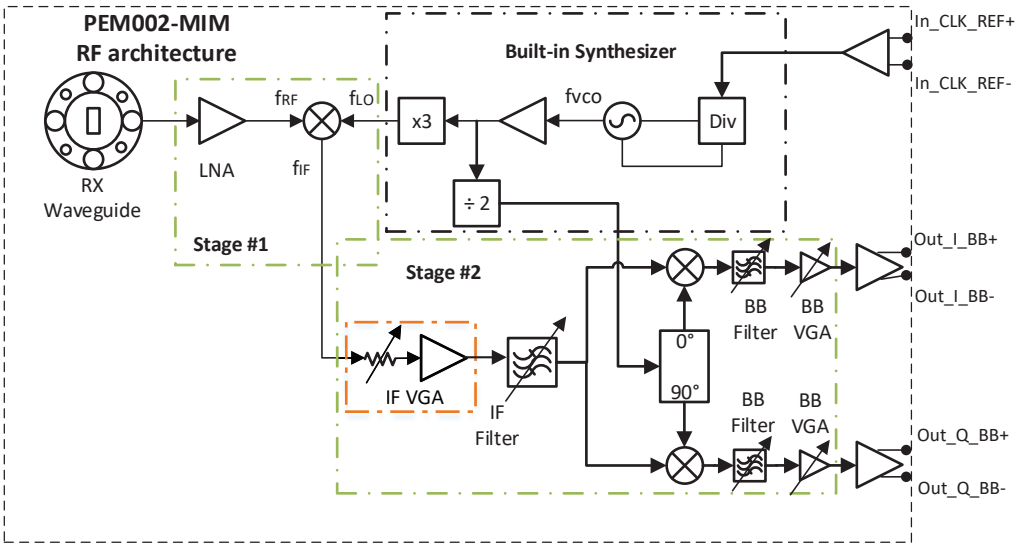

FIGURE 6.2: PEM009 two-step superheterodyne down-conversion architecture presented in the receiver (adapted from [185]).

6.3.3 Developed external CLK board

The reference clock source of both TX and RX devices might be shared to avoid additional distortions effects due to CFO. However, in a realistic environment scenario, both TX and RX are operating using independent clock sources, and thus CFO is inherently present. The bounds of the frequency difference between TX and RX clocks, can be computed from the frequency stability of the crystal oscillators located in each of TX/RX boards. For example, the ±25 ppm crystal oscillator implemented in both TX/RX boards of the PEM009, induces a maximum frequency shift between TX/RX of 1.5 MHz (considering a 60 GHz RF carrier). This impairment value may be impractical for some wireless PHY layers, and thus, a new crystal-based clock has been developed and attached at both TX/RX equipments, as shown in Fig. 6.3. The chosen crystal oscillator was the M6300 supplied by MtronPTI, and has the following features: LVPECL differential output at 308.571 MHz, and frequency stability of around 0.5 ppm. The M6300 clock measured phase-noise values at 100 Hz, 1kHz and 10 kHz are given in 6.2.

Consequently, using such oscillator, the CFO presented in the PEM009 is now reduced to a maximum theoretical value of 30 kHz.

6.4 PEM009 RF impairments characterisation

In this section the RF impairments of the PEM009 VUBIQ 60 GHz development system [185] are assessed. Its TX board is therefore, characterised in terms of transmitted power, carrier and side-band RF leakages and IMD products. Similar measurements

TABLE 6.2
MEASURED PHASE-NOISE OF M6300 OSCILLATOR CLOCK, AT 308.571 MHZ.

Freq. Offset [Hz]	**Phase-noise [dBc/Hz]**
10	-62
100	-78.5
1000	-80
10000	-99
100000	-118
1000000	-124

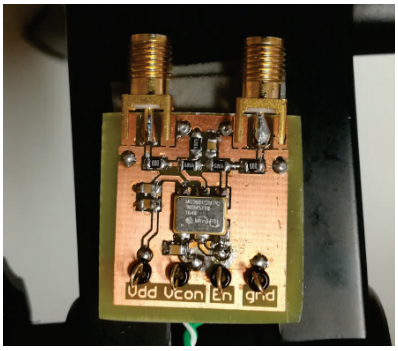

FIGURE 6.3: Developed external reference clock source (M6300 oscillator) board.

were conducted on the RX board. In addition, the system is characterised by its IF-IF frequency response magnitude, IQ and DC voltage offset imbalances. These results will be essential for mmWave RF impairments modelling, as well for the design of appropriate digital signal processing compensation algorithms, and, ultimately, for EVM link budget estimation purposes.

6.4.1 Transmitter

Output power and gain

Although several amplification stages are present and embedded in the mmWave TX, as seen in Fig. 6.1, no information regarding their gains are provided [192]. Therefore an extensive RF measurement on the TX output power was conducted. The utilised setup for such experiment is illustrated in Fig. 6.4, where the TX board input Continuous Wave (CW) signals are generated by a Vector Signal Generator (VSG) (ROHDE & SCHWARZ SMJ 100 A), and then split into two similar branches. Since TX input connector ports are differential, a 180° splitter is used to convert both single-ended interfaces into differential ones. The signal power level of both baseband signals is set to the recommended −26 dBm value. Finally, the output signal power is measured by connecting the mmWave TX wave-guide port to the ZVA 67 VNA, operating in SA mode. Results are summarised in Fig. 6.5, considering single tone baseband signals of

10 MHz (f_{FO}), and f_C values of 57.24 GHz, 59.4 GHz, 61.56 and 63.72 GHz. Average output power levels of 4, -4 and -23 dBm were obtained for IF_{Att} values of 0, 8 and 20 dB, respectively. Moreover, Fig. 6.6a shows the output signal power dependency on IF_{Att} values at $f_{RF} = 57.25$ GHz. It can be clearly seen that the analogue IF attenuator does not changes linearly with the GUI configuration value. A maximum gain of 32 dB, was obtained for an IF_{Att} of 0 dB, as it is illustrated in Fig. 6.6b.

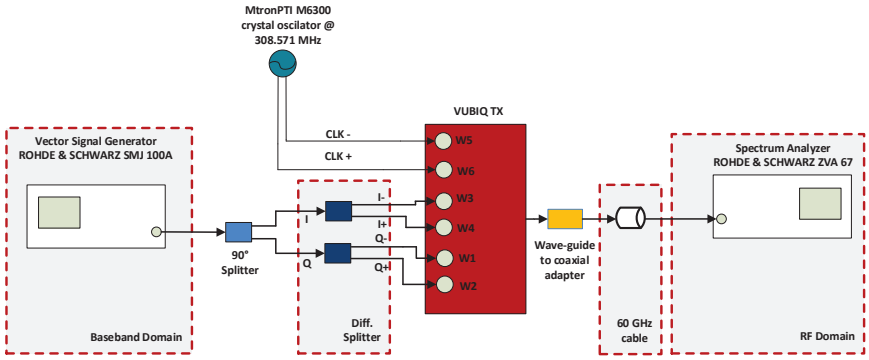

(a)

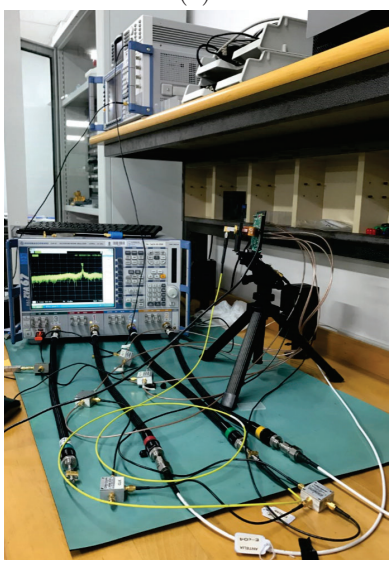

(b)

FIGURE 6.4: Block diagram of the transmitted output power measurement setup in a), and its picture in b).

Intermodulation distortion products

Non-linear distortion in wireless RF Front-Ends are usually characterised by 2nd and 3rd-order IMD products. Such products are mainly generated by cascaded amplifiers

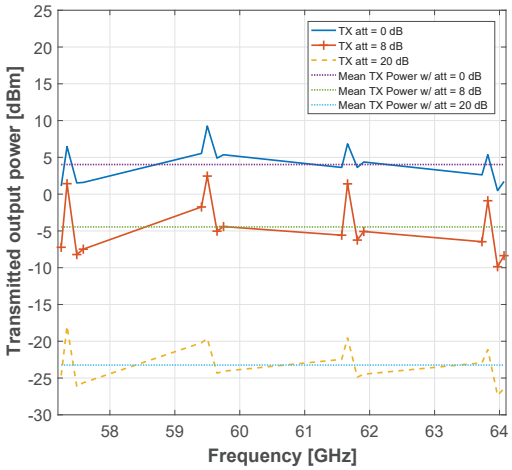

FIGURE 6.5: Transmission output power performance versus f_{RF} and IF_{Att} values.

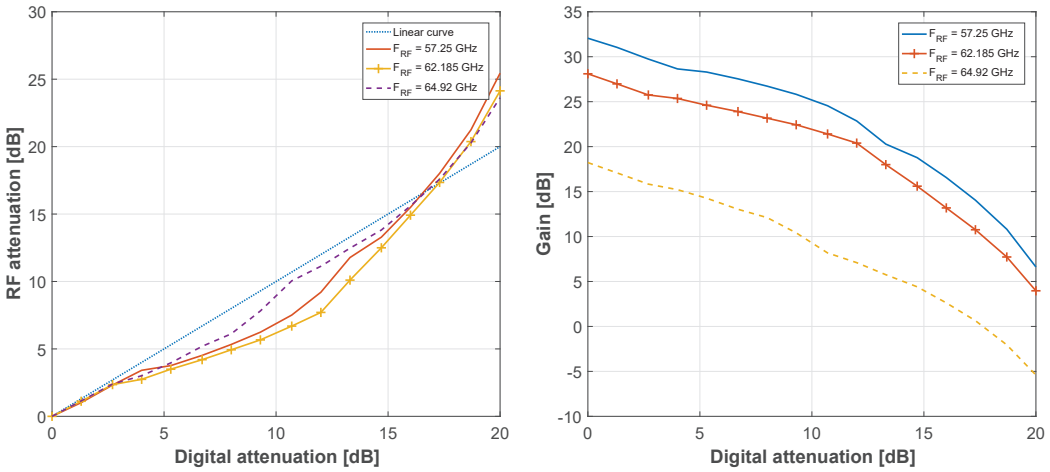

(a) (b)

FIGURE 6.6: Digital attenuation values versus: a) RF attenuation, and b) signal gain, considering a input power of -26 dBm.

and mixers present in the up-conversion, due its analogue design architecture. Power levels of both 2nd and 3rd distortion products are measured at the output of TX board, utilising the same measurement setup of Fig. 6.4. However, a baseband signal consisting of two tone frequencies, at 50 MHz and 52.44 MHz, is considered instead.

The power level difference between 2nd and 3rd intermodulation products and both fundamental tones are presented (in dBc values) in Tables 6.3, 6.4, 6.5 and 6.6, for f_C values of 57.24, 59.4, 61.56 and 63.72 GHz, respectively. Additionally, for each of the f_C values, 0, 8, 12 and 20 dB values for IF_{Att} are used.

Moreover, the most significant IMD products (lowest IMD dBc value) are shown in Fig.6.7, for each f_C and IF_{Att} combinations. As it is depicted, and as expected, the power ratio between IMD products and carrier increases as the digital attenuation increases.

TABLE 6.3
POWER LEVEL DIFFERENCE BETWEEN IMD PRODUCTS AND BOTH FUNDAMENTAL TONES, CONSIDERING $f_C = 57.24$ GHz.

IMD product	**Relative Power [dBc]**			
	Att. = 0*	**Att. = 8***	**Att. = 12***	**Att. = 20***
f_2-f_1	35.37	38.32	38.84	39.44
$2f_1$-f_2	30.4	29.06	**26.51**	39.56
f_1	-0.8	-0.52	-0.47	-0.7
f_2	0	0	0	0
$2f_2$-f_1	**28.36**	31.22	31.33	39.56
$2f_1$	42.32	43.54	45.07	38.95
f_1+f_2	36.96	37.52	37.83	38.92
$2f_2$	43.86	43.82	45.71	**38.88**
$3f_1$	37.11	37.42	39.17	39.12
$2f_1$+f_2	28.45	**27.56**	27.8	39.14
f_1+$2f_2$	29.18	28.04	28	39.18
$3f_2$	39.38	38.74	40.61	39.21

(†) in dB.

TABLE 6.4
POWER LEVEL DIFFERENCE BETWEEN IMD PRODUCTS AND BOTH FUNDAMENTAL TONES, CONSIDERING $f_C = 59.4$ GHz.

IMD product	**Relative Power [dBc]**			
	Att. = 0*	**Att. = 8***	**Att. = 12***	**Att. = 20***
f_2-f_1	32.36	42.75	35.8	40.03
$2f_1$-f_2	37.53	**30.24**	**27.42**	40.42
f_1	-1.63	-0.97	-1.29	-1.27
f_2	0	0	0	0
$2f_2$-f_1	**23.58**	34.12	30.11	40.67
$2f_1$	38.29	46.97	43.99	42.09
f_1+f_2	33.63	41.78	37.5	42.12
$2f_2$	41.05	48.29	44.05	42.16
$3f_1$	32.05	41.33	37.95	41.39
$2f_1$+f_2	23.59	32.67	28.18	**39.35**
f_1+$2f_2$	24.44	33.45	28.28	41.23
$3f_2$	35.4	43.11	39.14	41.18

(†) in dB.

This implies that cascaded amplifiers start operating far below their saturation point as the IF attenuation is increased. The maximum difference between fundamental tones

TABLE 6.5
POWER LEVEL DIFFERENCE BETWEEN IMD PRODUCTS AND BOTH FUNDAMENTAL TONES, CONSIDERING $f_C = 61.56$ GHz.

IMD product	**Relative Power [dBc]**			
	Att. = 0*	**Att. = 8***	**Att. = 12***	**Att. = 20***
f_2-f_1	31.79	43.13	35.27	39.18
$2f_1$-f_2	33.11	33.28	**26.38**	37.84
f_1	-1.63	0	0	-1.99
f_2	0	-1.41	-0.54	0
$2f_2$-f_1	**21.51**	32.41	29.5	39.40
$2f_1$	37.66	44.37	42.12	39.46
f_1+f_2	32.23	39	36.45	39.45
$2f_2$	40.82	47.08	42.63	39.44
$3f_1$	31.96	39.92	36.83	39.23
$2f_1$+f_2	23.91	30.98	28.43	**37.53**
f_1+$2f_2$	24.75	**31.22**	29.56	39.2
$3f_2$	37.42	41.75	37.69	39.18

(†) in dB.

TABLE 6.6
POWER LEVEL DIFFERENCE BETWEEN IMD PRODUCTS AND BOTH FUNDAMENTAL TONES, CONSIDERING $f_C = 63.72$ GHz.

IMD product	**Relative Power [dBc]**			
	Att. = 0*	**Att. = 8***	**Att. = 12***	**Att. = 20***
f_2-f_1	37.28	42.38	36.63	36.3
$2f_1$-f_2	26.33	36.43	26.35	**35.33**
f_1	-3.65	-1.99	-0.64	-0.25
f_2	0	0	0	0
$2f_2$-f_1	26.17	32.61	32.44	37.62
$2f_1$	38.94	46.87	42.68	38.22
f_1+f_2	32.59	41.99	37.01	38.22
$2f_2$	40.17	48.33	43.62	38.21
$3f_1$	32.16	40.63	36.98	37.43
$2f_1$+f_2	**22.11**	28.42	25.72	37.36
f_1+$2f_2$	23.53	**27.57**	**25.58**	37.27
$3f_2$	36.43	37.88	37.56	37.21

(†) in dB.

and IMD products power is 39.35 dBc, and happens for an IF_{Att} equals to 20 dB and a f_C of 59.4 GHz.

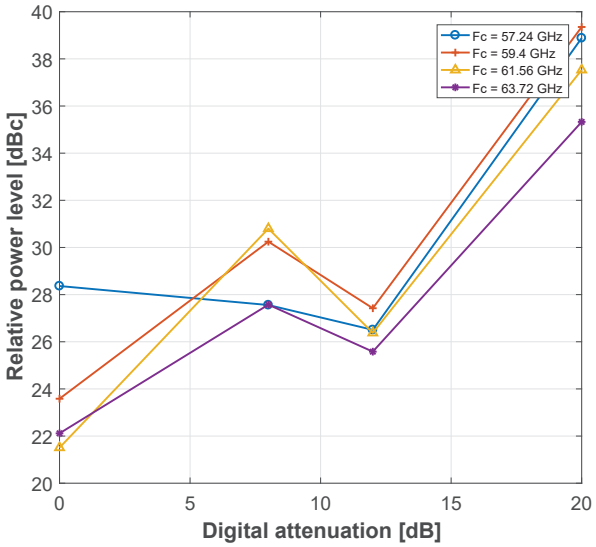

FIGURE 6.7: IMD product power when related to the carrier value, for each f_C and digital attenuation configurations.

Other figures of merit to evaluate IMD products are the 2nd and 3rd order Intercept Points, IP2 and IP3, respectively. Such values indicate when both 2nd/3rd order power levels overtake the fundamental tone, at a particular input power. IP2 and IP3 are constituted by two coordinate points, Input Intercept Point (IIP_n) and Output Intercept Point (OIP_n), where n indicates the IMD order. The OIP_n is defined as follows:

$$OIP_n = P_{out} + \frac{\Delta P}{n-1}, \tag{6.2}$$

where P_{out} and ΔP denote the fundamental tone output power and the difference between P_{out} and the IMD product power level, respectively. Consequently, IIP_n can be obtained by:

$$IIP_n = OIP_n - G, \tag{6.3}$$

where G is the linear gain of the device.

Particularly, for the VUBIQ TX (input power is constant), only OIP_2 and OIP_3 values are measured. Furthermore, OIP_2 is obtained considering the IMD tone of $f_1 + f_2$, and OIP_3 is calculated by:

$$\begin{cases} OIP_{3(low)} = P(f_1) + \frac{P(f_2) - P(2f_1 - f_2)}{2} \\ OIP_{3(high)} = P(f_2) + \frac{P(f_1) - P(2f_2 - f_1)}{2} \end{cases}, \tag{6.4}$$

where $P(2f_1 - f_2)$ and $P(2f_2 - f_1)$ are the power of the low and high frequency signals of the intermodulation signal, respectively.

The obtained values for OIP_2 is given in Table 6.7 considering the same TX parameter combinations of previous measurements. Similarly, values for OIP_3 are shown in Table 6.8 for a f_C of 57.24 GHz and 59.4 GHz and in Table 6.9 OIP_3 for 61.56 GHz and 63.72 GHz.

TABLE 6.7
MEASURED OIP_2 VALUES CONSIDERING A f_C OF 57.24 GHZ, 59.4 GHZ, 61.56 GHZ AND 63.72 GHZ.

Att.	**OIP$_2$ [dBm]**			
[dB]	**57.24 GHz**	**59.4 GHz**	**61.56 GHz**	**63.72 GHz**
0	42.32	41.76	38.21	33.72
8	36.37	45.25	40.55	40.83
12	31.99	36.6	32.96	30.48
20	15.98	15.98	17.19	15.53

TABLE 6.8
MEASURED $OIP_{3(low)}$ AND $OIP_{3(high)}$ VALUES FOR $f_C = 57.24$ GHZ AND $f_C = 59.4$ GHZ.

	F$_c$ = 57.24 GHz		**F$_c$ = 59.4 GHz**	
Att. [dB]	**OIP$_{3(low)}$ [dBm]**	**OIP$_{3(high)}$ [dBm]**	**OIP$_{3(low)}$ [dBm]**	**OIP$_{3(high)}$ [dBm]**
0	21.36	19.94	28.52	20.74
8	13.9	14.72	19.56	21.01
12	7.89	10.06	14.1	14.8
20	-2.46	-2.81	1.62	1.11

TABLE 6.9
MEASURED $OIP_{3(low)}$ AND $OIP_{3(high)}$ VALUES FOR $f_C = 61.56$ GHz AND $f_C = 63.72$ GHz.

	$\mathbf{F_c = 61.56\ GHz}$		$\mathbf{F_c = 63.72\ GHz}$	
Att. [dB]	**$\mathbf{OIP_{3(low)}}$ [dBm]**	**$\mathbf{OIP_{3(high)}}$ [dBm]**	**$\mathbf{OIP_{3(low)}}$ [dBm]**	**$\mathbf{OIP_{3(high)}}$ [dBm]**
0	24.16	17.55	17.96	16.05
8	17.48	17.75	19.04	16.14
12	9.42	11.25	6.96	10.01
20	-1.35	-1.57	-4.77	-3.75

RF carrier and side-band leakages

Usually in IQ up-conversion architectures, such as the one represented in Fig. 6.1, not only the modulated signal is transmitted, but also its undesired image and RF carrier, which may harm adjacent wireless channels. The transmission of an undesired RF carrier results from the presence of DC voltage offset in both I/Q branches that can be either introduced by both I and Q signal inputs or from analogue hardware imperfections present in the RF modulator.

In order to evaluate both undesired signals at the PEM009 TX board, metrics as carrier and image (also known as side-band) leakages, are considered. Both metrics measure the power level difference between both desired and undesired transmitted signals. For this system analysis, the measurement setup of Fig. 6.4 is considered, as well as, using the same input TX combination parameters of previous analysis. The summary of these results are detailed in Fig. 6.8. As it can be seen from this figure, although a carrier suppression is verified in average, around 11 dBc, for $IF_{\text{Att}} = 20$ dB, the side-band leakage presents more power than the desired signal (also in average). For example, a -1.6 dBc value is verified for $IF_{\text{Att}} = 0$ dB. Therefore, according to these results, TX board induces relevant IQ imbalances into baseband signals.

6.4.2 Receiver

In this subsection, a detailed RF characterisation analysis is performed on the mmWave integrated PEM009 receiver chip-set. Clock and synthesiser leakages, IMD products and power sensitivity are the considered metrics for such evaluation.

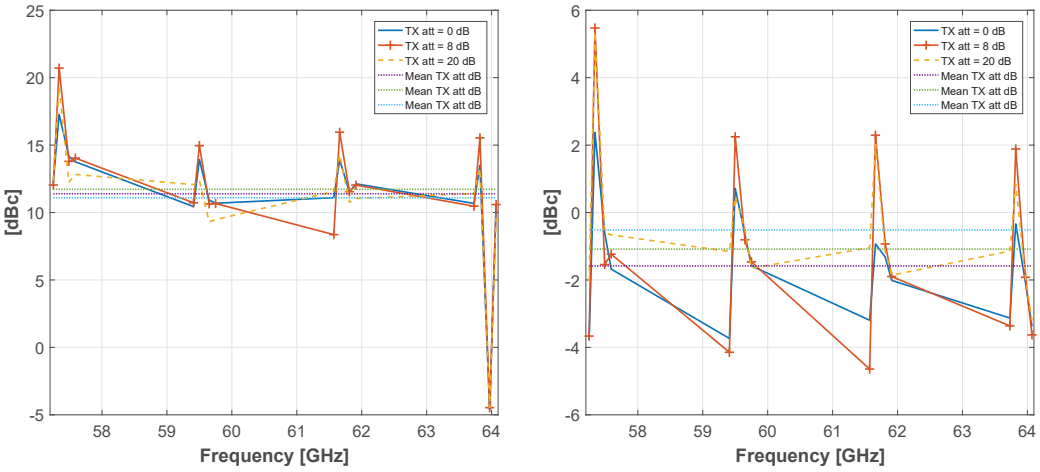

FIGURE 6.8: Both carrier a) and b) side-band suppressions, considering different combinations of f_C and f_{FO} frequency values.

Direct clock leakages

In order to investigate and identify possible hardware imperfections on the receiver side, a spectrum analysis on the received baseband signal is performed when the RX board is either turned OFF or ON. In this way, one can not only verify possible direct leakages from the clock source, but can also evaluate possible synthesiser leakages into both baseband I/Q channels. The considered measurement setup is illustrated in Fig. 6.9.

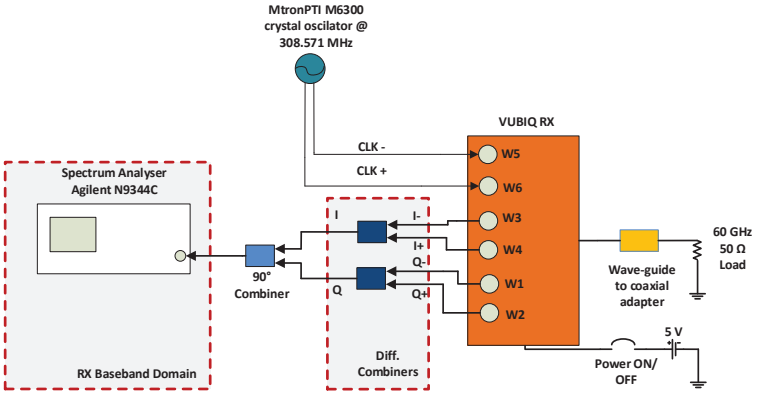

FIGURE 6.9: Block diagram of the clock leakage measurement setup.

From Fig. 6.10, results demonstrate that when RX is powered OFF, signal leakages from the external source clock are present in both I/Q channels, since its fundamental tone at 308.571 MHz and its third harmonic frequency component, at 925.713 MHz,

are approximately -78 dBm and -83 dBm, for I and Q baseband channels, respectively. As such, clock input ports are not isolated from I/Q RX baseband ports, exhibiting an attenuation of 68 dB (for a clock input power level of -10 dBm).

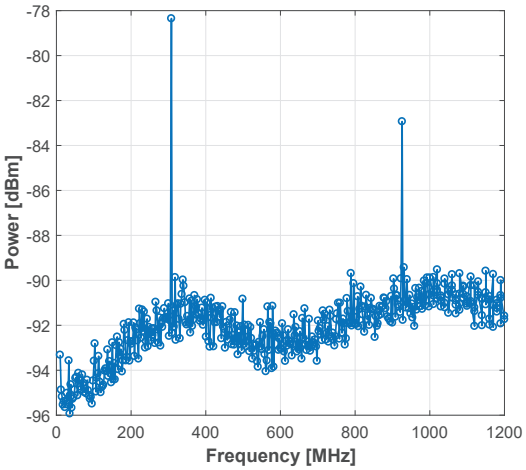

FIGURE 6.10: Direct signals leakage from the external clock reference signal to the baseband I/Q channels.

A similar study is carried out for all f_C values available in the RX input parameters (switching between 15 carriers spaced by 540 MHz), when RX is powered ON. These results are shown in Fig.6.11 for f_C values from 57.24 GHz up to 63.72 GHz. Moreover it is clearly seen that undesirable signal tones are present all over the system bandwidth, meaning that a WB received I/Q signal will be interfered with such leaks, unless f_C is chosen to be 60.48 GHz. At this frequency, the signal is able to lock without generating harmonics. In addition, from these results, it is demonstrated that the received signal noise floor of the RX is around -70 dBm, and -60 dBm, respectively for an IF digital attenuation of 0 dB and 16 dB. Therefore, leakages from the previous study (depicted Fig. 6.10) are masked by noise, not affecting the system performance.

Intermodulation distortion products

The IMD products from 2nd and 3rd-order are now being evaluated on both received I/Q baseband channels, after demodulation, instead of being measured at 60 GHz. The block diagram of the measurement setup is illustrated in Fig. 6.12. The signal is transmitted through a coaxial cable with enough attenuation to avoid the receiver saturation, and next, it is demodulated by the mmWave integrated RX IC and captured by an Agilent N9344C SA. Based on the receiver clock leakage results, a f_C equal to 60.48 GHz is chosen for this characterisation.

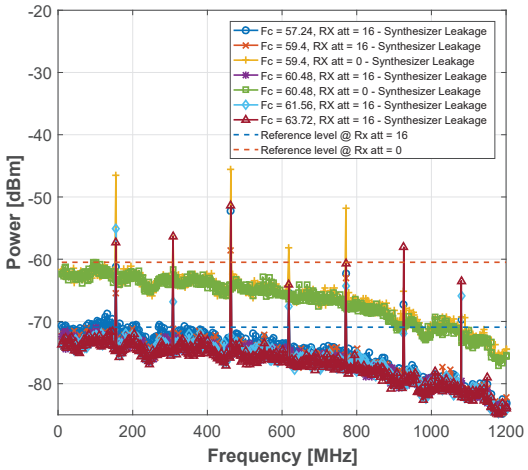

FIGURE 6.11: Overlapped IQ baseband frequency responses for f_C values of 57.24 GHz, 59.4 GHz, 60.48 GHz, and for 63.72 GHz.

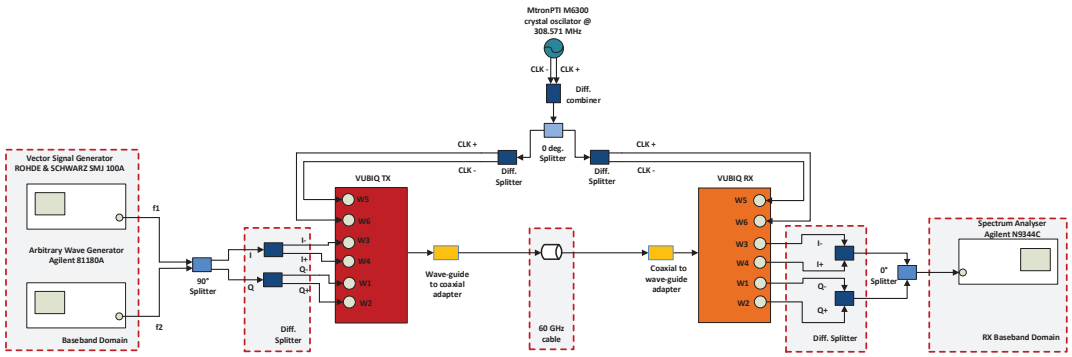

FIGURE 6.12: VUBIQ RX IMD characterisation measurement setup.

The power level assessment for IMD products is performed also for different combination values of TX and RX IF_{Att}. While changing the TX IF_{Att} from 0, 8, 12 and 20 dB, the RX IF_{Att} values are fixed, and vice-versa. Results for the former configurations are summarised in Table 6.10, and in Table 6.11, respectively. It is verified that in order to mitigate non-linearity effects from amplification stages, TX and RX IF attenuations must be set to 20 and 12 dB, respectively, for a power difference of 35 dBc between the fundamental tone and IMD products.

Receiver power sensitivity and gain

To evaluate the receiver gain, it is necessary to assess the received power at the input port of the RX 60 GHz wave-guide. Therefore, taking into account the transmitted output power and the measurement setup illustrated in Fig. 6.12, the estimated received power level at the RX wave-guide can be calculated by:

$$P_r = P_t - L_{cable} - 2 \times L_{connector}, \tag{6.5}$$

TABLE 6.10
SUMMARY OF 2ND AND 3RD-ORDER IMD PRODUCTS, CONSIDERING $f_C = 60.48$ GHz, $RX\ IF_{ATT} = 20$ dB, AND TX IF_{ATT} SET FROM 0 dB UP TO 20 dB.

IMD product	**Relative Power [dBc](*)**			
	Att.$_{TX}$=0†	**Att.$_{TX}$=8†**	**Att.$_{TX}$=12†**	**Att.$_{TX}$=20†**
f_2-f_1	31.95	29.96	33.36	32.76
$2f_1$-f_2	**22.25**	22.3	**18.11**	**30.66**
f_1	-1.7	0	0	0
f_2	0	-0.4	-3.29	-1.04
$2f_2$-f_1	23.6	**21.5**	18.41	31.16
$2f_1$	40.26	38.2	39.11	‡
f_1+f_2	30.2	31.2	36.61	‡
$2f_2$	43.4	45.5	44.11	‡
$3f_1$	38	32.6	33.11	‡
$2f_1$+f_2	22.5	22.2	23.11	‡
f_1+$2f_2$	24.5	34.1	26.41	‡
$3f_2$	42	38.5	37.31	‡

(*) RX digital attenuation is fixed to 20 dB;
(†) in dB;
(‡) Not sufficient dynamic range available in the SA.

TABLE 6.11
SUMMARY OF 2ND AND 3RD-ORDER IMD PRODUCTS, CONSIDERING $f_C = 60.48$ GHz, $TX\ IF_{ATT} = 20$ dB, AND RX IF_{ATT} SET FROM 0 dB UP TO 20 dB.

IMD product	**Relative Power [dBc](*)**		
	Att.$_{RX}$=0†	**Att.$_{RX}$=8†**	**Att.$_{RX}$=12†**
f_2-f_1	61.6	56.8	53.4
$2f_1$-f_2	**33.3**	**34.6**	**35**
f_1	-1	-0.8	-0.5
f_2	0	0	0
$2f_2$-f_1	36.96	36.45	36.8
$2f_1$	‡	‡	‡
f_1+f_2	‡	‡	‡
$2f_2$	‡	‡	‡
$3f_1$	‡	‡	‡
$2f_1$+f_2	‡	‡	‡
f_1+$2f_2$	‡	‡	‡
$3f_2$	‡	‡	‡

(*) TX digital attenuation is fixed to 20 dB;
(†) in dB;
(‡) Not sufficient dynamic range available in the SA.

where P_r, P_t, L_{cable}, and $L_{connector}$, are the received power, transmitted power, cable, and connector losses, respectively. Hence, the received RF power for different combinations of f_C, and f_{FO} values, is given in Table 6.12.

TABLE 6.12
RECEIVED RF POWER VS TONE AND CARRIER FREQUENCY.

TX GUI config.	**Received Power Tone [dBm]**			
	10 MHz	**100 MHz**	**250 MHz**	**350 MHz**
(57.24, 0)	-73.4	-68.56	-73.04	-73.1
(59.4, 0)	-73.12	-67.55	-72.47	-72.63
(61.56, 0)	-74.96	-71.50	-75.26	-75.32
(63.72, 0)	-79.49	-75.45	-80.34	-79.75
(57.24, 8)	-81.73	-73.61	-82.77	-82.17
(59.4, 8)	-80.39	-74.35	-82.4	-82.4
(61.56, 8)	-84.17	-76.95	-85.14	-84.77
(63.72, 8)	-88.59	-81.71	-90.69	-89.84
(57.24, 20	-99.15	-92.98	-100.73	-100.33
(59.4, 20)	-98.86	-96.43	-101.71	-102.06
(61.56, 20)	-101.04	-97.88	-103.78	-104.17
(63.72, 20)	-105.05	-101.93	-108.19	-107.9

Consequently, considering both received tones power levels at RF and baseband frequencies, it is possible to estimate the RX gain. For example, in Table 6.13, the RX overall gain is 49.2 and 44.2 dB for RX IF_{Att} values of 0 dB and 8 dB, respectively.

TABLE 6.13
VUBIQ RX GAIN, CONSIDERING TX IF_{ATT}=20 DB, AND RX IF_{ATT} SET TO EITHER 0 DB OR 8 DB.

Digital Att. [dB]	**RX Gain [dB]**
0	49.2
8	44.2

6.4.3 Loop-back system characterisation

Overall IF-IF frequency response magnitude

In this section the transmitted to received (IF-IF) magnitude response, of the PEM009 is evaluated. The measurement setup block diagram similar to the one illustrated in Fig.6.12, whereas both input and outputs of the RF front-end are directly connected to the VNA simultaneously. Results of the transceiver Frequency Response (FR) are illustrated in Fig. 6.13, for $f_C = 60.48$ GHz and TX $IF_{Att} = 20$ dB, for RX IF_{Att} values of 0, 8, 12 and 20 dB.

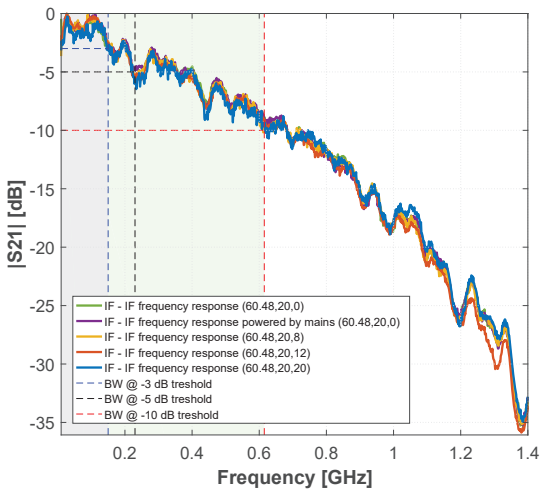

FIGURE 6.13: PEM009 magnitude IF-IF response over its operation frequency range.

From 6.13, it is verified that the PEM009 frequency magnitude response is not flat across its entire "announced" 1.2 GHz bandwidth. Instead, it has actually a shape similar to what is seen in a LPF. According to the results, the effective 3 dB BW of the RF front-end is around 150 MHz (Δf_1). However, even considering a threshold level of 5 dB or 10 dB below, the BW increases to 230 MHz (Δf_2) and 615 MHz (Δf_3), respectively. In this context, due to the robustness of the equaliser DSP block in compensating channel magnitude attenuations up to 20 dB, a 10 dB threshold is considered, which from the point of view of the author, is a reasonable trade-off between magnitude variation response versus B.

IQ and DC offset imbalances assessment

In order to evaluate and characterise IQ imbalances introduced on baseband signals by the RF front-end, the following measurement process was conducted: SDR presented in Section 4.2 was used to generate CW I/Q signals 90° out of phase and connected to the TX board. At the output of RX, both received I/Q signals are connected to the input ports of a 20 GSPS wideband *Keysight Technologies* S-series oscilloscope, and remotely acquired by a host PC to be post-processed. A picture of the measure setup is shown in Fig. 6.14.

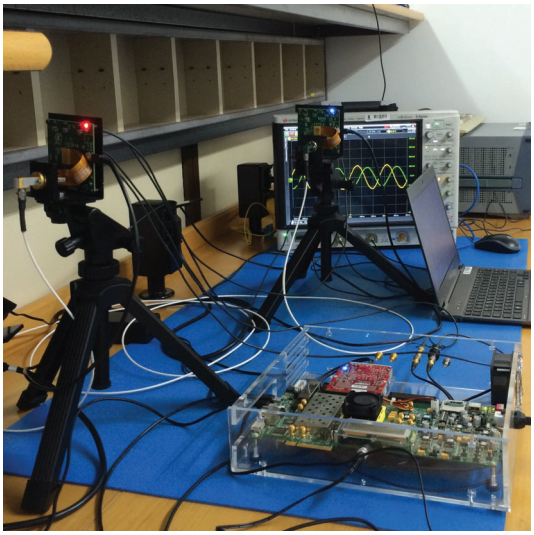

FIGURE 6.14: Photograph of the IQ imbalances bench test measurement setup.

To calculate both phase and gain imbalances present in both I/Q captured signals, some mathematical considerations are needed. Firstly, amplitude imbalance is defined as [193]:

$$\alpha = 10\log_{10}(1 + \frac{a_I - a_Q}{a_I + a_Q})[dB], \tag{6.6}$$

where a_I and a_Q, are the amplitude on I and Q branches, respectively. Secondly, phase imbalance (β) is calculated as:

$$\beta = 90 - \Delta\theta, \tag{6.7}$$

where constant 90 represents the reference phase offset between both sine (I) and cosine (Q) waveforms, and $\Delta\theta$ is phase difference between both received branches, which ideally is 90°.

The DC voltage offset is calculated processing the same data used in the IQ imbalances assessment. The obtained results are summarised in Fig. 6.15, considering f_C equals to 60.48 GHz, and TX/RX $IF_{\text{Att}} = 17.3$ dB.

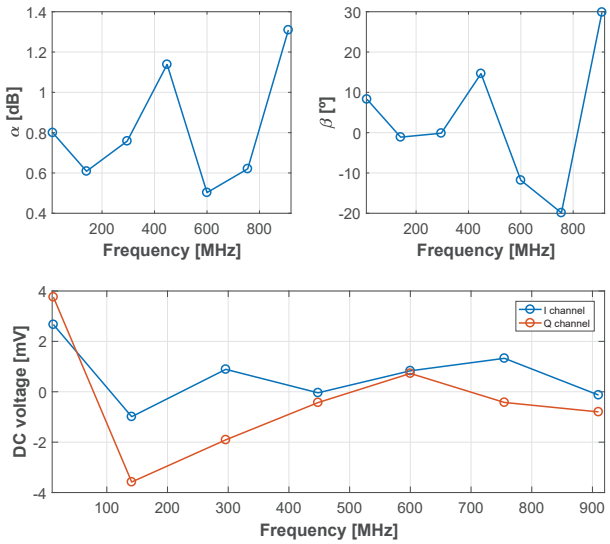

FIGURE 6.15: Results for PEM009 imbalances: a) gain; b) phase and c) DC voltage offset over its frequency range.

Carrier frequency offset and demodulator frequency stability

In previous measurement sections, the same clock reference source was used on both TX and RX devices, to avoid additional distortions effects from CFO. However, in a realistic environment, both TX and RX must be operating with independent clock sources, and thus CFO is always present. In order to assess this phenomena on the PEM009, two clock boards, as the one presented in Fig. 6.3, were used. The measurement setup is very similar to the one illustrated in Fig. 6.12, whereas a single tone (293 MHz) is transmitted instead, and each TX/RX device has their own independent clock source. At the received side, baseband signals are connected to a SA. The demodulated signal spectrum is used to measure both CFO value and the frequency stability of the RX. The measured signal FR is depicted in Fig. 6.16, where a replica of the demodulated signal spaced 2.2 kHz is visible. Unlike the IT RF front-end, significant spectrum difference

is noticed between both clock configurations. Additionally, other frequency spurious are verified in both shared and independent clock configurations. The minimum SFDR values for both clock configurations, are approximately −21, and −24.7 dBc. This might be due to carrier modulation of TX IMD products, which will eventually appear at the RX baseband signal spectrum.

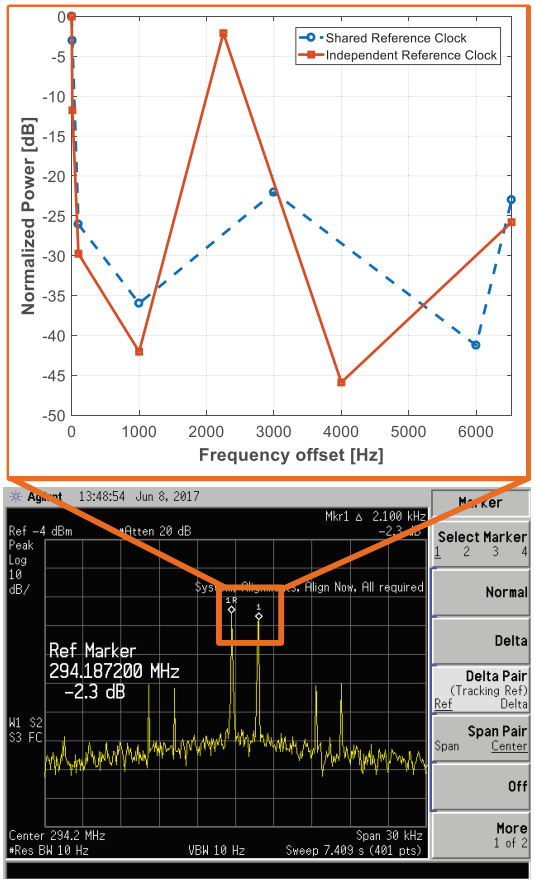

FIGURE 6.16: Results of PEM009 signal frequency stability assessment considering both shared and independent clock configurations.

6.5 Impact of PEM009 non-linearities on OFDM transmission performance

Similarly to what has been presented for the IT RF front-end in Chapter 5, the effect of RF impairments on the quality of OFDM transmission over-the-air using PEM009 system, is evaluated for different SNIR conditions at the receiver. The experimental

setup is shown in Fig. 6.17, where both TX/ RX wave-guide devices are connected to 25 and 0 dBi horn antennas, respectively, and spaced 64.5 cm apart (enough distance to avoid saturation of the RX LNA). In addition, VUBIQ RF IF settings were set to 20 dB in both TX/RX devices, and the centre carrier frequency set to 60.48 GHz, in order to mitigate the presence of non-linearities, as it was verified in the results from the previous section. Again, QoS is assessed through EVM, BER, and digital modulation analysis.

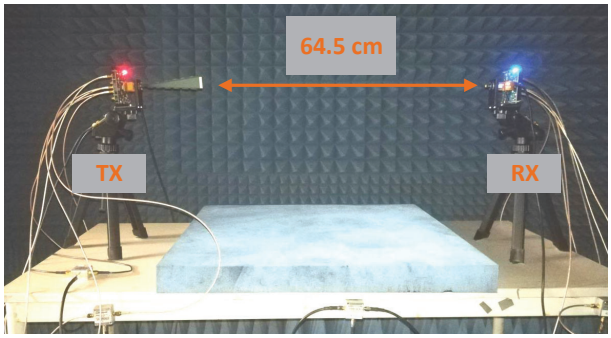

FIGURE 6.17: MmWave link employed for OFDM performance assessment (PEM009 as RF front-end).

Average EVM results under different conditions of SNIR have been summarised in Table 6.14, for IF4 OFDM transmissions. The minimum average EVM value, -14.34 dB, is verified for an input power of -16.72 dBm when both TX/ RX devices are clocked using the same source. Comparing these results with the ones obtained in Section 5.2.1, it is clearly seen that PEM009 induces much more severe RF impairments in the OFDM system than the IT RF front-end. In fact, there is an EVM degradation of 18.65 dB, by just considering the PEM009 system instead. Also, for a subjective quality assessment metric of this EVM value (-14.34 dB), 4- and 16-QAM received constellations, are depicted in both Fig. 6.18a and Fig. 6.18b, respectively. While, for the 4-QAM constellation the scatter points are well separated, in the 16-QAM a relatively high distortion of the received scatter symbols is clearly visible, since they are quite close from each other, therefore indicating that it is very likely to obtain erroneous decoded data.

Additionally, when both TX and RX are either operating independently or using I and Q branches, the performance degradation is very severe. This is, data is not even successfully decoded for 4-QAM ($EVM > -2$ dB). Results for remaining IF values are summarised in Fig. 6.19a. From such results, average EVM is always below the target -10 dB for a 4-QAM BER lower than 10^{-3}, for all IF values. Consequently, average EVM performance degradation results of a mmWave transmission using PEM009, for all

TABLE 6.14
SNIR VS EVM RESULTS USING IF4 OFDM MODULATION FOR BOTH SHARED AND INDEPENDENT CLOCK CONFIGURATIONS, FOR PEM009

Gain Sel.	**Analogue* Att. [dB]**	**TX Input Power [dBm]**	**Analogue RX SNIR [dB]**	$\overline{EVM}^{\dagger}$ [%]	$\overline{EVM}^{\dagger}$ [dB]	$\overline{EVM}^{\ddagger}$ [%]	$\overline{EVM}^{\ddagger}$ [dB]	$\overline{EVM}^{\dagger\dagger}$ [%]	$\overline{EVM}^{\dagger\dagger}$ [dB]
	0	-25.63	26.46	32.06	-9.85	143.44	3.75	72.62	-2.71
0	5	-30.63	20.74	64.87	-3.66	160.64	4.51	-§	-§
	10	-35.63	14.80	134.60	2.61	201.21	6.26	-§	-§
	0	-19.76	25.64	27.30	-11.24	100.84	1.16	78.67	-2.04
1	5	-24.76	28.65	55.98	-4.79	124.23	2.99	-§	-§
	10	-29.76	24.76	78.34	-2.06	163.30	4.75	-§	-§
	0	-17.83	20.30	29.33	-10.63	97.54	0.99	75.49	-2.23
2	5	-22.83	27.43	31.92	-5.89	120.47	2.35	-§	-§
	10	-27.83	26.27	50.74	-5.89	102.47	1.42	-§	-§
	0	-16.21	17.03	22.66	-12.77	63.63	-2.92	72.75	-2.65
3	5	-21.21	22.47	23.54	-12.06	83.65	-0.96	-§	-§
	10	-26.21	30.92	31.26	-9.80	137.71	3.57	-§	-§
	0	-14.83	16.48	24.61	-12.02	100.02	0.71	70.72	-2.88
4	5	-19.83	21.06	25.27	-11.79	87.77	0.12	-§	-§
	10	-24.83	30.06	52.20	-5.11	100.59	0.98	-§	-§
	0	-13.64	16.55	23.88	-12.05	84.95	-0.46	67.86	-3.22
5	5	-18.64	18.42	26.25	-11.79	85.21	-0.05	-§	-§
	10	-23.64	28.20	34.74	-8.70	102.14	1.13	-§	-§
	0	-12.62	17.47	23.13	-12.66	97.24	0.77	72.34	-2.65
6	5	-17.62	18.20	28.99	-10.41	113.84	1.94	-§	-§
	10	-22.62	26.41	33.26	-9.11	106.82	1.38	-§	-§
	0	-11.72	17.07	26.19	-11.61	93.91	0.79	74.73	-2.42
7	5	-16.72	**26.35**	**19.01**	**-14.34**	109.36	1.65	-§	-§
	10	-21.72	23.70	31.69	-9.52	88.48	0.94	-§	-§

(*) Variable attenuator placed between the SDR and transmitter;
(†) Shared clock source configuration;
(‡) Independent clock source configuration;
(††) IQ configuration with shared clock source;
(§) Not considered.

IF values, are shown in Fig. 6.19b. This EVM degradation is the EVM difference when using IF back-to-back and using mmWave PEM009 chip-set. A minimum degradation value of 27.17 dB, 18.17 %, is achieved for $IF = 312.5$ MHz. For this best case scenario, it is possible to estimate the TX input power operating range. According to Fig. 6.20, such range is approximately 10 dB, which means RF front-end system ensures a relatively good performance for TX input power between $[-26.5, -16.5]$ dBm (considering an EVM threshold of -10 dB). It is clearly seen that such system operates also in a lower input dynamic power range, leading to a reduction of approximately 11 dB when compared with the IT RF front-end.

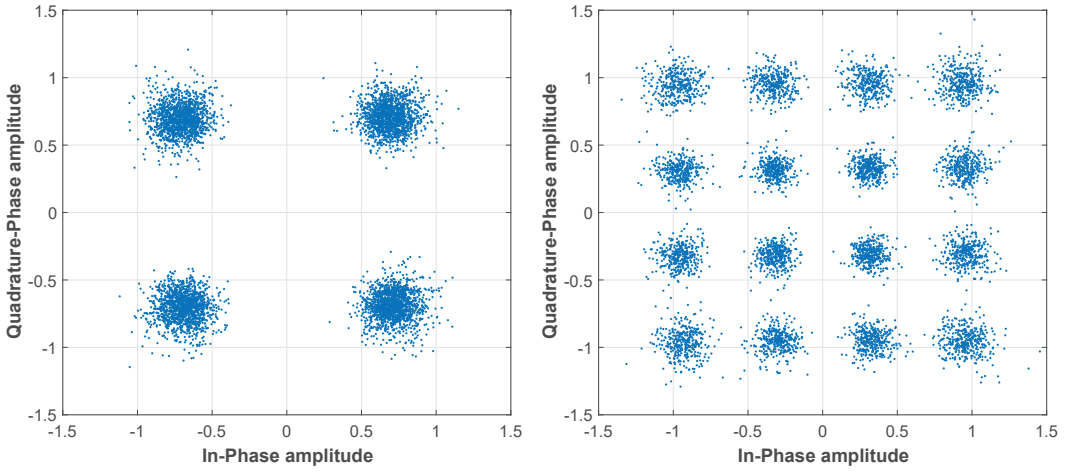

(a) (b)

FIGURE 6.18: Received scatter constellation plots for: a) 4-QAM, and b) 16-QAM, considering an IF4 OFDM power transmission of −16.72 dBm on the PEM009 TX.

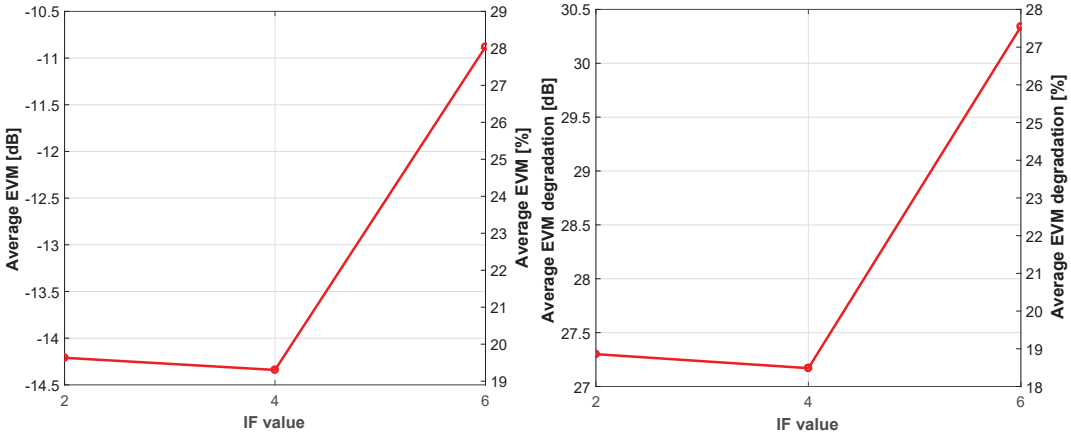

(a) (b)

FIGURE 6.19: Results of EVM: a) performance, and b) degradation, considering PEM009 with absence of CFO.

6.6 mmWave EVM link budget

It is well known that OFDM performance is inherently dependent on the SNR present, which can be easily measured using a spectrum analyser placed at the receiver. To this extent, SNR and EVM metrics can be related by (A.94), as detailed in Section A.4.3. However, that is only verified in the absence of any RF impairments. Therefore, in order to assess the maximum radio link range, for a certain performance threshold, the RX EVM must be accurately estimated. For example, as it is illustrated in Fig. 6.21, PA in-band intermodulation products can significantly reduce this ratio. Hence, such impairment is characterised by the SNIR ratio instead, and is mainly caused by the PA saturation power level, which can be assessed following the proposed method described in

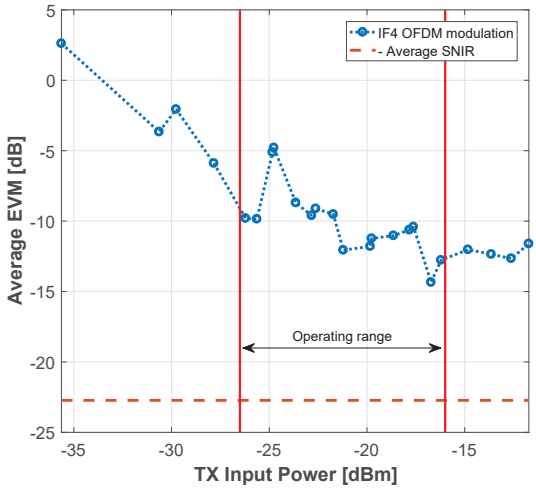

FIGURE 6.20: PEM009 input power versus EVM, for IF4 OFDM with absence of CFO.

section 6.4. On the other hand, PN from local oscillators can also play a very important role on the overall mmWave system performance. Despite the fact that this impairment does not contribute to the SNIR, its impact might result in severe EVM degradation. In order to evaluate this, PN must be accurately measured, modelled and its individual impact on the OFDM system performance assessed through measurement.

6.6.1 LO's PN measure, modelling and performance degradation effect on OFDM systems

In order to assess the individual PN effect on OFDM systems, the measurement setup depicted in Fig. 6.22 must be considered, where the rubidium clock is used as reference signal to both ADC/ DAC sample clock rate. In addition to all DSP algorithms presented in the proposed SDR (see Fig. 4.9b), a phase-noise generator source was included in the receiver OFDM chain. The PN generator was implemented following the algorithm of [194], and based on the 60 GHz measured PN values of Fig. 6.23a, which compiles the PN experimental curves for the IT RF front-end (of Fig. 5.4), PEM009 RF front-end (of Fig. 6.16) and the rubidium clock for reference. The PN values of the rubidium clock were extracted from Table. 5.1. To validate this algorithm, PSD comparison of real-time generated noise samples with the average measured values were performed. As it can be verified from Fig. 6.23b, a good match between both modelled and measured curves is obtained, in particular for both PEM009 and IT RF front-ends.

Measured EVM results versus modelled PN for each source, is presented in Table 6.15. In this table, the performance degradation is characterised in terms of $\triangle EVM$, which is the difference between measured $\overline{EVM}$ in the presence and absence of PN from the mmWave LO. Two additional PN sources are modelled and presented in Fig. 6.23a (curves A and B) to assess different PNs' impact on OFDM's EVM performance. These

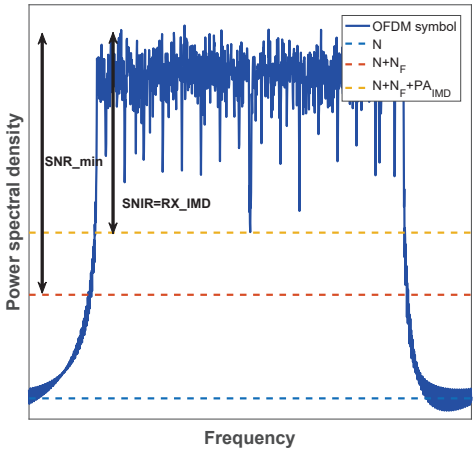

FIGURE 6.21: Illustration of the SNR metric.

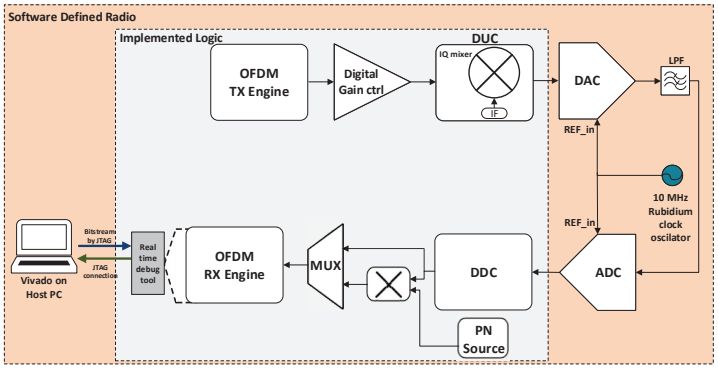

FIGURE 6.22: Block diagram of the PN assessment setup.

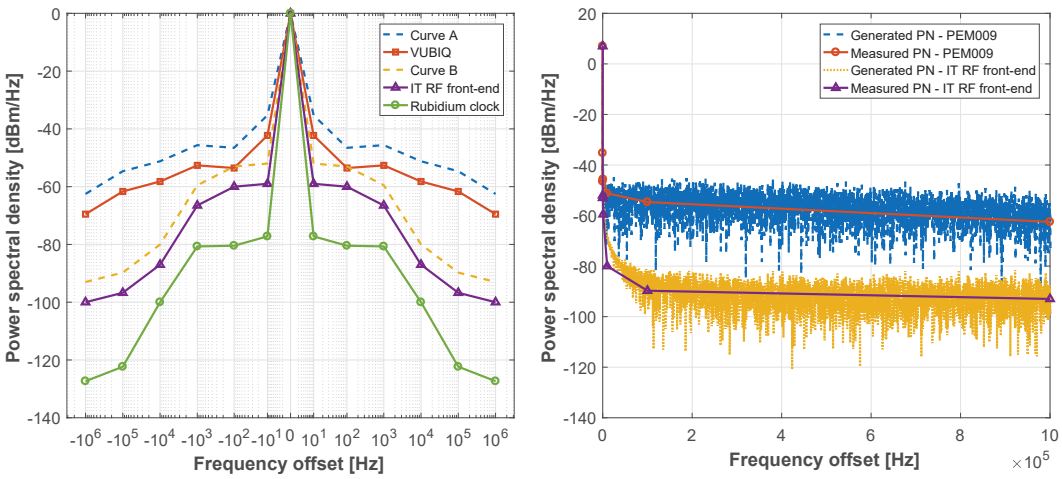

(a) (b)

FIGURE 6.23: PSD comparison of a) measured PN curves from both M6300 and Rubidium oscillators with both 60 GHz RF front-ends, and b) generated PN modelling curves for both IT and VUBIQ PEM009 systems, with their PN measurements curve values.

results show that PN noise has a significant impact on the OFDM EVM performance. That is, when PN model is not implemented, $\overline{SNR} = -\overline{EVM}$ [dB], which is in agreement with (A.94), while $|\overline{EVM}| = \overline{SNR} - 9$ and $|\overline{EVM}| = \overline{SNR} - 23$, when IT and VUBIQ PEM009 RF front-ends are considered, respectively. This is in line with the results from Table 5.3, when $SNIR = 37.81$ dB yielded an average EVM of -32.58 dB, when using IT's RF system. These results also show that OFDM degradation performance is more relevant when considering the VUBIQ PEM009's, which is explained by its higher PN PSD values versus frequency offset, when compared with IT's.

TABLE 6.15
EVM PERFORMANCE DEGRADATION VALUES FOR VUBIQ PEM009 AND IT REFERENCE RF FRONT-END PN CURVES.

PN curve source	$\overline{SNR}$ **[dB]**	$\overline{EVM}$ **[dB]**	$\triangle EVM$ **[dB]**
No PN (baseband only)		-42	N/A
IT RF model		-33	9
Curve B	42	-31.6	10.4
VUBIQ PEM009 model		-19	23
Curve A		-14.4	27.6

6.6.2 Proposed method

As it was verified in the previous subsection, a measured high SNR value does not always translate into good system performance. Therefore, minimum SNR, SNR_{min}, value must be accurately estimated for a certain EVM value, in order to properly manage the TX power. In other words, optimum SNR value must be estimated based on the maximum system's performance in terms of EVM. In this context, the following practical EVM link budget formulation, which takes into account both PA and PN impairments, is proposed.

1. $SNR_{min} = |EVM_{PN}|$, where EVM_{PN} is the average EVM floor value of the system performance under PN conditions;

2. Since 1) is just verified if $RX_{IMD} > |EVM_{PN}|$, where RX_{IMD} is the power difference between the fundamental tone with the IMD product, an additional margin should be considered to mitigate the PA non-linearities. Therefore, $SNR_{min} \geq |EVM_{PN}| + IR_{IMD}$, where IR_{IMD} is the third order IMD power-to-noise ratio.

Moreover, since the EVM versus PN measurement indicated in the previous subsection could be impractical in same RF systems, such can be estimated from the following mathematical equation (6.8), obtained from polynomial curve fitting.

$$\overline{EVM}(PSD_0) = 0.01343.PSD_0^2 + 2.511.PSD_0 + 73.12, \tag{6.8}$$

where PSD_0 is the PSD of PN at 1kHz. This allows the calculation of average EVM for PSD values from -80.7 up to -45.6 dBm/Hz at 1kHz of CFO, and has been extrapolated from Fig.6.24.

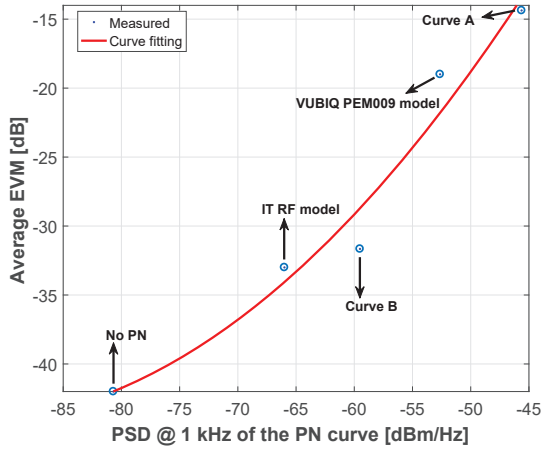

FIGURE 6.24: $\overline{EVM}$ with PN PSD @ 1 kHz ($\overline{SNR} = 42$ dB).

Moreover, the maximum separation between end points (d_{max}) of a system in presence of the joint effect of both PA and PN impairments, considering the estimated SNR_{min}, can be expressed using (3.17), following the conversion from SNR to E_b/N_o outlined in Section A.4.3.

6.7 Interim conclusions

In this chapter, a study on the impact of RF impairments in a complete multi-Gigabit/s radio in-the-loop OFDM mmWave communication system, implemented according to the LTE advanced, for high data rate applications, and considering 4-, and 16 QAM, was presented for the PEM009 RF front-end. Additionally, PEM009 system measurements for: PN characteristic curve, TX output power and gain, TX/ RX IMD products, TX RF carrier and side-band leakages, RX clock leakage, RX sensitivity

and gain, IQ imbalances, DC offset, bandwidth and finally CFO, were evaluated. The performance assessment of the OFDM system was conducted through EVM, BER, and spectral efficiency per stream analysis, considering a real-time transmission of pseudo-random bits over LOS radio channels located inside anechoic chamber.

It has been shown through an extensive measurement campaign for the PEM009 RF front-end, that the most significant spurious frequency from TX/ RX IMD products are about 39.35 and 35 dB below the desired tone, respectively. Both minimum carrier suppression, and side-band leakages values are in average 11 dBc, and -1.6 dBc, which means, mutual interference between adjacent TX channels will occur. Moreover, the carrier frequency of 60.48 GHz is the only option which ensures no significant clock leakages from the PLL circuit into both I/Q baseband channels. However, even for this RF carrier, PEM009 IQ imbalances and DC offset impairments are very significant and frequency dependent. Finally, the available PEM009 RF front-end bandwidth considering a -3 dB threshold was found to be approximately 150 MHz. However, typical OFDM systems might handle FR attenuations up to 10 dB and, consequently its bandwidth is increased to 625 MHz.

It has also been concluded that PEM009 fails to provide a reliable TX/ RX independent end-to-end communication, since the CFO replica present in the received baseband channels leads to severe signal interference and therefore data is not successfully demodulated (relatively high EVM). However, it is believed that employing a LVPECL clock waveform type with the same measured PN of the rubidium signal, such issue would be overcome. Therefore, PEM009 in the presented configuration is recommended to be used in a shared clock configuration. Nevertheless, the spectral efficiency of the system is relatively low. For example, even considering its measured B (615 MHz), the data rate would still be limited to 2.5 Gbps, consequently failing to meet the 5G requirements. On the other hand, from the results provided in Chapter 5, IT Front-end has proven to be a more reliable choice, being able to provide a data rate up to 16 Gbps, when employing 256-QAM (considering a 2 GHz channel). In fact, the use of mmWave frequencies to transmit data has been demystified, since the possibility of having a 60 GHz link with the same EVM requirement of Wi-Fi at 2.4 GHz was demonstrated.

Furthermore, it has been demonstrated that IQ imbalances induce the largest performance degradation in the OFDM waveform, when using the PEM009 RF front-end. In fact, this is in line with the performed RF measurements, where it has been shown that such impairment is not only significant (max 1.4 dB, and 30° of both amplitude and phase distortion), it also frequency dependent over the RF front-end bandwidth. With the consideration of low-IF OFDM transmissions, the uncoded OFDM performance in terms of average EVM has been decreased from -2 dB to -14 dB, with BER below 10^{-3}. In addition, in absence of this impairment, the phase-noise effect turns out to be main limiting factor. In other words, it is dictating the overall system

EVM floor value. This has also been validated by the implementation of a PN model in the receiver chain of the OFDM FPGA design, that modulated PN characteristic curve values for both PEM009 and the IT RF front-end at 60 GHz. For example, in the PEM009 system, despite the presence of a SNR of 42 dB at RX, the minimum average EVM value is only -19 dB, yielding to an EVM degradation of 23 dB. This is the main reason why IT RF front-end outperforms the PEM009 performance (only 9 dB of EVM degradation due to PN), and thus enables modulation orders up to 256-QAM.

Results presented in this work also demonstrate that RF impairments from analogue up-conversion/ down-conversion stages are the most restrictive factor in mmWave transmissions, limiting both data rate and spectral efficiency. Therefore, currently COTS CMOS-based RF front-end technology is not yet ready to tackle 5G communication requirements, and must evolve. While non-linearites from PA and PN can be compensated by backing off the PA input power, and choosing a very stable LO, IQ imbalances should be completely mitigated by performing the IQ mixing process in the digital domain. Finally, this work might be an important guide to establish mmWave real-time OFDM links meeting 5G requirements. In this context, a practical link budget formulation for accurate EVM estimation based on the presented mmWave RF measurements, is proposed.

The work performed in this chapter was successfully disseminated in one international journal publication, and in one webinar:

J. R. Gomes, L. Sismeiro, C. Ribeiro, T. Fernandes, M. Sanchez, Akram Hammoudeh, R. F. S. Caldeirinha„ **"Will COTS RF front-ends really cope with 5G requirements at mmWave?"**, *IEEE Access*, vol. 6, no. -, pp. 38745 - 38769, July 2018. doi: 10.1109/ACCESS.2018.2851781. **Impact Factor = 3.557, Q1;**

W. IEEE ComSoc Webinar: **"Meeting the Challenges of RF with mmWave for 5G", delivered by Prof. Rafael Caldeirinha** – *IEEE ComSoc* – 30 Oct. 2018.

This page is intentionally left blank.

CHAPTER 7

A mmWave use case: augmented versus virtual reality

This chapter presents a very high throughput wireless data transmission solution for AR Head Mounted Devices (HMDs) in the 60 GHz band. Its feasibility is assessed in an OFDM down-link communication towards five UE devices, placed at different locations inside an indoor classroom environment scenario. Key performance indicators as EVM, SNR, and path loss are considered for QoS assessment. Experimental results demonstrate the reliability of the proposed mmWave system, where a data rate of 312.5 Mbps is achieved over distances of 1, 2.4 and 4.1 m, regardless of the UE position.

7.1 Augmented and virtual reality: a state-of-the-art

In the last decades, computer technology has demonstrated that is a necessary resource in teaching and a learning improvement tool for students [195]. Recently, VR and AR technologies with HMD are intended to play an even more important role in the reduction of the student's average learning curve. The study reported in [196], shows that students interacting with virtual objects, have exhibited more improvements in learning, when compared to those who use of desktop computers. Also, in [197], an AR approach for teaching magnetic fields using virtual environments helped students to observe and grasp fields generated by multiple magnetic sources and allows it to be manipulated by them, within the system visualization point, i.e. Field-of-View (FoV).

In AR, the user has a live view of virtual elements *augmented* in a real world environment scenario. Therefore, AR concept is a mixed reality spectrum, which can enhance human senses such as, visual, auditory, and haptic, from computer-generated perceptual information. Although being similar technology, VR's occluded displays immerse the user in a new and artificial world, with no iteration between real and virtual worlds. Nevertheless, both AR's transparent OHMD and VR's HMD require similar hardware processing unit specifications. Such devices have to display video content at

relatively high frame rate and pixel resolution, in order to *trick* the user's brain into believing that the virtual objects are real. Additionally, relatively low latency is also required, which prevents simulation sickness [198], and consequently, a very high system throughput and computational capacity are a demand in the communication of AR/ VR devices with the video source.

In Table 7.1, a full overview on the comparison of both main AR/ VR system specifications is presented according to [198, 199]. In summary, it is recommended that both systems should support video resolutions up to 16k, at least 90 frames-per-second (fps), latencies lower than 20 ms between the server (source) and HMD/ OHMD devices. Due to this strict system requirements, their devices are currently divided in two types: wired and wireless [200]. The first enables a more immersive experience to the user than the other (graphical processing is done in a dedicated graphic card outside the display), at the expense of user mobility. In order to overcome this mobility drawback, video transmission must be performed over the air. However, in wireless devices, the graphical computation and video display are carried out within HMD/ OHMD devices, which leads to loss of graphical processing power. This is evident when considering the most relevant AR/ VR devices available on the market as presented in Table 7.2, where wireless HMD/ OHMD typically support lower resolution, frame rate, FoV, and consequently lower data rate, when compared to the wired ones. The main reasons for this, rely on battery life-time and overheating constraints [201], as Graphics Processing Units (GPUs) are high power consuming devices [202]. Nevertheless, even the wired technology struggles to cope with the AR/ VR specifications [203–206]. For example, a system with more than 16 bits per pixel, a frame rate of 120 Hz and supporting 8k display resolution per eye, a HEVC encoder [207], would require a data transmission rate higher than 509.6 Mbps, which is approximately x34 times more than the rate of state-of-the-art VR wired HTC Vive model, see Table 7.2, can deliver [203–206].

Considering the above AR/ VR technology limitations, such systems might only achieve their full potential considering the next wireless communication standard of mobile communications. Merging the fifth wireless communication generation (5G), intended to be released by 2020 [12], with the AR/ VR technologies seems to be the most promising solution to overcame the current handicap on both wired and wireless devices. In fact, the 5G is envisioned to have a peak data rate of 20 Gbps, with a maximum end-to-end latency of 1 ms [198], which easily meets the major specifications established for VR/AR systems. In addition, one of the 5G verticals is education, where it is predicted a mainstream use of AR devices [208]. In order to mitigate the larger mmWave path losses, in comparison with the sub-6 GHz, a massive MIMO beamforming antenna array, as the one reported in [96] should be also considered. This allows the generation of individual beams for each UE, reducing possible signal interferences between adjacent users, and maximising the received power signal at each one UEs. In this context, an

TABLE 7.1
SUMMARY OF THE RECOMMEND VR AND AR SYSTEM SPECIFICATIONS.

Specification	VR	AR
Screen	Occluded	Transparent
Display	HMD	OHMD
Main Application	Entertainment	Industry & Education
Environment	Virtual	Real & Virtual
6DoF‡	✓	✓
Frame Rate	$\geq$ 90 fps	$\geq$ 90 fps
Bit resolution	16	
MTP*	$\leq$ 20 ms	$\leq$ 15 ms
Video resolution	Full HD/4k/ 8k/16k	Full HD/4k/ 8k/16k
Data Rate	200-1000 Mbps	200-1000 Mbps
Latency	$<$ 20 ms (end-to-end)	$<$ 20 ms (end-to-end)
Processing power	6000 GFLOPS	

(‡) 6 Degrees of Freedom: freedom of movement in a three-dimensional space;
(*) Motion-to-Photon: latency between user's motion and the display updates.

extensive study on the feasibility of OFDM modulated data transmission over the air at 60 GHz, in a typical indoor classroom environment, as the one illustrated in Fig. 7.1, is presented in the sections below. In such usage case, the AR server is intended to deliver multi-Gigabit/s of data transmission towards multiple users (students) simultaneously in a LOS scenario.

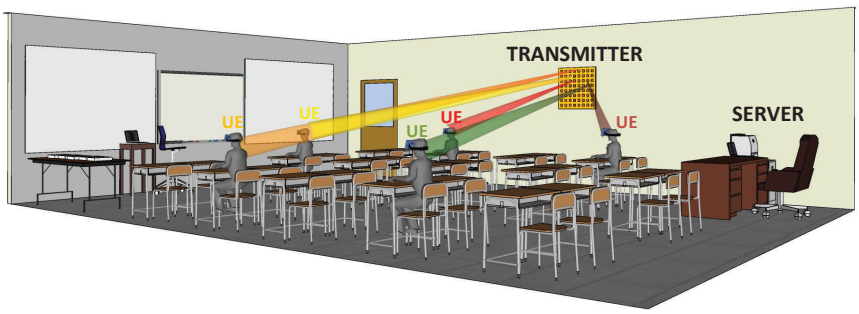

FIGURE 7.1: Proposed use case scenario for AR applications in an indoor classroom environment.

Table 7.2
List of the most relevant AR/ VR devices available on the market [203–206].

Specs	VR		AR	
	Wired	**Wireless**	**Wired**	**Wireless**
Model	HTC Vive	Samsung Gear	Meta 2	Microsoft Hololens
Resolution ($W \times H^{\dagger}$)	1080x1200 (per eye)	Native to phone	1280x1440 (per eye)	1268x720p (per eye)
Frame Rate	90 fps	60 fps	60 fps	60 fps
FoV	110°	101°	90°	33.4°
MTP*	7-15 ms	$\leq$ 10 ms	NA [$]	$\leq$ 2 ms
Estimated Data Rate [Mbps]	14.9	14.2 ‡	14.2	7

([†]) Width (W) and Height (H) of the frame image;
([*]) b_{pp} = 16 & compression = 250:1;
([$]) Not available;
(‡) With Galaxy S8's 1280x1440 (per eye) resolution.

7.2 mmWave radio prototype system

The mmWave radio prototype system considered in this work, is composed by both OFDM SDR , which has a maximum EVM performance of -42 dB, and COTS 60 GHz PEM009 RF front-end, introduced in Sections 4.6 and 6.3, respectively. Both DAC/ ADC converters were configured for a sampling frequency clock of 1250 MHz, with filters at the DAC output in order to eliminate *Nyquist* signal replicas above 625 MHz. Similar to other chapters, QoS assessment results, in terms of EVM, are calculated with the aid of an ILA, which captures samples to be processed in a host PC.

FPGA technology has been chosen over GPU one, since it offers thousands of Giga Multiply-Accumulate operations per Second (GMACS), with the interconnection of multiple dedicated logic resource blocks, at much higher power efficient than the GPUs. This reduces power consumption, thermal and space constraints [202], enabling its hardware integration in smaller housings. Moreover, comparison processing capabilities between both units is reported in [202], and results show that FPGA ensures a power efficiency higher than 70 Giga Floating Point Operations per Second (GFLOPS)/W, against 20 GFLOPS/W achieved for the state-of-art GPU model available on the market. Furthermore, considering that for the deployment of AR, a 6000 GFLOPs is

required [199], the power consumption in both IC platforms would be 85 W, and 300 W, respectively for FPGA and GPU.

7.3 Link budget assessment

The performance of the aforementioned OFDM prototype has been evaluated for link distances of 0.5, 1, 2, and 4m, inside an anechoic chamber, as depicted in Fig. 7.2a. A high-level block diagram of the setup is presented in Fig. 7.2b. As it can be seen from this figure, the DAC output signal is connected to a variable attenuator, in order to allow the variation of its output power level, and consequently the TX signal power level at 60 GHz. Received data is then converted to baseband and captured simultaneously by the ADC and the Agilent N9344C SA, for EVM and SNR metric calculations, respectively.

The link-budget was assessed for all link distances and for an EVM of −15 dB at RX. Therefore, the TX baseband output signal power ($P_{TX_{BB}}$), after the variable attenuator, was calculated for each link distance, following (7.1).

$$\begin{aligned} P_{TX_{BB}} = P_{RX_{BB}} - G_{VubiqTX} - G_{AntTX} + L_{pathloss} \\ -G_{AntRX} - G_{VubiqRX} + IL, \end{aligned} \tag{7.1}$$

where both $G_{\mathrm{VubiqTX}} = 6$ dB, and $G_{\mathrm{VubiqRX}} = 47$ dB are the VUBIQ RF TX/RX gain, respectively, $G_{AntTX} = 25$ dBi, and $G_{AntRX} = 0$ dBi, are the TX/ RX antenna gain, respectively, and $IL = 9$ dB is the implementation loss. The free space losses are represented by $L_{pathloss}$. Baseband RX signal power level is given by $P_{RX_{BB}}\ [dBm] = N\ [dBm] + SNR\ [dB]$, where N is the RX noise power level, and $SNR = -EVM + M_1$, where M_1 is the excess signal power required for the synchronisation algorithm [18]. Finally, when considering $N = -54$ dBm for a signal bandwidth of 156.25 MHz (measured with an SA resolution bandwidth of 10 kHz), and $SNR = 33$ dB, the $P_{TX_{BB}}$ is equal to -28, -22, -16, and -10 dBm, respectively, for link distances of 0.5, 1, 2, and 4 m. Measured EVM versus $P_{TX_{BB}}$ are depicted in Fig. 7.3, where it can be verified that for all link distances the established KPI for the AR mmWave radio prototype is always met.

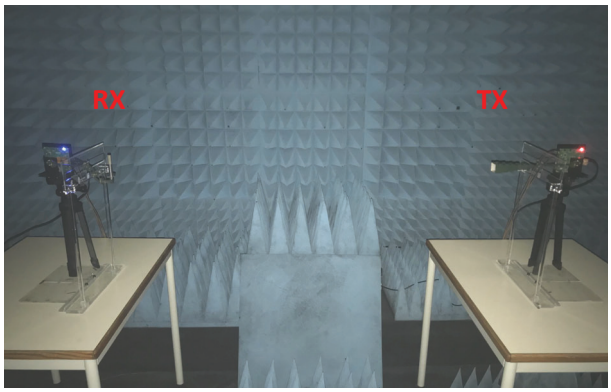

(a)

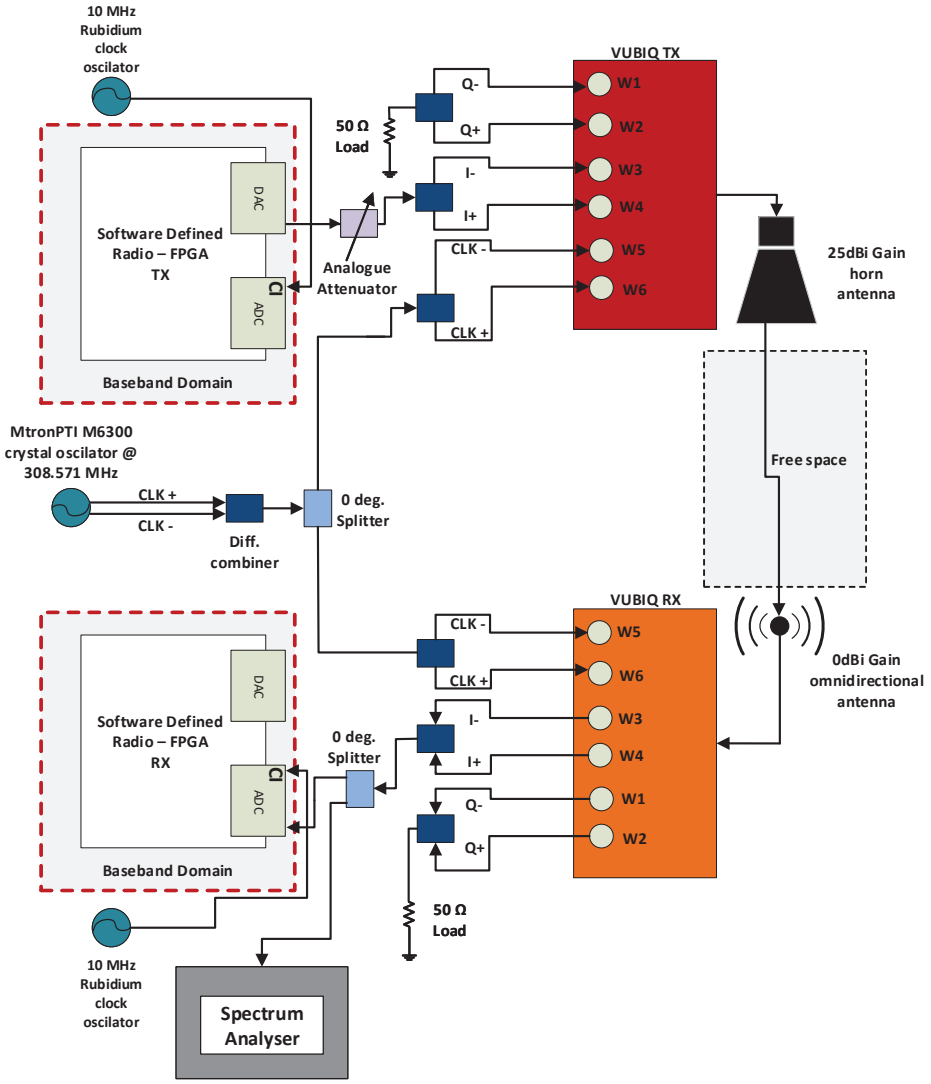

(b)

FIGURE 7.2: AR prototype system dynamic range assessment setup: a) picture, and b) block diagram of the mmWave system.

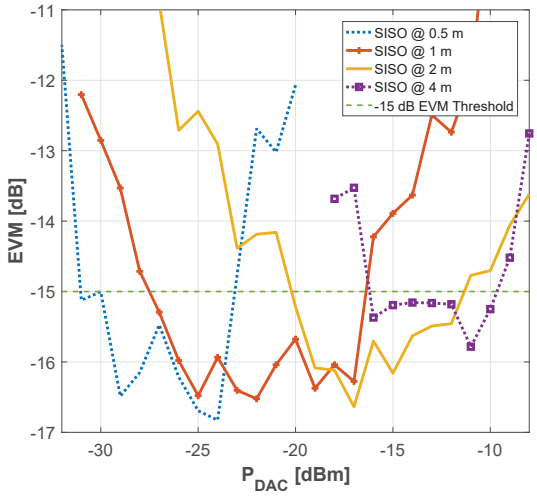

FIGURE 7.3: EVM versus $P_{TX_{BB}}$ for the link range of interest.

7.4 Classroom indoor experiments

7.4.1 Measurement setup

To show the feasibility of using the 60 GHz band for the proposed AR usage case, see Fig. 7.1, indoor RF measurements were conducted in one of the classrooms available at Instituto de Telecomunicações in Leiria, as shown in Fig. 7.4a. In such environment, a 312.5 Mbps downlink (QPSK) OFDM transmission was assessed for five individual users (A-E) placed in different desks, as illustrated in 7.4b. The source antenna and UE antennae heights are set to 1.1 m from the floor, respectively, where the UE antenna is placed 40 cm high from each desk, which mimics the Optical Head Mounted Displays (OHMD) device. Moreover, according to the results from Subsection 7.3, the EIRP of the mmWave transmitter was set to 9, 15, 21 dBm, enabling distances between the source and the receiver device of 1, 2.4, and 4.1 m, respectively.

Furthermore, since the development of an multi-beam antenna structure is out-of-scope of this work, the TX antenna beam can be manually rotated from -90 to 90 degree of azimuth for each individual user, as it is depicted in Fig.7.5.

7.4.2 Downlink OFDM performance

Fixed LOS point measurements were done at each UE position, following the location matrix, as shown in Fig. 7.6 for the user A. This mimics the user head movement and enables the evaluation of the prototype system under different multipath fading conditions. Results for the downlink performance are shown in Fig. 7.7, for the UE A, as average EVM (out from 500 OFDM frames), SNR and RX baseband power level, considering all the location points. In addition to this, Table 7.3 summarises the results

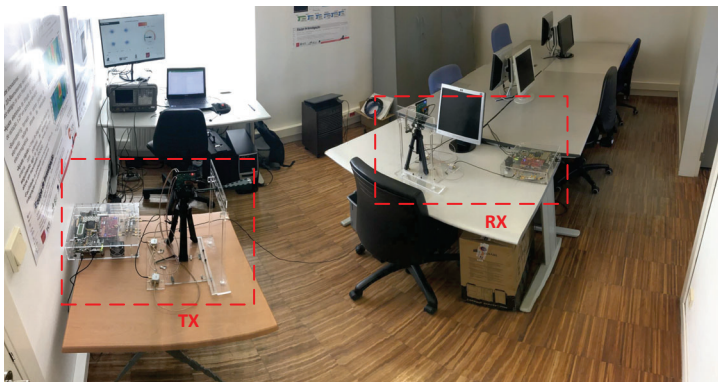

(a)

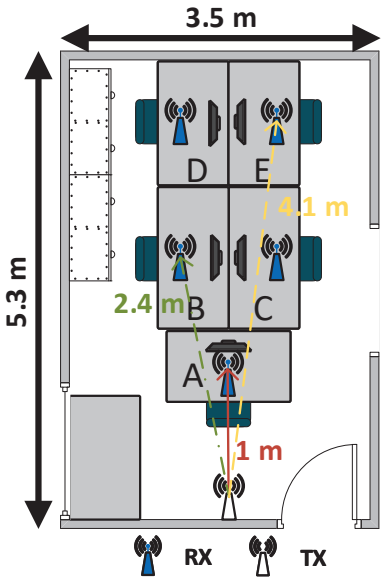

(b)

FIGURE 7.4: Classroom measurement setup: a) picture, and b) room floor-plan.

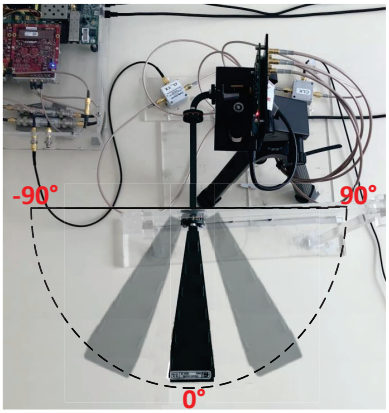

FIGURE 7.5: TX angular beam antenna coverage.

for all UEs, considering as well the average path loss and the 50 % values of the EVM CDF. From these results, it is clearly seen that the average EVM is below −10 dB, as well as its CDF values at 50%, regardless of the position of the UE in the room. This metric indicates that it is very unlikely to obtain erroneous QPSK decoded data [18]. In addition, average SNR, at the receiver, is always higher than 28 dB under the same conditions. These KPIs demonstrate that the proposed system is robust enough to enable AR device communication.

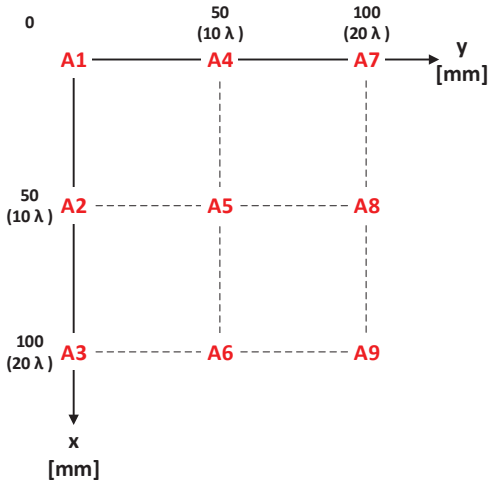

FIGURE 7.6: UE location matrix for diversity measurement.

TABLE 7.3
SUMMARY OF THE SYSTEM PERFORMANCE INDICATOR RESULTS FOR ALL UES.

UE	$\overline{EVM}$ **[dB]**	$\overline{SNR}$ **[dB]**	$\overline{PathLoss}$ **[dBm]**	**CDF of EVM [dB] at 50%**
A	-16.15	28	81	-14.61
B	-14.08	28	89	-12.09
C	-14.57	30	86	-12.45
D	-13.83	29	87	-12.17
E	-14.76	30	88	-13.36

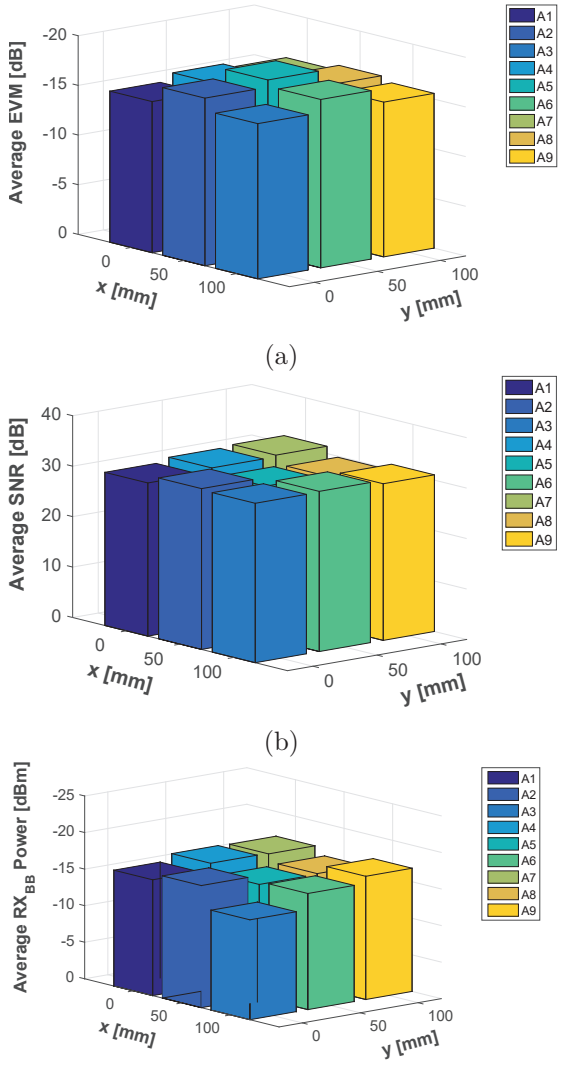

FIGURE 7.7: Summary of the system performance indicator results for the UE A, as: a) average EVM performance, b) SNR, and c) ADC input power.

7.5 Interim conclusions

This chapter details an experimental trial on mmWave OFDM downlink communications over-the-air in a classroom indoor environment. Its scope is to assess if 60 GHz band transmissions is a feasible choice to replace the current wired/wireless AR communication standards, which only support tens of Mbps of data rate. It has been shown through an extensive measurement campaign that the flexibly of a baseband SDR combined with an COTS PEM009 RF front-end, enables an overall system dynamic range of 18 dB, which is enough for a short-range communication link, e.g., 4 m. Additionally, indoor experimental results demonstrate not only the feasibly of the proposed wireless system to provide 312.5 Mbps of data rate, but also the effectiveness of the 60 GHz band. It has been demonstrated that all the user equipments placed in the measurement room plan have a relatively high quality of service. In other words, average EVM and SNR are always below -10 dB and higher than 28 dB, receptively, despite the user location. Finally, this work might be an important guide to establish mmWave real-time OFDM links in indoor environments.

The work performed in this chapter was disseminated in one international conference publication:

C. R. Gomes, L. Sismeiro, C. Ribeiro, M. G. Sanchéz, A. Hammoudeh and R. F. S. Caldeirinha, **"A mmWave solution to provide wireless Augmented Reality in classrooms"**, *2018 15th International Symposium on Wireless Communication Systems (ISWCS), Lisbon, 2018*, vol. -, no. -, pp. 1 - 6, Aug. 2018. doi: 10.1109/ISWCS.2018.8491103.

This page is intentionally left blank.

CHAPTER 8

A novel multi-Gigabit/s MIMO-OFDM architecture for emerging 5G applications

This chapter introduces a highly scalable multi-Gigabit/s real-time wideband MIMO OFDM processing chain for 5G applications. In 5G deployment scenarios, both very high system throughput and spectral efficiency are a demand. Although massive MIMO is seen as the strongest candidate to enable such requirements, it requires an enormous amount of digital processing resources and energy consumption. The proposed pipelined HW architecture fully explores logical resources to boost MIMO OFDM systems HW utilisation. Sharing the OFDM transceiver chain resources among all antenna paths, we demonstrate that the system complexity does not significantly increases with the considered antenna configuration. We present an FPGA implementation where a single OFDM transceiver chain real-time processes a 8×8 MIMO configuration at LTE's highest sampling rate of 30.72 MHz. In applications, where diversity is not a demand, other antenna configurations such as 1×1 (SISO), 2×2, 4×4 can also be provided, enabled at sampling rates of 245.76, 122.88, and 61.44 MHz, respectively. Moreover, exploring the pipelined hardware architecture and the reduced footprint, multiple parallel OFDM transceiver chains might be implemented. For example, in a Xilinx Virtex 7 XC7VX485T, it is demonstrated that a second processing branch might be implemented, leading to a 5 Gbps (using 1024-QAM)) SISO link or a 16×16 MIMO configuration, running a sample rate of at 30.72 MHz.

8.1 Related works: a state-of-the-art

A number of articles addressing data rates of multi-Gigabit/s are already available in the scientific literature. However, none of them are RT based prototypes. For example, in [99], authors achieve 10 Gbps, but the transmitted data is initially stored in a dedicated FPGA memory and played back in loop. At the receiver, samples that are acquired by an

ADC are stored in another memory for subsequent post-processing. Moreover, despite of the existence of a few articles describing architectures, implementations and platforms that offer the possibility to implement and test algorithms for MIMO-OFDM-based systems, to the author's knowledge, none of them present a signal processing efficiency close to the one proposed in this work. For example, in [209], for a 2×2 MIMO antenna configuration, the input data stream is multiplexed in two parallel SISO paths, doubling the system's complexity when compared with SISO. Similarly, in [210–212] the same concept is adopted, where one pair of IFFT/FFT is used for each MIMO transceiver path. In [213, 214], although a 128×8 MIMO antenna configuration is considered, only the receiver detector is implemented in hardware. The real-time SISO LTE platform presented in [215], is limited to 20 MHz of signal Bandwidth, which leads to a very limited potential to process post-4G UWB systems. Finally, in the prototype Massive MIMO testbed reported in [52, 53], HW efficiency seems to be an issue, since each Xilinx Kintex-7 FPGA processes a single antenna path, resulting in a bulky and power consuming system.

Unlike the state of art, this paper proposes a high-performance OFDM TRX engine for the prototyping of advanced 5G communications systems, capable of achieving multi-Gigabit/s RT transmission. Moreover, it also addresses the design of various MIMO configurations exploring the single OFDM processing path. Experimental results show that a single TRX path implemented in a *Xilinx* Virtex 7 FPGA, running at 250 MHz, enables an aggregated bandwidth higher than 246 MHz, achieving data rates over 2 Gbps, with a processing load over twenty GMACS. The structured design approach enables a single TRX OFDM engine to process data for different antenna configurations at the expense of system bandwidth, i.e., it supports a 8×8 MIMO antenna configuration utilising a single pair of IFFT/FFT processing blocks, targeting LTE's maximum sample rate of 30.72 MHz. This feature significantly reduces the hardware footprint needed to implement MIMO systems, by reusing the processing potential of the TRX. This work is a major evolution from [18], where the fully pipelined hardware architecture was used to implement an over-the-air OFDM SISO transceiver, achieving a maximum baseband bandwidth of 61.44 MHz. An FPGA hardware implementation will be used to assess the overall OFDM engine performance over an AWGN channel and under the presence of CFO, considering as metrics EVM, also known as received constellation error, and BER.

8.2 Modular architecture for wireless prototyping: overview

The suitable choice of the implementation architecture and system-level design flow (and associated tools) may dictate the success or failure of the platform. Statistics shows that 60-70% of the entire product cycle for a complex logic system is targeted to verification tasks [216]. System level development flows, like the ones proposed by *Matlab's Simulink* together with *Xilinx's* SysGen can lead to the design of a synchronous multirate system, resorting to clock enabling. This clocking architecture enables a faster development and simpler verification of the system with the provided debugging tools. Design and verification need not to be concerned with pipelining or registering. However, the simpler clocking structure hides longer critical paths that limit the system's maximum clock frequency (therefore leading to sub-optimal performance), and the need to distribute a low-skew clock to the entire design, with significantly more demanding clock driving and associated power consumption. In this context, the Modular Architecture for Wireless Prototyping (MAWP) considered in this work is based on the one proposed in [18], where it has been demonstrated that its utilisation successfully reduces the length of clock paths, leading to increased overall performance/ throughput of the system, by pushing the system's maximum clock rate. The decoupling of the processing in each block, leads to different processing duty-cycles for the different blocks, opening way to the use of energy efficient techniques (like clock gating) to reduce the system's overall power consumption.

The adopted architecture allows the designer to reduce the time to market requirements from the system design to its deployment, due to the ability of the user to validate each processing block individually and independently from the full digital processing chain. Also, the use of interfacing First-In First-Out (FIFO) memories constraints the clock signal path to small synchronous islands, and thus, inter-block strict timing synchronisation requirements are relaxed. The modular architecture of MAWP is the key feature that sets it apart from other hardware architectures. The digital signal processing templates for transmitter and receiver are presented in Fig. 8.1, and as can be seen from the figure, each one has independent processing (*proc.*) and control ($proc.CTL$) elements, resulting in a fully decentralized architecture with parallel processing. The template for both sides is similar. The difference resides in the organization of the individual elements in the blocks, imposed by the presence of analogue-to-digital interfaces.

The DSP algorithm is implemented in the $Proc.$ block. The processing is under the control of a Finite State Machine (FSM) present in the $proc.CTL$ element. A FIFO buffer element, $BufferFIFO$, is the block responsible to interface adjacent processing blocks and provides the fill level indication signal, to the buffer level monitoring element

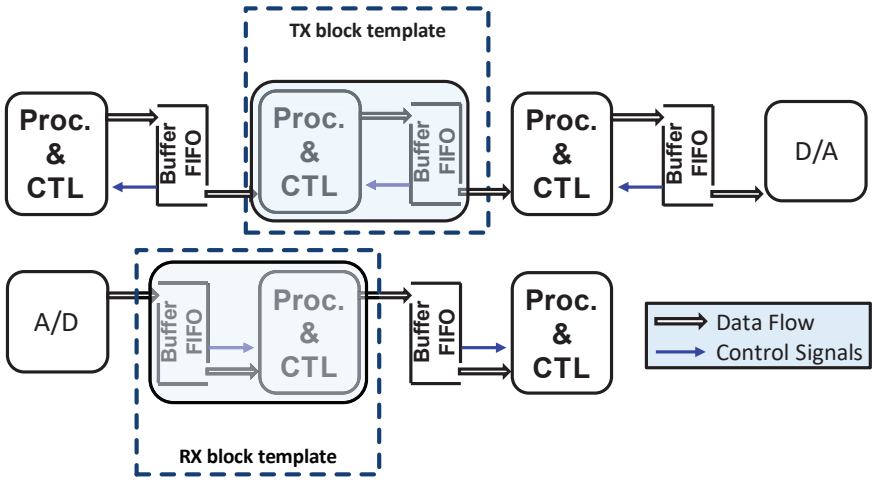

FIGURE 8.1: Conceptual transmitter (top) and receiver (bottom) chains (adapted from [18]).

BufCTL. Each processing block implements a soft handshake with the neighbouring blocks to control the generation/consumption of processed data.

8.3 Hardware design method for MIMO-OFDM systems

MIMO is envisaged to be one of the key technology to be adopted in future 5G wireless communications systems [217]. For example, exploiting the spatial multiplexing of the antennas at both TX/ RX ends, spectral efficiency and data rates are significantly boosted when compared to SISO systems. However, in conventional MIMO implementations, hardware complexity linearly increases with the number of used antennas. This might lead to enormous amounts of digital processing resources and energy consumption, in particular, when the number of antennas in the MIMO configuration tends to hundreds. In order to overcome the hardware constraints associated with MIMO implementations, a novel MIMO-OFDM hardware architecture design is suggested to attain significant HW resource savings. The proposed architecture, depicted in Fig. 8.2, is composed of a single OFDM processing engine present at both TX/ RX which modulate and demodulate data symbols, from l independent antenna streams, respectively. Therefore, an interface block between *MIMO OFDM TX* and *MIMO OFDM RX* engines and multi-processing data sources such as MIMO pre-coding, and MIMO decoder along and/or MIMO post-coding (green blocks in Fig. 8.2), is required. Such would allow, for example, the implementation of analogue-digital (hybrid) beamforming techniques in massive MIMO configurations, in order to mitigate user interference in ultra-dense 5G scenarios [218], while saving significant amount of logical resources.

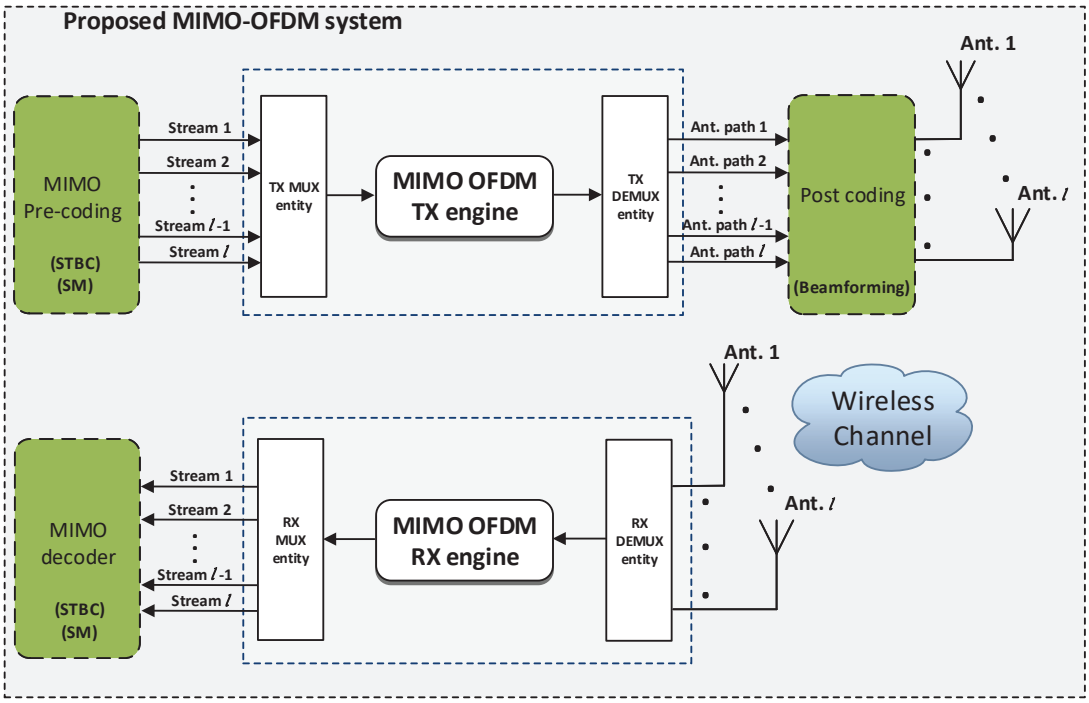

FIGURE 8.2: Block diagram of the proposed architecture in a MIMO-OFDM system.

Since the scope of this work is to enable an hardware efficient OFDM modulation/ demodulation scheme, no additional details are provided regarding MIMO pre-coding/ decoder algorithms. Such is achieved through the use of multiplexing and demultiplexing entities to convert low speed parallel to high speed serial streaming data, which enables data to be processed by a single processing path. In addition, to ensure that the MIMO information is transmitted at the same rate as data is being generated, both *MIMO OFDM TX engine* and *MIMO OFDM RX engine* entities have to operate at a rate greater than l times higher than the rate of both MIMO pre-coding/ decoding blocks, where l is the number of antennas at both ends. With this, multiple antenna configurations are enabled by re-using the main functional DSP blocks from a typical single OFDM TRX chain. This enables higher number of paths to be processed, when compared with conventional MIMO-OFDM FPGA designs [209–212], with a reduced increment of the HW resources and footprint of the target circuit. To demonstrate this, a study on the hardware resource usage, for 2×2, 4×4 and 8×8 MIMO OFDM configurations, employing both conventional and proposed hardware architecture designs, is conducted. Designs are implemented in a *Xilinx* VC707 FPGA development board. The results are presented in the following subsections.

Furthermore, the proposed architecture might be used in the design of massive MIMO-OFDM systems. The consideration of N parallel MIMO OFDM TX/RX engines would enable the necessary processing power for M antenna paths, by considering $N = \lfloor M/l \rfloor$, where each MIMO-OFDM TX/RX engines process l streams.

8.3.1 Detailed description of the MIMO-OFDM architecture

Integration of new transmission schemes, air-interfaces, MIMO coders/ decoders in the proposed MIMO-OFDM architecture is straightforward, as it is illustrated in Fig. 8.2. For example, from this figure, a MIMO coder can be directly connected to our MIMO OFDM TX engine, which processes and modulates the pre-coder output data for each antenna path, and delivers the samples to be transmitted to all antennas simultaneously. However, this work intends to demonstrate that MIMO systems can be deployed using much less hardware resources than the ones found in literature [209–212]. In this context, the complete TRX MIMO-OFDM system of Fig. 8.3 was considered, without using any particular MIMO/beamforming coder/decoder algorithms.

As a reference, a single OFDM TX/ RX chain was implemented. At the transmitter, multiple SISO modulators are implemented to emulate the *MIMO modulator* block. They generate individual antenna streaming data for configurations up to 8 antenna paths. This entity is composed of a bank of parallel random binary generators together with QAM modulators and pilot sub-carrier assignment algorithms. Following this, its output data is connected to the *TX MUX* entity, which performs a Serial-to-Parallel (S/P) path conversion and selects the correct antenna path to be processed by the *MIMO OFDM TX Engine* DSP block (controlled by the antenna selector control signal). This entity, unlike conventional MIMO architectures, is not replicated for each antenna processing path. It performs the OFDM modulation (IFFT transform operation, CP insertion) and the appending of a PHY preamble on the transmitted OFDM frame, for multiple antenna paths. Next, its output data is connected to the *TX DEMUX* block, which performs the opposite operation of the *TX MUX* block. Along with memory banks and processing control FSMs, it converts serial OFDM streaming data into parallel paths, and assigns them to their respective antenna path ensuring the synchronicity of the transmission. Each antenna TX path is directly connected to the corresponding RX antenna path (as depicted in Fig. 8.3), since the MIMO pre-coding and decoding are beyond the scope of this work. At the receiver, the counterpart of this process is implemented. Prior to the *MIMO OFDM RX Engine*, which is responsible to mitigate CFO, to perform FFT, and CP removal, a joint timing synchronisation and CFO estimation is considered, following the algorithm reported in [219]. The blocks implemented in the MIMO-OFDM TX/RX engines perform all the processing required for over the air transmission. Finally, the *MIMO demodulator* entity performs the operations needed to recover the transmitted bits in each SISO path (deframing, channel estimation, equalisation and demapping).

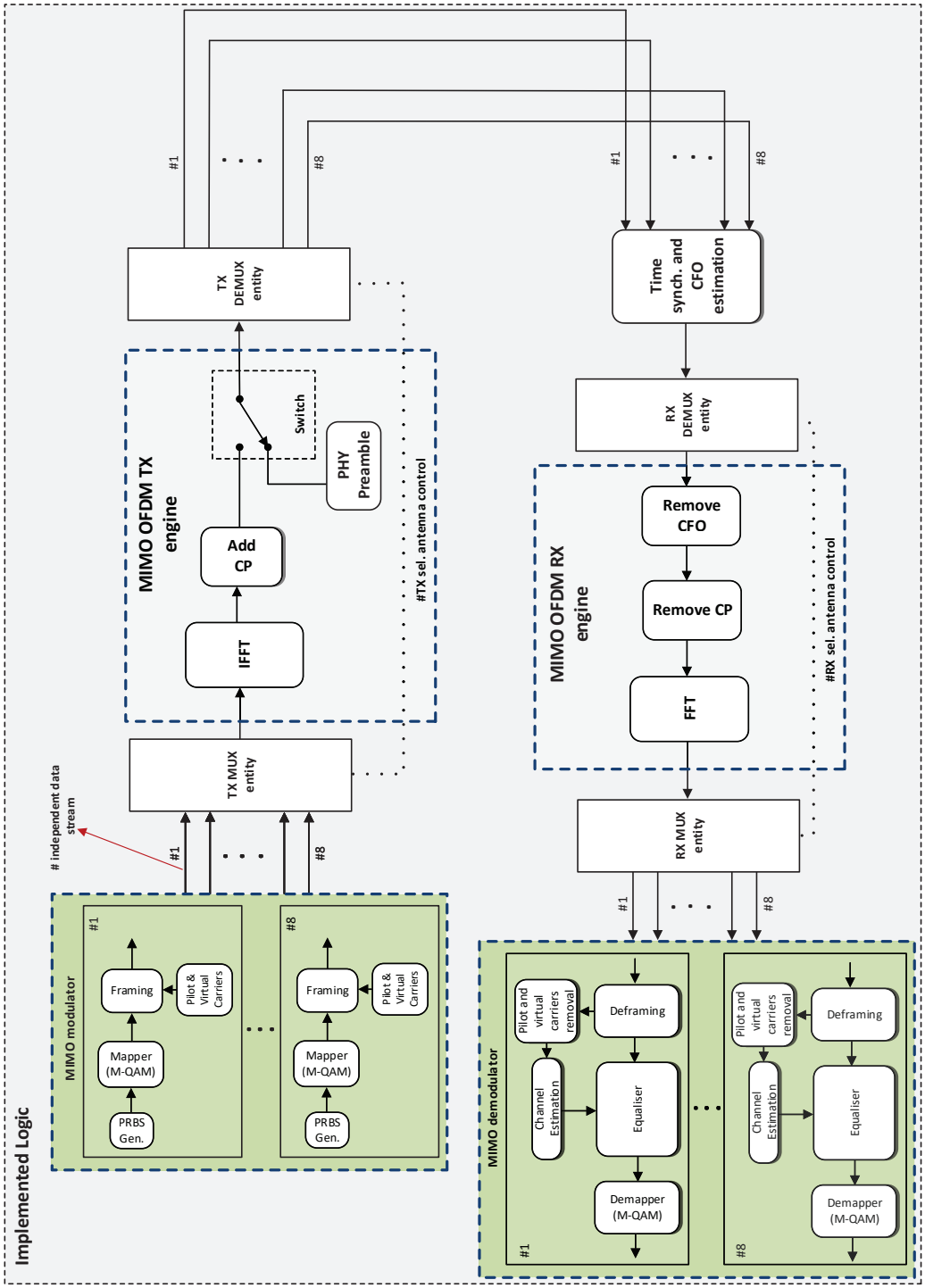

FIGURE 8.3: Block diagram of the implemented MIMO-OFDM based engine for multiple antenna configurations.

The key features of the proposed architecture, and what sets it apart from the conventional method, are the consideration of $MUX/DEMUX$ entities, and the implementation of high performance OFDM TX/RX engines in the MIMO-OFDM design. For example, only one IFFT/FFT pair is enough to process multiple MIMO antenna configurations. For the hardware design of such algorithms, the MAWP concept, presented in Section 8.2, was considered and significantly enhanced to meet the new performance requirements. Detailed hardware design of both $TX\ MUX$ and $TX\ DEMUX$ blocks are illustrated in Figs. 8.4a, and 8.4b, respectively. From the top figure, it can be verified that a P/S path conversion is accomplished by the use of a main FSM unit (*Proc.* element), two primitive multiplexers, one counter and two FIFOs (one for each I/Q source path). The processing control unit operates as follow: depending on the chosen MIMO configuration, it selects sequentially which sources are read from the $MIMO\ modulator$ and how many samples are written to the interface memories. Hence, there is a read enable bit for each individual data source, namely, Re_out_i, where i is the antenna index. In the reading process of the first source path, Re_out_0 is set to '1' and the remaining are set to '0'. After the required number of samples needed for an OFDM frame are reached (set in the counter limit value), Re_out_0 is set to 0 and Re_out_1 is set to '1'. This means that data source from the second antenna path starts to be read, and it stops when a frame is reached. This process is repeated for all paths. After the information from last source path is processed, the first antenna is read once again. This reading loop only stops if either interface FIFOs are either empty or full, which are monitored by the other $TX\ Buffer\ CTRL$ FSM. In this event, both counter and FIFO writing enabling bits (en and We_data), respectively, are set to '0'. Otherwise, these bits are set to '1'.

Similar algorithm implementation was done for the $TX\ DEMUX$ block. A main FSM unit *Path sel.* is also responsible to control and decide when the individual FIFO's write enable bits (we_i) are asserted, while output data, namely $Data\_i\_I\_in$, and $Data\_i\_Q\_in$, are being read simultaneously from all memories and assigned to their respective i TX antenna. The number of FIFOs at the $DEMUX$ entity can be adjusted depending on the considered MIMO configuration. For example, in a 2×2 MIMO system, only 2 FIFOs are used per I/Q paths. In both figures, blue lines indicate the input data buses coming from the adjacent DSP block in the architecture, dark lines represent the internal bus connections in the algorithm and green ones the output data buses. In particularly, $ANT[2:0]$ bus sets the MIMO configuration chosen by the user, i.e., when it has values equal to 0, 2, 4, and 8, SISO, 2×2, 4×4, and 8×8 system arrangements are selected, respectively. Finally, $RX\ MUX$ and $RX\ DEMUX$ were implemented just as the TX ones by adjusting the interface FIFO placement arrangement, following the template presented in Fig. 8.1.

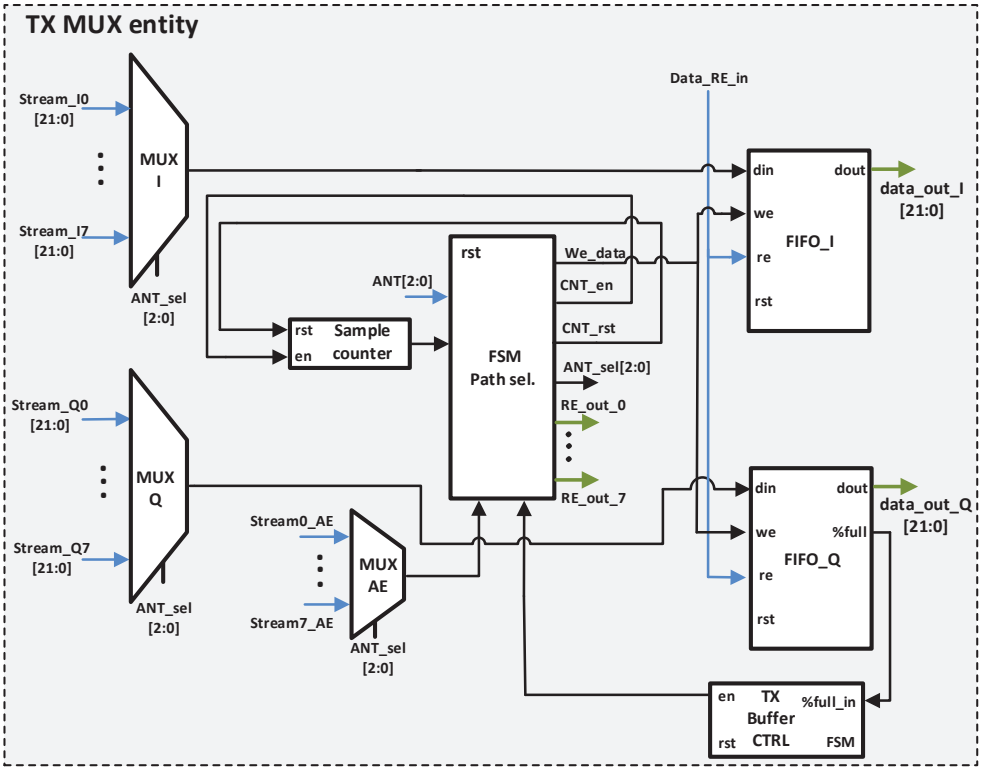

(a)

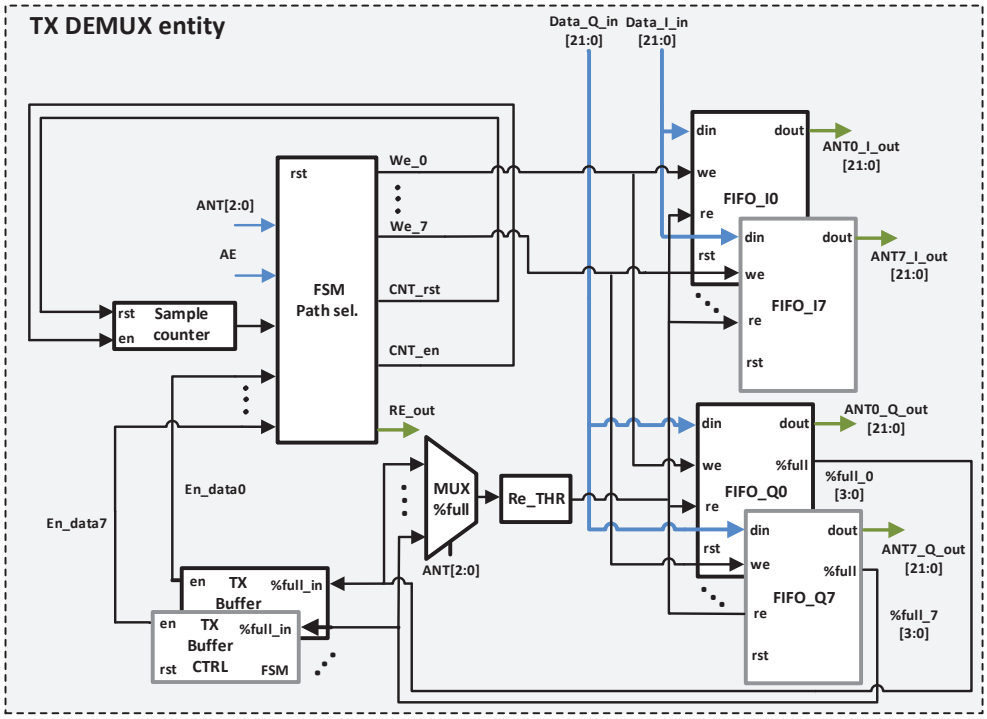

(b)

FIGURE 8.4: Detailed block diagrams of: a) MUX and b) DEMUX DSP block algorithm entities, considered in the proposed MIMO-OFDM method.

The considered OFDM waveform design parameters based on the LTE downlink Physical (PHY) layer [37], with the operating parameters given in Table 8.1, for 4-, 16-, 64-, 256- and 1024-QAM for 1×1 / 2×2 / 4×4 / 8×8 MIMO antenna configurations, which is in line with the 5G NR specifications reported in [79, 220].

TABLE 8.1
MAIN PARAMETERS CONSIDERED IN THE DESIGN OF OFDM WAVEFORM, BASED ON THE LTE STANDARD [37] .

Parameter	Value
FFT size block	1024
Data block size	800
Sub-carrier bandwidth	240/120/60/30 kHz
Modulation	16-/ 64-/ 256-/ 1024-QAM
Guard time interval	256 samples
MIMO config.	SISO / 2×2 / 4×4 / 8×8
Sample rates per path	245.76 / 122.8 / 61.44 / 30.72 MHz
Maximum aggregate data rate	2.46 Gbps
OFDM frame samples	6400

8.4 Hardware implementation efficiency: conventional vs. proposed method

8.4.1 Used logical resources and power consumption

The MIMO-OFDM transceiver illustrated in Fig. 8.3, was implemented in a *Xilinx* Virtex7 XC7VX485T considering both conventional and proposed MIMO-OFDM design methods, for SISO, 2×2, 4×4, and 8×8 antenna configurations. Following this, the amount of used logic resources was analysed in terms of the number of slices, Look-Up Tables (LUTs), Flip-Flops (FFs), DSP48E1 elements, and 36k bits Block RAMs (BRAM36k). A slice in the VC707 corresponds to 4 LUTs, 8 FFs, multiplexers and carry logic. Partially occupied slices are also included in the implementation report. Therefore, slice number is not a very accurate figure of merit for resource utilisation. However, it can be used to evaluated if mapping, routing and timing constraints of the hardware design are easily met. The hardware efficiency inherent from the utilisation of the proposed MIMO system is characterised by the amount of saved DSP48E1 slices,

BRAM36k, LUTs and FFs, when compared against conventional MIMO systems. From Fig. 8.5a, it can be verified that the amount of saved DSP48E1s and FFs resource blocks go up to 81% and 65%, respectively, in a 8×8 configuration. In fact, DSP48E1 slice is the HW primitive which leads to a major contribution to the overall chip dimension. Additionally, when DSP48E1 slices, LUTS, and FFs are converted to logic gates, the total amount of saved gates is 70%, for this MIMO arrangement, as indicated in Fig. 8.5b. It should be mentioned that such results were obtained considering that 1 DSP48E1 slice occupies 456 LUTs and 139 FFs in the VC707, and 1 FF and 1 LUT are equivalent to 7 and 8 logic gates, respectively.

The graphical illustration of the implemented logic area (subjective analysis) in the VC707 using the proposed MIMO method is illustrated in Fig. 8.6 for all MIMO configurations. From this figure, it is clearly seen that the utilised logic region does not linearly increase with the number of antennas considered in the MIMO configuration.

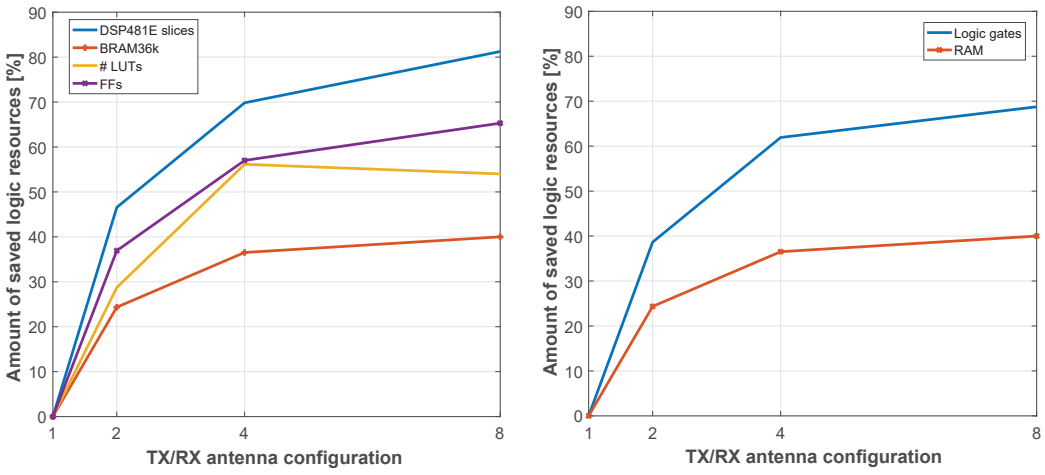

(a) (b)

FIGURE 8.5: Amount of saved logical resources, when using the proposed MIMO design against a conventional one, for 1×1, 2×2, 4×4, and 8×8 antenna configurations, considering: a) resource blocks; and b) logic gates and RAM.

Summary of the logical resource utilisation for both conventional and proposed MIMO-OFDM system's implementations is given in Table 8.2. Results demonstrate that using our MIMO architecture, the number of occupied resources in the FPGA are significantly reduced, when compared with the conventional one. For example, from Table 8.2, in a 8×8 MIMO antenna configuration, only 38.1% of the total VC707 slices capacity is utilised, against 78.5% in a conventional system implementation. Hence, this method not only successfully reduces the hardware complexity, but also enables a

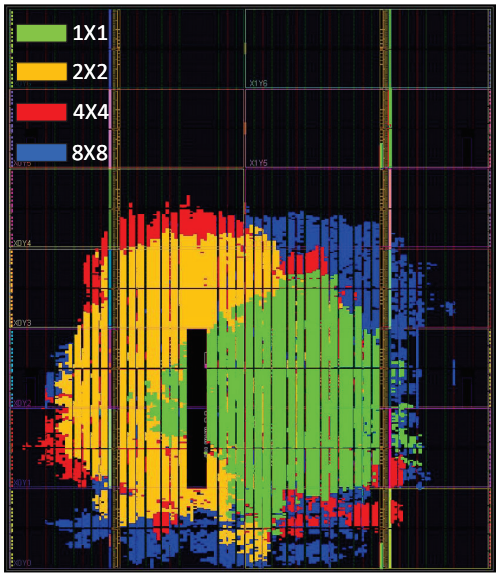

FIGURE 8.6: Occupied hardware footprint for 1×1 (SISO), 2×2, 4×4, and 8×8 antenna configurations, in a *Xilinx* Virtex7 XC7VX485T.

second TRX MIMO-engine branch to be operating in parallel (enabling the system to provide 16×16 antenna configurations), considering that two engines would occupy 76% of the total number of slices in the VC707. And yet, this value is lower than the 78.5% verified in the conventional method. This explains the fact that in Fig. 8.6, the occupied implementation area from the VC707 does not significantly increase with the number of antennas.

TABLE 8.2
TRX FPGA RESOURCES USAGE FOR BOTH CONVENTIONAL AND PROPOSED MIMO-OFDM METHODS IMPLEMENTATION.

config.	**Method**	# of slices	# of LUTs	# of FFs	# of DSP48E1 slices	# of BRAM36ks
1×1	conventional	7443 (9.8%*)	23268 (7.7%)	25947 (4.3%)	58 (2.1%)	57.5 (5.6%)
	proposed	7443 (9.8%*)	23268 (7.7%)	25947 (4.3%)	58 (2.1%)	57.5 (5.6%)
2×2	conventional	14886 (19.6%)	46536 (15.3%)	51894 (8.5%)	116 (4.1%)	115 (11.1%)
	proposed	10883 (14.3%)	33163 (10.9%)	32734 (5.3%)	62 (2.2%)	87 (8.4%)
4×4	conventional	29772 (39.2%)	93072 (30.6%)	103788 (17.1%)	232 (8.3%)	230 (22.3%)
	proposed	13951 (18.4%)	40815 (13.4%)	44618 (7.3%)	70 (2.5%)	146 (14.1%)
8×8	conventional	**59544 (78.5%)**	**186144 (61.3%)**	**207576 (34.2%)**	**464 (16.6%)**	**460 (44.7%)**
	proposed	**28957 (38.1%)**	**85609 (28.2%)**	**72034 (11.8%)**	**87 (3.1%)**	**276 (26.8%)**

(*) Used logic capacity of the VC707, in percentage.

Furthermore, results of logic resource usage for the TRX presented in Table 8.3 can be further detailed into the amount of logic utilised in both TX and RX processing chains, for the MIMO-OFDM system. It is evident that the RX requires much more hardware resources than TX. For example, receiver implementation requires in average more than 75% of slices, LUTs, FFs, DSP48E1 slices in comparison with the TX one. In order to understand this value, Table 8.4 shows the TX/RX engines breakdown in a 1×1 antenna configuration. From this, it can be verified that not only the MIMO-OFDM RX engine requires almost twice the HW of the TX one, but also that algorithms for channel estimation, CFO compensation, and timing synchronisation require a significant amount of logical resources. Moreover, the results presented in Table 8.4 confirm that higher cost units, in terms of logical resources usage, are in both OFDM TX/RX engines, which are precisely the ones that are not replicated in the proposed MIMO-OFDM method.

Table 8.3
Transmitter and receiver FPGA resources usage for the proposed MIMO-OFDM method implementation.

Array size	**TX antenna configuration**				
	1	2	4	8	*average** [%]
# of slices	1650 (22.2%*)	2026 (18.6%)	3159 (22.6%)	5100 (17.6%)	20.25
# of LUTs	4527 (19.5%)	5276 (16%)	7823 (19.2%)	12243 (14.3%)	17.25
# of FFs	6367 (24.5%)	7418 (22.7%)	9618 (21.6%)	13955 (19.4%)	22.05
# of DSP48E1 slices	16 (27.6%)	16 (25.8%)	16 (22.9%)	16 (18.4%)	23.7
# of BRAM36ks	28 (48.7%)	41.5 (47.7%)	68.5 (46.9%)	122.5 (44.4%)	46.9
Array size	**RX antenna configuration**				
	1	2	4	8	*average** [%]
# of slices	5793 (77.8%)	8857 (81.4%)	10792 (77.4%	23857 (82.4%)	79.75
# of LUTs	18741 (80.5%)	27887 (84%	32992 (80.8%	73366 (85.7%)	82.75
# of FFs	19580 (75.5%)	25316 (77.3%	35000 (78.4%)	58079 (80.6%)	77.95
# of DSP48E1 slices	42 (72.4%)	46 (74.2%)	54 (77.1%)	71 (81.6%)	76.325
# of BRAM36ks	29.5 (51.3%)	45.5 (52.3%)	77.5 (53.1%)	153.5 (55.6%)	53.075

(*) Average percentage of required logic resources for the TX and RX, from the overall TRX implementation, for each antenna configuration.

Finally in Table 8.5, the TRX MIMO-OFDM power consumption for each antenna configuration is summarised. In this table, *clk_gen_*0 and *clk_gen_*1 are the two MMCM blocks utilised for the generation of clocks in the design, and *Data source* is composed by the QAM modulator, pilot generation, and frequency framing. Similarly, *Data decoder*, is composed by QAM demodulator, channel estimation, equaliser, pilot

TABLE 8.4
TX/ RX ENGINES RESOURCE USAGE BREAKDOWN ON A *Xilinx* VIRTEX7 XC7VX485T FPGA FOR A SISO ANTENNA CONFIGURATION.

Main Unit	# of slices	# of LUTs	# of FFs	# of DSP48E1 slices	# of BRAM36ks
QAM modulator	227	633	465	0	5
Pilot Gen.	39	92	98	0	1
Framing	68	180	162	0	2.5
TX MUX	47	138	109	0	0
MIMO OFDM TX engine	**1115**	**3312**	**5163**	**16**	**14.5**
TX DEMUX	3	0	4	0	0
Synch algorithm	1923	6714	4984	14	0
RX MUX	3	1	3	0	0
MIMO OFDM RX engine	**2189**	**7249**	**9392**	**24**	**13.5**
RX DEMUX	30	82	90	0	0
Chan. est.	822	2542	2656	4	6.5
QAM demodulator	74	183	177	0	0
Deframing	530	1709	1754	0	0.5

removal, and frequency deframing. Results show that 1.77, 2.16, 2.67 and 4.1 W are required to power up the MIMO system, for 1×1, 2×2, 4×4, and 8×8 antenna configurations. Nevertheless, due to the trade-off between HW savings and power consumption, it has been decided to sacrifice energy savings in benefit of HW efficiency in the proposed architecture. However, the power consumption increment was kept to a minimum. For example, in a 2×2 MIMO "worst case" power consumption comparison to traditional OFDM implementations (where it is considered that power consumption scales linearly with the footprint), the proposed architecture presents a power consumption penalty of 7.1%. The total power value for a traditional 2×2 MIMO-OFDM architecture was calculated as follows. Firstly, power consumption values of each main unit, given in Table 8.4, present in the SISO configuration has been divided by two, except for both *clk_gen_*0, and *clk_gen_*1 units (their power consumption are approximately the same regardless of the MIMO configuration). Secondly, former values were summed together and its resulting value was multiplied by 2 (number of complete OFDM chains presented at both TX/RX ends). It is also noticed, as expected, that power consumption of a certain DSP block is linearly dependent with its clock speed. For example, the synchronisation algorithm requires 0.4 W in a 1×1 configuration (operating at 245.76 MHz), while in a 2×2 configuration clocked at 122.88 MHz, the same block only requires 0.2 W, half the former value.

8.4.2 Processing efficiency

In the above implementation results, the clock speed of both TX/RX OFDM engines was boosted to 250 MHz, targeting the LTE maximum sample rate of 30.72 MHz in a 8×8 configuration. Such requires a processing load of 22 GMAC/s, which results

TABLE 8.5
FPGA IMPLEMENTATION POWER CONSUMPTION FOR THE PROPOSED MIMO-OFDM SYSTEM.

Main unit	**Power consumption [mW]**			
	SISO	2×2	4×4	8×8
clk_gen_0	115	115	115	115
clk_gen_1	118	117	112	122
FIFOs	69	80	112	167
Data source	54	106	216	424
TX MUX	2	3	5	4
MIMO OFDM TX engine	**200**	**276**	**325**	**207**
TX DEMUX	1	1	1	1
Sync. algorithm	400	200	100	50
RX MUX	1	1	2	4
MIMO OFDM RX engine	**549**	**617**	**620**	**565**
RX DEMUX	2	2	2	2
Data decoder	260	640	1060	2420
Total Power	1770	2158	2670	4081

from a clock rate and a total number of used DSPs equal to 250 MHz and 87 (as shown in Table 8.2), respectively. This is quite remarkable, since, for example, in the hardware implementation of the MIMO detector in [221], several critical paths of 10 ns are present, which severely limits the design to go beyond the implemented 90 MHz clock. The processing efficiency achieved in the proposed MIMO-OFDM implementation, is assessed in terms of the ratio between maximum clock rate and sample rate, for a 1×1 antenna configuration. Results are presented in Table 8.6, along with a review of the literature on hardware implementation efficiency. From this table, it can be verified that the processing efficiency has been significantly improved, when compared to the work reported in [18], which was the previous state of art. It is a two fold enhancement, where both system clock and bandwidth have been increased from 150 to 250 MHz and from 61.44 to 245.46 MHz, respectively.

Moreover, both maximum clock speed and signal bandwidth results depicted in Table 8.6, for the proposed MIMO-OFDM implementation, can be further increased by replacing the current target hardware (FPGA) by an ASIC. In fact, FPGA hardware implementations can be relatively easily re-mapped in ASIC, and according to [142], by doing so, clock speeds can be significantly increased by a multiplier factor of 3.4. Therefore, the hardware implementation of the considered TRX MIMO architecture in an ASIC would result in data rate of 8.4 Gbps (836 MHz of aggregated signal bandwidth), considering a 1×1 antenna configuration, and employing 1024-QAM, as it is depicted

TABLE 8.6
TRX PROCESSING EFFICIENCY.

Implementation Technique	**B [MHz]**	**Max. CLK [MHz]**	**Proc. Eff [%]**
Proposed	245.76	250	98.3
Ribeiro [18]	61.44	150	41
Park [222]	40	100	40
Wang [212]	20	220	9
Wu(*) [213]	20	317	6.3

(*) Relation B/clk imposed by the number of IFFT clock cycles required to process data.

in Fig. 8.7. Targeting the LTE's maximum sample rate, a 27×27 MIMO configuration would also be enabled by each processing path.

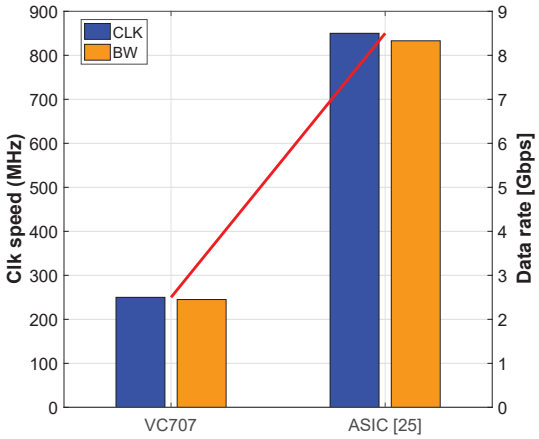

FIGURE 8.7: Comparison of the TRX SISO OFDM performance in terms of clock speed and signal bandwidth by considering both VC707 and ASIC as target hardware platforms.

8.5 Real-time performance assessment of the MIMO-OFDM hardware design

In this subsection, performance of the proposed multi-Gigabit/s MIMO OFDM TRX architecture, in a real-time environment, using BER, and EVM analysis, as performance metrics, for 4-, 16-, 64-, 256-, and 1024-QAM, under the presence of a noisy channel, is evaluated. Additionally, the robustness of the system against CFO is also assessed. Therefore, in addition to those DSP blocks implemented for usage logic resources and FPGA footprint assessment, as illustrated in Fig. 8.3, a wireless channel and CFO generator blocks were also included in the implemented design. The former was modelled as an AWGN channel, allowing real-time measurements of the BER for different Signal-to-Noise Ratio (SNR) values, while the latter was modeled as an digital IQ mixer (frequency shifter), as depicted in Fig. 8.8. Mismatch of carrier frequency values are therefore induced by a digital oscillator connected to an IQ mixer, at the receiver. In particular for system performance evaluation, since signals received at all RX antennas are affected by similar delays and CFO values, the joint synch and CFO estimation algorithm only uses the samples from the first antenna, to reduce the HW footprint. Moreover, both decoded bitstream data or equalised QAM constellation symbols are acquired with the aid of a real-time debugging tool.

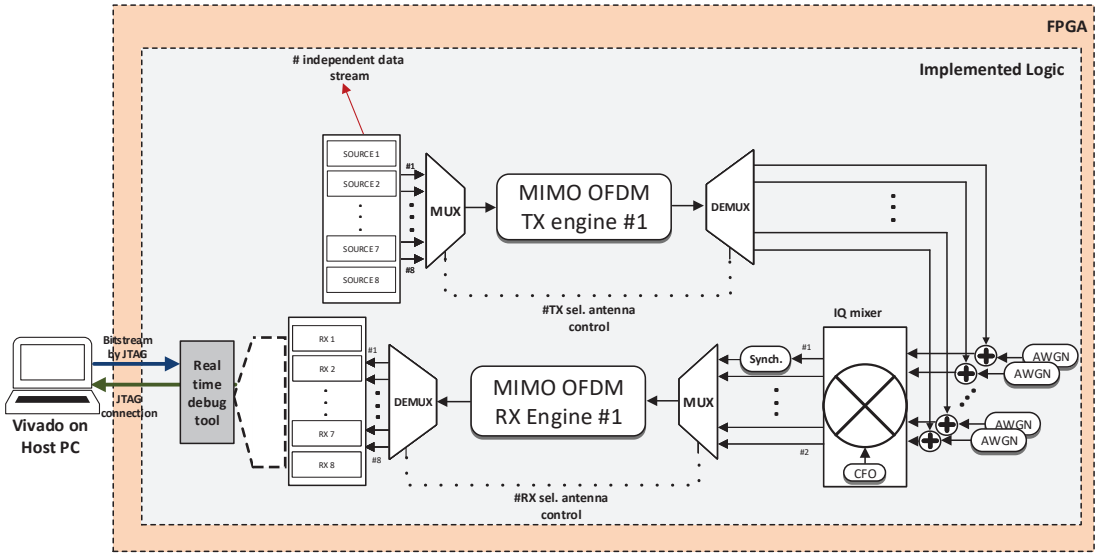

FIGURE 8.8: Block diagram of real-time measurement setup utilised in the system performance assessment.

In an OFDM system, the orthogonality between sub-carriers is only maintained if both the independent LO at the receiver is in synchronism with the one used at the transmitter, and if *Doppler* effect is negligible. Otherwise, carrier frequency mismatch will occur at RX, which might result in ICI and high BER values. To overcome this, such CFO must be estimated and compensated by the receiver. In this work, in order to mitigate this impairment, its value is estimated using the *Beek* algorithm, presented in [18], and it is compensated through the implementation of a CORDIC DSP block, with angular frequency inversely proportional to the estimated CFO value. The mathematical expression of such operation is given as follows:

$$\begin{aligned} z(n) = y(n).\exp(-j\omega) &= \Big[y_R(n) + jy_I(n)\Big].\exp(-j\omega) \\ &= \underbrace{y_R(n).\cos(j\omega) + y_I(n).\sin(j\omega)}_{\text{In-Phase}} + \\ &\qquad \underbrace{-y_R(n).j\sin(j\omega) + y_I(n).j\cos(j\omega)}_{\text{Quadrature-Phase}}, \end{aligned} \quad (8.1)$$

where n is the sample index of each frame, $z(n)$, is the CFO compensated signal, and y_R, y_I are the OFDM received real and imaginary signal parts, respectively. The estimated angular frequency (ω) is given by $2.\pi\epsilon.n$, where ϵ, is the rotation angle obtained by the *Beek* algorithm, which is then accumulated along each received OFDM symbol.

Figure 8.9 shows the measured average EVM values for each MIMO-OFDM configuration under the presence of CFO. From these results, it is clearly demonstrated that the considered MIMO TRX system can deal with relatively high range of carrier frequency offsets. However, such robustness depends on the sub-carrier spacing in the OFDM system design, i.e., the *Beek* algorithm is only able to estimate CFO values up to half the sub-carrier bandwidth value. In this context, the higher the number of antennas in the MIMO configuration, the lower is the maximum CFO value the system can deal with. On one hand, a SISO configuration, where sub-carrier spacing is 240 kHz, can deal with CFO values up to 120 kHz with no performance degradation (EVM values are always around -60 dB (0.1%). On the other hand, a 8×8 MIMO configuration can only compensate CFO values up to 15 kHz. Nevertheless, this value does not represent a significant design limitation in transmissions over the air. For example, in order to have a CFO value higher than this from *Doppler* effect, a mobile equipment would have to be travelling at a speed higher than 6750 km/h, in a LTE environment, which is very unlikely to occur. Furthermore, as it can be seen in Fig. 8.10, when carrier offset mismatch is compensated, 16-, 64-, 256- and 1024 QAM constellations do not present significant scattering distortion on the received symbols. This subjective quality evaluation indicates that the proposed MIMO architecture is very accurate, remarkably

showing potential for 4096-QAM implementations, since the scatter points are visible well separated the 1024-QAM constellation.

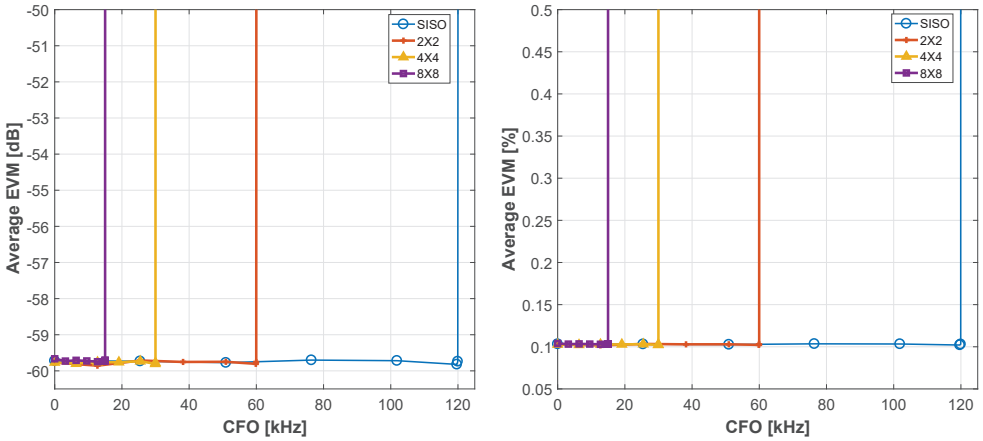

(a) (b)

FIGURE 8.9: EVM performance of the MIMO-OFDM engine for all antenna configurations, under presence of CFO.

Measured BER results have been computed for 1×1, 2×2, 4×4 and 8×8 OFDM MIMO configurations, for 4-, 64-, and 1024-QAM orders. A comparison between these values and those obtained from the theoretical expression, given in (A.91), for OFDM transmissions over AWGN channels, has also been considered. From Fig. 8.11, results exhibit a good match with the theoretical ones (dash lines), in which the small gap between both lines can be attributed to the limited fixed-point bus format resolution adopted in the hardware design.

8.6 Interim conclusions

In this chapter, a novel method for hardware efficient MIMO-OFDM designs is presented for 1×1, 2×2, 4×4, and 8×8 antenna configurations, and implemented in a VC707 *Xilinx* FPGA. In particular, the 8×8 MIMO arrangement targets a sampling rate of 30.72 MHz, and thus, it might be used in LTE advanced deployment scenarios. Therefore, OFDM waveform design is based on the LTE standard, but considering higher QAM modulation orders, such as 64-, 256, 1024-QAM. Moreover, flexibility on changing the MIMO antenna arrangement through a control signal, allows the user to

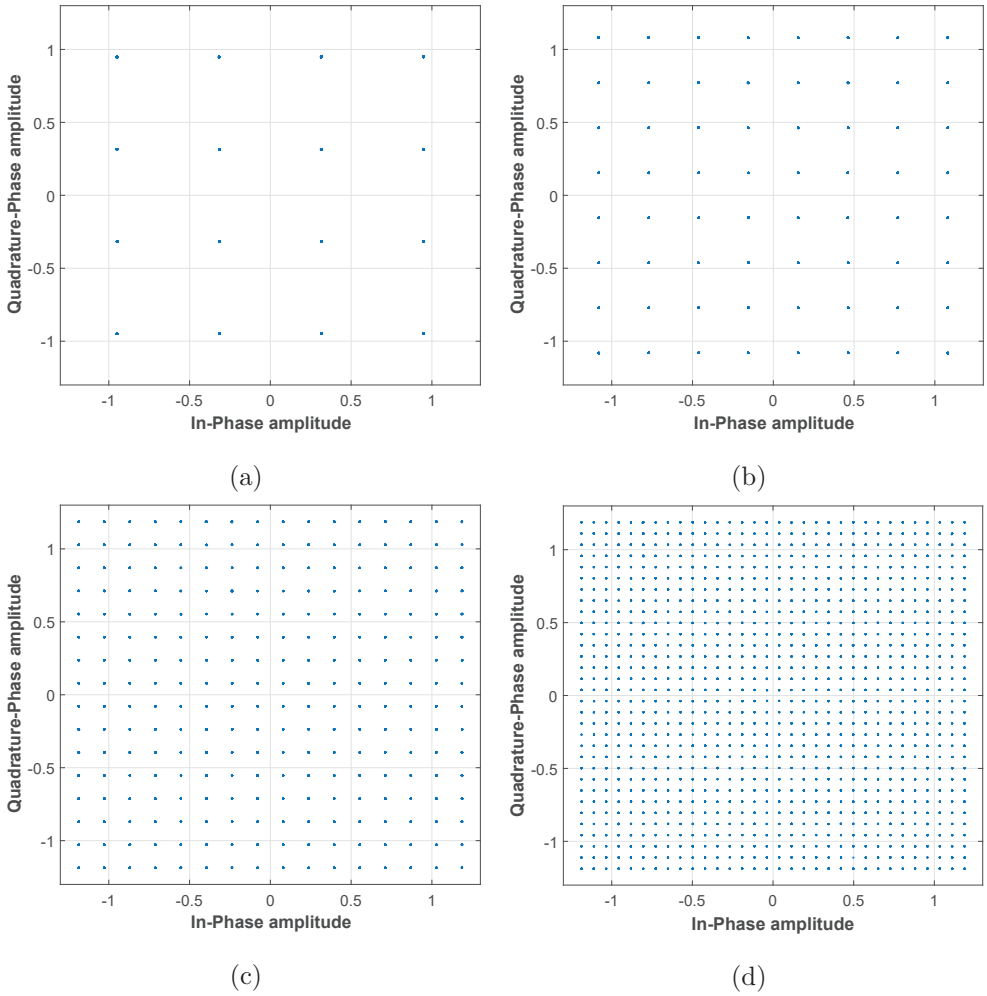

FIGURE 8.10: Received scatter constellation plots for: a) 16-QAM, b) 64-QAM, c) 256-QAM, and d) 1024-QAM, presented in all MIMO configurations when CFO is compensated.

change from 8×8 to 1×1, in real-time, enabling 2.46 Gbps of data rate transmissions for radio in-the-loop communication systems.

The proposed MIMO-OFDM system efficiently utilises a fully pipelined modular architecture with a processing efficiency of over 98.3%, (to the best of the author's knowledge it goes significantly beyond the state-of-the-art). Due to its ability to reduce the design timing constraints, a maximum clock speed of 250 MHz has been achieved in the VC707 implementation. Additionally, it has been demonstrated that the proposed architecture re-uses the most HW consuming DSP algorithms present in a MIMO-OFDM architecture. Sharing the transceiver chain resources among all antenna paths reduces more than 80% hardware in terms of DSP48E1 slices, when compared with conventional design methods. This allows, for example, the implementation of 2 parallel MIMO-OFDM engines in a single *Xilinx* Virtex7 XC7VX485T FPGA, enabling the

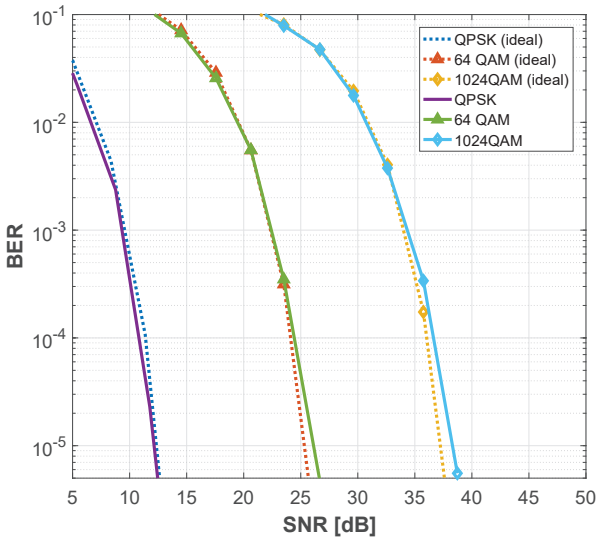

FIGURE 8.11: BER performance of the MIMO-OFDM engine for all antenna configurations, considering 4-, 64-, and 1024-QAM.

deployment of a 16×16 MIMO antenna configuration, fulfilling LTE maximum signal bandwidth, resulting in a complete 5 Gigabit/s wireless communication system.

Moreover, it has been demonstrated through RT EVM measurements, that the proposed MIMO-OFDM TRX has negligible system performance degradation in presence of CFO, with an EVM always below -60 dB. The receiver is able to compensate CFO values up to 15, 30, 60, and 120 kHz, for 8×8, 4×4, 2×2, and 1×1 antenna configurations, respectively. Furthermore, experimental BER curve results of MIMO-OFDM transmissions over an AWGN channel, are very close to the ideal ones, which proves that a 22-bit bus format is a good compromise between both system complexity and performance. Finally, the presented herein might be an important guide to establish RT massive MIMO links over the air in future 5G wireless communication systems, at the minimum expense of hardware resources. The proposed architecture is flexible to be scalable to hundreds of antenna paths, at both radio ends, depending on the footprint of the target integrated circuit. Therefore, time for evaluation and validation of new MIMO coder/decoder envisaged for future wireless communications systems might be significantly reduced, when using the suggested MIMO architecture.

The work performed in this chapter was submitted in one international journal publication:

J. C. Ribeiro, R. Gomes, L. Duarte, R. F. S. Caldeirinha, Akram Hammoudeh, **"Multi-Gigabit/s real-time based transceiver engine aiming at emerging 5G MIMO applications"**, *Physical Communication - Elsevier*, (under review: submitted on Jan. 2019). **Impact Factor = 1.522, Q2.**

This page is intentionally left blank.

CHAPTER 9

Review and conclusions

9.1 Introduction

In this chapter it is summarised and evaluated the work undertaken during this research project, while outlining the main contributions to science and possible directions for further work. The chapter is divided into four sections: critical review of the developed work, by mentioning the main achievements; overview of the most relevant outcomes from the research work present in this document; summary of the main contribution to knowledge by outlining the published work (deliverables); suggestion/guidelines for further scientific investigation and developments.

9.2 Review of the thesis

The scope of this Ph.D thesis was aimed at the research and development of a novel multi-Gigabit/s prototype mmWave system, targeting in particular, applications for future wireless communication systems. To accomplish such objective, a software-defined radio solution composed of two distinct parts, a baseband unit and a radio unit was presented, as alternative to the fully commercially available testbeds present in the literature. While the first is responsible to enable digital modulation/demodulation of the most modern transmission scheme techniques, the former, up-converts/down-converts mmWave signals. Such RF architecture have been detailed, designed, developed, extensively characterised and validated in a controlled environment as proof of concept. This yielded to the state of the art on mmWave testbeds at 60 GHz, at the time of this thesis submission, while meeting the minimum technical performance requirements of IMT-2020 envisioned for 5G. In this context and remarkably, the USW/IT testbed is the only prototype system, to the best of the author acknowledge, capable of processing a signal BW of 150 MHz in real-time, with modulation orders up to 1024 QAM (considering

the proposed novel MIMO-OFDM architecture), and employing OFDM as transmission scheme.

Finally, the feasibility of the proposed multi-Gigabit/s system in enabling AR applications (one of the usage cases envisioned for 5G), was assessed towards five UE devices, placed at different locations inside an indoor classroom environment scenario. Results demonstrated that the proposed system is robust enough to enable AR device communications over such scenario. The outcome of this research project is documented in several different chapters of this thesis, which are summarised below:

In Chapter 1, it was introduced the background of study and subsequent motivation that led to this research work. The main line of research was to provide and develop a fully customised wireless communication prototype system (which does not rely on a single wireless communication standard), as alternative to COTS solutions, targeting 5G multi-Gigabit/s applications. This was the main concept adopted in the initial Ph.D work-plan and it is the innovative key feature of this work. Finally, enumeration of the original research objectives and the structure of this thesis, were outlined.

In Chapter 2 was presented an extensive literature review addressing the most relevant topics towards the accomplishment of the proposed research work. It started by reviewing the current and future wireless communication standards, giving particular emphasis to the role of mmWave spectrum in enabling multi-Gigabit/s data rates, followed by an extensively description of the NR PHY layer. An appropriate state-of-the-art on mmWave testbeds was finally given, summarising the most up-to-date related works presented in the literature on this topic, and comparing them with the 5G testbed proposed in this thesis (USW/ IT).

In Chapter 3, it is introduced the developed mmWave simulation tool using *Matlab/ Simulink*. This was initially used for evaluating the performance of customised wireless communication systems under 60 GHz realistic channel and RF impairment models. At first, a complete OFDM multi-Gigabit/s system was simulated based on the 60 GHz PHY layer specifications of the IEEE 802.15.3c standard, but the inherent simulator's modular architecture enabled the study of other waveforms (not defined in this standard), such as FS-FBMC, the consideration of different order modulations, lengths of CP and FFT size.

The contents of Chapter 4 are related to the developments of the proposed novel FPGA based SDR for prototyping future wireless communication systems. Following the 5G system requirements, the hardware choice of its components was extensively detailed. Moreover, all the necessary firmware modifications from the original 4DSP DAC/ ADC FPGA designs, needed to stablish a real-time communication between them and the VC707 board (processor unit), were outlined. Furthermore, the motivation for consideration of a digital IF OFDM system architecture was also presented and

validated, firstly, in a back-to-back configuration and then in a OTA scenario, leading to the ideal SDR concept (only TX/ RX antennas and very high speed sampler converters were considered). The obtained experimental results of EVM $< -26dB$, for this former configuration (also known as all digital radio), indicate that the proposed OFDM SDR prototype system can be, for instance, a promising solution to implement the 5G NR PHY layer numerology that aims the sub-1 GHz band.

In Chapter 5 was presented a complete multi-Gigabit/s end-to-end 5G prototype communication system at mmWave. It has been demonstrated that the system's inherent real-time reconfigurability feature, allows to select, on-the-fly, for example, digital modulations from QPSK up to 256 QAM. Furthermore, results from an extensive OTA testbed characterisation, at 60 GHz, for different values of SNIR, were also provided, where minimums EVM values of -33 dB were achieved, considering an OFDM transmission. This indicates that the proposed *USW/IT* is a promising and feasible solution to implement the 5G NR PHY layer numerology that targets the mmWave band (24-52.6 GHz).

Chapter 6 presented the experimental evaluation of the integration of the SDR RT multi-Gigabit/s wireless OFDM system with two distinct RF front-ends designed for mmWave. Comparative analysis between 60 GHz cutting-edge COTS and reference RF front-ends, taking into account their intrinsic RF impairments and their impact on the overall system performance degradation, was given. In particular, proper RF measurements were performed to fully characterise the PEM009 VUBIQ RF front-end, in terms of output power and gain, RF carrier and side-band leakages, RX IMD products, RX power sensitivity and gain, overall IF-IF frequency response and IQ and DC offset imbalances. In addition, performance degradation in the OFDM waveform, when both IT RF front-end (reference) and PEM009 were assessed inside an anechoic chamber. Results demonstrated that RF impairments from analogue up-conversion/ down-conversion stages are the most restrictive factor in mmWave transmissions, limiting both data rate and spectral efficiency. The content presented in this chapter resulted in a paper publication on a highly reputed international journal.

In Chapter 7, it is assessed feasibility of the developed 60 GHz OFDM down-link communication, to replace the current wired/ wireless AR communication standards, which only support dozens Mbps of data rate. To this end, five UE devices, placed at different locations inside an indoor classroom environment scenario, were considered. Reported results, show that a baseband SDR combined with the PEM009 RF front-end, enabled short-range communication links up to 4m, while providing 312.5 Mbps of data rate over 60 GHz radio channels.

Chapter 8 presented the implementation and evaluation of a highly scalable multi-Gigabit/s real-time wideband OFDM processing chain for 5G applications, capable to enable MIMO-OFDM configurations up to 16×16 (massive MIMO) at the minimum

expense of HW utilisation. As proof of concept, a 8×8 MIMO configuration, at LTE's highest sampling rate of 30.72 MHz, was implemented in the VC707, where it was demonstrated that using such architecture, a processing efficiency of over 98.3% was achieved. Finally, the proposed fully pipelined modular MIMO-OFDM architecture can be of an extremely agile tool to validate massive MIMO pre-coding/ decoding algorithms for 5G and future generation of mobile communication systems, in an OTA real-time testbed. Currently, the majority of these algorithms, to best of author knowledge, rely mainly on simulations.

9.3 Conclusions

The work carried out in this research project contributed into three main areas: *i)* realistic simulation tools for the evaluation of wireless communication systems; *ii)* SDR design, development and characterisation, and *iii)* multi-Gigabit/s real-time OFDM testbed systems at mmWave. The work reported in this thesis was thoroughly supported by simulations and measurement campaigns, enabling several critical observations and conclusions to be drawn. The main contributions to each area may be summarised below.

Last but not the least, this thesis (as it is noticed from the above chapters description) has been an all-encompassing research project, spanning from advanced theory to prototyping and practical performance assessment.

9.3.1 Contribution to mmWave wireless communication simulation tools

In spite of the fundamentals on digital wireless communication standards systems are solid and well reported in the literature, this Ph.D. work contributed with a mmWave simulation framework capable to predict the performance of the most relevant transmissions schemes, namely, OFDM, SC-FDE and FBMC, under both channel and RF impairments at 60 GHz. This was accomplished by exploring the inherent modular architecture of *Simulink*, and its IP block library. This enabled, for example, a rapid system development of customised RF impairment models, waveforms, and algorithms for channel and time estimation. The proposed simulation framework was particularly based on the 60 GHz IEEE 802.15.3c standard, but can be adapted to any wireless specification.

Results obtained from a specific set of simulations, allowed to predict, overcome and avoid some of the most negative RF impairments in the developed mmWave real-time

OFDM testbed. In addition, they were disseminated in the literature with six direct publications in relevant forums.

9.3.2 Contribution to software-defined radio

The main outcome of this research project, resulted in the construction/ development of a mmWave software-defined radio for future wireless communication systems. The development of such system was motivated by interoperability problems between distinct wireless communication standards and air interfaces, that led to implementation of radio systems in dedicated hardware. In addition, the current state-of-the-art COTS SDRs only enable signal transmissions with relatively small bandwidths, and thus provide low data rate transmissions. For example, at sub-6GHz communications, USRP X310 [223] delivers signal bandwidths only up to 160 MHz. On the other hand, at mmWave, NI PXI mmWave TRX bundle [224], which cost around 200,000 £ [225], offer a maximum processing bandwidth of 2 GHz, however their current NI waveform generator can only cope with signal bandwidths up to 145 MHz [226]. In this work, it is provided a (much) more cost effective solution to tackle SISO mmWave/ sub-6 GHz communications, where all the TRX chains are fully customised, and baseband unit can be easily upgraded (with some minor firmware modifications) to process signal bandwidths up to 5 GHz (IQ). Notwithstanding, at the beginning of this research project, the aforementioned devices were not even available on the market. Thus, no mmWave SDR platform existed, at that time, capable to achieve multi-Gigabit/s data rate over mmWave frequency spectrum.

9.3.3 Contribution to 5G

MmWave communications is envisaged to be integrated in the next generation of mobile networks, namely enhanced mobile broadband (one of the 5G verticals). This is seen as the solution to increase the overall capacity of mobile radio cells, enabling the support of multi-Gigabit/s transmissions towards the mobile equipments. In this context, an extensive measurement campaign (in the controlled environment of an anechoic chamber) aimed at the characterisation of two distinct RF front-end technologies was included. Such study allowed one to conclude that the performance of an end-to-end multi-Gigabit/s OFDM downlink communication is mainly limited by the RF impairments induced by the RF architecture considered in the up-conversion/down-conversation of RF signals, limiting both system's data rate and spectral efficiency. The measurement also demonstrated that current COTS CMOS-based RF front-end technology is not ready yet to tackle 5G communication requirements, and must be evolved.

Finally, in order to provide a guide to establish mmWave real-time OFDM links meeting 5G requirements, in this work a practical link budget formulation for accurate

EVM estimations, was proposed. This part of the work contributed to the literature with one paper publication in a highly reputed IEEE journal.

9.4 Contributions to the knowledge

As contributions to knowledge, the research work presented in this Ph.D. has resulted in several scientific publications in relevant and recognised international Journals [J] and conferences [C], which further support the contents addressed in the chapters of this thesis. Moreover, the proposed real-time mmWave prototype system has been showcasing in several live demonstrators [D], in relevant national and international events. Particularly, the work present in Chapter 6 contributed to an IEEE ComSoc webinar [W].

9.4.1 Direct contributions

In terms of journals papers, at the submission time of this document, the research work carried out throughout this thesis has contributed directly to the scientific knowledge with five journal papers, four are already published and one is still under review. In addition, four peer-reviewed conference papers and four live demonstrators. All these contributions are listed below considering a chronological order (from the latest to oldest publication). Some of the published papers can be found on-line in various digital libraries, such as the *IEEE Xplore* website.

Papers in international journals:

J1. C. Ribeiro, R. Gomes, L. Duarte, R. F. S. Caldeirinha, Akram Hammoudeh, **"Multi-Gigabit/s real-time based transceiver engine aiming at emerging 5G MIMO applications"**, *Physical Communication-Elsevier*, (under review: submitted on February 2019). **Impact Factor = 1.522, Q2;**

J2. R. Gomes, L. Sismeiro, C. Ribeiro, T. Fernandes, M. Sanchez, Akram Hammoudeh, R. F. S. Caldeirinha„ **"Will COTS RF front-ends really cope with 5G requirements at mmWave?"**, *IEEE Access*, vol. 6, no. -, pp. 38745 - 38769, July 2018. doi: 10.1109/ACCESS.2018.2851781. **Impact Factor = 3.557, Q1;**

J3. R. Gomes, J. R. Reis, Zaid Al-Daher, A. Hammoudeh, R. F. S. Caldeirinha, **"5G: Performance and Evaluation of FS-FBMC against OFDM for High Data Rate Applications at 60 GHz**, *IET Signal Processing*, vol. 12, no. 5, pp. 620-628, Feb. 2018. doi: 10.1049/iet-spr.2016.0671 . **Impact Factor = 1.25, Q2;**

J4. R. Gomes, Akram Hammoudeh , R. F. S. Caldeirinha, Zaid Al-Daher, T. Fernandes, J. R. Reis, **"Towards 5G: Performance evaluation 60 GHz UWB OFDM communications under both channel and RF impairments"**, *Physical Communication-Elsevier*, vol. 25, no. 2, pp. 527-538, Oct. 2017. doi: 10.1016/j.phycom.2017.10.011. **Impact Factor = 1.522, Q2;**

J5. R. Gomes, R. F. S. Caldeirinha, Akram Hammoudeh, Pedro Pires, **"Performance Evaluation of 60 GHz OFDM Communications under Channel Impairments over Multipath Fading Channels at 60 GHz"**, *Sensors & Transducers Journal and Magazine*, vol. 204, no. 9, pp. 29-38, Sept.2016;

Papers in international conferences:

C1. R. Gomes, K. Sobaihi, R.F.S Caldeirinha and A. Hammoudeh, **"Performance Evaluation of a Dual-Mode OFDM and SC-FDE System at mmWave enabling Joint Radar and 5G Multi-Gigabit/s Wireless Communications"**, 2019 6th International Conference on Signal Processing and Integrated Networks (SPIN), India, 2019.

C2. R. Gomes, L. Sismeiro, C. Ribeiro, M. G. Sanchéz, A. Hammoudeh and R. F. S. Caldeirinha, **"A mmWave solution to provide wireless Augmented Reality in classrooms"**, *2018 15th International Symposium on Wireless Communication Systems (ISWCS), Lisbon, 2018*, vol. -, no. -, pp. 1 - 6, Aug. 2018. doi: 10.1109/ISWCS.2018.8491103.

C3. R. Gomes, R. F. S. Caldeirinha, Akram Hammoudeh, **"Uncompressed Full HD Video Transmission using Uncoded OFDM over Multipath Fading Channels at 60 GHz"**, *IARIA SIGNAL 2016*, vol. 0, no. 0, pp. 0-0, June 2016;

C4. R. Gomes, Zaid Al-Daher, Akram Hammoudeh, Khaled Sobaihi, R. F. S. Caldeirinha, T. Fernandes, **"Performance and evaluation of OFDM and SC - FDE over an AWGN propagation channel under RF impairments using simulink at 60GHz"**, *Loughborough Antennas and Propagation Conference (LAPC)*, Loughborough, 2014, pp. 685-689. doi: 10.1109/LAPC.2014.6996487

Live demonstrators/ showcases:

D1. Demonstrator: **"Showcase of a full-duplex 5G Radio TESTBED at mmWave: GbE-based OTA Live Streaming of 8 HD Videos"** – *Techdays ISWCS 2018 conference* – 28-31 December 2018 – Lisboa, Portugal, in a collaboration with TWEVO;

D2. Demonstrator: **"An End-to-End Multi-Gigabit/s 5G TESTBED at mm-Wave – the First Portuguese Trials"** – *encontro Ciência 2018 Centro de Congressos de Lisboa* – 2-4 July 2018 – Aveiro, Portugal, in a collaboration with TWEVO;

D3. Demonstrator: **"A complete Multi-Gigabit/s End-to-End 5G TESTBED at mmWave - the first Portuguese trials"** – *Techdays Aveiro 2017 Centro Exposições* – 12-14 October 2017 – Aveiro, Portugal, in a collaboration with TWEVO;

D4. Demonstrator: **"Design, Development and Implementation of a Milimetre Wave Wireless Radio System Prototype for Gigabit/s Multimedia Applications at 60 GHz"** – *2016 Engineering Showcase* – 20 April 2016 – University of South Wales, United Kingdom.

9.4.2 Indirect contributions

The author has also contributed to other relevant research work that resulted in several international publications in connection to the work presented in this thesis.

Papers as co-author in international journals:

J1. J. Reis; C. Ribeiro; L. Duarte; R. Gomes; N. Copner and R.F.S. Caldeirinha, **"On the impact of Electronic 2D Beamsteering in Emerging 5G New Radio"**, *International Journal on Communications Antenna and Propagation (IRECAP)* (article in press). **Impact Factor = 1.62, Q2**.

J2. J. Reis; N. Copner; A. Hammoudeh; Z. Al-Daher; R.F.S. Caldeirinha; T.R. Fernandes and R. Gomes, **"FSS-inspired Transmitarray for two Dimensional Antenna Beamsteering"**, *IEEE Transactions on Antennas and Propagation*, vol. 64, no. 6, pp. 2197-2206, June 2016. doi: 10.1109/TAP.2016.2543802. **Impact Factor = 2.957, Q1;**

Co-author in international webinar:

W1. IEEE ComSoc Webinar: **"Meeting the Challenges of RF with mmWave for 5G", delivered by Prof. Rafael Caldeirinha** – *IEEE ComSoc* – 30 Oct. 2018.

9.5 Recommendations for further work

With the obtained results documented in this thesis, possible extensions for further development can be suggested following identified lines of research. To this extent, proposals are grouped as follows: *i)* modelling of novel indoor and outdoor 5G channel models to be included in the proposed mmWave simulation framework. *ii)* development of new RF front-end at 26 GHz; *iii)* evolve the current SISO prototype system to accommodate higher signal bandwidths, and post-OFDM waveforms; *iv)* integration of the developed and implemented MIMO-OFDM architecture with the SDR FPGA design, in order allow OTA transmissions of new MIMO BF, and multi-user algorithms.

i) Study on novel indoor and outdoor 5G channel models to be included in the proposed mmWave simulation framework. In this context, some guidelines are already available in the literature. For example, in [227], an overview of the channel properties for outdoor urban micro-cellular and macro-cellular environment is presented. In particular, authors highly recommend that 5G channel models, for carries from 0.5 to 100 GHz, should comply with the 3GPP 3D channel model (characterisation of the scattering environment between the base section sector and the UE in both azimuth and elevation dimensions) [228]. Furthermore, an extensive study on the channel models for those frequencies can also be found in [229].

ii) Study and development of a new RF front-end designed to enable 5G applications, where the adopted frequency band must comply with the UK's communications regulator, OFcom. According to this regulator, 26 GHz spectrum band is envisioned to be the key enabler feature of 5G services, by stating:

> "The 26 GHz band covers the 3.25 GHz of spectrum between 24.25 GHz and 27.5 GHz and is being prioritised across Europe as the first high frequency band for 5G. This high frequency spectrum (known as 'mm-Wave spectrum'), offers very high data capacity and speeds but with a limited range [50]."

Following the above carrier specifications and an radio IF architecture, a new RF front-end was designed at 26 GHz. The block diagram of the transmitter can be seen in Fig. 9.1. The RF front-end was built using the state-of-art "drop-in" and drop-on" RF components from X-Microwave innovative Modular Drop-In Building Blocks (X-MWblocks) [230], as depicted in Fig. 9.2. These analogue components technology are sought to be easy to test, integrate, align and configure, from prototype to final production hardware. Each RF front-end will occupy an area of 98 mm by 61 mm (excluding the antennae). Assembling of the RF front-end

and OFDM performance over-the-air considering this RF front-end are yet to be carried out, since all the required X-Microwave components arrived in the final stage of the writing-up this project. However, considering the measured PN from the LO chain, depicted in Fig. 9.3, and using (6.8), it is expected an EVM performance below < -35 dB, which is quite satisfactory.

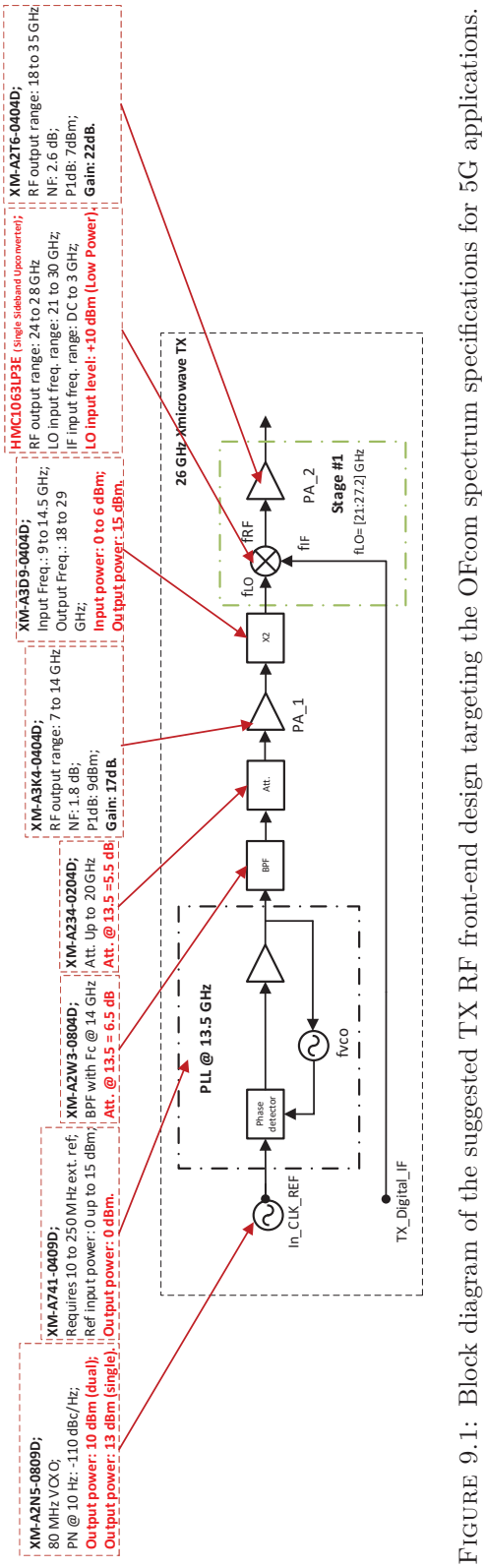

FIGURE 9.1: Block diagram of the suggested TX RF front-end design targeting the OFcom spectrum specifications for 5G applications.

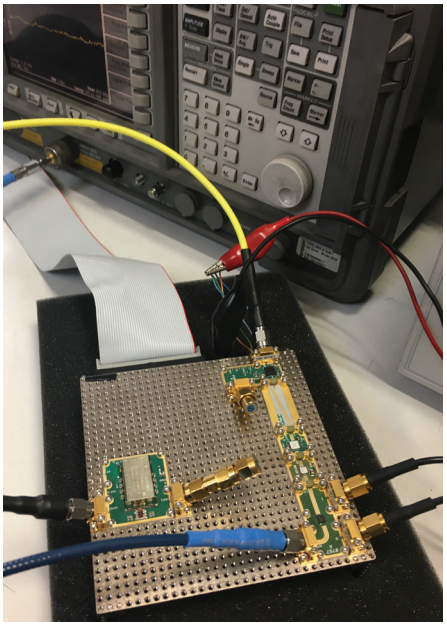

FIGURE 9.2: X-Microwave innovative modular building block system, considered in the development of the new 26 GHz RF front-end.

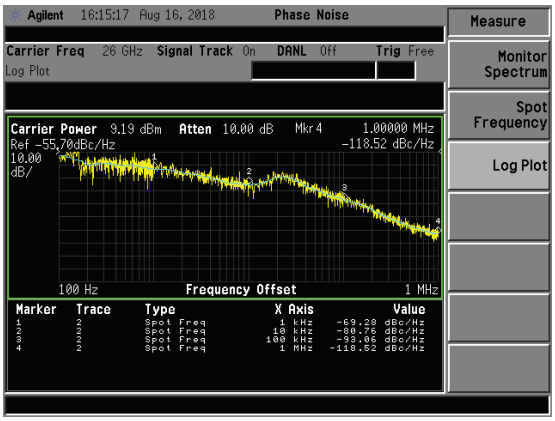

FIGURE 9.3: PN measured at the output of the multiplier (LO's mixer input), at 26 GHz.

iii) In order to evolve the current SISO mmWave transceiver system to accommodate (process in real-time) higher signal bandwidths, and consequently higher system throughput, both FMC230/ FMC126 converters must be set to their maximum sampling clock rate (5 GSPS). To this end, the ADC should be configured to operate in 1-channel mode, where the analogue signal is sampled at different phases in each of the four ADC channels, at 1.25 GSPS [151]. Since the ADC clock is driven to the DAC to overcome sampling mismatch, the DAC will be operating at 5 GSPS, as well. Nevertheless, since the firmware of both converters considers parallel data interface, a distributed OFDM waveform generation IP should be designed (a parallelism technique considering 8 processing paths must be addressed). With this, the distributed 8× interpolation/decimation filter is

not necessary, since the transmitted OFDM symbol will be utilizing the full DAC/ ADC bandwidth (2.5 GHz).

iv) Finally, in order to fully test the 5G NR PHY layer OTA, new MIMO BF and multi-user SysGen algorithm must be designed and integrated in the SDR FPGA design. In fact, some time has already been dedicated to this topic, and preliminary research on MIMO algorithms HW implementations have already been undertaken.

It is well known that over AWGN channels, BER decreases exponentially with the SNR, whereas in multipath fading channels, such as: a *Rayleigh* channel model, it decreases only linearly [231]. Over such channels, BER is limited by a relatively large channel attenuation, and consequently low instantaneous SNR. An effective method reducing the probability of low SNR, which consequently improves the system's performance, is by the consideration of spatial diversity techniques. With this, some information reaches the RX from statistically independent channels [231]. One of the most simple and common diversity MIMO coder/ decoder algorithms, is the *Alamouti* transmit/receive MIMO diversity scheme [232]. In this context, as proof of concept, a 2×2 MIMO system was designed following this scheme. Implementation of both *Alamouti* coding/ decoding, for a 2×2 MIMO diversity configuration are given in Fig. 9.4a and Fig. 9.4b, respectively, based on [232].

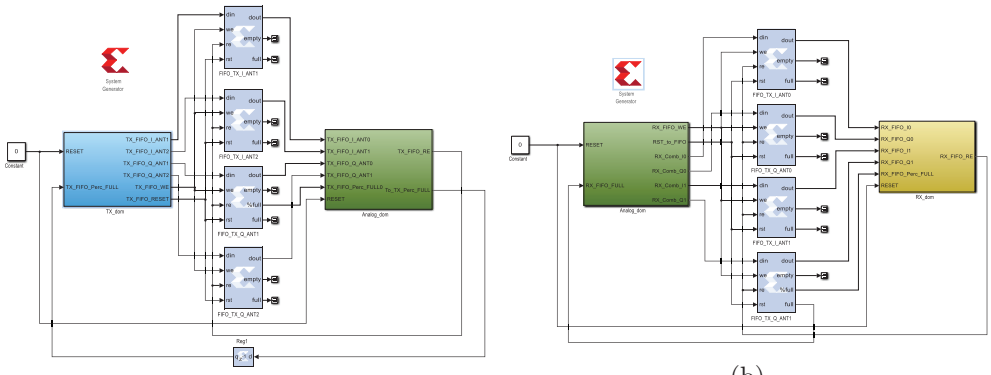

(a) (b)

FIGURE 9.4: *Alamouti* 2×2 diversity MIMO configurations: a) coder, and b) decoder SysGen designs.

In order to validate the above SysGen design, random channel coefficients have been considered, and BER analysis has been performed by a comparing the transmitted with the received bit-stream (considering that SNR is infinite). Results are shown in Fig. 9.5, where it can be verified that neither erroneous bits nor symbols are

present after demodulation. Nonetheless, the performance of *Alamouti* algorithm should be further assessed over realistic multipath fading channel under different SNR conditions, and then integrated in both MIMO-OFDM developed architecture and TRX firmware to be also evaluated OTA. Such tasks should be done in further work.

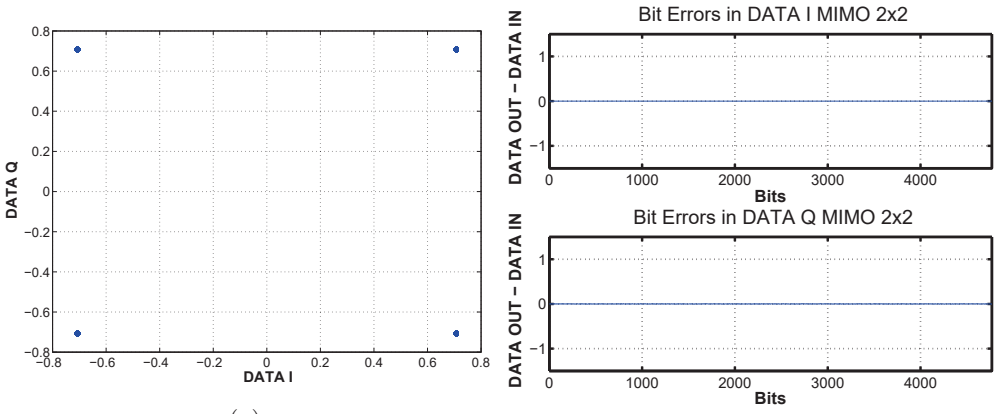

(a) (b)

FIGURE 9.5: Received data results for 2×2 receiver diversity scheme with: (a) received signal constellation and (b) bit errors on received data.

In addition, all the aforementioned suggestions for further work, in this topic, can be summarised in a roadmap, such as the one illustrated in Fig. 9.6.

FIGURE 9.6: Suggested roadmap to further enhance the features of the developed mmWave testbed.

References

[1] Z. Pi and F. Khan, "An Introduction to Millimeter-wave Mobile Broadband Systems," *IEEE Communications Magazine*, vol. 49, no. 6, pp. 101–107, June 2011.

[2] "The Evolution of Mobile Techonologies," https://www.qualcomm.com/media/documents/files/the-evolution-of-mobile-technologies-1g-to-2g-to-3g-to-4g-lte.pdf.

[3] "LTE Advanced," http://www.3gpp.org/technologies/keywords-acronyms/97-lte-advanced, accessed: 2018-03-08.

[4] T. S. Rappaport, J. N. Murdock, and F. Gutierrez, "State of the Art in 60-GHz Integrated Circuits and Systems for Wireless Communications," *Proceedings of the IEEE*, vol. 99, no. 8, pp. 1390–1436, Aug 2011.

[5] W. Paper, "Cisco Visual Networking Index: Forecast and Methodology, 2016-2021," Cisco, Tech. Rep., 6 2017.

[6] J. G. Andrews, S. Buzzi, W. Choi, S. V. Hanly, A. Lozano, A. C. K. Soong, and J. C. Zhang, "What Will 5G Be?" *IEEE Journal on Selected Areas in Communications*, vol. 32, no. 6, pp. 1065–1082, June 2014.

[7] G. Wunder, P. Jung, M. Kasparick, T. Wild, F. Schaich, Y. Chen, S. T. Brink, I. Gaspar, N. Michailow, A. Festag, L. Mendes, N. Cassiau, D. Ktenas, M. Dryjanski, S. Pietrzyk, B. Eged, P. Vago, and F. Wiedmann, "5GNOW: non-orthogonal, asynchronous waveforms for future mobile applications," *IEEE Communications Magazine*, vol. 52, no. 2, pp. 97–105, February 2014.

[8] D. Soldani and A. Manzalini, "Horizon 2020 and Beyond: On the 5G Operating System for a True Digital Society," *IEEE Vehicular Technology Magazine*, vol. 10, no. 1, pp. 32–42, March 2015.

[9] P. Demestichas, A. Georgakopoulos, D. Karvounas, K. Tsagkaris, V. Stavroulaki, J. Lu, C. Xiong, and J. Yao, "5G on the Horizon: Key Challenges for the Radio-Access Network," *IEEE Vehicular Technology Magazine*, vol. 8, no. 3, pp. 47–53, Sept 2013.

[10] G. Consortium, "5G Waveform Candidate Selection derivable 3.1," *5GNOW*, vol. 2013, no. 1, pp. 1–110, November 2013.

[11] S. Sasipriya and R. Vigneshram, "An overview of cognitive radio in 5G wireless communications," in *2016 IEEE International Conference on Computational Intelligence and Computing Research (ICCIC)*, Dec 2016, pp. 1–5.

[12] T. S. Rappaport, S. Sun, R. Mayzus, H. Zhao, Y. Azar, K. Wang, G. N. Wong, J. K. Schulz, M. Samimi, and F. Gutierrez, "Millimeter Wave Mobile Communications for 5G Cellular: It Will Work!" *IEEE Access*, vol. 1, pp. 335–349, 2013.

[13] M. Schellmann, Z. Zhao, H. Lin, P. Siohan, N. Rajatheva, V. Luecken, and A. Ishaque, "FBMC-based air interface for 5G mobile: Challenges and proposed solutions," in *2014 9th International Conference on Cognitive Radio Oriented Wireless Networks and Communications (CROWNCOM)*, June 2014, pp. 102–107.

[14] K.-C. Huang and Z. Wang, *Millimeter Wave Communication Systems*. John Wiley & Sons, Apr. 2011.

[15] T. Baykas, C. Sum, Z. Lan, J. Wang, M. A. Rahman, H. Harada, and S. Kato, "IEEE 802.15.3c: the first IEEE wireless standard for data rates over 1 Gb/s," *IEEE Communications Magazine*, vol. 49, no. 7, pp. 114–121, July 2011.

[16] R. Daniels, J. Murdock, T. Rappaport, and R. Heath, "60 GHz Wireless: Up Close and Personal," *IEEE Microwave Magazine*, vol. 11, no. 7, pp. 44–50, Dec. 2010.

[17] T. Yilmaz, E. Fadel, and O. B. Akan, "Employing 60 GHz ISM Band for 5G Wireless Communications," in *2014 IEEE International Black Sea Conference on Communications and Networking (BlackSeaCom)*, May 2014, pp. 77–82.

[18] C. Ribeiro and A. Gameiro, "A Software-defined Radio FPGA Implementation of OFDM-based PHY Transceiver for 5G," *Analog Integr. Circuits Signal Process.*, vol. 91, no. 2, pp. 343–351, May 2017. [Online]. Available: https://doi.org/10.1007/s10470-017-0939-x

[19] S. Yong, P. Xia, and A. Garcia, *60GHz Technology for Gbps WLAN and WPAN: From Theory to Practice*. Wiley Publishing, 2011.

[20] H. Yang, "Towards low-cost gigabit wireless systems at 60 GHz," Ph.D. dissertation, TUE : Department of Electrical Engineering, 2008.

[21] D. Pareit, B. Lannoo, I. Moerman, and P. Demeester, "The History of WiMAX: A Complete Survey of the Evolution in Certification and Standardization for IEEE 802.16 and WiMAX," *IEEE Communications Surveys Tutorials*, vol. 14, no. 4, pp. 1183–1211, Fourth 2012.

[22] R. B. Marks, "IEEE 802.16 Broadband Wireless Access Working Group," Tech. Rep., 2003.

[23] K. Etemad, "Overview of mobile WiMAX technology and evolution," *IEEE Communications Magazine*, vol. 46, no. 10, pp. 31–40, October 2008.

[24] S. Wang, Y. Zhang, Z. Liu, W. Zhou, and D. Liu, "A brief study on low-rate wireless personal network," in *2012 International Conference on Systems and Informatics (ICSAI2012)*, May 2012, pp. 1360–1363.

[25] "IEEE 802.15 Working Group." [Online]. Available: http://www.ieee802.org/15/

[26] "IEEE Standard for Information technology– Local and metropolitan area networks– Specific requirements– Part 15.1a: Wireless Medium Access Control (MAC) and Physical Layer (PHY) specifications for Wireless Personal Area Networks (WPAN)," *IEEE Std 802.15.1-2005 (Revision of IEEE Std 802.15.1-2002)*, pp. 1–700, June 2005.

[27] B. H. Walke, S. Mangold, and L. Berlemann, *IEEE 802 Wireless Systems: Protocols, Multi-hop Mesh/Relaying, Performance and Spectrum Coexistence*. New York, NY, USA: John Wiley & Sons, Inc., 2007.

[28] "IEEE Standard for Information technology-Telecommunications and information exchange between systems-Local and metropolitan area networks-Specific requirements Part 15.4: Wireless Medium Access Control (MAC) and Physical Layer (PHY) Specifications for Low-Rate Wireless Personal Area Networks (WPANs) Amendment 3: Alternative Physical Layer Extension to support the Japanese 950 MHz bands," *IEEE Std 802.15.4d-2009 (Amendment to IEEE Std 802.15.4-2006)*, pp. c1–27, April 2009.

[29] A. O. Ejeye and S. D. Walker, "Uncompressed quad-1080p wireless video streaming," in *2012 4th Computer Science and Electronic Engineering Conference (CEEC)*, Sept 2012, pp. 13–16.

[30] W. Paper, "Ultra-Wideband (UWB) Technology - Enabling high-speed wireless personal area networks," intel, Tech. Rep., 2004.

[31] G. Breed, "Wireless USB Uses Ultra Wideband (UWB) for High Data Rate," in *High Frequency Electronics*, Sep 2005.

[32] "IEEE 802.15 WPAN Task Group 3c." [Online]. Available: http://www.ieee802.org/15/pub/TG3c.html

[33] I. Guvenc, S. Gezici, Z. Sahinoglu, and U. C. Kozat, *Reliable Communications for Short-Range Wireless Systems*, 1st ed. New York, NY, USA: Cambridge University Press, 2011.

[34] C. J. Hansen, "WiGiG: Multi-gigabit wireless communications in the 60 GHz band," *IEEE Wireless Communications*, vol. 18, no. 6, pp. 6–7, December 2011.

[35] W. Paper, "802.11ac: The Fifth Generation of Wi-Fi," intel, Tech. Rep., 2018.

[36] "UMTS." [Online]. Available: http://www.3gpp.org/technologies/keywords-acronyms/103-umts

[37] "LTE." [Online]. Available: http://www.3gpp.org/technologies/keywords-acronyms/98-lte

[38] D. Pepe and D. Zito, "60-GHz transceivers for wireless HD uncompressed video communication in nano-era CMOS technology," in *Melecon 2010 - 2010 15th IEEE Mediterranean Electrotechnical Conference*, April 2010, pp. 1237–1240.

[39] "IEEE Standard for Information technology–Telecommunications and information exchange between systems–Local and metropolitan area networks–Specific requirements-Part 11: Wireless LAN Medium Access Control (MAC) and Physical Layer (PHY) Specifications Amendment 3: Enhancements for Very High Throughput in the 60 GHz Band," *IEEE Std 802.11ad-2012 (Amendment to IEEE Std 802.11-2012, as amended by IEEE Std 802.11ae-2012 and IEEE Std 802.11aa-2012)*, pp. 1–628, Dec 2012.

[40] "IEEE Standard for Information technology– Local and metropolitan area networks– Specific requirements– Part 15.3: Amendment 2: Millimeter-wave-based Alternative Physical Layer Extension," *IEEE Std 802.15.3c-2009 (Amendment to IEEE Std 802.15.3-2003)*, pp. 1–200, Oct 2009.

[41] J. Notor, "Overview of Current 60 GHz Spectrum Rules," Tech. Rep., July 2013.

[42] T. S. Rappaport, Y. Xing, G. R. MacCartney, A. F. Molisch, E. Mellios, and J. Zhang, "Overview of Millimeter Wave Communications for Fifth-Generation (5G) Wireless Networks—With a Focus on Propagation Models," *IEEE Transactions on Antennas and Propagation*, vol. 65, no. 12, pp. 6213–6230, Dec 2017.

[43] F. Giannetti, R. Reggiannini, M. Moretti, E. Adirosi, L. Baldini, L. Facheris, A. Antonini, S. Melani, G. Bacci, A. Petrolino, and A. Vaccaro, "Real-Time Rain Rate Evaluation via Satellite Downlink Signal Attenuation Measurement," *Sensors*, vol. 17, no. 8, p. 1864, 2017.

[44] "Recommendation ITU-R P.838-3," Tech. Rep., 2005.

[45] H. Yang, P. F. M. Smulders, and M. H. A. J. Herben, "Channel Characteristics and Transmission Performance for Various Channel Configurations at 60 GHz," *EURASIP J. Wirel. Commun. Netw.*, vol. 2007, no. 1, pp. 43–43, Jan. 2007. [Online]. Available: http://dx.doi.org/10.1155/2007/19613

[46] T. Rappaport, *Wireless Communications: Principles and Practice*, 2nd ed. Upper Saddle River, NJ, USA: Prentice Hall PTR, 2001.

[47] J. E. HILL, "Gain of directional antennas," Watkins-Johnson Tech-note, 3, (4), Tech. Rep., 1976.

[48] J. C. Williams, "A 36 GHz printed planar array," *Electronics Letters*, vol. 14, no. 5, pp. 136–137, March 1978.

[49] W. P. N. 9, "E-band and V-band - Survey on Status of Worldwide Regulation," ETSI, Tech. Rep., 2015.

[50] W. Paper, "5G spectrum access at 26 GHz and update on bands above 30 GHz," OFcom, Tech. Rep., 2017.

[51] L. Lu, G. Y. Li, A. L. Swindlehurst, A. Ashikhmin, and R. Zhang, "An Overview of Massive MIMO: Benefits and Challenges," *IEEE Journal of Selected Topics in Signal Processing*, vol. 8, no. 5, pp. 742–758, Oct 2014.

[52] O. Edfors, L. Liu, F. Tufvesson, N. Kundargi, and K. Nieman, *Massive MIMO for 5G: Theory, Implementation and Prototyping.* John Wiley & Sons, Ltd, 2016, pp. 189–230.

[53] W. Paper, "5G Massive MIMO Testbed: From Theory to Reality," NI, Tech. Rep., 2017.

[54] J. Vieira, S. Malkowsky, K. Nieman, Z. Miers, N. Kundargi, L. Liu, I. Wong, V. Öwall, O. Edfors, and F. Tufvesson, "A flexible 100-antenna testbed for Massive MIMO," in *2014 IEEE Globecom Workshops (GC Wkshps)*, Dec 2014, pp. 287–293.

[55] R. Bhusal and S. Moh, "Qualitative and Quantitative Comparison of IEEE 802.15.3c and IEEE 802.11ad for Multi-Gbps Local Communications," *Wireless Personal Communications*, vol. 75, pp. 2135–2149, 2014.

[56] T. Nitsche, C. Cordeiro, A. B. Flores, E. W. Knightly, E. Perahia, and J. C. Widmer, "IEEE 802.11ad: directional 60 GHz communication for multi-Gigabit-per-second Wi-Fi ," *IEEE Communications Magazine*, vol. 52, no. 12, pp. 132–141, December 2014.

[57] A. Note, "Wireless LAN at 60 GHz - IEEE 802.11ad Explained," Agilent Tecnologies, Tech. Rep., 2013.

[58] C. W. Pyo and H. Harada, "Throughput analysis and improvement of hybrid multiple access in IEEE 802.15.3c mm-wave WPAN," *IEEE Journal on Selected Areas in Communications*, vol. 27, no. 8, pp. 1414–1424, October 2009.

[59] A. Sadri, "Summary of the Usage models for 802.15.3c ," Tech. Rep., Nov. 2006.

[60] X. Zhu, A. Doufexi, and T. Kocak, "On the Performance of IEEE 802.15.3c millimeter-wave WPANs: PHY and MAC," in *2010 Wireless Advanced 2010*, June 2010, pp. 1–6.

[61] M. Sung, S. Cho, J. Kim, J. K. Lee, J. H. Lee, and H. S. Chung, "Demonstration of IFoF-Based Mobile Fronthaul in 5G Prototype With 28-GHz Millimeter wave," *Journal of Lightwave Technology*, vol. 36, no. 2, pp. 601–609, Jan 2018.

[62] "IMT Vision – Framework and overall objectives of the future development of IMT for 2020 and beyond," ITU-R M.2083, Tech. Rep., 2015.

[63] L. Kong, M. K. Khan, F. Wu, G. Chen, and P. Zeng, "Millimeter-Wave Wireless Communications for IoT-Cloud Supported Autonomous Vehicles: Overview, Design, and Challenges," *IEEE Communications Magazine*, vol. 55, no. 1, pp. 62–68, January 2017.

[64] G. Pocovi, H. Shariatmadari, G. Berardinelli, K. Pedersen, J. Steiner, and Z. Li, "Achieving Ultra-Reliable Low-Latency Communications: Challenges and Envisioned System Enhancements," *IEEE Network*, vol. 32, no. 2, pp. 8–15, March 2018.

[65] C. Bockelmann, N. Pratas, H. Nikopour, K. Au, T. Svensson, C. Stefanovic, P. Popovski, and A. Dekorsy, "Massive machine-type communications in 5g: physical and MAC-layer solutions," *IEEE Communications Magazine*, vol. 54, no. 9, pp. 59–65, September 2016.

[66] "5G Usage Scenarios in Non-Standalone (NSA) and Standalone (SA) Operation." [Online]. Available: https://www.testandverification.com/telecommunications/5g-usage-scenarios-nsa-sa/

[67] J. Mei, K. Zheng, L. Zhao, Y. Teng, and X. Wang, "A Latency and Reliability Guaranteed Resource Allocation Scheme for LTE V2V Communication Systems," *IEEE Transactions on Wireless Communications*, vol. 17, no. 6, pp. 3850–3860, June 2018.

[68] W. Shieh, C. J. Hsu, and T. Wang, "Vehicle Positioning and Trajectory Tracking by Infrared Signal-Direction Discrimination for Short-Range Vehicle-to-Infrastructure Communication Systems," *IEEE Transactions on Intelligent Transportation Systems*, vol. 19, no. 2, pp. 368–379, Feb 2018.

[69] N. Xia, H. Chen, and C. Yang, "Radio Resource Management in Machine-to-Machine Communications—A Survey," *IEEE Communications Surveys Tutorials*, vol. 20, no. 1, pp. 791–828, Firstquarter 2018.

[70] Z. Pi and F. Khan, "An Introduction to Millimeter-wave Mobile Broadband Systems," *IEEE Communications Magazine*, vol. 49, no. 6, pp. 101–107, June 2011.

[71] H. Ishii, Y. Kishiyama, and H. Takahashi, "A novel architecture for LTE-B :C-plane/U-plane split and Phantom Cell concept," in *2012 IEEE Globecom Workshops*, Dec 2012, pp. 624–630.

[72] B. Yang, Z. Yu, J. Lan, R. Zhang, J. Zhou, and W. Hong, "Digital Beamforming-Based Massive MIMO Transceiver for 5G Millimeter-Wave Communications," *IEEE Transactions on Microwave Theory and Techniques*, vol. 66, no. 7, pp. 3403–3418, July 2018.

[73] R. W. Heath, N. González-Prelcic, S. Rangan, W. Roh, and A. M. Sayeed, "An Overview of Signal Processing Techniques for Millimeter Wave MIMO Systems," *IEEE Journal of Selected Topics in Signal Processing*, vol. 10, no. 3, pp. 436–453, April 2016.

[74] W. Roh, J. Seol, J. Park, B. Lee, J. Lee, Y. Kim, J. Cho, K. Cheun, and F. Aryanfar, "Millimeter-wave beamforming as an enabling technology for 5G cellular communications: theoretical feasibility and prototype results," *IEEE Communications Magazine*, vol. 52, no. 2, pp. 106–113, February 2014.

[75] S. Zihir, O. D. Gurbuz, A. Karroy, S. Raman, and G. M. Rebeiz, "A 60 GHz single-chip 256-element wafer-scale phased array with EIRP of 45 dBm using sub-reticle stitching," in *2015 IEEE Radio Frequency Integrated Circuits Symposium (RFIC)*, May 2015, pp. 23–26.

[76] W. Hong, K. Baek, and S. Ko, "Millimeter-Wave 5G Antennas for Smartphones: Overview and Experimental Demonstration," *IEEE Transactions on Antennas and Propagation*, vol. 65, no. 12, pp. 6250–6261, Dec 2017.

[77] "Understanding the 5G NR Physical Layer," KEYSIGHT TECNOLOGIES, Tech. Rep., 2017.

[78] A. A. Zaidi, R. Baldemair, V. Moles-Cases, N. He, K. Werner, and A. Cedergren, "OFDM Numerology Design for 5G New Radio to Support IoT, eMBB, and MBSFN," *IEEE Communications Standards Magazine*, vol. 2, no. 2, pp. 78–83, JUNE 2018.

[79] S. Parkvall, E. Dahlman, A. Furuskar, and M. Frenne, "NR: The New 5G Radio Access Technology," *IEEE Communications Standards Magazine*, vol. 1, no. 4, pp. 24–30, Dec 2017.

[80] "The first 5G standard is complete - so what's next?" QUALCOMM, Tech. Rep., 2018.

[81] M. Shafi, A. F. Molisch, P. J. Smith, T. Haustein, P. Zhu, P. D. Silva, F. Tufvesson, A. Benjebbour, and G. Wunder, "5G:A Tutorial Overview of Standards, Trials, Challenges, Deployment, and Practice," *IEEE Journal on Selected Areas in Communications*, vol. 35, no. 6, pp. 1201–1221, June 2017.

[82] A. A. Zaidi, R. Baldemair, H. Tullberg, H. Bjorkegren, L. Sundstrom, J. Medbo, C. Kilinc, and I. D. Silva, "Waveform and Numerology to Support 5G Services and Requirements," *IEEE Communications Magazine*, vol. 54, no. 11, pp. 90–98, November 2016.

[83] J. Jeon, "NR Wide Bandwidth Operations," *IEEE Communications Magazine*, vol. 56, no. 3, pp. 42–46, MARCH 2018.

[84] S. Lien, S. Shieh, Y. Huang, B. Su, Y. Hsu, and H. Wei, "5G New Radio: Waveform, Frame Structure, Multiple Access, and Initial Access," *IEEE Communications Magazine*, vol. 55, no. 6, pp. 64–71, 2017.

[85] "Ran1 chairma's notes," 3GPP TSG RAN WG1 Meeting 85, Tech. Rep., 2016.

[86] "Study on New Radio Access Tecnology Physical Layer aspects," 3GPP, Tech. Rep., 2017.

[87] Y. Ghasempour, C. R. C. M. da Silva, C. Cordeiro, and E. W. Knightly, "IEEE 802.11ay: Next-Generation 60 GHz Communication for 100 Gb/s Wi-Fi," *IEEE Communications Magazine*, vol. 55, no. 12, pp. 186–192, DECEMBER 2017.

[88] "IEEE Draft Standard for Information Technology–Telecommunications and Information Exchange Between Systems Local and Metropolitan Area Networks–Specific Requirements Part 11: Wireless LAN Medium Access Control (MAC) and Physical Layer (PHY) Specifications–Amendment: Enhanced Throughput for Operation in License-Exempt Bands Above 45 GHz," *IEEE P802.11ay/D2.0, July 2018*, pp. 1–673, Jan 2018.

[89] e. a. Alexander Maltsev, "Channel Models for IEEE 802.11ay - doc.: IEEE 802.11-15/1150r9," Tech. Rep., may 2016.

[90] P. Zhou, K. Cheng, X. Han, X. Fang, Y. Fang, R. He, Y. Long, and Y. Liu, "Ieee 802.11ay-based mmwave wlans: Design challenges and solutions," *IEEE Communications Surveys Tutorials*, vol. 20, no. 3, pp. 1654–1681, thirdquarter 2018.

[91] D. Stanleyl, *IETF 95-Wireless Tutorial: IEEE 802.11 - doc.: IEEE 802.11-16/0500r0*, march 2016.

[92] "3GPP Defined 5G Requirements and Evaluation Conditions," *NTT DOCOMO Tecnical Journal*, vol. 19, no. 3, pp. 13–23, Jan. 2018.

[93] "mmWave Access and Backhaul Link Tests and Presentation of Final Demonstrator D6.5," MiWaveS, Tech. Rep. 1, June 2017.

[94] "PXI Express - NI PXIe-1085 Series User Manual," 2018. [Online]. Available: http://www.ni.com/pdf/manuals/373712j.pdf

[95] G. Yue, Z. Wang, L. Chen, L. Cheng, J. Tang, X. Zou, Y. Zeng, and L. Li, "Demonstration of 60 GHz Millimeter-wave Short-range Wireless Communication System at 3.5 Gbps Over 5 M Range," *Science China Information Sciences*, vol. 60, no. 8, p. 080306, Jun 2017.

[96] T. Obara, T. Okuyama, Y. Aoki, S. Suyama, J. Lee, and Y. Okumura, "Indoor and outdoor experimental trials in 28-GHz band for 5G wireless communication systems," in *2015 IEEE 26th Annual International Symposium on Personal, Indoor, and Mobile Radio Communications (PIMRC)*, Aug 2015, pp. 846–850.

[97] J. Mashino, K. Satoh, S. Suyama, Y. Inoue, and Y. Okumura, "5G Experimental Trial of 28 GHz Band Super Wideband Transmission Using Beam Tracking in Super High Mobility Environment," in *2017 IEEE 85th Vehicular Technology Conference (VTC Spring)*, June 2017, pp. 1–5.

[98] "Final Radio Interface Concepts and Evaluations for Mm-Wave Mobile Communications D4.2," Millimetre-Wave Based Mobile Radio Access Network for Fifth Generation Integrated Communications (mmMAGIC), Tech. Rep. 1, June 2017.

[99] D. Shin, S. Suyama, H. Suzuki, and K. Fukawa, "10 Gbps Millimeter-wave OFDM Experimental System with Iterative Phase Noise Compensation," in *2013 IEEE Radio and Wireless Symposium*, Jan 2013, pp. 184–186.

[100] J. Zhang, X. Zhang, P. Kulkarni, and P. Ramanathan, "OpenMili: A 60 GHz Software Radio with a Programmable Phased-array Antenna: Demo," in *Proceedings of the 22Nd Annual International Conference on Mobile Computing and Networking*, ser. MobiCom '16. New York, NY, USA: ACM, 2016, pp. 485–486. [Online]. Available: http://doi.acm.org/10.1145/2973750.2985614

[101] D. Cvetkovski, E. Grass, T. Hälsig, and B. Lankl, "Hardware-in-the-loop demonstration of a 60 GHz line-of-sight 2x2 MIMO link," in *IEEE EUROCON 2017 -17th International Conference on Smart Technologies*, July 2017, pp. 631–636.

[102] P. Zetterberg and R. Fardi, "Open Source SDR Frontend and Measurements for 60-GHz Wireless Experimentation," *IEEE Access*, vol. 3, pp. 445–456, 2015.

[103] K. Sobaihi, A. Hammoudeh, and D. Scammell, "64.8 GHz Wireless Personal Area Network Characterisation Using Single-carrier Frequency Domain Equalisation for Indoor Channels," *IET Microwaves, Antennas Propagation*, vol. 7, no. 8, pp. 635–643, June 2013.

[104] Y. Inoue, Y. Kishiyama, S. Suyama, J. Kepler, M. Cudak, and Y. Okumura, "Field Experiments on 5G mmW Radio Access with Beam Tracking in Small Cell Environments," in *2015 IEEE Globecom Workshops (GC Wkshps)*, Dec 2015, pp. 1–6.

[105] S. Mittal, S. Gupta, and S. Dasgupta, "System generator : The state-of-art fpga design tool for dsp applications," 2009.

[106] Y. Choand and W. Yang, *MIMO-OFDM Wireless Communications with MATLAB*. Wiley.

[107] J. Zhang and Z. Zhang, "Simulation and analysis of OFDM system based on simulink," in *2010 International Conference on Communications, Circuits and Systems (ICCCAS)*, Jul. 2010, pp. 28–31.

[108] W. Y. Yang, Y. S. Cho, W. G. Jeon, J. W. Lee, J. H. Paik, J. K. Kim, M.-H. Lee, K. I. Lee, K. W. Park, and K. S. Woo, *MATLAB/Simulink for Digital Communication*, second edition ed. A-Jin Publishing Co, 2009.

[109] B. Farhang-Boroujeny, "OFDM Versus Filter Bank Multicarrier," *IEEE Signal Processing Magazine*, vol. 28, no. 3, pp. 92–112, May 2011.

[110] Fabrizio Pancaldi, Giorgio M. Vitetta, Reza kalbasi, Naofal Al-Dhahir, Murat Uysal, and Hakam Mheidat, "Single-Carrier Frequency Domain Equalization - A Focus on Wireless Applications," *IEEE SIGNAL PROCESSING MAGAZINE*, Sep. 2008.

[111] Y. Wang and X. Dong, "Comparison of Frequency Offset and Timing Offset Effects on the Performance of SC-FDE and OFDM Over UWB Channels," *IEEE Transactions on Vehicular Technology*, vol. 58, no. 1, pp. 242–250, Jan 2009.

[112] A. Sahin, I. Guvenc, and H. Arslan, "A Survey on Multicarrier Communications: Prototype Filters, Lattice Structures, and Implementation Aspects," *Communications Surveys Tutorials, IEEE*, vol. 16, no. 3, pp. 1312–1338, Third 2014.

[113] "FBMC Physical Layer: A Primer," Tech. Rep. 1, June 2010.

[114] M. Bellanger, "FS-FBMC: A Flexible Robust Scheme for Efficient Multicarrier Broadband Wireless Access," in *Globecom Workshops (GC Wkshps), 2012 IEEE*, Dec 2012, pp. 192–196.

[115] U. H. Rizvi, G. J. M. Janssen, and J. H. Weber, "Impact of RF Impairments on the Performance of Multi-carrier and Single-carrier based 60 GHz Transceivers," in *2007 14th IEEE Symposium on Communications and Vehicular Technology in the Benelux*, Nov 2007, pp. 1–5.

[116] F. M. Gardner, *Phaselock Techniques: Third Edition*. Wiley, 07 2005.

[117] C.-S. Choi, Y. Shoji, H. Harada, R. Funada, S. Kato, K. Maruhashi, I. Toyoda, and K. Takahashi, "RF impairment models for 60 GHz-band SYS/PHY simulation - doc.: IEEE 802.15-06-0477-01-003c," IEEE P802.15 Working Group for Wireless Personal Area Networks (WPANs), Tech. Rep., Nov. November 2006.

[118] S. C. Cripps, *Advanced Techniques in RF Power Amplifier Design*. Norwood, MA, USA: Artech House, Inc., 2002.

[119] ——, *RF Power Amplifiers for Wireless Communications*. Norwood, MA, USA: Artech House, Inc., 2006.

[120] Christoph Rapp, "Effects of HPA-nonlinearity on a 4-DPSK/OFDM-signal for a Digital Sound Broadcasting System," 1991.

[121] V. Erceg et al, "60 GHz Impairments Modeling," Tech. Rep., Nov. 2009.

[122] M. Varonen, M. Karkkainen, and K. A. I. Halonen, "Millimeter-wave Amplifiers in 65-nm CMOS," in *ESSCIRC 2007 - 33rd European Solid-State Circuits Conference*, Sep. 2007, pp. 280–283.

[123] Su-Khiong Yong, "TG3c Channel Modeling Sub-committee Final Report," Tech. Rep., Mar. 2007.

[124] A. A. M. Saleh and R. Valenzuela, "A Statistical Model for Indoor Multipath Propagation," *IEEE Journal on Selected Areas in Communications*, vol. 5, no. 2, pp. 128–137, February 1987.

[125] Q. H. Spencer, B. D. Jeffs, M. A. Jensen, and A. L. Swindlehurst, "Modeling the Statistical Time and Angle of Arrival Characteristics of an Indoor Multipath Channel," *IEEE Journal on Selected Areas in Communications*, vol. 18, no. 3, pp. 347–360, March 2000.

[126] Hiroshi Harada, Ryuhei Funada, Hirokazu Sawada, and Shuzo Kato, *CM MATLAB Release Support Document*, Mar. 2007.

[127] P. Gallo, S. Loi, and P. Priotti, "Transmission Range Analysis of IEEE 802.15.3c Technology in Residential Environments," in *Telecommunications: The Infrastructure for the 21st Century*, Sep. 2010, pp. 1–6.

[128] T. Baykas, M. Lei, C.-S. Sum, R. Funada, Y. Nishiguchi, and R. Kimura, "Operation Range Estimation of Reed-Solomon Coded SC-FDE System in 60-GHz WPANs," in *10th International Conference on Advanced Communication Technology, 2008. ICACT 2008*, vol. 1, Feb. 2008, pp. 167–170.

[129] M. Lei, I. Lakkis, H. Harada, and S. Kato, "MMSE-FDE Based on Estimated SNR for Single-Carrier Block Transmission (SCBT) in Multi-Gbps WPAN (IEEE 802.15.3c)," in *IEEE International Conference on Communications Workshops, 2008. ICC Workshops '08*, May 2008, pp. 52–56.

[130] N. Bonello, S. Chen, and L. Hanzo, "Design of Low-density Parity-check Codes: An Overview," *IEEE VechicularTechnology Magazine*, vol. 6, no. 4, pp. 16–23, Dec. 2011.

[131] C. E. Shannon, "A Mathematical Theory of Communication," *The Bell System Technical Journal*, vol. 27, no. 3, pp. 379–423, July 1948.

[132] Henrik Schulze and Christian Luders, *Theory and Applications of OFDM and CDMA*. Wiley.

[133] H. K. Kim et al, *IAENG Transactions on Engineering Technologies : Special Edition of the World Congress on Engineering and Computer Science 2011* . Springer Science & Business Media, sep 2012.

[134] B. M. Popovic, "Efficient Golay Correlator," *Electronics Letters*, vol. 35, no. 17, pp. 1427–1428, Aug 1999.

[135] M. Lei and Y. Huang, "CFR and SNR Estimation Based on Complementary Golay Sequences for Single-Carrier Block Transmission in 60-GHz WPAN," in *IEEE Wireless Communications and Networking Conference, 2009. WCNC 2009*, Apr. 2009, pp. 1–5.

[136] H. Bouhadda, H. Shaiek, D. Roviras, R. Zayani, Y. Medjahdi, and R. Bouallegue, "Theoretical Analysis of BER Performance of Nonlinearly Amplified FBMC/OQAM and OFDM Signals," *EURASIP Journal on Advances in Signal Processing*, vol. 2014, no. 1, p. 60, 2014. [Online]. Available: http://asp.eurasipjournals.springeropen.com/articles/10.1186/1687-6180-2014-60

[137] V. Berg, J. B. Dore, and D. Noguet, "A Flexible FS-FBMC Receiver for Dynamic Access in the TVWS," in *Cognitive Radio Oriented Wireless Networks and Communications (CROWNCOM), 2014 9th International Conference on*, June 2014, pp. 285–290.

[138] Q. He and A. Schmeink, "Comparison and Evaluation between FBMC and OFDM Systems," in *WSA 2015; 19th International ITG Workshop on Smart Antennas; Proceedings of*, Mar. 2015, pp. 1–7.

[139] R. W. Stewart, K. W. Barlee, D. S. W. Atkinson, and L. H. Crockett, *Software Defined Radio Using MATLAB & Simulink and the RTL-SDR*. UK: Strathclyde Academic Media, 2015.

[140] "Software-defined radio," https://www.winradio.com/home/facts.htm, accessed: 2017-10-18.

[141] S. Bronckers, A. Roc'h, and B. Smolders, "Wireless Receiver Architectures Towards 5G: Where Are We?" *IEEE Circuits and Systems Magazine*, vol. 17, no. 3, pp. 6–16, thirdquarter 2017.

[142] I. Kuon and J. Rose, "Measuring the Gap Between FPGAs and ASICs," *IEEE Transactions on Computer-Aided Design of Integrated Circuits and Systems*, vol. 26, no. 2, pp. 203–215, Feb 2007.

[143] "Field Programmable Gate Array (FPGA)," https://www.xilinx.com/products/silicon-devices/fpga/what-is-an-fpga.html, accessed: 2017-03-08.

[144] W. Paper, "FPGA vs ASIC," Xilinx, Tech. Rep., 2006.

[145] "VITA 57 (FMC) opens the I/O pipe to FPGAs." [Online]. Available: http://vita.mil-embedded.com/articles/vita-fmc-opens-io-pipe-fpgas/

[146] W. Paper, "I/O Design Flexibility with the FPGA Megazzine Card (FMC)," Xilinx, Tech. Rep., 2009.

[147] https://www.xilinx.com/support/documentation/selection-guides/ultrascale-plus-fpga-product-selection-guide.pdf.

[148] https://www.xilinx.com/products/boards-and-kits/ek-v7-vc707-g.html.

[149] https://www.xilinx.com/support/documentation/selection-guides/7-series-product-selection-guide.pdf.

[150] "FMC Cards." [Online]. Available: https://www.xilinx.com/products/boards-and-kits/fmc-cards.html

[151] "http://www.4dsp.com/FMC126.php."

[152] "http://www.4dsp.com/FMC230.php."

[153] UM009 FMC12x, "FMC122/FMC125/FMC126: User Manual," 4DSP, Tech. Rep., 2014.

[154] UM023 FMC230, "FMC230: User Manual," 4DSP, Tech. Rep., 2015.

[155] "EV10AQ190 Datasheet," https://www.teledyne-e2v.com/resources/account/download-datasheet/1735, accessed: 2017-01-08.

[156] "12-output clock generator with integrated 2.8 ghz vco - datasheet."

[157] "11-/14-bit, 5.7 gsps, rf digital-to-analog converter - datasheet."

[158] CD336 VC707 + FMC230, "FMC230: Reference Firmware for VC707," 4DSP, Tech. Rep., 2015.

[159] CD244 VC707 + FMC230, "FMC126: Reference Firmware for VC707," 4DSP, Tech. Rep., 2015.

[160] W. Paper, "Designing IP Subsystems Using IP Integrator," Xilinx, Tech. Rep., 2018.

[161] 4DSP, "4FM Gettting Started Guide," 4DSP, Tech. Rep., 2012.

[162] UG940, "Vivado Design Suite Tutorial: Embedded Processor Hardware Design," Xilinx, Tech. Rep., 2017.

[163] UG761, "AXI Reference Guide," Xilinx, Tech. Rep., 2011.

[164] PCA9548A, "Low Voltage 8-Channel I2C Switch with Reset," Texas Instruments, Tech. Rep., 2015.

[165] "System Generator for DSP:Define, Test and Implement high-performance DSP Designs," https://www.xilinx.com/products/design-tools/vivado/integration/sysgen.html.

[166] W. Paper, "Model-Based Design with Simulink, and Xilinx System Generator for DSP," MathWorks, Tech. Rep., 2012.

[167] P. P. Vaidyanathan, "Multirate digital filters, filter banks, polyphase networks, and applications: a tutorial," *Proceedings of the IEEE*, vol. 78, no. 1, pp. 56–93, Jan 1990.

[168] A. Mertins and D. A. Mertins, *Signal Analysis: Wavelets, Filter Banks, Time-Frequency Transforms and Applications (chapter 6)*. New York, NY, USA: John Wiley & Sons, Inc., 1999.

[169] B. Farhang-Boroujeny, "Filter Bank Spectrum Sensing for Cognitive Radios," *IEEE Transactions on Signal Processing*, vol. 56, no. 5, pp. 1801–1811, May 2008.

[170] T. Pereira, M. Violas, J. Lourenço, A. Gameiro, A. Silva, and C. Ribeiro, "An FPGA Implementation of OFDM Transceiver for LTE Applications," *Intrnl. Journal On Advances in Systems and Measurements*, vol. 6, no. 1-2, pp. 224–234, June 2013.

[171] W. Wenzhao, C. Yaqin, and Z. Qi, "Implementation of Mixed Feedback/Feedforward Analog and Digital AGC," in *ICMMT 4th International Conference on, Proceedings Microwave and Millimeter Wave Technology, 2004.*, Aug 2004, pp. 377–381.

[172] "MAX2090 Analogue VGA," https://www.maximintegrated.com/en/products/comms/wireless-rf/MAX2090.html, accessed: 2017-09-18.

[173] "Analog Devices HMC1030," http://www.analog.com/en/products/rf-microwave/rf-power-detectors/envelope-peak-detectors/hmc1030.html#product-overview, accessed: 2017-09-18.

[174] J. H. Jang and H. J. Choi, "A fast automatic gain control scheme for 3gpp lte tdd system," in *2010 IEEE 72nd Vehicular Technology Conference - Fall*, Sep. 2010, pp. 1–5.

[175] L. Verma, M. Fakharzadeh, and S. Choi, "WiFi on Steroids: 802.11ac and 802.11ad," *IEEE Wireless Communications*, vol. 20, no. 6, pp. 30–35, December 2013.

[176] P. Smulders, "Exploiting the 60 GHz band for Local Wireless Multimedia Access: Prospects and Future Directions," *IEEE Communications Magazine*, vol. 40, no. 1, pp. 140–147, Jan 2002.

[177] H. Xu, V. Kukshya, and T. S. Rappaport, "Spatial and Temporal Characteristics of 60-GHz Indoor Channels," *IEEE J.Sel. A. Commun.*, vol. 20, no. 3, pp. 620–630, Sep. 2006. [Online]. Available: http://dx.doi.org/10.1109/49.995521

[178] R. C. Daniels and R. W. H. Jr., "60 GHz Wireless Communications: Emerging Requirements and Design Recommendations," *IEEE Vehicular Technology Magazine*, vol. 2, no. 3, pp. 41–50, Sept 2007.

[179] J. Kim, J.-J. Lee, and W. Lee, "Strategic Control of 60 GHz Millimeter-Wave High-Speed Wireless Links for Distributed Virtual Reality Platforms," vol. 2017, pp. 1–10, 01 2017.

[180] F. Gutierrez, S. Agarwal, K. Parrish, and T. S. Rappaport, "On-chip Integrated Antenna Structures in CMOS for 60 GHz WPAN Systems," *IEEE Journal on Selected Areas in Communications*, vol. 27, no. 8, pp. 1367–1378, October 2009.

[181] "TP Link WiGig Router," http://static.tp-link.com/AD7200_V2_User%20Guide.pdf, accessed: 2017-09-18.

[182] "Netgear WiGig Router," https://www.netgear.com/images/datasheet/netw\orking/wifirouter/R9000.pdf, accessed: 2017-09-18.

[183] "Dell Latitude," https://www.dell.com/en-us/work/shop/dell-laptops-and-notebooks/latitude-5414/spd/latitude-14-5414-laptop/xctol541414us, accessed: 2017-09-18.

[184] "EK1HMC6350 RF Front-End," http://www.analog.com/media/en/techni\cal-documentation/user-guides/EK1HMC6350-UG-1031.pdf, accessed: 2017-09-18.

[185] "PEM009 RF Front-End," https://www.pasternack.com/images/ProductPDF/PEM009-KIT.pdf, accessed: 2017-09-18.

[186] T. Wei and X. Zhang, "mTrack: High-Precision Passive Tracking Using Millimeter Wave Radios," in *Proceedings of the 21st Annual International Conference on Mobile Computing and Networking*, ser. MobiCom '15. New York, NY, USA: ACM, 2015, pp. 117–129. [Online]. Available: http://doi.acm.org/10.1145/2789168.2790113

[187] Y. Zeng, P. H. Pathak, Z. Yang, and P. Mohapatra, "Poster Abstract: Human Tracking and Activity Monitoring Using 60 GHz mmWave," in *2016 15th ACM/IEEE International Conference on Information Processing in Sensor Networks (IPSN)*, April 2016, pp. 1–2.

[188] A. Olivier, "Design, Simulation and Experimental Evaluation of Indoor Localization Schemes for 60 GHz Millimeter Wave Systems," Master's thesis, Dep. of Information Eng., University of Padova, Italy, 2015.

[189] Y. Ghasempour and E. W. Knightly, "Decoupling Beam Steering and User Selection for Scaling Multi-User 60 GHz WLANs," in *Proceedings of the 18th ACM International Symposium on Mobile Ad Hoc Networking and Computing*, ser. Mobihoc '17. New York, NY, USA: ACM, 2017, pp. 10:1–10:10. [Online]. Available: http://doi.acm.org/10.1145/3084041.3084050

[190] R. N. Foster et al, "Beam-Steering Performance of Flat Luneburg Lens at 60 GHz for Future Wireless Communications," 2017.

[191] T. Nitsche, G. Bielsa, I. Tejado, A. Loch, and J. Widmer, "Boon and Bane of 60 GHz Networks: Practical Insights into Beamforming, Interference, and Frame Level Operation," in *Proceedings of the 11th ACM Conference on Emerging Networking Experiments and Technologies*, ser. CoNEXT '15. New York, NY, USA: ACM, 2015, pp. 17:1–17:13. [Online]. Available: http://doi.acm.org/10.1145/2716281.2836102

[192] "PEM009 TX Board," https://www.pasternack.com/images/ProductPDF/PE\M010.pdf, accessed: 2017-09-18.

[193] A. Tarighat, R. Bagheri, and A. H. Sayed, "Compensation Schemes and Performance Analysis of IQ Imbalances in OFDM Receivers," *IEEE Transactions on Signal Processing*, vol. 53, no. 8, pp. 3257–3268, Aug 2005.

[194] N. J. Kasdin, "Discrete Simulation of Colored Noise and Stochastic Processes and 1/f Alpha; Power Law Noise Generation," *Proceedings of the IEEE*, vol. 83, no. 5, pp. 802–827, May 1995.

[195] M. Billinghurst and A. Duenser, "Augmented Reality in the Classroom," *Computer*, vol. 45, no. 7, pp. 56–63, July 2012.

[196] S. Barma, S. Daniel, N. Bacon, M.-A. Gingras, and M. Fortin, "Observation and Analysis of a Classroom Teaching and Learning Practice Based on Augmented Reality and Serious Games on Mobile Platforms," *International Journal of Serious Games*, vol. 2, no. 2, jun 2015. [Online]. Available: https://doi.org/10.17083/ijsg.v2i2.66

[197] S. Matsutomo, T. Manabe, V. Cingoski, and S. Noguchi, "A Computer Aided Education System Based on Augmented Reality by Immersion to 3-D Magnetic Field," *IEEE Transactions on Magnetics*, vol. 53, no. 6, pp. 1–4, June 2017.

[198] W. Paper, "Augmented and Virtual Reality: the First Wave of 5G Killer Apps," ABI Research, Qualcomm, Tech. Rep., 2017.

[199] J. M. F. H. Alisha Seam; Amy Poll; Remound Wright, "Enabling Mobile Augmented and Virtual Reality with 5G Networks," AT&T Foundry, Tech. Rep., 2017.

[200] C. Anthes, R. J. García-Hernández, M. Wiedemann, and D. Kranzlmüller, "State of the Art of Virtual Reality Technology," in *2016 IEEE Aerospace Conference*, March 2016, pp. 1–19.

[201] M. Schneider, J. Rambach, and D. Stricker, "Augmented Reality Based on Edge Computing Using the Example of Remote Live Support," in *2017 IEEE International Conference on Industrial Technology (ICIT)*, March 2017, pp. 1277–1282.

[202] W. Paper, "GPU vs FPGA Performance Comparison," BERTEN Digital Signal Processing, Tech. Rep., 5 2016.

[203] "HTC Vive Pro," https://www.vive.com/us/product/vive-pro/, accessed: 2018-03-08.

[204] "Samsung Gear VR," http://www.samsung.com/pt/gear-vr/, accessed: 2018-03-08.

[205] "Meta Vision," http://www.metavision.com, accessed: 2018-03-08.

[206] "Microsoft Hololens," https://www.microsoft.com/pt-pt/hololens, accessed: 2018-03-08.

[207] T. Research, "The First Billion Users: Powering Virtual Reality with Advanced Video Encoding & Rendering," 2018.

[208] W. Paper, "IEEE 5G and Beyond Technology Roadmap," IEEE, Tech. Rep., 2017.

[209] N. T. Hieu, B. H. Phu, V. D. Thanh, and Y. Ogawa, "FPGA Implementation of MIMO OFDM Eigenbeam-Space Division Multiplexing Systems for Future Wireless Communications Networks," in *2013 IEEE 78th Vehicular Technology Conference (VTC Fall)*, Sept 2013, pp. 1–5.

[210] T. H. Liu, Y. J. Chen, Y. K. Ko, Y. C. Lin, and Y. S. Chu, "Hardware Implementation of the Compressed Beamforming Weights Calculation for the Practical Wireless MIMO-OFDM Communication System," *IEEE Transactions on Circuits and Systems II: Express Briefs*, vol. PP, no. 99, pp. 1–1, 2017.

[211] K. Neshatpour, M. Mahdavi, and M. Shabany, "A Low-complexity High-throughput ASIC for the SC-FDMA MIMO Detectors," in *2012 IEEE International Symposium on Circuits and Systems*, May 2012, pp. 3065–3068.

[212] G. Wang, B. Yin, K. Amiri, Y. Sun, M. Wu, and J. R. Cavallaro, "FPGA Prototyping of a High Data Rate LTE Uplink Baseband Receiver," in *2009 Conference Record of the Forty-Third Asilomar Conference on Signals, Systems and Computers*, Nov 2009, pp. 248–252.

[213] F. Wu, Y. Li, and M. Zhao, "Estimation of TX I/Q Imbalance at the RX Side with RX I/Q Imbalance and Carrier Frequency Offset for OFDM Systems," in *2014 IEEE Globecom Workshops (GC Wkshps)*, Dec 2014, pp. 960–965.

[214] M. Wu, C. Dick, J. R. Cavallaro, and C. Studer, "High-Throughput Data Detection for Massive MU-MIMO-OFDM Using Coordinate Descent," *IEEE Transactions on Circuits and Systems I: Regular Papers*, vol. 63, no. 12, pp. 2357–2367, Dec 2016.

[215] R. Gupta, T. Vogel, N. Kundargi, A. Ekbal, A. Morelli, V. Mancuso, V. Sciancalepore, R. Ford, and S. Rangan, "LabVIEW Based Platform for Prototyping Dense LTE Networks in CROWD Project," in *2014 European Conference on Networks and Communications (EuCNC)*, June 2014, pp. 1–5.

[216] "How to choose a verification methodology | EE Times." [Online]. Available: http://www.eetimes.com/document.asp?doc_id=1217826

[217] E. L. Bengtsson, F. Rusek, S. Malkowsky, F. Tufvesson, P. C. Karlsson, and O. Edfors, "A Simulation Framework for Multiple-Antenna Terminals in 5G Massive MIMO Systems," *IEEE Access*, vol. 5, pp. 26 819–26 831, 2017.

[218] D. Castanheira, P. Lopes, A. Silva, and A. Gameiro, "Hybrid Beamforming Designs for Massive MIMO Millimeter-Wave Heterogeneous Systems," *IEEE Access*, vol. 5, pp. 21 806–21 817, 2017.

[219] J. J. van de Beek, M. Sandell, and P. O. Borjesson, "ML Estimation of Time and Frequency Offset in OFDM Systems," *IEEE Transactions on Signal Processing*, vol. 45, no. 7, pp. 1800–1805, Jul 1997.

[220] W. Paper, "Making 5G NR a commercial reality," Qualcomm, Tech. Rep., 12 2016.

[221] A. Salari, S. M. Fakhraie, and A. Abbasfar, "Algorithm and FPGA Implementation of Interpolation-based Soft Output MMSE MIMO Detector for 3GPP LTE," *IET Communications*, vol. 8, no. 4, pp. 492–499, March 2014.

[222] J. S. Park and T. Ogunfunmi, "Efficient FPGA-Based Implementations of MIMO-OFDM Physical Layer," *Circuits, Systems, and Signal Processing*, vol. 31, no. 4, pp. 1487–1511, 2012.

[223] "USRP X310," https://www.ettus.com/product/details/X310-KITl.

[224] W. Paper, "Introduction to the NI mmWave Transceiver System Hardware," NI, Tech. Rep., 2018.

[225] "NI PXI mmWave Transceiver Bundle," http://sine.ni.com/nips/cds/view/p/lang/pt/nid/213722l.

[226] "NI PXI waveform genator," https://www.ni.com/pt-pt/shop/select/pxi-waveform-generator.

[227] K. Haneda, J. Zhang, L. Tan, G. Liu, Y. Zheng, H. Asplund, J. Li, Y. Wang, D. Steer, C. Li, T. Balercia, S. Lee, Y. Kim, A. Ghosh, T. Thomas, T. Nakamura, Y. Kakishima, T. Imai, H. Papadopoulos, T. S. Rappaport, G. R. MacCartney, M. K. Samimi, S. Sun, O. Koymen, S. Hur, J. Park, C. Zhang, E. Mellios, A. F. Molisch, S. S. Ghassamzadeh, and A. Ghosh, "5G 3GPP-Like Channel Models for Outdoor Urban Microcellular and Macrocellular Environments," pp. 1–7, May 2016.

[228] 3GPP, "Study on 3D channel model for LTE," 3GPP 36.873 (V12.2.0), Tech. Rep., July 2015.

[229] E. T. . 901, "5G; Study on channel model for frequencies from 0.5 to 100 GHz," 3GPP TR 38.901 version 14.3.0 Release 14, Tech. Rep., January 2018.

[230] "X microwave Getting Started Guide," X microwave, Tech. Rep., 2018.

[231] A. F. Molisch, *Wireless Communications*, 2nd ed. Wiley Publishing, 2011.

[232] S. M. Alamouti, "A Simple Transmit Diversity Technique for Wireless Communications," *IEEE Journal on Selected Areas in Communications*, vol. 16, no. 8, pp. 1451–1458, Oct 1998.

[233] T. F. Collins, R. Getz, D. Pu, and A. M. Wyglinski, *Software-Defined Radio for Engineers*. Analog Devices, 2018.

[234] M. Patzold, *Mobile Fading Channels: Modelling,Analysis and Simulation*. New York, NY, USA: John Wiley & Sons, Inc., 2001.

[235] K.-L. Du and M. N. S. Swamy, *Wireless Communication Systems: From RF Subsystems to 4G Enabling Technologies*. New York, NY, USA: Cambridge University Press, 2010.

[236] H. Yang, Smulders, and Herben, "Indoor Channel Measurements and Analysis in the Frequency Bands 2 GHz and 60 GHz," in *2005 IEEE 16th International Symposium on Personal, Indoor and Mobile Radio Communications*, vol. 1, Sept 2005, pp. 579–583.

[237] S. Deng, M. K. Samimi, and T. S. Rappaport, "28 Ghz and 73 Ghz Millimeter-wave Indoor Propagation Measurements and Path Loss Models," in *2015 IEEE International Conference on Communication Workshop (ICCW)*, June 2015, pp. 1244–1250.

[238] J. A. Dabin, N. Ni, A. M. Haimovich, E. Niver, and H. Grebel, "The effects of antenna directivity on path loss and multipath propagation in UWB indoor wireless channels," in *IEEE Conference on Ultra Wideband Systems and Technologies, 2003*, Nov 2003, pp. 305–309.

[239] M. Ibnkahla, *Adaptive Signal Processing in Wireless Communications*, 1st ed. Boca Raton, FL, USA: CRC Press, Inc., 2008.

[240] J. Nsenga, W. V. Thillo, F. Horlin, A. Bourdoux, and R. Lauwereins, "Comparison of OQPSK and CPM for Communications at 60 GHz with a Nonideal Front End," *EURASIP Journal on Wireless Communications and Networking*, vol. 2007, no. 1, p. 086206, Mar. 2007. [Online]. Available: http://jwcn.eurasipjournals.com/content/2007/1/086206/abstract

[241] H. Mehrpouyan et al, "Improving Bandwidth Efficiency in E-band Communication Systems," *IEEE Communications Magazine*, vol. 52, no. 3, pp. 121–128, 2014.

[242] N. Guo, R. C. Qiu, S. S. Mo, and K. Takahashi, "60-GHz Millimeter-Wave Radio: Principle, Technology, and New Results," *EURASIP Journal on Wireless Communications and Networking*, vol. 2007, no. 1, p. 068253, Dec. 2006. [Online]. Available: http://jwcn.eurasipjournals.com/content/2007/1/068253/abstract

[243] P. Cruz, H. Gomes, and N. Carvalho, "Receiver Front-End Architectures – Analysis and Evaluation," in *Advanced Microwave and Millimeter Wave Technologies*, M. Mukherjee, Ed. Rijeka: IntechOpen, 2010, ch. 25. [Online]. Available: https://doi.org/10.5772/8744

[244] F. Ellinger, *Radio Frequency Integrated Circuits and Technologies*, 2nd ed. Springer Publishing Company, Incorporated, 2008.

[245] J. Mitola, "The Software Radio Architecture," *IEEE Communications Magazine*, vol. 33, no. 5, pp. 26–38, May 1995.

[246] J. Chu, "Nonlinear Distortion in Wireless Systems [BookSoftware Reviews]," *IEEE Microwave Magazine*, vol. 16, no. 2, pp. 106–107, March 2015.

[247] P. Roblin, M. Rawat, and V. Ratnasamy, "RF Front-End Flexibility, Self-Calibration, and Self-Linearization: Characterizing and Mitigating Nonlinearities in SDR MIMO Systems for Concurrent Multiband Operation," *IEEE Microwave Magazine*, vol. 19, no. 2, pp. 49–61, March 2018.

[248] Q. Zou, A. Tarighat, and A. H. Sayed, "Joint Compensation of IQ Imbalance and Phase Noise in OFDM Wireless Systems," *IEEE Transactions on Communications*, vol. 57, no. 2, pp. 404–414, February 2009.

[249] C. Yih, "Analysis and Compensation of DC Offset in OFDM Systems Over Frequency-Selective Rayleigh Fading Channels," *IEEE Transactions on Vehicular Technology*, vol. 58, no. 7, pp. 3436–3446, Sept 2009.

[250] M. Windisch and G. Fettweis, "Blind Estimation and Compensation of I/Q Imbalance in OFDM Receivers with Enhancements Through Kalman Filtering," in *2007 IEEE/SP 14th Workshop on Statistical Signal Processing*, Aug 2007, pp. 754–758.

[251] R. Lyons, *Understanding Digital Signal Processing (3rd Edition)*, 08 2011.

[252] "Defining and Testing Dynamic Parameters in HighSpeed ADCs," Maxim Integrated, Tech. Rep., 2001.

[253] W. Misch, "Understand SINAD, ENOB, SNR, THD, THD + N, and SFDR so You Don't Get Lost in the Noise Floor," Tech. Rep., 2009.

[254] Y. Geerts, M. Steyaert, W. Sansen, S. M. Geerts, Y., and M. Sansen, *Design of Multi-bit Delta-sigma A/D Converters*. In The international series in engineering and computer science: Kluwer Academic Publishers, 2003, vol. 686.

[255] S. Semenov and E. Krouk, *Modulation and Coding Techniques in Wireless Communications*, 1st ed. Wiley Publishing, 2011.

[256] "Digital Modulation in Communication Systems," Agilent Tecnologies, Tech. Rep., 2001.

[257] R. A. Shafik, M. S. Rahman, and A. R. Islam, "On the Extended Relationships Among EVM, BER and SNR as Performance Metrics," in *2006 International Conference on Electrical and Computer Engineering*, Dec 2006, pp. 408–411.

This page is intentionally left blank.

APPENDIX A

Communication theory

A.1 Introduction

In nowadays, the design of modern communication systems requires the combination of digital processing with analogue RF architectures. For example, digital signal processing has progressed to such an extent that in advanced systems, the majority of the PHY layer functions are implemented in re-configurable hardware [233]. This enables the typical RF components of a radio communication system, e.g. mixers, filters, amplifiers, detector, to be implemented by software, in the digital domain. Such systems are traditionally composed of a high performance digital processing unit, e.g. FPGA that takes care of the heavy computation, complemented by a RF front-end that is responsible for the radio signal conditioning inherent to transmission and reception. To this extent, in the development advanced radio communication systems it is required not only a solid knowledge in signal processing techniques, but also in signals and systems, and in analogue RF baseband/ passband processing. Several aspects of communication theory are addressed, in this Appendix, in three distinct sections, namely: radio, signal processing and digital fundamentals.

In particular, this appendix introduces the theoretical background necessary to build the simulation framework outlined in Chapter 3, which was used, in this work, to predict the performance of a complete multi-Gigabit/s wireless communication system under channel and RF impairments at 60 GHz, and in the development of the proposed *USW/IT* 5G testbed, addressed in Chapter 4. In particular, a critical review on the most common techniques for up-converting and down-converting RF signals is presented, and a mathematical formulation of the effect of RF impairments induced in an In-Phase and Quadrature-phase demodulation is performed. Furthermore, a review on the most relevant digital modulations for mmWave communication is also presented.

A.2 Radio communication: fundamentals

A.2.1 Radio propagation phenomena

In a wireless communication system, the medium between both transmitter and receiver ends, including the antennas, is called radio channel. Such medium is responsible for the propagation of the radiated signal, which may experience different propagation paths before arriving at RX. This phenomena is usually caused by either the reflection or/ and the diffraction of the transmitted signal, from its interaction with different interacting objects present in the radio path. Typically in outdoor scenarios, these objects can be houses, mountains, walls, and windows [231], as it is illustrated in Fig. A.1a.

Furthermore, each of the propagation paths have a specific amplitude, time of delay, and specular angular profile [231]. Consequently, when multiple replicas of the transmitted signal are arriving at RX, with different phases and amplitudes, they will interfere with each other. This interference can be either constructive or destructive, depending only on the phase of those replicas, which in turn depends on the geographical positions of the interacting objects, in the propagation environment. As it is illustrated in Fig. A.1b, when two sinusoidal signals are arriving at the RX in phase and with the same amplitude, the result will be a sinusoidal signal with twice the amplitude of both replicas (less likely), whereas, if they are 180° out of phase they will cancel (fade) each other. For this reason, amplitude fluctuations on the received signal will occur. Moreover, when one of the TX/ RX stations are moving, the LOS multipath component might be obstructed by for example a building, and as consequence the average received signal power will significantly be reduced. This phenomenon is known as shadowing.

In sum, radio waves can mainly br affected by reflection, diffraction and scattering. The definition of each one is as follows [106]:

- **Reflection** - occurs when a radio wave collides on an obstacle's surface with relatively large dimensions compared to the wavelength. As result, transmitted signal is re-directed to other direction, rather than going straight to the receiver;
- **Diffraction** - in the presence of a surface characterised by either sharp irregularities or small opening in the propagation path between TX/ RX, radio wave is spread out leading to the generation of secondary waves.
- **Scattering** - occurs when a radio wave impinges a obstacle with small dimensions, compared to the wavelength. Signals are re-radiated towards other directions, deviating the transmitted signal from the receiver path. Obstacles that might induce scattering are: foliage, street signs, lamp posts, rough surfaces etc. Illustration of this phenomena is depicted in Fig. A.2.

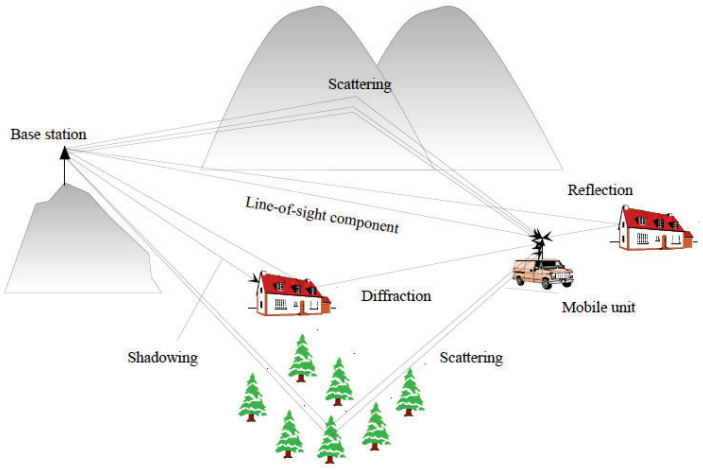

(a)

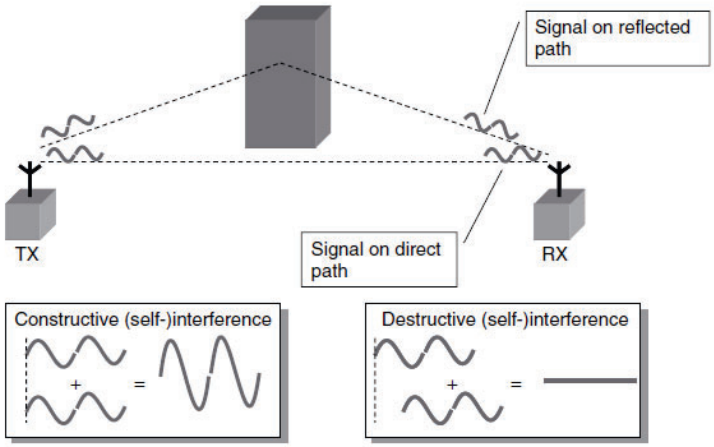

(b)

FIGURE A.1: Illustration: a) of signal replicas arriving at RX caused by reflections on buildings, and b) of the consequence that phase mismatch of different replicas might have on the combined received signal (images extracted from [231, 234]).

So far, it has been discussed that the wireless channel effect might lead to destructive interference at RX. In fact, contrary to wired channels, the wireless channel is rather dynamic and unpredictable [106]. Therefore, understanding and modelling the radio channel is crucial for the proper design of advanced wireless communication systems.

A.2.2 Channel characterisation

As aforementioned, a multipath channel can lead to the dissipation of the received signal's energy in amplitude, phase and time, making it a very significant source of signal degradation in wireless communication systems [106]. To this end, fading channels can

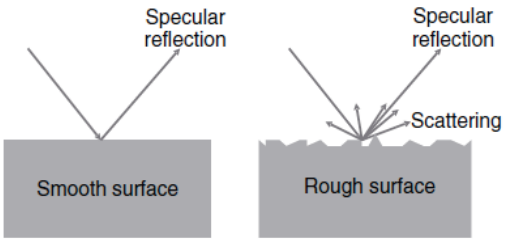

FIGURE A.2: Representation of scattering induced by a rough surface (image extracted from [231]).

be characterised according to various aspects, as depicted in Fig. A.3. In this context, a fading channel is classified into two main categories: large-scale and small-scale fading.

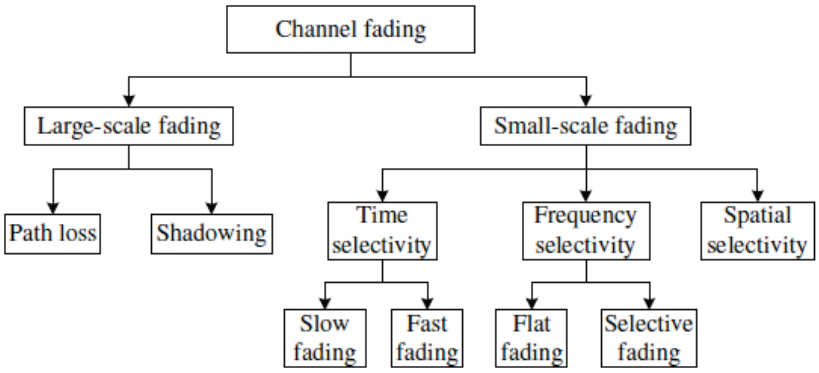

FIGURE A.3: Block diagram of how channel fading can be classified (image extracted from [231]).

Large-scale fading refers to the variation of the received signal power level when RX moves through a relatively large distance (typically greater than 100 wavelengths [231]). On the other hand, small-scale fading refers to variations on the received signal power around a mean value, on a very-short-distance scale. Such fluctuations occur on a scale comparable with one wavelength [231], and are the result of constructive and destructive interference phenomena (Fig. A.1b). Visually, these two distinct types of fading can be identified from a characteristic received signal power curve versus link distance, as the one illustrated in Fig. A.4.

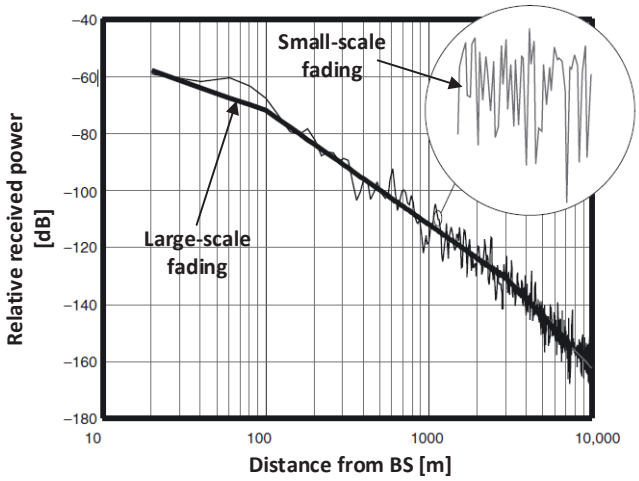

FIGURE A.4: Generic characteristic of the received power curve versus link distance (figure reproduced from [231]).

Narrow and wideband systems

Usually, in a Linear Time-Invariant (LTI) fading channel, when excited by an impulse signal, several echoes of this signal will arrive at RX. One of the best ways to understand this phenomenon is with the ellipse model (only valid in static scenarios), reported in [231], and highlighted in Fig. A.5. In such model, both TX/ RX are placed at the focal points of multiple ellipses, and the transmitted rays experience a single interaction with the object. Moreover, rays iteration with several interacting objects placed on a particular ellipse will arrive precisely at the same time. On the other hand, if transmitted signals interact with objects from different ellipses, they will arrive at different instant times. A radio medium that behaves in this way is defined as a time dispersive channel and characterised by a CIR.

Furthermore, by definition a receiver cannot distinguish between echoes (τ and $\tau + \Delta\tau$), if [231]:

$$\Delta\tau \ll \frac{1}{B}, \tag{A.1}$$

where B is the baseband bandwidth of the transmitted signal, and $\frac{1}{B}$ is equals to the transmitted symbol duration (T_s). Thus, when the condition presented in (A.1) is meet, all echoes will arrive at the same time. This corresponds to the first ellipse region illustrate in Fig. A.5. Therefore, a channel can be "considered" non-dispersive if the inverse of the signal bandwidth is negligible to the instant between delays. Subsequently, a system is said to be narrowband if [231]:

$$T_s \gg \tau_{max}, \tag{A.2}$$

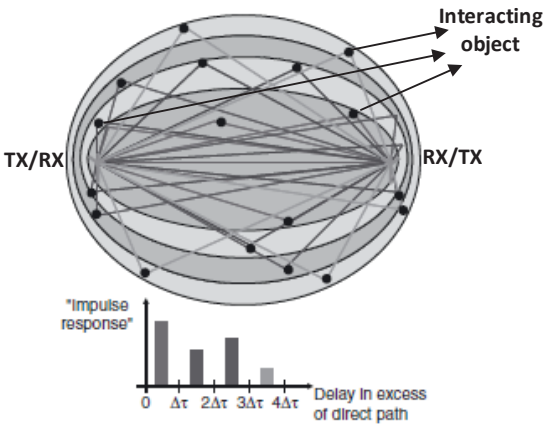

FIGURE A.5: Ellipse model for scattered components with different delays. (image adapted from [231]).

where τ_{max} is the time span of the channel impulse response. Otherwise it is characterised as a wideband system, where the arriving echoes have longer duration than the transmitted signal. Moreover, while in a narrowband system a single delay bin can represent the CIR of all echoes, in a wideband system, CIR is modelled as a group of bins, where the time resolution of each one is determined by the signal bandwidth [20].

Additionally, delay dispersion can be equivalent to frequency selectivity, if a impulse response has a finite length. This is, *Fourier* transform of a channel impulse response results into: $\mathcal{F}\{h(\tau)\} = H(f)$, where $H(f)$ is frequency transfer function of a LTI channel, given by $h(\tau)$ [231]. To this extent, the effect of multipath channel propagation induces in both wideband and narrowband systems, can be evaluated from either the channel transfer frequency function or impulse response. Finally, from Fig. A.6, it can be seen that in practice any system can be either narrowband or wideband, it only depends on the considered transmitted signal bandwidth, where $|H(f)|$ is the received signal amplitude frequency response over the bandwidth of interest, and $|H_s(f)|$, $|H_c(f)|$, are the amplitude frequency responses of the transmitted signal and fading channel, respectively. Particularly, in the section it is addressed the modelling of wide multipath fading channels. It is worth noting that a real channel is frequency selective when measured over a relatively large bandwidth [231].

Channel: stochastic versus deterministic modelling

The accurate modelling of a radio propagation channel must be carried out before any system design. This was evident in the development of any wireless standards such as: IEEE 802.11n, IEEE 802.15.3c, and IEEE 802.11ad [19], where the performance of these radio technologies and signal processing techniques were assessed and improved by the means of simulations. In general, a channel modelling depends on carrier frequency,

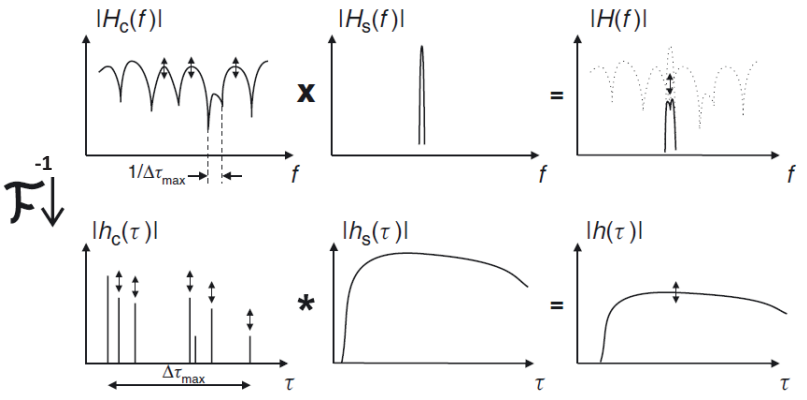

(a)

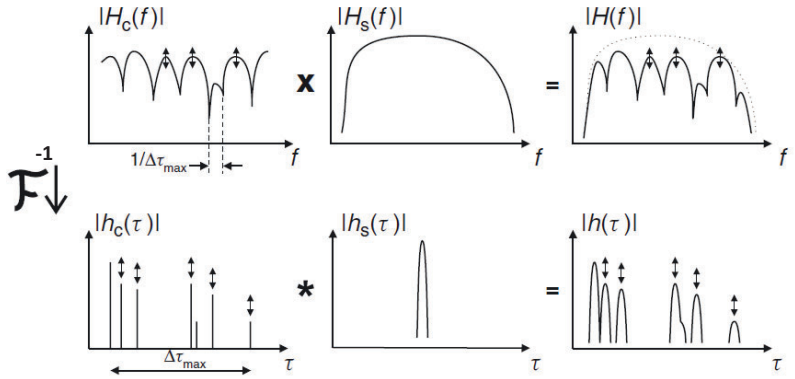

(b)

FIGURE A.6: Representation of the relation between impulse response and transform function using *Fourier* transform in: a) narrowband channel, and b) wideband channel (images adapted from [231]).

signal bandwidth and type of environment, antenna radiation pattern and gain, which might lead to complex and diverse mathematical models. Thus, such involves a trade-off between accuracy and simplicity [19].

Typically, channel modelling can be classified into one of the following two main categories: deterministic and stochastic [19]. The first is considered to model a channel where no randomness is involved. Hence, such mathematical model will always produce the same output value for the same input condition. Whereas, in stochastic systems, the channel's output will follows a certain probability distribution value. On one hand, a deterministic channel model extracts data collected from radio measurements to provide a closed-form expression. The main drawback of this approach is that such model is site-specific. On the other hand, stochastic channel models are derived from data collected in a large number of channel measurements at different locations, which leads to a statistical representation of the channel [19], which enables the derivation of the probability density function (pdf) of the channel. Due to this reason, stochastic modelling is the most popular approach.

In the previous section, the modelling of LTI wireless channels have been addressed. These type of systems are characterised by the impulse response given by $h(\tau)$. However, channels from realistic wireless communications systems are time variant, and thus the CIR is a time dependent equation described by $h(t, \tau)$, where t and τ are the absolute time and delay instant, respectively. The channel's output ($y(t)$) can be calculated by the convolution of $h(t, \tau)$, with the input signal ($x(t)$), as follows [231]:

$$y(t) = \int_{-\infty}^{+\infty} x(t - \tau)h(t, \tau)d\tau, \tag{A.3}$$

where $h(t, \tau)$ characterises the phase and amplitude of the received multipath component at the time instant $x(t - \tau)$. Moreover, the *Fourier* transformation of arbitrary CIR in function to τ, results in the following time-variant transfer function [231]:

$$H(t, f) = \int_{-\infty}^{+\infty} h(t, \tau) \exp(-j2\pi f\tau)d\tau, \tag{A.4}$$

Consequently, performing the *Fourier* transform of $H(t, f)$, the following equation is obtained:

$$B(v, f) = \int_{-\infty}^{+\infty} s(v, \tau) \exp(-j2\pi f\tau)d\tau, \tag{A.5}$$

which is known as the *Doppler*-variant transfer function. This means, that each multipath component might experience a distinct *Doppler* effect. Furthermore, from above equations it can be verified that four equivalent representations of the CIR are

possible to obtain. Figure A.7 shows the correspondence of these equations with the *Fourier* transform. Note that all these equations are in fact deterministic.

Finally, inverse *Fourier* transform of $B(v, f)$ with respect to t results in the *Doppler*-variant impulse response represented in (A.6).

$$s(v, \tau) = \int_{-\infty}^{+\infty} h(t, \tau) \exp(-j2\pi vt) dt, \tag{A.6}$$

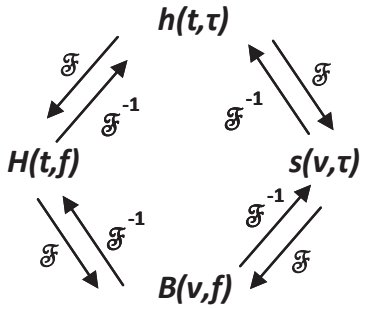

FIGURE A.7: Interrelation of the *Fourier* transform between channel frequency response, channel impulse response, and both *Doppler* impulse and frequency responses (image adopted from [231]).

By definition, the stochastic model of a fading channel is a joint pdf of the complex amplitudes for all possible combinations of τ and t [235]. However, this would lead to a very complex mathematical formulation. Instead the four functions: $h(t, \tau)$, $H(t, f)$, $s(v, \tau)$, $B(v, f)$ are described as single stochastic Autocorrelation Function (ACF), as follows [231]:

$$\begin{cases} h(t,\tau) \Rightarrow R_h(t, t', \tau, \tau') = E\{h^*(t,\tau)h(t',\tau')\} \\ H(t,f) \Rightarrow R_H(t, t', f, f') = E\{H^*(t,f)H(t',f')\} \\ s(v,\tau) \Rightarrow R_s(v, v', \tau, \tau') = E\{s^*(v,\tau)s(v',\tau')\} \\ B(v,f) \Rightarrow R_B(v, v', f, f') = E\{B^*(v,f)B(v',f')\} \end{cases}, \tag{A.7}$$

where $E\{.\}$ is the expectation operator, $(.)^*$ is the complex conjugate, $t' = t + \Delta t$, $f' = f + \Delta f$, and $v' = v + \Delta v$. Analogously, the received signal, denoted by $y(t) = x(t) \circledast h(t, \tau)$, is obtained as follows[235]:

$$R_{yy} = \int_{-\infty}^{+\infty} \int_{-\infty}^{+\infty} R_{xx}(t - \tau, t' - \tau') R_h(t, t', \tau, \tau') d\tau d\tau', \tag{A.8}$$

where $R_{xx}(t-\tau, t'-\tau')$ and $R_h(t, t', \tau, \tau')$ are the ACFs of the input signal and channel, respectively. Particularly, the input signal ACF is given by [235]:

$$R_{xx}(t-\tau, t'-\tau') = E[x^*(t-\tau)x(t'-\tau')] \tag{A.9}$$

The most common stochastic wideband channel model in radio communications is the Wide-Sense Stationary Uncorrelated Scattering (WSSUS) [231]. Wide-Sense Stationary (WSS) means that the statistical properties of the channel do not change over time. This is, the instantaneous amplitude of the multipath components can change, while the mean power and the *Doppler* spectrum, of a particular channel, remain the same with time. In practise, this is only fulfilled over an area of about 10λ [231]. In this context, $R_h(t, t', \tau, \tau')$, detailed in (A.7), is equivalent to $R_h(\Delta t, \tau, \tau')$[235]. Furthermore, Uncorrelated Scatterers (US) definition, means that multipath components arriving at different delays are uncorrelated [231]. In the frequency domain, this condition means that R_H only depends on the frequency difference $\Delta f = f' - f$, leading to the following equivalence: $R_H(t, t', f, f') = R_H(t, t', \Delta f)$. Combining above assumptions, stochastic ACFs equations are simplified into two variables as follows [235]:

$$\begin{cases} R_h(t, t', \tau, \tau') = P_h(\Delta t, \tau)\delta(\tau - \tau') \\ R_H(t, t', f, f') = R_H(\Delta t, \Delta f) \\ R_s(v, v', \tau, \tau') = P_s(v, \tau)\delta(v - v')\delta(\tau - \tau') \\ R_B(v, v', f, f') = R_B(v, \Delta f)\delta(v.v') \end{cases}, \tag{A.10}$$

where P_h is the delay cross-power spectral density, R_H is the time-frequency correlation function, P_s is the scattering function, P_B is the *Doppler* cross power spectral density and $\delta(.)$ is the *Dirac* delta function.

The most common WSSUS model for wideband channels, is the N-tap *Rayleigh*-fading model, which follows a tapped delay line structure. This is, amplitude of all multipath components are subject to a *Rayleigh* distribution [231]. This model is mathematically formulated as [231]:

$$h(t, \tau) = a_0\delta(\tau, \tau_0) + \sum_{i=1}^{N} c_i(t)\delta(\tau - \tau_i), \tag{A.11}$$

where a_0 is the complex amplitude of the specular path, N is the number of taps corresponding to one group of closely spaced multipath components, and $c_i(t)$ are the time-dependent complex channel coefficients that follow zero-mean *Gaussian* random distribution. However, such is only accurate when:

- The effect of reflection and diffraction coefficients due to the presence of interacting objects in the environment, is constant over the signal bandwidth;
- Signal bandwidth relative to the carrier should be much smaller than 1.

For high-data data systems, ($B > 500$ MHz), the aforementioned statements are not verified. Different frequency components from the transmitted signal might experience distinct propagation conditions [231]. For example, higher frequency components are often more attenuated. In particular, for 60 GHz indoor applications, a generic complex baseband directional CIR derived from the extension of the Saleh-Valenzuela (SV) model [124] to the angular domain by the authors from [125], is adopted [123]. It is assumed that multipath components (rays) arrive in clusters according to a *Poisson* distribution [124], where each cluster can be seen as a group of rays arriving at, approximately, same phase and time [19]. CIR mathematical formulation is given (A.12), and its graphical representation can be seen in Fig. A.8.

$$h(t,\phi,\theta) = \underbrace{\beta\delta(t,\phi,\theta)}_{\text{LOS}} + \underbrace{\sum_{l=0}^{L}\sum_{k=0}^{K_l}\alpha_{k,l}\delta(t-T_l-\tau_{k,l})\delta(\phi-\Omega_l-\omega_{k,l})(\theta-\psi_l-\Psi_{k,l})}_{\text{Clusters}} \tag{A.12}$$

where *LOS* term models a distinct strong LOS path on top of the clustering phenomenal (only present when directive antennas are employed especially in the LOS scenario). Moreover, L is the total number of clusters and K_l is the total number of rays in the l^{th} cluster. Scalars $\alpha_{k,l}$, $\tau_{k,l}$, $\omega_{k,l}$ and $\Psi_{k,l}$, are the complex amplitude, Time of Arrival (TOA), Angle of Arrival (AOA), and Angle of Departure (AOD) of the k^{th} ray of the l^{th} cluster, respectively. In addition, T_l Ω_l, ψ_l, are the mean TOA, AOA, and AOD of the l^{th} cluster.

Large-scale fading

In general, the average received signal decreases monotonically with the increasing of the link distance, mainly due to shadowing from the presence of large buildings, intervening terrains, and vegetation [46]. This effect is called large-scale fading, which can be predicted by a Path Loss (PL) equation (ratio of the received signal power level to the transmitted one), a very important metric in wireless network planing [19].

As it was discussed in Section 2.2, PL is more severe at mmWave than at lower frequencies, e.g., the free space loss itself increases by 22 dB (at 60 GHz) when compared to a 5 GHz band. Although PL for wideband systems is both frequency and distance (d) dependent, in order to simplify its modelling, (A.13) is usually adopted [19]. Therefore,

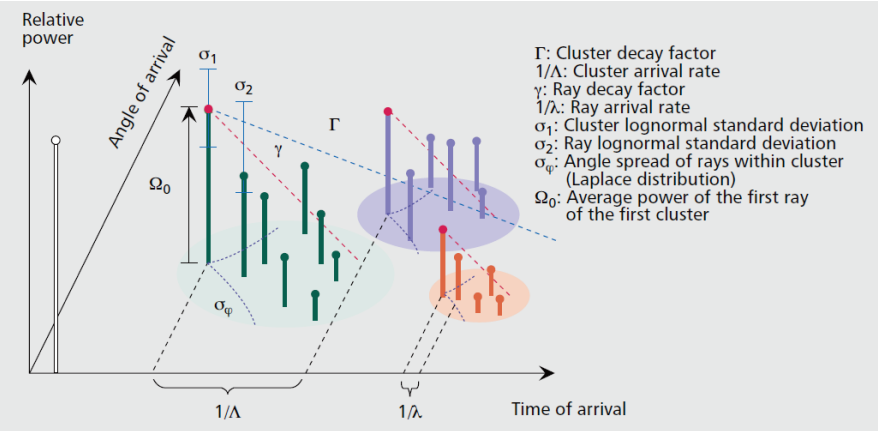

FIGURE A.8: Graphical representation of the CIR as a function of TOA and AOA (image extracted from [15]).

it is assumed that PL is only distance dependent.

$$PL(d)[dB] = \overline{PL}(d)[dB] + X_\tau[dB], \tag{A.13}$$

where $\overline{PL}(d)$ is the average PL and X_τ is the shadowing fading margin, which is considered to ensure that the minimum received power is exceed in 90% of all cases, with respect to the mean of the normalised received power at a fixed distance [231]. Therefore, X_τ is typically a zero mean *Gaussian* distributed variable with standard deviation τ [236]. Consequently, $\overline{PL}(d)$ is given by [19]:

$$\overline{PL}(d)[dB] = PL_{d_0}[dB] + 10 \times n \log_{10}(\frac{d}{d_0}) + \sum_{q=1}^{Q} X_q \quad (d \geq d_o), \tag{A.14}$$

where PL_{d_0} is the path loss at a reference distance (d_0), usually $d_0 = 1$ m, and n is the path loss exponent. Moreover, the term X_q takes into account additional attenuation from specific obstruction by objects, such as penetration losses. Furthermore, n highly depends on the transmission environment, which tends to increase whenever multipath phenomena is more relevant [106]. Table A.1, shows n values for difference indoor/ outdoor environments.

From Table A.1 it is noted that for typical indoor LOS environments, n value is slightly lower than the theoretical free space propagation exponent one ($n = 2$). Also, in [237] results obtained were 1.3, 1.7 for corridor and laboratory environments. This is explain due to the accumulation of multipath energy [238], also known as wave-guide effect. In other words, multipath interference is more constructive than destructive.

Table A.1
Path loss exponent for several indoor and outdoor environments [46].

Environment	Path loss exponent (n)
Free space	2
Urban area cellular radio	2.7-3.5
Shadowed urban cellular radio	3-5
In building LOS	1.6-1.8
Obstructed in buildings	4-6
Obstructed in factories	2-3

Small-scale fading

Small-scale fading characterises the fast variations of amplitude of radio wave signal over either a short period of time or travel distance [46]. For this reason, large scale path loss can be ignored when analysing the effect of this phenomenon. Additionally, a small-scale fading channel can be further classified either as time selective or frequency selective or even as spatial selective. Time selectivity of a channel is induced by the *Doppler* effect, present in a non-static environment. To this regard, depending on the time variation due to movements of both TX, RX, or even movement of interacting object, this channel can be considered as either fast fading or slow fading, depending on how fast the channel changes compared to the signal bandwidth (data rate) [20]. Multipath time dispersion of the transmitted signal leads to a frequency selective channel, which can also be characterised as flat fading of frequency selective channel, depending on the relation between both transmitted signal and channel bandwidths [46]. Finally, spatial selectivity is the result of multipath components arriving at a particular angle spread, which is a measure of how signal replicas are arriving with respect to the mean arrival angle. In other words, the received power level could be more relevant at certain angles of arrival than others [239]. For example, BF can be seen as a technique to achieve spatial selectivity, since it can modify the direction of the main lobe of a certain antenna. In sum, depending on the relation between both signal and channel parameters, the transmitted information can experience different types of small-scale fading.

A schematic showing how to classify multipath fading channels is outlined in Fig. A.9 [46]. From this figure, it is clearly seen that while multipath delay spread leads to either a flat fading channel or a frequency selective fading, *Doppler* spread leads to either fast fading channel or slow fading channel. These two propagation metrics are independent from each other. For example, a channel can be frequency selective and being also characterised by a fast fading. In this context, a transmitted signal experiences a flat

fading if [46]:

$$B_s \ll B_c \tag{A.15}$$

and

$$T_s \gg \tau_{RMS}, \tag{A.16}$$

where T_s and B_s are the transmitted symbol duration and bandwidth, respectively; and τ_{RMS} and B_c are RMS delay spread and Coherence bandwidth (B_c), respectively.

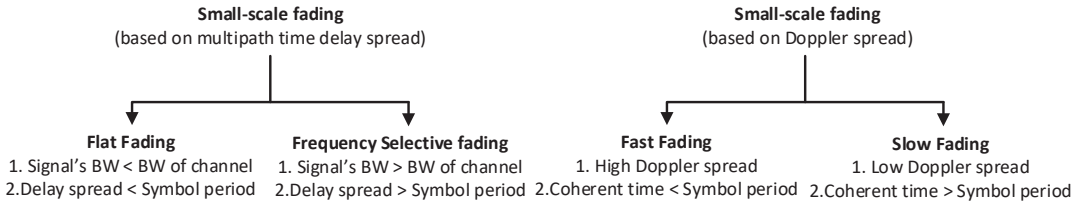

FIGURE A.9: Schematic illustrating how to characterise a small-scale fading channel (image adapted from [46]).

In (A.16), it is verified that τ_{RMS} is used as a quantitative metric for the evaluation of the frequency selectivity of a fading channel, in particular, by comparing it with the transmitted symbol time interval. To this extent, if delay spread from a certain channel impulse response is negligible compared to T_s, then a channel can be classified as flat fading. Otherwise, it is characterised as frequency selective. In other words, if (A.15), and (A.16) are met, the radio channel yields a constant gain and linear phase response over the signal bandwidth, and no excess delay is experienced at the receiver [46].

The RMS delay spread and coherence bandwidth are channel parameters that can be determined from a PDP, also known as delay power spectral density, $P_h(\tau)$. Such contains information regarding the received power from a transmitted delta pulse with unit energy that undergoes in multipath fading channel. According to [231], it can be calculated from the CIR as follows:

$$P_h(\tau) = \lim_{T\to\infty} \frac{1}{2T} \int_{-T}^{+T} |h(t,\tau)|^2 dt \tag{A.17}$$

Note that in practice the integral presented in (A.17) can be extend over the time span the channel is considered as quasi-stationary [231]. This means that $R_H(t, t', f, f')$

can be simplified into $R_H(0, \Delta f)$, and consequently it can be obtained from the *Fourier* transform of the PDP. Under such assumption, ACF of the channel's transfer function can be calculated as:

$$R_H(0, \Delta f) = \int_{-\infty}^{+\infty} H(f) H^*(f + \Delta f)\, d\Delta f, \tag{A.18}$$

where $H(f)$ is the complex transfer function of the channel, Δf is the frequency shift and (.)*denotes the complex conjugate.

While (A.17) is used to obtain either the RMS delay spread or mean excess delay, (A.18) can be considered to calculate the channel coherence bandwidth. In Fig. A.10 shows a PDP sample, along with the indication of RMS delay spread, mean excess delay and maximum excess delay. Note that the dynamic range of the average PDP is computed considering all multipath components which are 10 dB above the noise floor [46]. Furthermore, RMS delay spread is the square root of the second central moment of the channel of the PDP, defined by [46]:

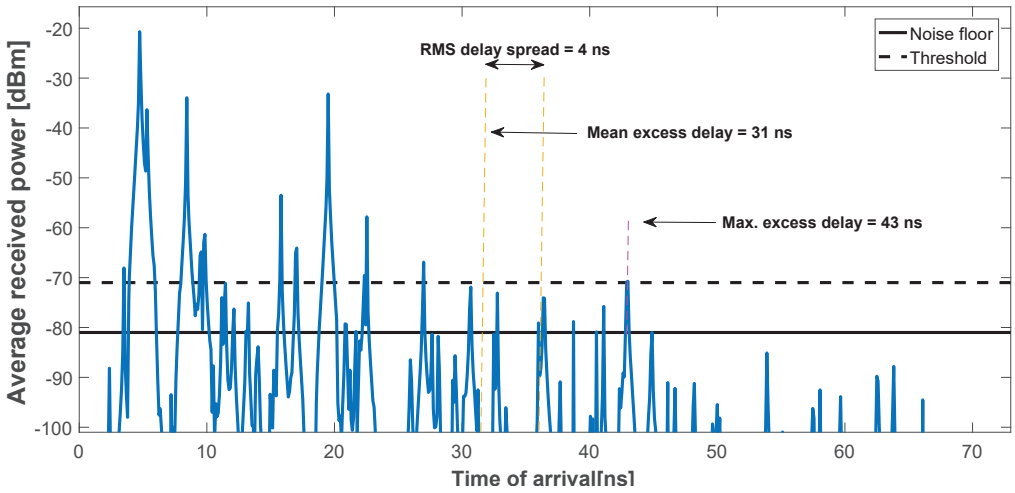

FIGURE A.10: Representation of the metrics: RMS delay spread, mean excess delay and maximum excess delay, for a particular PDP sample.

$$\tau_{RMS} = \sqrt{\overline{\tau^2} - (\overline{\tau})^2}, \tag{A.19}$$

where $\overline{\tau}$ and $\overline{\tau^2}$ are the mean excess delay and the second central moment of the considered PDP, which are calculated by (A.20) and eq. (A.21), respectively:

$$\overline{\tau} = \frac{\sum_i P(\tau_i)\tau_i}{\sum_i P(\tau_i)} \tag{A.20}$$

$$\overline{\tau^2} = \frac{\sum_i P(\tau_i)\tau_i^2}{\sum_i P(\tau_i)}, \tag{A.21}$$

Furthermore, the B_c is a key metric involved in expressing the performance of any digital wireless system over a fading channel, since if the system requires a bandwidth larger than B_c, amplitude and phase distortion of the signal will occur. In this case, the fading channel is considered as a frequency-selective fading, making the digitally modulated data experience ISI. As example of a frequency selective channel is depicted in Fig. A.11, where it can be seen that signal bandwidth (B_2) is much greater than B_c (B_1), which is caused by multipath delay components arriving at a instant of time equal or higher than T_s. Despite B_c can be calculated by (A.18) for a particular correlation coefficient value, it can also be obtained by the following approximation [106]:

$$B_c \approx \frac{1}{\tau_{RMS}} \tag{A.22}$$

Additionally, B_c can also be defined as the maximum frequency difference at which two signals are highly correlated and a correlation of 0.5 ($B_{c_{0.5}}$) and 0.9 ($B_{c_{0.9}}$), as follows:

$$B_{c_{0.5}} \approx \frac{1}{5\tau_{RMS}} \tag{A.23}$$

$$B_{c_{0.9}} \approx \frac{1}{50\tau_{RMS}} \tag{A.24}$$

Fast and slow fading are related to how CIR varies within a certain transmitted symbol duration. This variation in the time domain is related to the movement of either TX or/and RX or/ and of any object present in the channel, which leads to a spread in the frequency domain (*Doppler* shift). In general $T_c \approx 1/f_m$, where f_m is the maximum *Doppler* frequency shift [46], which is given by:

$$f_m = \frac{v}{\lambda} cos(\gamma) = -f_c \times \frac{v}{c_o} cos(\gamma), \tag{A.25}$$

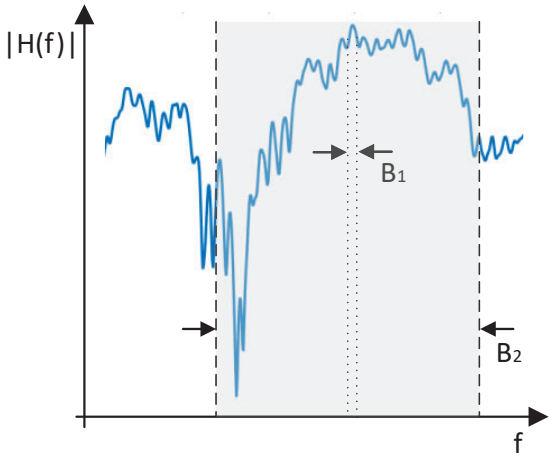

FIGURE A.11: Illustration of a frequency selective fading channel.

where λ is the wavelength of the transmitted carrier, γ is the direction of wave propagation, f_c is the carrier frequency and c_o is the speed of light. To this extent, a channel is characterised as slow fading if [46]:

$$T_s \ll T_c \tag{A.26}$$

and

$$B_s \gg B_d, \tag{A.27}$$

where T_C is the coherence time (period of time in which the CIR is considered static) and B_d is the bandwidth of *Doppler* spread ($B_d = 2f_m$) [106]. Therefore, $T_s > T_c \Rightarrow B_d > B_s$. Furthermore, if $T_s >> T_c$ means that the channel is static over one or several transmitted symbols. Additionally, in [46] it is suggested that, for modern digital communication systems, that T_c can be approximately using:

$$T_c \approx \sqrt{\frac{9}{16\pi f_m^2}}, \tag{A.28}$$

Finally, all stated considerations, can be summarised in the fading matrix depicted in Fig. A.12.

A.2.3 RF front-end architectures

A RF front-end is responsible to modulate a signal into a certain carrier frequency. As result, multiple wireless services can operate simultaneously without interfering in each other. However, the choice of the best RF front-end architecture can be

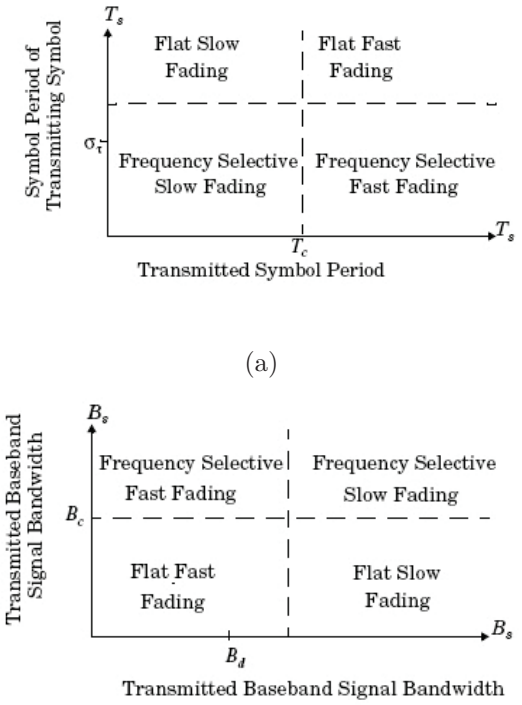

FIGURE A.12: Matrix of type of channel fading experience by the transmitted signal as function of: a) symbol duration, and b) baseband signal bandwidth (images extracted from [46]).

critical, particularly for 5G mobile receivers [141]. As stated in Section 2.4.1, 3GPP has established a new PHY, the 5G NR, which envisage the utilisation of bandwidths up to 400 MHz, at mmWave, to enable data rates higher than 1 Gbps. Hence, more flexible (the carrier frequency will depend on the sub-carrier numerology), low-power and high-performance RF front-ends are necessary in 5G systems [141].

In particular at 60 GHz, there are some drawbacks that must be taken into account, which are mostly related to the non-linearities of the RF front-ends [240]. For example, PN floor, presented in the oscillators, is significantly increased at mmWave frequencies [241]. For instance, if the desired frequency at the input of the mixer is f and the original frequency from the reference source is f_o, the final phase noise will be $20\log_{10}(f/f_o)$ dB above the original level, thus, signal conversions from baseband to mmWave induce higher PN in comparison to lower frequencies [242]. In addition, the up-conversion of baseband signals at the transmitter and their down-conversion back to baseband at the receiver, using IQ mixers, causes the RF front-ends to induce several critical non-idealities affecting both transmitted and received radio signals. Such non-linearities, including IQ imbalances and PA non-linear distortions, should also be taken into account in radio design and link quality. These issues become even more critical in handset devices, in which low power consumption and small form factors are a must [19].

According to [141], the most common receiver architectures are: the superheterodyne, homodyne and low-Intermediate Frequency (IF). The first architecture is the traditional choice in wireless receivers. This is, depending on the selected IF and filters, high selectivity and sensitivity can be achieved by employing a two down-conversion method [19, 141]. In other words, the received signal is demodulated into an IF stage and then converted to baseband. The block diagram of this approach considering an IQ quadrature mixing (required in more sophisticated wireless systems) is depicted in Fig. A.13a, and its description is given below [19]:

1. A RF bandpass filter is considered to reject possible out-of-band emissions among the signals acquired by the antenna;
2. The filtered in-band signals are amplified by the means of a LNA and another bandpass filter is utilised to suppress possible image signals which might overlap with the intended signal after the first mixing process;
3. The first mixer down-converts the received RF signal into an IF, and then channel selection is performed, using highly selective filters;
4. A VGA adjust the signal power level for optimum In-phase and Quadrature-phase demodulation;
5. Finally, after splitting the IF signal of 4) into two branches, these IF signals are down-converted into baseband with the aid of two other mixers a second quadrature LO. After this process, additional anti-aliasing filtering is carried out before the conversion of these signals to the digital domain.

The aforementioned architecture allows a relatively lower signal power level at the receiver input, good performance in attenuating undesired signals, and its robust to the effect of DC offset [243]. However, it has one main issue. It requires image signal cancellation techniques, which can be implemented either by employing filtering, or *Hartley* or *Weaver* image rejection architectures [244]. The effect of this image signal replica can be mathematically demonstrated. Considering that the baseband signal: $x(t) = A\cos(2\pi f_o t)$, has been modulated with a high frequency carrier, $c(t) = \cos(2\pi f_c t)$, the information transmitted over the channel, $y(t)$, is expressed by:

$$y(t) = \frac{A}{2}\cos\left(2\pi t(f_c - f_o)\right) + \frac{A}{2}\cos\left(2\pi t(f_c + f_o)\right), \tag{A.29}$$

where f_o is the frequency of the baseband signal, and f_c is the carrier frequency. At the receiver, $y(t)$ is down-converted to an IF frequency through the first mixer stage, as

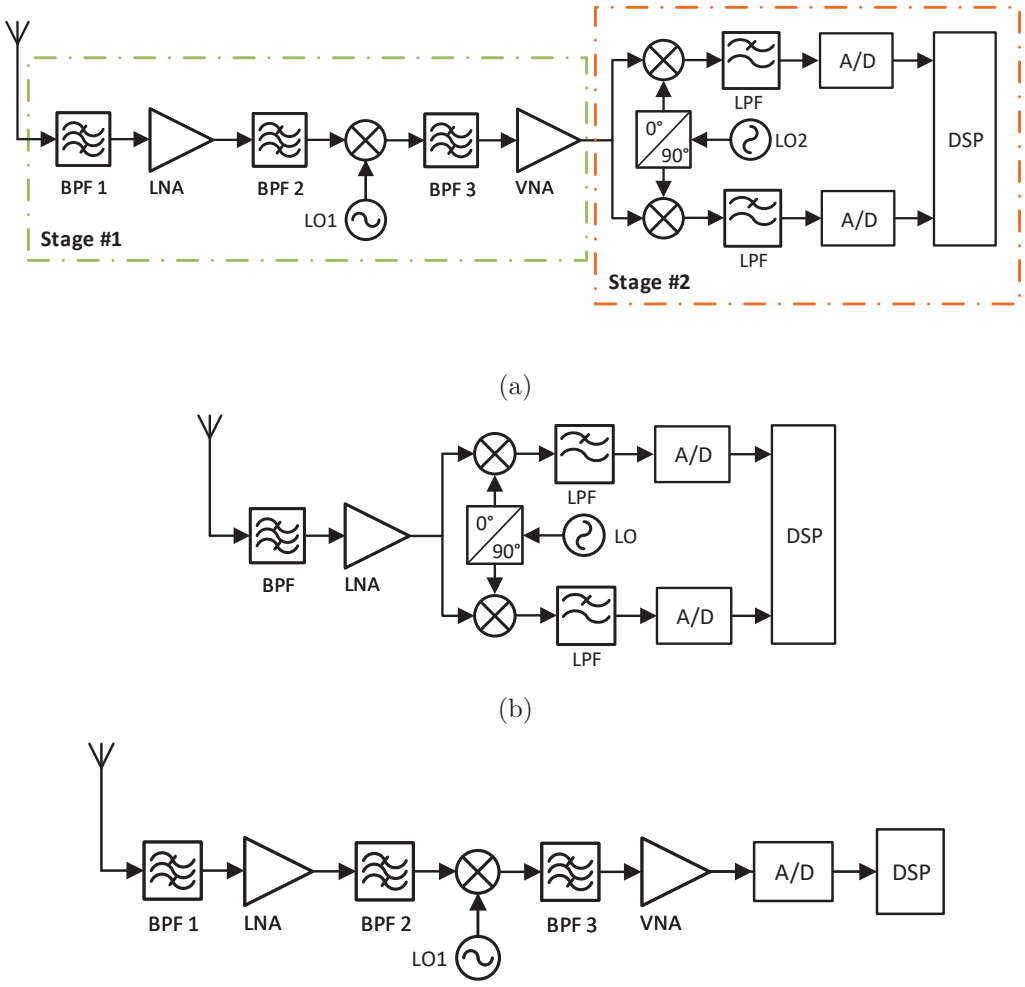

FIGURE A.13: The most common receiver architectures: (a) superheterodyne (b) homodyne and (c) low-IF. (images adapted from [141]).

follows:

$$g(t) = \frac{A}{4}\cos(2\pi t(f_c - f_o - f_{LO1})) + \frac{A}{4}\cos(2\pi t(f_c + f_o - f_{LO1}))+ \underbrace{\frac{A}{4}\cos(2\pi t(f_c - f_o + f_{LO1}))}_{\text{High frequency components}} + \underbrace{\frac{A}{4}\cos(2\pi t(f_c + f_o + f_{LO1}))}_{\text{High frequency components}}, \quad \text{(A.30)}$$

where f_{LO1} is the frequency of the first LO, which value is lower than f_c. Consequently, after filtering the higher frequency signal components of $g(t)$, highlighted in (A.30), with a bandpass filter, the resultant signal is mixed again with a second LO frequency. Note $f_{LO2} = f_c - f_{LO1}$. With this, the equation of the demodulated baseband signal is given in (A.31). It is clearly seen that at baseband, the image signal will overlap with the desired signal, which might lead to severe loss of performance in the demodulation

process. Moreover, frequency domain representation of the aforementioned stages is shown in Fig. A.14.

$$bb(t) = \underbrace{\frac{A}{4}\cos(2\pi t(f_c - f_o - f_{LO1}))}_{\text{image signal}} \times \cos(2\pi t(f_c - f_{LO1})) + \underbrace{\frac{A}{4}\cos(2\pi t(f_c + f_o - f_{LO1}))}_{\text{desired signal}} \cos(2\pi t(f_c - f_{LO1})), \quad \text{(A.31)}$$

$$\iff bb(t) = \frac{A}{8}\cos(2\pi t(2f_c - f_o - 2f_{LO1})) + \underbrace{\frac{A}{8}\cos(2\pi t(f_o))}_{\text{image signal}} + \frac{A}{8}\cos(2\pi t(2f_c + f_o - 2f_{LO1})) + \underbrace{\frac{A}{8}\cos(2\pi t(f_o))}_{\text{desired signal}}, \quad \text{(A.32)}$$

Moreover, high manufacture costs and power consumption (it utilises a significant number of analogue components) of superheterodyne architectures make this approach not the preferred one for mobile devices [19, 141]. For instance, a solution to design a more costly and power effective architecture might be accomplished with the employment of a homodyne architecture, also known as either direct conversion or zero-IF, instead. In fact, as it is seen in Fig. A.13b, such architecture is a simplified version of the superheterodyne one (it requires fewer number of analogue components). This is, it converts the received signal directly to baseband [19]. After filtering, amplification and splitting of the RF signal, baseband signals are obtained from a direct IQ down-conversion, with LO operating at the same frequency of the RF carrier. However this approach also have a few limitations. Firstly, considering the mmWave band, this configuration might be very challenge to implement, since the frequency required for the LO is very high. Another issue is that the leakage of LO signal to the input of the mixer can result in self mixing, leading to a time-varying DC offset at the output of the mixer [243, 244]. Such does not only distort the desired signal, but might lead to its saturation in the following analogue states. In addition, this architecture also induce IQ imbalances and flicker noise into the baseband signal [141]. Finally, as advantage this architecture does not present image signal [141].

Furthermore, a low-IF architecture, also referred to digital IF might be considered. This architecture is similar to the super-heterodyne one, but the second IQ mixing stage is performed in the digital domain instead, as shown in Fig. A.13c. On one hand, this approach leads to the increasing of the ADC sampling rate, where a relatively high dynamic range is required [19]. On the other hand, it is the one that achieves higher

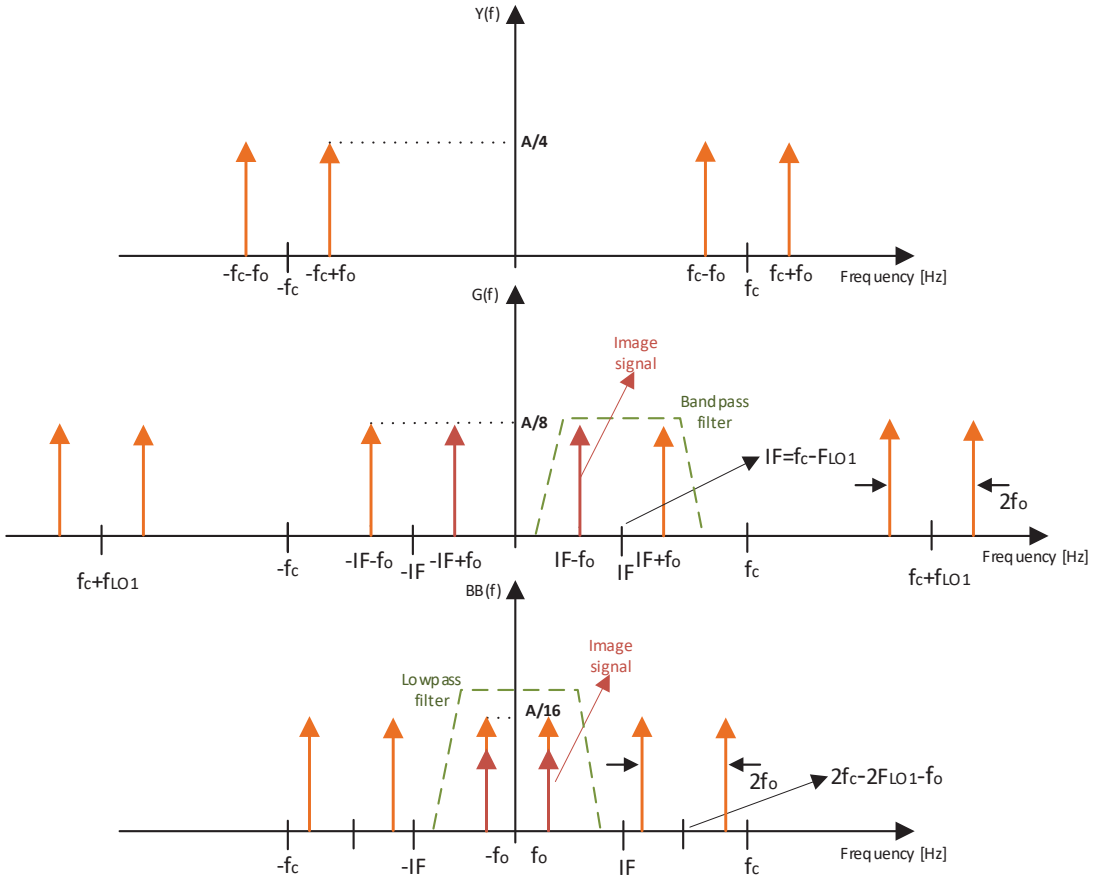

FIGURE A.14: Frequency domain representation of the RF stages presented in a generic two-step superheterodyne architecture.

flexibility, when compared to the other aforementioned architectures. Moreover, contrary to the homodyne architecture, the low receiver is not sensitive to DC offset, LO leakage and flicker noise [244]. In fact, it presents a good compromise between zero-IF and the superheterodyne architectures. Due to this fact, such approach is becoming popular for advanced radio transceivers, where the digital approach avoid possible amplitude and phase imbalances issues from analogue IQ stages [244].

Comparison of the receiver architectures, in terms of RF complexity, IC integration, RF power consumption and main advantages/ disadvantages, is outlined in Table A.2, based on the work reported in [243, 244].

Finally, when it comes to transmitter architectures, their main role is: modulation of binary information, frequency up-conversion and power amplification. Since, high power level signals are usually transmitted OTA, RF band selection and noise are not a constraint [244]. Therefore, transmitter architectures are simpler and, in general, less approaches are found in literature when compared to receiver systems [244]. Figure A.15 shows a typical architecture of a digital IF transmitter, where the baseband signal is

TABLE A.2
COMPARISON OF THE RECEIVER ARCHITECTURES, IN TERMS OF RF COMPLEXITY, IC INTEGRATION, RF POWER CONSUMPTION AND MAIN ADVANTAGES/ DISADVANTAGES.

Features	**Two step superheterodyne**	**Zero IF**	**Digital IF**
Complexity	high	low	very low
IC integration	No*	yes	yes
Power consumption	high	low	low/moderate
Flexibility	low	low	moderate
Advantages	Selectivity Sensitivity Immune DC offset	Simplicity IC integration	Immune DC offset Simplicity No IQ issues
Drawbacks	Image signal I/Q mismatch Noise figure Non-linear behaviour	Strong DC issues I/Q mismatch Flicker noise Even/Odd distortion	Image signal high ADC sampling rate and dynamic range

* Off-chip image reject and channel select filter is required;
† High selectivity with high attenuation on the interfering signals, require high filter orders.

firstly up-converted to RF, bandpass filtered, amplified and lowpass filtered and, at last, transmitted by the antenna.

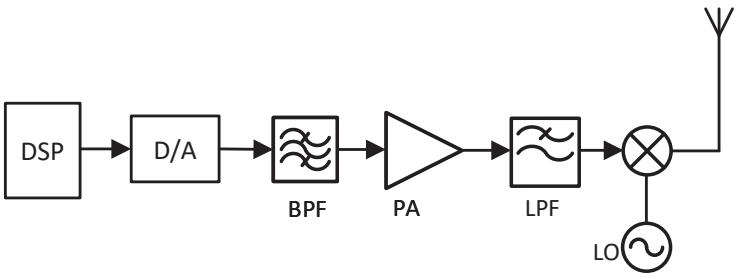

FIGURE A.15: Generic architecture of digital IF transmitter (image adapted from [244])

Ultimately, the best architecture solution would be to perform all the analogue stages in the digital domain, which would give the ability to configure the receiver path to operate at different radio bands or/and signal bandwidths [141]. This method is known as ideal SDR receiver, and it was initially proposed by *Mitola* [245]. However, this would be extremely challenging at mmWave, since both DAC/ ADC would required almost hundreds of GHz of bandwidth [14]. As it was addressed in Chapter 4.

A.2.4 RF impairments

PA non-linearities

In general, active RF components from TX/RX architectures, such as the ones illustrated in Figs. A.13 and A.15, are characterised by non-linear transfer curves [19]. Nevertheless, it is well known that the PA, placed at TX, is the most dominant non-linear source in wireless transceiver. Particularly at mmWave frequencies, this issue is even more relevant, since silicon-based IC amplifier cannot provide enough power transmission while maintaining a relatively high linearity [19]. Note that the generation of high power level signals is required to overcome attenuations from the signal path loss at those frequencies, as discussed in Section 2.4.1, in order to achieve reasonable coverage ranges.

A typical power characteristic transfer curve, of a SiGe PA is illustrated in A.16a. From this figure, it is evident that at an input power higher than -20 dBm, the linearity of the output curve is no longer verified. In other words, the output power of the PA does not follow the input power multiplied by a constant gain. This is explained by the input/ output power characteristics of the active transistor considered in the PA design [246]. In addition, it is also seen that PA efficiency is higher close to its output saturation point. Since PA accounts for the most significant portion of power consumption in a RF architecture, it is recommended to drive a PA close to this point [19]. However, this might result in severe signal distortion. The easiest way to evaluate such distortion is to extract the non-linear model parameters from measured data, at a particular frequency [246]. Considering that the PA has a time-invariant input-output power response, such can be modelled by a polynomial equation. Assuming that the PA output ($y(t)$) is modelled by [19]:

$$y(t) = a_1 x(t) + a_2 x^2(t) + a_3 x^3(t), \tag{A.33}$$

where a_1, a_2, a_3 are the polynomial coefficients, and $x(t)$ is the PA's input signal, defined as: $x(t) = Acos(2\pi t)$. With this, (A.33) becomes:

$$\begin{aligned} y(t) &= a_1[Acos(2\pi ft)] + a_2[(Acos(2\pi ft))^2] + a_3[(Acos(2\pi ft))^3] \\ \iff y(t) &= \underbrace{A^2\frac{a_2}{2}}_{\text{DC component}} + \underbrace{cos(2\pi ft).[Aa_1 + A^3\frac{3a_3}{4}]}_{\text{desired signal}} + \\ &\quad \underbrace{cos(4\pi ft).[A^2\frac{a_2}{2}]}_{\text{2nd harmonic}} + \underbrace{cos(6\pi ft).[A^3\frac{a_3}{4}]}_{\text{3rd harmonic}} \end{aligned} \tag{A.34}$$

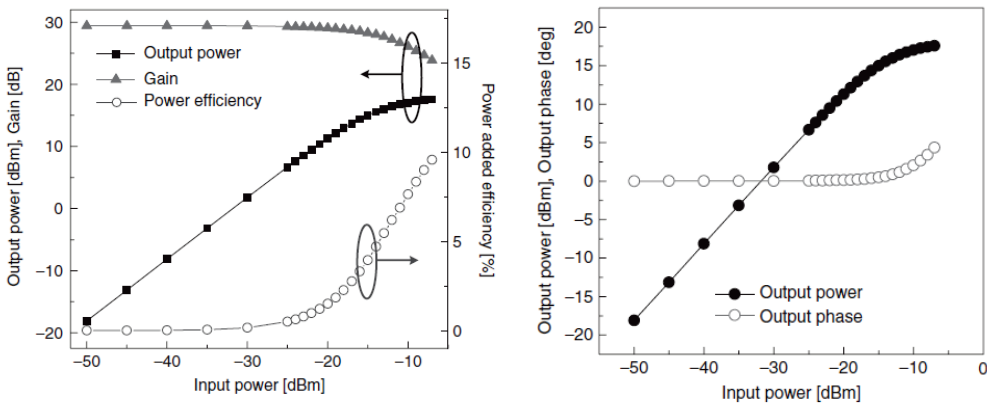

(a) (b)

FIGURE A.16: Example of a 60 GHz SiGe PA characteristic transfer curves: a) Input power versus output power, gain and power efficiency; b) relation of input power with output power and phase (image extracted from [19])

From (A.34) it is demonstrated that the PA not only amplifies the desired signal, but also produces harmonics, which can lead to adjacent channel interference. Moreover, when $x(t) = Acos(2\pi f_1 t) + Acos(2\pi f_2 t)$, $y(t)$ becomes:

$$
\begin{aligned}
y(t) &= a_1[Acos(\omega_1 t) + Acos(\omega_2 t)] + a_2[(Acos(\omega_1 t) + Acos(\omega_2 t))^2] + \\
&\quad a_3[(Acos(\omega_1 t) + Acos(\omega_2 t))^3] \\
\iff y(t) &= \underbrace{A^2 a_2}_{\text{DC component}} + \underbrace{cos(\omega_1 t).[Aa_1 + A^3\frac{9a_3}{4}]}_{\text{desired signal\_1}} + \underbrace{cos(\omega_2 t).[Aa_1 + A^3\frac{9a_3}{4}]}_{\text{desired signal\_2}} + \\
&\quad \underbrace{cos((\omega_1+\omega_2)t).[A^2 a_2] + cos((\omega_1-\omega_2)t).[A^2 a_2]}_{\text{second-order IMD}} + \underbrace{cos((2\omega_1)t).[A^2\frac{a_2}{2}]}_{\text{2nd harmonic}} + \\
&\quad \underbrace{cos((2\omega_2)t).[A^2\frac{a_2}{2}]}_{\text{2nd harmonic}} + \underbrace{cos((2\omega_1+\omega_2)t).[A^3\frac{3a_3}{4}] + cos((2\omega_1-\omega_2)t).[A^3\frac{3a_3}{4}]}_{\text{third-order IMD}} \\
&\quad \underbrace{cos((\omega_1+2\omega_2)t).[A^3\frac{3a_3}{4}] + cos((\omega_1-2\omega_2)t).[A^3\frac{3a_3}{4}]}_{\text{third-order IMD}} + \\
&\quad \underbrace{cos((3\omega_2)t).[A^3\frac{a_3}{4}]}_{\text{3rd harmonic}} + \underbrace{cos((3\omega_1)t).[A^3\frac{a_3}{4}]}_{\text{3rd harmonic}}
\end{aligned}
\tag{A.35}
$$

Similarly, in addition to the harmonics of both tones, second-order and third-order Intermodulation Distortion (IMD) products are presented at the output of the PA, when the input signal is constituted by two tones. Thus, when a multi-tone signal is

amplified, not only adjacent channel interference can occur, but also in band distortions might arise. For example, when $f_2 = nf_1$, the n^{th} harmonic of the lower-band signal overlaps with the higher one, as it is illustrated in Fig. A.17 [247].

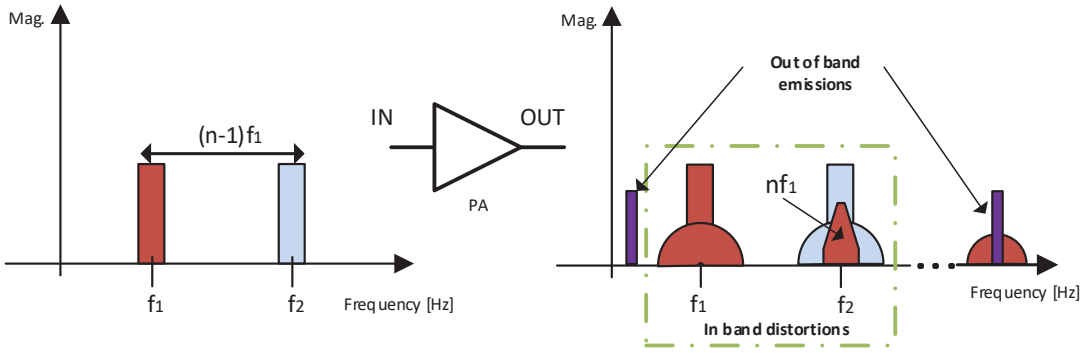

FIGURE A.17: Illustration of dual-band transmission, where the n^{th} harmonic interfere with the second signal bandwidth (image adapted [247])

Furthermore, the third order IMD products are particularly important, because they are present very close to the desired signals and cannot be easily filtered, and their tones amplitude increase by a factor of three relative to the power level of the fundamental tones. Consequently, they might cause significant bandwidth signal distortions, when for example a complex waveform, such as OFDM, is transmitted. Intermodulation products of two particular sub-carriers will overlap with the information carried by the others leading to an in-band interference.

Finally, as it can be seen in Fig. A.16b, the PA non-linearity is also responsible to deviate the phase of the input signal by an angle that depends on the input power [246]. This characteristic curve is known as the AM-PM of a PA. Several empirical behavioural models are presented in the literature to describe both PA AM-AM and AM-PM non-linearities. According to [19], the *Rapp* model [120] is appropriate to characterise power transfer curves of 60 GHz solid-state PAs. However, it does not consider memory effects, i.e., both AM-AM/ AM-PM characteristics curves remain the same regardless the frequency of the input signal. More details regarding this model are present in Chapter 3.

Phase noise and carrier frequency offset

Frequency variations are the dominant impairment in a LO [246], i.e., its output signal is not locked at a particular frequency, in fact, its amplitude and phase change over time.

This issue is modelled as random phase fluctuations, known as PN. In this context, the effect of PN in the performance of the IQ homodyne receiver demodulator depicted in Fig. A.18, is formulated.

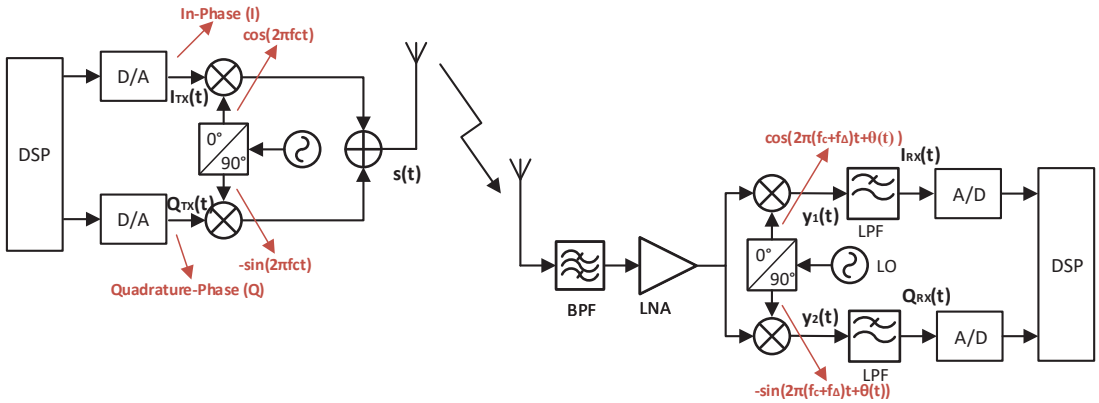

FIGURE A.18: Homodyne transceiver architecture with presence of both PN and CFO at the direct down-conversion stage (image adapted [248]).

Considering that at TX is performed an ideal direct up-conversion, and at RX, only PN is presented at the LO(s), the demodulated IQ baseband $y_1(t)$ and $y_2(t)$ signals are expressed as follows:

$$\begin{cases} y_1(t) = s(t).\cos(2\pi f_c t + \theta(t)) \\ y_2(t) = s(t).(-1)\sin(2\pi f_c t + \theta(t)) \end{cases}, \tag{A.36}$$

where the transmitted pass-band signal $s(t)$ can be represented as:

$$s(t) = I_{TX}(t)\cos(2\pi f_c t) - Q_{TX}(t)\sin(2\pi f_c t), \tag{A.37}$$

where $I_{TX}(t)$ and $Q_{TX}(t)$ are the TX's IQ baseband signals, respectively. With this, (A.36) becomes:

$$\begin{cases} y_1(t) = \frac{1}{2}I_{TX}(t)[\cos(\theta(t)) + \cos(4\pi f_c t + \theta(t))] - \frac{1}{2}Q_{TX}(t)[-\sin(\theta(t)) + \sin(4\pi f_c t + \theta(t))] \\ \\ y_2(t) = -\frac{1}{2}I_{TX}(t)[\sin(\theta(t)) + \sin(4\pi f_c t + \theta(t))] + \frac{1}{2}Q_{TX}(t)[\cos(\theta(t)) - \cos(4\pi f_c t + \theta(t))] \end{cases}$$

$$\iff \begin{cases} y_1(t) = \frac{1}{2}[I_{TX}(t)\cos(\theta(t)) + Q_{TX}(t)\sin(\theta(t))] + \\ \underbrace{\frac{1}{2}[I_{TX}t)\cos(4\pi f_c t + \theta(t)) - Q_{TX}(t)\sin(4\pi f_c t + \theta(t))]}_{\text{High frequency components}} \\ y_2(t) = \frac{1}{2}[-I_{TX}(t)\sin(\theta(t)) + Q_{TX}(t)\cos(\theta(t))] \\ \underbrace{-\frac{1}{2}[I_{TX}(t)\sin(4\pi f_c t + \theta(t)) + Q_{TX}(t)\cos(4\pi f_c t + \theta(t))]}_{\text{High frequency components}} \end{cases} \tag{A.38}$$

Finally, after proper filtering the high frequency components, highlighted in (A.38), baseband signals $I_{RX}(t)$ and $Q_{RX}(t)$ can be described as:

$$\begin{cases} I_{RX}(t) = \frac{1}{2}.[I_{TX}(t)\cos(\theta(t)) + Q_{TX}(t)\sin(\theta(t))] \\ Q_{RX}(t) = \frac{1}{2}.[-I_{TX}(t)\sin(\theta(t)) + Q_{TX}(t)\cos(\theta(t))] \end{cases}, \tag{A.39}$$

where $\theta(t)$ is the phase noise term. From (A.39), it is clearly seen that PN results into loss of orthogonality between I and Q channels, i.e., part of the signal energy at I channel goes to Q channel and vice-versa. From a *Cartesian* plot of both transmitted and demodulated signals (accounting for a scaling factor of 2), it is easier to understand the effect of such impairment in the demodulator accuracy. Considering that both $I_{TX}(t)$ and $Q_{TX}(t)$ have constant amplitude values and are time-invariant, PN leads to a rotation of the transmitted symbols, as it is illustrated in Fig. A.19. Moreover, when either the LO's phase is fluctuating or a very small frequency error is presented at RX, received symbols will be slightly spinning around part of the $\sqrt{(I_{RX}^2 + Q_{RX}^2)}$ circle. This means that under such conditions it will be difficult for the demodulator to recover the original TX information.

Another source of signal distortion induced by a RF front-end system, appears when both TX/ RX local oscillators are tuned at two distinct frequencies. The frequency difference between these reference signals is denoted as f_Δ, and it is known as CFO. Considering that PN is now negligible, $y_1(t)$ and $y_2(t)$ signals can be expressed as:

$$\begin{cases} y_1(t) = s(t).\cos(2\pi(f_c + f_\Delta)t) \\ y_2(t) = s(t).(-1)\sin(2\pi(f_c + f_\Delta)t) \end{cases} \tag{A.40}$$

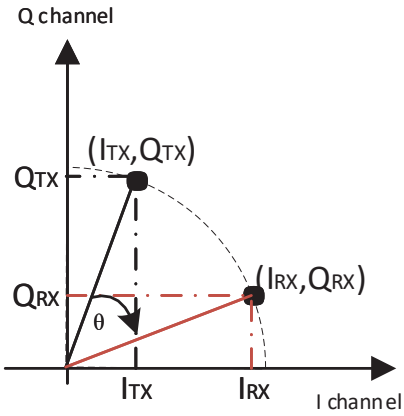

FIGURE A.19: Illustration of the PN effect in the *Cartesian* plane.

With the same considerations performed to obtain (A.39), (A.40) is simplified into:

$$\begin{cases} I_{RX}(t) = \frac{1}{2}.[I_{TX}(t)\cos(2\pi f_{\Delta}t)) + Q_{TX}(t)\sin(2\pi f_{\Delta}t)] \\ Q_{RX}(t) = \frac{1}{2}.[-I_{TX}(t)\sin(2\pi f_{\Delta}t) + Q_{TX}(t)\cos(2\pi f_{\Delta}t)] \end{cases} \tag{A.41}$$

From (A.41) it is demonstrated that when CFO is presented at RX, similar to the PN's effect, received symbols (I_{RX}/Q_{RX}) will be constantly spinning around the $\sqrt{(I_{RX}^2 + Q_{RX}^2)}$ full circle. However in this particular case, $\theta(t)$ varies linearly in the interval $[0 : 2\pi]$, which leads to a significant distortion of the received symbols.

While PN is intrinsic property of the LO, CFO between TX/ RX can be mitigated (considering that CFO induced by the channel as *Doppler* effect is negligible), by synchronising the carrier with the RX's LO frequency. In order to attain this requirement, PLL devices are usually employed as carrier synchronisation circuits at both system ends. A typical 60 GHz PLL architecture is given in Fig. A.20, where PFD, CP and VCO stand for Phase/frequency detector, charge pump and voltage-controlled oscillator, respectively. VCO has the function of generating a sinusoidal signal whose frequency and phase is being controlled by the PFD. This circuit compare the phase and frequency of the PLL's output signal divided by N, and if such has different phase and frequency from the input reference signal, a control signal proportional to this phase error is generated. Finally, VCO is controlled by a current provided by the CP, which is proportional to that error. With this loop, VCO will tend to a very frequency stable value.

Additionally, from the PLL components illustrated in Fig. A.20, the ones that contribute the most for PN are the input reference clock and the VCO [19]. From Fig. A.21 it is clearly noted that the input clock reference is the dominant source at relatively low frequency offsets, while at higher offset values, VCO becomes the dominant

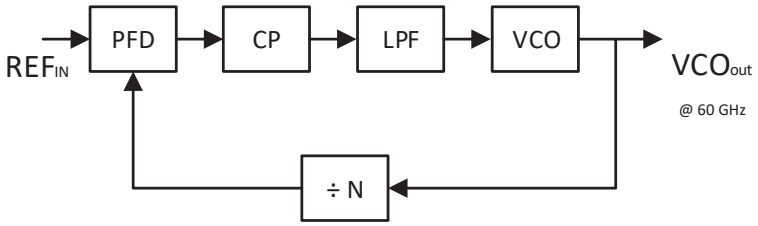

FIGURE A.20: Block diagram of a typical 60 GHz PLL architecture (image adapted from [19]).

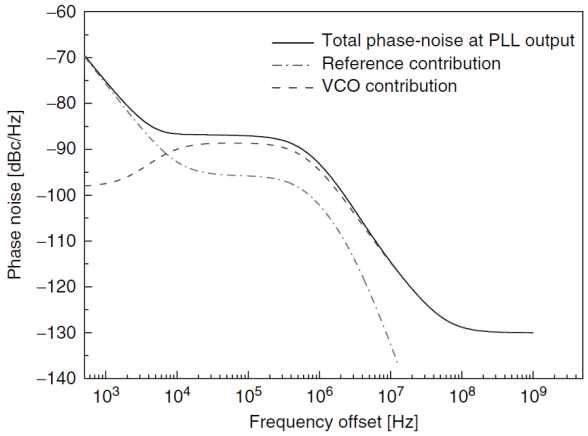

FIGURE A.21: Illustration of the contribution that both input reference clock and VCO have on the overall PLL phase-noise (image extracted from [19]).

source of phase-noise. This is explained by the fact that at flicker noise is only presented in the reference input clock [19].

DC offset

The transmission of an undesired RF carrier, results from the presence of DC voltage offset in both IQ branches. Such can be either introduced by both I and Q signal inputs (from non-ideal DAC stages [249]) or coming from analogue hardware imperfections presented in the RF modulator. At the transmitted signal, such phenomena appears as an interfering source centred at the frequency of LO. In order to understand the effect of DC offset in the demodulator performance, let's consider the transceiver architecture illustrated in Fig. A.22, where both sampled IQ baseband signals, namely d_I and d_Q, respectively, are subject to an individual DC offset value given by A_1/ A_2, respectively. Mathematically, the transmitted signal can be represented as:

$$s(t) = [A_1 + I_{TX}(t)]\cos(2\pi f_c t) - [A_2 + Q_{TX}(t)]\sin(2\pi f_c t) \tag{A.42}$$

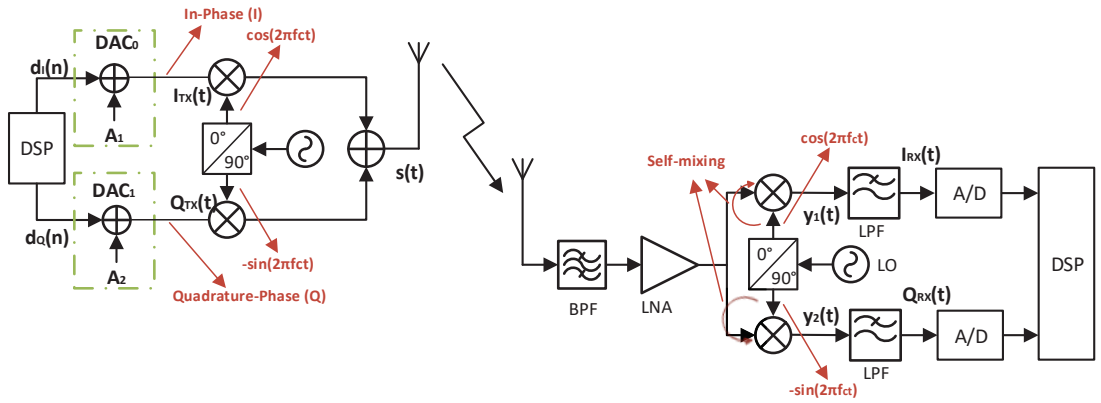

FIGURE A.22: Illustration of a homodyne transceiver with DC offset.

With the use of some trigonometric identities, and considering $I_{TX}(t)$ and $I_{TX}(t)$ equal to $A_i \cos(2\pi f_i t)$ and $A_q \cos(2\pi f_i t)$, (A.42) becomes:

$$s(t) = \underbrace{A_1 \cos(2\pi f_c t)}_{\text{DC offset}} + \frac{A_i}{2}[\cos(2\pi(f_c + f_i)t) + \cos(2\pi(f_c - f_i)t)] - \underbrace{A_2 \sin(2\pi f_c t)}_{\text{DC offset}} + \frac{A_q}{2}[\sin(2\pi(f_c + f_i)t) + \sin(2\pi(f_c - f_i)t)] \quad \text{(A.43)}$$

At RX, other sources of DC offset are the LO leakage self-mixing, which can lead to signal saturation at certain analogue stages of RX, and the ADC sampling [249] process. Mathematically, demodulated signals, $I_{RX}(t)$ and $Q_{RX}(t)$, can be expressed by:

$$\begin{cases} I_{RX}(t) = LPF\{s(t).\cos(2\pi f_c t) + S_I \cos(2\pi f_c t).\cos(2\pi f_c t)\} \\ Q_{RX}(t) = LPF\{s(t).(-1)\sin(2\pi f_c t) + S_Q \sin(2\pi f_c t).\sin(2\pi f_c t)\} \end{cases}, \quad \text{(A.44)}$$

where the second term in each of the above equations represents the self-mixing component, highlighted in Fig.A.22. Replacing $s(t)$ by (A.42), (A.44) can be simplified as:

$$\begin{cases} I_{RX}(t) = \frac{1}{2}[A_1 + I_{TX}(t) + S_I] \\ Q_{RX}(t) = \frac{1}{2}[A_2 + Q_{TX}(t) + S_Q] \end{cases}, \quad \text{(A.45)}$$

where both S_I and S_Q are the self-mixing signal amplitude in both LO's from the IQ mixing process. According to [249], these DC values can be considered static, however A_1 and A_2 might be considered as dynamic since they can change due to the variation of the wireless channel conditions.

Finally, the most straightforward technique to mitigate DC offset is to employ a high-pass filter at both TX/ RX baseband stages. Nevertheless, it might require prohibitively large capacitors [249].

IQ imbalances

The source of imbalances between I and Q branches are caused by the limited accuracy of the analogue hardware components presented in both up-conversion and down-conversion RF stages, which is more relevant in Zero-IF TX/ RX architectures. Such is mainly caused from different gains in both I/ Q branches and from the inaccuracy of the mixer's phase shifter [250], which induce significant signal distortions in sophisticated waveforms. For example, in OFDM systems, such non-idealities introduces severe distortion among sub-carriers, i.e., sub-carrier indices become mirrored around the tone $N/2+1$, where N is the total number os sub-carriers used in the designed of OFDM [193]. This results from the transmission of an image signal which after demodulation overlaps with the desired baseband signal. In this context, image signal transmission, and distortion on both received I/Q baseband signals due to IQ imbalances are formulated in this section, following the transceiver architecture shown in Fig. A.23.

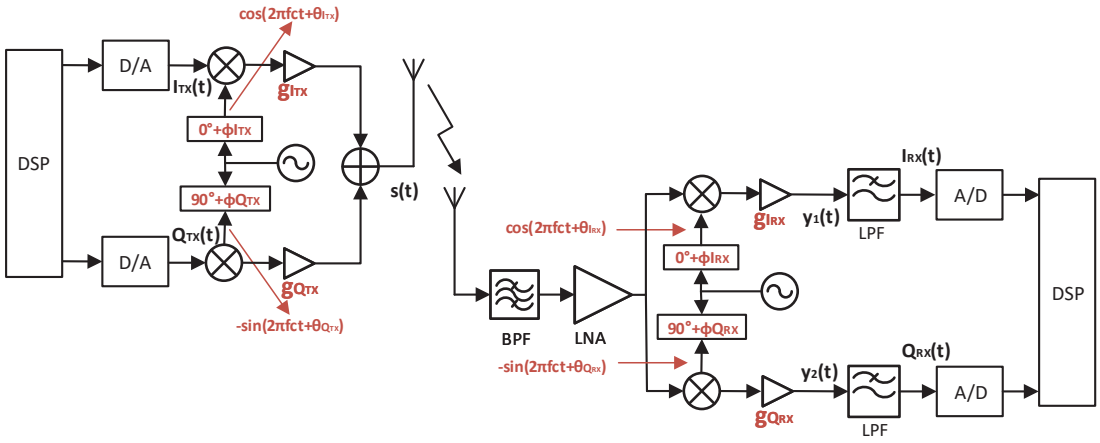

FIGURE A.23: Illustration of generic homodyne transceiver with TX/ RX IQ imbalances (image adapted from [250]).

In case of no IQ imbalances are verified at TX, both $g_{I_{TX}}$, $g_{Q_{TX}}$ are set to 1, and both ϕI_{TX}, $\phi_{Q_{TX}}$ are set to 0. With this, the RF carrier, from an IQ modulation, can be described by (A.46), leading to the carrier frequency domain representation illustrated in Fig. A.24, where it can be seen that both negative I/ Q mixing terms cancel each

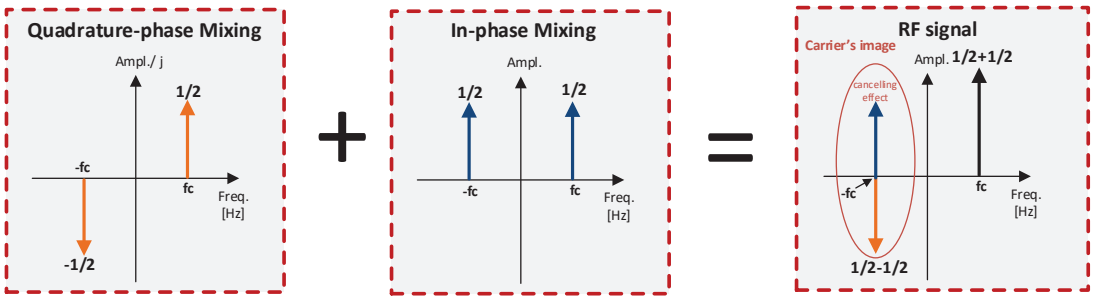

FIGURE A.24: Illustration of the frequency spectrum of the IQ modulator's RF carrier, in the absence of IQ imbalances.

other when added together. This means that no image signal is transmitted.

$$c(t) = \underbrace{\frac{1}{2}e^{j2\pi f_c t} + \frac{1}{2}e^{-j2\pi f_c t}}_{\text{real part = I-phase mixing}} + \underbrace{\frac{j}{2}e^{j2\pi f_c t} - \frac{j}{2}e^{-j2\pi f_c t}}_{\text{imaginary part = Q-phase mixing}} \tag{A.46}$$

It can be verified from Fig. A.24, that the image signal is only completely attenuated when both I and Q carriers have the same amplitude and phase. Otherwise, the transmitted carrier is described as:

$$c(t) = g_{I_{TX}} \cos(2\pi f_c t + \phi_{I_{TX}}) - g_{Q_{TX}} \sin(2\pi f_c t + \phi_{Q_{TX}}), \tag{A.47}$$

Expressing the sinusoidal functions as complex exponentials, yields:

$$\begin{aligned} c(t) = \frac{g_{I_{TX}}}{2}\Big[e^{j(2\pi f_c t+\phi_{I_{TX}})} + e^{-j(2\pi f_c t+\phi_{I_{TX}})}\Big] - \\ \frac{g_{Q_{TX}}}{2j}\Big[e^{j(2\pi f_c t+\phi_{Q_{TX}})} - e^{-j(2\pi f_c t+\phi_{Q_{TX}})}\Big] \\ \iff c(t) = \frac{g_{I_{TX}}}{2}\Big[e^{j(2\pi f_c t)}.e^{j(\phi_{I_{TX}})} + e^{-j(2\pi f_c t)}.e^{-j(\phi_{I_{TX}})}\Big] + \\ \frac{jg_{Q_{TX}}}{2}\Big[e^{j(2\pi f_c t)}.e^{j(\phi_{Q_{TX}})} - e^{-j(2\pi f_c t)}.e^{-j(\phi_{Q_{TX}})}\Big] \end{aligned} \tag{A.48}$$

Furthermore, considering the *Euler's* formula: $e^{j(A)} = \cos(A) + j\sin(A)$ and $e^{-j(A)} = \cos(A) - j\sin(A)$, (A.48) becomes:

$$\begin{aligned} c(t) = \frac{g_{I_{TX}}}{2}\Big[e^{j(2\pi f_c t)}.\Big(\cos(\phi_{I_{TX}}) + j(\sin(\phi_{I_{TX}})\Big) + e^{-j(2\pi f_c t)}. \\ \Big(\cos(\phi_{I_{TX}}) - j\sin(\phi_{I_{TX}})\Big)\Big] + \frac{jg_{Q_{TX}}}{2}\Big[e^{j(2\pi f_c t)}.\Big(\cos(\phi_{Q_{TX}}) + j\sin(\phi_{Q_{TX}})\Big) \\ - e^{-j(2\pi f_c t)}.\Big(\cos(\phi_{Q_{TX}}) - j\sin(\phi_{Q_{TX}})\Big)\Big] \end{aligned} \tag{A.49}$$

When both imaginary and real parts are placed separately, (A.49) is simplified into:

$$\begin{cases} real\{c(t)\} = \frac{g_{I_{TX}}}{2} e^{j(2\pi f_c t)}.\cos(\phi_{I_{TX}}) + \frac{g_{I_{TX}}}{2} e^{-j(2\pi f_c t)}.\cos(\phi_{I_{TX}}) - \\ \frac{g_{Q_{TX}}}{2} e^{j(2\pi f_c t)}.\sin(\phi_{Q_{TX}}) - \frac{g_{Q_{TX}}}{2} e^{-j(2\pi f_c t)}.\sin(\phi_{Q_{TX}}) \\ \\ imag\{c(t)\} = j\frac{g_{I_{TX}}}{2} e^{j(2\pi f_c t)}.\sin(\phi_{I_{TX}}) - j\frac{g_{I_{TX}}}{2} e^{-j(2\pi f_c t)}.\sin(\phi_{I_{TX}}) + \\ j\frac{g_{Q_{TX}}}{2} e^{j(2\pi f_c t)}.\cos(\phi_{Q_{TX}}) - j\frac{g_{Q_{TX}}}{2} e^{-j(2\pi f_c t)}.\cos(\phi_{Q_{TX}}) \end{cases} \tag{A.50}$$

Finally, based on (A.50), the frequency domain representation of $c(t)$ is depicted in Fig. A.25, where $A = \frac{g_{I_{TX}}}{2}.\cos(\phi_{I_{TX}})$, $B = \frac{g_{Q_{TX}}}{2}\sin(\phi_{Q_{TX}})$, $C = \frac{g_{I_{TX}}}{2}\sin(\phi_{I_{TX}})$, and $D = \frac{g_{Q_{TX}}}{2}.\cos(\phi_{Q_{TX}})$. It is demonstrated that if both out-of-phase difference between LO's is not exactly 90°, and the carrier's image is transmitted. However, if the amplitude of both I and Q branches are not the same, the undesired signal is not perfectly cancelled.

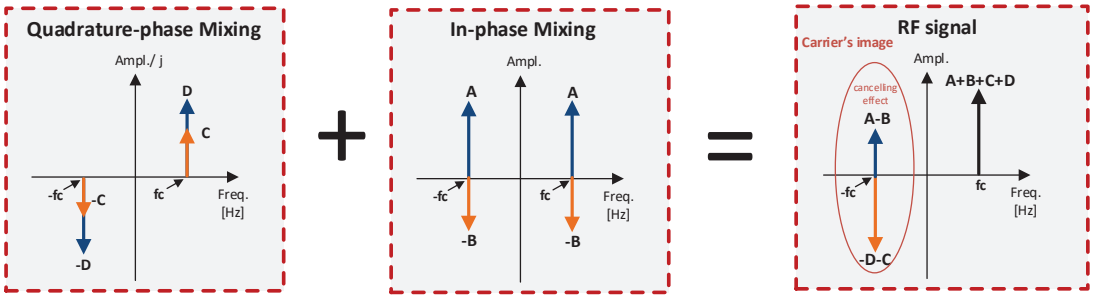

FIGURE A.25: Illustration of the frequency spectrum of the IQ modulator's RF carrier, in the presence of IQ imbalances.

At RX, IQ impairments distort both desired signal baseband signals, and consequently affect the demodulator accuracy. Mathematically this can be demonstrated, as follows:

$$\begin{cases} I_{RX}(t) = LPF\{s(t).(g_{I_{RX}}\cos(2\pi f_c t + \phi_{I_{RX}}))\} \\ Q_{RX}(t) = LPF\{s(t).(-g_{Q_{RX}}\sin(2\pi f_c t + \phi_{Q_{RX}}))\} \end{cases}, \tag{A.51}$$

where $s(t)$ is given by (A.52), which yields to (A.53).

$$s(t) = g_{I_{TX}}.I_{TX}(t)\cos(2\pi f_c t + \phi_{I_{TX}}) - g_{Q_{TX}}.Q_{TX}(t)\sin(2\pi f_c t + \phi_{Q_{TX}}) \tag{A.52}$$

$$\begin{cases} I_{RX}(t) = \frac{g_{I_{TX}} g_{I_{RX}} I_{TX}(t)}{2}[\cos(\phi_{I_{TX}} - \phi_{I_{RX}})] - \frac{g_{Q_{TX}} g_{I_{RX}} Q_{TX}(t)}{2}[\cos(\phi_{Q_{TX}} - \phi_{I_{RX}})] \\ Q_{RX}(t) = \frac{g_{Q_{TX}} g_{Q_{RX}} Q_{TX}(t)}{2}[\cos(\phi_{Q_{TX}} - \phi_{Q_{RX}})] - \frac{-g_{I_{TX}} g_{Q_{RX}} I_{TX}(t)}{2}[\sin(\phi_{I_{TX}} - \phi_{Q_{RX}})] \end{cases}, \tag{A.53}$$

where $g_{I_{RX}}$, $g_{Q_{RX}}$ are the RX's gain in each I/ Q branch, respectively, and ϕI_{RX}, $\phi_{Q_{RX}}$, are the phase mismatch present in both RX's LO's. Furthermore, from (A.53) it is verified that the demodulated baseband symbols might suffer not only phase rotation, given by the sin and cos terms, but also amplitude distortion. In addition, both TX/ RX impairments might fluctuate over time in wideband systems, like the ones operating at mmWave. For example, according to [213], while imbalances caused by I/ Q mixers might be considered frequency independent, the ones caused by filter mismatch are usually frequency dependent.

A.3 Signal processing: fundamentals

A.3.1 Discrete *Fourier* transform

As it has been discussed in Section A.2.2, *Fourier* transform is the mathematical procedure that relates time and frequency domains, of a particular signal. In fact, if a signal is affected in one domain, it will be also changed in the other domain. For example, convolution in the time domain corresponds to a multiplication in the frequency domain [233]. Moreover, according to [251], Discrete Fourier Transform (DFT) is one of the most powerful signal processing algorithms utilised in today, in the field of engineering. It can be used to manipulate, analyse and synthesise signals in such way that would not be possible in the analogue (continuous) domain. *Fourier* transform of a continuous signal $x(t)$ is defined in (A.54) [233].

$$X(\omega) = \int_{-\infty}^{+\infty} x(t) e^{-j\omega t}\, dt, \tag{A.54}$$

where ω is the angular frequency given by $2\pi f$. Consequently, the discrete version of (A.54) is given by [251]:

$$X(m) = \sum_{n=0}^{N-1} x(n) e^{-j2\pi nm/N}, \tag{A.55}$$

where $x(n)$ is a discrete time-domain sequence from sampled values of $x(t)$, and both m and N are the index of the DFT output in the frequency domain and the total number of samples of $x(n)$, respectively. Consequently, considering the *Euler's* formula:

$e^{j(A)} = \cos(A) + j\sin(A)$ and $e^{-j(A)} = \cos(A) - j\sin(A)$, (A.55) becomes:

$$X(m) = \sum_{n=0}^{N-1} x(n)[\cos(2\pi nm/N) - j\sin(2\pi nm/N)] \tag{A.56}$$

From (A.56), the output of DFT is the sum of the product between $x(n)$ and a complex sinusoid, where, each of the frequency points $X(m)$ correspond, in fact, to the fundamental frequency of each the real and imaginary sinusoids, given by $\frac{mf_s}{N}$, where f_s is the sampling rate. Finally, the spectral content of the input $x(t)$ is given at N equally spaced frequency points [251]. Since, the output of a DFT is a complex value, phase relation between the various signal spectral components can be obtained from: $X_\phi(m) = tan^-1\frac{X_{imag}(m)}{X_{real(m)}}$. Consequently, power spectrum can be obtaining by the sum of each real/ imaginary squared magnitude. In sum, the main features of DFT operation are [251]:

- For real input values, a N-point DFT output is characterised by $N/2+1$ independent terms (total frequency range from DC up to $\frac{f_s}{2}$);
- The DFT output of the sum of two input sequences, $x_{sum} = x_1(n) + x_2(n)$ is equal to the sum of their individually DFT output, given by $X_{sum} = X_1(m) + X_2(m)$;
- The magnitude of the DFT's output is proportional to the length of the input sequence;
- The frequency resolution is $\frac{f_s}{N}$;
- Spectral resolution of the DFT operation can be enhanced by increasing N. As rule of thumb, to attain a certain frequency resolution ($freq_{res}$), it is required to collect $\frac{1}{freq_{res}}$ seconds of non-zero time samples.

Moreover, there is a DFT spectrum leakage when the input sequence has frequency components non multiples of $\frac{f_s}{N}$. For example, the DFT's amplitude response of from a arbitrary real sinusoid is given by the following sinc response [251]:

$$X(m) = \frac{A_o N}{2}.\frac{sin[\pi(k-m)]}{sin[\pi(k-m)]}, \tag{A.57}$$

where A_o is the amplitude of the sampled input sinusoid, and k is the number of the sine-wave cycles in the N-point input sequence length. This is extremely important since spectral components from the input sequence can be masked by the side-lobes of the sinc function. In order to mitigate this, input data is usually multiplied with a window function prior to DFT [251].

Furthermore, the DFT of an all-ones rectangular window function as input sequence $x(n)$, is also characterised by the following sinc function [251]:

$$X(m) = \frac{sin[\pi m]}{sin[\frac{\pi m}{N}]}, \tag{A.58}$$

where $x(n)$ is equal to 1 in the range of $-(N-1)/2$ to $(N-1)/2$, and N is the size of DFT, which is the same number of the $x(n)$ samples.

Finally, since it is not possible to calculate continuous *Fourier* transform (it has an infinitely value of frequency resolution) of an discrete time-domain sequence in Digital Signal Processing (DSP), DFT considers that both time and frequency responses of any particular input signal are periodic [233].

A.3.2 Fast *Fourier* transform

The major drawback of the DFT calculation method described above, is its computation inefficiency. This is, as N tends to a relatively large value, the amount of complex multiplications operations become impractical, leading to relatively large computation time [233]. However, in 1965 a FFT algorithm was proposed, by *Cooley* and *Tukey*, to implement the DFT in a very efficient way, while maintaining the aforementioned DFT features [251].

One of the most popular FFT algorithms is known as radix-2 FFT, which aims to reduce the redundant arithmetic operation present in the DFT operation. This algorithm splits a relatively large DFT into several 2-point DFT, which significantly reduces the number of necessary complex multiplications (these mathematical routines are well described in [251]). As result, while a typical N-DFT requires N^2 multiplications, a N-FFT only needs $\frac{N}{2}\log_2(N)$. Complexity comparison between these two algorithms is highlighted in Fig. A.26 for several input sequence length values (N). In particular, when $N = 2^{15}$, the result would be 1.07×10^9 and 2.4×10^5 complex multiplications, for DFT and FFT, respectively. It is worth noting that, if a multiplication is carried out in 1 ns, the DFT case would consume 1.07 s, while the FFT one would only require 2.4×10^{-4} s (0.0224% of the DFT time).

The main particularity of radix-2 FFT algorithm is that the input sequence must always have a integer number of samples that satisfies the condition: $N = 2^k$, where k is any positive integer value. Otherwise, the number of input samples must be zero-padding until the former condition is met [251]. Furthermore, the number of input samples should be calculated depending on the target spectral resolution of a certain signal frequency response analysis, which is given by (A.59) [251]. For example, if a spectral

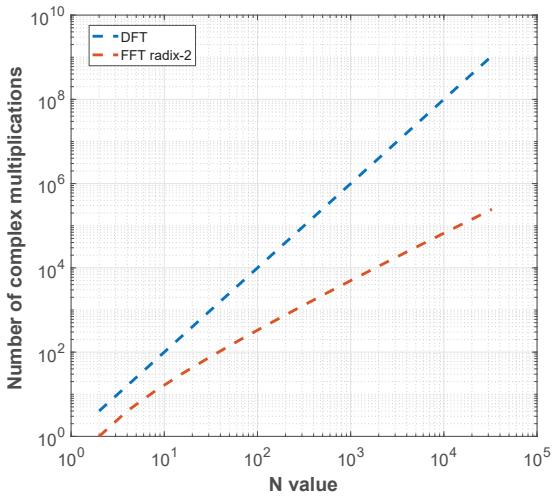

FIGURE A.26: Comparison of DFT with radix-2 FFT in terms of number of complex multiplications versus N.

resolution of 10 Hz is necessary, then the number of samples required are $0.1 f_s$. Once again, if the obtained value is not a power of two, zero padding should be performed.

$$N = \frac{f_s}{freq_{res}} \tag{A.59}$$

Additionally, the SNR at the output of the FFT increases with the increasing of N. Thus, this SNR value can be defined as the SNR of the input signal minus the FFT gain process, given by $10\log(\frac{N}{2})$ [233]. This is similar to the behave of a narrowband SA, where its noise floor decreases with the decreasing of the resolution bandwidth.

A.3.3 Sampling theory

A continuous analogue signal can be converted into a discrete-time digital sequence by sampling the continuous-time signal at discrete interval times. Next, a quantiser is responsible to convert the time-discrete amplitude samples into a digital format [233]. The device where both aforementioned processes are performed is called ADC. Similarly, a discrete-time signal can be converted to its continuous-time version by a reconstruction performed by the DAC. According to [233], the sampling method is known as either uniform sampling or periodic sampling. Such consists on the acquisition of samples from the continuous-time original signal repeatedly every interval sampling period (T_s). This can be mathematically expressed by [233]:

$$x_s(t) = x(t)p(t) = x(t)\sum_{k=-\infty}^{\infty}\delta(t - kT_s), \tag{A.60}$$

where $p(t)$ is the sampling function, and $x(t)$ the original time-continuous signal. Despite from (A.60), sampling seems to be quite straightforward task, a major concern rise upon how fast should ADC/ DAC operate to ensure that original signal content is preserved. For example, considering that a sinewave is being sampled at a certain rate, it might not be possible to evaluate if the fundamental frequency of the discrete-time signal is actually the same of its original continuous-time version. From [251], it has been demonstrated that a sampled version of a sinewave is given by:

$$x(n) = \sin(2\pi f_o n T_s) = \sin(2\pi(\underbrace{f_o + k f_s}_{\text{signal replicas}})nT_s) \tag{A.61}$$

where f_s is the sampling rate, and f_o is the fundamental frequency of the sinewave.

From (A.61), it is clearly noted that sampled values of a f_o sinewave also represents other sinewaves at frequencies kf_s, where k can be any positive/ negative integer value. In fact, this is in line from what have been discussed in the above section. This is, any sampled discrete sequence has a periodic spectrum at multiple integer values of f_s. Having in mind that the band of interest is from $[-\frac{f_s}{2}, \frac{f_s}{2}]$, signal replicas given by $f_o + kf_s$ could not appear in such interval. Otherwise, the signal of interest will be characterised by other frequency tones instead. This is known as frequency ambiguity or as aliasing [251]. As an example, it is considered that a $f_o = 7$ kHz sinewave was sampled at $f_s = 6$ kHz, and that $k = -1$. In this particular case, a signal replica will appear at $7 - 6 = 1$ kHz. This issue is shown in Fig. A.27, where samples of sinewave #2, which has a frequency 7 times higher than sinewave #1, are the same of sinewave #1, when f_s is 0.86 times slower than the frequency of sinewave #2. Therefore, it is not possible to assess from each sinewave the sequence of sampled values belong to. In other others, the integrity of the sampled signal really depends on the sampling rate (f_s). In order to overcome this problem, at least two samples per period of a particular sinewave must be taken, i.e., $f_s > 2f_o$. This is known as the *Nyquist* sampling theorem [233].

Finally, in case $x(n)$ is a sampled version of a bandlimited continuous-time signal, $x(t)$, with bandwidth from $[-B, B]$, aliasing will also occur in its discrete spectrum if the *Nyquist* condition is not met. The spectral relation between f_s, and the aliasing effect, for a particular signal bandwidth, is illustrated in Fig. A.28b and Fig. A.28c, considering that $\frac{f_s}{2} > B$ and $\frac{f_s}{2} < B$, respectively. Particularly, from the former figure, it is clearly seen that signal replicas are overlapping the continuous spectrum in the desired band of interest ($[-\frac{f_s}{2}, \frac{f_s}{2}]$). This means, that under such condition, the original signal will not be able to be retrieved after a DAC process (part of the spectral information within the band of $-B$ to B Hz has been corrupted).

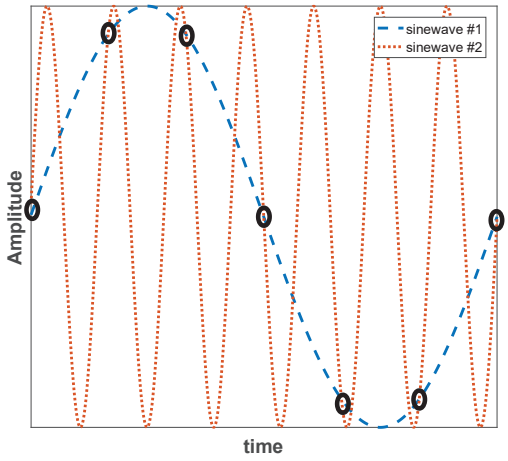

FIGURE A.27: Frequency ambiguity effects of sampling at 7 kHz sinewave at a sample rate of 6 kHz. (image adapted from [251])

A.3.4 *Nyquist* zones

As it aforementioned above, converting a continuous-time signal into a discrete sampled sequence will generate replicas of the original signal, centred at multiples of f_s, in the frequency domain. In this context, the spectrum of any discrete signal can be divided into an infinitive number of *Nyquist* zones, which are characterised with a bandwidth of $\frac{f_s}{2}$, as highlighted in Fig. A.29 for the spectrum's magnitude over multiples of the sampling rate). Moreover, this means that any interfering signal located above $\frac{f_s}{2}$ or below $-\frac{f_s}{2}$ in the continuous-time original signal will be aliased into the first *Nyquist* zone (band of interest), as it is depicted in Fig. A.30a. Therefore, prior to any sampling process, an analogue low-pass filter, also known as anti-aliasing filter [251], must be placed at the input of the ADC. As it is illustrated in Fig. A.30b, frequency replicas of the interfering signal would no longer aliase with the desired signal, when the interfering signals are suppressed by the filter.

A.3.5 DAC and ADC characterisation metrics

Digital-to-analogue and analogue-to-digital converters are one of the most important blocks in a radio testbed, since they perform the bridge between digital and analogue domains. In order to understand the hardware limitations in both ADC and DAC conversions, a series of measurements can be conducted to evaluate their performance boundaries. In order to quantify signal distortion induced by both converters, measurement setups shown in Fig. A.31a and Fig. A.31b are typically considered, respectively for the DAC and ADC converters. In general, a single tone signal is generated either in the continuous-time domain or in the digital-domain (depending on the considered converter) and its spectral purity is assessed trough several performance indicators.

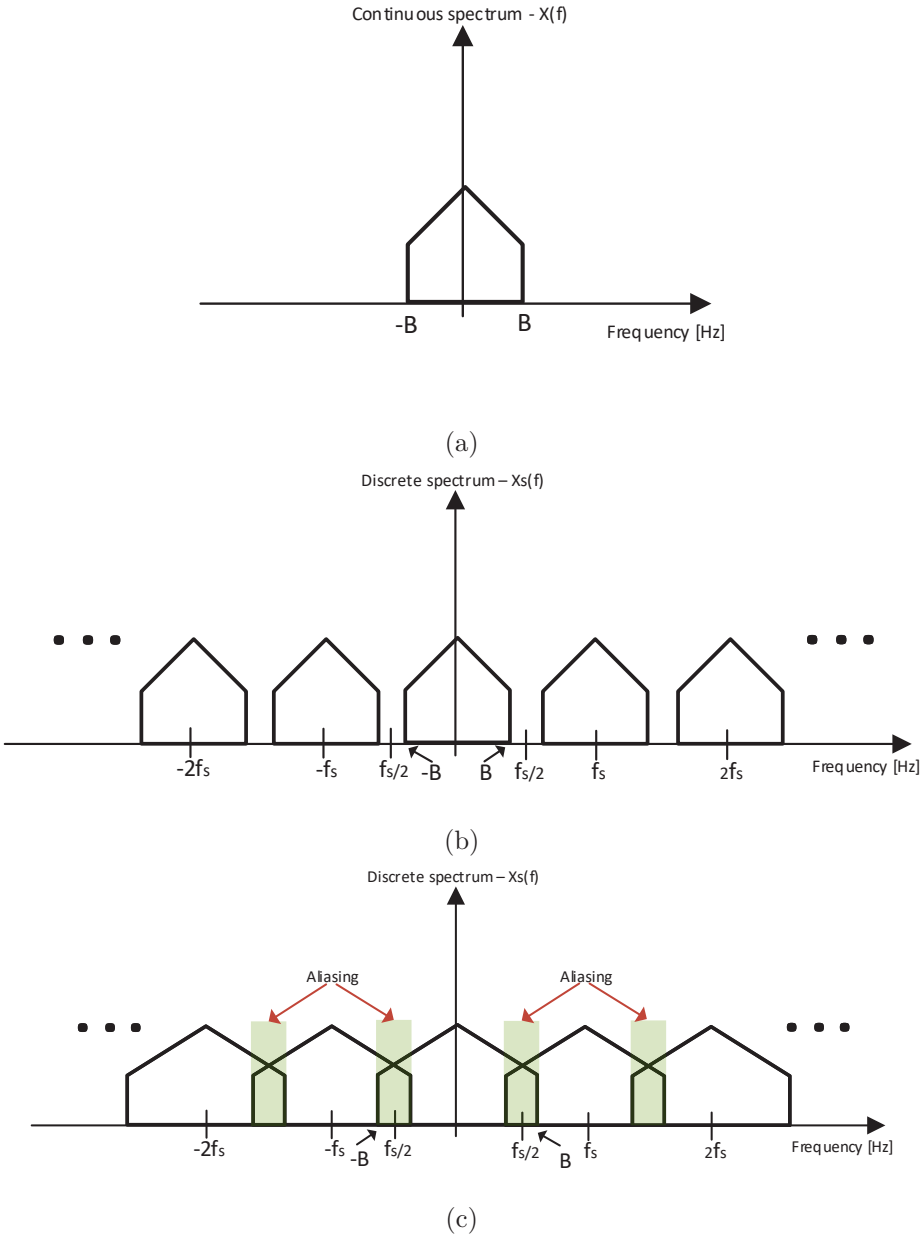

FIGURE A.28: Frequency spectrum of: (a) original continuous-time signal; (b) discrete version of the original signal when $fs/2 > B$; (c) discrete version of the original signal when $fs/2 < B$. (images adapted from [233]).

These are: SINAD, ENOB, and SFDR [233]. A description of the aforementioned metrics is given below, based on the work reported in [252, 253].

SINAD

SINAD gives an indication of a converter's overall dynamic range, as it expresses the ratio of the desired signal RMS amplitude (S) to the mean value of the root-sum-square of harmonic distortion components, presented at $| \pm kf_s \pm nf_o|$, plus noise. Both k and

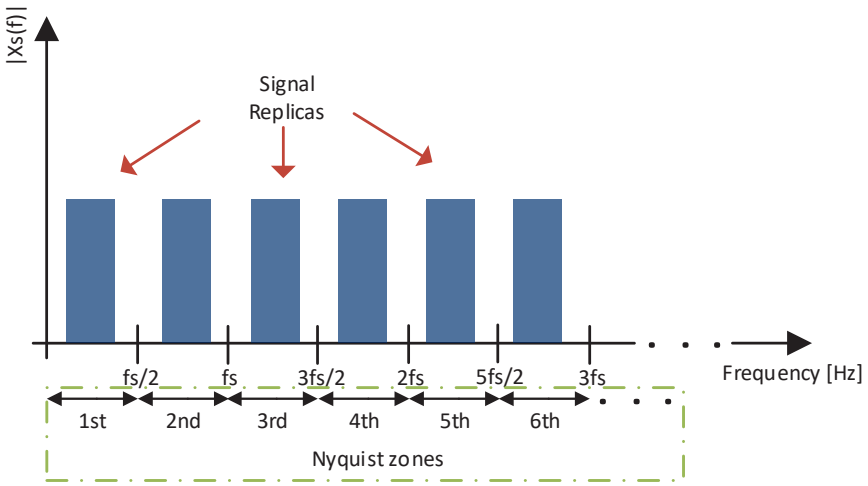

FIGURE A.29: Illustration of the *Nyquist* zones present in the magnitude frequency response of any discrete sampled signal.

n might have any integer number greater than 0, but only the harmonics that are in half of the *Nyquist* bandwidth are considered. It can be calculated as:

$$SINAD = 20\log_{10}\frac{S}{N+D}[dB] = -10\log_{10}.(10^{-SNR/10} + 10^{-THD/10})[dB], \quad \text{(A.62)}$$

where both SNR and Total Harmonic Distortion (THD) can be measured directly from the FFT/ spectral analyser outputs (sample averaging might be considered to smooth the random variation of noise). Nonetheless, in case of the ADC, FFT processing gain must be subtracted from the measured SNR value. THD is the ratio between S with the mean value of the root-sum-square of the tone (f_o) harmonics. These parameters change with both signal's frequency and amplitude, i.e., lower S value means lower SINAD and SNR. Moreover, it is worth noting that, ideal SNR can be calculated using (A.63), where N is the number of bits of the DAC/ ADC.

$$SNR = 6.02N + 1.76[dB] \quad \text{(A.63)}$$

As it can be verified from (A.63), lower number of bits leads to lower SNR levels, for a full-scale input signal. This is because quantisation process introduces random error samples. The maximum amplitude error in each sample is given by $\pm\frac{1}{2}\frac{V_{ref}}{2^N}$, where V_{ref} is the amplitude of the input signal at the convert. Moreover, according to [233], this error spread uniformly over the entire *Nyquist* bandwidth, and can be approximately modelled by a *Gaussian* distribution.

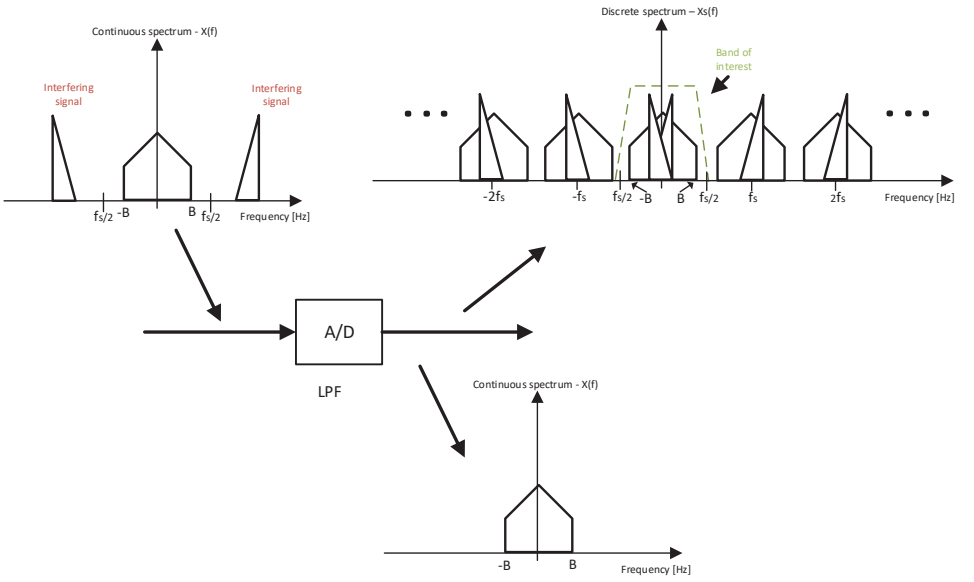

(a)

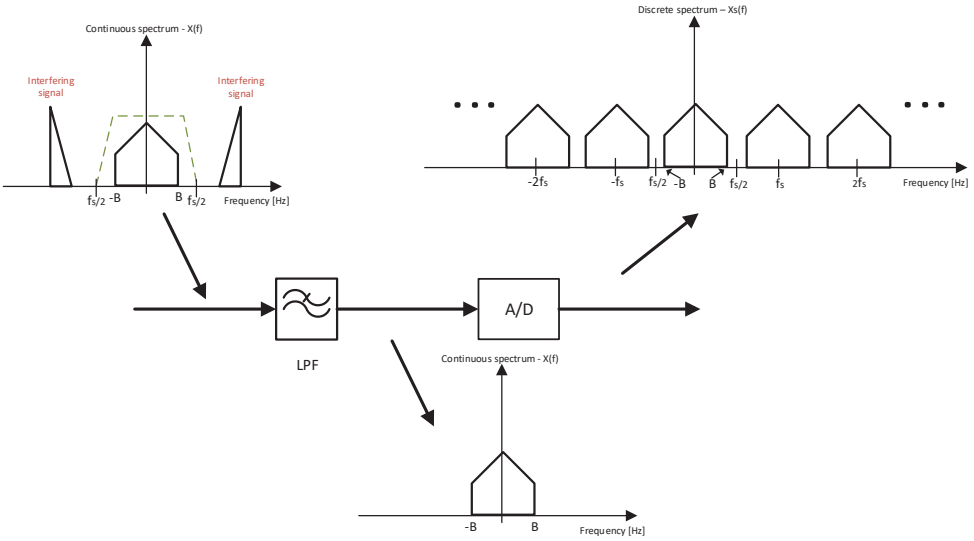

(b)

FIGURE A.30: Frequency spectrum of: (a) original continuous-time signal; (b) discrete version of the original signal when $fs/2 > B$; (c) discrete version of the original signal when $fs/2 < B$. (images adapted from [233]).

ENOB

The ENOB measures the bit resolution accuracy of both DAC/ ADC, at a particular fundamental frequency and sampling rate. In addition, ENOB can also be related to SINAD in dB and it is generally expressed as:

$$ENOB = \frac{SINAD - 1.76}{6.02}[dB], \tag{A.64}$$

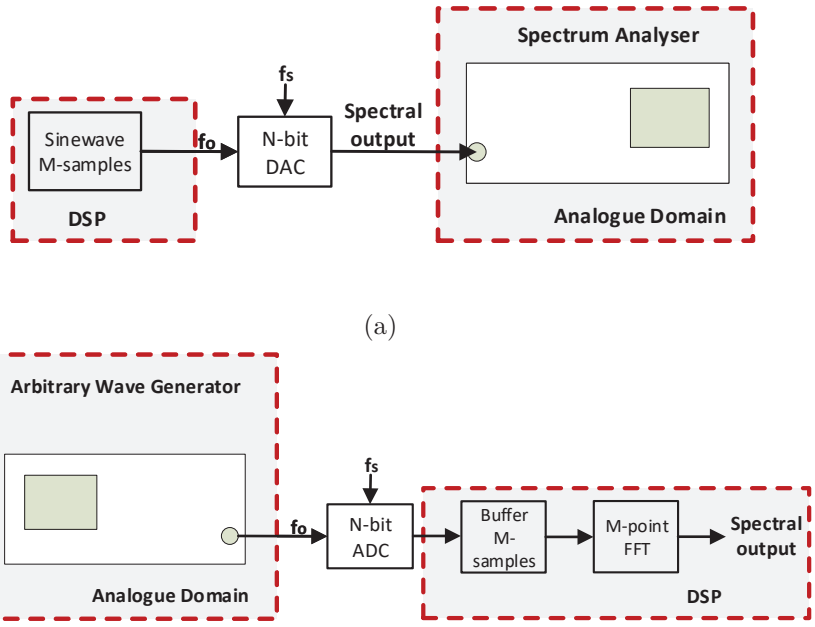

FIGURE A.31: Block diagram of the characterisation measurement setup in: a) DAC, and b) ADC.

where 1.76 refers to the quantisation error of an ideal DAC/ ADC [254] and 6.02 is equal to $20\log_{10}(2)$, which corresponds to conversion of the logarithmic base.

SFDR

Finally, SFDR is the ratio between the fundamental signal's RMS amplitude level to the worst distortion spur, i.e., with the highest amplitude level relative to other non-desired spectral components. Such spur could be a non-harmonic of the original signal. Such metric is also measured from the frequency response of the converter in the band of interest (DC up to $f_s/2$).

A.4 Digital communication: fundamentals

A.4.1 *Shannon* channel capacity

In Chapter 2, it has been discussed that mmWave technology can lead to an increase of the overall mobile cells capacity (since relatively large channel bandwidth is available), while enabling efficient frequency re-use of the spectrum utilisation. However, channel capacity does not increase linearly with the increasing of signal bandwidth. This is, even if B tens to infinity, the data rate will be limited by the received power, in a free

error transmission. This is known as the *Shannon* limit, which is expressed as [131]:

$$C = B \times \log_2(1 + SNR) \Leftrightarrow C = B \times \log_2(1 + \frac{P_{RX}}{N_0.B})[bps], \tag{A.65}$$

where C is the channel capacity, P_{RX} is the received power, and N_0 power spectral density of noise. Therefore, (A.65) describes the theoretical maximum non-erroneous data rate that a digital transceiver can achieve, for a particular signal bandwidth and SNR. In case error-correcting codes are considered to reduced the probability of bit error, channel capacity is reduced by the factor $\frac{k}{N}$ (signalling rate), where k and N are the message and codeword lengths. Furthermore, when $B \to \infty$, (A.65) can be simplified into [14]:

$$C = 1.44 \times \frac{P_{RX}}{N_0}[bps], \tag{A.66}$$

From (A.66) is mathematically demonstrated that even when signal bandwidth is unlimited, SNR is the major channel capacity limiting factor. This is clearly seen in Fig. A.32, where at a SNR value of 1 dB, channel capacity value remain rather low, even for relatively large signal bandwidths. This limitation is known as the *Shannon* AWGN capacity, and it is usually considered as the performance boundary in evaluating transmission schemes, under the assumption that the wireless channel is both non-dispersive and static.

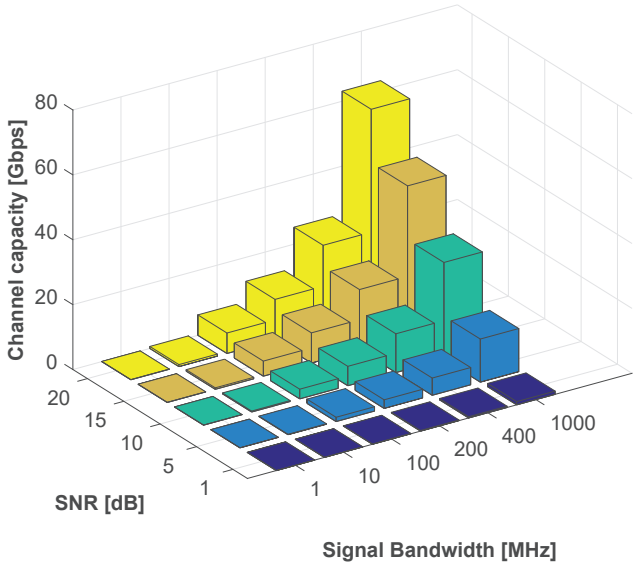

FIGURE A.32: *Shannon* limit versus SNR and signal bandwidth.

A.4.2 Digital modulations for mmWave communications

In this section, it is given an overview on the most relevant modern digital modulation techniques, particularly for mmWave communication systems. Digital modulation is the conversion of a bit stream data into analogue signal waveforms, which then will carry the information over a particular channel [231]. While at TX, a modulator converts bits into analogue waveforms, at RX, its counterpart (the demodulator) try to recover the original bit sequence from the received analogue information. Most modulations techniques have a intermediary step, where a group of k bits can be mapped in to one out of $M = 2^k$ symbols, which define the physical characteristics of the continuous carrier waveform in terms of amplitude and phase [233]. In fact, digital modulations can be classified depending on the carrier's amplitude and phase [14]. On one hand, modulations such as Phase Shift Keying (PSK) and Frequency Shift Keying (FSK), are characterised by a carrier with constant amplitude to carry the symbol's information in either phase or frequency variations, respectively. On the other hand, Amplitude Shift Keying (ASK) and QAM modulations transfer data in carrier amplitude variations. In sum, the method of mapping bits to symbols vary according to the modulation scheme, as well the bit rate, which is k times the transmission symbol rate.

The most evident way to manipulate the physical characteristics of a particular carrier is known as Pulse Amplitude Modulation (PAM), where data information is encoded in the amplitude of multiple signal pulses [233]. Consequently, PAM demodulation is performed by assessing the amplitude level of the carrier at a certain time interval [233]. Hence, in general, PAM signals, denoted as $s(t)$, can be interpreted as basis pulse $g(t)$, multiplied with a modulation coefficient c_i, as expressed below [231]:

$$s(t) = \sum_{i=-\infty}^{\infty} c_i g(t - iT_s), \tag{A.67}$$

where T_s is the symbol (pulse) duration, which means that $g(t)$ is only defined in this time interval, otherwise it is zero. From (A.67) it can be verified that the transmitted analogue symbol is composed by series of time-shifted $g(t)$, where the modulation presented in each pulse is independent of each other [231]. Different PAM can be realised by setting a particular coefficient value for a specific bit. For example the most basic arrangement between bits and PAM symbols, is when the binary digits "0" and "1" are mapped to two amplitude levels, as follows [233]:

$$\begin{cases} \text{"1"} \rightarrow s_1(t) \\ \text{"0"} \rightarrow s_2(t) \end{cases}, \tag{A.68}$$

where both $s_1(t)$ and $s_2(t)$ are characterised with the same basis pulse function given in (A.67), but with two distinct amplitudes. Moreover, according to [233], the energy of each symbol, can be calculated using (A.69).

$$E_s = \int_0^{T_s} s^2(t)dt[J] \tag{A.69}$$

Additionally, since it can be assigned M distinct amplitudes to PAM symbols, relation between average bit and symbol energies is given as follows: $\overline{E}_b = \frac{\overline{E}_s}{\log 2(M)}$. Furthermore, the minimum *Euclidean* distance among two symbols can be expressed as [233]:

$$d^2_{min} = min_{s_i(t),s_j(t),i\neq j} \int_0^{T_s} (s_i(t) - sj(t))^2 dt \tag{A.70}$$

Additionally, the effectiveness of converting bit(s) into a symbol in terms of the required transmitted power, is given by $\epsilon_p = \frac{d^2_{min}}{\overline{E}_b}$. According to [233], the maximum power efficiency a M-PAM signal can attain is $\epsilon_p = 4$. To this end, M-PAM modulation maximum amplitude coefficients should follow (A.71) [233].

$$c_i = A(2i - 1), \tag{A.71}$$

where i represents the index of the symbol. Moreover, A and its multiples represent the amplitude values that are assigned to symbols. This leads to the M-PAM signal constellation illustrated in Fig. A.33. Finally, expressions for both average symbol and

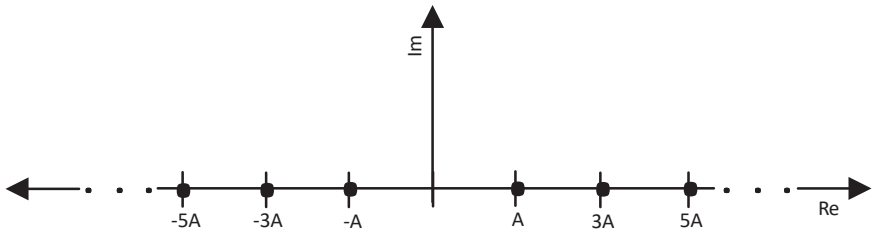

FIGURE A.33: Space diagram of a M-PAM signal constellation (image adapted from [233]).

bit energy, are given in (A.72) and (A.73), respectively [233].

$$\overline{E}_s = A^2 T_s \frac{M^2 - 1}{3} \tag{A.72}$$

$$\overline{E}_b = \frac{A^2 T_s (2^{2k}) - 1}{3k} \tag{A.73}$$

BPSK and QPSK

As aforementioned, PSK modulation manipulates the phase of a particular carrier in accordance with the transmitted bit stream. Such can be expressed as [255]:

$$s_i(t) = A.cos(2\pi f_c t + \phi_i), \tag{A.74}$$

where i is symbol index which can have values from 0 up to $M-1$, which is the number of different phases (symbols) PSK modulation carrier can represent, and and f_c is the carrier frequency. The most common type of this modulation is BPSK, which is the simplest and more robust digital phase modulation [256]. In BPSK each symbol corresponds to a single bit. Hence, the most logic approach is to separate them 180° apart, as follows [255]:

$$\begin{cases} s_1(t) = A.cos(2\pi f_c t + \pi), \; if \; bit \; 0 \\ s_2(t) = A.cos(2\pi f_c t + 0), \; if \; bit \; 1 \end{cases}, \tag{A.75}$$

where $\phi_i = \frac{2\pi i}{M}$. Furthermore, knowing that, the average power ($\overline{P}$) of a sinusoid signal is $\frac{A^2}{2}$ [W], and that $E_s = \overline{P}.T_s$ [J], (A.75) can be re-written as [255]:

$$\begin{cases} s_1(t) = -\sqrt{2\overline{P}}.cos(2\pi f_c t) = -\sqrt{\frac{2E_s}{T_s}}.cos(2\pi f_c t), \; if \; bit \; 0 \\ s_2(t) = \sqrt{2\overline{P}}.cos(2\pi f_c t) = \sqrt{\frac{2E_s}{T_s}}.cos(2\pi f_c t), \; if \; bit \; 1 \end{cases}, \tag{A.76}$$

From (A.76), it can be noted that BPSK modulation is equivalent to an amplitude modulation, since the carrier changes from A to $-A$, and vice-versa, depending on the bit to be sent, as it is illustrated in Fig. A.34. Thus, the BPSK intermediary step, is in fact a 2-PAM. Another very popular PSK modulation is known as QPSK, since it boosts two times the data rate of a BPSK modulation (in this case $M = 4$ leads to 2 bits per symbol) [256]. To this end, and based on (A.74), QPSK modulated analogue waveform, in function of the carrier phase, is expressed by (A.77) [255].

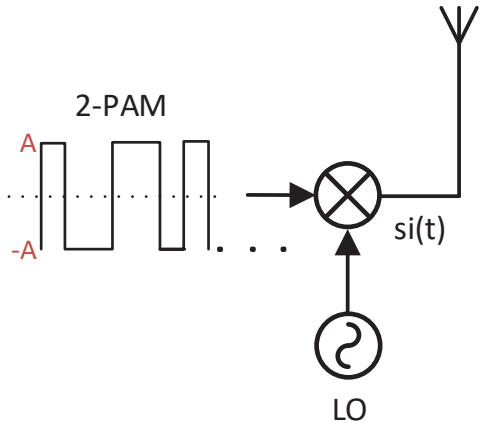

FIGURE A.34: BPSK analogue transmission (image adapted from [14]).

$$s_i(t) = \sqrt{\frac{2E_s}{T_s}}.cos(2\pi f_c t + \frac{\pi i}{2} + \phi_o), \tag{A.77}$$

where ϕ_o is an arbitrary phase offset, typically chosen as $\frac{\pi}{4}$ [255]. One possible bit mapping for QPSK signals is the following:

$$\begin{cases} s_1(t) = \sqrt{\frac{2E_s}{T_s}}.cos(2\pi f_c t + \frac{\pi}{4}),\ if\ bit\ 00 \\ s_2(t) = \sqrt{\frac{2E_s}{T_s}}.cos(2\pi f_c t + \frac{3\pi}{4}),\ if\ bit\ 01 \\ s_3(t) = \sqrt{\frac{2E_s}{T_s}}.cos(2\pi f_c t + \frac{5\pi}{4}),\ if\ bit\ 10 \\ s_4(t) = \sqrt{\frac{2E_s}{T_s}}.cos(2\pi f_c t + \frac{7\pi}{4}),\ if\ bit\ 11 \end{cases}, \tag{A.78}$$

Additionally, applying the trigonometric identity $\cos(x+y) = \cos(x)\cos(y) - \sin(x)\sin(y)$ to (A.77), QPSK signals can also be expressed by (A.79), which is quite similar to the equation of an transmitted I/ Q signal detailed in (A.37). This yield to a two-dimensional signal space representation where both I-phase/ Q-phase mixing are carried out by the carriers given in (A.80) [255].

$$s_i(t) = \sqrt{\frac{2E_s}{T_s}}.[\cos(2\pi f_c t)\cos(\frac{\pi i}{2} + \frac{\pi}{4}) - \sin(2\pi f_c t)\sin(\frac{\pi i}{2} + \frac{\pi}{4})], \tag{A.79}$$

$$\begin{cases} \psi_1(t) = \sqrt{\frac{2}{T_s}}cos(2\pi f_c t) \\ \psi_2(t) = \sqrt{\frac{2}{T_s}}sin(2\pi f_c t) \end{cases}, \tag{A.80}$$

Consequently, this leads another possible bit mapping, given as follows:

$$\begin{cases} s_1(t) = \sqrt{\frac{2E_s}{T_s}}.\frac{\sqrt{2}}{2}\big[\cos(2\pi f_c t) - \sin(2\pi f_c t)\big],\ if\ bit\ 00 \\ s_2(t) = \sqrt{\frac{2E_s}{T_s}}.\frac{\sqrt{2}}{2}\big[-\cos(2\pi f_c t) - \sin(2\pi f_c t)\big],\ if\ bit\ 01 \\ s_3(t) = \sqrt{\frac{2E_s}{T_s}}.\frac{\sqrt{2}}{2}\big[-\cos(2\pi f_c t) + \sin(2\pi f_c t)\big],\ if\ bit\ 10 \\ s_4(t) = \sqrt{\frac{2E_s}{T_s}}.\frac{\sqrt{2}}{2}\big[\cos(2\pi f_c t) + \sin(2\pi f_c t)\big],\ if\ bit\ 11 \end{cases}, \tag{A.81}$$

From (A.81), it is easy to note that QPSK is in fact the sum of two independent BPSK modulations performed at both I/ Q chains. Therefore, QPSK can be implemented as either a phase modulation or as an amplitude modulation, as highlighted in Fig. A.35a, and in Fig. A.35b, respectively. In particular, in the former figure, it is seen that QPSK signal is composed of two sets of 2-PAM symbols, where each one carry 1 bit. This leads to the QPSK signals projection in function to $\psi_1(t)$ and $\psi_2(t)$ of Fig. A.36, where the distance between adjacent symbols (d) is equal to $2\sqrt{\frac{E_s}{2}}$. Due to this reason QPSK is also known as 4-QAM. Moreover, the amount of transmitted power required for each mapped bit is the same, regardless the symbol point in the space diagram, since signal amplitude is always equal to $\sqrt{(\pm\frac{E_s}{2})^2 + (\pm\frac{E_s}{2})^2}$.

Consequently, a QPSK demodulator can also be seen as two independent BPSK demodulation processes in each I/ Q channels. Therefore, after the I/Q down-conversion is carried out, a bit to symbol decision if performed considering the amplitude of each received baseband PAM symbol. Particularly for QPSK, receiver only evaluates whether the RX symbol magnitude is > 0 or < 0 in each I/Q branch. The aforementioned process is known as *hard decision demodulation*, where for QPSK the boundaries are defined by the real and imaginary axes.

M-QAM

As it was verified in Section 2.3, QAM is widely employed in the PHY layer of both current and emerging Gigabit/s wireless communication protocols, specially at mmWave. The motivation for its use, is mainly related to [231, 233]:

- More information (k bits) are transmitted per symbol, which leads to higher data rates;
- Higher spectral efficiency is achieved in comparison with other modulation schemes;
- Simple receiver structure;
- Despite being a straight amplitude modulation, it employs two independent double side-bands in the same spectrum.

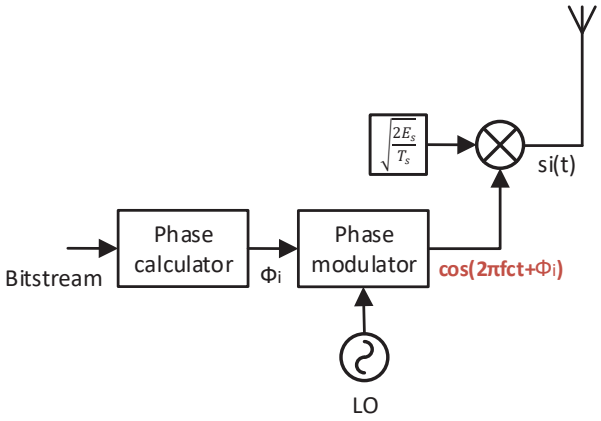

(a)

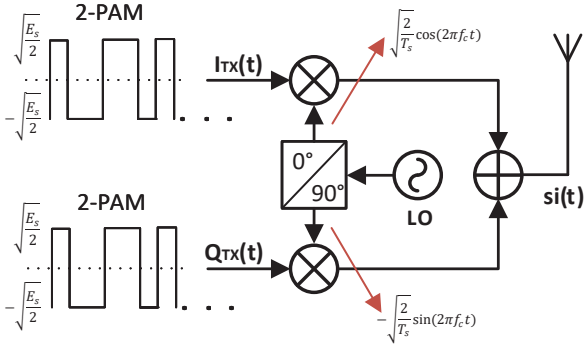

(b)

FIGURE A.35: Block diagram of the QPSK transmitter as: a) phase modulation (images adapted from [255]), and b) amplitude modulation.

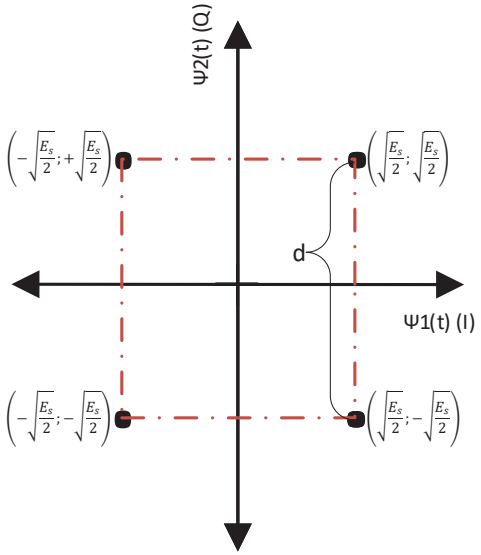

FIGURE A.36: QPSK constellation diagram (image adapted from [255]).

Similar to QPSK, M-QAM also adopts the transmission of parallel and independent symbols in both In-phase and Quadrature-phase components [231]. Therefore, M different waveforms can be represented as the transmission two orthogonal $\sqrt{M}$-PAM sequences. As a QPSK signal, M-QAM can also be visualised in a constellation diagram, where each of those M symbols are characterised by real and imaginary positions, as depicted in Fig. A.37. Additionally, according to [139], the most relevant amplitude-based digital amplitude modulation schemes are: 4-QAM, 16-QAM, and 64-QAM, where k varies from 2, 4, and 6 bits per symbol, respectively.

Mathematically, based on [14], QAM transmitted waveforms can be expressed as:

$$s_i(t) = A_I(t).\cos(2\pi f_c t) - A_Q(t).\sin(2\pi f_c t) = V_m(t)\cos(2\pi f_c t + \theta_m)$$
$$m = 1, 2, ..., M \; for \; 0 \leq t \leq T_s, \quad \text{(A.82)}$$

Where $A_I(t)$ and $A_Q(t)$ are the I/Q $\sqrt{M}$-PAM pulse waveforms, respectively, and $V_m = \sqrt{A_I^2 + A_Q^2}$ denote the transmitted signal amplitude, and $\theta_m = \tan^{-1}\frac{A_I}{A_Q}$ represents the phase, at each T_s interval.

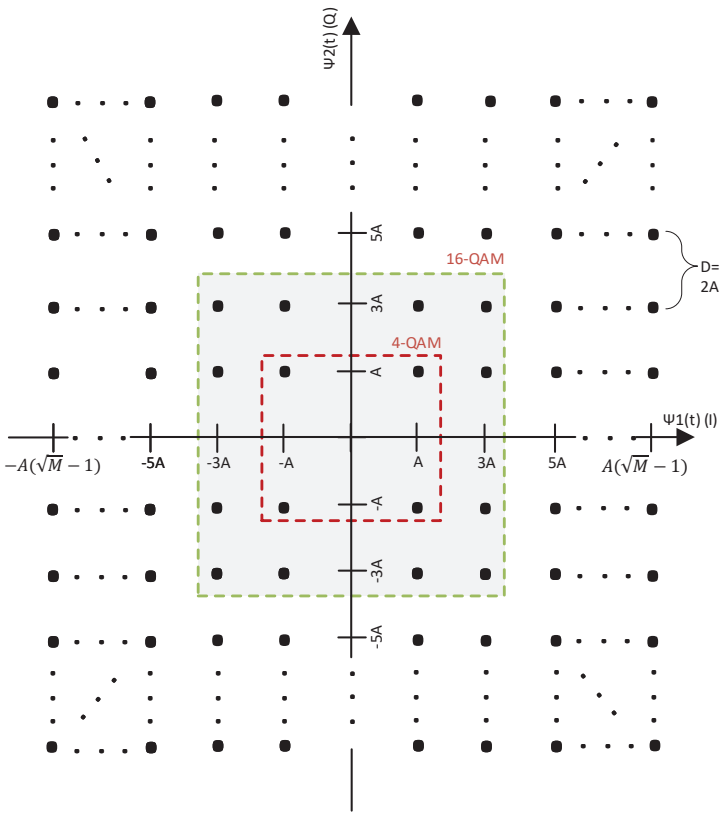

FIGURE A.37: Square M-QAM constellation signal diagram (image adapted from [233]).

The typical M-QAM receiver structure is depicted in Fig. A.38, where an analogue I/ Q demodulator converts the RF signal into two I/ Q baseband signals. Subsequently, each received symbol is compared with a threshold level to determine the estimated $k/2$ bit sequence [255] (which can be easily implemented in a DSP platform). Although such *hard bit decision* is similar to QPSK, when M is higher than 4, it is not enough to evaluate whether both I/ Q signal components are either greater or lower than zero to estimate the original bit sequence. As example, it is illustrated in Fig. A.39 a 16-QAM constellation with *Gray* mapping, where it is clearly seen that to decode a "0011" bit word, both real and imaginary received signal components should be higher than $2A$. Such threshold is calculated as the expected symbol amplitude ($3A$) minus half the distance between adjacent symbols, which is equal to A. However, when either noise or fading is presented in the transmission channel, received symbol samples might arrive with significant amplitude distortion. In other words, if the absolute value of either real or imaginary noisy component is greater than $\frac{d}{2}$ between adjacent constellation points, the original transmitted symbol will be erroneously decoded into any neighbour point, as it is also in Fig. A.39. The received symbol folds into the decision region of the word "0011" (nearest constellation point within the complex half *Euclidean* distance) instead of the "0001". Therefore, not always the nearest constellation point to the received I/ Q symbol corresponds to the original binary word.

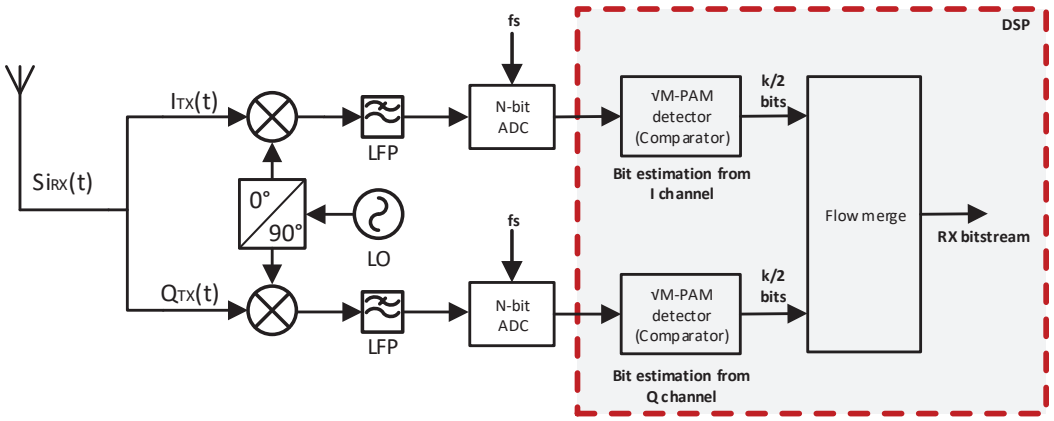

FIGURE A.38: Typical M-QAM receiver structure (image adapted from [233, 255])

Furthermore, expressions for both M-QAM average symbol and bit energy, are obtained replacing M by $\sqrt{M}$ in (A.72) and (A.73), respectively, resulting in the following equations [233]:

$$\overline{E}_s = A^2 T_s \frac{M-1}{3} \tag{A.83}$$

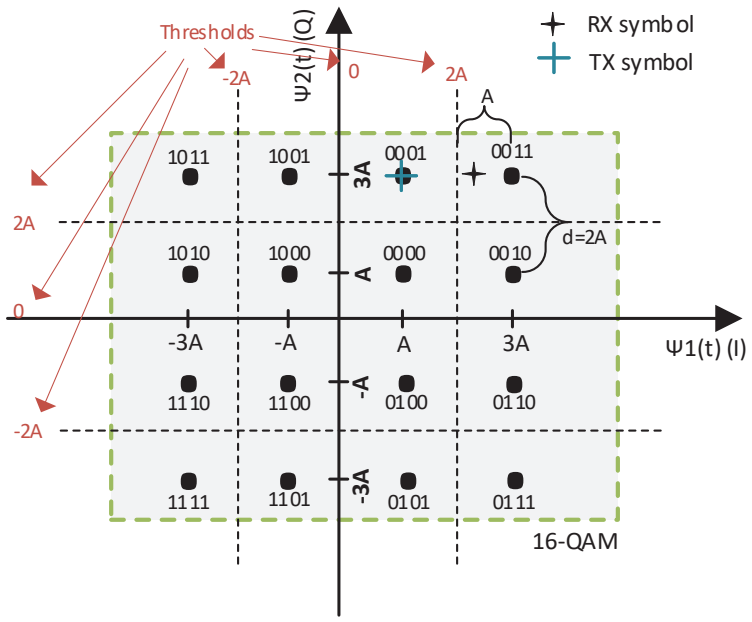

FIGURE A.39: Illustration of 16-QAM hard decision demodulation (image adapted from [255])

$$\overline{E}_b = A^2 T_s \frac{2^k - 1}{3k} \tag{A.84}$$

Despite a higher-order M-QAM constellation might be considered to achieve higher spectral efficiency, its output signal is characterised by higher PAPR values [231]. For example, the maximum symbol power for 4-, 16-, 64-, 256, 1024-QAM is $2A^2$, $18A^2$, $98A^2$, $450A^2$, $1922A^2$ [W], respectively. Consequently, average symbol power for the same QAM constellations becomes A^2, $5A^2$, $21A^2$, $85A^2$, $341A^2$ [W], respectively. This leads to the PAPR values, for each modulation, of (A.85).

$$\begin{cases} PAPR_{4-QAM} = 2 \\ PAPR_{16-QAM} = 3.6 \\ PAPR_{64-QAM} = 4.66 \\ PAPR_{256-QAM} = 5.3 \\ PAPR_{1024-QAM} = 5.6 \end{cases}, \tag{A.85}$$

From (A.85), it is clearly demonstrated that higher-order modulations have inherent higher PAPR. Therefore, in order to ensure that the maximum power of a higher order QAM is at the same level of a lower order one, the power present at every symbol that compose the constellation must be normalised to its maximum power. Therefore, in

practise A value for each M-QAM constellation is given in (A.86).

$$\begin{cases} 2A^2 = 1 \Leftrightarrow A = \frac{1}{\sqrt{2}},\ for\ 4-QAM \\ 18A^2 = 1 \Leftrightarrow A = \frac{1}{\sqrt{18}},\ for\ 16-QAM \\ 98A^2 = 1 \Leftrightarrow A = \frac{1}{\sqrt{98}},\ for\ 64-QAM \\ 450A^2 = 1 \Leftrightarrow A = \frac{1}{\sqrt{450}},\ for\ 256-QAM \\ 1922A^2 = 1 \Leftrightarrow A = \frac{1}{\sqrt{1922}},\ for\ 1024-QAM \end{cases}, \tag{A.86}$$

As it is verified in (A.86), A is greatly reduced as M increases, and thus, the constellation points in a M-QAM scheme have to be placed closer to each other, as the modulation order increases [14]. This leads to significant reduction of the distance among two adjacent symbols ($2A$).

Finally, when choosing the appropriate modulation format for a particular wireless communication system, a trade-off between error margin and data transmission reliability must be taken into account. To this end, a summary of the data handling of each modulation versus their error margin is outlined in Table A.3. For example, although 256-, and 1024-QAM modulations enable a relatively high spectral efficiency, their error margins are below 0.05. Therefore, probability of decoding erroneous bits is also significantly increased [231], which will be discussed later in this section. Due to this reason, the sensitivity to noise, and both RF front-end and channel impairments is dramatically increased in 256 and 1024-QAM configurations, which explains why these modulations are traditionally not preferable in the design of mmWave systems [14].

Table A.3
Summary of the data handling of each modulation versus error margin

Modulation scheme	**Data rate [bps]**	**bits/symbol**	**Error margin***
BPSK	$1 \times f_s$	1	1
QPSK	$2 \times f_s$	2	0.71
16-QAM	$4 \times f_s$	4	0.23
64-QAM	$6 \times f_s$	6	0.1
256-QAM	$8 \times f_s$	8	0.05
1024-QAM	$10 \times f_s$	10	0.02

* Half the distance between two adjacent transmitted symbols, which is equal to A.

Bandwidth efficiency

As it as been cited in Section A.3.1, the DFT of rectangular pulse (window function) is characterised by a sinc function, where its side-lobes extend over a significant large bandwidth. This when applied to the aforementioned digital modulations, will not only lead to the decreasing of system's spectral efficiency, but also might induce adjacent channel interference. In order to prevent this issue, the frequency response of the transmitted signal must be modified to present a stronger roll-off. According to [231], the most common way to attain this, is by the multiplication of the TX baseband signal with a raised cosine window. This allows to control the amount of excess bandwidth (roll-off factor) by changing the design parameter α [231]. In this context, it is summarised in Table A.4, the relation between the spectral efficiency of several modulations with and without the consideration of a pulse shaping filter. It is verified that a raised cosine pulse with $\alpha = 0.5$, leads to significant increase in terms of bandwidth efficiency. Such will also reduce the bandwidth of the transmitted signal, which is calculated by (A.87) [256].

$$BW = f_s.(1 + \alpha) \tag{A.87}$$

Table A.4
Spectral efficiency versus modulation scheme [231].

Modulation scheme	**Spectral efficiency for 90 % of total energy [bit/s/Hz]***	**Spectral efficiency for 90 % of total energy [bit/s/Hz]†**
BPSK	0.59	1.02
QPSK/ 4-QAM	1.18	2.04
16-QAM	2.36	4.08
64-QAM	3.54	6.12
256-QAM	4.72	8.16
1024-QAM	5.9	10.2

* Without considering a pulse shaping filter;
† Considering a pulse shaping filter with $\alpha = 0.5$;

A.4.3 Performance metrics for wireless communication systems

It is well known that joint distortion effects of coexisting of noise, multipath fading channel, and RF impairments, lead to the performance degradation of a mmWave radio

transceiver [J4]. This is explained by the fact that, under such impairments, received symbols can be shifted out from the correct binary region, which induces significantly losses on the demodulation process. In order to minimise this, *Gray* QAM constellation mapping is often considered, leading to reduction of the overall system's bit error probability [14]. For each point of a M constellation, adjacent (neighbours) symbols differ by only one bit. This is clearly seen in Fig. A.39, for 16-QAM.

In order to evaluate the QoS of a digital wireless communication system, three main performance metrics are considered, namely: SNR, EVM, and BER [257]. While SNR, at receiver, is a straightforward measure of the relative power of signal level to the noise floor of the RF front-end, EVM is a measure of how close received symbols are relative to expected (ideal) one [256]. On the other hand, BER is a one-to-one binary decision which assesses if a demodulated bit is erroneous or not. For example, the relationship among these performance indicators is of extremely importance in adaptive modulation systems, where a algorithm has to receive feedback from the receiver, and assess if it is necessary or not to change the MCS [257]. Mathematical formulation for these metrics is formulated below.

SNR

Assuming an AWGN channel in an I/ Q transmission, average SNR can be measured from the received symbols as [257]:

$$\overline{SNR} = \left[\frac{\frac{1}{T}\sum_{t=1}^{T}[(I_t)^2 + (Q_t)^2]}{\frac{1}{T}\sum_{t=1}^{T}(n_{I,t})^2 + (n_{Q,t})^2]} \right], \tag{A.88}$$

where both I_t, Q_t, $n_{I,t}$, and $n_{Q,t}$ are the I/Q signal components of the $M-ary$ QAM constellation, and of the complex noise, respectively. Finally, T represents the time window symbols are being acquired.

EVM

As it was cited above, EVM measures the quality of the demodulation process by comparing the received signal to a reference. The difference between these two signals denotes the demodulation error, which can be characterised by either an error vector, or by both magnitude and phase errors [256], as it is illustrated in Fig. A.40. This means that EVM is a performance metric obtained before symbols are converted into bits.

In general, and as it was discussed in Section 2.3, the frame structure, of any particular wireless system, usually carry information with more than one modulation scheme. For example, WiGig's training sequences, see Fig. 2.8b, is modulated by BPSK, while the payload is modulated by either QPSK or 16-QAM. To avoid the

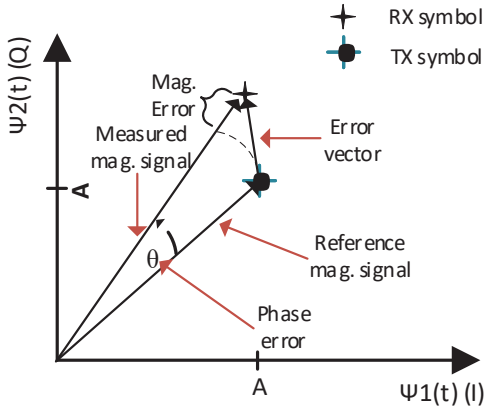

FIGURE A.40: Illustration of error vector measurement. (image adapted from [256])

need of computing EVM for each different modulation scheme, authors' in [257] have derived a closed-form EVM expression, given in (A.89), which does not depend on the modulation's constellation.

$$EVM_{RMS} = \left[\frac{\frac{1}{T}\sum_{n=1}^{T} |I_t - I_{0,t}|^2 + |Q_t - Q_{0,t}|^2}{\frac{1}{N}\sum_{n=1}^{N} (I_{0,n})^2 + (Q_{0,n})^2} \right]^{\frac{1}{2}}, \tag{A.89}$$

where N is the number of unique constellation's points, $I_t = V_{I,t}.|B|$ and $Q_t = V_{Q,t}.|B|$, represent the normalised I/ Q voltage of the received symbols, respectively, and $I_{0,t} = V_{I_{0,t}}.|B_0|$ and $Q_t = V_{Q_{0,t}}.|B_0|$ are the normalised I/Q voltage of the ideal constellation symbols. Moreover, both $|B_0|$ and $|B|$ are calculated as follows [257]:

$$\begin{cases} |B_0| = \sqrt{\frac{N}{\sum_{n=1}^{N}[(V_{I_{0,n}})^2 + (V_{Q_{0,n}})^2]}} \\ |B| = \sqrt{\frac{T}{P_v}} = \sqrt{\frac{T}{\sum_{t=1}^{T}[(V_{I,t})^2 + (V_{Q,t})^2]}} \end{cases}, \tag{A.90}$$

where P_v is the total power of transmitted symbols over the time interval of T seconds, and V_I and V_Q are the RMS voltage levels of both received I/Q signal components, respectively.

BER

BER provides a evaluation of the performance by attributing the percentage of bit errors for a given number of transmitted bits. According to [257], BER against SNR is one of the most preferred performance metrics in recent communication systems. This is mainly due to the fact that the EVM's mathematical operations, described above, might be considered too complex to be carried out, on the fly, by a digital processor

engine [257]. However, when BER is considered, transmitted data must be known at RX, and thus for large packets such metric is typically avoided [257].

The analytical BER expressions for M-ary QAM over both AWGN and *Rayleigh* channels are given in (A.91), and in (A.92), respectively [106].

$$BER_{AWGN} = \frac{2(M-1)}{M\log_2(M)} Q\left(\sqrt{\frac{6E_b}{N_o}\frac{\log_2(M)}{M^2-1}}\right), \tag{A.91}$$

where M is the modulation order, E_b/N_o is the energy per bit to noise power spectral density ratio and $Q(.)$ is the standard Q-function. Converting to SNR to E_b/N_o is performed according to: $SNR[dB] = E_b/N_o[dB] + 10\log_{10}(k)$, where k, is the number of information bits per symbol.

$$BER_{Rayleigh} = \frac{M-1}{M\log_2(M)}\left(1 - \sqrt{\frac{3\gamma\log_2 M/(M^2-1)}{3\gamma\log_2 M/(M^2-1)+1}}\right), \tag{A.92}$$

where γ denote E_b/N_o.

Relation between EVM with BER and SNR

From (A.89), it verified that EVM is the normalised error magnitude between the measured and ideal symbols, for a particular M-ary constellation. If the channel is considered AWGN, such magnitude difference represents both I/ Q noise components [257]. In this context, (A.89) can be simplified as:

$$EVM_{RMS} = \left[\frac{\frac{1}{T}\sum_{t=1}^{T}(|n_{I,t}|^2 + |n_{I,t}|^2)}{P_{ref}}\right]^{\frac{1}{2}}, \tag{A.93}$$

where P_{ref} is the power of transmitted constellation, and $\frac{1}{T}\sum_{t=1}^{T}(|n_{I,t}|^2 + |n_{I,t}|^2)$ is the normalised noise power. To this extent, SNR and EVM metrics can be related by (A.94) [257].

$$EVM_{RMS} \approx \left[\frac{1}{SNR}\right]^{\frac{1}{2}} = \left[\frac{N_o}{E_s}\right]^{\frac{1}{2}}, if\ T \gg N$$
$$\Leftrightarrow -EVM|_{dB} \approx SNR|_{dB} \tag{A.94}$$

Finally, considering that $SNR \approx \frac{1}{EVM_{RMS}^2}$, BER expression given in (A.91) can be rewritten in function of EVM as:

$$BER_{AWGN} = \frac{2(M-1)}{M\log_2(M)} Q\left(\sqrt{\frac{6\log_2(M)}{(M^2-1)EVM_{RMS}^2.\log_2(M)}}\right) \Leftrightarrow \frac{2(M-1)}{M\log_2(M)} Q\left(\sqrt{\frac{6}{(M^2-1)EVM_{RMS}^2}}\right), \quad \text{(A.95)}$$

It is worth noting that above mathematical formulations are only valid if the channel is considered as an AWGN model, and no RF impairments are presented in the system.

A.5 Interim conclusions

This chapter introduces the theoretical background required in the development of both proposed end-to-end mmWave multi-Gigabit/s waveform simulator framework, and real-time 5G testbed, detailed in Chapters 3, and 4, respectively.

Firstly, the radio propagation phenomena and its modelling is addressed, where for example, it is verified that the channel frequency selectivity really depends on the BW of the receiver. To this extent, in order to model a wideband multipath fading channel, CIR samples must be acquired at very high sampling rates. Secondly, the most common types of RF analogue transceiver architectures are introduced and compared in terms of complexity, IC integration, power consumption and flexibility. Compared to the superheterodyne, the Zero IF architectures have the advantage of low cost and power consumption and easy IC integration, however they are characterised with severe RF impairments, from the imperfection of its analogue components, modelled by PA non-idealities, PN, DC offset, CFO, and IQ imbalances. Digital IF seems to be the most promising solution for 5G transceivers since it is immuned to both DC offset and IQ issues, and it is even simpler than Zero IF. Nevertheless, the effect that these impairments induce in an I/ Q demodulator's accuracy has been formulated and illustrated by the means of a *Cartesian* plot.

Furthermore, the most relevant digital modulations for mmWave communications have been introduced, where it is demonstrated by the *Shannon* theorem that the dominant effect on the performance, in terms of data rate, of any particular system is the SNR, and not the signal bandwidth. Also, it is concluded that both BPSK and QPSK are widely adopted in communication standards, since they are quite simple and robust against noise, and other impairments (error margins are significantly large in comparison with M-ary QAM modulations). Finally, the most important performance

assessment metrics for wireless communications systems are described, and the relation between EVM, BER and SNR is addressed.

This page is intentionally left blank.

APPENDIX B

Detailed functional block diagrams of the FMC230

In this appendix, both original and modified block diagrams of the FMC230 FPGA interface firmware, are presented. Firstly, Fig. B.1 shows a high-level block diagram of the data interface inside the FMC board, while also detailing its sample rate clock tree. Secondly, Fig. B.2 highlights the FPGA data interface design required to exchange real-time data with the DAC core. Finally, in Fig. B.3, it is illustrated where the custom SysGen IP was connected, considering the original DAC 4DSP firmware.

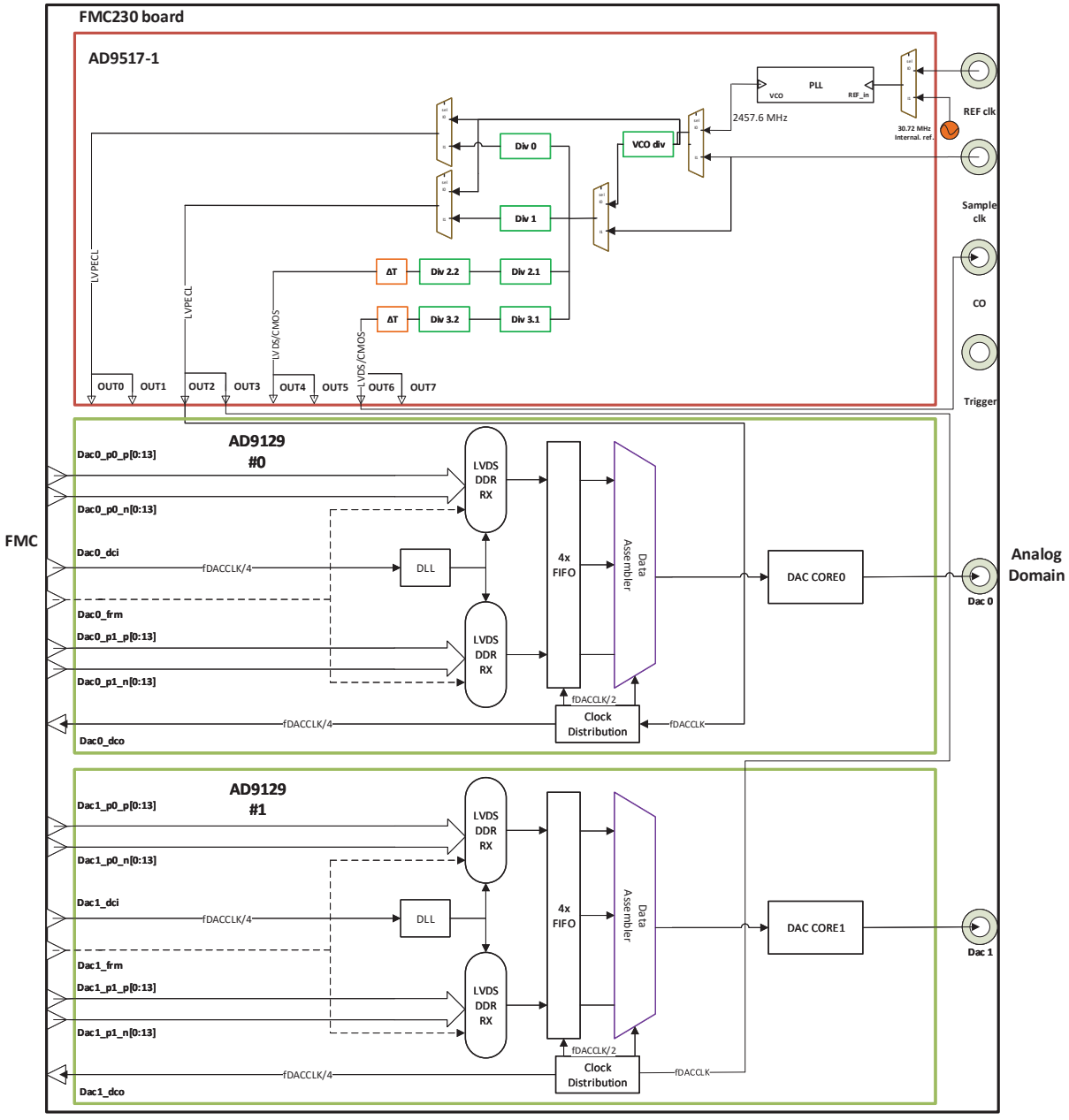

FIGURE B.1: Detailed FMC230 functional block diagram.

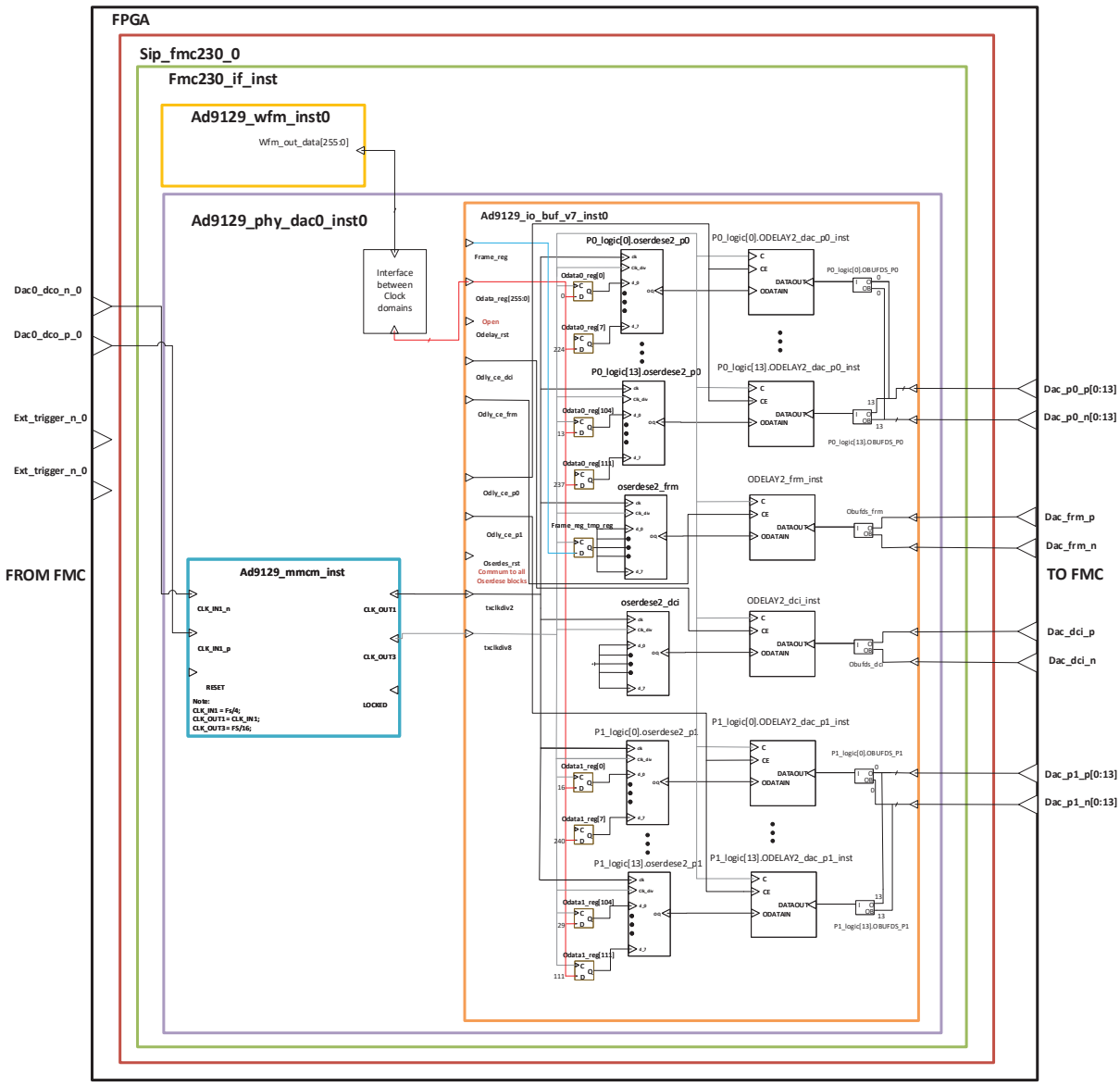

FIGURE B.2: Block diagram of the data interface between the FPGA and FMC230 for the DAC0.

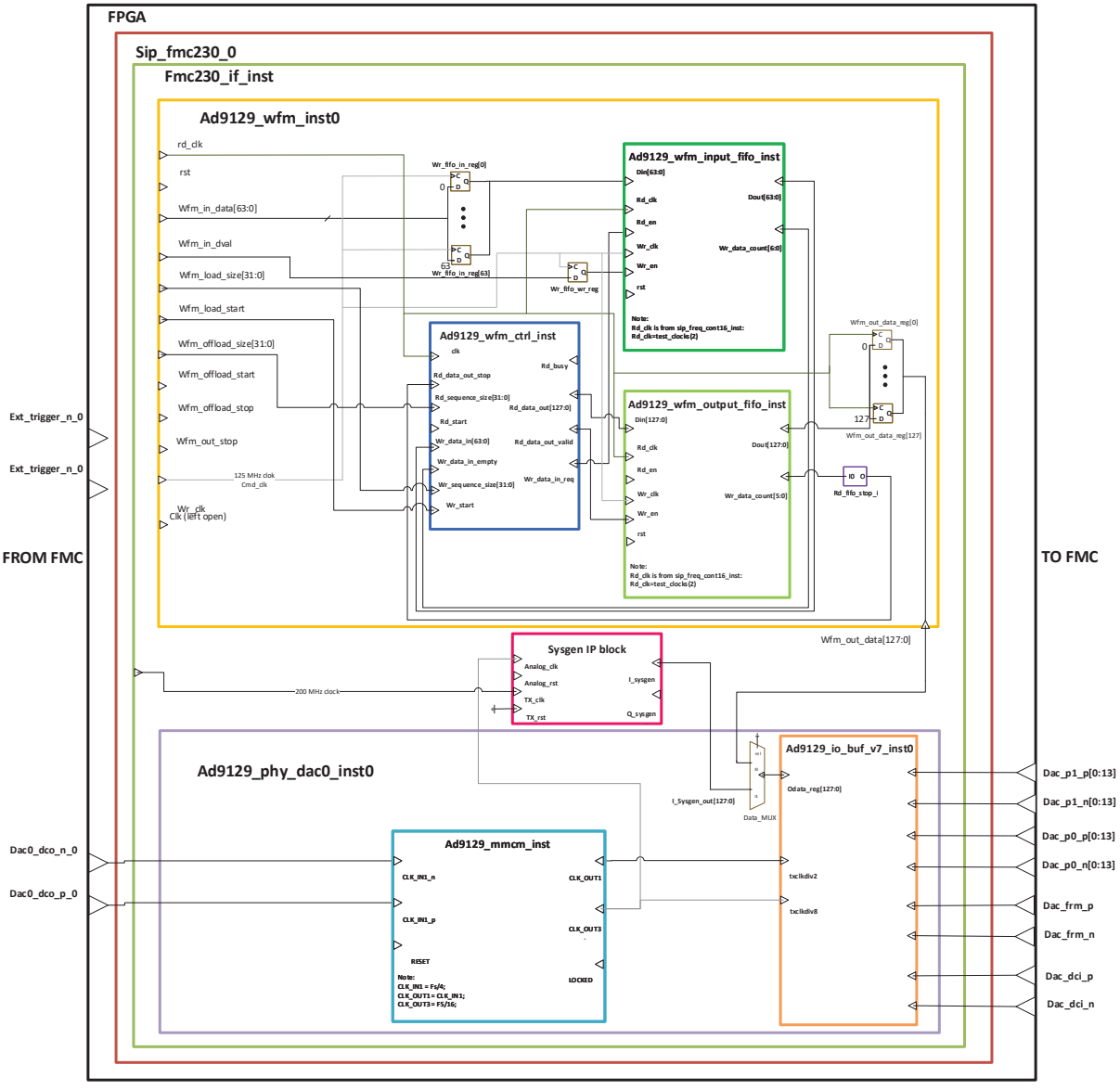

FIGURE B.3: Block diagram of the integration of the TX custom IP with the FMC230 firmware.

APPENDIX C

SysGen implemented models

This appendix presents some snapshots of the designed SysGen TRX IF architecture. In particular, both Figs. C.1 and C.2 show the design of the distributed filters employed at TX, and RX, respectively. Subsequently, Figs. C.3 and C.4 show the design of the distributed CORDICs considered at TX, and RX, respectively. Finally, Fig. C.5 shows how the OFDM real-time engine was connected to both distributed interpolation filter and CORDIC, at the TX side.

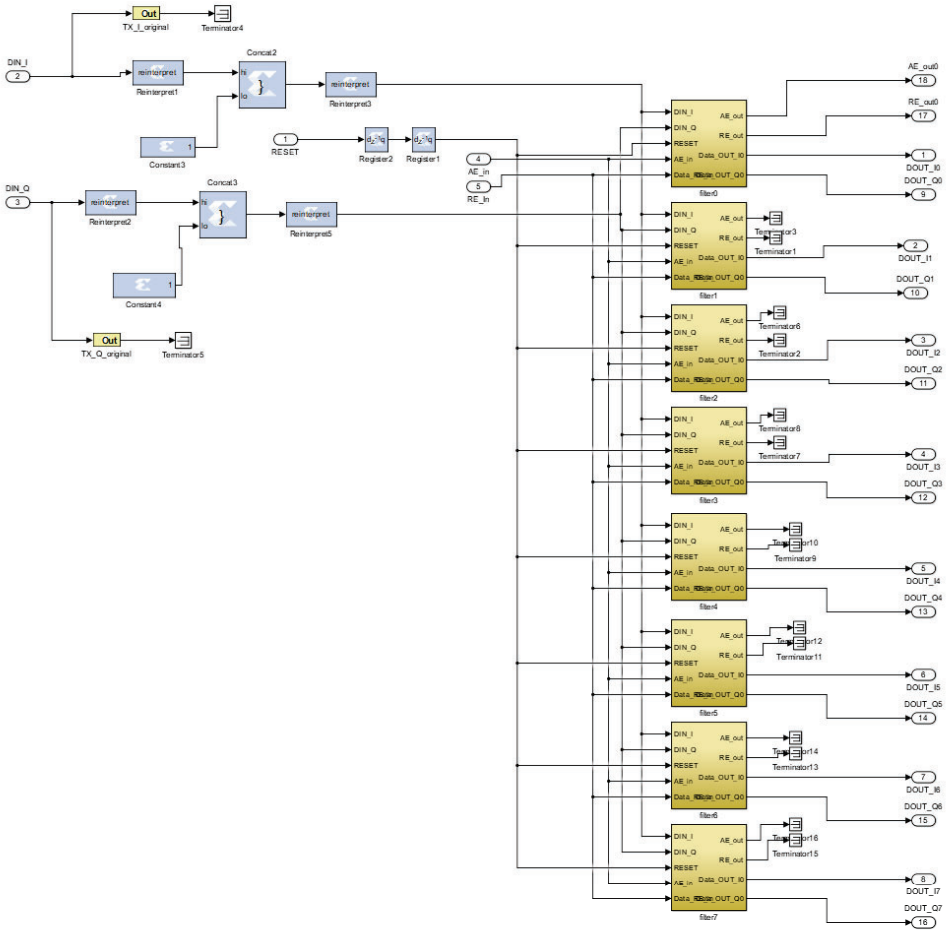

FIGURE C.1: SysGen design of the distributed filters, at TX.

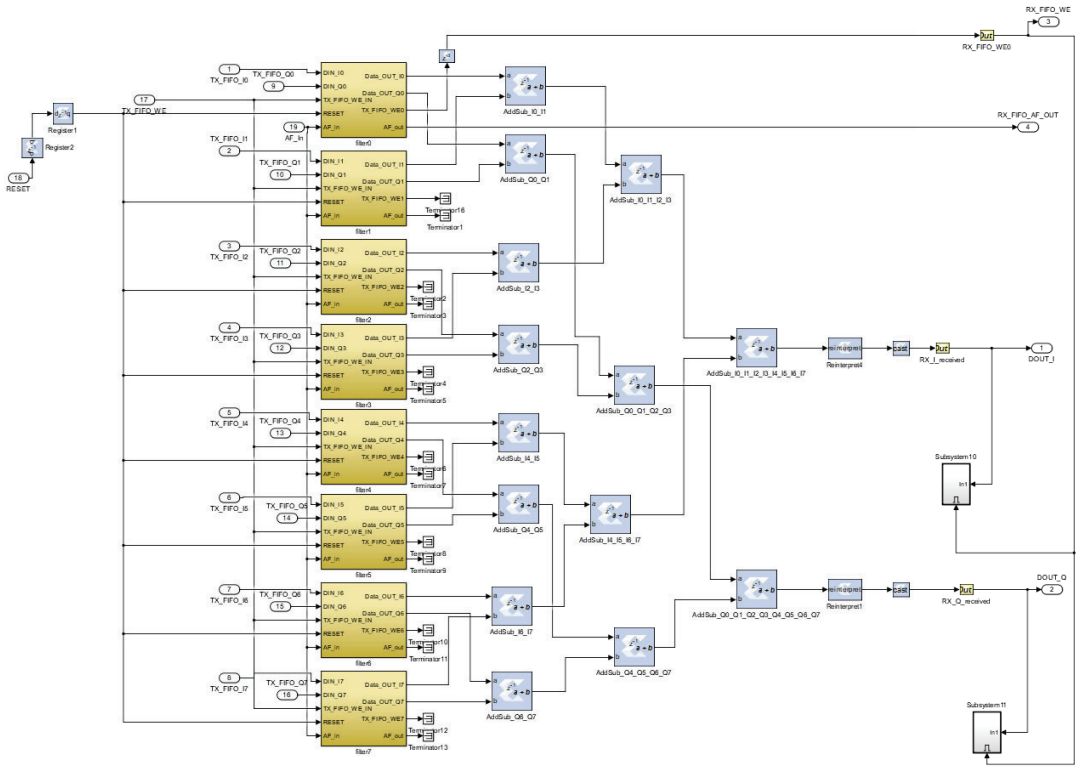

FIGURE C.2: SysGen design of the distributed filters, at RX.

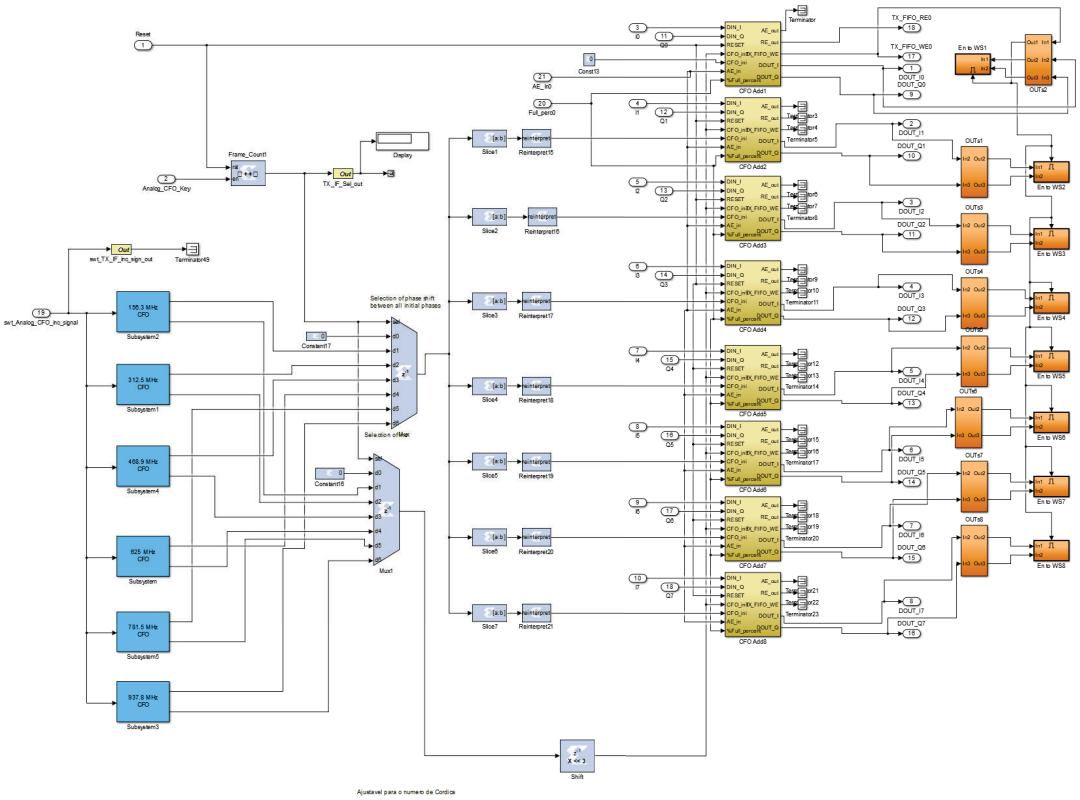

FIGURE C.3: SysGen design of the distributed CORDICs, at TX.

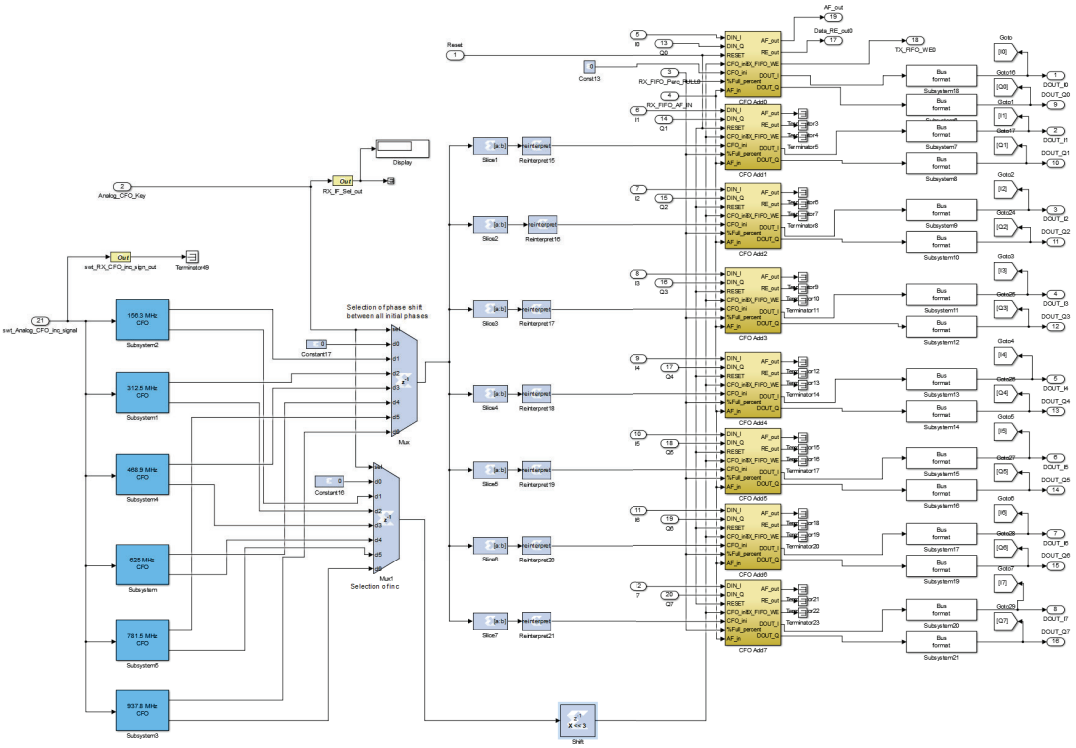

FIGURE C.4: SysGen design of the distributed CORDICs, at RX.

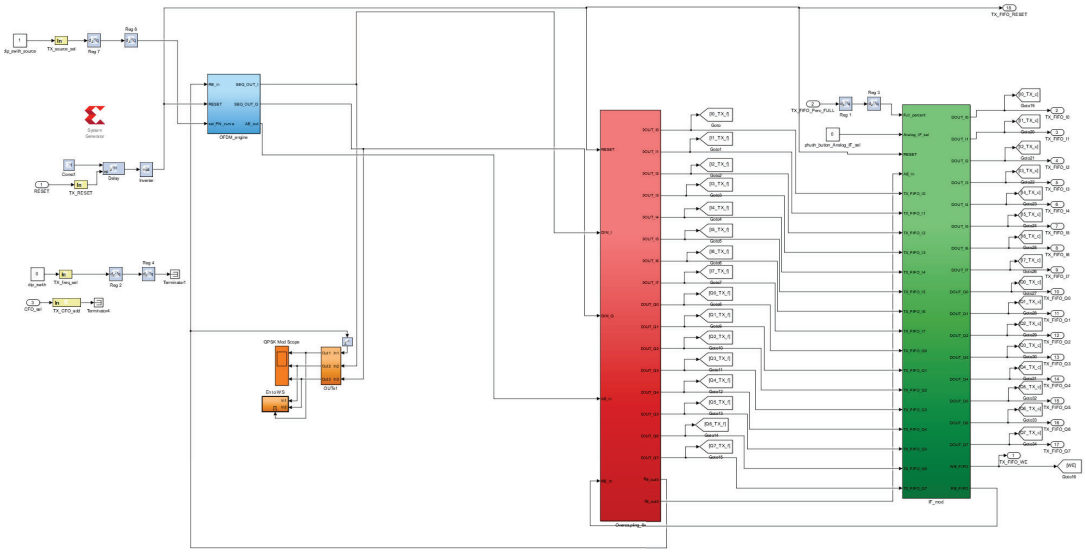

FIGURE C.5: SysGen OFDM integration, at TX.

APPENDIX D

Bandwidth of the considered omnidirectional antenna

This appendix presents the measurement of the S11 parameter of the antenna considered in the performance assessment of the proposed low-IF OFDM testbed OTA.

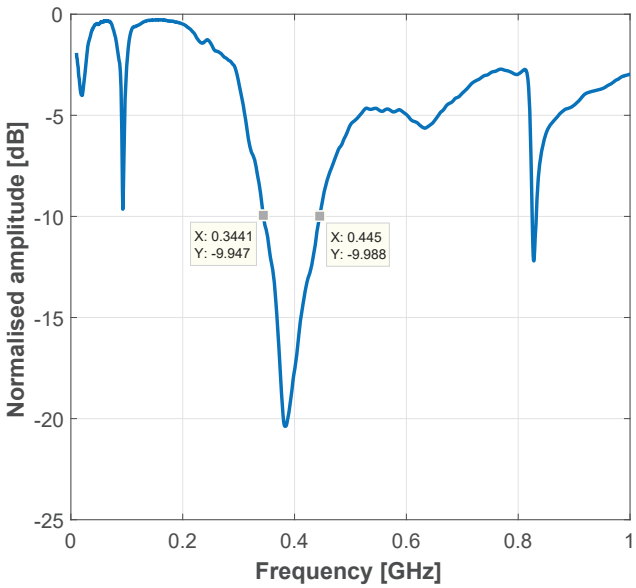

FIGURE D.1: Measured S11 parameter of the considered omnidirectional antenna.

This page is intentionally left blank.

APPENDIX E

Real-time KPI monitoring tool

This appendix introduces the real-time monitoring tool used in showcases, so the performance of the mmWave OFDM testbed could be assessed on the fly.

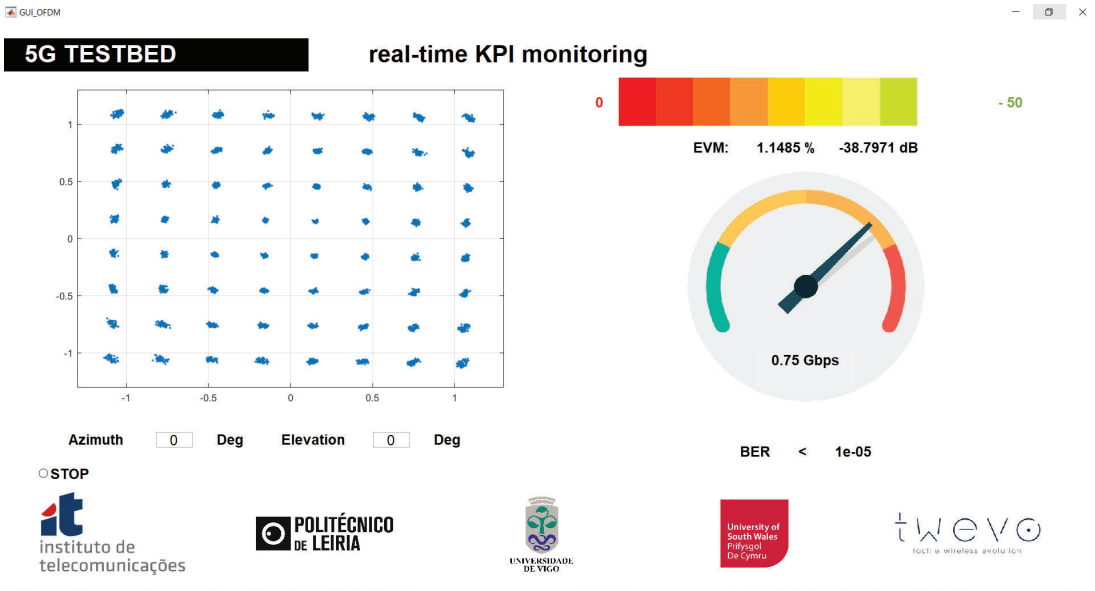

FIGURE E.1: Real-time monitoring tool used in showcases.

This page is intentionally left blank.